Epidemics on Networks

Analysis, Network Reconstruction and Prediction

Prasse, B.

DOI
10.4233/uuid:d8bdaccc-e926-4a98-ad05-eea449a915aa

Publication date
2021

Document Version
Final published version

Citation (APA)
Prasse, B. (2021). *Epidemics on Networks: Analysis, Network Reconstruction and Prediction*. [Dissertation (TU Delft), Delft University of Technology]. https://doi.org/10.4233/uuid:d8bdaccc-e926-4a98-ad05-eea449a915aa

EPIDEMICS ON NETWORKS

ANALYSIS, NETWORK RECONSTRUCTION AND PREDICTION

EPIDEMICS ON NETWORKS

ANALYSIS, NETWORK RECONSTRUCTION AND PREDICTION

Dissertation

for the purpose of obtaining the degree of doctor
at Delft University of Technology
by the authority of Rector Magnificus Prof.dr.ir. T.H.J.J. van der Hagen,
chair of the Board for Doctorates,
to be defended publicly on
Monday 17 May 2021 at 12:30 o'clock

by

Bastian PRASSE

Master of Science in Engineering
and Master of Science RWTH Aachen University
(T.I.M.E. double degree programme),
KTH Royal Institute of Technology, Sweden,
and RWTH Aachen University, Germany,
born in Troisdorf, Germany.

This dissertation has been approved by the promotors.

Composition of the doctoral committee:

Rector Magnificus	chairperson
Prof.dr.ir. P.F.A. Van Mieghem	Delft University of Technology, promotor
Dr.ir. E. Smeitink	Delft University of Technology, KPN, copromotor
Independent members:	
Prof.dr.ir. R.E. Kooij	Delft University of Technology
Prof.dr. C.M. Scoglio	Kansas State University, USA
Prof.dr. E. Cator	Radboud University
Dr. J.L.A. Dubbeldam	Delft University of Technology
Prof.dr. T. Britton	Stockholm University, Sweden
Prof.dr.ir. G.J.T. Leus	Delft University of Technology, reserve member

Keywords: Complex Networks, Epidemics on Networks, Network Reconstruction, Prediction of Epidemics, Structural and Functional Brain Networks

Printed by: Ipskamp Printing, Enschede

Front & Back: Designed by Verena Hild, based on a template from https://www.canva.com/.

ISBN 978-94-6421-330-0

An electronic version of this dissertation is available at
http://repository.tudelft.nl/.

CONTENTS

SUMMARY

The field of epidemiology encompasses a broad class of spreading phenomena, ranging from the seasonal influenza and the dissemination of fake news on online social media to the spread of neural activity over a synaptic network. The propagation of viruses, fake news and neural activity relies on the contact between individuals, social media accounts and brain regions, respectively. The contact patterns of the whole population result in a network. Due to the complexity of such contact networks, the understanding of epidemics is still unsatisfactory. In this dissertation, we advance the theory of epidemics and its applications, with a particular emphasis on the impact of the contact network.

Our first contribution focusses on the analysis of the N-Intertwined Mean-Field Approximation (NIMFA) of the Susceptible-Infected-Susceptible (SIS) epidemic process on networks. We propose a geometric approach to clustering for epidemics on networks, which reduces the number of NIMFA differential equations from the network size N to the number $m < N$ of clusters (Chapter 2). Specifically, we show that exact clustering is possible if and only if the contact network has an equitable partition, and we propose an approximate clustering method for arbitrary networks. Furthermore, for arbitrary contact networks, we derive the closed-form solution of the nonlinear NIMFA differential equations around the epidemic threshold (Chapter 3). Our solution reveals that the topology of the contact network is practically irrelevant for the epidemic outbreak around the epidemic threshold. Lastly, we study a discrete-time version of the NIMFA epidemic model (Chapter 4). We derive that the viral state is (almost always) monotonically increasing, the steady state is exponentially stable, and the viral dynamics is bounded by linear time-invariant systems.

In the second part, we consider the reconstruction of the contact network and the prediction of epidemic outbreaks. We show that, for the stochastic SIS epidemic process on an individual level, the exact reconstruction of the contact network is impractical. Specifically, the maximum-likelihood SIS network reconstruction is NP-hard, and an accurate reconstruction requires a tremendous number of observations of the epidemic outbreak (Chapter 5). For epidemic models between groups of individuals, we argue that, in the presence of model errors, accurate long-term predictions of epidemic outbreaks are not possible, due to a severely ill-conditioned problem (Chapter 6). Nonetheless, short-term forecasts of epidemics are valuable, and we propose a prediction method which is applicable to a plethora of epidemic models on networks (Chapter 7). As an intermediate step, our prediction method infers the contact network from observations of the epidemic outbreak. Our key result is paradoxical: even though an accurate network reconstruction is impossible, the epidemic outbreak can be predicted accurately. Lastly, we apply our network-inference-based prediction method to the outbreak of COVID-19 (Chapter 8).

The third part focusses on spreading phenomena in the human brain. We study the relation between two prominent methods for relating structure and function in the

brain: the eigenmode approach and the series expansion approach (Chapter 9). More specifically, we derive closed-form expressions for the optimal coefficients of both approaches, and we demonstrate that the eigenmode approach is preferable to the series expansion approach. Furthermore, we study cross-frequency coupling in magnetoencephalography (MEG) brain networks (Chapter 10). By employing a multilayer network reconstruction method, we show that there are strong one-to-one interactions between the alpha and beta band, and the theta and gamma band. Furthermore, our results show that there are many cross-frequency connections between distant brain regions for theta-gamma coupling.

SAMENVATTING

Het vakgebied van epidemiologie omvat een brede klasse van verspreidingsverschijnselen, variërend van de seizoensgriep en de verspreiding van nepnieuws op sociale media tot de verspreiding van neurale activiteit via een synaptisch netwerk. De verspreiding van virussen, nepnieuws en neurale activiteit is afhankelijk van het contact tussen individuen, sociale-media-accounts en hersengebieden. De contacten van alle individuen samen vormen een netwerk. Vanwege de complexiteit van dergelijke contactnetwerken is het gedrag van epidemische processen nog steeds niet geheel doorgrond. In dit proefschrift dragen wij bij aan de ontwikkeling van de theorie en toepassing van epidemische processen, waarbij we ons concentreren op het onderliggende contactnetwerk.

Onze eerste bijdrage is gerelateerd aan de *N-Intertwined Mean-Field Approximation* (NIMFA) van het *Susceptible-Infected-Susceptible* (SIS) virusverspreidingsmodel op netwerken. We stellen een geometrische benadering voor voor het clusteren van individuen in het contactnetwerk, die het aantal NIMFA-differentiaalvergelijkingen reduceert van de netwerkgrootte N tot het aantal $m < N$ clusters (Hoofdstuk 2). In het bijzonder laten we zien dat een exacte clustering mogelijk is dan en slechts dan het contactnetwerk een *gelijkwaardige partitie* heeft, en we stellen een benaderende clustermethode voor voor algemene netwerken. Verder leiden we voor algemene contactnetwerken de gesloten oplossing af van de niet-lineaire NIMFA-differentiaalvergelijkingen rond de epidemische drempelwaarde (Hoofdstuk 3). Onze oplossing laat zien dat de topologie van het contactnetwerk praktisch irrelevant is voor een virusuitbraak rond de epidemische drempelwaarde. Ten slotte bestuderen we een discrete-tijdversie van het NIMFA-epidemisch model (Hoofdstuk 4). In het bijzonder laten we zien dat de virale toestand (bijna altijd) monotoon toeneemt, de stabiele toestand exponentieel stabiel is en de het tijdsafhankelijke proces wordt begrensd door lineaire tijdinvariante systemen.

In het tweede deel gaan we in op de reconstructie van het contactnetwerk en de voorspelling van virusuitbraken. We tonen aan dat de reconstructie van het contactnetwerk voor het SIS process op individueel niveau praktisch onmogelijk is. In het bijzonder is de meest aannemelijke schatter van de SIS-netwerkreconstructie NP-moeilijk, en een nauwkeurige reconstructie vereist een enorm aantal observaties van de virusuitbraak (Hoofdstuk 5). Voor epidemische metapopulatiemodellen stellen we dat, in de aanwezigheid van modelfouten, nauwkeurige langetermijnvoorspellingen van epidemische uitbraken niet mogelijk zijn omdat het probleem slecht geconditioneerd is (Hoofdstuk 6). Desalniettemin zijn kortetermijnvoorspellingen van epidemische processen waardevol, en we stellen een voorspellingsmethode voor die toepasbaar is op een breed scala aan epidemische modellen op netwerken (Hoofdstuk 7). Als tussenstap leidt onze voorspellingsmethode het contactnetwerk af op basis van het aantal geobserveerde zieke personen tijdens de epidemie. Ons belangrijkste resultaat is paradoxaal: hoewel een nauwkeurige netwerkreconstructie onmogelijk is, kan de virusuitbraak nauwkeurig worden voorspeld. Ten slotte passen we onze voorspellingsmethode toe op het uitbre-

ken van COVID-19 (Hoofdstuk 8).

Het derde deel richt zich op het bestuderen van verspreidingsverschijnselen in het menselijk brein. We bestuderen twee prominente benaderingsmethoden om de structuur en functie in de hersenen aan elkaar te relateren: de eigenmode-benadering en de reeksontwikkelingsbenadering (Hoofdstuk 9). We leiden gesloten uitdrukkingen af voor de optimale coëfficiënten van beide benaderingen, en we tonen aan dat de eigenmode-benadering de voorkeur geniet boven de reeksontwikkelingsbenadering. Verder bestuderen we kruisfrequentieverbindingen in magnetoencephalography (MEG) hersennetwerken (Hoofdstuk 10). Door een meerlaagse netwerkreconstructiemethode toe te passen, laten we zien dat er sterke een-op-een interacties zijn tussen de alfa- en bètaband en de thèta- en gammaband. Bovendien laten onze resultaten zien dat er veel kruisfrequentieverbindingen zijn tussen verre hersengebieden voor thèta-gammakoppeling.

1

INTRODUCTION

EPIDEMIOLOGY originates from the study of infectious diseases such as gonorrhoea, cholera and the flu [1, 2], with seminal works by Bernoulli [3] and Snow [4]. Human beings do not only transmit infectious diseases from one individual to another, but also opinions, online social media content and innovations. Furthermore, man-made structures exhibit epidemic phenomena, such as the propagation of failures in power networks or the spread of a malicious computer virus via the internet. Modern epidemiology has evolved into the study of general spreading processes [5–7]. The mutual characteristic of spreading processes is that they can be modelled by a viral infection: every individual is either healthy, or infected with the virus, opinion, social media content; and the virus spreads from one individual to another, provided that the individuals are "in contact", for instance by physical proximity (e.g., closer than 1.5 meters), a friendship or a connection on an online social media platform.

The spread of a virus is governed by the interplay of two interdependent parts: the *viral dynamics*, which characterises the transmission of the virus, given by the infectiousness, the incubation time, and the time to recover from an infection; and the *contact network*, which specifies the individuals that are in contact. The essential interplay of function and structure is explicitly taken into account in modern, sophisticated epidemic models [5, 6]. In theory, if the contact network and the viral dynamics were accurately known, epidemic models would be capable of providing accurate descriptions of the evolution of an epidemic. However, the staggering complexity of contact networks poses a major challenge to the analysis, prediction and control of real-world epidemics: First, the modern world is densely connected – both digitally and physically, via the internet and an unprecedented mobility of individuals. Thus, most epidemics spread among large populations, with a corresponding contact network of tremendous size. Second, the contact patterns between individuals are very diverse, ranging from isolated individuals, with barely any regular social contacts, to "superspreaders" [8–11]. Hence, the majority of contact networks are highly heterogeneous. Third, the contact network may change over time [12–15]. For instance, during the COVID-19 pandemic, the very aim of lockdown policies is the explicit, time-varying control of contacts among the popula-

tion [16, 17]. In summary, obtaining an accurate description of the contact network is a tremendous, and perhaps impossible, challenge. The analysis and prediction of spreading processes, despite the unavailability of the network, lie at the heart of this thesis.

1.1. MODELLING EPIDEMICS ON NETWORKS

In this section, we introduce two epidemic models which are central to this thesis. We consider a contact network of N nodes, where every node $i = 1, ..., N$ corresponds to an individual or a group of similar individuals. If the nodes i, j are in contact, then node i and node j can infect one another with the virus. We denote the $N \times N$ adjacency matrix by A and its elements by a_{ij}. If there is a link from node j to node i, then $a_{ij} = 1$, and $a_{ij} = 0$ otherwise. Hence, the virus spreads from node j to node i only if $a_{ij} = 1$.

The vast majority of epidemic models assumes that every individual is in either one compartment [1, 2, 5, 6]. Every compartment describes another stage of the disease, such as healthy, infected or deceased. The NIMFA model and the SIR model presented below are prominent instances of compartmental epidemic models.

1.1.1. THE NIMFA (SIS) EPIDEMIC MODEL

The first epidemic model that we consider has two compartments: every individual is either *susceptible* $\mathcal{S}$ (healthy) or *infectious* $\mathcal{I}$. Susceptible individuals can be infected by a contact to infectious individuals, and infected individuals can cure and become susceptible again. At any time $t \geq 0$, every node i has a *viral state* $v_i(t)$, whose evolution is governed by a set of nonlinear differential equations:

Definition 1.1 (Heterogeneous NIMFA epidemic model [18, 19])**.** For every node $i = 1, ..., N$, the viral state $v_i(t)$ evolves in continuous time $t \geq 0$ as

$$\frac{dv_i(t)}{dt} = -\delta_i v_i(t) + (1 - v_i(t)) \sum_{j=1}^{N} \tilde{\beta}_{ij} a_{ij} v_j(t), \tag{1.1}$$

where $\delta_i > 0$ is the *curing rate* of node i, and $\tilde{\beta}_{ij} > 0$ is the *infection rate* from node j to node i.

The differential equations (1.1) can be interpreted in two ways. On the one hand, if the nodes correspond to individuals, then the differential equations (1.1) follow from a mean-field approximation of the stochastic SIS process [20, 21], and the viral state $v_i(t)$ approximates the expected value $\mathrm{E}[X_i(t)]$ of the zero-one state $X_i(t)$ of the stochastic Susceptible-Infected-Susceptible (SIS) epidemic process. Thus, the viral state $v_i(t)$ approximates the probability that individual i is infected at time t. In the remainder of this thesis, we refer to (1.1) as NIMFA, which is an acronym for "N-Intertwined Mean-Field Approximation" [20, 21]. On the other hand, if the nodes correspond to groups [18, 22–25], then the viral state $v_i(t)$ can be interpreted as the fraction of infectious individuals in group i.

We denote the $N \times 1$ viral state vector by $v(t) = (v_1(t), ..., v_N(t))^T$. Lajmanovich and Yorke [18] showed that $v(0) \in [0, 1]^N$ implies that $v(t) \in [0, 1]^N$ at every time $t \geq 0$. Hence, NIMFA (1.1) is well-defined if the viral state $v_i(t)$ is interpreted as probability or fraction.

We define the $N \times N$ diagonal matrix $S = \text{diag}(\delta_1, ..., \delta_N)$ whose diagonal is given by the curing rates δ_1, ..., δ_N. Then, stacking the differential equations (1.1) yields that

$$\frac{dv(t)}{dt} = -Sv(t) + \text{diag}(u - v(t))\, Bv(t), \tag{1.2}$$

where the $N \times N$ infection rate matrix B is composed of the elements $\beta_{ij} = \tilde{\beta}_{ij} a_{ij}$, and $u = (1, ..., 1)^T$ is the $N \times 1$ all-one vector.

In its simplest form [20], NIMFA assumes the same infection rate β and curing rate δ for all nodes. More precisely, for *homogeneous NIMFA* the governing equations (1.2) reduce to

$$\frac{dv(t)}{dt} = -\delta v(t) + \beta \text{diag}(u - v(t))\, Av(t). \tag{1.3}$$

For the vast majority of epidemiological, demographical, and ecological models, the *basic reproduction number* R_0 is an essential quantity [26, 27]. The basic reproduction number R_0 is defined [28] as "The expected number of secondary cases produced, in a completely susceptible population, by a typical infective individual during its entire period of infectiousness". For NIMFA (1.1), the basic reproduction number R_0 is given by [18, 29]

$$R_0 = \rho(S^{-1}B), \tag{1.4}$$

where $\rho(M)$ denotes the spectral radius of a square matrix M. Lajmanovich and Yorke [18] showed that there is a bifurcation around the *epidemic threshold* $R_0 = 1$. If $R_0 \leq 1$, then the origin (the all-healthy state) is the only equilibrium of NIMFA (1.1), and it holds that $v(t) \to 0$ as $t \to \infty$. If $R_0 > 1$, then there is a second equilibrium, the $N \times 1$ steady-state[1] vector v_∞, with positive components, and it holds that $v(t) \to v_\infty$ as $t \to \infty$ if $v(0) \neq 0$. Thus, the steady state v_∞ corresponds to the endemic viral state. By setting (1.2) to zero, we obtain that the steady state v_∞ satisfies

$$(B - S)\, v_\infty = \text{diag}(v_\infty)\, Bv_\infty. \tag{1.5}$$

1.1.2. THE SIR EPIDEMIC MODEL

The second fundamental epidemic model is the Susceptible-Infected-Removed (SIR) model, which assumes that cured individuals are immune to the disease, which is modelled by the compartment *removed* $\mathcal{R}$. Hence, the key difference between the SIS and the SIR model is that, after curing from the disease, individuals either can be reinfected or are immune, respectively. At every time t, the 3×1 SIR viral state of node i is denoted by $v_i(t) = (\mathcal{S}_i(t), \mathcal{I}_i(t), \mathcal{R}_i(t))^T$. If nodes correspond to groups of individuals, then $\mathcal{S}_i(t)$, $\mathcal{I}_i(t)$ and $\mathcal{R}_i(t)$ describe the fraction of susceptible, infected and removed individuals in group i at time t.

[1] Strictly speaking, the origin $v(t) = 0$ is always a steady state of the NIMFA model (1.2). In this thesis, we only refer to the non-zero equilibrium v_∞ as steady state.

Definition 1.2 (Heterogeneous SIR epidemic model [30, 31])**.** For every node i, the SIR viral state $v_i(t) = (\mathcal{S}_i(t), \mathcal{I}_i(t), \mathcal{R}_i(t))^T$ evolves in continuous time t as

$$\begin{aligned} \frac{d\mathcal{I}_i(t)}{dt} &= -\delta_i \mathcal{I}_i(t) + (1 - \mathcal{I}_i(t) - \mathcal{R}_i(t)) \sum_{j=1}^{N} \beta_{ij} \mathcal{I}_j(t) \\ \frac{d\mathcal{R}_i(t)}{dt} &= \delta_i \mathcal{I}_i(t) \end{aligned} \tag{1.6}$$

and the fraction of susceptible individuals follows as $\mathcal{S}_i(t) = 1 - \mathcal{I}_i(t) - \mathcal{R}_i(t)$. Here, β_{ij} denotes the *infection rate* from node j to node i, and δ_i is the *curing rate* of node i.

Similarly to NIMFA (1.1), if nodes i correspond to individuals, Youssef and Scoglio [31] derived the differential equations (1.6) as a first-order mean field approximation of the stochastic SIR epidemic process, where the components of the viral state $v_i(t)$ approximate the probability that individual i is in the respective compartment $\mathcal{S}$, $\mathcal{I}$ or $\mathcal{R}$.

1.2. NOTATION

The following notation is used throughout this thesis. The number of nodes in the contact network is denoted by N. The $N \times N$ diagonal matrix with a vector $x \in \mathbb{R}^N$ on its diagonal is denoted by $\operatorname{diag}(x)$. The Frobenius norm of a matrix M is denoted by $\|M\|_F$. For a square matrix M, we denote the spectral radius by $\rho(M)$. If the matrix M is symmetric, then M can be diagonalised as [32]

$$M = X \operatorname{diag}(\lambda_1, ..., \lambda_N) X^T$$

with the $N \times N$ matrix $X = (x_1, ..., x_N)$, where λ_i denotes the eigenvalue to the $N \times 1$ eigenvector x_i of the matrix M. For two $N \times 1$ vectors y, z, the inequalities $y > z$ and $y \geq z$ denote that $y_i > z_i$ or $y_i \geq z_i$, respectively, for every element $i = 1, ..., N$. The $N \times N$ identity matrix is denoted by I, and, for an arbitrary integer m, I_m denotes the $m \times m$ identity matrix. Similarly, the $N \times 1$ all-one vector is denoted by u, and u_m denotes the $m \times 1$ all-one vector. The $N \times 1$ basic vector is denoted by e_i, whose entries are given by $(e_i)_i = 1$ and $(e_i)_j = 0$ if $j \neq i$.

1.3. DOCUMENT STRUCTURE

This thesis consists of three parts, which are divided into several chapters.

I. Analysis of Epidemics on Networks The first part consists of three chapters and focusses on the mathematical analysis of the NIMFA epidemic model (1.1). In Chapter 2, we consider the grouping of nodes to obtain a low-complexity description of the viral state dynamics. More precisely, we study structural conditions on the contact network which allow for an exact or approximate description of the viral dynamics by less than N differential equations. In Chapter 3, we derive the closed-form solution of the nonlinear NIMFA differential equations (1.1) around the epidemic threshold $R_0 = 1$. In Chapter 4, we study the viral dynamics of the NIMFA epidemic model in discrete time, with a particular focus on stability and speed of convergence to the steady state.

II. Network Reconstruction and Prediction of Epidemics The second part consists of four chapters and deals with the question: *Can we predict an epidemic outbreak without knowing the contact network?* In Chapter 5, we propose a Bayesian framework for reconstructing the contact network on *individual level* from observations of the stochastic SIS epidemic process. We prove that the SIS network reconstruction problem is NP-hard. Furthermore, based on designing an accurate, polynomial-time heuristic, we show that a tremendous number of observations is required for an accurate network reconstruction, which seems infeasible in practice. Chapter 6 demonstrates that, even under idealised conditions, the accuracy of predicting epidemics is subject to fundamental limits. For a general class of epidemic models on *group level*, Chapter 7 proposes a two-stage method for predicting epidemic outbreaks. First, the contact network is (partly) reconstructed from past observations of the epidemic spread. Second, the epidemic outbreak is predicted with the partly reconstructed network. In Chapter 8, we propose and evaluate a network-inference based method for predicting the spread of COVID-19.

III. Spreading in Brain Networks: Relating Function and Structure Beyond the spread of infectious diseases, the field of epidemics on networks encompasses general spreading dynamics over networks. The third part of the thesis consists of two chapters and focusses on the relation of function and structure for spreading in the brain. In this context, "function" refers to brain activity, such as functional Magnetic Resonance Imaging (fMRI) and magnetoencephalography (MEG) data, and "structure" refers to the anatomical network between brain regions. Chapter 9 considers the relation of function and structure in the brain. In particular, we compare two prominent methods, the *eigenmode approach* and the *series expansion approach*, both analytically and empirically. In Chapter 10, we propose a inter-layer connectivity reconstruction method for multilayer brain networks. Every layer corresponds to one MEG frequency band (e.g., alpha or beta band), and an interlayer link between two nodes describes the cross-frequency coupling of the two respective brain regions.

I

Analysis of Epidemics on Networks

2

CLUSTERING FOR EPIDEMICS ON NETWORKS: A GEOMETRIC APPROACH

Infectious diseases typically spread over a contact network with millions of individuals, whose sheer size is a tremendous challenge to analysing and controlling an epidemic outbreak. For some contact networks, it is possible to group individuals into clusters. A high-level description of the epidemic between a few clusters is considerably simpler than on an individual level. However, to cluster individuals, most studies rely on equitable partitions, a rather restrictive structural property of the contact network. In this chapter, we focus on Susceptible-Infected-Susceptible (SIS) epidemics, and our contribution is threefold. First, we propose a geometric approach to specify all *networks for which an epidemic outbreak simplifies to the interaction of only a few clusters. Second, for the complete graph and any initial viral state vectors, we derive the closed-form solution of the nonlinear differential equations of the N-Intertwined Mean-Field Approximation (NIMFA) of the SIS process. Third, by relaxing the notion of equitable partitions, we derive low-complexity approximations and bounds for epidemics on* arbitrary *contact networks. Our results are an important step towards understanding and controlling epidemics on large networks.*

This chapter is based on B. Prasse, K. Devriendt, and P. Van Mieghem, *Clustering for epidemics on networks: a geometric approach*, in preparation.

2.1. INTRODUCTION

The majority of viruses spread through a population of tremendous size, which renders individual-based modelling impractical. However, most applications do not require to model an epidemic on individual level. Instead, a mesoscale description of the epidemic often is sufficient. For instance, suppose the outbreak of a virus is modelled on the level of neighbourhoods. Then, sophisticated lockdown measures can be deployed which constrain neighbourhoods differently, depending on the prevalence of the virus in the respective neighbourhood. The natural way to obtain a mesoscale description of the epidemic is *clustering* (or grouping) of individuals, for instance, by assigning individuals with similar age or location to the same cluster. Thus, all individuals in one cluster are considered indistinguishable and exchangeable. Additionally to the complexity reduction, clustering for epidemics on networks has the advantage that, on a mesoscale description, temporal fluctuations of the individual-based contact network may average out.

Many papers deal with clustering of individuals into *communities* [33–35], where individuals within the same community are densely connected, and there are only few links between individuals of different communities. Hence, communities are defined by structural properties of the contact graph. Most results are of the type: if the network has a certain mesoscale structure, then also the dynamics have some structure [36–38]. In this chapter, we approach clustering from the other direction: we presume structure *in the dynamics* and aim to find all contact networks that are compatible with the structured dynamics. The central analysis tool in our analysis is the *Proper Orthogonal Decomposition* (POD) [39–41] of the $N \times 1$ viral state vector $v(t)$, which is given by

$$v(t) = \sum_{l=1}^{m} c_l(t) y_l \tag{2.1}$$

for some $m \leq N$. Here, the $N \times 1$ *agitation mode* vectors $y_1, ..., y_m$ are orthonormal[1], and the scalar functions $c_l(t) \in \mathbb{R}$ are obtained by projecting the viral state $v(t)$ onto the vector y_l, $c_l(t) = y_l^T v(t)$. Since any $N \times 1$ vector $v(t)$ can be written as the linear combination of N orthonormal vectors, the POD (2.1) is exact for *any* network if $m = N$. However, we are particularly interested in networks, for which the number of agitation modes m is (much) smaller than the number of nodes N. If (2.1) holds true, then the viral state vector $v(t)$ is element of the m-dimensional subspace

$$\mathcal{V} = \text{span}\{y_1, ..., y_m\} \tag{2.2}$$

at any time t, where the span (the set of all linear combinations) of the vectors $y_1, ..., y_m$ is denoted by

$$\text{span}\{y_1, ..., y_m\} = \left\{ \sum_{l=1}^{m} c_l y_l \middle| c_l \in \mathbb{R} \right\}.$$

With the POD (2.1), the viral state $v(t)$ can be described with less than N differential equations: denote the right side of the NIMFA (1.2) by $f_{\text{NIMFA}}(v(t)) \in \mathbb{R}^N$. Then, NIMFA

[1] A set of vectors $y_1, ..., y_m$ is orthonormal if $y_l^T y_k = 0$ for $l \neq k$ and $y_l^T y_k = 1$ for $l = k$.

(1.2) reads more compactly

$$\frac{dv(t)}{dt} = f_{\text{NIMFA}}(v(t)). \tag{2.3}$$

With the POD (2.1), we obtain that

$$\sum_{l=1}^{m} \frac{dc_l(t)}{dt} y_l = f_{\text{NIMFA}}\left(\sum_{l=1}^{m} c_l(t) y_l\right). \tag{2.4}$$

Since the vectors $y_1, ..., y_m$ are orthonormal, we can project (2.4) onto the agitation modes y_l to obtain the differential equations

$$\frac{dc_l(t)}{dt} = y_l^T f_{\text{NIMFA}}\left(\sum_{l=1}^{m} c_l(t) y_l\right), \quad l = 1, ..., m. \tag{2.5}$$

Hence, the POD (2.1) reduces the number of differential equations from the number of nodes N to the number of agitation modes m. We emphasise that the POD (2.1) is a hybrid of linear and nonlinear analysis: The viral state $v(t)$ equals to a linear combination of the agitation modes y_l, which are weighted by possibly nonlinear functions $c_l(t)$. In this chapter, we study under which conditions the POD (2.1) is *exact* for the NIMFA epidemic model (1.2). Furthermore, in Chapter 7, we show that the POD (2.1) holds *approximately* almost always, for a diverse class of dynamics on networks.

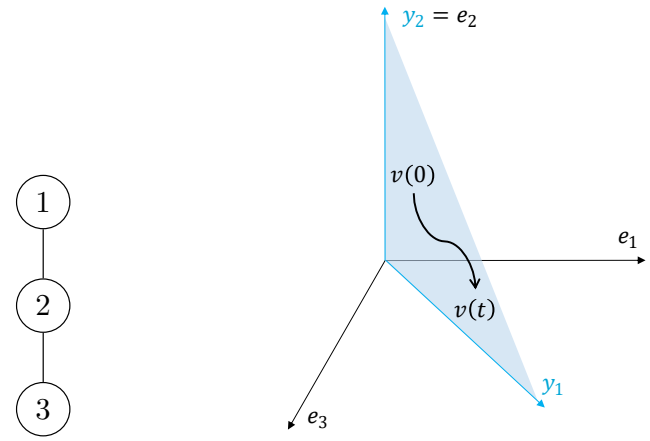

(a) Path graph. (b) Viral state space.

Figure 2.1: **Proper orthogonal decomposition for a path graph. (a)**: A path graph with $N = 3$ nodes. The top, middle and bottom nodes are labelled by 1, 2 and 3, respectively. **(b)**: The black curve depicts the trajectory of the viral state $v(t)$ in the Euclidean space $\mathbb{R}^3$. The shaded area illustrates the viral state set $\mathcal{V}$, which equals to the span of the vectors y_1, y_2, given by (2.8). Provided that $v(0) \in \mathcal{V}$, the viral state $v(t)$ remains in the subspace $\mathcal{V}$ at every time t.

Example 2.1. *Consider homogeneous NIMFA (1.3) on the path graph in Figure 2.1a, for*

which the viral state vector $v(t)$ evolves as

$$\begin{aligned}\frac{dv_1(t)}{dt} &= -\delta v_1(t) + \beta(1-v_1(t))\,v_2(t),\\ \frac{dv_2(t)}{dt} &= -\delta v_2(t) + \beta(1-v_2(t))\,(v_1(t)+v_3(t)),\\ \frac{dv_3(t)}{dt} &= -\delta v_3(t) + \beta(1-v_3(t))\,v_2(t).\end{aligned} \tag{2.6}$$

Suppose that the initial viral states of node 1 and 3 are equal, $v_1(0) = v_3(0)$. Then, it holds that $v_1(t) = v_3(t)$ at all times t due to the symmetry of the path graph. Hence, the viral state vector $v(t) = (v_1(t), v_2(t), v_3(t))^T$ satisfies

$$v(t) = c_1(t)y_1 + c_2(t)y_2, \tag{2.7}$$

where the orthonormal vectors y_1, y_2 are given by

$$y_1 = \frac{1}{\sqrt{2}}\begin{pmatrix}1\\0\\1\end{pmatrix}, \quad y_2 = \begin{pmatrix}0\\1\\0\end{pmatrix}. \tag{2.8}$$

As illustrated by Figure 2.1b, the viral state $v(t)$ remains in the $m = 2$ dimensional subspace $\mathcal{V} = \operatorname{span}\{y_1, y_2\}$ at all times t, provided that $v(0) \in \mathcal{V}$. On the subspace $\mathcal{V}$, (2.5) yields that the $N = 3$ differential equations (2.6) reduce to $m = 2$ equations

$$\begin{aligned}\frac{dc_1(t)}{dt} &= -\delta c_1(t) + \sqrt{2}\beta\left(1 - \frac{1}{\sqrt{2}}c_1(t)\right)c_2(t),\\ \frac{dc_2(t)}{dt} &= -\delta c_2(t) + 2\sqrt{2}\beta(1-c_2(t))\,c_1(t),\end{aligned}$$

from which the viral state $v(t)$ is obtained with (2.7).

Two conditions must hold for the set $\mathcal{V}$ to reduce NIMFA to m differential equations. First, the set $\mathcal{V}$ must be an m-dimensional subspace, spanned by the basis vectors $y_1, ..., y_m$. Second, if the initial viral state $v(0)$ is element of the set $\mathcal{V}$, then the viral state $v(t)$ must remain in the set $\mathcal{V}$ at every time $t > 0$. Hence, the set $\mathcal{V}$ must be an *invariant set* [42] of NIMFA. Thus, in this chapter, we consider the geometric problem:

Problem 2.2 (Clustering in NIMFA)**.** For a given number of nodes N and a given number $m \le N$ of agitation modes, find *all* $N \times N$ infection rate matrices B and the corresponding $N \times 1$ agitation modes $y_1, ..., y_m$, such that $\mathcal{V} = \operatorname{span}\{y_1, ..., y_m\}$ is an invariant set of NIMFA (1.2).

In contrast to Example 2.1, for which the agitation modes y_1, y_2 follow rather straightforwardly, Problem 2.2 considers the interdependency of arbitrary graphs and invariant sets $\mathcal{V}$ in full generality.

If $m \ll N$, then we expect that the invariant set $\mathcal{V}$, and its basis vectors y_l, reflect a macroscopic structure, or a clustering, of the contact graph. For instance, the agitation

mode y_1 in Example 2.1 indicates that the viral states $v_1(t)$ and $v_3(t)$ evolve equally and nodes 1 and 3 can be assigned to the same cluster.

Furthermore, the invariant set $\mathcal{V}$ allows for sophisticated, low-complexity control methods for the viral state $v(t)$, see [6] for a survey of control methods. More specifically, consider that an affine control method is applied to NIMFA (2.3),

$$\frac{dv(t)}{dt} = f_{\text{NIMFA}}(v(t)) + \sum_{l=1}^{m} g_l(t) y_l. \tag{2.9}$$

Here, the scalar function $g_l(t)$ is the control of the l-th agitation mode y_l. If the subspace $\mathcal{V} = \text{span}\{y_1, ..., y_m\}$ is an invariant set of NIMFA (1.2), then $\mathcal{V}$ is also an invariant set of (2.9). Hence, on the subspace $\mathcal{V}$, the viral state $v(t)$ can be controlled with only m distinct control inputs $g_1(t), ..., g_m(t)$. If the agitation mode y_l corresponds to a group of nodes, such as in Example 2.1, then the control $g_l(t)$ is applied to all nodes of that group. For instance, $g_l(t)$ could be the viral state control of individuals of a certain age group and location.

2.2. RELATED WORK

Clustering in NIMFA is closely related to *equitable partitions* [32, 43, 44]. We denote a general partition of the node set $\mathcal{N} = \{1, ..., N\}$ by[2] $\pi = \{\mathcal{N}_1, ..., \mathcal{N}_r\}$. Here, the *cells* $\mathcal{N}_1, ..., \mathcal{N}_r$ are disjoint subsets of the node set $\mathcal{N}$, such that $\mathcal{N} = \mathcal{N}_1 \cup ... \cup \mathcal{N}_r$. We adapt the definition of *equitable* partitions in [45, 46] as:

Definition 2.3 (Equitable partition)**.** Consider a symmetric $N \times N$ infection rate matrix B and a partition $\pi = \{\mathcal{N}_1, ..., \mathcal{N}_r\}$ of the node set $\mathcal{N} = \{1, ..., N\}$. The partition π is *equitable* if, for all cells $l, p = 1, ..., r$, the infection rates β_{ik} satisfy

$$\sum_{k \in \mathcal{N}_l} \beta_{ik} = \sum_{k \in \mathcal{N}_l} \beta_{jk} \quad \forall i, j \in \mathcal{N}_p.$$

For an equitable partition π, we define the degree from cell $\mathcal{N}_l$ to cell $\mathcal{N}_p$ as

$$d_{pl} = \sum_{k \in \mathcal{N}_l} \beta_{ik} \tag{2.10}$$

for some node $i \in \mathcal{N}_p$. Definition 2.3 states that, for an equitable partition π, the sum of the infection rates (2.10) is the same for all nodes $i \in \mathcal{N}_p$. We denote the $r \times r$ *quotient matrix* by B^π, whose elements are defined as $(B^\pi)_{pl} = d_{pl}$. Furthermore, we define the $r \times 1$ all-one vector $u_r = (1, ..., 1)^T$.

As shown by Bonaccorsi *et al.* [38] and Ottaviano *et al.* [46], NIMFA (1.2) can be reduced to r differential equations, provided that the infection rate matrix B has an equitable partition π with r cells. For our work, we summarise the results in [38, 46] as:

Theorem 2.4 ([38, 46])**.** *Consider NIMFA (1.2) on an $N \times N$ infection rate matrix B with an equitable partition $\pi = \{\mathcal{N}_1, ..., \mathcal{N}_r\}$. Assume that $\delta_i = \delta_j$ and $v_i(0) = v_j(0)$ for all nodes*

[2] Slightly deviating from common notation, we also refer to π as an (equitable) partition *of the infection rate matrix B*.

i, j in the same cell $\mathcal{N}_l$. Then, it holds that $v_i(t) = v_j(t)$ at every time $t > 0$ for all nodes $i, j \in \mathcal{N}_l$ and all $l = 1, ..., r$. Furthermore, define the $r \times 1$ reduced-size *viral state vector*

$$v^\pi(t) = \begin{pmatrix} v_{i_1}(t) & \dots & v_{i_r}(t) \end{pmatrix}^T$$

and the $r \times r$ reduced-size *curing rate matrix*

$$S^\pi = \operatorname{diag}\left(\delta_{i_1}, ..., \delta_{i_r}\right), \tag{2.11}$$

where i_l denotes an arbitrary node in the cell $\mathcal{N}_l$. Then, the reduced-size viral state vector $v^\pi(t)$ evolves as

$$\frac{dv^\pi(t)}{dt} = -S^\pi v^\pi(t) + \operatorname{diag}\left(u_r - v^\pi(t)\right) B^\pi v^\pi(t). \tag{2.12}$$

Remarkably, on both microscopic (1.2) and macroscopic (2.12) resolutions, the viral dynamics follow the same class of governing equation. For the Markovian Susceptible-Infectious-Susceptible (SIS) process, Simon et *al.* [47] proposed a lumping approach to reduce the complexity, which is an approximation and merges states of the SIS Markov chain, also see the work of Ward *et al.* [48]. In [49], a generalised mean-field framework for Markovian SIS epidemics has been proposed, which includes NIMFA as a special case. Beyond epidemics, analogous results to Theorem 2.4 have been proved for a diverse set of dynamics[3] on networks with equitable partitions [37, 54–57]. As a direct consequence of Theorem 2.4, equitable partitions are related to the proper orthogonal decomposition (2.1):

Corollary 2.5. *Consider NIMFA (1.2) on an $N \times N$ infection rate matrix B with an equitable partition $\pi = \{\mathcal{N}_1, ..., \mathcal{N}_r\}$. Assume that $\delta_i = \delta_j$ and $v_i(0) = v_j(0)$ for all nodes i, j in the same cell $\mathcal{N}_l$. Then, the subspace $\mathcal{V} = \operatorname{span}\{y_1, ..., y_m\}$ with $m = r$ is an invariant set, where the $N \times 1$ agitation modes y_l are given by*

$$\left(y_l\right)_i = \begin{cases} \frac{1}{\sqrt{|\mathcal{N}_l|}} & \text{if} \quad i \in \mathcal{N}_l, \\ 0 & \text{if} \quad i \notin \mathcal{N}_l, \end{cases}$$

and the scalar functions equal $c_l(t) = \sqrt{|\mathcal{N}_l|} v_l^\pi(t)$.

In other words, Corollary 2.5 states that every equitable partition π yields an invariant set $\mathcal{V}$, whose dimension equals the number of cells r in the partition π. Example 2.6 illustrates Theorem 2.4 and Corollary 2.5:

Example 2.6. *Consider NIMFA on a graph with $N = 6$ nodes, whose curing rate matrix equals $S = \operatorname{diag}\left(\tilde{\delta}_1, \tilde{\delta}_1, \tilde{\delta}_1, \tilde{\delta}_2, \tilde{\delta}_2, \tilde{\delta}_3\right)$ for some curing rates $\tilde{\delta}_1, \tilde{\delta}_2, \tilde{\delta}_3$. Furthermore, suppose*

[3] Specifically, we believe that Theorem 2.4 can be generalised to the dynamics $\frac{dv_i(t)}{dt} = -\delta_i v_i(t) + \sum_{j=1}^N \beta_{ij} g(v_i(t), v_j(t))$, where the arbitrary function $g(v_i(t), v_j(t))$ describes the "coupling" [50–53] between node i and j.

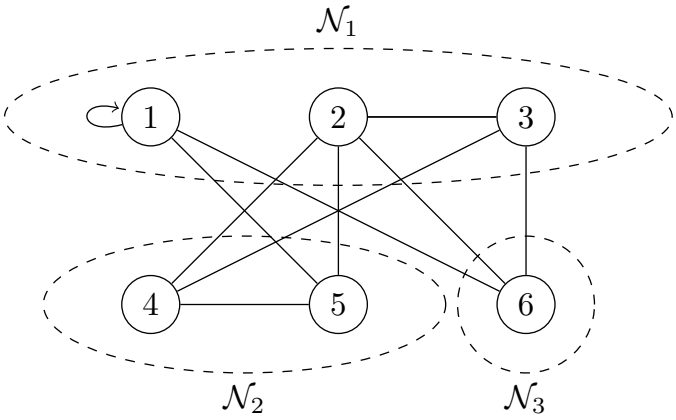

Figure 2.2: **Graph with a partition of the node set.** A graph with $N = 6$ nodes and the partition $\pi = \{\mathcal{N}_1, \mathcal{N}_2, \mathcal{N}_3\}$, whose cells are given by $\mathcal{N}_1 = \{1,2,3\}$, $\mathcal{N}_2 = \{4,5\}$ and $\mathcal{N}_3 = \{6\}$. For unit link weights, i.e., $\beta_{ij} = 1$ for all nodes i, j, the partition π is *not* equitable. If the link weights β_{ij} satisfy (2.13), as in Example 2.6, then the partition π is equitable.

that the infection rate matrix B is symmetric and given by the graph in Figure 2.2 as

$$B = \left(\begin{array}{ccc:ccc} \beta_{11} & 0 & 0 & 0 & \beta_{15} & \beta_{16} \\ 0 & 0 & \beta_{23} & \beta_{24} & \beta_{25} & \beta_{26} \\ 0 & \beta_{23} & 0 & \beta_{34} & 0 & \beta_{36} \\ \hdashline 0 & \beta_{24} & \beta_{43} & 0 & \beta_{45} & 0 \\ \beta_{15} & \beta_{25} & 0 & \beta_{45} & 0 & 0 \\ \hdashline \beta_{16} & \beta_{26} & \beta_{36} & 0 & 0 & 0 \end{array}\right). \tag{2.13}$$

Suppose that, for some degrees $d_{pl} > 0$, the infection rates β_{ij} satisfy: $\beta_{11} = \beta_{23} = d_{11}$; $\beta_{15} = \beta_{34} = d_{12}$ and $\beta_{24} = \beta_{25} = d_{12}/2$; $\beta_{16} = \beta_{26} = \beta_{36} = d_{13}$; and $\beta_{45} = d_{22}$. Then, the infection rate matrix B becomes

$$B = \left(\begin{array}{ccc:ccc} d_{11} & 0 & 0 & 0 & d_{12} & d_{13} \\ 0 & 0 & d_{11} & d_{12}/2 & d_{12}/2 & d_{13} \\ 0 & d_{11} & 0 & d_{12} & 0 & d_{13} \\ \hdashline 0 & d_{12}/2 & d_{12} & 0 & d_{22} & 0 \\ d_{12} & d_{12}/2 & 0 & d_{22} & 0 & 0 \\ \hdashline d_{13} & d_{13} & d_{13} & 0 & 0 & 0 \end{array}\right).$$

Thus, the matrix B has the equitable partition $\pi = \{\mathcal{N}_1, \mathcal{N}_2, \mathcal{N}_3\}$ with the cells $\mathcal{N}_1 = \{1,2,3\}$, $\mathcal{N}_2 = \{4,5\}$ and $\mathcal{N}_3 = \{6\}$. The quotient matrix equals

$$B^\pi = \begin{pmatrix} d_{11} & d_{12} & d_{13} \\ d_{12} & d_{22} & 0 \\ d_{13} & 0 & 0 \end{pmatrix}.$$

For the partition π, the reduced-size state can be chosen[4] *as* $v^\pi(t) = (v_1(t), v_4(t), v_6(t))^T$. *Theorem 2.4 states that the vector* $v^\pi(t) = (v_1(t), v_4(t), v_6(t))^T$ *evolves as*

$$\frac{dv^\pi(t)}{dt} = -S^\pi v^\pi(t) + \operatorname{diag}\left(u_3 - v^\pi(t)\right) B^\pi v^\pi(t),$$

with the 3×3 *reduced-size curing rate matrix* $S^\pi = \operatorname{diag}\left(\tilde{\delta}_1, \tilde{\delta}_2, \tilde{\delta}_3\right)$. *Furthermore, Corollary 2.5 states that the viral state* $v(t)$ *has the proper orthogonal decomposition*

$$v(t) = \sqrt{3} v_1^\pi(t) y_1 + \sqrt{2} v_2^\pi(t) y_2 + v_3^\pi(t) y_3$$

with the agitation modes

$$y_1 = \frac{1}{\sqrt{3}} \begin{pmatrix} 1 & 1 & 1 & 0 & 0 & 0 \end{pmatrix}^T,$$
$$y_2 = \frac{1}{\sqrt{2}} \begin{pmatrix} 0 & 0 & 0 & 1 & 1 & 0 \end{pmatrix}^T,$$
$$y_3 = \begin{pmatrix} 0 & 0 & 0 & 0 & 0 & 1 \end{pmatrix}^T.$$

2.3. EXACT CLUSTERING

Theorem 2.4 and Corollary 2.5 only give an incomplete answer to Problem 2.2: if the infection rate matrix B has an equitable partition π, then there exists an invariant set $\mathcal{V}$. But are there invariant sets $\mathcal{V}$, even if the matrix B does not have an equitable partition π?

We denote the *orthogonal complement* of the viral state set $\mathcal{V}$ by

$$\mathcal{V}^\perp = \left\{ w \in \mathbb{R}^N \mid w^T v = 0, \quad \forall v \in \mathcal{V} \right\}.$$

The dimension of the set $\mathcal{V}$ equals m. Thus, the dimension of the orthogonal complement $\mathcal{V}^\perp$ equals $N - m$. Since the orthogonal complement $\mathcal{V}^\perp$ is a subspace, there is a set of $N - m$ orthonormal basis vectors $y_{m+1}, ..., y_N$ such that

$$\mathcal{V}^\perp = \operatorname{span}\{y_{m+1}, ..., y_N\}. \tag{2.14}$$

The *direct sum* of two subspaces $\mathcal{S}_1, \mathcal{S}_2 \subseteq \mathbb{R}^N$ is defined as the subspace

$$\mathcal{S}_1 \oplus \mathcal{S}_2 = \{s_1 + s_2 \mid s_1 \in \mathcal{S}_1, s_2 \in \mathcal{S}_2\}. \tag{2.15}$$

Thus, the Euclidean space is the direct sum $\mathbb{R}^N = \mathcal{V} \oplus \mathcal{V}^\perp$ of the two subspaces $\mathcal{V}, \mathcal{V}^\perp$.

We rely on four assumptions to solve Problem 2.2.

Assumption 2.7. *For every viral state* $v \in \mathcal{V}$, *it holds that* $\operatorname{diag}(\delta_1, ..., \delta_N)\, v \in \mathcal{V}$.

Suppose that the curing rates are homogeneous, i.e., $\delta_i = \delta$ for all nodes i. Then, Assumption 2.7 is satisfied, since $\operatorname{diag}(\delta_1, ..., \delta_N)\, v = \delta v \in \mathcal{V}$ for every viral state $v \in \mathcal{V}$. More generally, Assumption 2.7 states that the viral state set $\mathcal{V}$ is an invariant subspace of the curing rate matrix $\operatorname{diag}(\delta_1, ..., \delta_N)$. Intuitively speaking, the curing rates $\delta_1, ..., \delta_N$ are "set in accordance to" the clustering given by the viral state set $\mathcal{V}$, such as in Example 2.6.

[4] But, for instance, $v^\pi(t) = (v_2(t), v_5(t), v_6(t))^T$ is possible as well.

Assumption 2.8. *There is a viral state $v \in \mathcal{V}$ whose entries satisfy $v_i > 0$ for every node $i = 1, ..., N$.*

There is a unique steady-state v_∞ with positive components $v_{\infty,i} > 0$ if $R_0 > 1$ and the matrix B is irreducible [18]. Since every viral state v converges to the steady state v_∞, the steady state v_∞ is element of the invariant set $\mathcal{V}$. Hence, Assumption 2.8 is always satisfied if $R_0 > 1$, provided the matrix B is irreducible.

Assumption 2.9. *The curing rates are positive and the infection rates are non-negative, i.e., $\delta_i > 0$ and $\beta_{ij} \geq 0$ for all nodes i, j.*

Assumption 2.9 is rather technical, since only non-negative curing rates and infection rates have a physical meaning.

Assumption 2.10. *The infection rate matrix B is symmetric and irreducible.*

Assumption 2.10 holds if and only if the infection rate matrix B corresponds to a connected undirected graph [58]. Under Assumption 2.10, the matrix B is diagonalisable [32] as

$$B = X \Lambda X^T. \tag{2.16}$$

Here, we denote the $N \times N$ diagonal matrix $\Lambda = \mathrm{diag}(\lambda_1, ..., \lambda_N)$ whose diagonal entries are given by the real eigenvalues $\lambda_1 \geq \lambda_2 \geq ... \geq \lambda_N$, and the columns of the $N \times N$ matrix $X = (x_1, ..., x_N)$ are given by the corresponding eigenvectors x_i.

Lemma 2.11 states that the invariant set $\mathcal{V}$ and the orthogonal complement $\mathcal{V}^\perp$ are spanned by eigenvectors of the infection rate matrix B:

Lemma 2.11. *Suppose that Assumptions 2.7 and 2.10 hold, and consider an invariant set $\mathcal{V} = \mathrm{span}\{y_1, ..., y_m\}$ of NIMFA (1.2) and the complement $\mathcal{V}^\perp = \mathrm{span}\{y_{m+1}, ..., y_N\}$. Then, there is some permutation $\phi : \{1, ..., N\} \to \{1, ..., N\}$, such that $\mathcal{V} = \mathrm{span}\{x_{\phi(1)}, ..., x_{\phi(m)}\}$ and $\mathcal{V}^\perp = \mathrm{span}\{x_{\phi(m+1)}, ..., x_{\phi(N)}\}$, where $x_{\phi(1)}, ..., x_{\phi(N)}$ denotes an orthonormal set of eigenvectors of the infection rate matrix B to the eigenvalues $\lambda_{\phi(1)}, ..., \lambda_{\phi(N)}$.*

Proof. Appendix A.1 □

We denote the span of the vectors $x_{\phi(l)}$ of the subspace $\mathcal{V}$ which correspond to a *non-zero* eigenvalue $\lambda_{\phi(l)} \neq 0$ as $\mathcal{V}_{\neq 0} = \mathrm{span}\{x_{\phi(l)} | l = 1, ..., m, \lambda_{\phi(l)} \neq 0\}$. Let the number of non-zero eigenvalues be denoted by m_1. Without loss of generality, we assume that, after the permutation ϕ, the *first* m_1 eigenvalues $\lambda_{\phi(1)}, ..., \lambda_{\phi(m_1)}$ are non-zero. Hence, the subspace $\mathcal{V}_{\neq 0}$ equals to

$$\mathcal{V}_{\neq 0} = \mathrm{span}\{x_{\phi(l)} | l = 1, ..., m_1\}. \tag{2.17}$$

Analogously to (2.17), we define the span of the vectors $x_{\phi(l)}$ of the subspace $\mathcal{V}$ which correspond to a *zero* eigenvalue $\lambda_{\phi(l)} = 0$ as

$$\begin{aligned} \mathcal{V}_0 &= \mathrm{span}\{x_{\phi(l)} | l = 1, ..., m, \lambda_{\phi(l)} = 0\} \\ &= \mathrm{span}\{x_{\phi(l)} | l = m_1 + 1, ..., m\}. \end{aligned}$$

Thus, the subspace $\mathcal{V}$ equals to the direct sum

$$\mathcal{V} = \mathcal{V}_{\neq 0} \oplus \mathcal{V}_0. \tag{2.18}$$

We emphasise that $\text{span}\{y_1,...,y_m\} = \text{span}\{x_{\phi(1)},...,x_{\phi(m)}\}$ does not imply that $y_l = x_{\phi(k)}$ for some k,l. An immediate consequence of Lemma 2.11 is that the infection rate matrix B can be decomposed as:

Lemma 2.12. *Suppose that Assumptions 2.7 and 2.10 hold, and consider an invariant set $\mathcal{V} = \text{span}\{y_1,...,y_m\}$ of NIMFA (1.2) and the complement $\mathcal{V}^\perp = \text{span}\{y_{m+1},...,y_N\}$. Then, the infection rate matrix B is decomposable as $B = B_{\mathcal{V}} + B_{\mathcal{V}^\perp}$, where*

$$B_{\mathcal{V}} = \begin{pmatrix} y_1 & ... & y_m \end{pmatrix} \tilde{B}_{\mathcal{V}} \begin{pmatrix} y_1^T \\ \vdots \\ y_m^T \end{pmatrix} \quad \text{and} \quad B_{\mathcal{V}^\perp} = \begin{pmatrix} y_{m+1} & ... & y_N \end{pmatrix} \tilde{B}_{\mathcal{V}^\perp} \begin{pmatrix} y_{m+1}^T \\ \vdots \\ y_N^T \end{pmatrix}$$

for some $m \times m$ matrix $\tilde{B}_{\mathcal{V}}$ and $(N-m)\times(N-m)$ matrix $\tilde{B}_{\mathcal{V}^\perp}$.

Proof. Appendix A.2. □

Lemma 2.12 shows that the sets $\mathcal{V}$ and $\mathcal{V}^\perp$ are invariant subspaces of the matrix B. In particular, the viral state dynamics on the invariant set $\mathcal{V}$ are the same for all infection rate matrices $B^{(1)}, B^{(2)}$ with the same submatrix $B^{(1)}_{\mathcal{V}} = B^{(2)}_{\mathcal{V}}$ but different submatrices $B^{(1)}_{\mathcal{V}^\perp} \neq B^{(2)}_{\mathcal{V}^\perp}$.

Example 2.13. *Suppose that Assumptions 2.7 and 2.10 hold. For some degrees d_{11}, d_{12}, d_{22} and some scalar ξ, consider the infection rate matrix*

$$B = \left(\begin{array}{ccc} d_{11}+\xi & d_{11}-\xi & d_{12} \\ d_{11}-\xi & d_{11}+\xi & d_{12} \\ \hdashline d_{12} & d_{12} & d_{22} \end{array}\right)$$

with the equitable partition $\pi = \{\mathcal{N}_1, \mathcal{N}_2\}$, where $\mathcal{N}_1 = \{1,2\}$ and $\mathcal{N}_2 = \{3\}$, and the quotient matrix

$$B^\pi = \begin{pmatrix} d_{11} & d_{12} \\ d_{12} & d_{22} \end{pmatrix}.$$

Corollary 2.5 states that the subspace $\mathcal{V} = \text{span}\{y_1, y_2\}$ is an invariant set of NIMFA (1.2), where the agitation modes equal to $y_1 = \frac{1}{\sqrt{2}}(1,1,0)^T$ and $y_2 = (0,0,1)^T$. The orthogonal complement follows as $\mathcal{V}^\perp = \text{span}\{y_3\}$, where $y_3 = \frac{1}{\sqrt{2}}(1,-1,0)^T$. Furthermore, Lemma 2.12 states that the infection rate matrix can be decomposed as $B = B_{\mathcal{V}} + B_{\mathcal{V}^\perp}$, where

$$B_{\mathcal{V}} = \begin{pmatrix} y_1 & y_2 \end{pmatrix} \begin{pmatrix} 2d_{11} & \sqrt{2}d_{12} \\ \sqrt{2}d_{12} & d_{22} \end{pmatrix} \begin{pmatrix} y_1^T \\ y_2^T \end{pmatrix} = \begin{pmatrix} d_{11} & d_{11} & d_{12} \\ d_{11} & d_{11} & d_{12} \\ d_{12} & d_{12} & d_{22} \end{pmatrix}$$

and

$$B_{\mathcal{V}^\perp} = 2\xi y_3 y_3^T = \begin{pmatrix} \xi & -\xi & 0 \\ -\xi & \xi & 0 \\ 0 & 0 & 0 \end{pmatrix}.$$

The eigenvectors $x_{\phi(1)}$, $x_{\phi(2)}$ equal to a linear combination of the agitation modes y_1, y_2, and the third eigenvector equals $x_{\phi(3)} = y_3$.

Theorem 2.14 states our main result:

Theorem 2.14. *Suppose that Assumptions 2.7 to 2.10 hold. Then, any invariant set $\mathcal{V} = \operatorname{span}\{y_1, ..., y_m\}$ of NIMFA (1.2) is equal to the direct sum $\mathcal{V} = \mathcal{V}_{\neq 0} \oplus \mathcal{V}_0$ of two subspaces $\mathcal{V}_{\neq 0}$,$\mathcal{V}_0$. Here, the orthonormal basis vectors $y_1, ..., y_{m_1}$, where $m_1 \leq m$, of the subspace $\mathcal{V}_{\neq 0} = \operatorname{span}\{y_1, ..., y_{m_1}\}$ are given by*

$$(y_l)_j = \begin{cases} \frac{1}{\sqrt{|\mathcal{N}_l|}} & \text{if } j \in \mathcal{N}_l, \\ 0 & \text{if } j \notin \mathcal{N}_l, \end{cases} \tag{2.19}$$

for some equitable partition $\pi = \{\mathcal{N}_1, ..., \mathcal{N}_{m_1}\}$ of the infection rate matrix B. If $m_1 = m$, then the subspace $\mathcal{V}_0$ is empty. Otherwise, if $m_1 < m$, then $\mathcal{V}_0 = \operatorname{span}\{x_{\phi(l)} \,|\, l = m_1 + 1, ..., m\}$ for some eigenvectors $x_{\phi(l)}$ of the infection rate matrix B belonging to the eigenvalue 0.

Proof. Appendix A.3. □

The Euclidean space $\mathbb{R}^N$ is always an invariant set of NIMFA. For $\mathcal{V} = \mathbb{R}^N$ and $\mathcal{V}_0 = \emptyset$, the equitable partition π in Theorem 2.14 becomes *trivial*, i.e., $\pi = \{\mathcal{N}_1, ..., \mathcal{N}_N\}$ with exactly one node in every cell $\mathcal{N}_l$. On the other hand, if there is an invariant set $\mathcal{V}$ of dimension $m < N$, then Theorem 2.14 implies that the matrix B is equitable with $m_1 \leq m$ cells.

If $\mathcal{V}_0 = \emptyset$, then Theorem 2.14 essentially reverts Corollary 2.5. Thus, every equitable partition π corresponds to an invariant set $\mathcal{V}_0$, and vice versa. *In other words, the macroscopic structure of equitable partitions π and the low-rank dynamics of invariant sets $\mathcal{V}$ are two sides of the same coin.* If $\mathcal{V}_0 = \emptyset$, then the dynamics on the invariant set $\mathcal{V} = \mathcal{V}_{\neq 0}$ are given by the reduced-size NIMFA system (2.12) with $m = m_1$ equations.

If $\mathcal{V}_0 \neq \emptyset$, then Theorem 2.14 is more general than the inversion of Corollary 2.5. Theorem 2.14 states that an invariant set of NIMFA equals to the direct sum $\mathcal{V} = \mathcal{V}_{\neq 0} \oplus \mathcal{V}_0$, where the subspace $\mathcal{V}_{\neq 0}$ corresponds to an equitable partition π of the infection rate matrix, and the subspace $\mathcal{V}_0$ is a subset of the kernel of the matrix B. If $\mathcal{V}_0 \neq \emptyset$, then the dynamics on the invariant set $\mathcal{V} = \mathcal{V}_{\neq 0} \oplus \mathcal{V}_0$ are described by the $m > m_1$ differential equations (2.5).

The curing rates δ_i satisfy Assumption 2.7 if there are some scalars $\tilde{\delta}_1, ..., \tilde{\delta}_{m_1}$ such that $\delta_i = \tilde{\delta}_l$ for all nodes i in cell $\mathcal{N}_l$, where $l = 1, ..., m_1$. However, Assumption 2.7 allows for more general curing rates. With Lemma 2.12 and Theorem 2.14, the infection rate matrix B can be constructed from specifying the agitation modes y_l, such that $\mathcal{V} = \operatorname{span}\{y_1, ..., y_m\}$ is an invariant set of NIMFA (1.2):

Example 2.15. *Consider NIMFA (1.2) on a network of $N = 5$ nodes and the subspaces $\mathcal{V}_{\neq 0} = \text{span}\{y_1, y_2\}$, $\mathcal{V}_0 = \text{span}\{y_3\}$, where the agitation modes equal*

$$y_1 = \frac{1}{\sqrt{3}}\begin{pmatrix}1 & 1 & 1 & 0 & 0\end{pmatrix}^T,$$
$$y_2 = \frac{1}{\sqrt{2}}\begin{pmatrix}0 & 0 & 0 & 1 & 1\end{pmatrix}^T,$$
$$y_3 = \frac{1}{\sqrt{6}}\begin{pmatrix}1 & -2 & 1 & 0 & 0\end{pmatrix}^T.$$

Furthermore, let y_4, y_5 be two vectors, with $y_4^T y_5 = 0$ and $y_4^T y_4 = y_5^T y_5 = 1$, that are orthogonal to the agitation modes y_1, y_2, y_3. With Lemma 2.12, define the infection rate matrix as

$$B = \begin{pmatrix}y_1 & y_2\end{pmatrix} \tilde{B}_{\mathcal{V}_{\neq 0}} \begin{pmatrix}y_1^T \\ y_2^T\end{pmatrix} + \begin{pmatrix}y_4 & y_5\end{pmatrix} \tilde{B}_{\mathcal{V}^\perp} \begin{pmatrix}y_4^T \\ y_5^T\end{pmatrix},$$

where the symmetric 2×2 matrices $\tilde{B}_{\mathcal{V}_{\neq 0}}$, $\tilde{B}_{\mathcal{V}^\perp}$ are chosen such that the matrix B is irreducible and contains only non-negative elements. Furthermore, consider the curing rate matrix $S = \text{diag}(\tilde{\delta}_1, \tilde{\delta}_2, \tilde{\delta}_1, \tilde{\delta}_3, \tilde{\delta}_3)$ for some curing rates $\tilde{\delta}_1, \tilde{\delta}_2, \tilde{\delta}_3 > 0$. Then, Assumptions 2.7 to 2.10 are satisfied, and Theorem 2.14 states that the subspace $\mathcal{V} = \mathcal{V}_{\neq 0} \oplus \mathcal{V}_0$ is an invariant set of NIMFA (1.2). (An alternative choice for the curing rate matrix is $S = \text{diag}(\tilde{\delta}_1, \tilde{\delta}_1, \tilde{\delta}_1, \tilde{\delta}_2, \tilde{\delta}_2)$, which also satisfies Assumption 2.7.)

2.3.1. DECOMPOSITION OF THE VIRAL DYNAMICS

Suppose the infection rate matrix B has an equitable partition π and the infection rates β_{ij} are the same between all nodes i, j in any two cells[5]. Then, we can decompose the dynamics of the viral state $v(t)$ as:

Theorem 2.16. *Consider NIMFA (1.2) on a symmetric $N \times N$ infection rate matrix B with an equitable partition $\pi = \{\mathcal{N}_1, ..., \mathcal{N}_r\}$. Furthermore, suppose that the curing rates δ_i are the same for all nodes i in any cell $\mathcal{N}_l$, and that the infection rates β_{ij} are the same for all nodes i in any cell $\mathcal{N}_l$ and all nodes j in any cell $\mathcal{N}_p$. Denote the subspace $\mathcal{V}_{\neq 0} = \text{span}\{y_1, ..., y_r\}$, with the basis vectors y_l defined in (2.19), and denote the kernel of the matrix B by $\ker(B) = \text{span}\{y_{r+1}, ..., y_N\}$. At every time $t \geq 0$, consider the viral state decomposition*

$$v(t) = \tilde{v}(t) + v_{\ker}(t),$$

where the projection of the viral state $v(t)$ on the subspace $\mathcal{V}_{\neq 0}$ equals

$$\tilde{v}(t) = \sum_{l=1}^{r} \left(y_l^T v(t)\right) y_l,$$

[5] If the matrix B is decomposable as $B = B_{\mathcal{V}} + B_{\mathcal{V}^\perp}$ as in Lemma 2.12, then the infection rates β_{ij} are the same between all nodes i, j in any two cells if and only if $B_{\mathcal{V}^\perp} = 0$.

and the projection of the viral state $v(t)$ on the kernel $\ker(B)$ *equals*

$$v_{\ker}(t) = \sum_{l=r+1}^{N} \left(y_l^T v(t)\right) y_l.$$

Furthermore, denote the $r \times 1$ reduced-size projection $\tilde{v}^\pi(t) = \left(\tilde{v}^\pi_{i_1}(t), ..., \tilde{v}^\pi_{i_r}(t)\right)^T$, where i_l denotes an arbitrary node in cell $\mathcal{N}_l$. Then, the reduced-size projection $\tilde{v}^\pi(t)$ evolves, independently of the projection $v_{\ker}(t)$, as

$$\frac{d\tilde{v}^\pi(t)}{dt} = -S^\pi \tilde{v}^\pi(t) + \operatorname{diag}\left(u_r - \tilde{v}^\pi(t)\right) B^\pi \tilde{v}^\pi(t) \tag{2.20}$$

with the quotient matrix B^π and the matrix S^π given by (2.11), and the projection $v_{\ker}(t)$ obeys

$$\frac{dv_{\ker}(t)}{dt} = -\left(S + \operatorname{diag}\left(B\tilde{v}(t)\right)\right) v_{\ker}(t). \tag{2.21}$$

Proof. Appendix A.4. □

In Theorem 2.16, the set $\mathcal{V}_0$ is equal to the kernel $\ker(B)$, which is equivalent to $\mathcal{V}^\perp = \emptyset$ and assuming the same infection rates β_{ij} between all nodes i, j in any two cells. In contrast to Theorem 2.4, we do not consider that the initial state satisfies $v_i(0) = v_j(0)$ for all nodes i, j in the same cell $\mathcal{N}_l$.

With the definition of the agitation mode y_l in (2.19), the viral state average in cell $\mathcal{N}_l$ follows from the projection of the viral state $v(t)$ on the vector y_l as

$$\frac{1}{|\mathcal{N}_l|} \sum_{i \in \mathcal{N}_l} v_i(t) = \frac{1}{\sqrt{|\mathcal{N}_l|}} y_l^T v(t)$$

for every cell $l = 1, ..., r$. Furthermore, the subspace $\mathcal{V}_{\neq 0}$ is spanned by the vectors y_1, ..., y_r. Hence, the dynamics of the projection $\tilde{v}(t)$ on the subspace $\mathcal{V}_{\neq 0}$ describes the evolution of viral state averages of every cell $\mathcal{N}_l$, which is described by r differential equations (2.20) on the quotient graph B^π. Since the steady state $v_{\infty,i}$ of every node i in the same cell $\mathcal{N}_l$ is the same [38, 46], it holds that $v_\infty \in \mathcal{V}_{\neq 0}$, which implies that $v_{\ker}(t) \to 0$ as $t \to \infty$. Furthermore, from Theorem 2.4 it follows that, if $v_{\ker}(0) = 0$, then $v_{\ker}(t) = 0$ at every time t. Thus, the evolution of the projection $v_{\ker}(t)$ describes convergence of the viral states $v_i(t)$ to the respective cell-averages. *By (2.20), Theorem 2.16 implies that the viral state cell-averages evolve independently of the dynamics on the kernel* $\ker(B)$. Schaub *et al.* [56] obtained an analogous result for linear dynamics on networks.

If we can derive the closed-form expression for the projection $\tilde{v}(t)$ by solving (2.20), then the dynamics $v_{\ker}(t)$ follow by the linear time-*varying* system (2.21). Furthermore, the reduced-size steady state $v^\pi_\infty = \left(\tilde{v}^\pi_{\infty,i_1}, ..., \tilde{v}^\pi_{\infty,i_r}\right)^T$ is an equilibrium of (2.20). Thus, if $\tilde{v}(t) = v_\infty$, then the dynamics of the projection $v_{\ker}(t)$ obey the linear time-*invariant* (LTI) system

$$\frac{dv_{\ker}(t)}{dt} = -\left(S + \operatorname{diag}\left(Bv_\infty\right)\right) v_{\ker}(t).$$

Thus, the affine subspace $\{v_\infty + v_{\ker} | v_{\ker} \in \ker(B)\}$ is an invariant set of NIMFA, on which the viral dynamics are linear.

Loosely speaking, Theorem 2.16 shows that a crucial challenge for solving NIMFA on graphs with equitable partitions is the dynamics of the projection $\tilde{v}(t)$, since solving the set of nonlinear equations (2.20) seems more difficult than solving the linear time-varying system (2.21) for a given $\tilde{v}(t)$. For a complete graph, the solution $\tilde{v}(t)$ to set of nonlinear equations (2.20) is one-dimensional and can be stated in closed form [59]. Thus, we obtain the solution of NIMFA on the complete graph, for *arbitrary* initial viral states $v(0)$, as:

Theorem 2.17. *Consider NIMFA (1.2) on the complete graph, whose infection rates equal $\beta_{ij} = \beta > 0$ for all nodes $i, j = 1, ..., N$. Suppose the curing rates satisfy $\delta_i = \delta$ for all nodes i. Then, for any initial viral state $v(0) \in [0,1]^N$, the solution of NIMFA (1.2) equals*

$$v(t) = c_1(t)\, y_1 + c_2(t)\, v_{\ker}(0),$$

with the agitation mode $y_1 = u/\sqrt{N}$, and the $N \times 1$ vector $v_{\ker}(0)$ given by

$$v_{\ker}(0) = \left(I - y_1 y_1^T\right) v(0).$$

The functions $c_1(t)$ and $c_2(t)$ follow explicitly as:

1. *If $\delta \neq \beta N$, then the scalar function $c_1(t)$ equals*

$$c_1(t) = \frac{w}{2\beta\sqrt{N}} \left(1 + \tanh\left(\frac{w}{2}\, t + \Upsilon_1(0)\right)\right) \tag{2.22}$$

with the viral slope *$w = \beta N - \delta$ and the constant*

$$\Upsilon_1(0) = \operatorname{arctanh}\left(2\frac{\beta\sqrt{N}}{w}\, y_1^T v(0) - 1\right),$$

and the scalar function $c_2(t)$ equals

$$c_2(t) = \Upsilon_2(0)\, e^{-\Phi t}\, \operatorname{sech}\left(\frac{w}{2}\, t + \Upsilon_1(0)\right) \tag{2.23}$$

with the constants $\Phi = w/2 + \delta$ and

$$\Upsilon_2(0) = \frac{v_{\ker}^T(0)\, v(0)}{\| v_{\ker}(0) \|_2^2} \cosh\left(\Upsilon_1(0)\right). \tag{2.24}$$

2. *If $\delta = \beta N$, then the scalar function $c_1(t)$ equals*

$$c_1(t) = \sqrt{N} \left(\delta\, t + \frac{\sqrt{N}}{y_1^T v(0)}\right)^{-1} \tag{2.25}$$

and the scalar function $c_2(t)$ obeys

$$c_2(t) = \tilde{\Upsilon}_2(0)\, e^{-\delta t} \left(\delta\, t + \frac{\sqrt{N}}{y_1^T v(0)}\right)^{-\frac{\beta N}{\delta}},$$

where the constant $\tilde{\Upsilon}_2(0)$ *is given by*

$$\tilde{\Upsilon}_2(0) = \frac{v_{\ker}^T(0)\, v(0)}{\| v_{\ker}(0) \|_2^2} \left(\frac{\sqrt{N}}{y_1^T v(0)} \right)^{\frac{\beta N}{\delta}}.$$

Proof. Appendix A.5. □

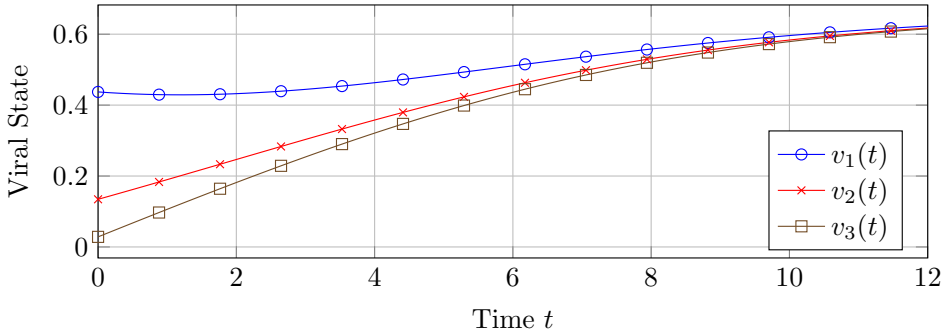

(a) Viral state $v(t)$ versus time t.

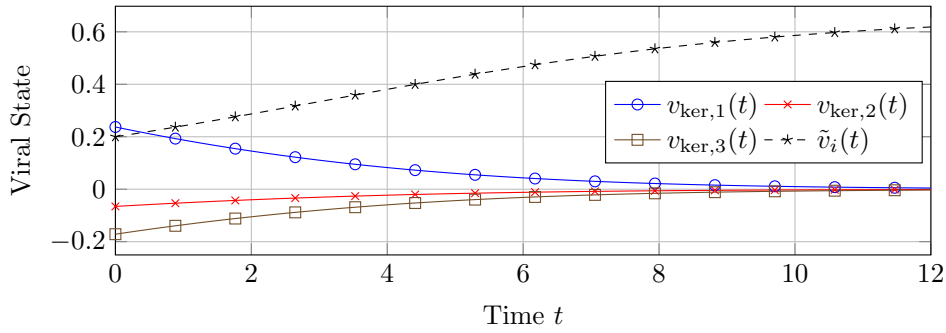

(b) Projections $\tilde{v}(t)$ and $v_{\ker}(t)$ versus time t.

Figure 2.3: **Closed-form solution of NIMFA on the complete graph.** The solution of NIMFA (1.1) for a complete graph with $N = 3$ nodes and homogeneous spreading rates. As stated by Theorem 2.16, the viral state satisfies $v(t) = \tilde{v}(t) + v_{\ker}(t)$, where $\tilde{v}(t)$ and $v_{\ker}(t)$ denote the projection of the viral state $v(t)$ on the subspace $\mathcal{V}_{\neq 0}$ and the kernel $\ker(B)$, respectively. **(a)**: The viral state $v_i(t)$ versus time t for every node i. **(b)**: The projections $\tilde{v}(t)$ and $v_{\ker}(t)$, which follow from Theorem 2.17 as $\tilde{v}_i(t) = c_1(t) v_{\infty,i}$ and $v_{\ker,i}(t) = c_2(t) (y_2)_i$ for all nodes i, where the scalar functions $c_1(t)$ and $c_2(t)$ are given by the closed-form expressions (2.22) and (2.23), respectively. Since the steady state $v_{\infty,i}$ is the same for every node i in the complete graph, it holds that $\tilde{v}_i(t) = \tilde{v}_j(t)$ for all nodes i, j.

Figure 2.3 illustrates the closed-form solution of NIMFA for complete graphs, as given by Theorem 2.17. As shown by Figure 2.3, even though the viral state average $\tilde{v}(t)$ is monotonically increasing, the viral state $v_1(t) = \tilde{v}_1(t) + v_{\ker,1}(t)$ is decreasing until $t \approx 1$, which is due to the dynamics of the projection $v_{\ker}(t)$ on the kernel $\ker(B)$.

2.4. APPROXIMATE CLUSTERING

As shown by Theorem 2.14, equitable partitions and low-dimensional viral state dynamics in NIMFA are equivalent. Many networks possess some macroscopic structure, which may *resemble* an equitable partition, but which *is not precisely* an equitable partition. *Is it possible to reduce the number of NIMFA equations, if the network has an "almost" equitable partition?*

Theorem 2.18 shows that NIMFA (1.2) on any network can be bounded by increasing or decreasing the spreading rates β_{ij},δ_i:

Theorem 2.18. *Consider two NIMFA systems with respective positive curing rates δ_i and $\tilde{\delta}_i$, non-negative infection rates β_{ij} and $\tilde{\beta}_{ij}$, and viral states $v_i(t)$ and $\tilde{v}_i(t)$. Suppose that the initial viral state $v_i(0)$,$\tilde{v}_i(0)$ are in $[0,1]$ for all nodes i and that the matrices B and $\tilde{B}$, with elements β_{ij} and $\tilde{\beta}_{ij}$, respectively, are irreducible. Then, if $\tilde{\delta}_i \leq \delta_i$ and $\tilde{\beta}_{ij} \geq \beta_{ij}$ for all nodes i, j, $\tilde{v}(0) \geq v(0)$ implies that $\tilde{v}(t) \geq v(t)$ at every time t.*

Proof. Appendix A.6. □

We emphasise that Theorem 2.18 does not assume symmetric infection rate matrices B, $\tilde{B}$. Building upon Theorem 2.18, we aim to bound the viral state $v(t)$ of any network at every time t by the viral state of networks with equitable partitions. In the following, we consider a partition $\pi = \{\mathcal{N}_1,...,\mathcal{N}_r\}$ of the node set $\mathcal{N} = \{1,...,N\}$ of an arbitrary network. We stress that π can be *any*, not necessarily equitable, partition. We define the minimum $d_{\min,pl}$ of the sum of infection rates from cell $\mathcal{N}_l$ to $\mathcal{N}_p$ as

$$d_{\min,pl} = \min_{i \in \mathcal{N}_p} \sum_{k \in \mathcal{N}_l} \beta_{ik} \tag{2.26}$$

and the maximum $d_{\max,pl}$ as

$$d_{\max,pl} = \max_{i \in \mathcal{N}_p} \sum_{k \in \mathcal{N}_l} \beta_{ik}. \tag{2.27}$$

Furthermore, we denote the $r \times r$ matrices $B_{\min}$ and $B_{\max}$, whose elements are given by $d_{\min,pl}$ and $d_{\max,pl}$, respectively. Analogously, we define the minimum $\delta_{\min,l}$ of the curing rates in cell $\mathcal{N}_l$ as

$$\delta_{\min,l} = \min_{i \in \mathcal{N}_l} \delta_i$$

and the maximum $\delta_{\max,l}$ as

$$\delta_{\max,l} = \max_{i \in \mathcal{N}_l} \delta_i. \tag{2.28}$$

We combine Theorem 2.4 and Theorem 2.18 to obtain:

Theorem 2.19. *Suppose that the Assumptions 2.9 and 2.10 hold. At every time t, consider the $r \times 1$ reduced-size lower bound $v_{\mathrm{lb},l}(t)$ and $r \times 1$ upper bound $v_{\mathrm{ub},l}(t)$, which evolve as*

$$\frac{d\,v_{\mathrm{lb}}(t)}{dt} = -\operatorname{diag}\left(\delta_{\max,1},...,\delta_{\max,r}\right) v_{\mathrm{lb}}(t) + \operatorname{diag}\left(u_r - v_{\mathrm{lb}}(t)\right) B_{\min}\, v_{\mathrm{lb}}(t) \tag{2.29}$$

and

$$\frac{dv_{\text{ub}}(t)}{dt} = -\operatorname{diag}\left(\delta_{\min,1},...,\delta_{\min,r}\right) v_{\text{ub}}(t) + \operatorname{diag}\left(u_r - v_{\text{ub}}(t)\right) B_{\max} v_{\text{ub}}(t).$$

Then, if the initial states satisfy $v_{\text{lb},l}(0) \leq v_i(0) \leq v_{\text{ub},l}(0)$ *for all nodes* i *in any cell* $\mathcal{N}_l$*, the viral state* $v_i(t)$ *of all nodes* i *in any cell* $\mathcal{N}_l$ *is bounded by*

$$v_{\text{lb},l}(t) \leq v_i(t) \leq v_{\text{ub},l}(t) \quad \forall\, t \geq 0. \tag{2.30}$$

Proof. Appendix A.7. □

Theorem 2.19 states that the $N \times 1$ viral state $v(t)$ on *any* network is bounded by the $r \times 1$ viral states $v_{\text{lb}}(t)$, $v_{\text{ub}}(t)$ on networks with equitable partitions and r cells. Reducing the N-dimensional viral state dynamics to r-dimensional dynamics comes at the cost of an *approximate* description by the bounds in (2.30). If the partition π is equitable, then it holds that $d_{\min,pl} = d_{\max,pl}$, and the bounds in Theorem 2.19 can be replaced by the exact statement in Theorem 2.4.

Similarly to the lower bound and upper bound of the degrees in (2.26) and (2.27), respectively, we define the *average* degree from cell $\mathcal{N}_l$ to $\mathcal{N}_p$ for any partition π as

$$\bar{d}_{pl} = \frac{1}{|\mathcal{N}_p|} \sum_{i \in \mathcal{N}_p} \sum_{k \in \mathcal{N}_l} \beta_{ik}.$$

Then, we define the $r \times r$ reduced-size infection rate matrix $\bar{B}$, which consists of the elements $\bar{d}_{pl}$. Furthermore, we define the average curing rate of any cell $\mathcal{N}_l$ as

$$\bar{\delta}_l = \frac{1}{|\mathcal{N}_l|} \sum_{i \in \mathcal{N}_l} \delta_i.$$

Then, we approximate the viral state by $v_i(t) \approx \bar{v}_l(t)$ for all nodes i in any cell $\mathcal{N}_l$. Here, the $r \times 1$ reduced-size viral state vector $\bar{v}(t)$ evolves as

$$\frac{d\bar{v}(t)}{dt} = -\operatorname{diag}\left(\bar{\delta}_1,...,\bar{\delta}_r\right) \bar{v}(t) + \operatorname{diag}\left(u_r - \bar{v}(t)\right) \bar{B}\, \bar{v}(t), \tag{2.31}$$

and, for all cells $\mathcal{N}_l$, the initial state equals

$$\bar{v}_l(0) = \frac{1}{|\mathcal{N}_l|} \sum_{i \in \mathcal{N}_l} v_l(0).$$

If the matrix B has an equitable partition π and the rates δ_i, β_{ij} are the same between all nodes i, j in any two cells as in Theorem 2.16, then the approximation $\bar{v}(t)$ coincides with the projection $\tilde{v}(t)$ of the viral state $v(t)$ on the subspace $\mathcal{V}_{\neq 0}$.

To illustrate the accuracy of the bounds in Theorem 2.19 and the reduced-size viral state $\bar{v}(t)$ for networks without equitable partitions, we consider the *Stochastic Block-model* (SBM), originally introduced by Holland *et al.* [60]. We consider a network with $N = 1000$ nodes and a partition π with $r = 5$ cells $\mathcal{N}_1$, ..., $\mathcal{N}_5$. The cells are of size $|\mathcal{N}_1| = 400$, $|\mathcal{N}_2| = 250$, $|\mathcal{N}_3| = 200$, $|\mathcal{N}_4| = 100$ and $|\mathcal{N}_5| = 50$. With a probability of 0.7,

there are no links between two cells $\mathcal{N}_p$, $\mathcal{N}_l$, i.e., $\beta_{ij} = \beta_{ji} = 0$ for all nodes $i \in \mathcal{N}_p$ and $j \in \mathcal{N}_l$. Otherwise, with a probability of 0.3, we denote the mean of the links between the cells $\mathcal{N}_p$, $\mathcal{N}_l$ by $\bar{\beta}_{pl} = \bar{\beta}_{lp}$, which is set to a uniform random number in $[0.1, 0.2]$. Then, the infection rate $\beta_{ij} = \beta_{ji}$ for all nodes $i \in \mathcal{N}_p$ and $j \in \mathcal{N}_l$ is set to a random number $[\bar{\beta}_{pl}, \bar{\beta}_{pl}(1+\sigma_{\text{rel}})]$, where we vary the *relative variance* σ_{rel} for different scenarios in the numerical evaluation. If $\sigma_{\text{rel}} = 0$, then the partition π is equitable. The larger the variance σ_{rel}, the "less equitable" the partition π. For every node i, the curing rate δ_i is set to a uniform random number in $[1, 1+\sigma_{\text{rel}}]$, and the initial viral state $v_i(0)$ is set to a uniform random number in $[0.01, 0.01(1+\sigma_{\text{rel}})]$. Hence, if the variance $\sigma_{\text{rel}} = 0$, then it holds that $v_{\text{lb},l}(t) = v_{\text{lb},l}(t) = v_i(t)$ for every node i in any cell $\mathcal{N}_l$. Lastly, the curing rates are decreased to $\delta_i \leftarrow c\delta_i$, where the scalar c is chosen such that the basic reproduction number (1.4) equals $R_0 = 3$. To obtain the viral state $v(t)$, we discretise NIMFA (1.1) with a sufficiently small sampling time, see Chapter 4 for a detailed analysis of the resulting discrete-time NIMFA model.

Figure 2.4 illustrates the accuracy of the bounds $v_{\text{lb},l}(t)$, $v_{\text{ub},l}(t)$ in Theorem 2.19 and the approximation accuracy of $\bar{v}(t)$ in (2.31) for the largest cell $\mathcal{N}_1$ and the smallest cell $\mathcal{N}_5$. For both $\sigma_{\text{rel}} = 0.25$ and $\sigma_{\text{rel}} = 0.5$, the approximation $\bar{v}_l(t)$ is close to the exact average viral state in cell $\mathcal{N}_l$,

$$v_{\text{avg},l}(t) = \frac{1}{|\mathcal{N}_l|} \sum_{i \in \mathcal{N}_l} v_l(t).$$

The accuracy of the bounds $v_{\text{lb},l}(t)$, $v_{\text{ub},l}(t)$ on any viral state $v_i(t)$ in cell $\mathcal{N}_l$ decreases when the variance σ_{rel} is increased. Nonetheless, the bounds $v_{\text{lb},l}(t)$, $v_{\text{ub},l}(t)$ are reasonably accurate for both $\sigma_{\text{rel}} = 0.25$ and $\sigma_{\text{rel}} = 0.5$.

2.4.1. CLUSTERING FOR EPIDEMICS ON REAL-WORLD NETWORKS

Approximating the viral state dynamics by $m < N$ equations requires the specification of a partition π of the nodes. In some cases, this partition is given *a priori*, as in the experiments in Figure 2.4, where the node partition π was chosen corresponding to the SBM blocks. In contrast, for real-world networks, it is more challenging to determine an appropriate clustering and, hence, to obtain an accurate description of the viral state dynamics by $m < N$ equations.

We consider a two-step approach to reduce NIMFA to $m = r < N$ equations. First, we obtain a partition π of the nodes by the Bethe spectral clustering algorithm [61], which makes use of the *Bethe Hessian* $H_{\pm} = (d_{\text{avg}} - 1)I \pm d_{\text{avg}}B + D$, with the average degree d_{avg} and the degree matrix $D = \text{diag}(d_1, \ldots, d_N)$. When the matrix B has an (approximate) SBM structure, the negative eigenvalues of $H_{\pm}$ have corresponding eigenvectors which are (approximately) piecewise constant on the blocks of B. The spectral clustering algorithm partitions the nodes of B based on a k-means clustering of the negative eigenvector entries of $H_{\pm}$. Second, we evaluate the accuracy of reduced-size viral state $\bar{v}(t)$ in (2.31) by the deviation of the prevalence,

$$\epsilon_{\text{avg}} = \sum_{k=1}^{n} \left| \frac{1}{N} \sum_{i=1}^{N} v_i(k\Delta t) - \frac{1}{N} \sum_{l=1}^{r} |\mathcal{N}_l| \, \bar{v}_l(k\Delta t) \right|. \tag{2.32}$$

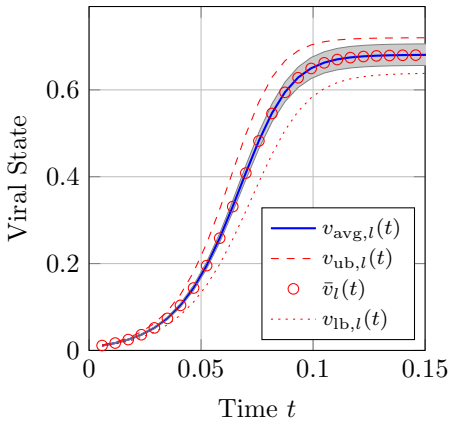

(a) Cell $\mathcal{N}_1$ and relative variance $\sigma_{\mathrm{rel}} = 0.25$.

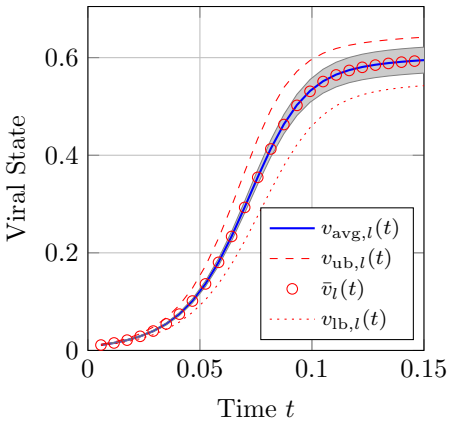

(b) Cell $\mathcal{N}_5$ and relative variance $\sigma_{\mathrm{rel}} = 0.25$.

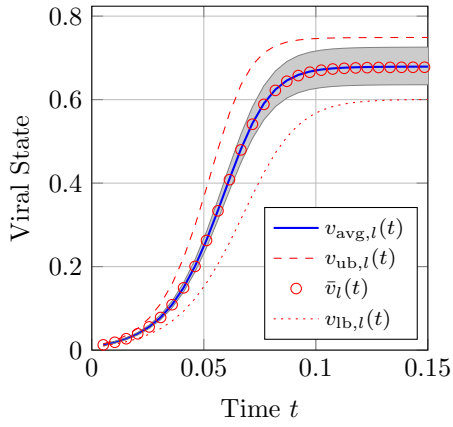

(c) Cell $\mathcal{N}_1$ and relative variance $\sigma_{\mathrm{rel}} = 0.5$.

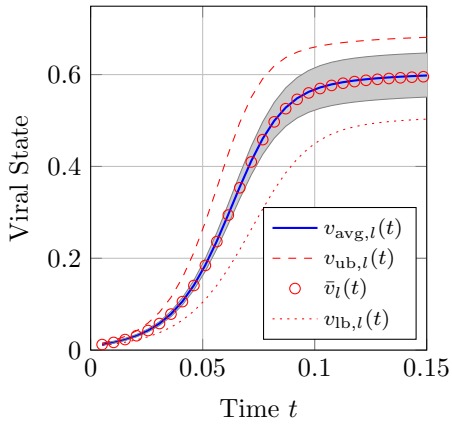

(d) Cell $\mathcal{N}_5$ and relative variance $\sigma_{\mathrm{rel}} = 0.5$.

Figure 2.4: **Low-dimensional approximation of the viral state dynamics.** For a stochastic blockmodel network with $N = 1000$ nodes and $r = 5$ cells, the accuracy of the approximation $\bar{v}_l(t)$ and the tightness of the bounds $v_{\mathrm{lb},l}(t)$, $v_{\mathrm{lb},l}(t)$ are depicted. The reduced-size viral states $\bar{v}(t), v_{\mathrm{lb}}(t)$ and $v_{\mathrm{lb}}(t)$ equal to the linear combination of $m = r = 5$ agitation modes y_l, each of which corresponds to one cell. The first and second row correspond to the relative variance $\sigma_{\mathrm{rel}} = 0.25$ and $\sigma_{\mathrm{rel}} = 0.5$, respectively. The left column corresponds to the largest cell $\mathcal{N}_1$, the right column corresponds to the smallest cell $\mathcal{N}_5$. The viral state $v_i(t)$ of every node i in the respective cell $\mathcal{N}_l$ is within the shaded grey area.

Here, Δt denotes the sampling time, k is the discrete time, and the number of observations n is chosen such that the viral state $v(n\Delta t)$ practically converged to the steady state v_∞.

We applied the Bethe clustering algorithm to three real-world networks, which were accessed through [62]: the *American football* network [63] with $N = 115$ nodes and $L = 613$ links, for which $r = 10$ clusters were detected; the *primary school* contact network (day 1) [64] with $N = 236$ nodes and $L = 5899$ links, resulting in $r = 8$ clusters; and the

train bombing network [65] with $N = 64$ nodes, $L = 243$ links and $r = 3$ identified clusters. For all networks, we considered homogeneous spreading rates β_{ij}, δ_i, which were set such that the basic reproduction number equals $R_0 = 3$. The initial viral state was set to $v_i(\Delta t) = 1/N$ for every node i. To evaluate the accuracy of the Bethe clustering approach, we additionally considered a collection of random partitions, which are obtained by randomly permuting the nodes in the partition π of the Bethe clustering.

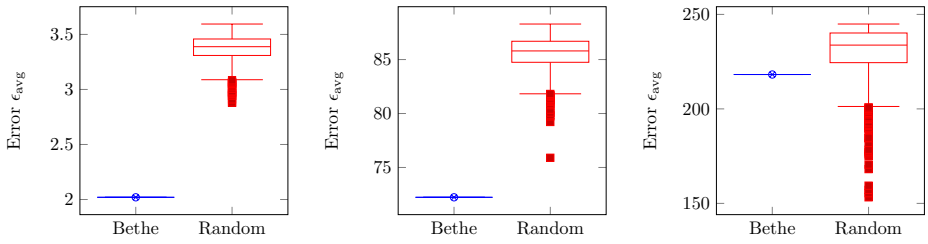

(a) American football. (b) Primary school. (c) Train bombing.

Figure 2.5: **Low-dimensional approximation of epidemics on real-world networks.** The error ϵ_{avg} of the reduced-size viral state $\bar{v}(t)$, in (2.31), for partitions obtained by Bethe clustering and random partitions.

Figure 2.5 shows that, for the football and the school network which have a clear community structure, the Bethe spectral clustering approach results in significantly more accurate low-dimensional viral dynamics $\bar{v}(t)$ than for random partitions. For the train network, which does not possess a clear community structure, there is a smaller advantage of Bethe clustering. Thus, our results indicate that if the network has an underlying community structure, then spectral clustering may be used to find an accurate low-dimensional approximation of the viral state dynamics.

Furthermore, for any partition π of the nodes, there are low-dimensional bounds $v_{\text{lb},l}(t)$, $v_{\text{ub},l}(t)$ of the viral state dynamics, as stated by Theorem 2.19. We define the errors ϵ_{ub} and ϵ_{lb} of the bounds $v_{\text{ub},l}(t)$ and $v_{\text{lb},l}(t)$ analogously to (2.32). Figure 2.6 demonstrates that the partition of the nodes by the Bethe clustering algorithm results in significantly more accurate lower bounds $v_{\text{lb},l}(t)$ than those obtained from random partitions, and somewhat more accurate upper bounds $v_{\text{ub},l}(t)$.

2.5. CONCLUSIONS

In this chapter, we focussed on reducing NIMFA on a network with N nodes to only $m \ll N$ differential equations. We believe that the geometric clustering approach outlined in this work can be applied to other dynamics on networks, particularly to general epidemic models, see Chapter 7, and the class of dynamics in [50–53]. Our contribution is composed of three parts. In the first part, we showed that the viral dynamics evolve on an m-dimensional subspace $\mathcal{V}$ *if and only if* the contact network has an equitable partition with $m_1 \leq m$ cells. Thus, low-dimensional viral state dynamics and the macroscopic structure of equitable partitions are equivalent.

In the second part, we focussed on equitable partitions π with the same spreading rates β_{ij} and δ_i for all nodes i, j in the same cell $\mathcal{N}_l$. We considered the decomposition of the viral state $v(t) = v_{\text{ker}}(t) + \tilde{v}(t)$ into two parts: the term $\tilde{v}(t)$ describes the vi-

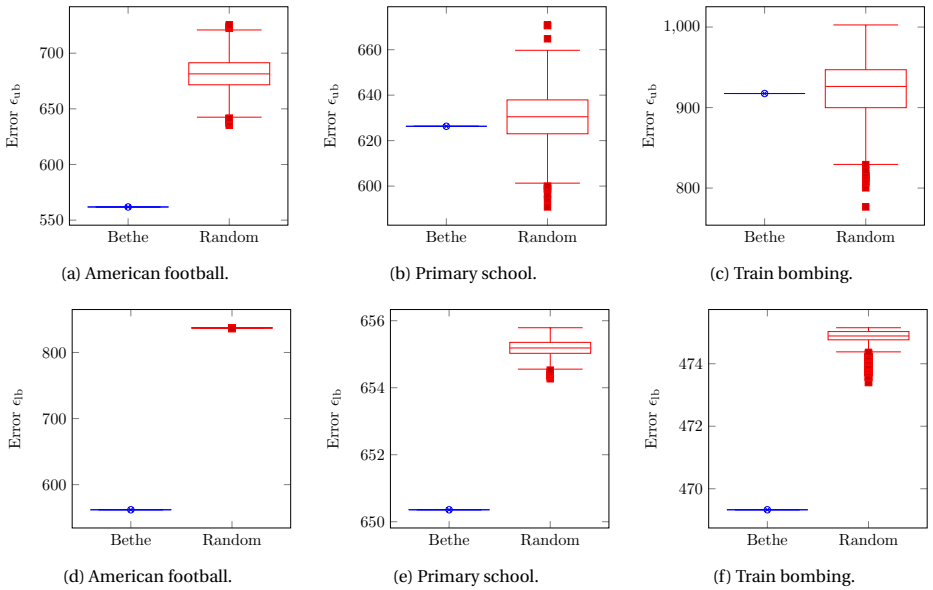

(a) American football. (b) Primary school. (c) Train bombing.

(d) American football. (e) Primary school. (f) Train bombing.

Figure 2.6: **Low-dimensional bounds of epidemics on real-world networks.** The errors of the low-dimensional bounds $v_{\mathrm{lb},I}(t)$ and $v_{\mathrm{ub},I}(t)$, stated by Theorem 2.19, for partitions obtained by Bethe clustering and random partitions. The subplots in the first and second row show the errors ϵ_{ub} and ϵ_{lb} of the upper bound $v_{\mathrm{ub},I}(t)$ and the lower bound $v_{\mathrm{ub},I}(t)$, respectively.

ral state average in every cell $\mathcal{N}_I$; and the term $v_{\mathrm{ker}}(t)$ equals the projection of the viral state $v(t)$ onto the kernel of the infection rate matrix B. By showing that the term $\tilde{v}(t)$ evolves independently from the projection $v_{\mathrm{ker}}(t)$ and the projection $v_{\mathrm{ker}}(t)$ obeys a linear time-varying system, we derived the solution of the NIMFA differential equations on the complete graph for *arbitrary* initial conditions $v(0)$.

Strictly speaking, most contact networks do not have an equitable partition, and an exact reduction of the number of NIMFA equations is not possible. In the third part, we considered arbitrary contact networks with a (not necessarily equitable) partition of the nodes into m cells. For any partition of the nodes, we derived bounds and approximations of the NIMFA epidemics with only m differential equations. The "more equitable" the partition, the more accurate the approximation. Thus, finding (almost) equitable partitions is crucial for reducing an epidemic outbreak in a large population to the interaction of only few groups of individuals.

ACKNOWLEDGEMENTS

We are grateful to Massimo Achterberg and Qiang Liu for helpful discussions on the material in this chapter.

3

THE SOLUTION OF NIMFA AROUND THE EPIDEMIC THRESHOLD

Most epidemic models are described by non-linear differential equations which do not have a closed-form solution. Due to the absence of a closed-form solution, the understanding of the precise dynamics of a virus is rather limited. We derive the solution of the NIMFA differential equations around the epidemic threshold. The solution applies to arbitrarily large and heterogeneous contact networks and heterogeneous spreading parameters, provided that the initial viral state vector is small. Numerical simulations demonstrate that the solution around the epidemic threshold is accurate, also above the epidemic threshold and for general initial viral states.

This chapter is based on [66].

3.1. INTRODUCTION

For real-world epidemics, the regime around epidemic threshold criterion $R_0 = 1$ is of particular interest. In practice, the basic reproduction number R_0 cannot be arbitrarily great, since natural immunities and vaccinations lead to significant curing rates δ_i and the frequency and intensity of human contacts constrain the infection rates β_{ij}. Furthermore, the basic reproduction number R_0 in (1.4) does take disease counter-measures (such as lockdown restrictions and quarantining) into account. Hence, if effective disease counter-measures are deployed, then the basic reproduction number R_0 may be close to 1, also for very contagious diseases. Beyond the spread of infectious diseases, many real-world systems seem to operate in the critical regime around a phase transition [67, 68].

The basic reproduction number R_0 only provides a coarse description of the dynamics of NIMFA (1.1). In this chapter, we aim to give a detailed, *quantitative* picture of the dynamics of the viral state $v(t)$ around the epidemic threshold $R_0 = 1$. More precisely, we derive the closed-form expression of the viral state $v_i(t)$ *for every node* i *at every time* t when $R_0 \downarrow 1$, given that the initial state $v(0)$ is small or parallel[1] to the steady-state vector v_∞. We remark that approximating the stochastic SIS epidemic process by NIMFA is least accurate around the epidemic threshold [20, 69]. Thus, the solution of NIMFA for $R_0 \downarrow 1$, which is derived in this chapter, might be less accurate for the description of the probabilistic SIS process.

In [59], NIMFA (1.3) was solved for a special case: If the adjacency matrix A corresponds to a regular graph and the initial state $v_i(0)$ is the same[2] for every node i, then NIMFA with time-varying, homogeneous spreading parameters $\beta(t), \delta(t)$ has a closed-form solution. Here, we focus on time-invariant but heterogeneous spreading parameters δ_i, β_{ij}, and we solve NIMFA (1.1) for *arbitrary large and heterogeneous* graphs around the threshold $R_0 = 1$.

3.2. NOTATIONS AND ASSUMPTIONS

The basic reproduction number $R_0 = \rho(S^{-1}B)$ is determined by the infection rate matrix B and the curing rate matrix S. Thus, the notation $R_0 \downarrow 1$ is imprecise, since there are infinitely many matrices B, S such that the basic reproduction number R_0 equals 1. To be more precise, we consider a sequence $\left\{\left(B^{(n)}, S^{(n)}\right)\right\}_{n\in\mathbb{N}}$ of infection rate matrices $B^{(n)}$ and curing rate matrices $S^{(n)}$ that converges[3] to a limit (B^*, S^*), such that $\rho\left((S^*)^{-1}B^*\right) = 1$ and

$$\rho\left(\left(S^{(n)}\right)^{-1}B^{(n)}\right) > 1 \quad \forall n \in \mathbb{N}.$$

For the ease of exposition, we drop the index n and replace $B^{(n)}$ and $S^{(n)}$ by the notation B and S, respectively. In particular, we emphasise that the assumptions below apply

[1] The initial state vector $v(0)$ is parallel to the steady-state vector v_∞ if $v(0) = \alpha v_\infty$ for some scalar $\alpha \in \mathbb{R}$.

[2] The steady-state $v_{\infty,i}$ is the same for every node i in a regular graph for homogeneous spreading parameters β, δ. Hence, the initial state $v_i(0)$ is the same for every node i if and only if the initial state $v(0)$ is parallel to the steady-state vector v_∞.

[3] By convergence of the sequence of tuples $\left(B^{(n)}, S^{(n)}\right)$ to the limit (B^*, S^*), we mean that, for all $\epsilon > 0$, there exists an $n_0(\epsilon) \in \mathbb{N}$ such that both $\|B^{(n)} - B^*\|_2 < \epsilon$ and $\|S^{(n)} - S^*\|_2 < \epsilon$ holds for all $n \geq n_0(\epsilon)$.

to every element $\left(B^{(n)}, S^{(n)}\right)$ of the sequence. In Section 3.3 to Section 3.5, we formally abbreviated the limit process $\left(B^{(n)}, S^{(n)}\right) \to (B^*, S^*)$ by the notation $R_0 \downarrow 1$. For the proofs in Appendix B, we use the lengthier but clearer notation $(B, S) \to (B^*, S^*)$. Furthermore, we use the superscript notation Ξ^* to denote the limit of any variable Ξ that depends on the infection rate matrix B and the curing rate matrix S. For instance, δ_i^* denotes the limit of the curing rate δ_i of node i when $(B, S) \to (B^*, S^*)$. The Landau-notation $f(R_0) = \mathcal{O}(g(R_0))$ as $R_0 \downarrow 1$ denotes that $|f(R_0)| \leq \sigma |g(R_0)|$ for some constant σ as $R_0 \downarrow 1$. For instance, it holds that $(R_0 - 1)^2 = \mathcal{O}(R_0 - 1)$ as $R_0 \downarrow 1$.

In the remainder of this chapter, we rely on three assumptions, which we state for clarity in this section.

Assumption 3.1. *For every basic reproduction number $R_0 > 1$, the curing rates are positive and the infection rates are non-negative, i.e., $\delta_i > 0$ and $\beta_{ij} \geq 0$ for all nodes i, j. Furthermore, in the limit $R_0 \downarrow 1$, it holds that $\delta_i \not\to 0$ and $\delta_i \not\to \infty$ for all nodes i.*

We consider Assumption 3.1 a rather technical assumption, since only non-negative rates δ_i and β_{ij} have a physical meaning. Furthermore, if the curing rates δ_i were zero, then the differential equations (1.1) would describe a Susceptible-Infected (SI) epidemic process. In this chapter, we focus on the SIS epidemic process, for which it holds that $\delta_i > 0$.

Assumption 3.2. *For every basic reproduction number $R_0 > 1$, it holds that $v_i(0) \geq 0$ and $v_i(0) \leq v_{\infty,i}$ for every node $i = 1, ..., N$. Furthermore, it holds that $v_i(0) > 0$ for at least one node i.*

For the description of most real-world epidemics, Assumption 3.2 is reasonable for two reasons. First, the total number of infected individuals often is small in the beginning of an epidemic outbreak. (Sometimes, there is even a single patient zero.) Second, a group i often contains many individuals. For instance, the viral state $v_i(t)$ could describe the prevalence of virus in municipality i. Thus, even if there is a considerable total number of infected individuals in group i, the initial *fraction* $v_i(0)$ would be small.

Assumption 3.3. *For every basic reproduction number $R_0 > 1$, the infection rate matrix B is symmetric and irreducible. Furthermore, in the limit $R_0 \downarrow 1$, the infection rate matrix B converges to a symmetric and irreducible matrix.*

Assumption 3.3 holds if and only if the infection rate matrix B (and its limit) corresponds to a connected undirected graph [58].

3.3. THE STEADY-STATE AROUND THE EPIDEMIC THRESHOLD

We define the $N \times N$ *effective infection rate matrix* W as

$$W = S^{-1} B. \tag{3.1}$$

In this section, we state an essential property that we apply to solve the NIMFA equations (1.1) when the basic reproduction number R_0 is close to 1: *The steady-state vector v_∞ converges to a scaled version of the principal eigenvector $x_1(W)$ of the effective infection rate matrix W when $R_0 \downarrow 1$.*

Under Assumptions 3.1 and 3.3, the effective infection rate matrix W is non-negative and irreducible. Hence, the Perron-Frobenius Theorem [58] implies that the matrix W has a unique eigenvalue $\lambda_1(W)$ which equals the spectral radius $\rho(W)$. As we show in the beginning of Appendix B.2, the eigenvalues of the effective infection rate matrix W are real and satisfy $\lambda_1(W) = \rho(W) > \lambda_2(W) \geq ... \geq \lambda_N(W)$. In particular, under Assumptions 3.1 and 3.3, the largest eigenvalue $\lambda_1(W)$, the spectral radius $\rho(W)$ and the basic reproduction number R_0 are the same quantity, i.e., $R_0 = \rho(W) = \lambda_1(W)$. In this chapter and in Appendix B, we shorten the notation $x_k(W)$ and $\lambda_k(W)$ by x_k and λ_k, respectively.

In [70, Lemma 4] it was shown that, for homogeneous NIMFA (1.3), the steady-state vector v_∞ converges to a scaled version of the principal eigenvector of the adjacency matrix A when $R_0 \downarrow 1$. We generalise the results of [70] to heterogeneous NIMFA (1.1):

Theorem 3.4. *Under Assumptions 3.1 and 3.3, the steady-state vector v_∞ obeys*

$$v_\infty = \gamma x_1 + \eta, \tag{3.2}$$

where the scalar γ equals

$$\gamma = (R_0 - 1) \frac{\sum_{l=1}^{N} \delta_l (x_1)_l^2}{\sum_{l=1}^{N} \delta_l (x_1)_l^3}, \tag{3.3}$$

and the $N \times 1$ vector η satisfies $\|\eta\|_2 \leq \mathcal{O}\left((R_0 - 1)^2\right)$ when the basic reproduction number R_0 approaches 1 from above.

Proof. Appendix B.2. □

3.4. THE VIRAL DYNAMICS AROUND THE EPIDEMIC THRESHOLD

In Subsection 3.4.1, we give an intuitive motivation of our solution approach for the NIMFA equations (1.1) when $R_0 \downarrow 1$. In Subsection 3.4.2, we state our main result.

3.4.1. MOTIVATION OF THE SOLUTION APPROACH

For simplicity, this subsection is confined to the homogeneous NIMFA equations (1.3). In numerical simulations, we observed that the proper orthogonal decomposition (2.1) yields an accurate approximation the viral state $v(t)$ for only $m \ll N$ agitation modes $y_1, ..., y_m$. Hence, it holds that $v(t) \approx c_1(t) y_1 + ... + c_m(t) y_m$ at every time t. We consider the most extreme case and represent the viral state $v(t)$ by a scaled version of only $m = 1$ vector y_1, which corresponds to $v(t) \approx c(t) y_1$ for a scalar function $c(t)$. (For simplicity, we replace the notation $c_1(t)$ by $c(t)$ in this chapter.) The viral state $v(t)$ converges to the steady-state vector v_∞ as $t \to \infty$. Hence, a natural choice for the vector y_1 is $y_1 = v_\infty$, which implies that $c(t) \to 1$ as $t \to \infty$. If $R_0 \approx 1$ and $v(0) \approx 0$, then the approximation $v(t) \approx c(t) v_\infty$ is accurate *at all times* $t \geq 0$ due to two intuitive reasons.

1. If $v(t) \approx 0$ when $t \approx 0$, then NIMFA (1.3) is approximated by the linearisation around zero. Hence, it holds that

$$\frac{dv(t)}{dt} \approx \left(\beta A - \delta I\right) v(t) \tag{3.4}$$

when $t \approx 0$. The state $v(t)$ of the linear system (3.4) converges rapidly to a scaled version of the principal eigenvector x_1 of the matrix $(\beta A - \delta I)$. Furthermore, Theorem 3.4 states that $v_\infty \approx \gamma x_1$ when $R_0 \approx 1$. Thus, the viral state $v(t)$ rapidly converges to a scaled version of the steady-state v_∞.

2. Suppose that the viral state $v(t)$ approximately equals to a scaled version of the steady-state vector v_∞. (In other words, the viral state $v(t)$ is "almost parallel" to the vector v_∞.) Then, it holds that

$$v(t) \approx c(t)\, v_\infty \tag{3.5}$$

for some scalar $c(t)$. We insert (3.5) into the NIMFA equations (1.3), which yields that

$$\frac{dc(t)}{dt} v_\infty \approx c(t) \left(\beta A - \delta I\right) v_\infty - \beta c^2(t) \text{diag}(v_\infty) A v_\infty. \tag{3.6}$$

For homogeneous NIMFA (1.3), the steady-state equation (1.5) becomes

$$\left(\beta A - \delta I\right) v_\infty = \beta \text{diag}\left(v_\infty\right) A v_\infty. \tag{3.7}$$

We substitute (3.7) in (3.6) and obtain that

$$\frac{dc(t)}{dt} v_\infty \approx \left(c(t) - c^2(t)\right) \left(\beta A - \delta I\right) v_\infty. \tag{3.8}$$

Since $v_\infty \approx \gamma x_1$ around the epidemic threshold, it holds that $A v_\infty \approx \rho(A) v_\infty$. Hence, we obtain that

$$\frac{dc(t)}{dt} v_\infty \approx \left(c(t) - c^2(t)\right) \left(\beta \rho(A) - \delta\right) v_\infty. \tag{3.9}$$

Left-multiplying (3.9) by v_∞^T and dividing by $v_\infty^T v_\infty$ yields that

$$\frac{dc(t)}{dt} \approx \left(c(t) - c^2(t)\right) \left(\beta \rho(A) - \delta\right). \tag{3.10}$$

The *logistic differential equation* (3.10) has been introduced by [71] as a population growth model and has a closed-form solution.

Due to the two intuitive steps above, NIMFA (1.3) reduces around the threshold $R_0 \approx 1$ to the one-dimension differential equation (3.10). Solving (3.10) for the function $c(t)$ gives an approximation of the viral state $v(t)$ by (3.5). The solution approach is also applicable to other dynamics on networks, see for instance [57].

However, the reasoning above is not rigorous for two reasons. First, the viral state vector $v(t)$ is not exactly parallel to the steady state v_∞. To be more specific, instead of (3.5) it holds that

$$v(t) = c(t)\, v_\infty + \xi(t) \tag{3.11}$$

for some $N \times 1$ *error vector* $\xi(t)$ which is orthogonal to the steady-state vector v_∞. In Subsection 3.4.2, we use (3.11) as an ansatz for solving NIMFA (1.1).

Second, the steady-state vector v_∞ is not exactly parallel to the principal eigenvector x_1. More precisely, we must consider the vector η in (3.2). Since $\eta \neq 0$, the step from (3.8) to (3.9) is affected by an error.

3.4.2. THE SOLUTION AROUND THE EPIDEMIC THRESHOLD

Based on the motivation in Subsection 3.4.1, we aim to solve the NIMFA differential equations (1.1) around the epidemic threshold criterion $R_0 = 1$. The ansatz (3.11) forms the basis for our solution approach. From the orthogonality of the error vector $\xi(t)$ and the steady-state vector v_∞, it follows that the function $c(t)$ at time t equals

$$c(t) = \frac{1}{\|v_\infty\|_2^2} v_\infty^T v(t). \tag{3.12}$$

The error vector $\xi(t)$ at time t follows from (3.11) and (3.12) as

$$\xi(t) = \left(I - \frac{1}{\|v_\infty\|_2^2} v_\infty v_\infty^T\right) v(t). \tag{3.13}$$

Our solution approach is based on two steps. First, we show that[4] the error term $\xi(t)$ satisfies $\xi(t) = \mathcal{O}((R_0-1)^2)$ at every time t when $R_0 \downarrow 1$. Hence, the error term $\xi(t)$ converges to zero *uniformly in time* t. Second, we find the solution of the scalar function $c(t)$ at the limit $R_0 \downarrow 1$.

Assumption 3.2 implies that the viral state $v(t)$ does not overshoot the steady-state v_∞:

Lemma 3.5. *Under Assumptions 3.1 to 3.3, it holds that $v_i(t) \le v_{\infty,i}$ for all nodes i at every time $t \ge 0$. Furthermore, it holds that $0 \le c(t) \le 1$ at every time $t \ge 0$.*

Proof. Appendix B.3. □

Theorem 3.6 states that the error term $\xi(t)$ converges to zero in the order of $(R_0-1)^2$ *uniformly in time* t when $R_0 \downarrow 1$.

Theorem 3.6. *Under Assumptions 3.1 to 3.3, there exist constants $\sigma_1, \sigma_2 > 0$ such that the error term $\xi(t)$ at any time $t \ge 0$ is bounded by*

$$\|\xi(t)\|_2 \le \|\xi(0)\|_2 e^{-\sigma_1 t} + \sigma_2 (R_0-1)^2$$

when the basic reproduction number R_0 approaches 1 from above.

Proof. Appendix B.4. □

We define the constant $\Upsilon(0)$, which depends on the initial viral state $v(0)$, as

$$\Upsilon(0) = \operatorname{artanh}\left(2\frac{v_\infty^T v(0)}{\|v_\infty\|_2^2} - 1\right). \tag{3.14}$$

Furthermore, we define the *viral slope* ϖ, which determines the speed of convergence to the steady-state v_∞, as

$$\varpi = (R_0 - 1)\sum_{l=1}^{N} \delta_l (x_1)_l^2 .$$

Then, building on Theorems 3.4 and 3.6, we obtain our main result:

[4] Theorem 3.4 implies that the steady-state v_∞ satisfies $\|v_\infty\|_2 = \mathcal{O}(R_0-1)$ when $R_0 \downarrow 1$. Thus, also $\|c(t)v_\infty\|_2 = \mathcal{O}(R_0-1)$ at every time t. Thus, a *linear* convergence of the error term $\xi(t)$ to zero, i.e., $\|\xi(t)\|_2 = \mathcal{O}(R_0-1)$, would not be sufficient to show that the viral state $v(t)$ converges to $c(t)v_\infty$ when $R_0 \downarrow 1$.

Theorem 3.7. *Suppose that Assumptions 3.1 to 3.3 hold and that, for some constant $p > 1$, $\|\xi(0)\|_2 = \mathcal{O}((R_0-1)^p)$ when $R_0 \downarrow 1$. Furthermore, define*

$$v_{\text{apx}}(t) = \frac{1}{2}\left(1+\tanh\left(\frac{\bar{\omega}}{2}t+\Upsilon(0)\right)\right)v_\infty. \tag{3.15}$$

Then, there exists some constant $\sigma > 0$ such that

$$\frac{\|v(t)-v_{\text{apx}}(t)\|_2}{\|v_\infty\|_2} \leq \sigma(R_0-1)^{s-1} \quad \forall t \geq 0, \tag{3.16}$$

where $s = \min\{p,2\}$, when the basic reproduction number R_0 approaches 1 from above.

Proof. Appendix B.5. □

We emphasise that Theorem 3.7 holds for any connected graph corresponding to the infection rate matrix B. Theorem 3.7 is in agreement with the universality of the SIS prevalence [72]. The bound (3.16) states a convergence of the viral state $v(t)$ to the approximation $v_{\text{apx}}(t)$ which is uniform in time t. Furthermore, since both the viral state $v(t)$ and the approximation $v_{\text{apx}}(t)$ converge to the steady-state v_∞, it holds that $\|v(t) - v_{\text{apx}}(t)\|_2 \to 0$ when $t \to \infty$. At time $t = 0$, we obtain from Theorem 3.7 and (3.13) that

$$\|v(0)-v_{\text{apx}}(0)\|_2 = \|\xi(0)\|_2.$$

Since $\|\xi(0)\|_2 = \mathcal{O}((R_0-1)^p)$ and, by Theorem 3.4, $\|v_\infty\|_2 = \mathcal{O}(R_0-1)$, we obtain that

$$\frac{\|v(0)-v_{\text{apx}}(0)\|_2}{\|v_\infty\|_2} = \mathcal{O}\left((R_0-1)^{p-1}\right).$$

Hence, for general $t \geq 0$ the approximation error $\|v(t)-v_{\text{apx}}(t)\|_2/\|v_\infty\|_2$ does not converge to zero faster than $\mathcal{O}\left((R_0-1)^{p-1}\right)$, and the bound (3.16) is best possible (up to the constant σ) when $p \leq 2$. With (3.13), the term $\|\xi(0)\|_2$ in Theorem 3.6 can be expressed explicitly with respect to the initial viral state $v(0)$ and the steady-state v_∞.

The vectors $\xi(t)$ and v_∞ are orthogonal. Thus, it holds that $\|v(t)\|_2 = \|c(t)v_\infty\|_2 + \|\xi(t)\|_2$, which implies that $\|\xi(0)\|_2 \leq \|v(0)\|_2$. Hence, if $\|v(0)\|_2 \leq \tilde{\sigma}(R_0-1)^2$ for some constant $\tilde{\sigma}$, then the condition $\|\xi(0)\|_2 = \mathcal{O}((R_0-1)^p)$ in Theorem 3.7 is satisfied for $p = 2$. Figure 3.1 illustrates the uniform convergence result in Theorem 3.7.

Furthermore, if the initial viral state $v(0)$ is parallel to the steady-state vector v_∞, then it holds that $\xi(0) = 0$. Thus, if the initial viral state $v(0)$ is small or parallel to the steady-state vector v_∞, then we obtain that $\xi(0) = 0$, and the bound (3.16) on the approximation error vector becomes

$$\frac{\|v(t)-v_{\text{apx}}(t)\|_2}{\|v_\infty\|_2} \leq \sigma(R_0-1) \quad \forall t \geq 0. \tag{3.17}$$

The solution to NIMFA (1.1) at the epidemic threshold criterion $R_0 = 1$ depends solely on the viral slope $\bar{\omega}$, the steady-state vector v_∞ and the initial viral state $v(0)$. The viral slope $\bar{\omega}$ converges to zero as $R_0 \downarrow 1$. Thus, Theorem 3.7 implies that the convergence time to the steady-state v_∞ goes to infinity when $R_0 \downarrow 1$, even though the steady-state v_∞ converges to zero. More precisely, it holds:

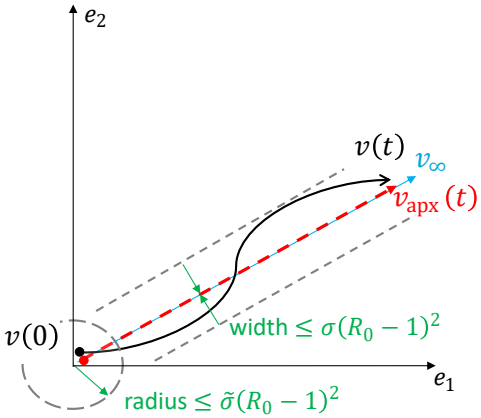

Figure 3.1: **Viral dynamics around the epidemic threshold** $R_0 = 1$**.** An illustration of the uniform convergence of Theorem 3.7 for a network with $N = 2$ nodes. The black curve shows the trajectory of the 2×1 viral state vector $v(t)$ as time t evolves. The blue line shows the steady state v_∞, which satisfies $v_\infty = \mathcal{O}(R_0 - 1)$ as $R_0 \downarrow 1$. The red curve depicts the trajectory closed-form approximation $v_{\text{apx}}(t) = c(t)v_\infty$, which is parallel to the steady state v_∞ at every time t. Theorem 3.7 yields: if the initial viral state $v(0)$ is positive and in the disk of radius $\tilde{\sigma}(R_0 - 1)^2$ for some constant $\tilde{\sigma}$, then the approximation error $\|v(t) - v_{\text{apx}}(t)\|_2$ is bounded by $\sigma(R_0 - 1)^2$ for some constant σ at every time t as $R_0 \downarrow 1$.

Corollary 3.8. *Suppose that Assumptions 3.1 and 3.3 hold and that the initial viral state $v(0)$ equals $v(0) = r_0 v_\infty$ for some scalar $r_0 \in (0,1)$. Then, for any scalar $r_1 \in [r_0, 1)$, the largest time t_{01} at which the viral state satisfies $v_i(t_{01}) \leq r_1 v_{\infty,i}$ for every node i converges to*

$$t_{01} = \frac{1}{\varpi} \log\left(\frac{r_1}{r_0}\frac{1-r_0}{1-r_1}\right)$$

when the basic reproduction number R_0 approaches 1 from above.

Proof. Appendix B.6. □

We combine Theorem 3.4 and Theorem 3.7 to obtain Corollary 3.9.

Corollary 3.9. *Suppose that Assumptions 3.1 to 3.3 hold and that, for some constant $p > 1$, $\|\xi(0)\|_2 = \mathcal{O}((R_0 - 1)^p)$ when $R_0 \downarrow 1$. Furthermore, define*

$$\tilde{v}_{\text{apx}}(t) = \left(1 + \tanh\left(\frac{\varpi}{2}t + \Upsilon(0)\right)\right)\frac{\gamma}{2}x_1. \tag{3.18}$$

Then, there exists some constant $\sigma > 0$ such that

$$\frac{\|v(t) - \tilde{v}_{\text{apx}}(t)\|_2}{\|v_\infty\|_2} \leq \sigma(R_0 - 1)^{s-1} \quad \forall\, t \geq 0,$$

where $s = \min\{p, 2\}$, when the basic reproduction number R_0 approaches 1 from above.

In contrast to Theorem 3.7, the approximation error $\|v(t) - \tilde{v}_{\text{apx}}(t)\|_2$ in Corollary 3.9 does *not* converge to zero when $t \to \infty$, since we replaced the steady-state v_∞ by the first-order approximation of Theorem 3.4. Corollary 3.9 implies that

$$\frac{v_i(t)}{v_j(t)} \to \frac{\tilde{v}_{\text{apx},i}(t)}{\tilde{v}_{\text{apx},j}(t)} = \frac{(x_1)_i}{(x_1)_j} \tag{3.19}$$

at every time t when $R_0 \downarrow 1$, provided that the initial viral state $v(0)$ is small or parallel to the steady-state vector v_∞. From (3.19) it follows that, around the epidemic threshold criterion $R_0 = 1$, the eigenvector centrality [32] fully determines the "dynamical importance" of node i versus node j.

For homogeneous NIMFA (1.3), the infection rate matrix B and the curing rate matrix S reduce to $B = \beta A$ and $S = \delta I$, respectively. Hence, the effective infection rate matrix becomes $W = \frac{\beta}{\delta} A$, and the principal eigenvector x_1 of the effective infection rate matrix W equals the principal eigenvector of the adjacency matrix A. Furthermore, the limit process $R_0 \downarrow 1$ reduces to $\tau \downarrow \tau_c$, with the *effective infection rate* $\tau = \frac{\beta}{\delta}$ and the *epidemic threshold* $\tau_c = 1/\rho(A)$. For homogeneous NIMFA (1.3), Theorem 3.7 reduces to:

Corollary 3.10. *Suppose that Assumptions 3.1 to 3.3 hold and consider the viral state $v(t)$ of homogeneous NIMFA (1.3). Furthermore, suppose that $\|\xi(0)\|_2 = \mathcal{O}\left((\tau - \tau_c)^p\right)$ for some constant $p > 1$ when $\tau \downarrow \tau_c$ and define*

$$v_{\text{apx}}(t) = \frac{1}{2}\left(1 + \tanh\left(\frac{(\tau - \tau_c)\delta}{2\tau_c}\, t + \Upsilon(0)\right)\right) v_\infty. \tag{3.20}$$

Then, there exists some constant $\sigma > 0$ such that

$$\frac{\|v(t) - v_{\text{apx}}(t)\|_2}{\|v_\infty\|_2} \leq \sigma(\tau - \tau_c)^{s-1} \quad \forall\, t \geq 0,$$

where $s = \min\{p, 2\}$, when the effective infection rate τ approaches the epidemic threshold τ_c from above.

Proof. Appendix B.7. □

From Corollary 3.10, we can obtain the analogue to Corollary 3.9 for NIMFA (1.3) with homogeneous spreading parameters β, δ. Furthermore, the approximation $v_{\text{apx}}(t)$ defined by (3.20) equals the exact solution [59] of homogeneous NIMFA (1.3) on a regular graph, provided that the initial state $v_i(0)$ is the same for every node i. In particular, the *net dose* $\varrho(t)$, a crucial quantity in [59, 73], is related to the viral slope ϖ via $\varrho(t) = \varpi t$.

As illustrated by Figure 3.1, the viral state $v(t)$ converges to the one-dimensional dynamics $v_{\text{apx}}(t)$ as $R_0 \downarrow 1$. *Are there networks for which the approximation $v_{\text{apx}}(t)$ is exact, for any basic reproduction number $R_0 > 1$?* The infection rate matrix B is *regular* if

$$\sum_{k=1}^{N} \beta_{ik} = \sum_{k=1}^{N} \beta_{jk} \tag{3.21}$$

for all nodes i, j. From Theorem 2.14, we obtain:

Corollary 3.11. *Suppose that Assumption 2.7 and Assumptions 3.1 to 3.3 hold and consider some fixed basic reproduction number $R_0 > 1$. Then, there is an $m = 1$ dimensional invariant set $\mathcal{V} = \text{span}\{y_1\}$ of NIMFA (1.2) if and only if $\mathcal{V}_0 = \emptyset$, the agitation mode equals either $y_1 = v_\infty / \|v_\infty\|_2$ or $y_1 = -v_\infty / \|v_\infty\|_2$ and the infection rate matrix B is regular. Furthermore, the approximation $v_{\text{apx}}(t)$ is exact if and only if the matrix B is regular and $v(0) = c(0)\, v_\infty$ for some scalar $c(0)$.*

Proof. Appendix B.8 □

3

Theorem 3.7 and Corollary 3.10 suggest that, around the epidemic threshold criterion $R_0 = 1$, the dynamics of heterogeneous NIMFA (1.1) closely resembles the dynamics of homogeneous NIMFA (1.3). In particular, we pose the question: *Can heterogeneous NIMFA (1.1) be reduced to homogeneous NIMFA (1.3) around the epidemic threshold criterion $R_0 = 1$ by choosing the homogeneous spreading parameters β, δ and the adjacency matrix A accordingly?*

Theorem 3.12. *Consider heterogeneous NIMFA (1.1) with given spreading parameters β_{ij}, δ_i. Suppose that Assumptions 3.1 to 3.3 hold and that, for some constant $p > 1$, $\|\xi(0)\|_2 = \mathcal{O}\left((R_0 - 1)^p\right)$ when the basic reproduction number R_0 approaches 1 from above. Define the homogeneous NIMFA system*

$$\frac{d\, v_{i,\text{hom}}(t)}{dt} = -\delta_{\text{hom}}\, v_{i,\text{hom}}(t) + \beta_{ii,\text{hom}} \left(1 - v_{i,\text{hom}}(t)\right) v_{i,\text{hom}}(t) + \left(1 - v_{i,\text{hom}}(t)\right) \beta_{\text{hom}} \sum_{j=1, j\neq i}^{N} v_{j,\text{hom}}(t), \tag{3.22}$$

where the homogeneous curing rate δ_{hom} equals

$$\delta_{\text{hom}} = \frac{\sum_{l=1}^{N} \delta_l\, (x_1)_l^3}{\sum_{l=1}^{N} (x_1)_l^3}, \tag{3.23}$$

the homogeneous infection rate β_{hom} equals

$$\beta_{\text{hom}} = \frac{\delta_{\text{hom}}}{\sum_{l=1}^{N} (x_1)_l} \left(1 + \gamma \sum_{l=1}^{N} (x_1)_l^3\right) \min_{l=1,\ldots,N} (x_1)_l \tag{3.24}$$

with the variable γ defined by (3.3), and the self-infection rates $\beta_{ii,\text{hom}}$ equal

$$\beta_{ii,\text{hom}} = \beta_{\text{hom}} \left(\frac{1}{\min_{l=1,\ldots,N} (x_1)_l} - \frac{1}{(x_1)_i} \right) \sum_{j=1}^{N} (x_1)_j + \beta_{\text{hom}}.$$

Then, if $v_{\text{hom}}(0) = v(0)$, there exists some constant $\sigma > 0$ such that

$$\frac{\|v(t) - v_{\text{hom}}(t)\|_2}{\|v_\infty\|_2} \leq \sigma (R_0 - 1)^{s-1} \quad \forall\, t \geq 0,$$

where $s = \min\{p, 2\}$, when the basic reproduction number R_0 approaches 1 from above.

Proof. Appendix B.9. □

In other words, when $R_0 \downarrow 1$, for any contact network and any spreading parameters δ_i, β_{ij}, heterogeneous NIMFA (1.1) can be reduced to homogeneous NIMFA (1.3) on a complete graph plus self-infection rates $\beta_{ii,\text{hom}}$. We emphasise that the sole influence of the topology on the viral spread is given by the self-infection rates $\beta_{ii,\text{hom}}$. *Thus, under Assumptions 3.1 to 3.3, the network topology has a surprisingly small impact on the viral spread around the epidemic threshold.*

3.5. NUMERICAL EVALUATION

We are interested in evaluating the accuracy of the closed-form expression $v_{\text{apx}}(t)$, given by (3.15), when the basic reproduction number R_0 is close, but not equal, to one. We generate an adjacency matrix A according to different random graph models. If $a_{ij} = 1$, then we set the infection rates β_{ij} to a uniformly distributed random number in $[0.4, 0.6]$ and, if $a_{ij} = 0$, then we set $\beta_{ij} = 0$. We set the *initial curing rates* $\delta_l^{(0)}$ to a uniformly distributed random number in $[0.4, 0.6]$. To set the basic reproduction number R_0, we set the curing rates δ_l to a multiple of the initial curing rates $\delta_l^{(0)}$, i.e. $\delta_l = \sigma\delta_l^{(0)}$ for every node l and some scalar σ such that $\rho(W) = R_0$. Thus, we realise the limit process $R_0 \downarrow 1$ by changing the scalar σ. Only in Subsection 3.5.2, we consider homogeneous spreading parameters by setting $\beta_{ij} = 0.5$ and $\delta_i^{(0)} = 0.5$ for all nodes i, j. Numerically, we obtain the "exact" NIMFA viral state sequence $v(t)$ by Euler's method for discretisation, i.e.,

$$\left.\frac{dv_i(t)}{dt}\right|_{t=k\Delta t} \approx \frac{v_i(k\Delta t) - v_i((k-1)\Delta t)}{\Delta t} \tag{3.25}$$

for a small sampling time Δt and a discrete time slot $k \in \mathbb{N}$. In Chapter 4, we derive an upper bound $\Delta t_{\max}$ on the sampling time Δt which ensures that the discretisation (3.25) of NIMFA (1.1) converges to the steady-state v_∞. We set the sampling time to $\Delta t = \Delta t_{\max}/100$. Except for Subsection 3.5.3, we set the initial viral state to $v(0) = 0.01\, v_\infty$. We define the convergence time t_{conv} as the smallest time t at which

$$\left|v_i(t_{\text{conv}}) - v_{\infty,i}\right| \leq 0.01$$

holds for every node i. Thus, at the convergence time t_{conv} the viral state $v(t_{\text{conv}})$ has practically converged to the steady-state v_∞. We evaluate Theorem 3.7 with respect to the approximation error ϵ_V, which we define as

$$\epsilon_V = \frac{1}{N t_{\text{conv}}} \sum_{i=1}^{N} \int_0^{t_{\text{conv}}} \frac{\left|v_i(\tilde{t}) - v_{\text{apx},i}(\tilde{t})\right|}{v_{\infty,i}} d\tilde{t}.$$

All results are averaged over 100 randomly generated networks.

3.5.1. APPROXIMATION ACCURACY AROUND THE EPIDEMIC THRESHOLD

We generate a Barabási-Albert random graph [8] with $N = 500$ nodes and the parameters $m_0 = 5$, $m_{\text{BA}} = 2$. Figure 3.2 gives an impression of the accuracy of the approximation of Theorem 3.7 around the epidemic threshold criterion $R_0 = 1$. For a basic reproduction

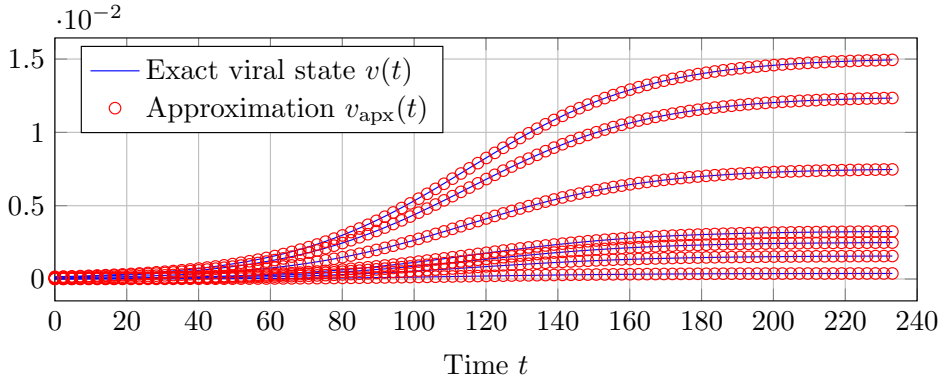

(a) Basic reproduction number $R_0 = 1.01$.

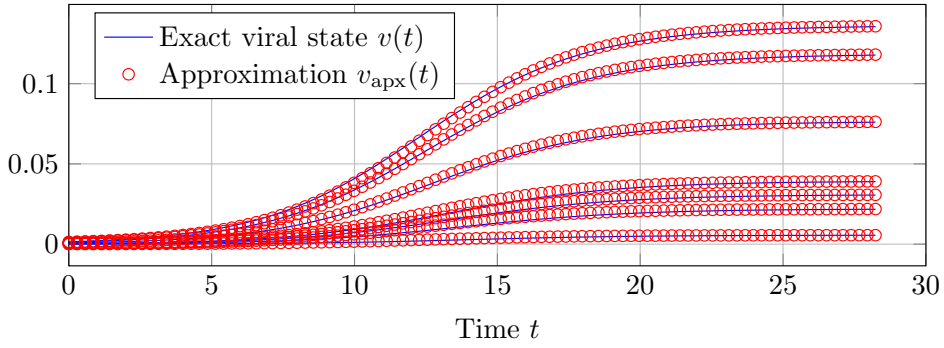

(b) Basic reproduction number $R_0 = 1.1$.

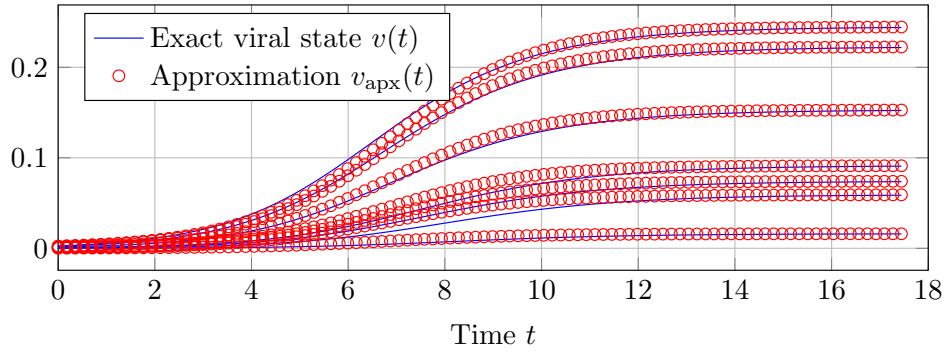

(c) Basic reproduction number $R_0 = 1.2$.

Figure 3.2: **Closed-form solution around the epidemic threshold.** For a Barabási-Albert random graph with $N = 500$ nodes, the approximation accuracy of Theorem 3.7 is depicted. Each of the sub-plots shows the viral state traces $v_i(t)$ of seven different nodes i, including the node i with the greatest steady-state $v_{\infty,i}$.

number $R_0 \leq 1.1$, the difference of the closed-form expression of Theorem 3.7 to the

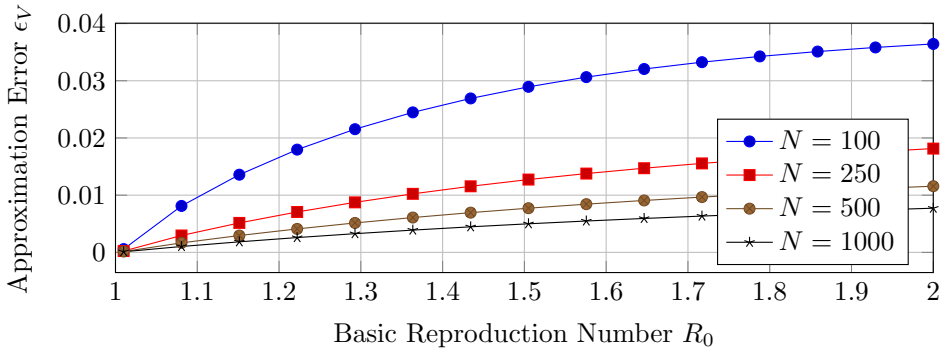

(a) Erdős-Rényi random graphs.

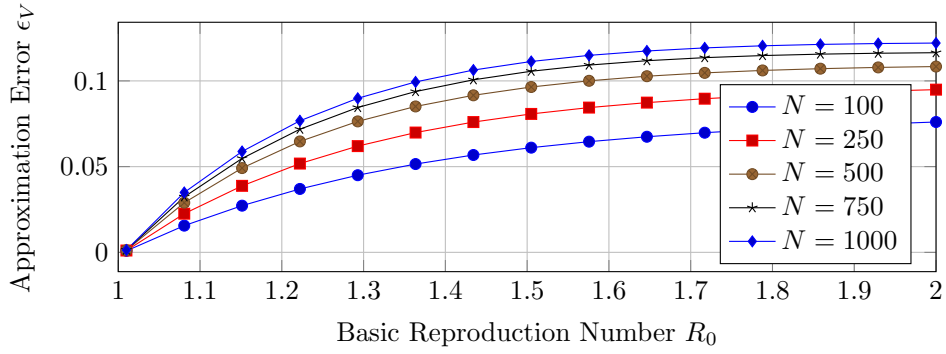

(b) Barabási-Albert random graphs.

Figure 3.3: **Accuracy of closed-form approximation versus the basic reproduction number R_0.** The approximation error ϵ_V of the NIMFA solution versus the basic reproduction number R_0 for different network sizes N.

exact NIMFA viral state trace is negligible.

We aim for a better understanding of the accuracy of the closed-form expression of Theorem 3.7 when the basic reproduction number R_0 converges to one. We generate Barabási-Albert and Erdős-Rényi connected random graphs with $N = 100, \ldots, 1000$ nodes. The link probability of the Erdős-Rényi graphs [74] is set to $p_{\text{ER}} = 0.05$. Figure 3.3 illustrates the convergence of the approximation of Theorem 3.7 to the exact solution of NIMFA (1.1). Around the threshold criterion $R_0 = 1$, the approximation error ϵ_V converges linearly to zero with respect to the basic reproduction number R_0, which is in agreement with Theorem 3.7. The greater the network size N, the greater is the approximation error ϵ_V for Barabási-Albert networks. The greater the network size N, the lower is the approximation error ϵ_V for Erdős-Rényi graphs.

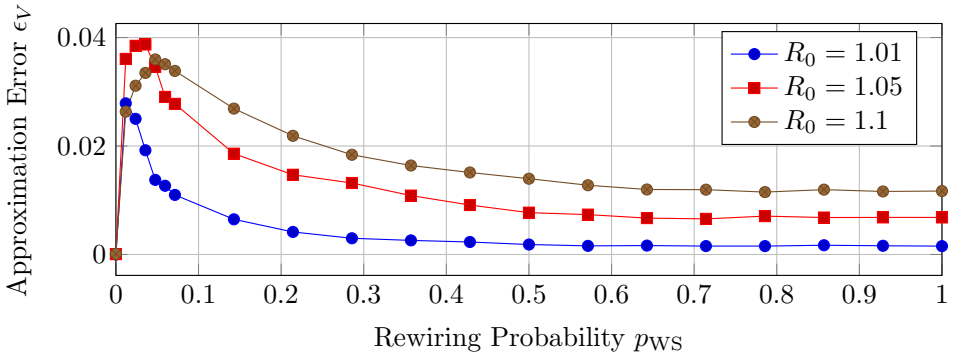

Figure 3.4: **Approximation accuracy versus degree heterogeneity.** The approximation error ϵ_V versus the link rewiring probability p_{WS} for Watts-Strogatz random graphs with $N = 100$ nodes and homogeneous spreading parameters β, δ.

3.5.2. IMPACT OF DEGREE HETEROGENEITY ON THE APPROXIMATION ACCURACY

For NIMFA (1.3) with homogeneous spreading parameters β, δ, the approximation $v_{\mathrm{apx}}(t)$ defined by (1.3) is exact if the contact network is a regular graph. We are interested how the approximation accuracy changes with respect to the heterogeneity of the node degrees. We generate Watts-Strogatz [75] random graphs with $N = 100$ nodes and an average node degree of 4. We vary the link rewiring probability p_{WS} from $p_{\mathrm{WS}} = 0$, which correspond to a regular graph, to $p_{\mathrm{WS}} = 1$, which corresponds to a "completely random" graph. Figure 3.4 depicts the approximation error ϵ_V versus the rewiring probability p_{WS} for homogeneous spreading parameters β, δ. Interestingly, the approximation error reaches a maximum and improves when the adjacency matrix A is more random.

3.5.3. GENERAL INITIAL VIRAL STATES

Theorem 3.7 required that the initial error $\xi(0)$ converges to zero, which means that the initial viral state $v(0)$ must be parallel to the steady-state v_∞ or, since $\|\xi(0)\|_2 \leq \|v(0)\|_2$, converge to zero. For general initial viral states $v(0)$ with $\xi(0) \neq 0$, it holds that $v_{\mathrm{apx}}(0) \neq v(0)$ since the approximation $v_{\mathrm{apx}}(0)$ is parallel to the steady-state vector v_∞. Hence, the approximation $v_{\mathrm{apx}}(t)$ cannot converge point-wise to the viral state $v(t)$ when $R_0 \downarrow 1$.

To investigate whether the approximation of Theorem 3.7 is accurate also when the initial error $\xi(0)$ does not converge to zero, we set the initial viral state $v_i(0)$ of every node i to a uniformly distributed random number in $(0, r_0 v_{\infty,i}]$ for some scalar $r_0 \in (0, 1]$. By increasing the scalar r_0, the initial viral state $v(0)$ is "more random". Figure 3.5 shows that the approximation error ϵ_V is almost unaffected by an initial viral state $v(0)$ that is neither parallel to the steady-state v_∞ nor small. Figure 3.6 shows that the viral state $v(t)$ converges rapidly to the approximation $v_{\mathrm{apx}}(t)$ as time t increases.

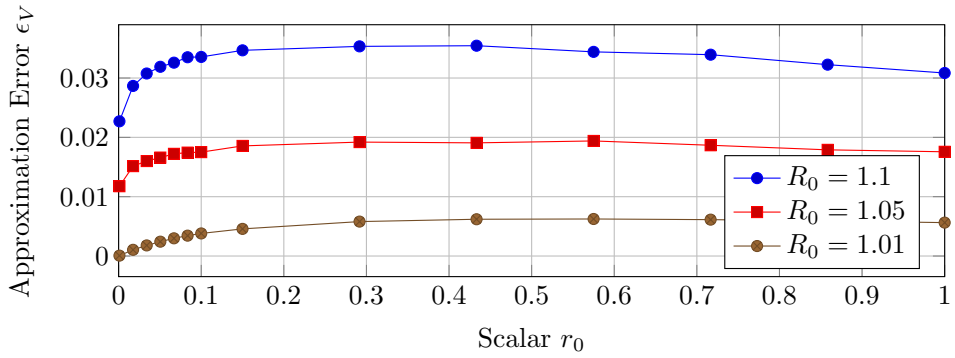

Figure 3.5: **Approximation accuracy versus variance of the initial viral state $v(0)$.** The approximation error ϵ_V versus the scalar r_0, which controls the variance of the randomly generated initial viral state $v(0)$, for Barabási-Albert networks with $N = 250$ nodes.

3.5.4. DIRECTED INFECTION RATE MATRICES

The proof of Theorem 3.7 relies on a symmetric infection rate matrix B as stated by Assumption 3.3. We perform the same numerical evaluation as shown in Figure 3.3 in Subsection 3.5.1 with the only difference that we generate strongly connected *directed* Erdős-Rényi random graphs. Figure 3.7 demonstrates the accuracy of the approximation $v_{\text{apx}}(t)$ for a directed infection rate matrix B, which leads us to:

Conjecture 3.13. *Suppose that Assumptions 3.1 and 3.2 hold and that the infection rate matrix B is irreducible but, in contrast to Assumption 3.3, not necessarily symmetric. Then, the viral state $v(t)$ is "accurately described" by the approximation $v_{\text{apx}}(t)$ when the basic reproduction number R_0 approaches 1 from above.*

3.5.5. ACCURACY OF THE CONVERGENCE TIME APPROXIMATION

Corollary 3.8 gives the expression of the convergence time t_{01} from the initial viral state $v(0) = r_0 v_\infty$ to the viral state $v(t_{01}) \leq r_1 v_\infty$ for any scalars $0 < r_0 \leq r_1 < 1$ around the epidemic threshold $R_0 = 1$. We set the scalars to $r_0 = 0.01$ and $r_1 = 0.9$ and define the approximation error

$$\epsilon_t = \frac{\left|\hat{t}_{01} - t_{01}\right|}{t_{01}},$$

where t_{01} denotes the exact convergence time and $\hat{t}_{01}$ denotes the approximate expression of Corollary 3.8.

We generate Barabási-Albert and Erdős-Rényi random graphs with $N = 100, \ldots, 1000$ nodes. Figure 3.8 shows that Corollary 3.8 gives an accurate approximation of the convergence time t_{01} when the basic reproduction number R_0 is reasonably close to one.

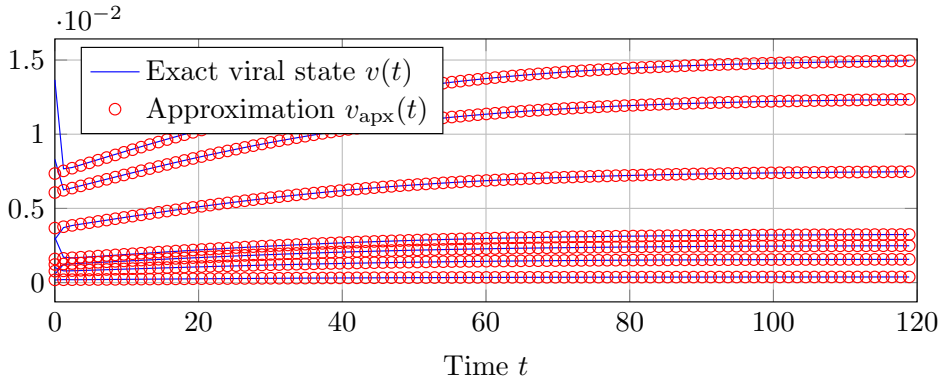

(a) Viral state $v(t)$ until time $t = 120$.

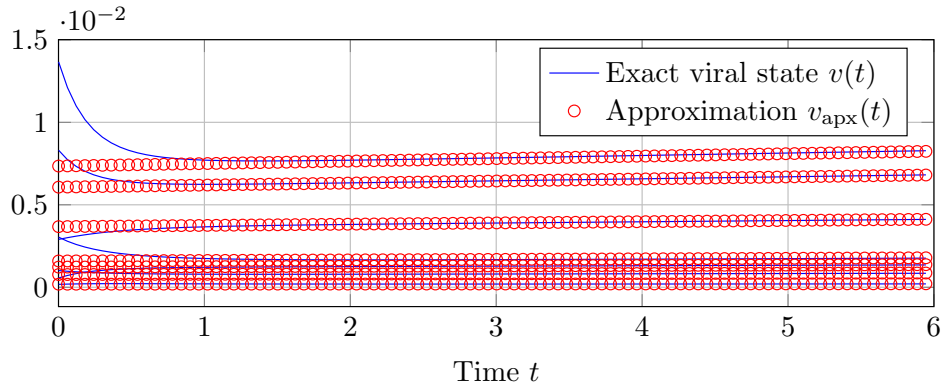

(b) Viral state $v(t)$ until time $t = 6$.

Figure 3.6: **Closed-form approximation for general initial viral states $v(0)$.** For a Barabási-Albert random graph with $N = 500$ nodes, a basic reproduction number $R_0 = 1.01$ and a randomly generated initial viral state $v(0)$, the approximation accuracy of Theorem 3.7 is depicted. The viral state traces $v_i(t)$ of seven different nodes i are depicted.

3.5.6. REDUCTION TO A COMPLETE GRAPH WITH HOMOGENEOUS SPREADING PARAMETERS

Theorem 3.12 states that, around the epidemic threshold, heterogeneous NIMFA (1.1) on any graph can be reduced to homogeneous NIMFA (1.3) on a complete graph. Figure 3.9 and Figure 3.10 show the approximation accuracy of Theorem 3.12 for Erdős-Rényi and Barabási-Albert random graphs, respectively. To accurately approximate heterogeneous NIMFA on Barabási-Albert graphs by homogeneous NIMFA on a complete graph, the basic reproduction number R_0 must be closer to 1 than for Erdős-Rényi graphs.

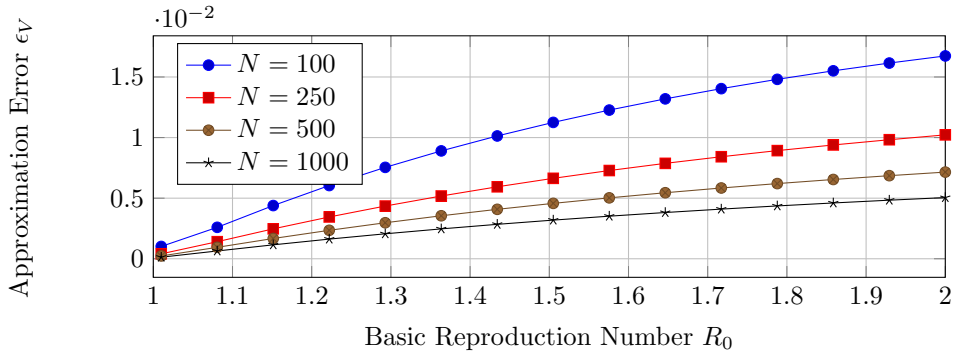

Figure 3.7: **Approximation accuracy for directed networks.** The approximation error ϵ_V of the NIMFA solution versus the basic reproduction number R_0 for *directed* Erdős-Rényi graphs for different network sizes N.

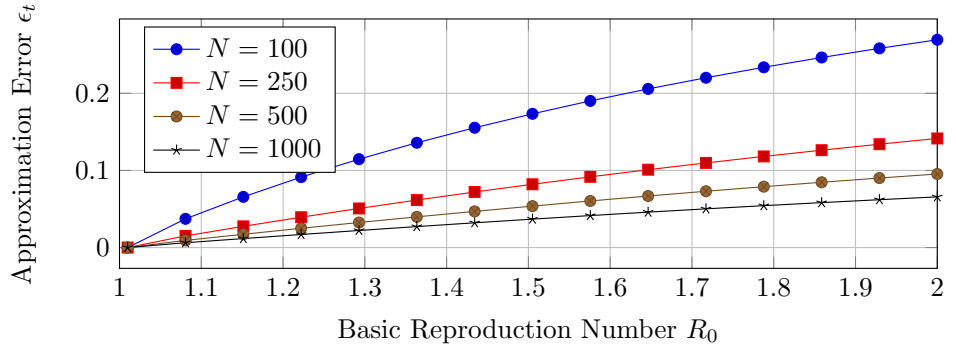

(a) Erdős-Rényi random graphs.

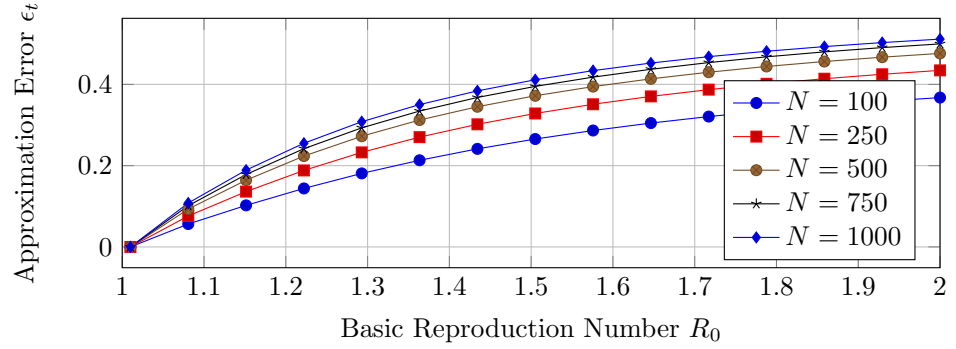

(b) Barabási-Albert random graphs.

Figure 3.8: **Closed-form approximation of the convergence time.** The approximation error ϵ_t of the convergence time t_{01} versus the basic reproduction number R_0 for different network sizes N.

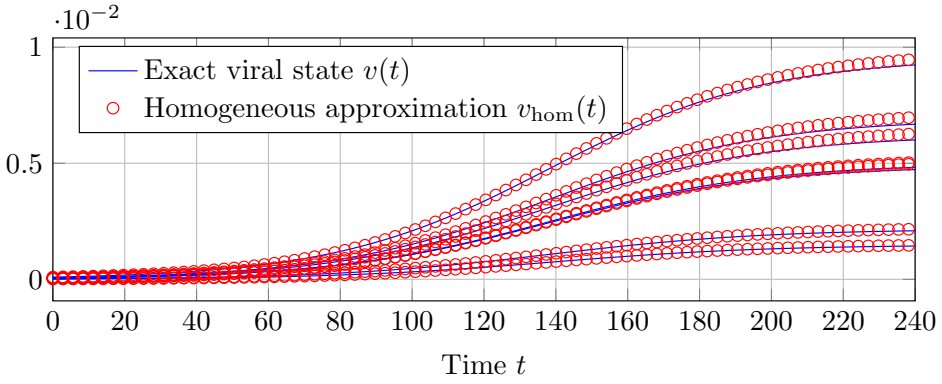

(a) Erdős-Rényi random graph and $R_0 = 1.01$.

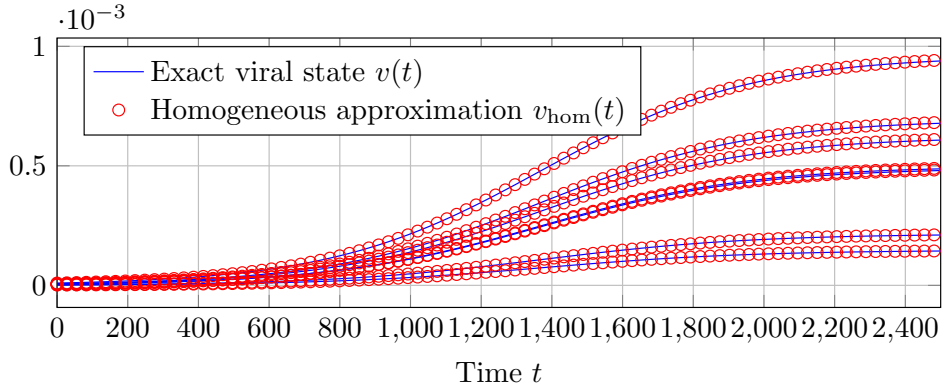

(b) Erdős-Rényi random graph and $R_0 = 1.001$.

Figure 3.9: **Reducing heterogeneous NIMFA on Erdős-Rényi graphs to NIMFA on a complete graph.** The approximation accuracy of Theorem 3.12 on a Erdős-Rényi random graph with $N = 100$ nodes. Each of the sub-plots shows the viral state traces $v_i(t)$ of seven different nodes i, including the node i with the greatest steady-state $v_{\infty,i}$.

3.6. CONCLUSIONS

We solved the NIMFA governing equations (1.1) with heterogeneous spreading parameters around the epidemic threshold when the initial viral state $v(0)$ is small or parallel to the steady-state v_∞, provided that the infection rates are symmetric ($\beta_{ij} = \beta_{ji}$). Numerical simulations demonstrate the accuracy of the solution when the basic reproduction number R_0 is close, but not equal, to one. Furthermore, the solution serves as an accurate approximation also when the initial viral state $v(0)$ is neither small nor parallel to the steady-state v_∞. We observe four important implications of the solution of NIMFA around the epidemic threshold.

First, the viral state $v(t)$ is almost parallel to the steady-state v_∞ for every time $t \geq 0$. On the one hand, since the viral dynamics approximately remain in a one-dimensional subspace of $\mathbb{R}^N$, an accurate network reconstruction around the epidemic threshold is

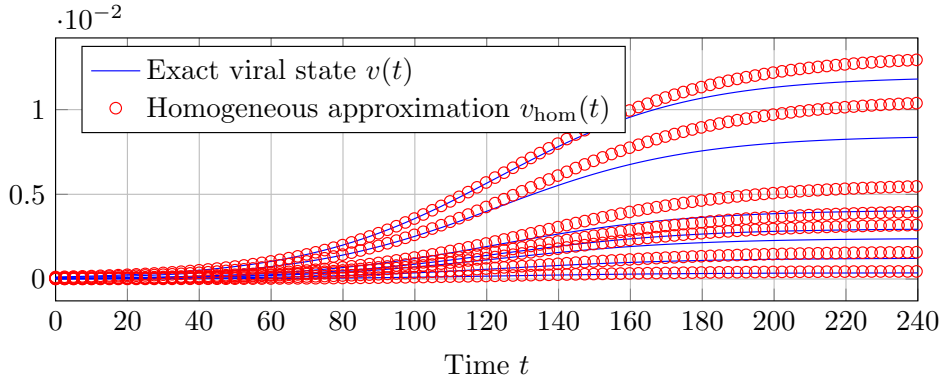

(a) Barabási-Albert random graph and $R_0 = 1.01$.

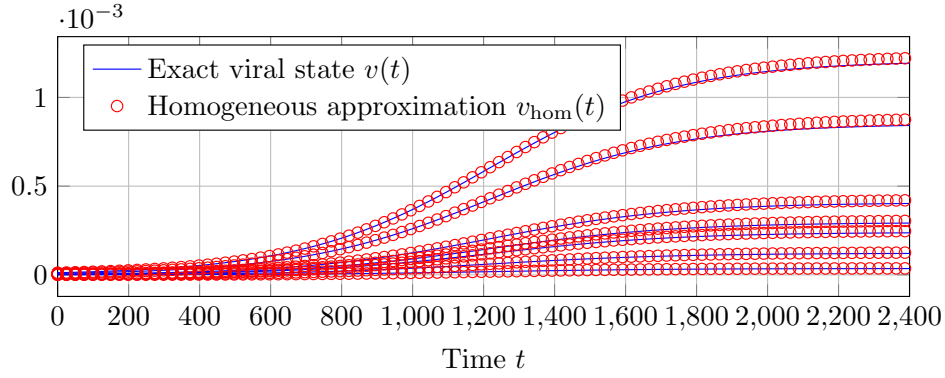

(b) Barabási-Albert random graph and $R_0 = 1.001$.

Figure 3.10: **Reducing heterogeneous NIMFA on Barabási-Albert graphs to NIMFA on a complete graph.** The approximation accuracy of Theorem 3.12 on a Barabási-Albert random graph with $N = 100$ nodes. Each of the sub-plots shows the viral state traces $v_i(t)$ of seven different nodes i, including the node i with the greatest steady-state $v_{\infty,i}$

numerically not viable around the epidemic threshold, see Chapter 7. Furthermore, when the basic reproduction number R_0 is large, then the viral state $v(t)$ rapidly converges to the steady-state v_∞, which, again, prevents an accurate network reconstruction. On the other hand, only the principal eigenvector x_1 of the effective infection rate matrix W and the viral slope ϖ are required to predict the viral state dynamics around the epidemic threshold. *Thus, around the epidemic threshold, the prediction of an epidemic does not require an accurate network reconstruction.*

Second, the eigenvector centrality (with respect to the principal eigenvector x_1 of the effective infection rate matrix W) gives a complete description of the dynamical importance of a node i around the epidemic threshold. *In particular, the ratio $v_i(t)/v_j(t)$ of the viral states of two nodes i, j does not change over time t.*

Third, around the epidemic threshold, we gave an expression of the convergence

time t_{01} to approach the steady-state v_∞. The viral state $v(t)$ converges to the steady-state v_∞ exponentially fast. *However, as the basic reproduction number R_0 approaches one, the convergence time t_{01} goes to infinity.*

Fourth, around the epidemic threshold, NIMFA with heterogeneous spreading parameter on any graph can be reduced to NIMFA with homogeneous spreading parameters on the complete graph plus self-infection rates.

Potential generalisations of the solution of NIMFA to non-symmetric infection rate matrices B or time-dependent spreading parameters $\beta_{ij}(t), \delta_I(t)$ stand on the agenda of future research.

ACKNOWLEDGEMENTS

We are grateful to Karel Devriendt for his help in proving Theorem 3.12.

4

THE DYNAMICS OF DISCRETE-TIME NIMFA

The majority of epidemic models are formulated in continuous time. However, processing real-world epidemic data and simulating epidemics is done digitally. Hence, continuous-time epidemic models are usually approximated in discrete time. The time-discretisation must be done carefully, since there is no guarantee that properties of continuous-time epidemic models, such as the stability of equilibria, also hold for the respective discrete-time approximation. In this chapter, we analyse NIMFA in discrete time for general, directed networks with heterogeneous spreading parameters. In particular, we show that the viral state is increasing and does not overshoot the steady-state, the steady-state is exponentially stable, and we provide linear systems that bound the viral state evolution. Thus, the discrete-time NIMFA model succeeds to capture the qualitative behaviour of a viral spread and provides a powerful means to study real-world epidemics.

This chapter is based on [76].

4.1. INTRODUCTION

Describing the evolution of an epidemic in discrete time $k \in \mathbb{N}$ is advantageous for two reasons. First, for the simulation of a viral spread, an implicit discretisation is performed for the majority of continuous-time epidemic models due to the absence of closed-form solutions. Hence, a more accurate approach is to directly study the epidemic model in discrete time. Second, data on real-world epidemics is often collected periodically. Thus, discrete-time models circumvent the challenge of incomplete knowledge of the viral state of time spans between two measurements. In Chapter 8, we use discrete-time epidemic models to predict the spread of COVID-19. Since the number of SARS-CoV-2 infections is reported daily, a natural choice is that the discrete time k corresponds to days.

The *discrete-time* NIMFA epidemic model is obtained from continuous-time NIMFA (1.1) by applying Euler's method [77], with a "sufficiently small" sampling time[1] $\Delta t > 0$, and the discrete-time curing and infection probabilities follow as $\delta_{\Delta t,i} = \delta_i \Delta t$ and $\beta_{\Delta t,ij} = \beta_{ij} \Delta t$, respectively.

Definition 4.1 (Discrete-Time NIMFA Model [25, 78])**.** The viral state $v_i[k]$ of the discrete-time NIMFA model evolves in discrete time $k = 1, 2, \ldots$ as

$$v_i[k+1] = (1 - \delta_{\Delta t,i}) v_i[k] + (1 - v_i[k]) \sum_{j=1}^{N} \beta_{\Delta t,ij} v_j[k] \tag{4.1}$$

for every group $i = 1, \ldots, N$. Here, $\delta_{\Delta t,i} > 0$ is the discrete-time *curing probability*, and $\beta_{\Delta t,ij} \geq 0$ is the discrete-time *infection probability* from group j to group i.

As vector equations, (4.1) reads

$$v[k+1] = \operatorname{diag}(u - \delta_{\Delta t}) v[k] + \operatorname{diag}(u - v[k]) B_{\Delta t} v[k], \tag{4.2}$$

where the viral state vector at discrete time k equals $v[k] = (v_1[k], \ldots, v_N[k])^T$, the curing probability vector equals $\delta_{\Delta t} = (\delta_{\Delta t,1}, \ldots, \delta_{\Delta t,N})^T$, and the $N \times N$ infection probability matrix $B_{\Delta t}$ is composed of the elements $\beta_{\Delta t,ij}$. The steady-state vector $v_\infty = (v_{\infty,1}, \ldots, v_{\infty,N})^T$ is, if existent, the non-zero equilibrium of the discrete-time NIMFA model (4.1), which satisfies $v[k+1] = v[k] = v_\infty$, and hence,

$$\sum_{j=1}^{N} \beta_{\Delta t,ij} v_{\infty,j} = \delta_{\Delta t,i} \frac{v_{\infty,i}}{1 - v_{\infty,i}}, \quad i = 1, \ldots, N. \tag{4.3}$$

For any sampling time Δt, the steady state of discrete-time NIMFA (4.1) coincides with the steady state of continuous-time NIMFA (1.1) given by the solution to (1.5).

In this chapter, we focus on four research questions:

1. *Under which conditions does the viral state $v[k]$ approach the endemic viral state v_∞?* To the best of our knowledge, the convergence of the viral state $v(t)$ to the steady-state v_∞ has only been shown [18, 79] for the *continuous-time* NIMFA model (1.1). In fact, Ahn and Hassibi [78] gave a counterexample for which the steady-state v_∞ of the discrete-time NIMFA (4.1) is unstable.

[1] We make the condition "sufficiently small" more precise by Assumption 4.3.

2. There does not seem to be a general closed-form solution of the NIMFA difference equation (4.1). *But, is there an approximate and simpler description of the viral state evolution?* Of particular interest is a worst-case scenario of the viral spread, i.e. an upper bound of the viral state $v_i[k]$ for any node i at any time k.

3. In practice, the viral state $v_i[k]$ often refers to a *cumulative and increasing* quantity. For instance [25], the viral state $v_i[k]$ of node i may refer to the fraction of deaths by cholera of group i up to time k. *Under which conditions is the viral state $v_i[k]$ increasing?*

4. *How quickly does the virus spread?* More specifically, how fast does the viral state $v[k]$ approach the steady-state v_∞?

4.2. NOTATIONS AND ASSUMPTIONS

We define the $N \times N$ matrix R as

$$R = I - \mathrm{diag}(\delta_{\Delta t}) + B_{\Delta t}. \tag{4.4}$$

Furthermore, in this chapter and in Appendix C, we shorten the eigenvector and eigenvalue notation $x_k(R)$, $\lambda_k(R)$ by x_k, λ_k, respectively.

Assumption 4.2. *The curing rates are positive and the infection rates are non-negative, i.e., $\delta_{\Delta t,i} > 0$ and $\beta_{\Delta t,ij} \geq 0$ for all nodes i, j.*

Assumption 4.3. *For every node $i = 1, \ldots, N$, the sampling time $\Delta t > 0$ satisfies*

$$\Delta t \leq \Delta t_{\max} = \frac{1}{\delta_i + \sum_{j=1}^{N} \beta_{ij}}. \tag{4.5}$$

The results of this chapter which rely on Assumption 4.3 hold true if the sampling time is sufficiently small, which we consider a rather technical assumption. The particular choice of the bound (4.5) is due to Lemma 4.11 in Section 4.3. Furthermore, we make the following assumption on the initial viral state $v_i[1]$.

Assumption 4.4. *For every node $i = 1, \ldots, N$, it holds that $0 \leq v_i[1] \leq v_{\infty,i}$.*

Assumption 4.4 is reasonable since the initial viral state $v[1]$ of many real-world epidemics is almost disease-free. For instance, at the beginning of the periodic outbreak of the flu, every geographical region is almost healthy. As another example, consider the spread of content (e.g., a novel tweet or a post) on online social media. The beginning of the epidemic outbreak (at time $k = 1$) would correspond to the first appearance of the online content. Hence, the viral state $v_i[1]$, where node i refers to a group of users, is close to 0.

Assumption 4.5. *The infection probability matrix $B_{\Delta t}$ is irreducible.*

Assumption 4.5 holds if and only if the infection probability matrix $B_{\Delta t}$ corresponds to a strongly connected graph[2]. Finally, as shown in [25], Assumption 4.6 avoids the trivial viral dynamics in which the virus dies out.

Assumption 4.6. *The spectral radius $\rho(R)$ of the matrix R is strictly greater than one.*

[2] In a strongly connected graph, there is a path from every node i to any other node j.

4.3. VIRAL DYNAMICS CLOSE TO THE STEADY-STATE

Paré *et al.* [25] showed that there is either one stable equilibrium, the healthy state $v[k] = 0$, or there are two equilibria, the healthy state and the steady-state v_∞ with positive components. For completeness, we recapitulate the results in [25] on the equilibria and the stability of the healthy state[3].

Theorem 4.7 ([25])**.** *Under Assumptions 4.2, 4.3 and 4.5, the following two statements hold true:*

1. *If $\rho(R) \leq 1$, then the healthy state $v[k] = 0$ is the only equilibrium of the discrete-time NIMFA model (4.2). Furthermore, $v[k] \to 0$ when $k \to \infty$ for any initial viral state $v[1]$ with $0 \leq v_i[1] \leq 1$ for every node i.*

2. *If $\rho(R) > 1$, then there are two equilibria of the discrete-time NIMFA model (4.2): The healthy state $v[k] = 0$ and a steady-state v_∞ with $v_{\infty,i} > 0$ for every node i.*

Many results in this chapter are based on the non-negativity of the matrix R in (4.4):

Lemma 4.8. *Suppose that Assumptions 4.2, 4.3 and 4.5 hold. Then, the matrix R is irreducible and non-negative.*

Proof. Appendix C.1. □

With the Perron-Frobenius Theorem [32], Lemma 4.8 implies that, under Assumptions 4.2, 4.3 and 4.5, there is a real eigenvalue λ_1 of the matrix R which equals the spectral radius $\rho(R)$ and that the principal eigenvector x_1 is positive. We generalise the bounds from [19, 20] for the steady-state vector v_∞ to the NIMFA model (4.1) with heterogeneous spreading parameters:

Lemma 4.9. *Suppose that Assumptions 4.2, 4.3, 4.5 and 4.6 hold. Then, the steady state $v_{\infty,i}$ of any node i is bounded by*

$$1 - \frac{\delta_{\Delta t,i}}{\sum_{j=1}^{N} \beta_{\Delta t,ij}} \leq v_{\infty,i} \leq 1 - \frac{\delta_{\Delta t,i}}{\delta_{\Delta t,i} + \sum_{j=1}^{N} \beta_{\Delta t,ij}}.$$

Proof. Appendix C.2. □

When replacing the probabilities $\beta_{\Delta t,ij}$ and $\delta_{\Delta t,i}$ by the rates β_{ij} and δ_i, Lemma 4.9 also holds for continuous-time NIMFA (1.1), which has the same steady state v_∞ as discrete-time NIMFA (4.1). We denote the difference of the viral state $v[k]$ to the steady state v_∞ by $\Delta v[k] = v[k] - v_\infty$. By considering the difference $\Delta v[k] = v[k] - v_\infty$, we obtain an equivalent representation of the discrete-time NIMFA equations (4.1).

Proposition 4.10 (NIMFA Equations as Difference to the Steady-State)**.** *Suppose that Assumptions 4.2, 4.3, 4.5 and 4.6 hold. Then, the difference $\Delta v[k] = v[k] - v_\infty$ from the viral state $v[k]$ to the steady state v_∞ of the discrete-time NIMFA model (4.2) evolves as*

$$\Delta v[k+1] = F \Delta v[k] - \operatorname{diag}(\Delta v[k]) B_{\Delta t} \Delta v[k], \tag{4.6}$$

[3] Theorem 4.7 follows immediately from merging [25, Theorems 1-2 and Proposition 2].

where the $N \times N$ matrix F is given by

$$F = I + \operatorname{diag}\left(\frac{\delta_{\Delta t,1}}{v_{\infty,1}-1},\ldots,\frac{\delta_{\Delta t,N}}{v_{\infty,N}-1}\right) + \operatorname{diag}(u - v_\infty)B_{\Delta t}. \tag{4.7}$$

Proof. Appendix C.3. □

For a sufficiently small sampling time Δt, Lemma 4.11 states that every element of matrix F is non-negative.

Lemma 4.11. *Suppose that Assumptions 4.2, 4.3, 4.5 and 4.6 hold. Then, the $N \times N$ matrix F defined by (4.7) is non-negative, i.e. $(F)_{ij} \geq 0$ for every $i, j = 1,\ldots,N$.*

Proof. Appendix C.4. □

Furthermore, Proposition 4.10 leads to:

Corollary 4.12. *Suppose that Assumption 4.2–4.6 hold. Then, it holds that $v_i[k] \leq v_{\infty,i}$ for every node i at every time $k \geq 1$.*

Proof. Appendix C.5. □

In other words, Corollary 4.12 states that the set $\{v | 0 \leq v_i \leq v_{\infty,i},\ \forall i = 1,\ldots,N\}$ is an invariant set of NIMFA (4.1), see the explanation above Problem 2.2. We emphasise that Corollary 4.12 does not imply that the viral state $v[k]$ increases monotonically.

To provide a graphical illustration of Corollary 4.12, we generate a random network with $N = 10$ nodes by creating a directed link $a_{ij} = 1$ from any node j to any node i with link probability $p_{\mathrm{ER}} = 0.25$ and we repeat this network generation if the resulting network is not strongly connected. If $a_{ij} = 1$, then we set the infection probability $\beta_{\Delta t,ij}$ to a uniformly distributed random number in $[0,1]$ and, if $a_{ij} = 0$, then we set $\beta_{\Delta t,ij} = 0$. The curing probability $\delta_{\Delta t,i}$ for every node i is set to a uniform random number in $[0.95\sigma, 1.05\sigma]$, where the constant σ is initially set to $\sigma = 10$. If the spectral radius $\rho(R) \leq 1 + 10^{-3}$, then we set the constant σ to $\sigma/1.1$ and generate new curing probabilities $\delta_{\Delta t,i}$. We repeat this generation of curing probabilities $\delta_{\Delta t,i}$ until $\rho(R) > 1 + 10^{-3}$. The sampling time Δt is set to $\Delta t = \Delta t_{\max}/10$, given by (4.5). For every node i, the initial viral state $v_i[1]$ is set to a uniform random number in $[0, 0.01\, v_{\infty,i}]$. Figure 4.1 depicts the resulting viral state traces $v_i[k]$ for every node i. As stated by Corollary 4.12, the viral state $v[k]$ approaches the steady state v_∞ from below without overshooting, but the viral state $v[k]$ is not strictly increasing. The absence of overshoot is not evident. For instance, in a Markovian SIS process overshoot is possible [72].

For applications in which the initial viral state $v[1]$ is close to zero, the NIMFA equations (4.8) can be replaced by linear time-invariant (LTI) systems in two different regimes: On the one hand, it holds for small times k that $v[k] \approx 0$. Hence, the representation (4.2) can be linearised around the origin $v[k] = 0$, which yields

$$v[k+1] \approx Rv[k], \tag{4.8}$$

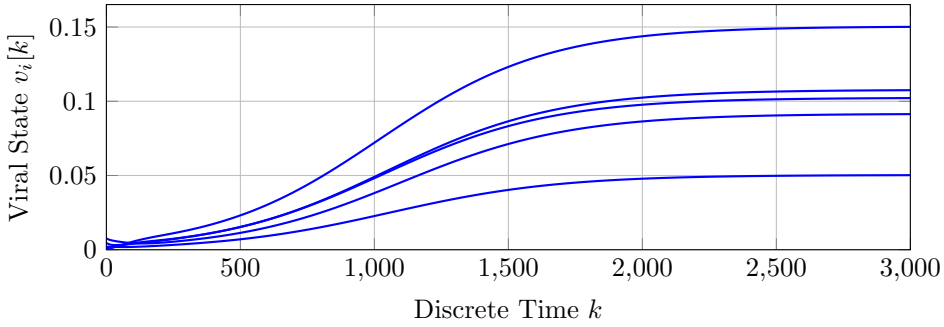

(a) Until discrete time $k = 3,000$.

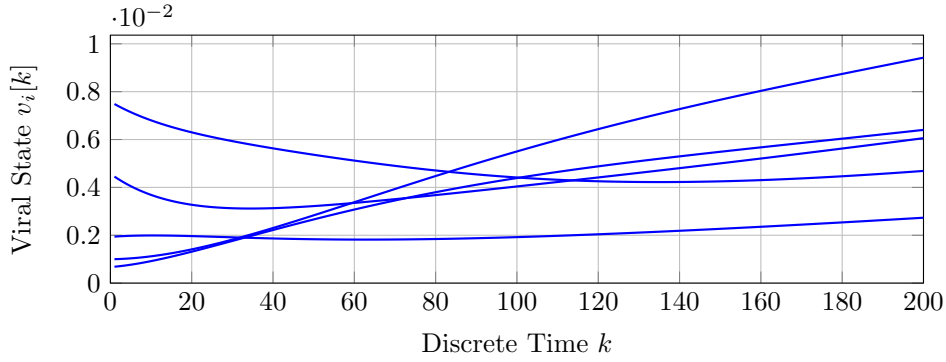

(b) Until discrete time $k = 200$.

Figure 4.1: **Viral state dynamics of NIMFA.** The upper sub-plot depicts the viral state traces $v_i[k]$, for a directed network with $N = 10$ nodes and heterogeneous spreading parameters $\delta_{\Delta t,i}, B_{\Delta t}$ until discrete time $k = 3000$. The viral states of only five nodes are depicted to avoid strongly overlapping curves. The lower sub-plot depicts the same viral state traces $v_i[k]$, $i = 1, ..., N$, but only the initial phase until discrete time $k = 200$.

for small times k. On the other hand, if the viral state $v[k]$ is close to the steady-state v_∞, which implies $\Delta v[k] \approx 0$, then the representation (4.6) can be linearised around the origin $\Delta v[k] = 0$, which gives

$$\Delta v[k+1] \approx F \Delta v[k]. \tag{4.9}$$

Furthermore, we obtain that the steady-state v_∞ is asymptotically stable[4].

Theorem 4.13 (Asymptotic Stability of the Steady-State)**.** *Under Assumptions 4.2, 4.3, 4.5 and 4.6, the steady-state v_∞ of the discrete-time NIMFA system (4.2) is asymptotically stable.*

Proof. Appendix C.6. □

[4]The steady-state v_∞ is asymptotically stable if there exists an $\epsilon > 0$ such that $\|v[1] - v_\infty\| < \epsilon$ implies that $v[k] \to v_\infty$ when $k \to \infty$.

Ahn and Hassibi [78] gave a counterexample for which the steady-state v_∞ of the discrete-time NIMFA system (4.2) is unstable. However, their counterexample does not satisfy Assumption 4.3. Hence, a sufficiently small sampling time Δt is decisive for the stability of the discrete-time NIMFA model (4.2). (Paré *et al.* [25] observed that the counterexample in [78] violates the third assumption in [25], which is closely related to Assumption 4.3.)

4.4. MONOTONICITY OF THE VIRAL DYNAMICS

In this section, we show that the viral state $v[k]$ is monotonically increasing, provided that the initial viral state $v[1]$ is small.

Definition 4.14 (Strictly increasing viral dynamics)**.** The viral state $v[k]$ is *strictly increasing at time k* if $v[k+1] > v[k]$. The viral state $v[k]$ is *globally strictly increasing* if $v[k]$ is strictly increasing at every time $k \geq 1$.

Lemma 4.15 states an inductive property of the monotonicity.

Lemma 4.15. *Under Assumptions 4.2–4.6, the viral state $v[k]$ is strictly increasing at time k if the viral state $v[k-1]$ is strictly increasing at time $k-1$.*

Proof. Appendix C.7. □

For any vector $y = (y_1, ..., y_N)^T$ we define $y^l = (y_1^l, ..., y_N^l)^T$. Theorem 4.16 states equivalent conditions to a globally strictly increasing viral state evolution.

Theorem 4.16 (Monotonicity of the Viral State Evolution)**.** *Suppose that Assumptions 4.2–4.6 hold. Then, the viral state $v[k]$ is globally strictly increasing if and only if one of the following two (equivalent) statements holds:*

1. *The initial viral state $v[1]$ satisfies*

$$\left(B_{\Delta t} - \operatorname{diag}(\delta_{\Delta t})\right) v[1] > \operatorname{diag}(\delta_{\Delta t}) \sum_{l=2}^{\infty} v^l[1]. \tag{4.10}$$

2. *It holds that*

$$\left(\operatorname{diag}(u - v_\infty) B_{\Delta t} \operatorname{diag}(u - v_\infty) - \operatorname{diag}(\delta_{\Delta t})\right) z > \operatorname{diag}(\delta_{\Delta t}) \sum_{l=2}^{\infty} z^l,$$

where the $N \times 1$ vector z is given by

$$z_i = \frac{v_i[1] - v_{\infty,i}}{1 - v_{\infty,i}}, \quad i = 1, ..., N.$$

Proof. Appendix C.8. □

For any scalar y with $|y| < 1$, the geometric series $\sum_{l=2}^{\infty} y^l = \frac{y^2}{1-y}$ gives an alternative form of the right-hand sides of statement 1 and 2 of Theorem 4.16. From Theorem 4.16, we obtain a corollary which states sufficient conditions for a globally strictly increasing viral state.

Corollary 4.17. *Suppose Assumptions 4.2–4.6 hold and that the initial viral state $v[1]$ equals either*

$$v[1] = \epsilon x_1 + \eta \tag{4.11}$$

or

$$v[1] = (1-\epsilon)v_\infty + \eta$$

for some small $\epsilon > 0$ and an $N \times 1$ vector η whose norm $\|\eta\|_2 = \mathcal{O}(\epsilon^p)$ for some scalar $p > 1$ which is independent of ϵ. Then, there exists an $\epsilon > 0$ such that the viral state $v[k]$ is globally strictly increasing.

Proof. Appendix C.9. □

Numerical simulations show that if the initial viral state $v[1]$ approaches zero from an *arbitrary* direction, which differs from (4.11), then the viral state $v[k]$ is in general *not* globally strictly increasing. However, the simulations also indicate that, if the initial viral state $v[1]$ is small, then the viral state seems "almost" globally strictly increasing, which is illustrated by Figure 4.1 and motivates us to state Definition 4.18.

Definition 4.18 (Quasi-increasing viral dynamics)**.** Define S_- as the set of times $k \geq 1$ at which the viral state $v[k]$ is not strictly increasing:

$$S_- = \left\{ k \in \mathbb{N} \,\middle|\, \exists i : \; v_i[k+1] \leq v_i[k] \right\}.$$

Then, the viral state $v[k]$ is *quasi-increasing with stringency ϵ*, if the set S_- is finite and $\|v[k+1] - v[k]\|_2 \leq \epsilon$ for every time k in S_-.

Thus, a quasi-increasing viral state $v[k]$ is strictly increasing at every time k not in the set S_-, and at the times k in the finite set S_- the viral state $v[k]$ is decreasing only within an ϵ-stringency. For the viral state trace $v[k]$ depicted in Figure 4.1, the set S_- equals $S_- = \{1, 2, ..., 165\}$. Theorem 4.19 states that the viral state $v[k]$ is quasi-increasing with an *arbitrarily small* stringency ϵ, provided that the initial viral state $v[1]$ is sufficiently small.

Theorem 4.19. *Suppose that Assumptions 4.2–4.6 hold and that $v[1] \neq 0$. Then, for any $\epsilon > 0$ there is a $\vartheta(\epsilon)$ such that $\|v[1]\|_2 \leq \vartheta(\epsilon)$ implies that the viral state $v[k]$ is quasi-increasing with stringency ϵ.*

Proof. Appendix C.10. □

4.5. BOUNDS ON THE VIRAL DYNAMICS

Due to the non-linearity of the NIMFA equations (4.2), an analysis of the *exact* viral state evolution is challenging. However, it is possible to bound the viral state $v[k]$ by LTI systems, which allows for an *approximate* analysis of the viral state evolution. As stated by Proposition 4.20, the linearisation (4.8) of the NIMFA model around zero directly yields an upper bound on the viral state $v[k]$.

Proposition 4.20. *Suppose that Assumptions 4.2–4.4 hold and define the LTI system*

$$v_{\text{ub}}^{(1)}[k+1] = R v_{\text{ub}}^{(1)}[k], \quad k \geq 1, \tag{4.12}$$

where the matrix R is given by (4.4). If $v_{\text{ub}}^{(1)}[1] \geq v[1]$, then it holds that $v_{\text{ub}}^{(1)}[k] \geq v[k]$ at every time $k \geq 1$. If $\rho(R) \geq 1$, then the LTI system (4.12) is unstable. If $\rho(R) < 1$, then the LTI system (4.12) is asymptotically stable.

Proof. Appendix C.11. □

In addition the upper bound in Proposition 4.20, the linearisation (4.9) of the NIMFA model around the steady-state v_∞ yields another upper bound on the viral state $v[k]$, as stated by Proposition 4.21.

Proposition 4.21. *Under Assumptions 4.2–4.6, denote an upper bound of the difference of the viral state $v[k]$ to the steady-state v_∞ at time k by $\Delta v_{\text{ub}}[k]$. Furthermore, define the LTI system*

$$\Delta v_{\text{ub}}[k+1] = F \Delta v_{\text{ub}}[k], \quad k \geq 1, \tag{4.13}$$

where the $N \times N$ matrix F is given by (4.7). Then, the following statements hold true:

1. *If $\Delta v_{\text{ub}}[1] \geq \Delta v[1]$, then it holds that $\Delta v_{\text{ub}}[k] \geq \Delta v[k]$ at every time $k \geq 1$.*
2. *If $\Delta v_{\text{ub}}[1] \leq 0$, then it holds that $\Delta v_{\text{ub}}[k] \leq 0$ at every time k.*

Proof. Appendix C.12. □

Hence, the LTI system (4.13) yields the upper bound

$$v_{\text{ub}}^{(2)}[k] := \Delta v_{\text{ub}}[k] + v_\infty \geq v[k]$$

on the viral state $v[k]$ at every time k. If Assumption 4.4 holds and $\Delta v_{\text{ub}}[1] = \Delta v[1]$, then it holds that $0 \geq \Delta v_{\text{ub}}[k] \geq \Delta v[k]$ for every time k. Thus, the convergence of $\Delta v[k]$ to 0 implies the convergence of $\Delta v_{\text{ub}}[k]$ to 0. The upper bound of Proposition 4.20 is tight when the viral state $v[k]$ is small, and the upper bound of Proposition 4.21 is tight when the viral state $v[k]$ is close to the steady-state v_∞. We combine Propositions 4.20 and 4.21 to obtain a tighter upper bound, for every node i, as

$$v_{\text{ub},i}[k] := \min\{v_{\text{ub},i}^{(1)}[k], v_{\text{ub},i}^{(2)}[k]\}. \tag{4.14}$$

Finally, Proposition 4.22 provides a lower bound on the viral state $v[k]$.

Proposition 4.22. *Suppose that Assumptions 4.2–4.6 hold and let there be an $N \times 1$ vector $v_{\min} > 0$ such that $v[k] \geq v_{\min}$ holds at every time $k \geq 1$. Furthermore, consider that $\Delta v_{\text{lb}}[1] = \Delta v[1]$, and define the LTI system*

$$\Delta v_{\text{lb}}[k+1] = F_{\text{lb}} \Delta v_{\text{lb}}[k], \quad k \geq 1, \tag{4.15}$$

where the $N \times N$ matrix F_{lb} is given by

$$F_{\text{lb}} = I + \operatorname{diag}\left(\frac{\delta_{\Delta t,1}}{v_{\infty,1} - 1}, \ldots, \frac{\delta_{\Delta t,N}}{v_{\infty,N} - 1}\right) + \operatorname{diag}(u - v_{\min}) B_{\Delta t}.$$

Then, the following statements hold true:

1. *It holds that* $\Delta v_{\mathrm{lb}}[k] \leq \Delta v[k] \leq 0$ *at every time* $k \geq 1$.

2. *Denote* $\gamma = \min_{i=1,\dots,N} v_{\max,i}$ *and* $\delta_{\Delta t,\min} = \min_{i=1,\dots,N} \delta_{\Delta t,i}$. *Then, it holds that*

$$\Delta v_{\mathrm{lb}}[k] \geq -\left(1 - \delta_{\Delta t,\min}\frac{\gamma}{1-\gamma}\right)^{k-1} v_\infty.$$

Hence, $\Delta v_{\mathrm{lb}}[k] \to 0$ *when* $k \to \infty$.

Proof. Appendix C.13. □

Hence, the LTI system (4.15) yields the lower bound

$$v_{\mathrm{lb}}[k] := \Delta v_{\mathrm{lb}}[k] + v_\infty \leq v[k] \tag{4.16}$$

on the viral state $v[k]$ at every time k. In particular, if the viral state $v[k]$ is globally strictly increasing, as discussed in Section 4.4, then the vector $v_{\min}$ can be chosen as $v_{\min} = v[1]$. Lemma 4.23 ensures the existence of a vector $v_{\min} > 0$ for every initial viral state $v[1] \neq 0$, which can be applied to Proposition 4.22.

Lemma 4.23. *Suppose that Assumptions 4.2–4.6 hold. Then, for any initial viral state* $v[1] > 0$, *there exists an* $N \times 1$ *vector* $v_{\min} > 0$ *such that* $v[k] \geq v_{\min}$ *holds at every time* $k \geq 1$. *Furthermore, for any initial viral state* $v[1] \neq 0$, *there exists an* $N \times 1$ *vector* $v_{\min} > 0$ *such that* $v[k] \geq v_{\min}$ *holds at every time* $k \geq N-1$.

Proof. Appendix C.14. □

Proposition 4.22 and Lemma 4.23 guarantee the existence of an LTI system (4.15) that lower-bounds the viral state $v[k]$. Thus, the viral state $v[k]$ converges to the steady-state v_∞ exponentially fast:

Corollary 4.24 (Steady-State is Exponentially Stable)**.** *Suppose that Assumptions 4.2–4.6 hold. Then, for any initial viral state* $v[1] \neq 0$ *there exist constants* $\alpha < 1$ *and* $k^* \leq N-1$ *such that*

$$\|v[k] - v_\infty\|_2 \leq \|v_\infty\|_2 \alpha^{k-1} \quad \forall k \geq k^*. \tag{4.17}$$

If the initial viral state $v[1] > 0$, *then the constant* k^* *can be set to* $k^* = 1$. *Furthermore, if the viral state* $v[k]$ *is globally strictly increasing (cf. Theorem 4.16) and* $v[1] > 0$, *then (4.17) is satisfied for*

$$\alpha = 1 - \delta_{\Delta t,\min}\frac{\gamma}{1-\gamma},$$

where $\gamma = \min_{i=1,\dots,N} v_{\max,i}$ *and* $\delta_{\Delta t,\min} = \min_{i=1,\dots,N} \delta_{\Delta t,i}$.

Proof. Appendix C.15. □

It is an open problem whether the steady-state v_∞ is exponentially stable for initial viral states $v[1]$ that do not satisfy Assumption 4.4. In the SIS epidemic process [5, 80], the *hitting time* T_{H_n} is the first time when the SIS process reaches a state with n infected nodes. As argued in [81], the average hitting time $\mathrm{E}[T_{H_n}]$ scales exponentially with respect to the number n of infected nodes, which is in agreement with the exponential convergence to the steady state v_∞ for the NIMFA epidemic model[5].

We provide a numerical evaluation of the upper bound $v_{\mathrm{ub}}[k]$, given by (4.14), and the lower bound $v_{\mathrm{lb}}[k]$, given by (4.16). We generate a directed Erdős-Rényi random graph with $N = 500$ nodes by creating a directed link $a_{ij} = 1$ from any node j to any node i with link probability $p_{\mathrm{ER}} = 0.05$. We generate another graph if the resulting graph is not strongly connected. If $a_{ij} = 1$, then we set the infection probability $\beta_{\Delta t,ij}$ to a uniformly distributed random number in $[0,1]$ and, if $a_{ij} = 0$, then we set $\beta_{\Delta t,ij} = 0$. The curing probability $\delta_{\Delta t,i}$ for every node i is set to a uniform random number in $[0.95\sigma, 1.05\sigma]$, where the constant σ is initially set to $\sigma = 10$. If the spectral radius $\rho(R) \leq 1 + 10^{-5}$, then we set the constant σ to $\sigma/1.005$ and generate new curing probabilities $\delta_{\Delta t}$. We repeat this generation of curing probabilities $\delta_{\Delta t,i}$ until $\rho(R) > 1 + 10^{-5}$. The sampling time Δt is set to $\Delta t = \Delta t_{\max}/20$, given by (4.5). For every node i, the initial viral state $v_i[1]$ is set to a uniform random number $[0, 0.1\, v_{\infty,i}]$. We initialise the bounds $v_{\mathrm{ub}}[k]$ and $v_{\mathrm{lb}}[k]$ on the viral state $v[k]$ at different bound-initialisation times $k_0 \geq 1$, i.e., $v_{\mathrm{lb}}[k_0] = v[k_0] = v_{\mathrm{ub}}[k_0]$. To obtain the lower bound $v_{\mathrm{lb}}[k]$, we set the vector $v_{\min}$ of Proposition 4.22 to

$$v_{\min,i} = \min_{k \geq k_0} v_i[k], \quad i = 1, \ldots, N.$$

We emphasise that if $v_i[k_0] > v_i[k_0 - 1]$ holds for every node i, then the vector $v_{\min}$ becomes $v_{\min} = v[k_0]$ due to Lemma 4.15. Figure 4.2 illustrates that, for a small bound-initialisation time k_0, the upper bound $v_{\mathrm{ub}}[k]$ results in a reasonable fit, whereas the lower bound $v_{\mathrm{lb}}[k]$ does not perform well. If the bound-initialisation time k_0 is greater, then both bounds $v_{\mathrm{lb}}[k]$ and $v_{\mathrm{ub}}[k]$ give a tight fit to the exact viral state $v[k]$.

4.6. CONCLUSIONS

In this chapter, we analysed the discrete-time NIMFA epidemic model with heterogeneous spreading parameters on directed graphs. Our contribution is threefold. First, we proved that the steady-state v_∞ is asymptotically stable, and we showed that the viral state $v[k]$ approaches the steady-state v_∞ without overshooting. Second, provided that the initial viral state $v[1]$ is sufficiently small, we showed that the viral state $v[k]$ is increasing. Third, we derived linear systems that give upper and lower bounds on the viral state $v[k]$, and we proved that the viral state $v[k]$ converges to the steady-state v_∞ exponentially fast.

In conclusion, we showed that the discrete-time NIMFA epidemic model captures the *qualitative* behaviour of real-world epidemics. Furthermore, since the spreading parameters are heterogeneous and the underlying contact network is directed, the NIMFA

[5] For an SIS process, the *spreading time* [82] is another measure for the time of convergence to the metastable state. For the spreading time, the convergence to the metastable state is defined differently for every realisation of the same SIS epidemic process. Hence, the spreading time is subject to random fluctuations, which approximately follow a lognormal distribution [81], contrary to the deterministic NIMFA model (4.1) and the average hitting time $\mathrm{E}[T_{H_n}]$ of an SIS process.

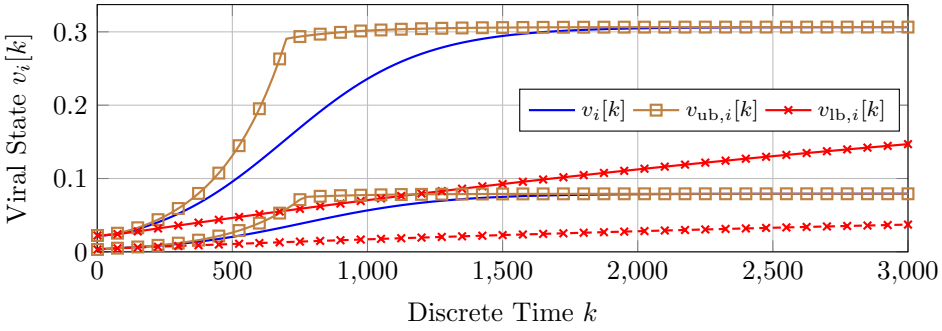

(a) Bounds initialised at time $k_0 = 1$.

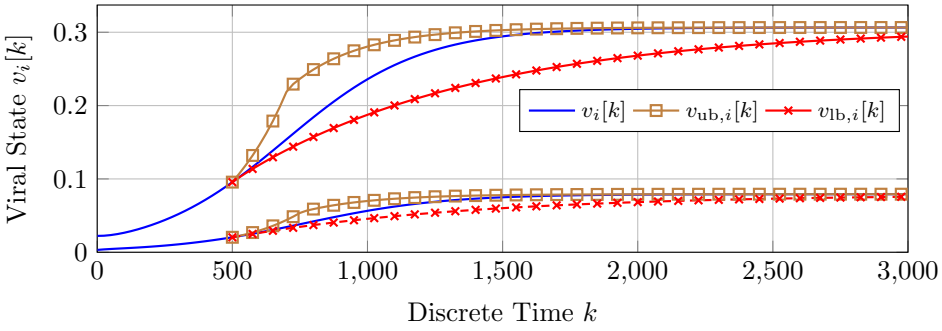

(b) Bounds initialised at time $k_0 = 500$.

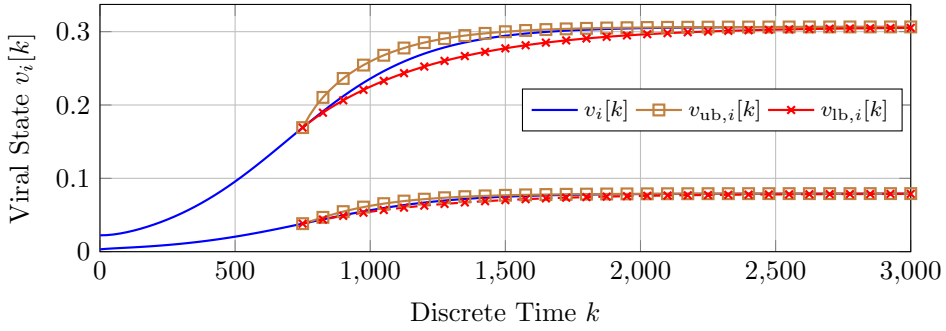

(c) Bounds initialised at time $k_0 = 750$.

Figure 4.2: **Linear bounds of the viral state dynamics.** For a directed Erdős-Rényi random graph with $N = 500$ nodes and heterogeneous spreading parameters $\delta_{\Delta t,i}, B_{\Delta t}$, the fit of the lower bound $v_{\mathrm{lb}}[k]$ and the upper bound $v_{\mathrm{ub}}[k]$ on the viral state $v[k]$ is depicted. The viral states $v_i[k]$ and the corresponding bounds $v_{\mathrm{lb},i}[k]$, $v_{\mathrm{ub},i}[k]$ of the two nodes with the maximal and minimal steady-state $v_{\infty,i}$ are shown. The sub-plots correspond to an initialisation of the bounds $v_{\mathrm{lb}}[k_0] = v[k_0] = v_{\mathrm{ub}}[k_0]$ at different times k_0.

model has a vast parameter space and can be fitted to various real-world epidemic data, which allows for *quantitative* predictions of the viral state evolution.

ACKNOWLEDGEMENTS

We are grateful to Qiang Liu for helpful discussions on the material in this chapter.

II

NETWORK RECONSTRUCTION AND PREDICTION OF EPIDEMICS

5

EXACT SIS NETWORK RECONSTRUCTION SEEMS INFEASIBLE

The knowledge of the network topology is imperative to precisely describing the viral dynamics of the stochastic Susceptible-Infected-Susceptible (SIS) epidemic process between individuals. In scenarios for which the network topology is unknown, one resorts to reconstructing the network from observing the viral state trace. Our contribution is threefold. First, we formulate the SIS network reconstruction as a Bayesian estimation problem, based on the sampled-time Markov chain of the SIS epidemic process. The resulting estimation problem is given by a mixed-integer optimisation problem. Second, we propose a novel method of constructing *a specific class of viral state traces from which the inference of the presence or absence of links is either easy or difficult. In particular, we use this construction to prove that the maximum-likelihood SIS network reconstruction is NP-hard. The NP-hardness holds for any connected contact graph. Third, we introduce an accurate, polynomial-time heuristic for the NP-hard SIS network reconstruction problem. With our heuristic, the network topology can almost always be exactly reconstructed. Notwithstanding, reconstructing the network with a reasonably high accuracy requires that the number of observations n grows with* $\log_{10}(n) \approx N^{\alpha} + b$*, where b is some constant,* $\alpha \approx 0.56$*, and N denotes the number of nodes. Such long observation periods are hardly realistic, which justifies the claim in the title.*

This chapter is based on [83] and [84].

5.1. INTRODUCTION

We consider the Markovian Susceptible-Infected-Susceptible (SIS) epidemic model [5, 58], where every node corresponds to an individual. The contact network is characterised by the symmetric $N \times N$ adjacency matrix A with elements a_{ij}, where N denotes the number of individuals. If $a_{ij} = 1$, then there is a link between individual i and j, and otherwise $a_{ij} = 0$. Every node i has an SIS viral state $x_i(t)$, which is a Bernoulli random variable, $x_i(t) \in \{0, 1\}$. At every continuous time $t \geq 0$, a node i is either susceptible (healthy) or infected, which is denoted by $x_i(t) = 0$ and $x_i(t) = 1$, respectively. Thus, there are two possible viral state transitions for every node, from susceptible to infected and vice versa. The Markovian SIS epidemic model assumes that the curing process per node i is a Poisson process with *curing rate* $\delta > 0$ and that the infection rate per link is a Poisson process with *infection rate* $\beta > 0$. The more general ϵ-SIS epidemic model additionally considers that a susceptible node may suffer from self-infections [85, 86]. The self-infection of a node i is a Poisson process with *self-infection* rate ϵ, which is independent of the infectious neighbours of node i. If $\epsilon = 0$, then the ϵ-SIS process reduces to the SIS-process.

The knowledge of the contact network A and the spreading parameters β,δ,ϵ is decisive for the prediction of an SIS epidemic outbreak and for the design of epidemic control strategies. However, in most applications, neither the contact network nor the spreading parameters are known. In this chapter, we consider the inverse problem of estimating both the adjacency matrix A and the spreading parameters β, δ, ϵ from observations of the SIS viral states $x_i(t)$ of all nodes $i = 1, ..., N$. Our approach is based on the sampled-time ϵ-SIS Markov chain, which is introduced in Section 5.3.

5.2. RELATED WORK

Vajdi and Scoglio [87] formulate the network reconstruction for the continuous-time SIS model in a Bayesian sense and propose a Gibbs sampling approach. For a discrete-time SIS process, Shen *et al.* [88] propose a network reconstruction method which is based on compressed sensing. Peixoto [89] proposes a Bayesian framework for joint SIS network reconstruction and community detection and employs a Markov Chain Monte Carlo approach. In this chapter, we propose a convex optimisation approach to reconstruct the network, based on the sampled-time Markov chain of the SIS process. Furthermore, we put an emphasis of the fundamental network reconstruction limits, by studying the computational complexity and the number of observations that are required for an accurate network reconstruction.

5.3. SAMPLED-TIME SIS EPIDEMIC PROCESS

The inverse problem of the reconstruction of the network topology and the estimation of the spreading parameters, given a number of measurements, is best described in discrete-time. For epidemic processes on computer systems, such as the spread of opinions on social media, the dynamics are inherently in discrete-time due to the digital design of hardware and software. For other epidemic processes, such as the spread of a disease, it is reasonable to assume that there is a limit to the temporal resolution of the empirical measurements.

We denote the transition probability of the continuous-time Markov chain of the SIS process from state i at time τ to state j at time $t+\tau$ by $P_{ij}(t)$. The sampled-time Markov chain with sampling time Δt is a discrete-time Markov chain [58], where the transition probabilities P_{ij} from state i to state j are given by the first-order Taylor expansion of $P_{ij}(t)$,

$$P_{ij} = P'_{ij}(0)\Delta t,$$

and the transition probabilities from state i to state i are given by

$$P_{ii} = 1 - \sum_{l=1}^{N} P_{il}.$$

The transition probabilities P_{ij} depend on the adjacency matrix A and the spreading parameters β, δ, ϵ. We assume that the sampling time Δt of the sampled-time Markov chain of the SIS process is sufficiently small. More precisely, we make two assumptions on the sampling time Δt. First, each viral state transition is observed, i.e., there is at most one transition in the interval $[kT,(k+1)\Delta t]$, where $k \in \mathbb{N}$ denotes the discrete time of the sampled-time Markov chain. Second, we assume that the higher-order terms of the Taylor expansion of the continuous-time SIS transition probabilities $P_{ij}(t)$ are negligible.

We denote the $N \times 1$ viral state vector of the sampled-time Markov chain at discrete time k by $x[k]$, and it holds that $x[k] \approx x(k\Delta t)$ if the sampling time Δt is small. There are three possible transitions from discrete time k to $k+1$ in the sampled-time Markov chain of the ϵ-SIS process:

1. Curing of a node A single node i changes from the infected state $x_i[k] = 1$ at discrete time k to the susceptible state $x_i[k+1] = 0$ at discrete time $k+1$. The probability of this transition is

$$\Pr\Big[x_i[k+1] = 0 \Big| x_i[k] = 1, x[k], A\Big] = \delta_{\Delta t}, \tag{5.1}$$

where the *curing probability* $\delta_{\Delta t}$ follows as $\delta_{\Delta t} = \delta\Delta t$.

2. Infection of a node A single node i changes from the susceptible state $x_i[k] = 0$ at discrete time k to the infected state $x_i[k+1] = 1$ at time $k+1$ with the probability

$$\Pr\Big[x_i[k+1] = 1 \Big| x_i[k] = 0, x[k], A\Big] = \epsilon_{\Delta t} + \beta_{\Delta t} N_i(A,k), \tag{5.2}$$

where $N_i(A,k)$ is the number of infected nodes adjacent to node i in A at time k. The *infection probability* equals $\beta_{\Delta t} = \beta\Delta t$, and the *self-infection probability* equals $\epsilon_{\Delta t} = \epsilon\Delta t$. The number of infected nodes $N_i(A,k)$ adjacent to node i at time k equals

$$N_i(A,k) = \sum_{j=1}^{N} a_{ij} x_j[k].$$

3. No change No node changes its viral state from time k to $k+1$. This constant transition occurs when neither a curing nor an infection takes place, and hence

$$\begin{aligned}\Pr\Big[x[k+1] = x[k] \Big| x[k], A\Big] = 1 &- \Pr\Big[\text{A node cures at } k+1 \Big| x[k], A\Big] \\ &- \Pr\Big[\text{A node gets infected at } k+1 \Big| x[k], A\Big],\end{aligned} \tag{5.3}$$

where the probabilities on the right-hand side follow from the transitions (5.1) and (5.2).

To ensure that (5.1), (5.2) and (5.3) are feasible expressions for probabilities, they have to be in $[0,1]$ for all viral states $x[k]$. Lemma 5.1 states an upper bound on the sampling time Δt, such that (5.1), (5.2) and (5.3) are in the interval $[0,1]$.

Lemma 5.1. *If the sampling time Δt satisfies*

$$\Delta t \leq \frac{4}{N^2\beta + 4N\max\{\epsilon,\delta\}}, \tag{5.4}$$

then (5.1), (5.2) and (5.3) are in $[0,1]$ for all adjacency matrices A and all viral states $x[k]$.

Proof. Appendix D.1 □

In the following, we assume that the sampling time Δt satisfies the bound (5.4).

5

5.4. ASSUMPTIONS

For formulating the SIS network reconstruction in a Bayesian sense in Section 5.5 and for the heuristic in Section 5.7, we rely on four assumptions.

Assumption 5.2. *There are known upper bounds $\beta_{\max} \geq \beta$, $\delta_{\max} \geq \delta$ and $\epsilon_{\max} \geq \epsilon$ on the spreading parameters. Furthermore, a non-zero lower bound $\beta_{\min} < \beta$ of the infection rate β is known.*

Assumption 5.3. *A priori, the adjacency matrix A, the spreading rates β, δ, ϵ and the initial viral state observation $x[1]$ are stochastically independent.*

Assumption 5.4. *The logarithm $\log(\Pr[A])$ of the prior distribution $\Pr[A]$ of the adjacency matrix A is concave when the range of elements of A is extended from $a_{ij} \in \{0,1\}$ to $a_{ij} \in [0,1]$.*

Every nonnegative concave function is logarithmically concave, but not the other way around [90].

Assumption 5.5. *The spreading rates β, δ and ϵ are a priori uniformly distributed in the intervals $[\beta_{\min}, \beta_{\max}]$, $[0, \delta_{\max}]$ and $[0, \epsilon_{\max}]$, respectively.*

Assumptions 5.3 to 5.5 are required for the Bayesian (maximum a posteriori) network reconstruction approach in Section 5.5 and in Section 5.7. However, we emphasise that Assumptions 5.3 to 5.5 could be omitted, if the network reconstruction is formulated as a maximum-likelihood estimation problem.

5.5. BAYESIAN FORMULATION OF THE NETWORK RECONSTRUCTION PROBLEM

In this section, we approach the SIS network reconstruction as a Bayesian estimation problem. We denote the tuple $\theta = (A, \beta, \delta, \epsilon)$, which consists of the parameters that must

be estimated. We denote all observations until the observation time n by the $N \times n$ matrix $X[n] = (x[n], x[n-1], ..., x[1])$. Furthermore, $f_{\Theta|X[n]}(\theta)$ denotes the conditional probability density function of the realisation θ of the parameters given the observations $X[n]$. We aim to find the parameters θ_{MAP} which maximise the posterior:

$$\theta_{\text{MAP}} = \arg\max_{\theta \in S_\theta} f_{\Theta|X[n]}(\theta), \tag{5.5}$$

where S_θ denotes the set of feasible solutions for the parameter tuple θ,

$$S_\theta = \mathcal{A} \times [\beta_{\min}, \beta_{\max}] \times [0, \delta_{\max}] \times [0, \epsilon_{\max}].$$

Here, the set of all unweighted $N \times N$ adjacency matrices A is denoted by $\mathcal{A}$, and $S_1 \times S_2$ is the Cartesian product of two sets S_1, S_2.

Under mild conditions, there are two crucial accuracy properties of Bayesian, or Maximum A Posteriori (MAP), estimation of continuous parameters. First, the Bayesian estimator is *unbiased*, which means that the expectation of the Bayesian estimator equals the true parameters [91, Theorem 4.16]. Second, the Bayesian estimator is *efficient*, which means that the Bayesian estimator satisfies the Cramér-Rao inequality [91–93] with equality. The Cramér-Rao inequality is a fundamental bound for the best possible accuracy of any estimator. If an unbiased efficient estimator exists, then the estimator coincides with the MAP estimator. The Cramér-Rao bound requires the parameters θ to be continuous. For the ϵ-SIS process in this chapter, the parameters in θ are not continuous due to the adjacency matrix A with zero-one elements. Nonetheless, based on the strength of the MAP estimator for continuous parameters, the vast majority of network reconstruction methods rely on maximum-likelihood or MAP estimation methods [94–99].

We translate (5.5) into a mixed-integer programme. Bayes' theorem gives

$$f_{\Theta|X[n]}(\theta) = \frac{\Pr[X[n]|\theta]\, f_\Theta(\theta)}{\Pr[X[n]]},$$

where $f_\Theta(\theta)$ denotes the prior distribution of the parameters θ. From the Markovianity of the SIS process [58], we obtain that

$$f_{\Theta|X[n]}(\theta) = \frac{\Pr[x[1]|\theta]}{\Pr[X[n]]} f_\Theta(\theta) \prod_{k=2}^{n} \Pr[x[k]|x[k-1], \theta] \tag{5.6}$$

The term $\Pr[X[n]]$ is not a function of θ. Furthermore, it holds that $\Pr[x[1]|\theta] = \Pr[x[1]]$, since θ and $x[1]$ are stochastically independent by Assumption 5.3. Hence, we can omit the first factor in (5.6), which yields that

$$\theta_{\text{MAP}} = \arg\max_{\theta \in S_\theta} f_\Theta(\theta) \prod_{k=2}^{n} \Pr[x[k]|x[k-1], \theta].$$

We denote the prior distributions of the parameters A, β, δ and ϵ by $\Pr[A]$, $f_{\text{beta}}(\beta)$, $f_{\text{delta}}(\delta)$ and $f_{\text{epsilon}}(\epsilon)$, respectively. Then, since the parameters A, β, δ and ϵ are stochastically independent under Assumption 5.3, we obtain that

$$\theta_{\text{MAP}} = \arg\max_{\theta \in S_\theta} \Pr[A] f_{\text{beta}}(\beta) f_{\text{delta}}(\delta) f_{\text{epsilon}}(\epsilon) \prod_{k=2}^{n} \Pr[x[k]|x[k-1], \theta].$$

The spreading parameters β, δ and ϵ are uniformly distributed under Assumption 5.5. Thus, the terms $f_{\text{beta}}(\beta)$, $f_{\text{delta}}(\delta)$ and $f_{\text{epsilon}}(\epsilon)$ are constant and can be omitted in the estimation. Then, by taking the logarithm (preserving the same optimum), we obtain that

$$\theta_{\text{MAP}} = \arg\max_{\theta \in S_\theta} \log(\Pr[A]) + \sum_{k=2}^{n} \log(\Pr[x[k]|x[k-1],\theta]). \tag{5.7}$$

We denote the set of the time instants of the infections of node i by

$$H_{01}[i] = \{k \in \mathbb{N}_n | x_i[k+1] = 1 \wedge x_i[k] = 0\},$$

where $\mathbb{N}_n = \{1,2,...,n\}$ denotes the set of natural numbers not greater than the observation length n. Furthermore, we denote the set of time instants which correspond to the curing of a node and to a constant transition as

$$H_{10} = \{k \in \mathbb{N}_n | \exists i \in \mathbb{N}_N : x_i[k+1] = 0 \wedge x_i[k] = 1\}$$

and

$$H_{\text{const}} = \{k \in \mathbb{N}_n | \forall i \in \mathbb{N}_N : x_i[k+1] = x_i[k]\},$$

respectively. Every addend of the optimisation problem (5.7) corresponds to some time k which is element of either $H_{01}[i]$, H_{10} or H_{const}. We rewrite (5.7) as

$$\theta_{\text{MAP}} = \arg\min_{\theta \in \Theta} f_{\text{obj}}(\theta),$$

where the objective function $f_{\text{obj}}(\theta)$ follows from the expressions for the transition probabilities as

$$\begin{aligned} f_{\text{obj}}(\theta) = &-\log(\Pr[A]) - \sum_{k \in H_{10}} \log(\delta_{\Delta t}) - \sum_{i=1}^{N} \sum_{k \in H_{01}[i]} \log\left(\epsilon_{\Delta t} + \beta_{\Delta t} \sum_{j=1}^{N} x_j[k] a_{ij}\right) \\ &- \sum_{k \in H_{\text{const}}} \log\left(1 - N\epsilon_{\Delta t} + (\epsilon_{\Delta t} - \delta_{\Delta t}) u^T x[k] + \beta_{\Delta t} \sum_{i,j} x_j[k](x_i[k]-1) a_{ij}\right). \end{aligned} \tag{5.8}$$

By formulating $\theta \in S_\theta$ as constraints, the MAP estimation is given by the following *mixed-integer programming* optimisation problem

$$\begin{aligned} \underset{\theta}{\text{minimise}} \quad & f_{\text{obj}}(\theta) \\ \text{subject to} \quad & a_{ij} \in \{0,1\} \quad \forall i,j \\ & \Delta t \beta_{\min} \le \beta_{\Delta t} \le \Delta t \beta_{\max} \\ & 0 \le \delta_{\Delta t} \le \delta_{\max} \Delta t \\ & 0 \le \epsilon_{\Delta t} \le \epsilon_{\max} \Delta t \end{aligned} \tag{5.9}$$

The solution to the above optimisation problem (5.9) is denoted by θ_{MAP}. If the considered graph is undirected and without self-loops, we add the constraints $a_{ij} = a_{ji}$ and $a_{ii} = 0$ to the optimisation problem.

5.6. MAXIMUM-LIKELIHOOD SIS NETWORK RECONSTRUCTION IS NP-HARD

The optimum θ_{MAP} of problem (5.9) can be found by a brute-force algorithm, where the minimum of the optimisation problem (5.9) is computed for every possible $N \times N$ adjacency matrix $A_1, A_2, ... \in \mathcal{A}$. For a fixed $A = A_m$, where $m = 1, ..., 2^{N(N-1)/2}$, the optimisation is performed with respect to the three spreading parameters $\beta_{\Delta t}, \delta_{\Delta t}, \epsilon_{\Delta t}$, and the objective function (5.8) is convex, since the objective function is a sum of composition of negative logarithms and linear functions. The brute-force approach yields $2^{N(N-1)/2}$ feasible points θ_m, one for each adjacency matrix candidate A_m, and the solution θ_{MAP} to the optimisation problem (5.9) is given by the feasible point which results in the minimal objective value. However, the computational complexity of $\mathcal{O}(2^{N(N-1)/2})$ renders the brute-force approach infeasible for large N. But perhaps the brute-force approach is too simple, and we wonder: *what is the computational complexity of the SIS network reconstruction (5.9)?*

Here, we consider a simpler problem than (5.9). Specifically, we assume that the spreading parameters β and δ are known and that $\epsilon = 0$. Furthermore, we focus on the maximum-likelihood (ML) network reconstruction, which follows from (5.9) if the prior distribution $\Pr[A]$ is constant for all $A \in \mathcal{A}$. In this section, we make a distinction between the three variables A, $\hat{A}$ and A_{ML}: in contrast to the *true* adjacency matrix A, which generated the viral states $x[k]$, the *optimisation variable* in the ML estimation problem is denoted as $\hat{A}$. The *solution* to the ML estimation problem, i.e., the adjacency matrix $\hat{A}$ which maximises the likelihood, is denoted by A_{ML}. Then, the ML network reconstruction is stated as:

Definition 5.6 (Maximum-likelihood SIS network reconstruction)**.** Given the viral state observations $x[k] \in \{0,1\}^N$ from time $k = 1$ to $k = n$ which originate from a sampled-time SIS process on an unknown adjacency matrix $A \in \mathcal{A}$, find the adjacency matrix A_{ML} which maximises the log-likelihood:

$$\begin{aligned} A_{\text{ML}} = \arg\max_{\hat{A}} \quad & \log\left(\Pr\left[x[1], ..., x[n] \middle| \hat{A}\right]\right) \\ \text{s.t.} \quad & \hat{a}_{ij} \in \{0,1\}, \quad i,j = 1, ..., N \\ & \hat{a}_{ij} = \hat{a}_{ji}, \quad i,j = 1, ..., N \\ & \hat{a}_{ii} = 0, \quad i = 1, ..., N \end{aligned} \tag{5.10}$$

We emphasise that the problem (5.10) is easier than the problem (5.9), since the spreading parameters are assumed to be known. An instance of the optimisation problem (5.10) is fully specified by the viral state observations $x[1]$, ..., $x[n]$.

We prove that the ML estimation (5.10) is NP-hard with respect to the number of nodes N for *any* connected adjacency matrix $A \in \mathcal{A}$. The idea of the proof is as follows: We aim to show that there is a polynomial-time reduction from the maximum-cut problem to the ML estimation for the sampled-time SIS process (5.10). Since the maximum cut problem is NP-complete [100], this polynomial-time reduction proves that the ML estimation (5.10) is NP-hard. As introduced in Subsection 5.6.1, the maximum cut problem can be stated as zero-one unconstrained quadratic programme (UQP). By comparison, we make the observation that the zero-one UQP which results from the maximum

cut problem resembles the ML estimation (5.10). We show that for every graph G of the maximum cut problem, there is an SIS viral state sequence $x[1], ..., x[n]$ such that solving the ML estimation (5.10) is equivalent to solving the maximum cut problem on the graph G. The polynomial-time reduction is presented in Subsection 5.6.2.

5.6.1. MAXIMUM CUT

We consider an undirected and unweighted graph $G = (\mathcal{N}, \mathcal{L})$, where $\mathcal{N} = \{1, ..., N\}$ is the set of nodes and $\mathcal{L}$ is the set of L links.

Definition 5.7 (Cut set [101, 102])**.** For a non-empty node subset $\mathcal{V} \subset \mathcal{N}$ of a graph and its complement $\bar{\mathcal{V}} = \mathcal{N} \setminus \mathcal{V}$, the cut-set $\partial\mathcal{V}$ is the set of all links that connect nodes in $\mathcal{V}$ to nodes in $\bar{\mathcal{V}}$:

$$\partial\mathcal{V} = \left\{(i, j) \in \mathcal{L} \middle| i \in \mathcal{V}, j \in \bar{\mathcal{V}}\right\}.$$

The cut size of a cut-set $\partial\mathcal{V}$ equals the number of links in the cut-set and is denoted as $|\partial\mathcal{V}|$. The maximum cut problem and the corresponding decision problem are as follows.

Definition 5.8 (Maximum cut problem)**.** Given a graph G, find a cut $\partial\mathcal{V}$ of maximal cut size $|\partial\mathcal{V}|$.

Definition 5.9 (Maximum cut decision problem)**.** Given a natural number κ and a graph G, is there a cut $\partial\mathcal{V}$ such that its cut size $|\partial\mathcal{V}|$ is at least κ?

The maximum cut decision problem is NP-complete, as shown by Garey *et al.* [103]. Hence, the maximum cut problem is NP-hard [104]. The maximum cut problem can be equivalently stated as zero-one unconstrained quadratic programming (UQP) [105]

$$\begin{aligned} \underset{y_1,...,y_N}{\text{maximise}} \quad & \sum_{i=1}^{N} \sum_{j=i+1}^{N} a_{ij}(y_i(1-y_j) + y_j(1-y_i)) \\ \text{subject to} \quad & y_i \in \{0,1\}, \quad i = 1, ..., N. \end{aligned} \tag{5.11}$$

The binary variable y_i equals 1 if node i is in the node set $\mathcal{V}$, and $y_i = 0$ if node i is in the node set $\bar{\mathcal{V}}$. The optimisation problem (5.11) is equivalent to

$$\begin{aligned} \underset{y_1,...,y_N}{\text{maximise}} \quad & \sum_{i=1}^{N} \sum_{j=i+1}^{N} b_{ij} y_i y_j + \sum_{l=1}^{N} b_l y_l \\ \text{subject to} \quad & y_i \in \{0,1\}, \quad i = 1, ..., N. \end{aligned} \tag{5.12}$$

The coefficients of the objective function of (5.12) are given by

$$b_{ij} = -2a_{ij} \tag{5.13}$$

and the degree of node l

$$b_l = \sum_{j=1}^{N} a_{lj}. \tag{5.14}$$

Since the elements a_{ij} of the adjacency matrix A are either zero or one, the coefficients are in the sets

$$b_{ij} \in \{-2, 0\} \tag{5.15}$$

and

$$b_l \in \{0, 1, ..., N-1\}. \tag{5.16}$$

The objective function f of the optimisation problem (5.12) is a quadratic function which maps N binary variables to a non-negative integer, $f : \{0,1\}^N \mapsto \mathbb{N}_0$. Hence, the optimisation problem (5.12) is a special case of pseudo-Boolean optimisation [106], in which the objective function f maps N binary variables to a real number, $f : \{0,1\}^N \mapsto \mathbb{R}$. Rosenberg [107] showed that the optimisation of any pseudo-Boolean function can always be reduced in polynomial time to the optimisation of a quadratic pseudo-Boolean function. The general optimisation of a quadratic pseudo-Boolean function is of the form (5.12) with the difference that the coefficients b_{ij} and b_l may attain any value in $\mathbb{R}$ - not only the integer values in (5.15) and (5.16) - and is NP-hard [108]. If the coefficients b_{ij} are non-negative real numbers, then the zero-one UQP (5.12) is polynomially solvable [109]. There are other special cases for the range of values of the coefficients b_{ij} and b_l for which the zero-one UQP (5.12) is solvable in polynomial time [110, 111].

5.6.2. REDUCTION OF MAXIMUM CUT TO SIS NETWORK RECONSTRUCTION

We aim to show that any instance of the zero-one UQP (5.12) with coefficients b_{ij} and b_l in the sets (5.15) and (5.16), and thus any instance of the maximum cut problem, can be translated to an SIS network reconstruction problem (5.10) in polynomial time. Hence, the SIS network reconstruction (5.10) is NP-hard. Since the zero-one UQP (5.12) is not NP-hard for certain ranges [109–111] of values of the coefficients b_{ij} and b_l, we emphasise that the conditions (5.15) and (5.16) are crucial (at least sufficient) for the NP-hardness of the zero-one UQP (5.12). Thus, our aim is to show that the SIS network reconstruction problem (5.10) can be translated to a zero-one UQP (5.12) with *any*[1] coefficients b_{ij} and b_l in the sets given by (5.15) and (5.16). Since the SIS network reconstruction problem (5.10) is fully specified by the viral state observations $x[1], ..., x[n]$, we aim to find viral state transitions $x[1], ..., x[n]$ such that solving the SIS network reconstruction problem (5.10) is equivalent to solving the zero-one UQP (5.12). The proof of the NP-hardness of the SIS network reconstruction problem (5.10) is based on four lemmas, which are stated below and whose proofs are given in the Appendices D.2 to D.6.

Since a graph G given by an adjacency matrix A in $\mathcal{A}$ is connected, there is a node l such that the graph G remains connected if node l is removed: Indeed, in any connected graph, there exists a spanning tree that connects all the nodes. In any tree, there exists a node l with degree one (a leaf node), whose removal does not disconnect the spanning tree and hence neither the graph. Without loss of generality, we label this node l as node 1.

[1] More precisely, the coefficients b_{ij} and b_l do not attain any values in $\{-2, 0\}$ and $\{0, 1, ..., N-1\}$ independently. Due to (5.13) and (5.14), it holds $b_l = -\frac{1}{2}\sum_{j=1}^{N} b_{lj}$. We show the *stronger* statement that, independently of the coefficients b_{ij}, the coefficients b_l may attain any value in $\{0, 1, ..., N-1\}$.

Our approach is based on stating a reduced-size version of the ML estimation (5.10), namely only with respect to the links a_{1i} which are incident to node 1. Since the graph given by an adjacency matrix A in $\mathcal{A}$ is connected, node 1 has at least one neighbour. Without loss of generality, we label this neighbour as node 2. Furthermore, we consider that $a_{12} = 1$ is known. In the following, we abbreviate

$$\Pr\left[x[1],...,x[n]\middle|\hat{a}_{13},...,\hat{a}_{1N},\hat{a}_{12}=a_{12},\hat{a}_{ij}=a_{ij}\ \forall i,j\geq 2\right],$$

i.e., the likelihood when the elements $\hat{a}_{12}$ and $\hat{a}_{ij}$ for $i,j\geq 2$ are fixed to the true values, formally by

$$\Pr\left[x[1],...,x[n]\middle|\hat{a}_{13},...,\hat{a}_{1N}\right],$$

and we introduce the following reduced-size SIS network estimation problem:

5

Definition 5.10 (Reduced-size SIS network reconstruction)**.** Given the links $a_{12}=1$ and a_{ij}, where $i\geq 2$ and $j\geq 2$, of the matrix $A\in\mathcal{A}$ and the viral state observations $x[k]\in\{0,1\}^N$ from time $k=1$ to time $k=n$, which resulted from a sampled-time SIS process with the adjacency matrix A, find the links $(A_{\mathrm{ML}})_{13},...,(A_{\mathrm{ML}})_{1N}$ which maximise the log-likelihood:

$$\begin{aligned}((A_{\mathrm{ML}})_{13},...,(A_{\mathrm{ML}})_{1N}) = \underset{\hat{a}_{13},...,\hat{a}_{1N}}{\arg\max} \quad & \log\left(\Pr\left[x[1],...,x[n]\middle|\hat{a}_{13},...,\hat{a}_{1N}\right]\right)\\ \text{s.t.} \quad & \hat{a}_{1i}\in\{0,1\},\quad i=3,...,N.\end{aligned} \tag{5.17}$$

Lemma 5.11 states that solving the reduced-size SIS network reconstruction (5.17) is equivalent to solving a zero-one UQP with particular coefficients:

Lemma 5.11 (Reduced-size SIS network reconstruction as zero-one UQP)**.** *For some natural numbers m_0, m_{1l}, $m_{2l}\in\mathbb{N}$, $l\in\{3,...,N\}$, define the coefficients*

$$c_{ij}\in\{-2,0\},\qquad i,j=3,...,N, \tag{5.18}$$

$$c_l=\frac{m_{1l}}{m_0}\lambda_+ + \frac{m_{2l}}{m_0}\lambda_- + \eta_l,\qquad l=3,...,N, \tag{5.19}$$

where $\lambda_+>0$, $\lambda_-<0$ and $\eta_l\geq 0$ are constant and are given by (D.26), (D.27) and (D.28), respectively. For any coefficients c_{ij} and c_l given by (5.18) and (5.19) and for any connected adjacency matrix $A\in\mathcal{A}$, there is a viral state sequence $x[k]$ from time $k=1$ to a finite time $k=n$ such that the reduced-size SIS network reconstruction problem (5.17) becomes:

$$\begin{aligned}\max_{\hat{a}_{13},...,\hat{a}_{1N}} \quad & \sum_{i=3}^{N}\sum_{j=i+1}^{N} c_{ij}\hat{a}_{1i}\hat{a}_{1j} + \sum_{l=3}^{N} c_l\hat{a}_{1l}\\ \text{s.t.} \quad & \hat{a}_{1i}\in\{0,1\},\quad i=3,...,N\end{aligned} \tag{5.20}$$

Proof. Appendix D.2. □

Comparing the objective function of (5.20) to the objective function in the zero-one UQP (5.12) shows that they are of the same form[2]: the binary variables y_j in (5.12) correspond to $\hat{a}_{1j}$, and the coefficients b_{ij} and b_l in (5.12) are replaced by c_{ij} and c_l in (5.20), respectively.

As stated in the beginning of Section 5.6.2, a crucial condition for the NP-hardness of the zero-one UQP (5.12) is that its coefficients are in the sets $b_{ij} \in \{-2,0\}$ and $b_l \in \{0,1,...,N-1\}$. To show the NP-hardness of the zero-one UQP (5.20), we have to show that also the coefficients c_{ij} and c_l attain *any* value in $\{-2,0\}$ and $\{0,1,...,N-1\}$, respectively. As stated by (5.18), the coefficients c_{ij} may attain either value in $\{-2,0\}$. The remaining condition that the coefficients c_l, given by (5.19), may attain any value in $\{0,1,...,N-1\}$ *exactly* does generally not hold. Nevertheless, the coefficients c_l may approach any $b_l \in \{0,1,...,N-1\}$ *arbitrarily close*, as stated by Lemma 5.12.

Lemma 5.12 (Coefficients approach any number)**.** *The coefficients c_l of the optimisation problem (5.20), given by (5.19), may approach any numbers $b_l \in \mathbb{R}$, $l = 3,...,N$, arbitrarily close for suitably chosen natural numbers $m_0, m_{1l}, m_{2l} \in \mathbb{N}$:*

$$\forall \varepsilon_{\text{th},l} \in \mathbb{R}^+, l \in \{3,...,N\}, z_l \in \mathbb{R}: \ \exists m_0, m_{1l}, m_{2l} \in \mathbb{N} \quad \textit{such that} \quad |c_l - b_l| \leq \varepsilon_{\text{th},l} \tag{5.21}$$

Proof. Appendix D.3. □

If the deviation $(c_l - b_l)$ is positive and not greater than a threshold $\varepsilon_{\text{th},l} = \frac{1}{N}$, then we can solve any instance of the maximum-cut problem by solving an instance of the reduced-size SIS network reconstruction (5.17):

Lemma 5.13 (Sufficiently small errors on the UQP coefficients)**.** *If $c_l \geq b_l$ and $c_l - b_l < \frac{1}{N}$ for all $l \in \{3,...,N\}$, then the solution to the reduced-size SIS network reconstruction problem (5.20) is also a solution to the zero-one UQP (5.12).*

Proof. Appendix D.4. □

Lemma 5.11, Lemma 5.12 and Lemma 5.13 prove the NP-hardness of the reduced-size SIS network reconstruction (5.17). Lemma 5.14 states how to obtain the reduced-size SIS network reconstruction (5.12) from the original, full-size SIS network reconstruction problem (5.10).

Lemma 5.14 (From full-size to reduced-size SIS network reconstruction)**.** *For all connected adjacency matrices $A \in \mathcal{A}$ and all viral state sequence $x[1],...,x[n_1]$, there is a viral state sequence $x[1],...,x[n_2]$ with $n_2 > n_1$, such that the solution A_{ML} to the full-size SIS network reconstruction (5.10) satisfies:*

1. *The following elements of A_{ML} equal the elements of the true adjacency matrix A:*

$$(A_{\text{ML}})_{12} = a_{12} = 1 \quad \textit{and} \quad (A_{\text{ML}})_{ij} = a_{ij} \quad \textit{for all } i,j \geq 2$$

[2] The reduced-size SIS network reconstruction (5.17) for a graph with N nodes results in a zero-one UQP (5.12) with $N-2$ optimisation variables $\hat{a}_{13},...,\hat{a}_{1N}$. Strictly speaking, to obtain the zero-one UQP (5.12) with N optimisation variables, one has to consider the reduced-size SIS network reconstruction (5.17) for graphs with $N+2$ nodes. For ease of exposition, we omit the detail of the deviation of the number of optimisation variables of the two optimisation problems (5.12) and (5.17).

2. *The other elements of A_{ML} are the solution to the reduced-size SIS network reconstruction problem (5.17) whose objective function is changed by an additive term:*

$$\begin{aligned}((A_{\mathrm{ML}})_{13},\dots,(A_{\mathrm{ML}})_{1N}) = \underset{\hat{a}_{13},\dots,\hat{a}_{1N}}{\arg\max} \quad & \log\Big(\Pr\Big[x[1],\dots,x[n_1]\Big|\hat{a}_{13},\dots,\hat{a}_{1N}\Big]\Big) \\ & + \sum_{l=2}^{N} \kappa_l \log\big(1-\delta_{\Delta t}-\beta_{\Delta t} d_l(A)-\beta_{\Delta t}\hat{a}_{1l}\big) \\ \text{s.t.} \quad & \hat{a}_{1l}\in\{0,1\}, \quad l=3,\dots,N. \end{aligned} \tag{5.22}$$

Here, $d_l(A)=\sum_{m=2}^{N} a_{ml}$ denotes the degree of node l when node 1 is removed from the graph given by the adjacency matrix A, and κ_l is a natural number which is independent of the optimisation variables $\hat{a}_{13},\dots,\hat{a}_{1N}$.

Proof. Appendix D.5. □

The optimisation problem (5.22) resembles the reduced-size SIS network reconstruction (5.17), but the objective functions differ by the additive term

$$\sum_{l=2}^{N} \kappa_l \log\big(1-\delta_{\Delta t}-\beta_{\Delta t} d_l(A)-\beta_{\Delta t}\hat{a}_{1l}\big).$$

We show in Appendix D.6 that the additive term does not have an impact on the difficulty: The NP-hardness of the reduced-size SIS network reconstruction (5.17) implies the NP-hardness of the optimisation problem (5.22). Since solving the full-size SIS network reconstruction problem (5.10) with the viral state sequence $x[1],\dots,x[n_2]$ as input implies solving the NP-hard optimisation problem (5.22).

Theorem 5.15 (SIS network reconstruction is NP-hard)**.** *For all connected adjacency matrices $A\in\mathcal{A}$, the SIS network reconstruction problem (5.10) is NP-hard.*

Proof. Appendix D.6. □

We emphasise that the NP-hardness holds for *any* class of connected adjacency matrices $A\in\mathcal{A}$, also for simple topologies such as paths or star graphs.

5.7. HEURISTIC NETWORK RECONSTRUCTION

Since the SIS network reconstruction is NP-hard, we resort to designing a heuristic for (5.9). A commonly employed heuristic for solving mixed integer programming problems is based on the solution of a convex optimisation problem which results from relaxing the integer constraint [90], i.e., replacing $a_{ij}\in\{0,1\}$ by $a_{ij}\in[0,1]$. However, the objective function f_{obj} given by (5.8) contains the terms βa_{ij} which render f_{obj} non-convex also when applying the convex relaxation of the integer constraint.

The intuitive approach of introducing a new variable $\tilde{a}_{ij}=\beta_{\Delta t}a_{ij}$ and relaxing the binary constraint $\tilde{a}_{ij}\in\{0,\beta_{\Delta t}\}$ to $\tilde{a}_{ij}\in[0,\beta_{\Delta t}]$ cannot be straightforwardly employed. First, there is no guarantee that expressing $\log(p[A])$ by $\tilde{a}_{ij}$ (and possibly by $\beta_{\Delta t}$) results in a convex function. Second, even if A is assumed to be uniformly distributed

and the term $\log(p[A])$ can hence be omitted, replacing $\beta_{\Delta t} a_{ij}$ by $\tilde{a}_{ij}$ would erase $\beta_{\Delta t}$ in the objective f_{obj}, and $\beta_{\Delta t}$ would only appear in the constraints $\tilde{a}_{ij} \in [0, \beta_{\Delta t}]$ and $\Delta t \beta_{\min} \leq \beta_{\Delta t} \leq \Delta t \beta_{\max}$. Thus, setting $\beta_{\Delta t} = \Delta t \beta_{\max}$ would always be a solution to the corresponding convex optimisation problem since the constraint $[0, \Delta t \beta_{\max}]$ is the least restrictive interval for $\tilde{a}_{ij}$. It is not obvious how to infer an estimate $\beta_{\Delta t}$ which does not equal $\Delta t \beta_{\max}$, and furthermore, how to deduce $a_{ij} = 0$ or $a_{ij} = 1$ from a solution $0 < \tilde{a}_{ij} < \Delta t \beta_{\max}$.

We propose a heuristic by translating the non-convex optimisation problem (5.9) into w separate convex optimisation problems with the solutions $\tilde{\theta}_{\text{cvx},l}$ for $l = 1, ..., w$. The translation is achieved by a transformation of the optimisation variables, i.e., $\tilde{\theta} = h(\theta)$ for a bijective function h, a piecewise-linear approximation of non-convex terms of the objective function with w line segments and a convex relaxation of the binary constraint $a_{ij} \in \{0, 1\}$. The greater the number of line segments w, the more accurate is the piecewise-linear approximation. We refer the reader to Appendix D.7 for details of the heuristic.

The solutions $\tilde{\theta}_{\text{cvx},l} = (A_{\text{cvx},l}, \tilde{\beta}_{\text{cvx},l}, \tilde{\delta}_{\text{cvx},l}, \tilde{\epsilon}_{\text{cvx},l})$, $l = 1..., w$, correspond to non-binary link estimates. More specifically, $(A_{\text{cvx},l})_{i,j}$ may not be element of $\{0, 1\}$. Since the link weights a_{ij} must be either zero or one, we employ a heuristic to find an estimate that approximates the exact solution θ_{MAP} of the original optimisation problem (5.9). For each $\tilde{\theta}_{\text{cvx},l}$, we perform two steps.

1. The solution $\tilde{\theta}_{\text{cvx},l}$ of the optimisation problem (D.55) corresponds to a non-binary valued adjacency matrix $A_{\text{cvx},l}$. To obtain a binary-valued solution, we round the elements of $A_{\text{cvx},l}$ to the nearest integer, which results in the heuristic estimate denoted by

$$\left(A_{\text{heur},l}\right)_{ij} = \begin{cases} 1 & \text{if } \left(A_{\text{cvx},l}\right)_{ij} \geq \frac{1}{2}, \\ 0 & \text{if } \left(A_{\text{cvx},l}\right)_{ij} < \frac{1}{2}. \end{cases} \tag{5.23}$$

2. The binary-valued heuristic estimates for the adjacency matrix $A_{\text{heur},l}$, together with the estimates $\tilde{\beta}_{\text{cvx},l}, \tilde{\delta}_{\text{cvx},l}, \tilde{\epsilon}_{\text{cvx},l}$ for the spreading parameters obtained by the convex problems (D.55), do realise a feasible point to the original optimisation (5.9). However, we obtain a better estimation of the three rates, for the given $A_{\text{heur},l}$, as follows.

   When A is fixed to $A_{\text{heur},l}$, the objective of the original problem (5.9) becomes a function of the three rates,

$$f_{\text{obj},l}(\beta_{\Delta t}, \delta_{\Delta t}, \epsilon_{\Delta t}) = f_{\text{obj}}(A_{\text{heur},l}, \beta_{\Delta t}, \delta_{\Delta t}, \epsilon_{\Delta t}). \tag{5.24}$$

   The function $f_{\text{obj},l}(\beta_{\Delta t}, \delta_{\Delta t}, \epsilon_{\Delta t})$ is convex with respect to $\beta_{\Delta t}, \delta_{\Delta t}, \epsilon_{\Delta t}$. Hence, the function $f_{\text{obj},l}(\beta_{\Delta t}, \delta_{\Delta t}, \epsilon_{\Delta t})$ can be efficiently minimised with respect to these three variables, whereby the constraints of the original optimisation problem (5.9) have to be considered (the constraints are also convex with respect to $\beta_{\Delta t}, \delta_{\Delta t}, \epsilon_{\Delta t}$). The reduced-size optimisation problem is also called *convex restriction* [112] of the original optimisation problem at the point $A_{\text{heur},l}$.

The refinement of the spreading parameters by convex optimisation results in a heuristic estimate, which is denoted by $\theta_{\text{heur},l} = (A_{\text{heur},l}, \beta_{\text{heur},l}, \delta_{\text{heur},l}, \epsilon_{\text{heur},l})$. The heuristic is performed for every line segment $l = 1, ..., w$. Thus, we obtain w solution candidates $\theta_{\text{heur},l}$.

The final estimate of the presented heuristic estimation approach is denoted by θ_{heur} and is given by the candidate $\theta_{\text{heur},l}$ which results in the minimal value of the objective function (5.8),

$$\theta_{\text{heur}} = \arg\min \left\{ f_{\text{obj}}\left(\theta_{\text{heur},l}\right) \middle| l = 1, ..., w \right\}.$$

We denote the corresponding value of the objective function by $f_{\text{heur}} = f_{\text{obj}}(\theta_{\text{heur}})$.

In pseudocode, the approach for determining a heuristic estimate θ_{heur} is given by Algorithm 5.1. The presented algorithm allows for parallelisation in a straightforward manner since $\theta_{\text{heur},l}$ can be obtained independently for the different line segments l.

Algorithm 5.1 Heuristic SIS network reconstruction

Input: SIS observations $X[n]$
Output: Heuristic for MAP estimate θ_{heur}
$f_{\text{heur}} \leftarrow \infty$
for $l = 1, ..., w$ **do**
  Obtain $\tilde{\theta}_{\text{cvx},l} = (A_{\text{cvx},l}, \tilde{\beta}_{\text{cvx},l}, \tilde{\delta}_{\text{cvx},l}, \tilde{\epsilon}_{\text{cvx},l})$ by solving (D.55)
  Obtain binary $A_{\text{heur},l}$ from non-binary $A_{\text{cvx},l}$ by rounding (5.23)
  Obtain $\left(\beta_{\text{heur},l}, \delta_{\text{heur},l}, \epsilon_{\text{heur},l}\right)$ by minimising $f_{\text{obj},l}(\beta_{\Delta t}, \delta_{\Delta t}, \epsilon_{\Delta t})$ in (5.24)
  if $f_{\text{obj}}\left(A_{\text{heur},l}, \beta_{\text{heur},l}, \delta_{\text{heur},l}, \epsilon_{\text{heur},l}\right) < f_{\text{heur}}$ **then**
    $\theta_{\text{heur}} \leftarrow \left(A_{\text{heur},l}, \beta_{\text{heur},l}, \delta_{\text{heur},l}, \epsilon_{\text{heur},l}\right)$
    $f_{\text{heur}} \leftarrow f_{\text{obj}}(\theta_{\text{heur}})$
  end if
end for

5.8. NUMERICAL EVALUATION

We perform numerical evaluations for both the heuristic estimation approach and the brute-force approach. We generate multiple Erdős-Rényi graphs and, for each of these graphs, generate the nodal infection state matrix $X[n]$ by a random number generator, according to the transition probabilities of the sampled-time ϵ-SIS process. Then, we give the nodal states $X[n]$ as input to the estimation procedures. We obtain a solution to the optimisation problems (D.55) by the Matlab command `fmincon`.

We choose the link probability p_{ER} of the Erdős-Rényi model such that the generated random graphs are connected with a high probability, which holds if p_{ER} is significantly greater than the threshold $\log(N)/N$. By setting $p_{\text{ER}} = 0.7$, we ensure $p_{\text{ER}} > 2\log(N)/N$ for all networks considered in the numerical evaluation, which are of size $N = 4$ or greater. For Erdős-Rényi random graphs, the logarithm of the prior distribution of the adjacency matrix A is given by

$$\log\left(\Pr[A]\right) = \frac{1}{2} N(N-1) \log\left(1 - p_{\text{ER}}\right) + \log\left(\frac{p_{\text{ER}}}{1 - p_{\text{ER}}}\right) \sum_{i=1}^{N} \sum_{j=1}^{N} a_{ij}.$$

Only the second addend depends on A and has to be considered for the optimisation. Alternatively, prior information on the link density could be considered by replacing $\log(\Pr[A])$ by $\rho \sum_{ij} a_{ij}$, where ρ is the sparsity parameter [97].

We compare the brute-force and the heuristic estimation of Section 5.7 for small networks, with $N = 4,5,6$ nodes, and for observation lengths ranging from $n = 100$ to $n = 5000$. Furthermore, the heuristic estimation approach is numerically evaluated for larger networks up to $N = 24$ nodes and observation lengths ranging from $n = 10^3$ to $n = 10^6$. For each pair of number of nodes N and observation length n, we generate 10^3 Erdős-Rényi random graphs with $p = 0.7$ – except for the comparison of brute-force and heuristic in Subsection 5.8.1, where $2 \cdot 10^3$ networks are created.

The spreading parameters are set to $\beta = 2/3$, $\delta = 1$ and $\epsilon = 0.01$. The upper bounds on the parameters are set to $\beta_{\max} = 1$, $\delta_{\max} = 1$ and $\epsilon_{\max} = 1$. The lower bound on the infection rate is set to $\beta_{\min} = 0.1\beta = 2/30$. The sampling time Δt is set as large as possible, considering the upper bound (5.4). Every node is set initially to the infected state, i.e., $x[1] = u$. For the heuristic approach presented in Section 5.7, we set the number of line segments to $w = 10$.

We compare the accuracy of the resulting estimates as follows. For the spreading parameters β, δ and ϵ, the error of the estimates is defined as the relative deviation $(\beta - \hat{\beta})/\beta$, where $\hat{\beta}$ is the estimate and β the true value. The errors of the rates δ and ϵ are defined analogously. For the adjacency matrix A, we define the error as

$$\varepsilon_A = \frac{1}{L} \sum_{i=1}^{N} \sum_{j=1}^{N} \left| \hat{a}_{ij} - a_{ij} \right|,$$

where $\hat{a}_{ij}$ and a_{ij} are the elements of the estimated and true adjacency matrix, respectively, and $L = (N-1)N/2$ is the number of possible links.

5.8.1. EVALUATION OF THE HEURISTIC ESTIMATION METHOD

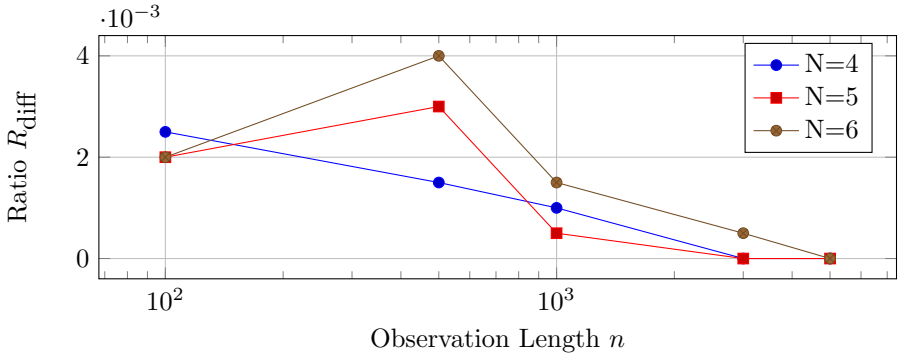

Figure 5.1: **Accuracy of the heuristic.** Fraction R_{diff} of 2,000 randomly generated graphs for which the results of the heuristic and the exact brute-force methods do not coincide.

Figure 5.1 shows that for almost every randomly generated graph the heuristic and the brute-force estimates are identical. Figure 5.2 demonstrates the difference in computation time of the heuristic and exact brute-force approach.

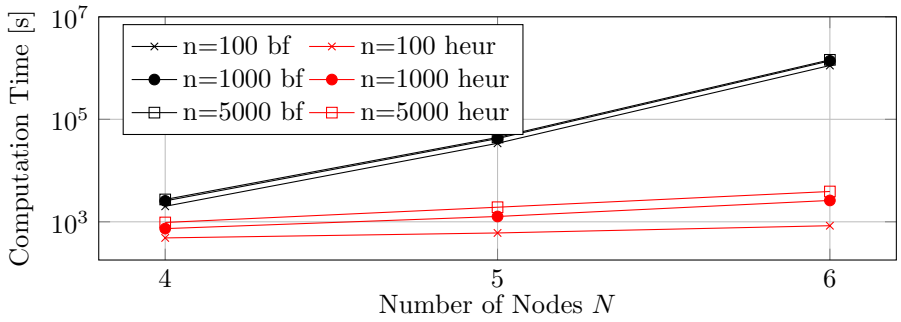

Figure 5.2: **Computation time of the heuristic.** Comparison of computation time of heuristic (heur) and brute-force (bf) approach in dependency of the number of nodes N.

5.8.2. ACCURACY OF ESTIMATION DEPENDING ON OBSERVATION LENGTH

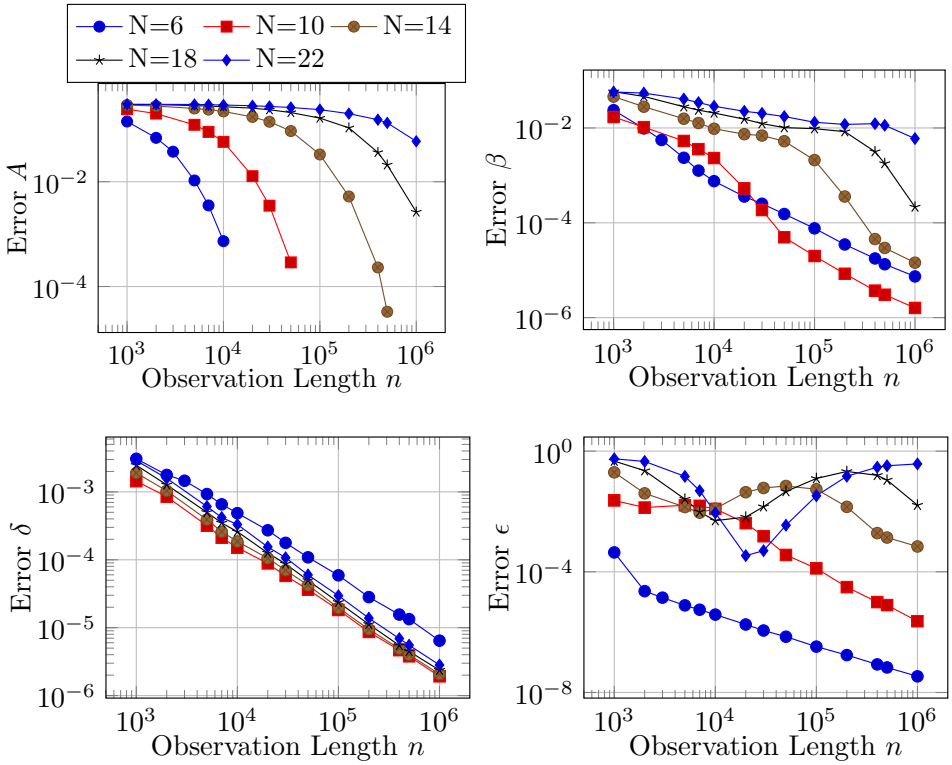

Figure 5.3: **Network reconstruction accuracy versus observation length.** The accuracy of the reconstructed network and estimated parameters in dependency of the observation length n. Discontinued graphs in the top left plot refer to zero errors of the estimate of A.

Figure 5.3 shows the accuracy of the estimate θ_{heur} versus the observation length

n. For a large observation length n, the adjacency matrix A is almost always exactly reconstructed. Furthermore, the network size N does not have a considerable impact on the estimation accuracy of the curing rate δ. In contrast, the estimation accuracy of the rates β and ϵ does depend significantly on the network size N. For a small observation length n, for which the adjacency matrix A is reconstructed poorly, the accuracy of the estimate of the self-infection rate ϵ is not monotonically increasing.

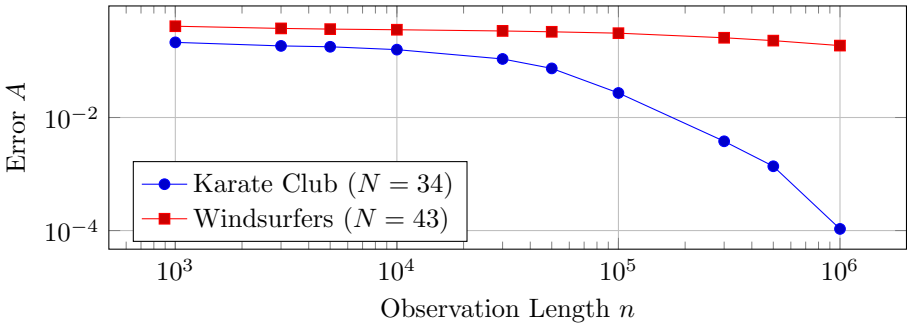

Figure 5.4: **Network reconstruction for real-world networks.** The accuracy of the reconstructed network and estimated parameters in dependency of the observation length n, for two real-world networks.

We evaluate our network reconstruction method for two real-world networks, the Zachary karate club [113] with $N = 34$ nodes and the network of windsurfers [114] with $N = 43$ nodes. Both networks were accessed via the *Konect* network collection [62].

For the two networks, 100 different SIS viral state sequences $x[1], ..., x[n]$ were created. Since the prior distribution $\Pr[A]$ is not available, we perform an ML estimation by omitting the term $\log(\Pr[A])$ in the objective function (5.7). Figure 5.4 shows the network reconstruction accuracy, averaged over the 100 different SIS viral state traces, in dependency of the observation length n. For both networks, a reasonable estimation accuracy requires a large number of observations n.

5.8.3. REQUIRED OBSERVATION LENGTH AND COMPUTATION TIME

Figure 5.5 and Figure 5.6 show the observation length n and the computation time T_{comp}, respectively, versus the network size N, to attain a given network reconstruction accuracy. Since none of the data points in Figure 5.3 coincides exactly with either of the desired error on the estimate of A, we perform linear interpolation to obtain Figure 5.5 and Figure 5.6. Both the observation length n and the computation time grow nearly exponentially with respect to the number of nodes N. Indeed, the number of observations n approximately grows as $\log_{10}(n) \approx N^{\alpha} + b$. Similarly, we find that the computation time T_{comp} approximately obeys $\log_{10}(T_{\text{comp}}) \approx mN + d$. The parameters α, b, m and d are given by Table 5.1.

For the Zachary karate club network [113] of size $N = 34$, Algorithm 5.1 took approximately 75 minutes on a *2.5GHz Intel® Xeon® Processor E5-2670 v2* for a reasonable net-

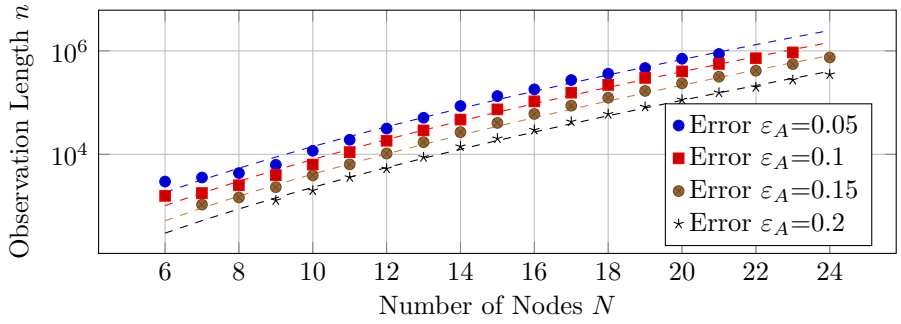

Figure 5.5: **Observation length versus network size.** The required observation length n to attain a given link error ε_A of the estimate of A versus the number of nodes N. The points are obtained by interpolation and the fitted dependencies are given by the dashed graphs.

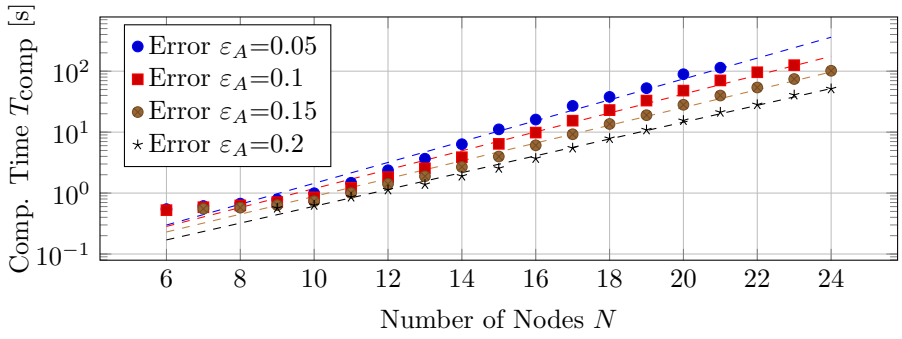

Figure 5.6: **Computation time versus network size.** The required computation time T_{comp} to attain a given link error ε_A of the estimate of A versus the number of nodes N. The points are obtained by interpolation and the fitted dependencies are given by the dashed graphs.

work reconstruction accuracy (an average fraction of erroneous links $\varepsilon_A \approx 10^{-4}$). As illustrated by Figure 5.6, the computation time for a desired average fraction of erroneous links ε_A grows nearly exponentially with the network size N, which poses a severe practical constraint, even if the large number of observations n given by Figure 5.5 is available.

5.9. CONCLUSIONS

We propose a Bayesian formulation for the SIS network reconstruction from viral state observations, based on the sampled-time SIS process. Our contribution is twofold. First, we considers the computational complexity of finding the maximum-likelihood estimate of the network topology. Instead of reconstructing a network for a *given* viral state sequence, we considered the reverse problem of *designing* a viral state sequence such that estimating the presence or absence of links either becomes computationally difficult (Lemma 5.11) or easy (first statement of Lemma 5.14). Specifically, we showed that the maximum-likelihood network reconstruction for SIS processes is NP-hard.

Table 5.1: **Fitted parameters for the observation length and the computation time versus the number of nodes.** Parameters obtained by fitting the number of observations n and the computation time T_{comp} in dependency of the number of nodes N, respectively.

Error A	0.2	0.15	0.1	0.05
α	0.5548	0.5596	0.5566	0.5549
b	-0.2259	0.0097	0.2985	0.5621
m	0.1380	0.1459	0.1551	0.1712
d	-1.5966	-1.5138	-1.4777	-1.5518

Second, we proposed an efficient, polynomial-time heuristic for the Bayesian SIS network reconstruction problem. Numerical evaluations indicate that our heuristic performs almost optimally for small networks. Thus, our heuristic is a good candidate for reconstructing larger networks, whose size render the solution of the optimal, NP-hard network reconstruction problem computationally infeasible. For sufficiently many observations n, our heuristic reconstructs the contact network and the spreading rates accurately. However, to attain a given network reconstruction accuracy, the number of observations n grows rapidly with respect to the network size N. In particular, we found the approximate relation $\log_{10}(n) \approx N^{\alpha} + b$, where $\alpha \approx 0.56$. In practical applications, the underlying network is only available in exceptional cases, and an accurate network reconstruction seems infeasible due to the tremendous observation lengths n.

ACKNOWLEDGEMENTS

We are grateful to Jaron Sanders for helpful discussions on the proof of the NP-hardness.

6

On the Accuracy of Predicting Epidemic Outbreaks

During an epidemic outbreak, perhaps the greatest concern is the future evolution: How many people will be infected and which regions will be affected the most? The accurate prediction of an epidemic enables targeted disease counter-measures (e.g., allocating medical staff and quarantining). But, when can we trust the prediction of an epidemic to be accurate? The contribution of this chapter is twofold. First, we demonstrate the ill-conditioning of predicting the logistic function, which is central to epidemic models. In particular, an epidemic can be predicted reliably only in the short term, or once the number of infections has passed the peak value. Second, we show that it is possible to compare the accuracy of predictions performed at two different observation times, without knowing the future number of infections.

This chapter is based on [115].

6.1. INTRODUCTION

Predictions of the epidemic outbreaks are a decisive tool for policy makes: if the future course of an epidemic is known, then appropriate disease counter-measures, such as societal lockdowns, can be deployed. A great body of research proposed various methods for predicting epidemic outbreaks. Predictions are valuable only if the prediction accuracy is known. Here, our focus are the fundamental limits of predicting epidemic outbreaks, which apply to any prediction method.

In this chapter, we focus on a homogeneous population, whose individuals are interchangeable. We consider two epidemic models. First, the SIS epidemic model, which assumes that infected individuals can cure and become susceptible again:

Definition 6.1 (SIS model in a homogeneous population [1, 116])**.** Consider a population of individuals, which are either susceptible $\mathcal{S}$ or infected $\mathcal{I}$ at every time $t \geq 0$. Denote the infection rate by $\beta > 0$ and the curing rate by $\delta > 0$. Then, the fraction of infected individuals $\mathcal{I}(t)$ evolves according to

$$\frac{d\mathcal{I}(t)}{dt} = \beta \mathcal{S}(t)\mathcal{I}(t) - \delta \mathcal{I}(t), \tag{6.1}$$

and the fraction of susceptible individuals follows as $\mathcal{S}(t) = 1 - \mathcal{I}(t)$.

The SIS epidemic model for a homogeneous population (6.1) is a special case of the NIMFA epidemic model on networks in Definition 1.1. More specifically, by setting[1] $N = 1$, $\beta_{ii} = \beta$ and $\delta_i = \delta$, the NIMFA equations (1.1) reduce to (6.1). From the fraction of the infected individuals $\mathcal{I}(t)$, the number of infected individuals follows as $N_{\text{pop}}\mathcal{I}(t)$, where N_{pop} denotes the number of all individuals in the population.

Second, we consider the SIR epidemic model in a homogeneous population. The SIR model assumes that cured individuals are immune to the disease, which is modelled by the compartment *removed* $\mathcal{R}$.

Definition 6.2 (SIR model in a homogeneous population [30])**.** Consider a population of individuals, which are either susceptible $\mathcal{S}$, infected $\mathcal{I}$ or removed $\mathcal{R}$ at every time $t \geq 0$. Denote the infection rate by $\beta > 0$ and the curing rate by $\delta > 0$. Then, the fraction of infected individuals $\mathcal{I}(t)$ evolves according to

$$\frac{d\mathcal{I}(t)}{dt} = \beta \mathcal{S}(t)\mathcal{I}(t) - \delta \mathcal{I}(t),$$

the fraction of removed individuals $\mathcal{R}(t)$ evolves according to

$$\frac{d\mathcal{R}(t)}{dt} = \delta \mathcal{I}(t), \tag{6.2}$$

and the fraction of susceptible individuals follows as $\mathcal{S}(t) = 1 - \mathcal{I}(t) - \mathcal{R}(t)$.

Analogously to the SIS model (6.1), the SIR epidemic model for a homogeneous population in Definition 6.1 is a special case of the SIR epidemic model *on networks* in Definition 1.2.

[1] More generally, the SIS model in a homogeneous population (6.1) describes NIMFA (1.1) on a *regular* infection rate matrix B, see Corollary 3.11.

The prediction of an epidemic translates to estimating the value of the compartments $\mathcal{S}(t)$, $\mathcal{I}(t)$, $\mathcal{R}(t)$ at future times t. For both the SIS and SIR model in homogeneous populations, we argue that the prediction of an epidemic is inherently difficult, independently of the particular prediction algorithm.

6.2. RELATED WORK

Several studies approach the prediction limits of epidemic outbreaks from different angles. Cirillo and Taleb [117] demonstrate that the number of fatalities of various past epidemics is strongly fat-tailed, which renders long-term predictions of epidemics outbreaks impossible. Castro *et al.* [118] and Paggi [119] study extensions of the SIR model and show that, even though the respective model accurately fits the past epidemic outbreak, a reliable prediction is not possible. The same conclusion is drawn by Alberti and Faranda [120], who directly fit a logistic function to the number of infections. In this chapter, we aim to *quantify* the predictability of an epidemic. We show that the predictability is limited by the initial exponential growth of the epidemic, and we propose a metric to quantify exponential growth. Based on the growth metric, it is indeed possible to obtain quantitative statements on the predictability of an epidemic.

6.3. THE LOGISTIC FUNCTION IN EPIDEMIC MODELS

At the heart of both the SIS and the SIR epidemic model lies the logistic function $f(t)$, which has been introduced by Verhulst [71] as

$$f(t) = \frac{y_\infty}{1 + e^{-K(t-t_0)}}. \tag{6.3}$$

Here, we denote the *steady-state* fraction of infections (also called the prevalence) by $y_\infty > 0$, the *inflection point* (peak of the number of new infections) by t_0 and the logistic *growth rate* by $K > 0$. For both the SIS and the SIR epidemic model, we denote the *effective infection rate* by $\tau = \beta/\delta$. Proposition 6.3 states that the solution of the SIS model is given by a logistic function. Proposition 6.3 is not a novel contribution but is included for completeness.

Proposition 6.3. *Consider the SIS epidemic model and assume that $\beta > \delta$ and $\mathcal{I}(0) > 0$. Then, the fraction of infected individuals $\mathcal{I}(t)$ is given by a logistic curve*

$$\mathcal{I}(t) = \frac{y_\infty}{1 + e^{-K(t-t_0)}}.$$

Here, the steady state equals $y_\infty = 1 - \frac{1}{\tau}$, the logistic growth rate equals $K = \beta - \delta$, and the inflection point equals

$$t_0 = \frac{1}{K} \log\left(\frac{1}{\mathcal{I}(0)}\left(1 - \frac{1}{\tau}\right) - 1\right).$$

Also for the SIS epidemic model *on networks*, the logistic curve gives an approximation and bounds for describing the number of infected individuals, see [72] and Chapter 3.

Similarly to Proposition 6.3, in the SIR epidemic model, the solution for the removed compartment $\mathcal{R}(t)$ can be approximated by a logistic function, as shown in the seminal work of Kermack and McKendrick [30].

Proposition 6.4 ([30])**.** *Consider the SIR epidemic model and assume that* $\mathcal{R}(0) = 0$ *and* $\mathcal{I}(0) > 0$*. Then, if* $\mathcal{R}(t) \ll \delta/\beta$ *holds true at all times* t*, the fraction of removed individuals* $\mathcal{R}(t)$ *can be approximated by a logistic curve at all times* $t \geq 0$ *as*

$$\mathcal{R}(t) \approx \sigma_1 + \frac{\sigma_2 - \sigma_1}{1 - \frac{\sigma_2}{\sigma_1} e^{-\frac{1}{2}\tau^2(\sigma_2-\sigma_1)\delta t}}.$$

Here, the constants σ_1 *and* σ_2 *equal to*

$$\sigma_l = \begin{cases} \frac{1}{s_0\tau^2}\left((s_0\tau - 1) + \sqrt{(s_0\tau-1)^2 + 2s_0(1-s_0)\tau^2}\right) & \text{if} \quad l = 1, \\ \frac{1}{s_0\tau^2}\left((s_0\tau - 1) - \sqrt{(s_0\tau-1)^2 + 2s_0(1-s_0)\tau^2}\right) & \text{if} \quad l = 2. \end{cases}$$

Proposition 6.4 states that the removed individuals $\mathcal{R}(t)$ is approximated by a logistic function *plus the offset* σ_1. By the definition of the SIR model in (6.2), the fraction of infections $\mathcal{I}(t)$ is proportional to the derivative of the removed individuals $\mathcal{R}(t)$. Thus, Proposition 6.4 implies that the *cumulative* number of infections

$$\mathcal{I}_c(t) = \int_0^t N_{\text{pop}} \mathcal{I}(z)\, dz, \tag{6.4}$$

where N_{pop} is the size of the population, is approximated by a logistic function (plus offset σ_1). Then, the peak of the epidemic, i.e., the largest *increase* of infections, occurs at the inflection point t_0.

In contrast to the deterministic SIS process of Definition 6.1, the logistic function $f(t)$ is not an accurate description of the *stochastic* SIS process in some settings [72, 121]. In particular, the prevalence of the stochastic SIS process can exhibit a local minimum, before converging to the metastable state. However, the cumulative number of infections $\mathcal{I}_c(t)$ is non-decreasing, and most real-world epidemics are well described by a sigmoid curve, without local minima.

6.4. PREDICTING EPIDEMIC OUTBREAKS

Proposition 6.3 and Proposition 6.4, and variations thereof, motivate the application of the logistic function (6.3) to the prediction of an epidemic outbreak. In particular, the logistic function has been applied to forecast the Coronavirus Virus Disease 2019 (COVID-19) outbreak in China [122–126] and Italy [127]. Furthermore, the logistic function has been applied to predict other phenomena than COVID-19, including tuberculosis [128] and product sales [129, 130]. We consider the prediction of the cumulative number of infections $\mathcal{I}_c(t)$, as defined in (6.4). Real-world epidemic data is collected in a periodic manner, i.e., in discrete time intervals. For instance, the Dutch National Institute for Public Health and the Environment (RIVM) reports the number of COVID-19 infections in the Netherlands on a daily basis[2]. We consider that the number of infections is reported at discrete times $t = \Delta t, 2\Delta t, \ldots, n\Delta t$ for some sampling time Δt, where n denotes

[2] See https://www.rivm.nl/coronavirus-covid-19/actueel.

the number of observations. (Typically, the sampling time Δt equals one day for reporting infections.) For a given sampling time Δt, we denote the number of infections at discrete time $k = 1,\ldots,n$ by $\mathcal{I}_c[k] = \mathcal{I}_c(k\Delta t)$. Furthermore, we denote the *observation time* by $t_{\text{obs}} = n\Delta t$.

In a real-world epidemic, the infections $\mathcal{I}_c[k]$ do not exactly follow a logistic function $f(k\Delta t)$. Instead, the infections $\mathcal{I}_c[k]$ satisfy

$$\mathcal{I}_c[k] = f(k\Delta t) + w[k] \tag{6.5}$$

for some logistic function $f(k\Delta t)$ and the unknown *model error* $w[k]$ at time k. To predict the number of infections $\mathcal{I}_c[k]$ at times $k > n$, we consider a two-step approach. First, we obtain parameter estimates $\hat{y}_\infty, \hat{t}_0, \hat{K}$ of the logistic function $f(t)$ by solving the constrained non-linear least-squares problem

$$\begin{aligned}(\hat{y}_\infty, \hat{t}_0, \hat{K}) = \underset{y_\infty, t_0, K}{\operatorname{argmin}} \sum_{k=1}^{n} \left(\mathcal{I}_c[k] - \frac{y_\infty}{1+e^{-K(k\Delta t - t_0)}}\right)^2, \\ \text{s.t.} \quad 0 \le y_{\infty,i} \le N_{\text{pop}}, \\ K \ge 0, \\ t_0 \ge 0.\end{aligned} \tag{6.6}$$

We solve the optimisation problem (6.6) by the Matlab command `GlobalSearch`. As initial conditions, we provide $y_\infty^{(0)} = \mathcal{I}_c[n]$, $K^{(0)} = 1$ and $t_0^{(0)} = t_{\text{obs}}$.

Second, we predict the number of infections $\mathcal{I}_c[k]$ at times $k > n$ by the logistic function (6.3) as $\hat{\mathcal{I}}_c[k] \approx \hat{f}(k\Delta t)$, where the estimate of the logistic function $f(t)$ equals

$$\hat{f}(t) = \frac{\hat{y}_\infty}{1+e^{-\hat{K}(t-\hat{t}_0)}}.$$

Schultz [131] analysed the impact of errors of the parameters $\hat{y}_\infty, \hat{K}, \hat{t}_0$ on the deviation of the logistic function $f(t)$ to its estimate $\hat{f}(t)$. The remainder of this section consists of two parts. First, we focus on the simplified problem of fitting the logistic function $f(t)$ to three points in Subsection 6.4.1. Second, we argue that the prediction of epidemics is ill-conditioned in Subsection 6.4.2.

6.4.1. FITTING THE LOGISTIC FUNCTION TO THREE EQUIDISTANT POINTS

As shown below, a central quantity for fitting the logistic function $f(t)$ is the *growth metric* $\Phi(y_1, y_2, y_3)$:

Definition 6.5. For some function $g(t)$, with $g(t) > 0$ at all times t, consider three equidistant points $y_1 = g(0)$, $y_2 = g(t_{\text{obs}}/2)$, $y_3 = g(t_{\text{obs}})$. Then, the growth metric is defined by

$$\Phi(y_1, y_2, y_3) = \frac{y_2}{y_3} - \frac{y_1}{y_2}. \tag{6.7}$$

The growth metric $\Phi(y_1, y_2, y_3)$ can be interpreted in two ways. First, consider the sign of the growth metric $\Phi(y_1, y_2, y_3)$. It holds that $\Phi(y_1, y_2, y_3) > 0$ if and only if [3] to

[3] Furthermore, $y_3/y_2 = y_2/y_1$ is equivalent to $\log(y_3) - \log(y_2) = \log(y_2) - \log(y_1)$. Thus, $\Phi(y_1, y_2, y_3) = 0$ if and only if the three equidistant points y_1, y_2, y_3 lie on a line in a semilogarithmic plot (see also Figure 6.1).

$y_3/y_2 < y_2/y_1$. In other words, the relative increase y_3/y_2 from time $t = t_{\text{obs}}/2$ to $t = t_{\text{obs}}$ must be smaller than the relative increase y_2/y_1 from time $t = 0$ to $t = t_{\text{obs}}/2$. By definition of exponential growth, it would hold that $y_3/y_2 = y_2/y_1$ if the three points y_1, y_2 and y_3 were on an exponential function, i.e., $y_1 = b^t$, $y_2 = b^{t+t_{\text{obs}}/2}$ and $y_3 = b^{t+t_{\text{obs}}}$ for some basis $b \geq 0$. Thus, $\Phi(y_1, y_2, y_3) > 0$ and $\Phi(y_1, y_2, y_3) < 0$ indicates that the function $g(t)$ grows slower or faster, respectively, than an exponential function from time $t = 0$ to time $t = t_{\text{obs}}$.

Second, the growth metric $\Phi(y_1, y_2, y_3)$ is related to the logarithmic derivative of the function $g(t)$. Denote the logarithm of the function $g(t)$ as $h(t) = \log(g(t))$. The first derivative of $h(t)$ equals $h'(t) = g'(t)/g(t)$. For small sampling times Δt, the derivative $h'(t)$ is approximated by the difference quotient

$$h''(t) \approx \frac{1}{\Delta t}\left(\frac{g'(t+\Delta t)}{g(t+\Delta t)} - \frac{g'(t)}{g(t)}\right).$$

Analogously, both derivatives $g'(t+\Delta t)$ and $g'(t)$ can be approximated by difference quotients, which yields that

$$\begin{aligned} h''(t) &\approx \frac{1}{\Delta t^2}\left(\frac{g(t+\Delta t) - g(t)}{g(t+\Delta t)} - \frac{g(t) - g(t-\Delta t)}{g(t)}\right) \\ &= -\frac{1}{\Delta t^2}\left(\frac{g(t)}{g(t+\Delta t)} - \frac{g(t-\Delta t)}{g(t)}\right). \end{aligned}$$

Hence, by identifying $y_1 = g(t-\Delta t)$, $y_2 = g(t)$ and $y_3 = g(t+\Delta t)$, we obtain that

$$\Phi(y_1, y_2, y_3) \approx -\Delta t^2 h''(t).$$

Particular, if $\Phi(y_1, y_2, y_3) > 0$ and the sampling time Δt is sufficiently small, then the function $g(t)$ is strictly logarithmically concave [90].

Pearl and Reed [132] showed that the logistic function $f(t)$ can be fitted in closed form to three points y_1, y_2 and y_3 at equidistant time points[4] $t = 0$, $t = t_{\text{obs}}/2$ and $t = t_{\text{obs}}$. We observe that the results in [132] can be stated in dependency on the growth metric $\Phi(y_1, y_2, y_3)$ as:

Proposition 6.6. *Consider three points $y_3 > y_2 > y_1 > 0$ and an observation time $t_{\text{obs}} > 0$. Then, there exists a logistic function $f(t)$ with $f(0) = y_1$, $f(t_{\text{obs}}/2) = y_2$ and $f(t_{\text{obs}}) = y_3$ if and only if*

$$\Phi(y_1, y_2, y_3) > 0. \tag{6.8}$$

Furthermore, the logistic function $f(t)$ is unique, and the steady-state equals

$$y_\infty = y_1 + \frac{(y_1 - y_2)^2}{y_2}\frac{1}{\Phi(y_1, y_2, y_3)}, \tag{6.9}$$

[4] Without loss of generality, we assume that the first point y_1 corresponds to time $t = 0$. Otherwise, if the first point y_1 corresponds to some time $\tilde{t} > 0$, then consider a time shift by formally replacing t with $t + \tilde{t}$.

the logistic growth rate equals

$$K = -\frac{2}{t_{\text{obs}}} \log\left(\frac{y_1}{y_2} + \frac{y_1}{y_1 - y_2}\Phi\left(y_1, y_2, y_3\right)\right), \tag{6.10}$$

and the inflection point equals

$$t_0 = \frac{1}{K} \log\left(\frac{\left(y_1 - y_2\right)^2}{y_1 y_2} \frac{1}{\Phi(y_1, y_2, y_3)}\right). \tag{6.11}$$

Proof. Appendix E.1. □

We emphasise that condition (6.8) implies that a logistic function $f(t)$ can only be fitted exactly to three points y_1, y_2, y_3 whose relative increase is slower than exponential. Figure 6.1 shows that the growth metric $\Phi(f(0), f(t/2), f(t))$ is close to zero for small times t. Thus, the logistic function $f(t)$ is practically indistinguishable[5] from an exponential function at small times t. As we argue in Subsection 6.4.2, the strong resemblance of the logistic function $f(t)$ and an exponential function is decisive for the prediction limits of an epidemic outbreak.

6.4.2. ILL-CONDITIONING OF PREDICTING EPIDEMIC OUTBREAKS

If the model errors $w(t)$ in (6.5) are sufficiently small, then the solution $\hat{y}_\infty, \hat{t}_0, \hat{K}$ to the least-squares problem (6.6) approximately equals to the true parameters y_∞, t_0, K. However, it is not clear what "sufficiently small" means. Thus, we face the fundamental question: *How much do small, but non-zero, model errors $w(t)$ affect the accuracy of the estimate $\hat{f}(t)$?*

To quantify the deviation of the estimated logistic function $\hat{f}(t)$ to the true function $f(t)$, we apply Proposition 6.6, which states that every logistic function can be parameterised by specifying three points y_1, y_2 and y_3. We set the three points of the true logistic function $f(t)$ in (6.5) to $y_1 = f(0)$, $y_2 = f(t_{\text{obs}}/2)$ and $y_3 = f(t_{\text{obs}})$. Analogously, we denote the corresponding points of the estimate $\hat{f}(t)$, obtained by (6.6), as $\hat{y}_1 = \hat{f}(0)$, $\hat{y}_2 = \hat{f}(t_{\text{obs}}/2)$ and $\hat{y}_3 = \hat{f}(t_{\text{obs}})$. The points $\hat{y}_1, \hat{y}_2, \hat{y}_3$ depend on the unknown model error $w(t)$. If the model error $w(t) \to 0$ at every time $t \in [0, t_{\text{obs}}]$, then it holds that $\hat{y}_i \to y_i$ for $i = 1,2,3$, which implies that $\hat{f}(t) \to f(t)$ at every time t.

We consider the *best case* and assume that, due to non-zero model errors $w[k]$, the estimate $\hat{f}(t)$ differs from the true function $f(t)$ in only one of the points y_1, y_2, y_3. More precisely, we consider that $\hat{y}_1 = y_1$, $\hat{y}_2 = y_2$ and $\hat{y}_3 = y_3 + \epsilon$ for some small perturbation ϵ. Thus, $\epsilon \to 0$ implies that $\hat{f}(t) \to f(t)$ at every time t. For now, we focus on the sensitivity of estimating the steady state y_∞. We define $\hat{y}_\infty(\epsilon)$ as the estimate of the steady state y_∞, given the perturbation $\hat{y}_3 = y_3 + \epsilon$. By applying Taylor's Theorem to (6.9), we obtain for a small perturbation ϵ that

$$\hat{y}_\infty(\epsilon) = y_\infty + \epsilon\kappa_1(t_{\text{obs}}) + \mathcal{O}\left(\epsilon^2\right), \tag{6.12}$$

[5] Here, we consider logistic functions $f(t)$ whose inflection point $t_0 \gg 0$, such that $f(t) \approx y_\infty e^{K(t-t_0)}$ when t is small.

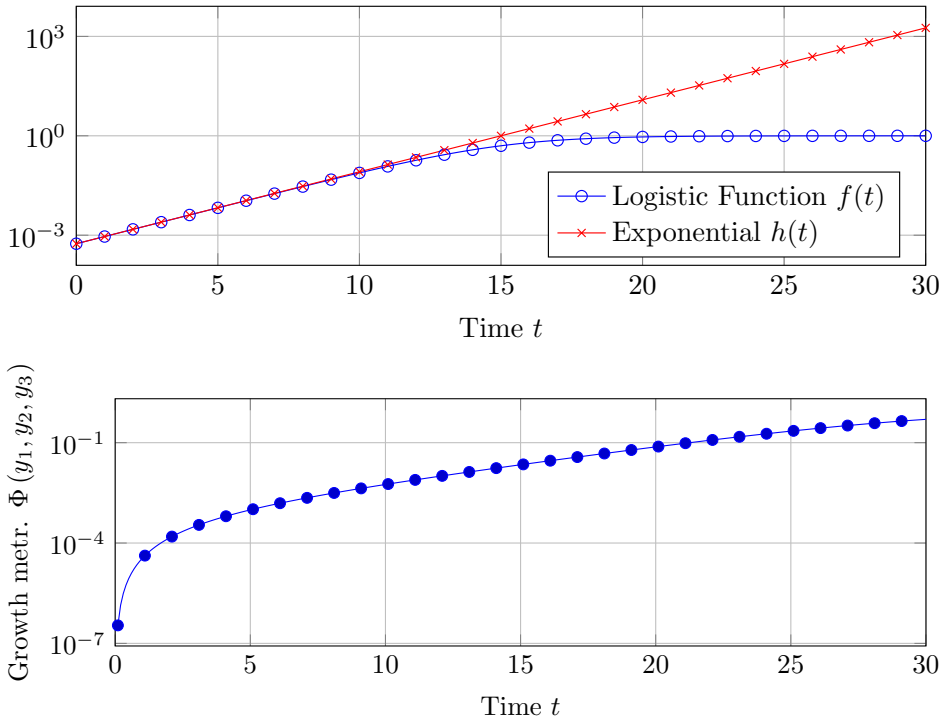

Figure 6.1: **Growth metric for a logistic function.** Upper subplot: The logistic function $f(t)$ with parameters $K = 0.5$, $t_0 = 15$ and $y_\infty = 1$ and the exponential function $h(t) = y_\infty e^{\hat{K}(t-t_0)}$ on a semi-logarithmic scale. Lower subplot: The growth metric $\Phi(y_1, y_2, y_3)$ for the points $y_1 = f(0)$, $y_2 = f(t/2)$, $y_3 = f(t)$ versus time t on a semi-logarithmic scale.

where we define[6] the *condition number* $\kappa_1(t_{\text{obs}})$ as

$$\kappa_1(t_{\text{obs}}) = \frac{\partial}{\partial y_3}\left(y_1 + \frac{(y_1 - y_2)^2}{y_2}\frac{1}{\Phi(y_1, y_2, y_3)}\right). \tag{6.13}$$

The condition number $\kappa_1(t_{\text{obs}})$ depends on the observation time t_{obs}, since the three points are given by $y_1 = f(0)$, $y_2 = f(t_{\text{obs}}/2)$ and $y_3 = f(t_{\text{obs}})$. From (6.12) it follows that the condition number $\kappa_1(t_{\text{obs}})$ describes the impact, or the amplification, of a small error $\epsilon = \hat{y}_3 - y_3$ on the estimate $\hat{y}_\infty(\epsilon)$. *The greater the condition number $\kappa_1(t_{\text{obs}})$, the harder it is to estimate the steady state y_∞.* Analogously to the condition number $\kappa_1(t_{\text{obs}})$ for the estimate of the steady state $y_\infty(\epsilon)$, we define the condition numbers $\kappa_2(t_{\text{obs}})$ and $\kappa_3(t_{\text{obs}})$ for the growth rate estimate $\hat{K}(\epsilon)$ and the inflection point estimate $\hat{t}_0(\epsilon)$, respectively. (See also Appendix E.2.)

[6] For a matrix A, the most common definition of the condition number is $\kappa(A) = \sigma_{\max}/\sigma_{\min}$, where $\sigma_{\max}$ and $\sigma_{\min}$ denote the greatest and smallest singular value of the matrix A. Analogously to (6.13), the condition number $\kappa(A)$ describes the sensitivity the solution x of the linear system $Ax = b$, when the vector b is perturbed [133].

Proposition 6.7 (Condition numbers of estimating the logistic function parameters)**.** *Consider three points $y_1 = f(0)$, $y_2 = f(t_{\text{obs}}/2)$ and $y_3 = f(t_{\text{obs}})$ on the logistic function $f(t)$. With respect to a small perturbation ϵ of the point y_3, the condition number of the steady-state estimate $\hat{y}_\infty(\epsilon)$ equals*

$$\kappa_1(t_{\text{obs}}) = \frac{(y_1 - y_2)^2}{y_3^2} \frac{1}{\Phi^2(y_1, y_2, y_3)}, \tag{6.14}$$

the condition number of the growth-rate estimate $\hat{K}(\epsilon)$ equals

$$\kappa_2(t_{\text{obs}}) = \frac{2}{t_{\text{obs}}} \frac{y_2^2}{y_3^2} \frac{1}{y_1 - y_2 + y_2 \Phi\left(y_1, y_2, y_3\right)}, \tag{6.15}$$

and the condition number of the inflection-point estimate $\hat{t}_0(\epsilon)$ equals

$$\kappa_3(t_{\text{obs}}) = \frac{1}{K} \frac{y_2}{y_3^2} \left(\frac{1}{\Phi(y_1, y_2, y_3)} - \frac{2 t_0 y_2}{t_{\text{obs}}} \frac{1}{y_1 - y_2 + y_2 \Phi\left(y_1, y_2, y_3\right)} \right). \tag{6.16}$$

Proof. Appendix E.2. □

To assess the difficulty of estimating the parameters y_∞, K, t_0, we consider an exemplary logistic function $f(t)$ with $K = 0.5$, $t_0 = 10$ and $y_\infty = 1$. Figure 6.2 shows that the condition numbers $\kappa_1(t)$, $\kappa_2(t)$, and $\kappa_3(t)$ are very large. For instance, at time $t = 5 = t_0/2$, the magnitude of the condition number $|\kappa_1(5)|$ is greater than 100. Thus, the steady-state estimate $\hat{y}_\infty(\epsilon)$ is distorted by the error ϵ times a factor of 100. Furthermore, Figure 6.2 indicates that the estimation of the growth rate parameter K is most robust against model errors $w(t)$, since the condition number $\kappa_2(t)$ is the smallest. We emphasise that, for simplicity, Proposition 6.7 considers the best case: the perturbation of only one point y_3. If the points y_1 and y_2 are also perturbed, then the condition numbers can become even greater than the expressions in Proposition 6.7.

The condition numbers in Proposition 6.7 are given by rather complicated expressions. To obtain a better understanding of the condition numbers, we derive bounds as:

Proposition 6.8 (Lower bounds on the condition numbers)**.** *Consider three points $y_1 = f(0)$, $y_2 = f(t_{\text{obs}}/2)$ and $y_3 = f(t_{\text{obs}})$ on the logistic function $f(t)$, whose inflection point $t_0 \geq 0$. For every observation time $t_{\text{obs}} > 0$, the condition number of the steady-state estimate $\hat{y}_\infty(\epsilon)$ is bounded by $\kappa_1(t_{\text{obs}}) > \kappa_{1,\text{lb}}(t_{\text{obs}})$, where*

$$\kappa_{1,\text{lb}}(t_{\text{obs}}) = 1 + \frac{4}{K^2} \frac{1}{t_{\text{obs}}^2} e^{2K(t_0 - t_{\text{obs}})}, \tag{6.17}$$

the condition number of the growth-rate estimate $\hat{K}(\epsilon)$ is bounded by $|\kappa_2(t_{\text{obs}})| > \kappa_{2,\text{lb}}(t_{\text{obs}})$, where

$$\kappa_{2,\text{lb}}(t_{\text{obs}}) = \frac{y_2^2}{y_3^2} \frac{1}{y_\infty} \frac{K}{1 + \frac{1}{2} K t_{\text{obs}}} \frac{1}{\Phi\left(y_1, y_2, y_3\right)}, \tag{6.18}$$

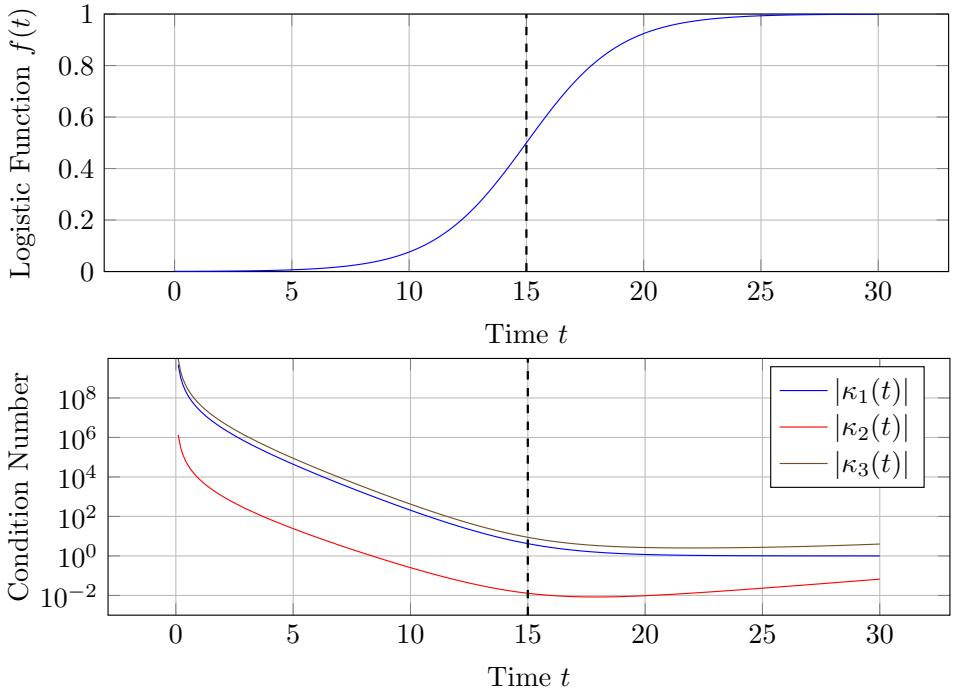

Figure 6.2: **Condition numbers of estimating the parameters of a logistic function.** Upper subplot: The logistic function $f(t)$ versus time t. Lower subplot: The absolute value of the condition numbers $\kappa_1(t)$, $\kappa_2(t)$, and $\kappa_3(t)$ versus time t on a semi-logarithmic plot. The dashed lines indicate the inflection point $t_0 = 15$.

and the condition number of the inflection-point estimate $\hat{t}_0(\epsilon)$ *is bounded by* $\kappa_3(t_{\text{obs}}) > \kappa_{3,\text{lb}}(t_{\text{obs}})$*, where*

$$\kappa_{3,\text{lb}}(t_{\text{obs}}) = \frac{1}{K}\frac{y_2}{y_3^2}\frac{1}{\Phi\left(y_1, y_2, y_3\right)}. \tag{6.19}$$

Proof. Appendix E.3. □

Figure 6.3 shows that the lower bounds of Proposition 6.8 are accurate, where we use the same parameters for the logistic function as in Figure 6.1. From Proposition 6.8, we obtain two statements on the prediction limits of epidemic outbreaks. First, the lower bound (6.17) grows exponentially with $(t_0 - t_{\text{obs}})$. *Thus, only if the epidemic has been observed until the inflection point* $t_{\text{obs}} \approx t_0$ *(or longer), the steady state* y_∞ *can be estimated accurately.* Second, the lower bounds (6.18) and (6.19) depend on the reciprocal of the growth metric $\Phi\left(y_1, y_2, y_3\right)$. The more the epidemic growth from $y_1 = f(0)$ to $y_3 = f(t_{\text{obs}})$ resembles an exponential, the smaller the growth metric $\Phi\left(y_1, y_2, y_3\right)$, see Subsection 6.4.1. But real epidemics grow practically exponentially in the beginning of the outbreak. *Hence, the growth rate* K *and the inflection point* t_0 *cannot be estimated accurately at early stages of an epidemic.* Or, as a simple rule of thumb: as long as the

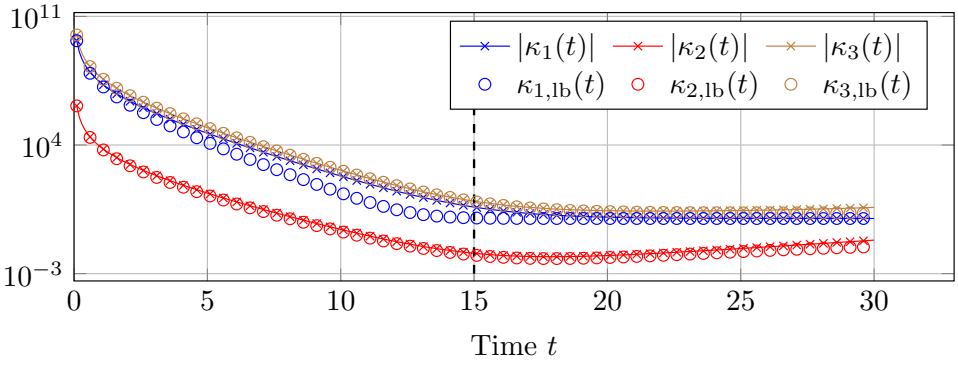

Figure 6.3: **Lower bounds on the condition numbers.** The absolute value of the condition numbers $\kappa_i(t)$, where $i = 1,2,3$, and the respective lower bounds $\kappa_{i,\mathrm{lb}}(t)$ versus time t on a semi-logarithmic plot. The dashed line indicates the inflection point $t_0 = 15$.

infections $\mathcal{I}_c(t)$ are on a straight line in a semi-logarithmic plot, the epidemic outbreak cannot be predicted accurately.

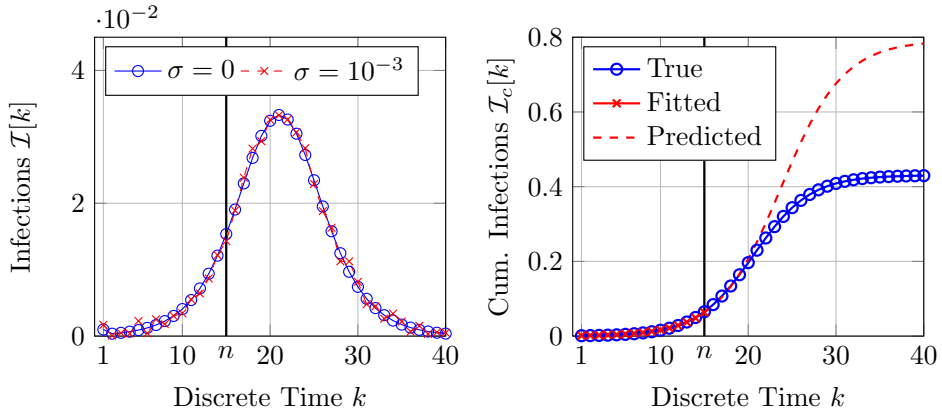

Figure 6.4: **Sensitivity of predicting an epidemic outbreak.** The left subplot shows the logistic function (6.5) with and without Gaussian model errors $w[k]$ with a standard deviation of $\sigma = 10^{-3}$. The randomly generated parameters of the logistic function $f(t)$ are $t_0 = 20.5, K = 0.31$ and $y_\infty = 0.43$. The right subplot shows the cumulative number of infections $\mathcal{I}_c[k]$ and the predicted value $\hat{\mathcal{I}}_c[k]$, based on the logistic function plus model errors $w[k]$.

We perform numerical simulations to illustrate the sensitivity of predicting an epidemic outbreak subject to model errors $w[k]$. We generate the model errors $w[k]$ in (6.5) as Gaussian random variables with zero mean and standard deviation σ, at all discrete times $k = 1,\ldots,n$. The model errors $w[k]$ and $w[\tilde{k}]$ are stochastically independent for all $k \neq \tilde{k}$. If the cumulative number of infections $\mathcal{I}_c[k]$, resulting from (6.5), is negative, then we set $\mathcal{I}_c[k] \leftarrow |\mathcal{I}_c[k]|$. Figure 6.4 shows that small model errors $w[k]$ have a severe impact on the accuracy of the estimated number of infections $\hat{I}_c[k]$. The prediction of the

number of infections $I_c[k]$ is accurate only in the short term. We emphasise that, for real epidemics, the model errors $w[k]$ are significantly larger than in Figure 6.4.

6.4.3. COVID-19 PREDICTION

We consider the prediction of the first wave of COVID-19 in several countries: Belgium, Italy, the Netherlands and South Africa. We obtain the infection data from the COVID-19 Dashboard of the Johns Hopkins University [134] and determine the period of the first wave to be: from March 1 until June 16 (Belgium), from February 16 until June 17 (Italy), from February 22 until July 11 (the Netherlands), from April 30 until October 7 (South Africa). The sampling time Δt equals one day. In the subsequent plots, the discrete time $k = 1$ denotes the first day of the respective country. For instance, time $k = 1$ corresponds to February 22, 2020, for the Netherlands.

Figure 6.5 shows a crucial contrast: the logistic function $f(t)$ fits the number of infections until observation time t_{obs}. But the logistic function $f(t)$ does not yield accurate predictions for the number of infections. Only short-term predictions, until day $t \approx t_{\text{obs}} + 4$, are possible. We emphasise that we chose an observation time t_{obs} before the peak of the epidemic, i.e., before the inflection point t_0. If the observation time $t_{\text{obs}} \gg t_0$, then the prediction becomes more accurate.

When can we trust the predictions to be accurate? Proposition 6.7 and Proposition 6.8 suggest that the growth metric $\Phi(y_1, y_2, y_3)$ is decisive for the prediction accuracy. We compute the prediction accuracy in three steps. First, by fitting a logistic function to the number of infections of the *complete* first wave, we obtain the "exact" steady-state y_∞, growth rate K and inflection point t_0. Second, to reduce erratic fluctuations, we apply a moving average of window length five to the estimates $\hat{y}_\infty$, $\hat{K}$, $\hat{t}_0$ and the growth metric $\Phi(y_1, y_2, y_3)$. For instance, we replace the steady-state estimate $\hat{y}_\infty(t_{\text{obs}})$ at observation time t_{obs} by the average of the steady-state estimates $\hat{y}_\infty(t_{\text{obs}})$, $\hat{y}_\infty(t_{\text{obs}} - \Delta t)$, ..., $\hat{y}_\infty(t_{\text{obs}} - 4\Delta t)$. Third, we define the absolute error of the steady-state estimate $\hat{y}_\infty$ as $\varepsilon(y_\infty, \hat{y}_\infty) = \left|\hat{y}_\infty - y_\infty\right|$. Analogously, for the growth rate estimate $\hat{K}$ and the inflection point estimate $\hat{t}_0$, the respective absolute errors are denoted by $\varepsilon(K, \hat{K})$ and $\varepsilon(t_0, \hat{t}_0)$.

Figure 6.6 and Figure 6.7 show that there is a strong correlation between the estimation errors $\varepsilon(K, \hat{K})$, $\varepsilon(t_0, \hat{t}_0)$ and inverse growth metric $\Phi(y_1, y_2, y_3)$, which is in line with Proposition 6.8. The red lines in Figures 6.6–6.8 are obtain by robust linear regression with the Matlab command `fitlm`. The linear regression is performed without intercept, i.e., the red lines go through the origin. Here, we define the *relative error* Δ_K of the linear regression as the average of the absolute deviation of $\varepsilon(K, \hat{K})$ to the linear curve, divided by the maximum value of the error $\varepsilon(K, \hat{K})$. The relative error Δ_{y_∞} and Δ_{t_0} are defined analogously. Furthermore, Figure 6.8 shows[7] that the estimation error $\varepsilon(y_\infty, \hat{y}_\infty)$ of the steady state y_∞ is reasonably correlated with the inverse growth metric $\Phi(y_1, y_2, y_3)$, except for South Africa.

We emphasise that the growth metric $\Phi(y_1, y_2, y_3)$ is computed solely based on past data until the observation time t_{obs}. *Hence, it is possible to quantify the prediction accuracy only based on past data.* For instance, suppose that the growth metric $\Phi(y_1, y_2, y_3)$ increases by a factor μ from time t_{obs} to $\tilde{t}_{\text{obs}} > t_{\text{obs}}$. Then, we can expect that the accuracy

[7] For clarity, we removed four outliers from Figure 6.8(a), because the axis range would be too large. The linear regression and the relative error Δ_{y_∞} consider all points, including the outliers.

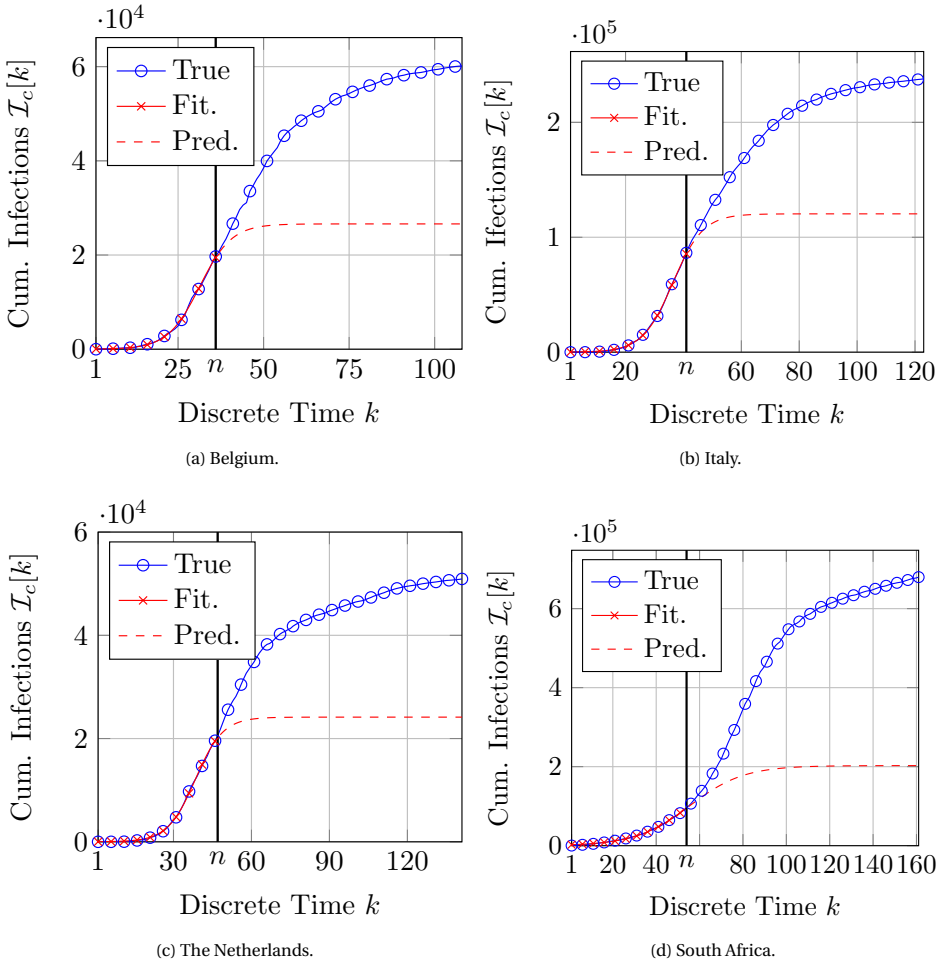

(a) Belgium.

(b) Italy.

(c) The Netherlands.

(d) South Africa.

Figure 6.5: **Difficulty of predicting COVID-19.** The blue curves show the cumulative number of the first wave of confirmed infections with SARS-CoV-2. The red curves shows the logistic curve which is fitted to the infections from day $k = 1$ until day n and used for predictions at times $k > n$.

of the estimates $\hat{K}$, $\hat{t}_0$ and $\hat{y}_\infty$ increases by the factor μ.

6.5. CONCLUSIONS

For many epidemic models, the cumulative number of infections resembles a logistic function, at least approximately. In this chapter, we showed that the prediction of a logistic function is ill-conditioned. More specifically, a good fit of a logistic function $\hat{f}(t)$ to the epidemic data until some observation time t_{obs} does *not* imply that the function $\hat{f}(t)$ yields accurate predictions at times $t > t_{\text{obs}}$. Hence, even under idealised conditions, the prediction of an epidemic is inherently difficult, regardless of the particular prediction algorithm.

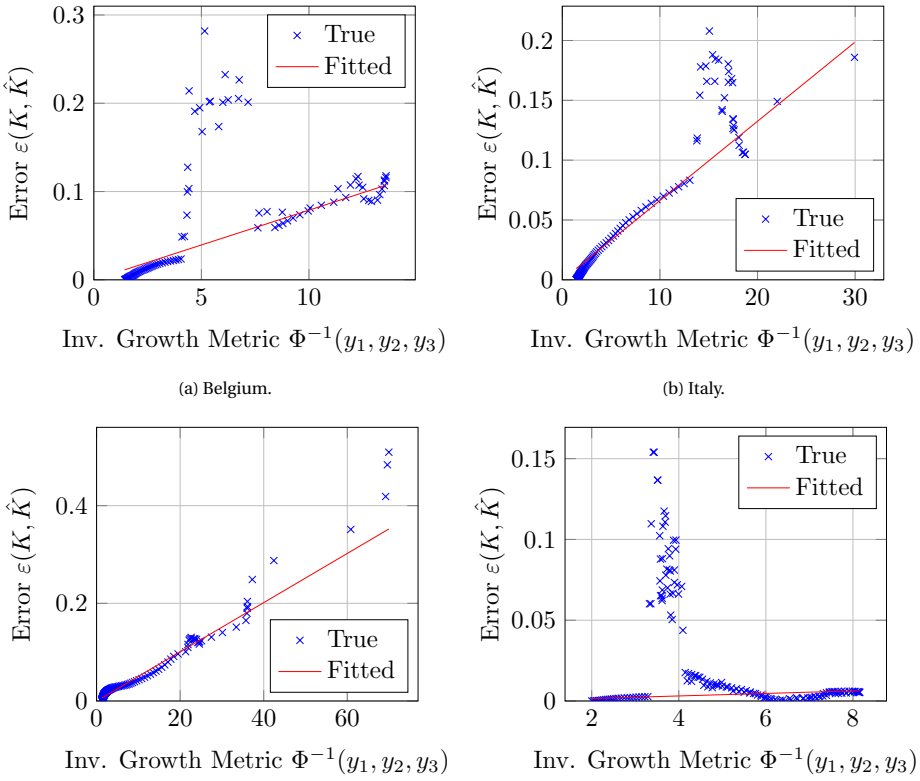

(a) Belgium.

(b) Italy.

(c) The Netherlands.

(d) South Africa.

Figure 6.6: **Assessing the growth rate estimation accuracy via the growth metric Φ.** In blue: the error $\varepsilon(K,\hat{K})$ of growth-rate estimate $\hat{K}$ at different times t_{obs} versus the inverse of the growth metric $\Phi(y_1,y_2,y_3)$, where $y_1 = \mathcal{I}_c(0)$, $y_2 = \mathcal{I}_c(t_{\text{obs}}/2)$ and $y_3 = \mathcal{I}_c(t_{\text{obs}})$. In red: curve obtained by linear regression. The relative error Δ_K of the linear regression equals: (a) $\Delta_K = 0.11$, (b) $\Delta_K = 0.03$, (c) $\Delta_K = 0.01$, (d) $\Delta_K = 0.15$.

Furthermore, we introduced the growth metric $\Phi(y_1,y_2,y_3)$, which quantifies the exponential growth of the epidemic. The more exponential the epidemic growth, the more difficult the prediction of the epidemic. In particular, the estimation error of the epidemic parameters correlates strongly with the inverse of the growth metric $\Phi(y_1,y_2,y_3)$, which enables quantitative statements on the prediction accuracy: Suppose that the epidemic is predicted at two different observation time t_{obs} and $\tilde{t}_{\text{obs}} > t_{\text{obs}}$. Then, the fraction of the respective growth metrics $\Phi(y_1,y_2,y_3), \tilde{\Phi}(y_1,y_2,y_3)$ approximates the change of the prediction accuracy from time t_{obs} to $\tilde{t}_{\text{obs}}$.

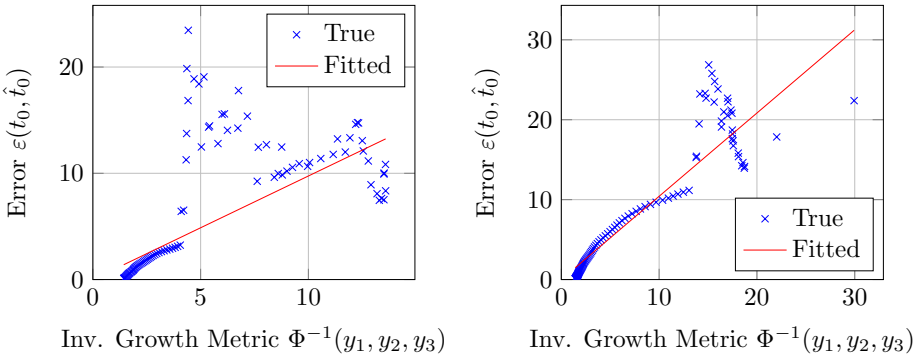

(a) Belgium.

(b) Italy

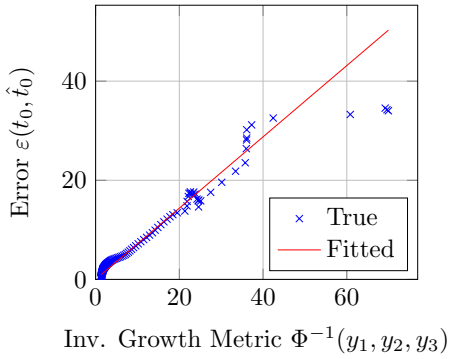

(c) The Netherlands.

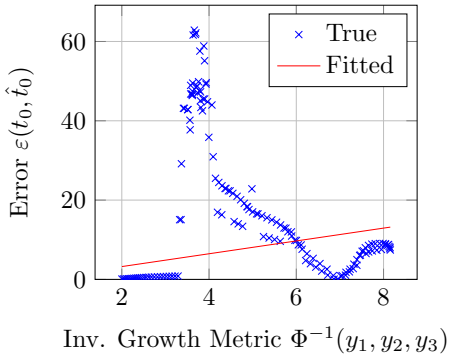

(d) South Africa.

Figure 6.7: **Assessing the inflection point estimation accuracy via the growth metric Φ.** In blue: the error $\varepsilon(t_0, \hat{t}_0)$ of inflection-point estimate $\hat{t}_0$ at different times t_{obs} versus the inverse of the growth metric $\Phi(y_1, y_2, y_3)$, where $y_1 = \mathcal{I}_c(0)$, $y_2 = \mathcal{I}_c(t_{\text{obs}}/2)$ and $y_3 = \mathcal{I}_c(t_{\text{obs}})$. In red: curve obtained by linear regression. The relative error Δ_{t_0} of the linear regression equals: (a) $\Delta_{t_0} = 0.14$, (b) $\Delta_{t_0} = 0.05$, (c) $\Delta_{t_0} = 0.03$, (d) $\Delta_{t_0} = 0.24$.

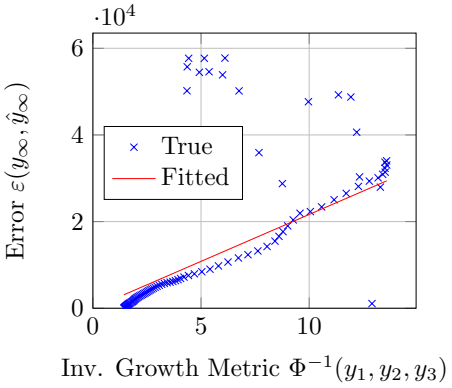

(a) Belgium.

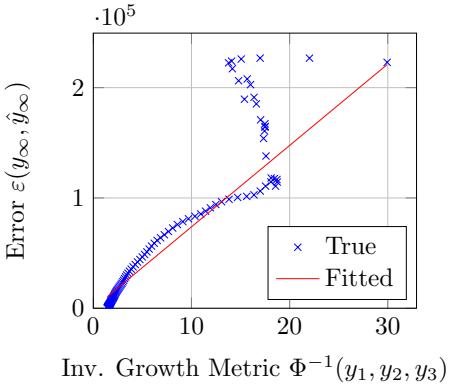

(b) Italy.

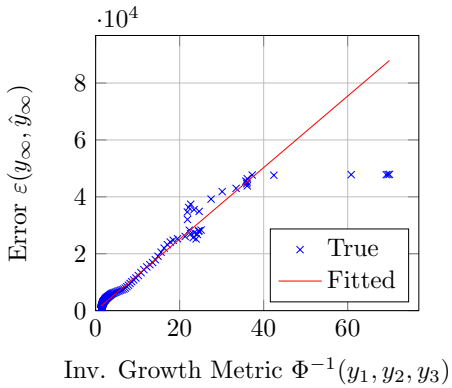

(c) The Netherlands.

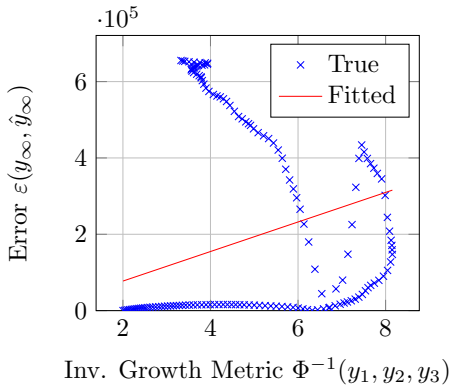

(d) South Africa.

Figure 6.8: **Assessing the steady state estimation accuracy via the growth metric Φ.** In blue: the error $\varepsilon(y_\infty, \hat{y}_\infty)$ of steady-state estimate $\hat{y}_\infty$ at different times t_{obs} versus the inverse of the growth metric $\Phi(y_1, y_2, y_3)$, where $y_1 = \mathcal{I}_c(0)$, $y_2 = \mathcal{I}_c(t_{\text{obs}}/2)$ and $y_3 = \mathcal{I}_c(t_{\text{obs}})$. In red: curve obtained by linear regression. The relative error Δ_{y_∞} of the linear regression equals: (a) $\Delta_{y_\infty} = 0.01$, (b) $\Delta_{y_\infty} = 0.08$, (c) $\Delta_{y_\infty} = 2.8 \cdot 10^{-4}$, (d) $\Delta_{y_\infty} = 0.36$.

7

NETWORK RECONSTRUCTION AND PREDICTION FOR GENERAL EPIDEMIC MODELS

The underlying core of most epidemic models is the graph that specifies the contacts between healthy and infected individuals. However, in the majority of applications, the contact network is unknown. To understand and predict an epidemic outbreak nonetheless, network reconstruction methods aim to estimate the contact network from viral state observations. This chapter considers general compartmental epidemic models (GEMF) in discrete time, which describe the viral spread between groups of individuals. The reconstruction of the network translates into a set of linear equations that is severely ill-conditioned. Counterintuitively, the contact network cannot be reconstructed from one epidemic outbreak with any finite machine precision, although an accurate prediction of the epidemic outbreak is possible.

This chapter is based on [135] and [53].

7.1. INTRODUCTION

The contact graph between individuals has a great impact on the spread of the virus [5, 9]. However, in the study of real-world epidemics, there is often not much known about the contact graph other than high-level properties such as, for instance, the degree distribution [10]. To obtain a better understanding of the viral spread, network reconstruction methods aim to infer the unknown contact graph from observing the viral state evolution. If the contact graph can be reconstructed, then the epidemic outbreak can be predicted. However, as we will show in this chapter, the prediction of epidemic outbreaks is surprisingly less related to network reconstruction, despite the clear dependence of the dynamic equations of epidemic spread on the contact graph (see equation (7.4) below). *In particular, we show that the network cannot be reconstructed although the epidemic outbreak can be predicted.*

The majority of network reconstruction methods focussed on inferring the contact network from viral state observations of every single individual [87–89, 97, 99]. Network reconstruction methods from viral state observations of single individuals are subject to two fundamental limitations. First, it is hardly practical to determine the viral state of every individual at every time in real-world epidemics. Second, an accurate network reconstruction requires a tremendous number n of viral state observation, see Chapter 5. Thus, inferring the contact network between single individuals only seems possible long after the virus reached the endemic state or, if the virus dies out, by observing multiple epidemic outbreaks, both of which seems impractical. To overcome the challenges of reconstructing the contact network of individual-based models, we describe the evolution of the virus on a coarser level between groups, or communities, of similar individuals. The prevalence of a virus within a group is accessible by sampling representative individuals.

In this chapter, we focus on the viral spread over a network with N nodes, where each node corresponds to a group of individuals such as households or geographical regions. Hence, we use the words *node* and *group* interchangeably. We consider that the viral spread between groups follows a discrete-time version of the Generalised Epidemic Mean-Field (GEMF) model [136] with heterogeneous spreading parameters on a directed contact network. The GEMF model considers C viral state compartments, which unifies a myriad of diverse epidemic models. For instance, in SIR model in Definition 1.2 there are $C = 3$ compartments. The viral state of node i at continuous time $t \geq 0$ is denoted by $\nu_i(t) = \left(\nu_{i,1}(t), ..., \nu_{i,C}(t)\right)^T \in [0,1]^C$, where $\nu_{i,p}(t)$ describes the fraction of individuals of group i in compartment p at time t.

7.2. THE DISCRETE-TIME GEMF EPIDEMIC MODEL

Originally, Sahneh *et al.* [136] derived the GEMF model as a mean-field approximation of *individual-based* Markovian spreading processes, where every node i corresponds to a single individual, whose viral state equals either one of C compartments. Then, the probability that the viral state of individual i equals the p-th compartment at time t is approximated by the state $\nu_{i,p}(t)$ of the GEMF model. In contrast, our interpretation of the viral state $\nu_{i,p}(t)$ as the fraction of individuals of group i in compartment p is in line with [18, 22, 23, 25]. Ideally, individuals in the same group are interchangeable for

describing the epidemic outbreak. The number of individuals in different groups i does not need to be the same.

We generalise the GEMF model [136] to heterogeneous spreading parameters and directed graphs. We state the GEMF model in discrete time and denote the viral state of group i at discrete time $k \in \mathbb{N}$ by $v_i[k] \in [0,1]^C$. Thus, it holds that $v_i[k] = v_i(\Delta t k)$ for some sampling time Δt. Since $v_{i,p}[k]$ denotes the fraction of individuals of group i in compartment p and each individual is in exactly one compartment, it holds that $v_{i,1}[k] + ... + v_{i,C}[k] = 1$ at any time k. For every two compartments $p, q = 1, ..., C$, we denote the $N \times N$ zero-one adjacency matrix as A_{pq} with elements $a_{pq,ij}$. The adjacency matrices A_{pq} specify the contact network: If there is a directed link from compartment q of group j to compartment p of group i, then $a_{pq,ij} = 1$, and $a_{pq,ij} = 0$ otherwise. For instance, if compartment q denotes individuals that are in quarantine, then it holds that $A_{pq} = 0$ for all compartments $p \neq q$ since the quarantine-compartment q is isolated from all compartments $p \neq q$. In the GEMF model, there are two kinds of viral state transitions from time k to $k+1$:

1. *Nodal transitions* occur at a node i independently of the viral state $v_j[k]$ of the other nodes $j \neq i$. The $C \times C$ nodal transition probability matrix S_i specifies the probabilities of nodal transitions at node i. The probability that, via a nodal transition, an individual in group i changes from compartment p to compartment q equals $(S_i)_{pq}$.

2. In contrast, *edge-based transitions* do depend on the viral state $v_j[k]$ of the neighbours j of node i and, hence, on the contact network. The $C \times C$ edge-based transition probability matrix $B_{m,ij}$ specifies the probabilities of edge-based transitions at node i due to (for instance, an infection from) the individuals of group j in compartment m. More precisely, the probability that an individual in group i changes from compartment p to compartment q due to a fraction $v_{j,m}[k]$ of individuals of group j in compartment m equals $\left(B_{m,ij}\right)_{pq} v_{j,m}[k]$. We emphasise that the edge-based transition probability matrix $B_{m,ii}$ from group i to group i is not necessarily zero, because the individuals in group i can possibly interact with each other.

Since we consider discrete-time GEMF with sampling time Δt, the entries of both matrices S_i and $B_{m,ij}$ correspond to transition *probabilities*, with respective transition *rates* (for the continuous-time limit $\Delta t \downarrow 0$) given by the entries of $S_i/\Delta t$ and $B_{m,ij}/\Delta t$. The edge-based transition probability matrix $B_{m,ij}$ is related to the adjacency matrices as A_{pm}, for all compartments $p = 1, ..., C$, as follows. Since individuals of group j in compartment m have an impact on individuals of group i in compartment p only if there is a link from compartment m of group j to compartment p of group i, it holds

$$\left(B_{m,ij}\right)_{pq} = (\tilde{B}_{m,ij})_{pq} a_{pm,ij} \tag{7.1}$$

for some $C \times C$ matrix $\tilde{B}_{m,ij}$. Hence, it holds $a_{pm,ij} = 1$ only if[1] there is a compartment q such that $\left(B_{m,ij}\right)_{pq} > 0$. More precisely, we can obtain the entries $a_{pm,ij}$ of the adjacency

[1] Here, we make the technical assumption: if there is a link from compartment m of group j to compartment p of group i, then the probability $\left(B_{m,ij}\right)_{pq}$ is positive for at least one compartment q.

matrix A_{pm} by

$$a_{pm,ij} = \begin{cases} 1 & \text{if} \quad \exists q = 1,\ldots,C\colon \left(B_{m,ij}\right)_{pq} > 0, \\ 0 & \text{otherwise.} \end{cases} \tag{7.2}$$

Any GEMF model can be visualised as in Figure 7.1 by the *transition graph*, which we define as follows. All compartments of two (arbitrary) groups i, j are represented by a node in the transition graph. Regarding the compartments of group i, two nodes in the transition graph are connected by a directed link if there is a transition between the respective compartments of group i. (The transitions between the compartments of the other group j are omitted, since the transitions between the compartments of one group i suffice to specify the GEMF model.) A node-based transition of group i from compartment p to compartment q is represented by a simple arrow "$\rightarrow$" that is labelled with the transition probability $(S_i)_{pq}$. An edge-based transition of group i from compartment p to compartment q is represented by an arrow with the multiplier "$\otimes$" in the middle. If compartment m of group j has an influence on the edge-based transition of group i from compartments p to compartment q, then there is an arrow from compartment m of group j to the respective multiplier "$\otimes$", which is labelled with the transition probability $\left(B_{m,ij}\right)_{pq}$. We emphasise that, by definition (7.1), $\left(B_{m,ij}\right)_{pq} = 0$ if the respective link $a_{pm,ij} = 0$.

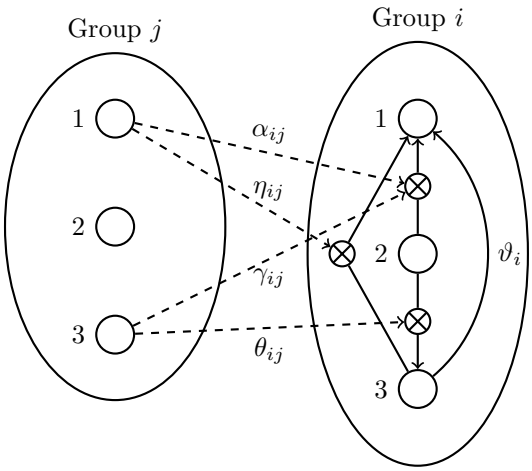

Figure 7.1: **GEMF transition graph.** The transition graph for an exemplary GEMF model with $C = 3$ compartments. The solid lines correspond to possible transitions between the three compartments of group i. The dashed lines illustrate which compartment of group j influences which edge-based transition between two compartments of group i.

Figure 7.1 illustrates an exemplary transition graph for a GEMF model with $C = 3$ compartments. In the following, we show how the transition graph in Figure 7.1 fully specifies the GEMF model, i.e. the node-based and edge-based transitions. In Figure 7.1, there is exactly one simple arrow from compartment 3 to compartment 1, which is labelled with the transition probability ϑ_i. Hence, the nodal transition probability matrix

S_i equals

$$S_i = \begin{pmatrix} 0 & 0 & 0 \\ 0 & 0 & 0 \\ \vartheta_i & 0 & 0 \end{pmatrix}. \tag{7.3}$$

There are two arrows from compartment 1 of group j to the edge-based transitions of group i: from compartment 2 to compartment 1 (labelled with α_{ij}), and from compartment 3 to compartment 1 (labelled with η_{ij}). Hence, the edge-based transition probability matrix $B_{1,ij}$ equals

$$B_{1,ij} = \begin{pmatrix} 0 & 0 & 0 \\ \alpha_{ij} & 0 & 0 \\ \eta_{ij} & 0 & 0 \end{pmatrix}.$$

There is no arrow from compartment 2 of group j to a transition of group i. Hence, compartment 2 of group j has no influence on the transitions of group i, and it holds that $B_{2,ij} = 0$. From the two arrows starting at compartment 3 of group j, we obtain the edge-based transition probability matrix $B_{3,ij}$ as

$$B_{3,ij} = \begin{pmatrix} 0 & 0 & 0 \\ \gamma_{ij} & 0 & \theta_{ij} \\ 0 & 0 & 0 \end{pmatrix}.$$

The matrices S_i and $B_{m,ij}$, where $m = 1,2,3$, for all groups i, j fully specify the transitions of the GEMF model. Furthermore, the links $a_{pm,ij}$ from compartment m of group j to compartment p of group i can be obtained from Figure 7.1 as follows. The link labelled with α_{ij} connects compartment 1 of group j to an edge-based transition *starting* at compartment 2 of group i (ending at compartment 1 of group i), which yields that $a_{21,ij} = 1$ if $\alpha_{ij} > 0$. Similarly, the link labelled with η_{ij} yields that $a_{31,ij} = 1$ if $\eta_{ij} > 0$. Both of the links labelled with γ_{ij} and θ_{ij} connect compartment 3 of group j with edge-based transitions *starting* at compartment 2 of group i, which yields that $a_{23,ij} = 1$ if $\gamma_{ij} > 0$ or $\theta_{ij} > 0$ (or both). For the other compartments p, m, which have not been mentioned above, it holds that $a_{pm,ij} = 0$.

Definition 7.1 (Discrete-Time GEMF Epidemic Model)**.** The discrete-time GEMF epidemic model describes the evolution of the viral state $\nu_i[k] \in \mathbb{R}^C$ for every group $i = 1, \ldots, N$ as

$$\nu_i[k+1] = \left(I_C - Q_i^T\right)\nu_i[k] - \sum_{j=1}^{N}\sum_{m=1}^{C} \nu_{j,m}[k] Q_{m,ij}^T \nu_i[k], \tag{7.4}$$

where $k \in \mathbb{N}$ denotes the discrete time slot. Here, the $C \times C$ Laplacian matrices of the nodal transition probability matrix S_i and the edge-based transition probability matrix $B_{m,ij}$ are denoted by $Q_i = \operatorname{diag}(S_i u) - S_i$ and $Q_{m,ij} = \operatorname{diag}\left(B_{m,ij} u\right) - B_{m,ij}$.

In Appendix F.1, we derive the discrete-time GEMF model (7.4) from the continuous-time GEMF model [136] by applying Euler's method. If the initial viral state $\nu_i[1]$ of every

node i satisfies $\nu_{i,1}[1]+\ldots+\nu_{i,C}[1]=1$, then [136] it holds that $\nu_{i,1}[k]+\ldots+\nu_{i,C}[k]=1$ at any time $k\geq 1$. Thus, the GEMF model (7.4) with CN compartments can be reduced to $(C-1)N$ non-linear difference equations.

Originally, the GEMF model was formulated for multi-layer networks [136]. The discrete-time GEMF model (7.4) does not explicitly model distinct network layers but directly *sums* the influences across all network layers. For instance, consider that infected individuals in group j infect susceptible individuals in group i via a link in the workplace network (network layer $l=1$) with the transition probability $\beta^{(1)}_{\Delta t,ij}$ or via a link in the friendship contact network (network layer $l=2$) with the transition probability $\beta^{(2)}_{\Delta t,ij}$. Then, an equivalent GEMF model is obtained by a total transition probability of $\beta_{\Delta t,ij}=\beta^{(1)}_{\Delta t,ij}+\beta^{(2)}_{\Delta t,ij}$ on one network layer. Since the value of the transition probability $\beta_{\Delta t,ij}$ completely determines the viral state dynamics of the GEMF model (7.4), it is only possible to estimate the transition probability $\beta_{\Delta t,ij}$ from viral state observations $\nu_i[1],\nu_i[2],\ldots$, but not the distinct addends $\beta^{(1)}_{\Delta t,ij}$ and $\beta^{(2)}_{\Delta t,ij}$ of the different layers.

7.2.1. SPECIAL CASES OF THE GEMF EPIDEMIC MODEL

In this chapter, we consider four special cases of the GEMF model (7.4). For the special cases of GEMF that are mentioned below, we refer to the transition probabilities δ_i and β_{ij} as curing probability and infection probability, respectively, to stress their physical meaning.

SIS (NIMFA) EPIDEMIC MODEL

The discrete-time NIMFA epidemic model in Definition 4.1 is a special case of the GEMF epidemic model (7.4). In this chapter, we refer to discrete-time NIMFA as *SIS epidemic model* for consistency with the other special cases of the GEMF model. Figure 7.2 shows the transition graph of the SIS epidemic model with the 2×1 viral state[2] vector $\nu_i[k]=(\mathcal{S}_i[k],\mathcal{I}_i[k])^T$.

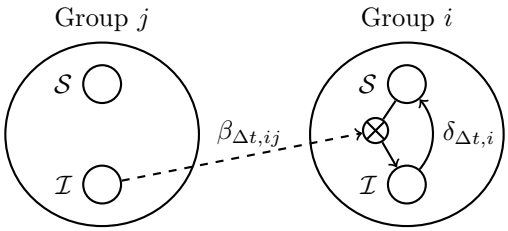

Figure 7.2: **SIS transition graph.** The transition graph for the discrete-time SIS (or NIMFA) epidemic model in Definition 4.1.

To be concise, we put a particular focus on the SIS model (4.1) in this chapter. However, the derivations hold for the general GEMF model (7.4) and are presented in Appendix F.

[2] In Chapter 4, the fraction of infected individuals $\mathcal{I}_i[k]$ was denoted by $\nu_i[k]$. The fraction of infected individuals follows as $\mathcal{S}_i[k]=1-\nu_i[k]$, and the infection probability follows as $\beta_{\Delta t,ij}=(B_{2,ij})_{12}$.

SIR EPIDEMIC MODEL

Applying Euler's method to the continuous-time SIR model in Definition 1.2 yields the discrete-time SIR epidemic model. Figure 7.3 shows the transition graph of the SIR epidemic model with the 2×1 viral state $v_i[k] = (\mathcal{S}_i[k], \mathcal{I}_i[k], \mathcal{R}_i[k])^T$.

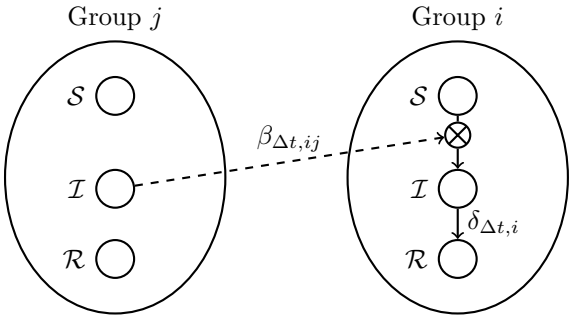

Figure 7.3: **SIR transition graph.** The transition graph for the discrete-time SIR epidemic model in Definition 1.2.

Definition 7.2 (Discrete-time SIR epidemic model)**.** For every group i, the viral state of the discrete-time SIR epidemic model equals $v_i[k] = (\mathcal{S}_i[k], \mathcal{I}_i[k], \mathcal{R}_i[k])^T$. Here, $\mathcal{S}_i[k]$, $\mathcal{I}_i[k]$ and $\mathcal{R}_i[k]$ denote the fraction of susceptible, infected, and recovered individuals in group i at time $k \in \mathbb{N}$, respectively. For every group i, the viral state evolves in discrete time k according to

$$\begin{aligned} \mathcal{I}_i[k+1] &= (1-\delta_{\Delta t,i})\mathcal{I}_i[k] + (1-\mathcal{I}_i[k]-\mathcal{R}_i[k]) \sum_{j=1}^{N} \beta_{\Delta t,ij}\mathcal{I}_j[k] \\ \mathcal{R}_i[k+1] &= \mathcal{R}_i[k] + \delta_{\Delta t,i}\mathcal{I}_i[k] \end{aligned} \tag{7.5}$$

and

$$\mathcal{S}_i[k] = 1 - \mathcal{I}_i[k] - \mathcal{R}_i[k] \tag{7.6}$$

at any time $k \in \mathbb{N}$. Here, $\beta_{\Delta t,ij}$ denotes the *infection probability* from group j to group i, and $\delta_{\Delta t,i}$ denotes the *curing probability* of group i.

SEIR EPIDEMIC MODEL

The third model that we consider has four compartments: the susceptible compartment $\mathcal{S}$, the exposed compartment $\mathcal{E}$, the infectious compartment $\mathcal{I}$, and the recovered (or removed) compartment $\mathcal{R}$. An individual transitions the compartments in the order $\mathcal{S} \to \mathcal{E} \to \mathcal{I} \to \mathcal{R}$. Individuals in the exposed compartment $\mathcal{E}$ have been infected by the disease but, in contrast to individuals in the infectious compartment $\mathcal{I}$, are not contagious yet. Individuals in the recovered compartment $\mathcal{R}$ have had the disease, but are not susceptible nor infectious any more (for instance, by immunisation or death). In the SEIR epidemic model, the only edge-based transition occurs from the susceptible compartment $\mathcal{S}$ to the exposed compartment $\mathcal{E}$, analogously to the $\mathcal{S} \to \mathcal{I}$ transition in the

SIS epidemic model. Furthermore, there are two nodal transitions in the SEIR epidemic model. First, the transition from the exposed compartment $\mathcal{E}$ to the infectious compartment $\mathcal{I}$, which occurs with the incubation probability $\gamma_{\Delta t,i}$ for an individual in group i. Second, the transition from the infectious compartment $\mathcal{I}$ to the recovered compartment $\mathcal{R}$, which occurs with the curing probability $\delta_{\Delta t,i}$ for an individual in group i. Both the transition graph and the systems equation of the SEIR epidemic model are stated in Appendix F.4.

SISIR EPIDEMIC MODEL

Lastly, we consider a two-staged infection process, with two different diseases and five compartments: the susceptible compartments $\mathcal{S}_l$, the infectious compartments $\mathcal{I}_l$, and the recovered (or removed) compartment $\mathcal{R}$, where $l = 1,2$ denotes the disease. In the SISIR epidemic model, individuals transition the compartments in the order $\mathcal{S}_1 \to \mathcal{I}_1 \to \mathcal{S}_2 \to \mathcal{I}_2 \to \mathcal{R}$. There are two edge-based transitions in the SISIR model, the infectious transitions $\mathcal{S}_1 \to \mathcal{I}_1$ and $\mathcal{S}_2 \to \mathcal{I}_2$, which occur analogously to the $\mathcal{S} \to \mathcal{I}$ transition in the SIS model, but with infection rates $\beta_{\Delta t,l,ij}$ that depend on the respective disease $l = 1,2$. The two nodal transitions $\mathcal{I}_1 \to \mathcal{S}_2$ and $\mathcal{I}_2 \to \mathcal{R}$ occur with the curing probabilities $\delta_{\Delta t,1,i}$ and $\delta_{\Delta t,2,i}$, respectively, for an individual in group i.

Our main motivation for studying the SISIR model is the technical challenge: the two contact networks corresponding to the two viruses are completely unrelated. Hence, the fact that node i can infect node j with virus 1 does not imply that node i can infect node j with virus 2. Thus, effectively a contact network with $2N$ nodes has to be reconstructed from the viral state observations of N groups.

An exemplary application of the SISIR model is the description of two viruses, which spread outside and inside a quarantine. The state $\mathcal{S}_1$ corresponds to healthy individuals. Individuals that are infected by the first virus are in the state $\mathcal{I}_1$ and are moved upon detection of the infection (with the curing probability $\delta_{\Delta t,1}$) to the state $\mathcal{S}_2$, which corresponds to the quarantine. In the quarantine, the spread of another virus takes place, which is modelled by an SIR process (the states $\mathcal{S}_2$,$\mathcal{I}_2$,$\mathcal{R}$). Both the transition graph and the systems equation of the SISIR epidemic model are stated in Appendix F.5.

7.2.2. CURING PROBABILITY CONTROL

So far, we assumed that the curing rates $\delta_{\Delta t,i}$ are constant or, equivalently, that the nodal transition probability matrices S_i do not change over time k. However, public health agencies react to an emerging epidemic outbreak by vaccinations and other disease control measures that do vary as time k evolves. In the SIS, SIR and SEIR epidemic models, we consider that the curing rates of every group i are time-dependent, i.e., the curing probability $\delta_{\Delta t,i}$ is replaced by

$$\tilde{\delta}_{\Delta t,i}[k] = \delta_{\Delta t,i} + \delta_{\mathrm{con},i}[k]. \tag{7.7}$$

Here, the scalar $\delta_{\mathrm{con},i}[k] \geq 0$ is the known *curing probability control* at time k (for instance the fraction of vaccinations), see [6, 137]. The constant curing probability term $\delta_{\Delta t,i} > 0$ in (7.7) corresponds to natural immunities and other influences which are unknown and have to be reconstructed from viral state observations to provide a full understanding of the viral spread. For the SISIR epidemic model, we consider that the curing rates of both diseases $l = 1,2$ are time-dependent and equal to $\tilde{\delta}_{\Delta t,l,i}[k] = \delta_{\Delta t,l,i} +$

$\delta_{\text{con},l,i}[k]$ for every group i. For the general GEMF model (7.4), the concept of time-varying curing rates (7.7) is generalised by replacing the nodal transition probability matrix S_i by the time-dependent $C \times C$ matrix $\tilde{S}_i[k] = S_i + S_{\text{con},i}[k]$. Here, the time-dependent $C \times C$ matrix $S_{\text{con},i}[k]$ describes the known controlled interventions to the viral state evolution, and the constant $C \times C$ matrix S_i is due to unknown terms of the nodal transitions. In Section 7.4, we will show that a non-zero curing probability control $\delta_{\text{con},i}[k] \neq 0$ is beneficial for the task of network reconstruction.

7.3. NETWORK RECONSTRUCTION AS LINEAR EQUATIONS

The focus of this chapter is the inverse problem of estimating the parameters of the GEMF model (7.4) from viral state observations. More precisely:

Problem 7.3 (GEMF network reconstruction)**.** Assume that the controlled interventions $S_{\text{con},i}[k]$ to the viral state evolution are either known or zero at every time k. Estimate the nodal transition probability matrix S_i and the edge-based transition probability matrix $B_{m,ij}$ for all nodes i, j and all compartments m from observations of the $C \times 1$ viral state vector $v_i[k]$ of every group i at every discrete time $k = 1, ..., n+1$, where $n \in \mathbb{N}$ denotes the *number of observed transitions*.

We emphasise that the adjacency matrices A_{pm} can be obtained from the matrices $B_{m,ij}$ by (7.2). For any $N \times N$ matrix A, we define the $N^2 \times 1$ vector that is obtained by stacking the columns of A as $\text{vec}(A) = (a_{11}, ..., a_{N1}, a_{12}, ..., a_{N2}, ...)^T$. The Kronecker product of a $k \times l$ matrix A and a $p \times q$ matrix B is denoted by $A \otimes B \in \mathbb{R}^{kp \times lq}$. Then, we obtain that, given the viral state observations $v_i[1], ..., v_i[n+1]$ of every group i, the GEMF model (7.4) is linear with respect to the Laplacian matrices Q_i and $Q_{m,ij}$.

Lemma 7.4. *Consider the GEMF model (7.4) with a nodal transition matrix $\tilde{S}_i[k] = S_i + S_{\text{con},i}[k]$, where the time-varying matrix $S_{\text{con},i}[k]$ is known (or equals zero). Denote the $C \times C$ Laplacian matrix of the known control matrix $S_{\text{con},i}[k]$ by*

$$Q^T_{\text{con},i}[k] = \text{diag}\left(S_{\text{con},i}[k]u\right) - S_{\text{con},i}[k].$$

For any group i, define the $Cn \times 1$ vector V_i as

$$V_i = \begin{pmatrix} v_i[2] - v_i[1] + Q^T_{\text{con},i}[1]v_i[1] \\ \vdots \\ v_i[n+1] - v_i[n] + Q^T_{\text{con},i}[n]v_i[n] \end{pmatrix},$$

and define the $Cn \times C^2$ matrices $W_i, R_{m,ij}$ as

$$W_i = -\left(I_C \otimes v_i[1], ..., I_C \otimes v_i[n]\right)^T$$

and

$$R_{m,ij} = \left(v_{j,m}[1]\left(I_C \otimes v_i[1]\right), ..., v_{j,m}[n]\left(I_C \otimes v_i[n]\right)\right)^T.$$

Furthermore, define the $Cn \times C^2(1+NC)$ *matrix* F_i *as*

$$F_i = \left(W_i, R_{1,i1}, ..., R_{1,iN}, R_{2,i1}, ..., R_{C,iN}\right)$$

and the $C^2(1+NC) \times 1$ GEMF parameter vector θ_i *as*

$$\theta_i = \left(\text{vec}(Q_i)^T, \text{vec}(Q_{1,i1})^T, ..., \text{vec}(Q_{1,iN})^T, \text{vec}(Q_{2,i1})^T, ..., \text{vec}(Q_{C,iN})^T\right)^T.$$

Then, the GEMF parameter vector θ_i *satisfies the linear system*

$$V_i = F_i \theta_i. \tag{7.8}$$

Proof. Appendix F.2. □

The entries of the $C^2 \times 1$ vectors $\text{vec}(Q_i)$ and $\text{vec}(Q_{m,ij})$ are linear combinations of the entries of the nodal transition probability matrix S_i and the edge-based transition probability matrix $B_{m,ij}$. Thus, the GEMF network reconstruction problem results in a set of equations (7.8) that is linear with respect to the matrices S_i and $B_{m,ij}$. For every node i, the maximum number of unknowns is bounded by the number $C^2(1+NC)$ of entries of the GEMF parameter vector θ_i. However, in most cases, many entries of the matrices S_i and $B_{m,ij}$ are a priori known to be zero, since some nodal or edge-based transitions cannot occur. For instance, at most one entry of the matrix S_i in (7.3) is non-zero. Furthermore, since the viral state $\nu_i[k]$ of every group i obeys $\nu_{i,1}[k] + ... + \nu_{i,C}[k] = 1$, there are n redundant equations in (7.8), and every N-th row of (7.8) can be omitted. Hence, the set of linear equations (7.8) can be often be expressed more compactly for particular GEMF models. To give an example, for the discrete-time SIS epidemic model (4.1) the linear system (7.8) can be expressed compactly as follows.

Lemma 7.5. *For any node* i*, the curing probability* $\delta_{\Delta t,i}$ *and the infection probabilities* $\beta_{\Delta t,i1}, ..., \beta_{\Delta t,iN}$ *of the SIS epidemic model (4.1) with time-varying curing rates* $\tilde{\delta}_{\Delta t,i}[k] = \delta_{\text{con},i}[k] + \delta_{\Delta t,i}$ *satisfy*

$$V_{\text{SIS},i} = F_{\text{SIS},i}\left(\delta_{\Delta t,i}, \beta_{\Delta t,i1}, ..., \beta_{\Delta t,iN}\right)^T. \tag{7.9}$$

Here, the $n \times 1$ *vector* $V_{\text{SIS},i}$ *equals*

$$V_{\text{SIS},i} = \begin{pmatrix} \mathcal{I}_i[2] - (1-\delta_{\text{con},i}[1])\mathcal{I}_i[1] \\ \vdots \\ \mathcal{I}_i[n+1] - (1-\delta_{\text{con},i}[n])\mathcal{I}_i[n] \end{pmatrix}$$

and the $n \times (N+1)$ *matrix* $F_{\text{SIS},i}$ *is given by*

$$F_{\text{SIS},i} = \begin{pmatrix} -\mathcal{I}_i[1] & \mathcal{S}_i[1]\mathcal{I}_1[1] & ... & \mathcal{S}_i[1]\mathcal{I}_N[1] \\ \vdots & \vdots & \ddots & \vdots \\ -\mathcal{I}_i[n] & \mathcal{S}_i[n]\mathcal{I}_1[n] & ... & \mathcal{S}_i[n]\mathcal{I}_N[n] \end{pmatrix}. \tag{7.10}$$

Analogously to Lemma 7.5, we state the linear system (7.8) more compactly for the discrete-time SIR, SEIR, and SISIR epidemic models in Appendix F.3, Appendix F.4, and Appendix F.5, respectively.

7.4. THE LIMITS OF NETWORK RECONSTRUCTION

On the first sight, it seems straightforward to infer the network from GEMF viral state observations, since the network reconstruction is equivalent to solving the linear system (7.8). However, as we show in the following, the linear system (7.8) is extremely ill-conditioned, which is a severe limitation to the GEMF network reconstruction problem itself – *regardless of the specific network reconstruction method.*

7.4.1. AGITATION OF THE VIRAL STATE DYNAMICS

For ease of exposition, we focus on the SIS epidemic model (4.1) in the following. However, the results also apply to other GEMF epidemic models. In Chapter 2 and Chapter 3, particularly below Lemma 2.12 and by Theorem 3.12, we showed that: if the POD (2.1) is *exact*, then there are many networks which cause the same SIS dynamics. In the following, we use the POD *approximately*. More precisely, at any time k, we approximate the SIS viral state vector $\mathcal{I}[k] = (\mathcal{I}_1[k], ..., \mathcal{I}_N[k])^T$ by

$$\mathcal{I}[k] \approx \sum_{l=1}^{m} c_l[k] y_l. \tag{7.11}$$

Here, the *agitation modes* $y_1, ..., y_m$ are some orthogonal vectors, and $c_l[k]$ denote some scalar functions. The greater the number m of agitation modes, the more accurate the approximation (7.11). If $m = N$, then the approximation (7.11) is exact, because any $N \times 1$ vector $\mathcal{I}[k]$ can be written as the linear combination of N orthogonal vectors. Intuitively speaking, if the POD (7.11) is accurate for $m \ll N$ modes, then the nodal state vector $\mathcal{I}[k]$ is barely agitated.

To approximate the viral state $\mathcal{I}[k]$ by the POD (7.11), we must specify the agitation modes y_l and the scalar functions $c_l[k]$. We obtain the agitation modes y_p numerically from viral state observations $\mathcal{I}[1]$, ..., $\mathcal{I}[n]$ in two steps [41]. First, we define the $N \times n$ viral state matrix as

$$M_{\mathcal{I}} = \begin{pmatrix} \mathcal{I}[1] & ... & \mathcal{I}[n] \end{pmatrix}.$$

Second, we obtain the agitation modes y_1, ..., y_m as the first m left-singular vectors of the nodal state matrix $M_{\mathcal{I}}$. At any time k, the scalar functions $c_l[k]$ follow as the inner product $c_l[k] = y_l^T \mathcal{I}[k]$.

Figure 7.4 shows that the proper orthogonal decomposition (7.11) is accurate at all times k. The number of agitation modes y_l equals $m = 5$, which is considerably lower than the network size N. We emphasise that the agitation modes y_l are computed from the nodal state $x[k]$ only until the observation time $k = n$. Nevertheless, the POD is accurate also at times $k > n$. Hence, during the observation interval $k = 1, ..., n$, the viral state $\mathcal{I}[k]$ quickly locks into only few agitation modes y_l, which govern the dynamics also for future time $k > n$. We stress that the POD (7.11) cannot be used (directly) to predict the nodal state $\mathcal{I}[k]$: Additionally to the agitation modes y_l, the coefficients $c_l[k] = y_l^T \mathcal{I}[k]$ at times $k > n$ require the future, unknown nodal state $\mathcal{I}[k]$.

Lemma 7.6. *Consider the SIS epidemic model (4.1) and suppose that the POD (2.1) is exact for m agitation modes. Then, the rank of the matrix $F_{\mathrm{SIS},i}$ in (7.10) is bounded by*

$$\operatorname{rank}\left(F_{\mathrm{SIS},i}\right) \leq 1 + m$$

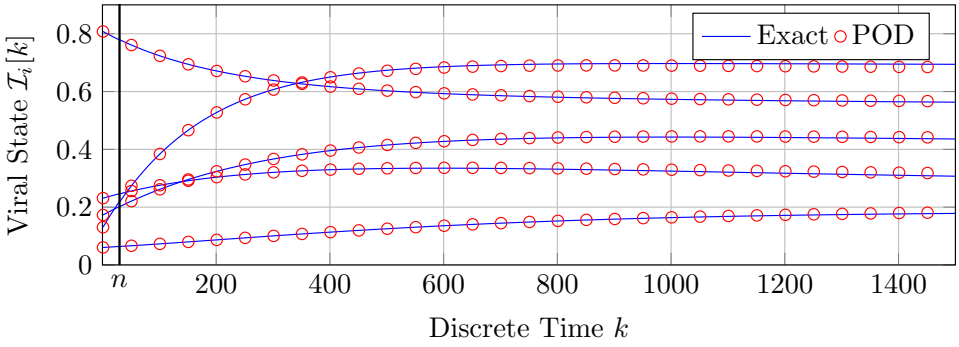

Figure 7.4: **Agitation of the viral state dynamics.** For a Barabási-Albert random graph with $N = 300$ nodes and heterogeneous spreading parameters $\delta_{\Delta t,i}$, $\beta_{\Delta t,ij}$ and a basic reproduction number $R_0 = 2$, the exact SIS viral state $\mathcal{I}_i[k]$ in blue and the POD approximation (7.11) in red. For readability, the viral state $\mathcal{I}_i[k]$ of only five nodes is depicted. The approximation equals the linear combination of $m = 5$ agitation modes y_1, ..., y_m, which are computed by observing the viral state vector $\mathcal{I}[k]$ until the observation time $n = 30$.

Proof. Appendix F.6 □

Lemma 7.6 shows that if the SIS viral state $\mathcal{I}[k]$ is not sufficiently agitated, then there are infinitely many networks that satisfy the linear system (7.9).

7.4.2. RECONSTRUCTION OF LARGE NETWORKS

The set of linear equations (7.8) can, in theory, be solved exactly if the rank of the matrix F_i equals the number of unknowns. However, any computer works with finite precision arithmetic, which causes small, but non-zero, round-off errors. In the worst case, even small round-off errors can accumulate and greatly affect the accuracy of the solution of the linear system (7.8). To solve the linear system (7.8) in practice, the *numerical* rank of the matrix F_i is decisive. The numerical rank of the matrix F_i equals the number of singular values of the matrix F_i that are greater than a small threshold ϵ_{rank}, which is set in accordance to the machine precision.

We perform numerical simulations to obtain the average numerical rank of the matrix F_i for the discrete-time SIS, SIR, SEIR and SISIR epidemic models. For the SIS, SIR, SEIR, and SISIR epidemic models, the adjacency matrices A_{12}, A_{12}, A_{13}, and both A_{12} and A_{34}, respectively, that correspond to the contact network between infected and susceptible nodes, are generated according to the Barabási-Albert random graph model [8], where the initial number of nodes is set to $m_0 = 3$ and the number of links per addition of a new node is set to $m = 3$. Furthermore, we set $a_{ii} = 1$ for every group i of the respective adjacency matrices, since we consider that individuals in group i can infect one another. On the one hand, we consider that there is no curing probability control, i.e., $\delta_{\text{con},i}[k] = 0$ for every group i at every time k. On the other hand, we set the curing probability control term $\delta_{\text{con},i}[k]$ to a uniformly distributed random number in $[0, \delta_{\text{max},i}]$ for every group i at every time k, where the maximum control value equals $\delta_{\text{max},i} = 0.01\delta_{\Delta t,i}$. Further details on the simulation parameters are given in Appendix F.8.

Without curing probability control, i.e., $\delta_{\text{con},i}[k] = 0$ for every group i at every time

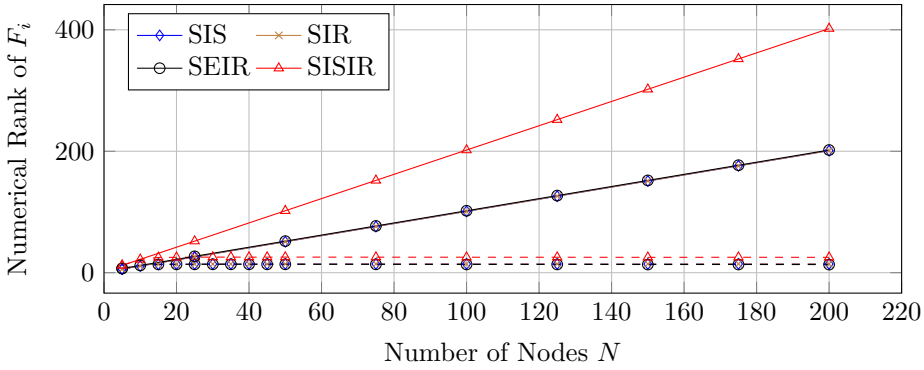

Figure 7.5: **Numerical rank for large networks.** The numerical rank of the matrix F_i versus the number of nodes N. The dashed and the solid lines depict the results without and with curing probability control, respectively. The results are averaged over 100 Barabási-Albert random graphs.

k, Figure 7.5 shows that the numerical rank of the matrix F_i, computed by the Matlab command `rank`, quickly stagnates as the number of groups N grows. Thus, the linear system (7.8) is very ill-conditioned. For instance, for the discrete-time SIS model (4.1), the numerical rank stagnates at approximately $\text{numrank}(F_i) \approx 15$, and the linear system (7.9) has practically not more than 15 independent equations. *Hence, large networks cannot be reconstructed from GEMF viral state observations of a single epidemic outbreak without curing probability control*[3], which is in agreement with other works [94, 138] that consider network reconstruction for *individual-based* epidemic models. For the SISIR model, the numerical rank of the matrix F_i is approximately twice as high as for the other epidemic models, which is intuitive since the contact network for the SISIR model is effectively of size $2N$. With curing probability control on the other hand, the numerical rank of the matrix F_i behaves very differently. In particular, the numerical rank of the matrix F_i equals the number of unknown parameters for the SIS, SIR, SEIR and SISIR epidemic model, also for large networks. *Hence, a time-varying control of the curing rates $\delta_{\Delta t,i}[k]$ is necessary for the reconstruction of large networks.*

In theory, we see two alternatives to controlling the curing rates for the reconstruction of large networks. However, we argue that neither of these two alternatives is applicable to real-world epidemics. First, a greater number of linearly independent equations (7.8) can be achieved by observing multiple epidemic outbreaks[139] with different initial viral states $v[1]$. Each epidemic outbreak results in a different matrix F_i, which can be stacked such that the linear system (7.8) has sufficiently many independent equations. However, the numerical rank of the matrix F_i stagnates when the number of nodes N increases. Thus, the greater the network size N the more epidemic outbreaks need to be observed to reconstruct the network. We believe that it is far from practical to observe multiple outbreaks for real-world epidemics, in particular for novel viruses that demand

[3] If the contact network is sparse, then compressed sensing [88] could be applied to the underdetermined system (7.8). Then, the required number of linearly independent equations for reconstructing a network with s non-zero elements grows at least proportionally to $s\log(N/s)$. However, since the rank of the matrix F_i *stagnates* for a growing number of nodes N, also compressed sensing methods fail for large networks.

rapid intervention.

Second, if some properties of the contact network are known a priori, then less equations are possibly needed to solve the GEMF network reconstruction problem. For instance, if the maximum in-degree of a node i is bounded by

$$\sum_{j=1}^{N} \beta_{\Delta t,ij} \leq d_{\max} \tag{7.12}$$

for some upper bound $d_{\max}$, then (7.12) can be included as a constraint in the linear system (7.9) of the SIS network reconstruction problem. However, the rank of the matrix F_i stagnates when the number of nodes N increases. Hence, the greater the network, the more constraints must be included in the linear system (7.8), which does not seem viable for a large network size N.

7.4.3. THE IMPACT OF MODEL ERRORS

A real-world virus does not exactly follow the difference equations of the GEMF model (7.4). Instead, the viral state $v_i[k]$ of any group i evolves according to

$$v_i[k+1] = f_{\text{GEMF},i}\,(v_1[k],...,v_N[k]) + w_i[k], \tag{7.13}$$

where $f_{\text{GEMF},i}\,(v_1[k],...,v_N[k])$ denotes the right-hand side of (7.4), and the $C \times 1$ vector $w_i[k]$ denotes the *model error* at group i and time k. To ensure that $v_{i,1}[k]+...+v_{i,C}[k] = 1$ at every time k, we set $w_{i,l}[k] = 0$ for exactly one compartment l. For the SIS, SIR, SEIR, and SISIR models, we choose the remaining compartment l as: $\mathcal{S}_i$, $\mathcal{S}_i$, $\mathcal{R}_i$, and $\mathcal{R}_i$, respectively.

To demonstrate the impact of model errors $w_i[k]$ on the network reconstruction problem, we perform numerical simulations of the SIS epidemic model (4.1) on a small Erdős-Rényi random graph with $N = 20$ nodes and link probability $p_{\text{ER}} = 0.1$. We set all parameters to the same values as in Subsection 7.4.2. We consider three cases for the maximum control value: $\delta_{\max,i} = 0$ (no curing probability control), $\delta_{\max,i} = 0.05\delta_i$ (small curing probability control), and $\delta_{\max,i} = \delta_i$ (large curing probability control). On the one hand, we consider a viral state evolution without model errors, i.e. $w_i[k] = 0$ for all nodes i and all times k. On the other hand, we consider that the SIS epidemic model (4.1) is subject to independently and identically distributed Gaussian model errors $w_{i,m}[k] \sim \mathcal{N}(0,\varsigma_i^2)$ with variance $\varsigma_i^2 = (0.05\Delta t)^2$.

Figure 7.6 illustrates that the evolution of the viral state $v_i[k]$ is virtually unaffected by the model error $w_i[k]$. If a real-world epidemic evolved with an equally small model error $w_i[k]$ as in Figure 7.6, then the SIS epidemic model (4.1) would be considered an outstanding fit to the epidemic data. On the first sight, Figure 7.6 suggests that it is possible to reconstruct the network from GEMF viral state observations $v_i[k]$ with a negligibly small model error $w_i[k]$. However, the GEMF network reconstruction problem is dramatically sensitive to small perturbations by model errors $w_i[k]$. The upper subplot in Figure 7.7 shows that, without curing probability control, only around five singular values $\sigma_j(F_{\text{SIS},i})$ of the matrix $F_{\text{SIS},i}$ remain largely unaffected by model errors $w_i[k]$. Hence, without curing probability control, even small networks cannot be reconstructed from GEMF viral state observations, also when the model errors $w_i[k]$ seem negligibly

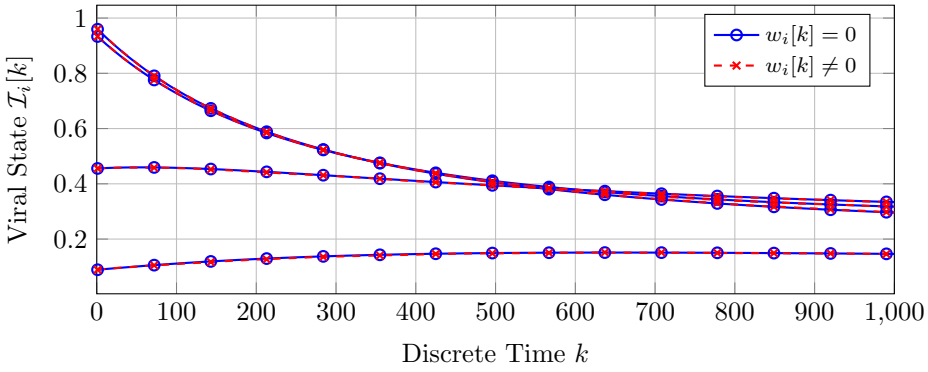

Figure 7.6: **SIS dynamics with small model errors.** The viral state $\mathcal{I}[k]$ of the discrete-time SIS epidemic model (4.1) for an Erdős-Rényi random graph with $N = 20$ groups without curing probability control ($\delta_{\max,i} = 0$), with and without model errors $w_i[k]$. The viral state $\mathcal{I}_i[k]$ of four of the twenty groups i is depicted.

small[4]. The lower sub-plot in Figure 7.7 shows that, for a sufficiently great curing probability control $\delta_{\text{con},i}[k]$, the model error $w_i[k]$ only slightly perturbs the singular values $\sigma_j(F_{\text{SIS},i})$. *Hence, curing probability control is necessary to reconstruct the network in the presence of model errors* $w_i[k]$ – but controlling the curing rates is possibly not *sufficient*, since we only studied the perturbation of the singular values $\sigma_j(F_{\text{SIS},i})$ but not the perturbation of the *whole* matrix $F_{\text{SIS},i}$.

7.5. NETWORK RECONSTRUCTION ALGORITHM

When the GEMF model (7.4) is subject to model errors $w_i[k]$, then the GEMF parameter vector θ_i does not satisfy the linear system (7.8) with equality. Thus, we resort to finding the vector θ_i as the minimiser of the Euclidean norm $\|V_i - F_i\theta_i\|_2^2$. More precisely, our network reconstruction method is based on the constrained LASSO [141]:

$$\begin{aligned} \hat{\theta}_i = \arg\min_{\theta_i} \quad & \|V_i - F_i\theta_i\|_2^2 + \rho_i \|\theta_i\|_1 \\ \text{s.t.} \quad & \theta_i \geq 0 \\ & (\theta_i)_j = 0 \quad \forall j \in \Omega_i \end{aligned} \tag{7.14}$$

The application of LASSO, and variations thereof, to network reconstruction is an established approach [88, 139, 142]. The ℓ_1-regularisation term $\|\theta_i\|_1$ in the objective favours the estimation of a sparse GEMF parameter vector θ_i, which is motivated by two reasons. First, the majority of real-world networks are indeed sparse [143]. Second, we follow the *bet on sparsity* principle: "Use a procedure that does well in sparse problems, since no procedure does well in dense problems" [141]. Tuning the *regularisation parameter* $\rho_i > 0$ in the objective of (7.14) controls the trade-off between a good fit to the model (first addend) and the sparsity of the GEMF parameter vector θ_i (second addend). We set the value of the scalar $\rho_i > 0$ by *cross-validation* [141]. In (7.14), the inequality

[4] Furthermore, the sensitivity to model errors renders model-free network inference methods [140] not suitable for the GEMF network reconstruction problem, since model-free methods per definition induce model errors.

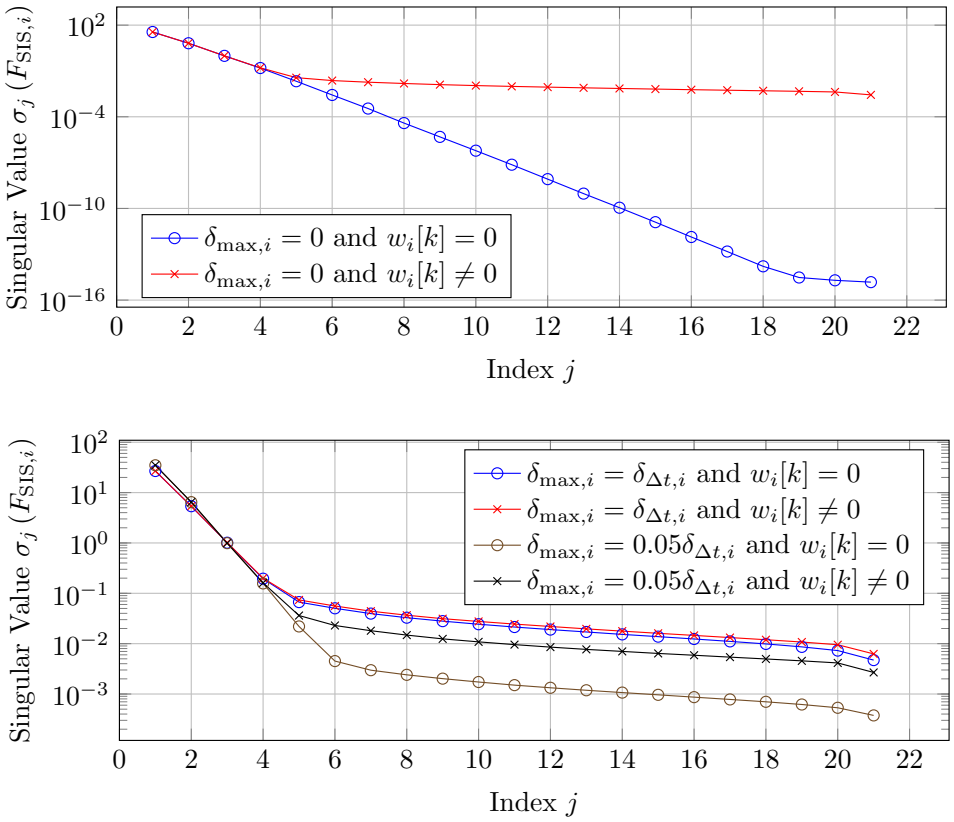

Figure 7.7: **Singular values of the linear network reconstruction problem.** The singular values $\sigma_j\,(F_{\mathrm{SIS},i})$ of the matrix $F_{\mathrm{SIS},i}$ of the linear system (7.9), with and without model errors $w_i[k]$. The upper sub-plot refers to no curing probability control ($\delta_{\max,i} = 0$), and the lower sub-plot considers a small and large value for the maximum value $\delta_{\max,i}$ of the curing probability control. The results are averaged over 100 Erdős-Rényi random graphs with $N = 20$ nodes.

$\theta_i \geq 0$ for the GEMF parameter vector θ_i holds element-wise. The indices j in the set $\Omega_i \subset \{1,...,C^2(1+NC)\}$ refer to entries $(\theta_i)_j$ that must be zero for the particular GEMF model. For instance, the 3×3 nodal transition matrix S_i in (7.3) has eight zero entries, which results in the inclusion of eight indices in the set Ω_i. To solve (7.14) numerically, we apply the interior point algorithm provided by the Matlab command `quadprog`. If there are no model errors, i.e., $w_i[k] = 0$ for every group i at every time k, then we do not estimate the GEMF parameter vector θ_i by the LASSO formulation (7.14). Instead, we apply the QR-solver provided by the Matlab command `mldivide` if the matrix F_i is of full rank, and we apply a basis pursuit approach [144] if the matrix F_i is not of full rank. For further details on the network reconstruction algorithm, we refer the reader to Appendix F.9.

7.5.1. INTERPRETATION AS BAYESIAN ESTIMATION

We show that the LASSO (7.14) can be interpreted as Bayesian estimation problem.

Assumption 7.7. *For every node i at every time k, the model error $w_i[k]$ in (7.13) follows the normal distribution $\mathcal{N}(0,\sigma_w^2)$ with zero mean and variance σ_w^2. Furthermore, the model errors $w_i[k]$ are stochastically independent and identically distributed at all times k and for all nodes i.*

Assuming that the model errors $w_i[k]$ follow a Gaussian distribution $\mathcal{N}(0,\sigma_w^2)$ allows for a simple analysis. If the distribution of the model errors $w_i[k]$ is not known, then Assumption 7.7 is in agreement with the *maximum entropy principle* [145]: Given a set of constraints on a probability distribution (e.g., specified mean), assume the "least informative" distribution, i.e., the distribution with maximum entropy that satisfies those constraint. Among all distributions on $\mathbb{R}$ with zero mean and variance σ_w^2, the Gaussian distribution $\mathcal{N}(0,\sigma_w^2)$ has the maximum entropy [146].

Assumption 7.8. *The parameter vector $\theta_i \geq 0$ follows the prior distribution*

$$\Pr[\theta_i] = \begin{cases} 0 & \text{if} \quad \exists j \in \Omega_i : (\theta_i)_j \neq 0, \\ \alpha \exp\left(-\sum_{j \notin \Omega_i} (\theta_i)_j\right) & \text{otherwise.} \end{cases}$$

Here, the normalisation constant α is set such that

$$\int_{\mathbb{R}_{\geq 0}^{C^2(1+NC)}} \Pr[\theta_i]\, d\theta_i = 1.$$

Furthermore, the parameter vector θ_i and the initial viral state $v_i[1]$ of all nodes i are stochastically independent.

Essentially, Assumption 7.8 states an exponential degree distribution of the contact network and transition probabilities. The Bayesian interpretation of the LASSO (7.14) is given by Theorem 7.9 below. We emphasise that Theorem 7.9 is not entirely novel, since it follows standard arguments in parameter estimation, see for instance [147]. Furthermore, Tibshirani elaborated on the Bayesian interpretation of the LASSO in the seminal paper [148]. Nevertheless, we believe that the presentation of Theorem 7.9, here in the context of network reconstruction, is valuable to the reader. For every time k, we define the $C \times N$ matrix $v[k] = (v_1[k], ..., v_N[k])$.

Theorem 7.9. *Suppose that Assumption 7.7 and Assumption 7.8 hold true and that the viral state $v_i[k]$ follows (7.13). Then, provided the regularisation parameter equals $\rho_i = 2\sigma_w^2$, the GEMF parameter vector $\hat{\theta}_i$, which is obtained by solving LASSO (7.14), coincides with the Bayesian estimate:*

$$\hat{\theta}_i = \underset{\theta_i \geq 0}{\operatorname{argmax}} \Pr\left[\theta_i \middle| v[1], ..., v[n+1]\right]. \tag{7.15}$$

Proof. Appendix E.7. □

7.6. NUMERICAL EVALUATION

To evaluate the quality of the network reconstruction, we compute the area under the receiver-operating-characteristic curve (AUC) [149]. The AUC ranges from 0 to 1, where an AUC of 1/2 is equivalent to flipping a coin to determine whether a link is presence or absence. If the estimated network equals the true network, then the AUC equals 1. We compute the AUC with respect to the estimates of the respective adjacency matrices A_{12}, A_{21}, and A_{13} of the SIS, SIR and SEIR model. For the SISIR model, we consider the mean of the two AUCs with respect to the adjacency matrices A_{12} and A_{34}. Furthermore, we define the *prediction error* $\epsilon_{\mathcal{I}}$ until the *prediction time* n_{pred} as

$$\epsilon_{\mathcal{I}} = \frac{1}{N}\frac{1}{n_{\text{pred}}-n}\sum_{k=n+1}^{n_{\text{pred}}}\sum_{i=1}^{N}\left|\mathcal{I}_i[k]-\hat{\mathcal{I}}_i[k]\right|.$$

Here, $\hat{\mathcal{I}}_i[k]$ denotes the predicted fraction of infectious individuals in group i at time k, which is obtained by iterating GEMF (7.4) without model errors from time $k=n$ to $k=n_{\text{pred}}$ with the parameter vector $\hat{\theta}_i$ that was estimated from the viral state observations $\nu_i[1],...,\nu_i[n]$ for every node i. For the SISIR model, we define the prediction error $\epsilon_{\mathcal{I}}$ as the sum of the two prediction errors with respect to the two compartments $\mathcal{I}_1$ and $\mathcal{I}_2$. Unless stated otherwise, all parameters are set to the same values as in Subsection 7.4.2.

7.6.1. ABSENCE OF MODEL ERRORS

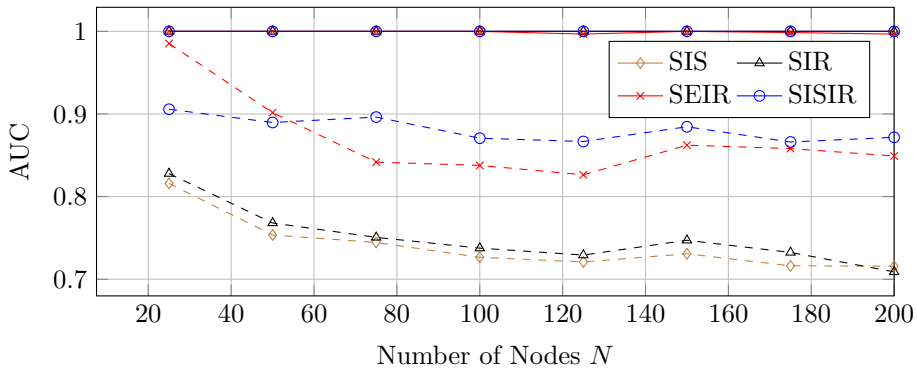

Figure 7.8: **Network reconstruction accuracy versus network size N.** The accuracy of the network reconstruction for four different epidemic models. The solid lines show the accuracy with curing probability control, $\delta_{\text{con},i}[k] \neq 0$, and the dashed lines show the accuracy without curing probability control, $\delta_{\text{con},i}[k] = 0$. The results are averaged over 100 Barabási-Albert random graphs, and the number of observations equals $n = 10N$.

For every group i, we set the maximum control value to $\delta_{\max,i} = 0.05\delta_{\Delta t,i}$ and the observation length to $n = 10N$. Figure 7.8 shows that, without model errors $w_i[k]$, the network reconstruction is almost always exact – provided that the curing rates are controlled ($\delta_{\max,i} = 0.05\delta_{\Delta t,i}$). Without curing probability control ($\delta_{\max,i} = 0$), the reconstructed network differs considerably from the true network when the number of nodes N is large, in agreement with Figure 7.5.

	SIS	SIR	SEIR	SISIR
AUC	0.52	0.52	0.54	0.52
$\epsilon_{\mathcal{I}}$	$3.72 \cdot 10^{-4}$	$3.49 \cdot 10^{-5}$	$4.28 \cdot 10^{-5}$	$6.25 \cdot 10^{-5}$

Table 7.1: **Network reconstruction accuracy versus prediction accuracy.** The prediction error $\epsilon_{\mathcal{I}}$ and the AUC for different epidemic models without curing probability control, where the number of observations equals $n = 100$ and the prediction time equals $n_{\text{pred}} = 1000$. The results are averaged over 100 Barabási-Albert random graphs with $N = 200$ nodes.

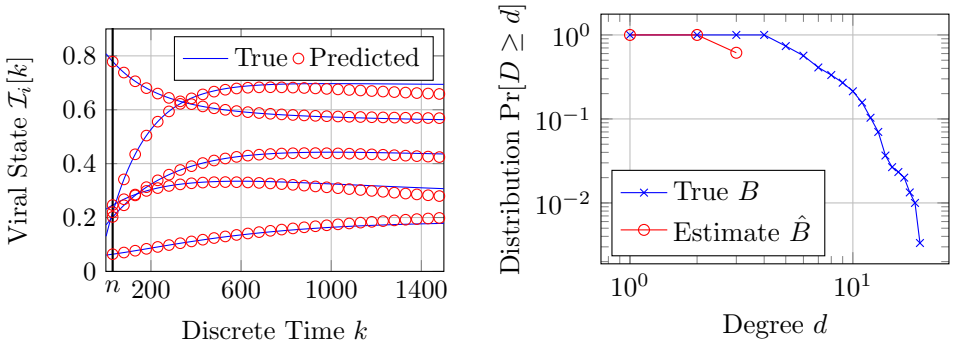

(a) Prediction accuracy.

(b) Network reconstruction accuracy (AUC = 0.51).

Figure 7.9: **Prediction accuracy versus network reconstruction accuracy.** For a Barabási-Albert random graph with $N = 300$ nodes, heterogeneous spreading parameters $\delta_{\Delta t,i}$, $\beta_{\Delta t,ij}$ and a basic reproduction number $R_0 = 2$: **(a)** shows the the exact SIS viral state $\mathcal{I}_i[k]$ in blue and the prediction for time $k > n$ in red, which is obtained by the LASSO (7.14) from observing the viral state $\mathcal{I}[k]$ until the observation time $n = 30$. For readability, the viral state $\mathcal{I}_i[k]$ of only five nodes is depicted; **(b)** shows the in-degree distribution of the estimated matrix $\hat{B}$ in red and the true matrix B in blue.

To evaluate the prediction error $\epsilon_{\mathcal{I}}$ in the absence of curing probability control, we reduce the observation length to $n = 100$ and set the prediction time to $n_{\text{pred}} = 1000$. Table 7.1 shows that the prediction error $\epsilon_{\mathcal{I}}$ is practically zero, even though the AUC is very low. Figure 7.9 juxtaposes the stark contrast of accurate prediction and inaccurate network reconstruction, with respect to the AUC score and the in-degree distribution[5]. *Thus, without curing probability control, fundamentally different contact networks result in virtually the same viral state sequence.*

7.6.2. PRESENCE OF MODEL ERRORS

As illustrated by Figure 7.7, we cannot expect that an accurate network reconstruction is possible in the presence of model errors $w_i[k]$. However, Table 7.1 shows that, at least

[5] The in-degree d_i of node i equals the number of links that end at node i. The in-degree distribution is given by $\Pr[D \geq d]$, where D is the degree of a randomly chosen node in the network.

in the absence of model errors $w_i[k]$, the prediction of the epidemic outbreak is surprisingly less related to an accurate network reconstruction. We consider Barabási-Albert random graphs with $N = 100$ nodes. For every group i at every time k, we generate the model error $w_i[k]$ as a Gaussian random variable with standard deviation $\varsigma_i = 0.1\Delta t$, and we set the sampling time to $\Delta t = \Delta t_{\max}/5$, where the maximum sampling time $\Delta t_{\max}$ is given in Appendix F.8. Furthermore, we consider curing rate control with $\delta_{\max,i} = 0.05\delta_{\Delta t,i}$.

Figure 7.10 gives an impression on the prediction accuracy for the SIS process (4.1), when the network is reconstructed from the viral state sequence $v[1],...,v[n]$ until the observation lengths $n = 50$ and $n = 100$, respectively. For an observation length $n = 50$, the AUC equals approximately 0.53 and the viral state prediction diverges from the true viral state $v[k]$ as time k evolves. However, the viral state prediction is accurate until discrete time $k \approx 125$, which is valuable for medium-term disease control measures. For an observation length $n = 100$, the AUC equals approximately 0.54 and the viral state prediction is relatively accurate at all times $k \geq n$ – taking the random model errors $w_i[k]$ into account. Hence, also in the presence of model errors $w_i[k]$, a prediction of the viral state $v[k]$ is generally possible, and the greater the number of observations n the more accurate the long-term viral state prediction.

To evaluate the prediction accuracy versus the observation length n, we consider the contact network of the *Infectious: Stay Away* exhibition [150] with $N = 410$ nodes, accessed via the *Konect* network collection [62]. Every node i corresponds to an individual, and there is a link between two nodes if the corresponding two individuals had at least one face-to-face contact for more than 20 seconds. We set the infection probability $\beta_{\Delta t,ij}$ proportional to the number of contacts between individual i and j, such that the infection probability $\beta_{\Delta t,ij}$ of the two individuals i, j that had the most face-to-face contacts is three times as great as the infection probability of two individuals that only had a single face-to-face contact. The self-infection probabilities $\beta_{\Delta t,ii}$ are set to zero for every group i. The curing probabilities $\delta_{\Delta t,i}$ are set as in Subsection 7.4.2, such that the basic reproduction number equals $R_0 = 1.5$. Figure 7.11 shows the AUC and the prediction error ϵ_{pred} versus the observation length n with and without model errors $w_i[k]$. In the presence of model errors $w_i[k]$, the prediction error ϵ_{pred} converges quickly to a small value, even though the AUC remains at around 0.5 for all observation lengths n.

7.7. CONCLUSIONS

In this chapter, we considered the reconstruction of the contact network and the prediction of epidemic outbreaks for general discrete-time compartmental epidemic models. Our contribution is composed of two parts.

In the first part, we proposed the GEMF model in discrete time, which generalises a plethora of diverse compartmental discrete-time epidemic models. We suggested the transition graph as an equivalent and compact visual representation of any particular GEMF model. Furthermore, the GEMF model can take multi-layer contact networks into consideration. Thus, the GEMF model is a powerful framework to study general spreading processes.

In the second part, we proposed a prediction framework which consists of two steps. First, the network is estimated from the viral state observations by the LASSO. Without

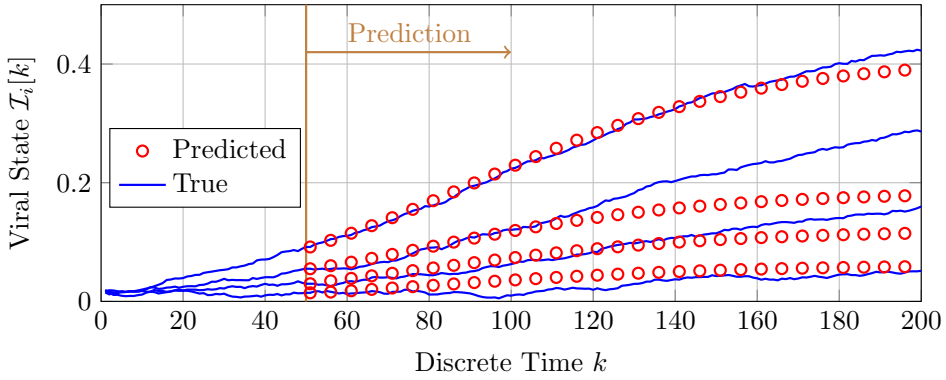

(a) Observation length of $n = 50$.

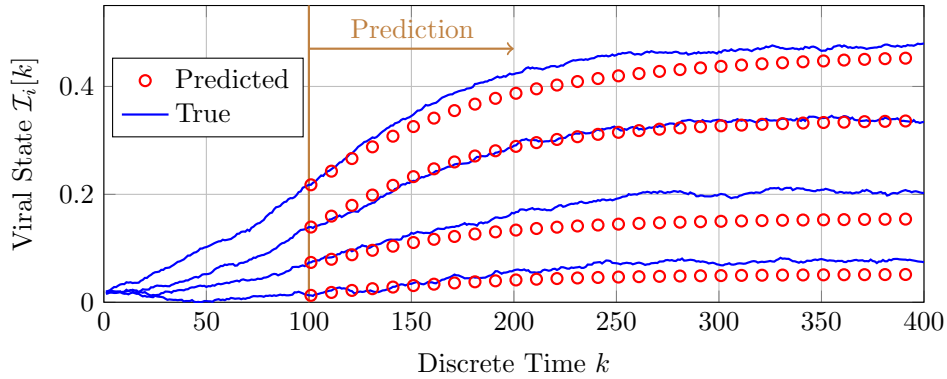

(b) Observation length of $n = 100$.

Figure 7.10: **Prediction of epidemics on networks.** The true and predicted viral state $\mathcal{I}_i[k]$ of the SIS model (4.1) of four nodes of a Barabási-Albert random graph with $N = 100$ nodes subject to model errors $w_i[k]$.

curing rate control, the first step seemingly fails, since the estimated network bears no *topological* similarity with the true network. Second, the viral state is predicted by iterating the dynamical model on the inaccurately estimated network. Counterintuitively, the prediction is accurate!

The network reconstruction and prediction accuracy do not match, because the viral state is barely agitated. Furthermore, the modes of agitation are hardly related to the network topology. Instead of the true topology, the estimated network does capture the interplay with the agitation modes.

We conclude with three points. First, the agitation modes depend on the initial viral state dynamics and, particularly, on the initial viral state $v[1]$. As a result, the estimated GEMF parameter vector $\hat{\theta}_i$ depends on the initial viral state $v[1]$. Thus, as confirmed by numerical simulations, the reconstructed network may be useless for the prediction of dynamics with a different initial state $\hat{v}[1] \neq v[1]$

Second, if there are no model errors and the curing rates are controlled, then the

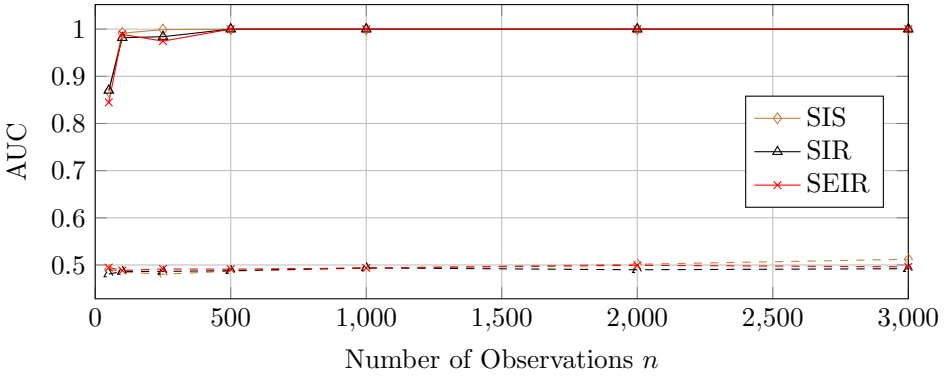

(a) Network reconstruction accuracy.

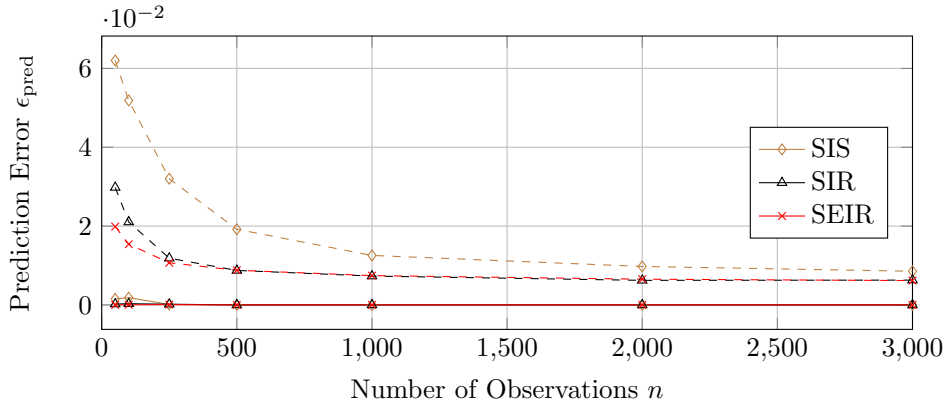

(b) Prediction accuracy.

Figure 7.11: **Accuracy of network reconstruction and epidemic outbreak prediction.** The AUC and the prediction error ϵ_{pred} versus the observation length n of the contact network of the *Infectious: Stay Away* exhibition [150] with $N = 410$ nodes. The solid and dashed lines correspond to the absence and presence of model errors $w_i[k]$, respectively. The results are averaged over 10 realisations of the respective epidemic model with different initial viral states $v[1]$.

network can be reconstructed. The viability of appropriate curing rate control for real epidemics is an open question.

Third, we could observe *multiple* epidemic outbreaks with different initial viral states $v[1]$ on the same network. For sufficiently many outbreaks, we would observe enough agitation modes to reconstruct the network exactly, by stacking the respective linear systems (7.8). However, Figure 7.5 shows that the numerical rank of the matrix F_i stagnates for large networks. Thus, the more nodes, the more time series must be observed to reconstruct the network.

8

NETWORK-INFERENCE-BASED PREDICTION OF THE COVID-19 OUTBREAK

At the moment of writing, the future evolution of the COVID-19 pandemic is unclear. Predictions of the further course of the outbreak are decisive to deploy targeted disease control measures. We consider a network-based model to describe the COVID-19 outbreak. The network is composed of geographical regions and their interactions (e.g., traffic flow). However, the precise interactions between the regions is unknown and must be inferred from observing the viral spread. We propose the Network-Inference-Based Prediction Algorithm (NIPA) to forecast the future prevalence of the COVID-19 in every region in the Netherlands and in the Chinese province Hubei. Numerical evaluations of NIPA and other prediction methods indicate that network-based forecasting is beneficial for an accurate forecast of the COVID-19 outbreak.

This chapter is based on B. Prasse, M. A. Achterberg, L. Ma, and P. Van Mieghem, *Network-inference-based prediction of the COVID-19 epidemic outbreak in the Chinese province Hubei*, Applied Network Science, **5**, 1 (2020) and M. A. Achterberg, B. Prasse, L. Ma, S. Trajanovski, M. Kitsak, and P. Van Mieghem, *Comparing the accuracy of several network-based COVID-19 prediction algorithms*, International Journal of Forecasting, to appear.

8.1. INTRODUCTION

In December 2019, the SARS-CoV-2 virus, which causes the Coronavirus Disease 2019 (COVID-19), emerged in the Chinese province Hubei [151]. The number of SARS-CoV-2 infections in China rose dramatically to almost 80,000 at the end of February. From China, COVID-19 quickly spread throughout the world, with almost eighty million cases at the end of December, 2020. Many countries imposed a nation-wide lockdown to mitigate the spread of COVID-19. A reliable forecast of the virus outbreak is key for targeted disease countermeasures and for the appropriate design of an exit strategy to lift the lockdown.

Unfortunately, as shown in Chapter 6, the prediction of epidemic outbreaks is subject to fundamental limits. There are two major sources of error. First, no model of the COVID-19 outbreak is perfect. Hence, there are *model errors* which quantify the deviation from the epidemic model to reality. Second, the available data on most epidemic outbreaks is limited, because epidemic time series are relatively short and carrying out large-scale and unbiased medical tests is challenging.

Nonetheless, many methods have been developed and applied to forecast the spread of COVID-19. Perhaps the simplest approach is based on fitting the number of infections to a sigmoid curve. The logistic function is a sigmoid curve of particular interest, because the logistic function is the (approximate) solution for the number of infected cases in the Susceptible-Infected-Susceptible (SIS) epidemic model and the number of removed cases in the Susceptible-Infected-Removed (SIR) epidemic model, see Chapter 3 and Chapter 6.

A great body of research proposes various prediction methods for COVID-19, including: Kalman filtering [152]; Bayesian methods [153]; approaches based on aeroplane networks, daily commute traffic or cell phone traffic [154]; adaptive neuro-fuzzy inference system [155]; Long Short-Term Memory (LSTM) [156]; the SIR epidemic model [156, 157]; and the SEIR epidemic model [158].

In this chapter, we apply a network-based prediction approach, where the network is composed of geographical regions and the population flow. The population flow clearly has an impact on the evolution of an epidemic. However, the exact population flow is unknown, and epidemic prediction methods must account for inaccuracies of population flow data. In this chapter, we consider the most extreme case by assuming no prior knowledge of the population flow. To forecast the COVID-19 outbreak, we design the Network-Inference-Based Prediction Algorithm (NIPA). NIPA is based on Chapter 7 and estimates the interactions between regions as an intermediate step.

8.2. THE NIPA PREDICTION ALGORITHM

We denote the discrete time by $k \in \mathbb{N}$. The difference Δt of time k to $k+1$ equals one day, and the number of *reported* infections is denoted by $N_{\text{rep},i}[k]$ at every time k for every region $i = 1, ..., N$. The reported fraction of infected individuals follows as

$$\mathcal{I}_{\text{rep},i}[k] = \frac{N_{\text{rep},i}[k]}{N_{\text{pop},i}},$$

where $N_{\text{pop},i}$ is the population size of region i.

From the observed infections $\mathcal{I}_{\text{rep},i}[1],...,\mathcal{I}_{\text{rep},i}[n]$, where n denotes the observation length, the Network-Inference-based Prediction-Algorithm (NIPA) estimates the number of infections at future times $k > n$. NIPA is based on the discrete-time SIR model in Definition 7.2, which assumes that the curing probabilities $\delta_{\Delta t,i}$ and the infection probabilities $\beta_{\Delta t,ij}$ do not change over time. Hence, we implicitly assume that the lockdown measures do not change significantly from time $k = 1$ to $k = n$. A generalisation of NIPA to time-varying parameters is a promising direction for future research, as shown by our initial results in [159]. We emphasise that $\beta_{\Delta t,ii} > 0$ since individuals within the same region i do interact with each other. Neither the curing probabilities $\delta_{\Delta t,i}$ nor the infection probabilities $\beta_{\Delta t,ij}$ are known for the spread of COVID-19. Potentially, it is possible to state bounds or estimates for the spreading parameters $\delta_{\Delta t,i}$ and $\beta_{\Delta t,ij}$ by making use of the people flow or geographical distances between the respective cities. Nevertheless, there would remain an uncertainty regarding the precise value of the spreading parameters $\delta_{\Delta t,i}$ and $\beta_{\Delta t,ij}$. In this chapter, we consider the most extreme case: there is no a priori knowledge on the curing probabilities $\delta_{\Delta t,i}$ nor the infection probabilities $\beta_{\Delta t,ij}$.

Before presenting the NIPA prediction method, we would like to know if the discrete-time SIR model in Definition 7.2 yields a well-defined viral state vector $v_i[k]$. More precisely: under which conditions are the quantities $\mathcal{S}_i[k]$, $\mathcal{I}_i[k]$ and $\mathcal{R}_i[k]$, which are interpreted as fractions, in the interval $[0,1]$ at every time k?

Assumption 8.1. *For all nodes i, j, it holds that $0 \leq \delta_{\Delta t,i} \leq 1$, $\beta_{\Delta t,ij} \geq 0$ and*

$$\sum_{j=1}^{N} \beta_{\Delta t,ij} \leq 1.$$

Under Assumption 8.1, the SIR viral state vector $v_i[k]$ is indeed well-defined, as stated by Lemma 3.5. Lemma 3.5 and its proof are inspired by [25, Lemma 1].

Lemma 8.2. *Suppose that the initial state of the discrete-time SIR model in Definition 7.2 satisfies $\mathcal{I}_i[1] \geq 0$, $\mathcal{R}_i[1] \geq 0$ and $\mathcal{S}_i[1] \geq 0$ for all nodes i. Then, under Assumption 8.1, it holds that $\mathcal{I}_i[k] \geq 0$, $\mathcal{R}_i[k] \geq 0$ and $\mathcal{I}_i[k] + \mathcal{R}_i[k] \leq 1$ for all nodes i at every time $k \in \mathbb{N}$.*

Proof. Appendix G.1. □

NIPA consists of three steps. First, we preprocess the raw data of reported infections $\mathcal{I}_{\text{rep},i}[k]$ obtain an SIR time series $v_i[1],...,v_i[n]$. Second, we obtain estimates $\hat{\delta}_{\Delta t,i}$ and $\hat{\beta}_{\Delta t,ij}$ of the unknown spreading parameters $\delta_{\Delta t,i}$ and $\beta_{\Delta t,ij}$ with an adaptation of the network inference method in Section 7.5. Third, the estimates $\hat{\delta}_{\Delta t,i}$ and $\hat{\beta}_{\Delta t,ij}$ result in an SIR model (7.5), which we iterate for future times $k = n, n+1,...$ to predict the evolution of COVID-19. We give an outline of the first two steps of NIPA below and refer the reader to Appendix G.3 for further details.

8.2.1. DATA PREPROCESSING

Based on the reported fraction of infections $\mathcal{I}_{\text{rep},i}[k]$, our goal is to obtain an SIR viral state vector $v_i[k] = (\mathcal{S}_i[k], \mathcal{I}_i[k], \mathcal{R}_i[k])^T$ for every node i at any time $k = 1,...,n$. We stress that, in contrast to Chapter 7, we do not observe every compartment of the viral state vector $v_i[k]$. The fraction of susceptible individuals follows as $\mathcal{S}_i[k] = 1 - \mathcal{I}_i[k] - \mathcal{R}_i[k]$ at

any time $k \geq 1$. Thus, it suffices to determine the fraction of infectious individuals $\mathcal{I}_i[k]$ and recovered individuals $\mathcal{R}_i[k]$.

We consider the reported fraction of infections $\mathcal{I}_{\text{rep},i}[k]$ as an *approximation* for the number of infectious individuals $\mathcal{I}_i[k]$. In fact, the reported fraction of infections $\mathcal{I}_{\text{rep},i}[k]$ is smaller than the true fraction of infected individuals $\mathcal{I}_i[k]$ for two reasons. First, not all infectious individuals are aware that they are infected. Second, the diagnosing capacities are limited, particularly when the number of infections increases rapidly. Hence, not all infections can be reported timely.

We do not know the fraction of removed individuals $\mathcal{R}_i[k]$. In the beginning of the outbreak, at time $k = 1$, it is reasonable to assume that $\mathcal{R}_i[1] = 0$ holds for every node i. At any time $k \geq 2$, the removed individuals $\mathcal{R}_i[k]$ could be obtained from (7.5), if the curing probability $\delta_{\Delta t,i}$ were known. However, we do not know the curing probability $\delta_{\Delta t,i}$. Hence, we consider 50 equidistant *candidate values* for the curing probability $\delta_{\Delta t,i}$, ranging from $\delta_{\min} = 0.01$ to $\delta_{\max} = 1$. We define the set of candidate values as $\Omega = \{\delta_{\min}, ..., \delta_{\max}\}$. For every candidate value $\delta_{\Delta t,i} \in \Omega$, the fraction of removed individuals $\mathcal{R}_i[k]$ follows from (7.5) at all times $k \geq 2$. Thus, we obtain 50 potential sequences $\mathcal{R}_i[1], ..., \mathcal{R}_i[n]$, each of which corresponding to one candidate value $\delta_{\Delta t,i} \in \Omega$. We estimate the curing probability $\delta_{\Delta t,i}$, and hence implicitly the sequence $\mathcal{R}_i[1], ..., \mathcal{R}_i[n]$, as the element in Ω that resulted in the best fit of the SIR model (7.5) to the reported number of infections.

The raw time series $\mathcal{I}_{\text{rep},i}[1], ..., \mathcal{I}_{\text{rep},i}[n]$ exhibits erratic fluctuations. To reduce the fluctuations, we apply a moving average, provided by the Matlab command `smoothdata`, to the time series $\mathcal{I}_{\text{rep},i}[1], ..., \mathcal{I}_{\text{rep},i}[n]$ of every node i. The preprocessed time series $\mathcal{I}_i[1], ..., \mathcal{I}_i[n]$ equals the output of `smoothdata`.

8.2.2. NETWORK INFERENCE

For every node i, the curing probability estimate $\hat{\delta}_{\Delta t,i}$ equals to one of the candidate values in the set Ω, as outlined in Subsection 8.2.1. The remaining task is to estimate the infection probabilities $\beta_{\Delta t,ij}$, which we perform analogously to Section 7.5. For every node i, we pose the optimisation problem:

$$\begin{aligned} \min_{\beta_{\Delta t,i1},...,\beta_{\Delta t,iN}} \quad & \left\| V_{\text{SIR},i} - F_{\text{SIR},i} \begin{pmatrix} \hat{\delta}_{\Delta t,i} \\ \beta_{\Delta t,i1} \\ \vdots \\ \beta_{\Delta t,iN} \end{pmatrix} \right\|_2^2 + \rho_i \sum_{j=1, j\neq i}^{N} \beta_{\Delta t,ij}, \\ \text{s.t.} \quad & \beta_{\Delta t,ij} \geq 0, \quad j = 1, ..., N, \\ & \sum_{j=1}^{N} \beta_{\Delta t,ij} \leq 1. \end{aligned} \tag{8.1}$$

The $2(n-1)\times 1$ vector $V_{\text{SIR},i}$ and the $2(n-1)\times(N+1)$ matrix $F_{\text{SIR},i}$ are defined in Lemma F.1. We choose to not penalise the probabilities $\beta_{\Delta t,ii}$, since we expect the infections among individuals within the same region i to be dominant. The last constraint in (8.1) ensures that the estimates for $\beta_{\Delta t,ij}$ result in a well-defined SIR model, as stated by Lemma 8.2.

We emphasise that the accurate prediction of an SIR epidemic outbreak does not

require an accurate network inference, see Appendix G.3. If the observed viral state sequence $v_i[1]$, ..., $v_i[n]$ exactly follows the discrete-time SIR model in Definition 7.2, then NIPA accurately predicts the infection state $\mathcal{I}_i[k]$. Furthermore, NIPA provides accurate *short-term* predictions, also in the presence of model errors $w_i[k]$. We refer the reader to Appendix G.3 for further details on NIPA.

8.3. EVALUATION OF THE PREDICTION ACCURACY

We denote the cumulative fraction of individuals of node i at time k by

$$\mathcal{I}_{c,i}[k] = \sum_{l=1}^{k} \mathcal{I}_i[l].$$

NIPA produces an estimate $\hat{\mathcal{I}}_{c,i}[k]$ for the cumulative number of infected cases at times $k > n$. We quantify the prediction error at time k by the symmetric Mean Absolute Percentage Error (sMAPE)

$$e[k] = \frac{2}{N} \sum_{i=1}^{N} \frac{\left|\mathcal{I}_{c,i}[k] - \hat{\mathcal{I}}_{c,i}[k]\right|}{\mathcal{I}_{c,i}[k] + \hat{\mathcal{I}}_{c,i}[k]},$$

which is commonly used in forecasting [160].

We compare the prediction accuracy of NIPA with two other methods:

Logistic function As we argued in Chapter 6, the logistic function is central to epidemic models. Independently for every region i, we fit the logistic function

$$y_i(t) = \frac{y_{\infty,i}}{1 + e^{-K_i(t - t_{0,i})}}$$

to the number of infections $\mathcal{I}_{c,i}[1]$,..., $\mathcal{I}_{c,i}[n]$ as described in Section 6.4.

Long Short-Term Memory (LSTM) networks Recurrent neural networks [161] (RNNs) are a powerful machine learning tool, for a broad spectrum of tasks. For instance, RNNs have been successfully applied to sequences [162], time series analysis and forecasting, speech recognition and natural language processing [163]. However, traditional RNNs do not work well[1] for data with long-term dependencies. For instance, for the prediction of time series, where the input at time k_0 influences the output at time $k \gg k_0$. Long Short-Term Memory (LSTM) networks [164] are specific types of RNNs that can deal with long-term dependencies. LSTM networks rely on introducing additional input, output and forget gates to the traditional RNN framework. The additional LSTM gates capture long-term dependencies in the data. For more details on and variations of LSTM networks, we refer to [165, 166, 166–168]. Here, we utilise one of the most common variations: an LSTM network with a forget gate. More specifically, we use an LSTM network with sequence and hidden sizes both equal to four in a single LSTM layer, a learning rate of 0.1 and Adam optimiser [169], with mean square error loss in 2000 epochs of training.

[1] More specifically, training RNNs for data with long-term dependencies can lead to vanishing or exploding gradients during the neural networks backpropagation.

8.3.1. HUBEI, CHINA

Figure 8.1: **Map of the cities in Hubei.** The 17 cities (prefecture-level divisions) of the Chinese province Hubei. The darker the city, the more infections per capita on February 14. We do not consider the city Shennongjia in this work.

We evaluate the prediction accuracy for the Chinese province Hubei. Hubei is divided into 17 cities (more precisely, prefecture-level divisions), as illustrated by Figure 8.1. We do not consider the city Shennongjia, since the number of infections in Shennongjia is small. Thus, we consider $N = 16$ cities. In December 2019, the first cases of COVID-19 were detected in Wuhan, the capital of Hubei. The first case outside Wuhan was reported on January 21. From January 24 onwards, the whole province Hubei was under lockdown, prohibiting any non-urgent travels. On February 15, the local government in Hubei changed the diagnosing policy[2], causing an erratic increase in the number of reported cases on February 15. Therefore, we restrict ourselves to the period from January 21 (day $k = 1$) to February 14, 2020. The number of newly reported infections for each city in Hubei is openly accessible via the website of the Hubei Province Health Committee[3] and stated in detail in Appendix G.2. There is a single outlier in city $i = 1$ (Wuhan) at time $k = 8$ (January 28, 2020), which we replace by $\mathcal{I}_{\text{rep},1}[8] = (\mathcal{I}_{\text{rep},1}[7] + \mathcal{I}_{\text{rep},1}[9])/2$.

To evaluate the prediction accuracy, we remove the data for a fixed number of days, say m, prior to February 14. The input to the prediction methods are the observations from 21 January up to $14 - m$ February, 2020. Then, we predict the course of the disease up to February 14. The course of the disease and the predictions are illustrated in

[2] See, for instance, www.nature.com/articles/d41586-020-00154-w.
[3] Under the link http://www.hubei.gov.cn/.

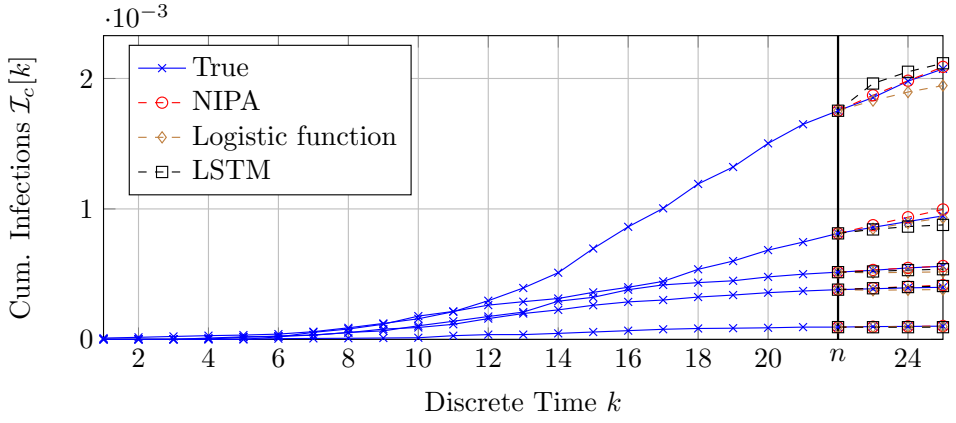

(a) Omitted days: $m = 3$.

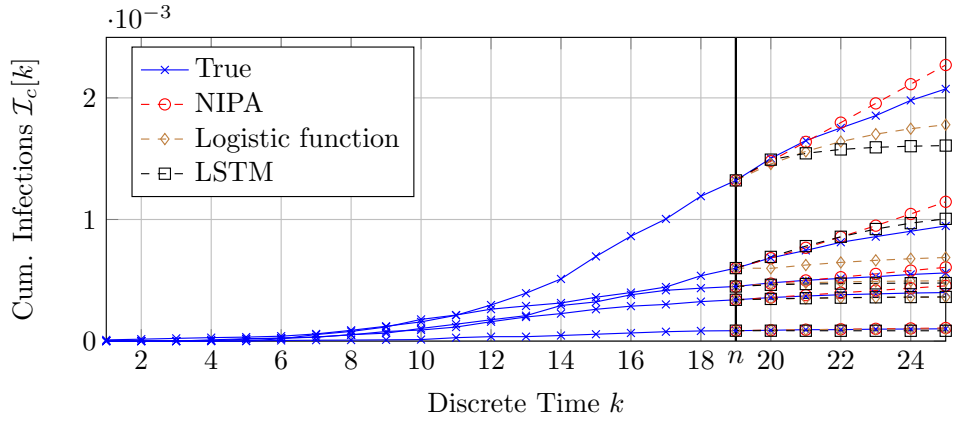

(b) Omitted days: $m = 6$.

Figure 8.2: **Prediction of the COVID-19 outbreak in Hubei.** The prediction of the COVID-19 outbreak in Hubei by NIPA, the logistic function and LSTM. For clarity, only five of the $N = 16$ cities are depicted. Each subfigure is obtained by omitting a number m of days prior to February 14, 2020, and subsequently predicting the same number of days ahead in time. The omitted number of data points is equal to: (a) $m = 3$ days and (b) $m = 6$ days. The first prediction data point, for instance February 13 in subfigure (a), coincides with the last day that has been observed.

Figure 8.2 for the removal of $m = 3$ and $m = 6$ days.

Figure 8.3 compares the accuracy of the predictions based on NIPA, LSTM and the logistic function. As time evolves and a growing amount of data is available, the sMAPE error in Figure 8.3 tends to decrease. The prediction accuracy decreases rapidly if the forecast horizon is increased. Especially, none of the considered algorithms accurately predicts the number of cases for five and six days ahead in time, as illustrated by Figures 8.3e and 8.3f, respectively. The prediction based on the logistic function are worse than the predictions of NIPA and LSTM. In agreement with [170], the predictions by

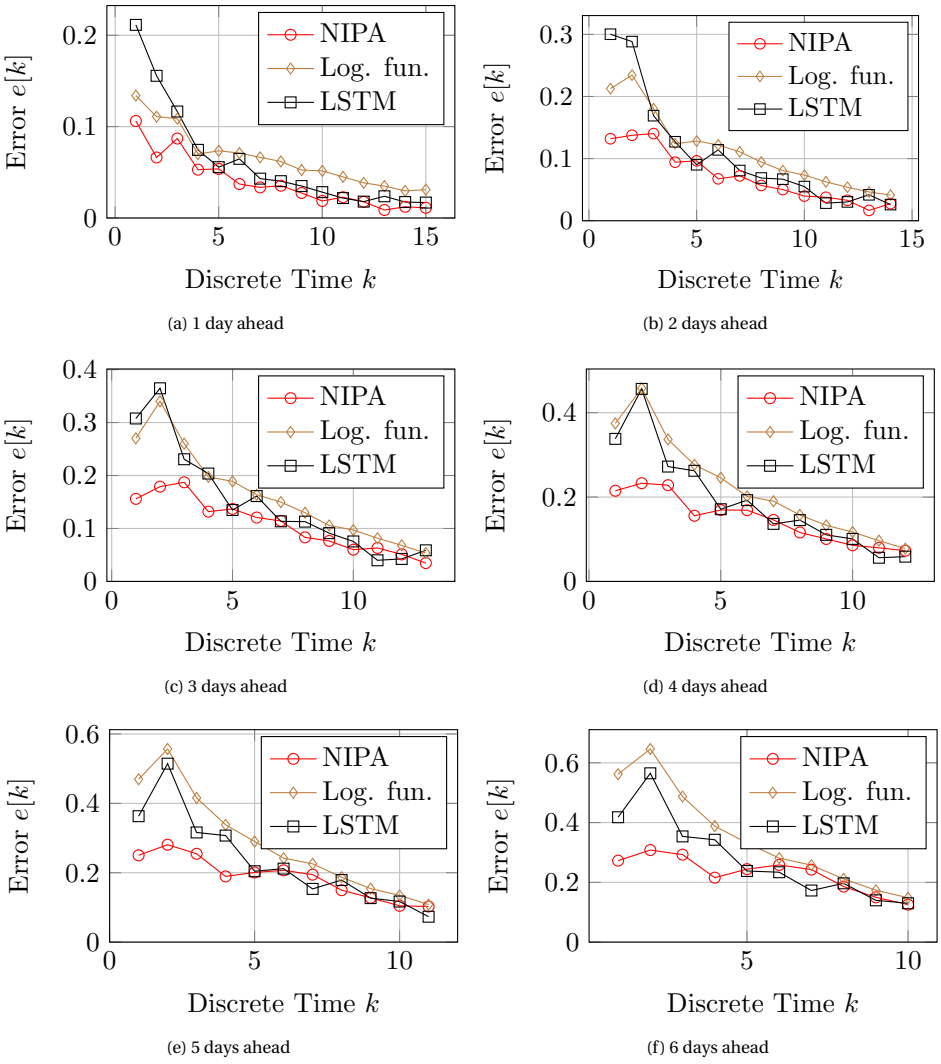

(a) 1 day ahead

(b) 2 days ahead

(c) 3 days ahead

(d) 4 days ahead

(e) 5 days ahead

(f) 6 days ahead

Figure 8.3: **Accuracy of predicting COVID-19 in Hubei versus time.** The subplots show the prediction accuracy for a forecast horizon from $m = 1$ day to $m = 6$ days. The initial time $k = 1$ corresponds to January 30, 2020.

LSTM are particularly inaccurate if the time series used for training is short. Table 8.1 states the average prediction errors of the different prediction methods.

8.3.2. THE NETHERLANDS

As a second case study, we consider the spread of COVID-19 in the Netherlands. On February 27 (day $k = 1$), the first individual in the Netherlands was diagnosed with COVID-

Algorithm	Prediction error
NIPA	0.122
Logistic function	0.186
LSTM	0.160

Table 8.1: **Average accuracy of predicting COVID-19 in Hubei.** The sMAPE prediction error $e[k]$ of NIPA, LSTM and logistic curve fitting, averaged over all nodes i and forecast horizons from $m = 1$ to $m = 6$ days.

Figure 8.4: **Map of the provinces in the Netherlands.** The 12 provinces of the Netherlands. The darker the province, the more infections per capita on May 19.

19. We consider the spread of COVID-19 among the $N = 12$ provinces in the Netherlands, which are shown in Figure 8.4. The number of SARS-CoV-2 infections is available from the Dutch National Institute for Public Health and the Environment[4] (*Rijksinstituut voor Volksgezondheid en Milieu* in Dutch).

Figure 8.5 shows the prediction accuracy for the Netherlands. Similarly to Subsection 8.3.1, NIPA outperforms the other prediction methods in most cases, particularly before April 1. Table 8.2 states the average prediction errors of the different prediction methods.

[4] Under the link https://www.rivm.nl/coronavirus-covid-19/actueel.

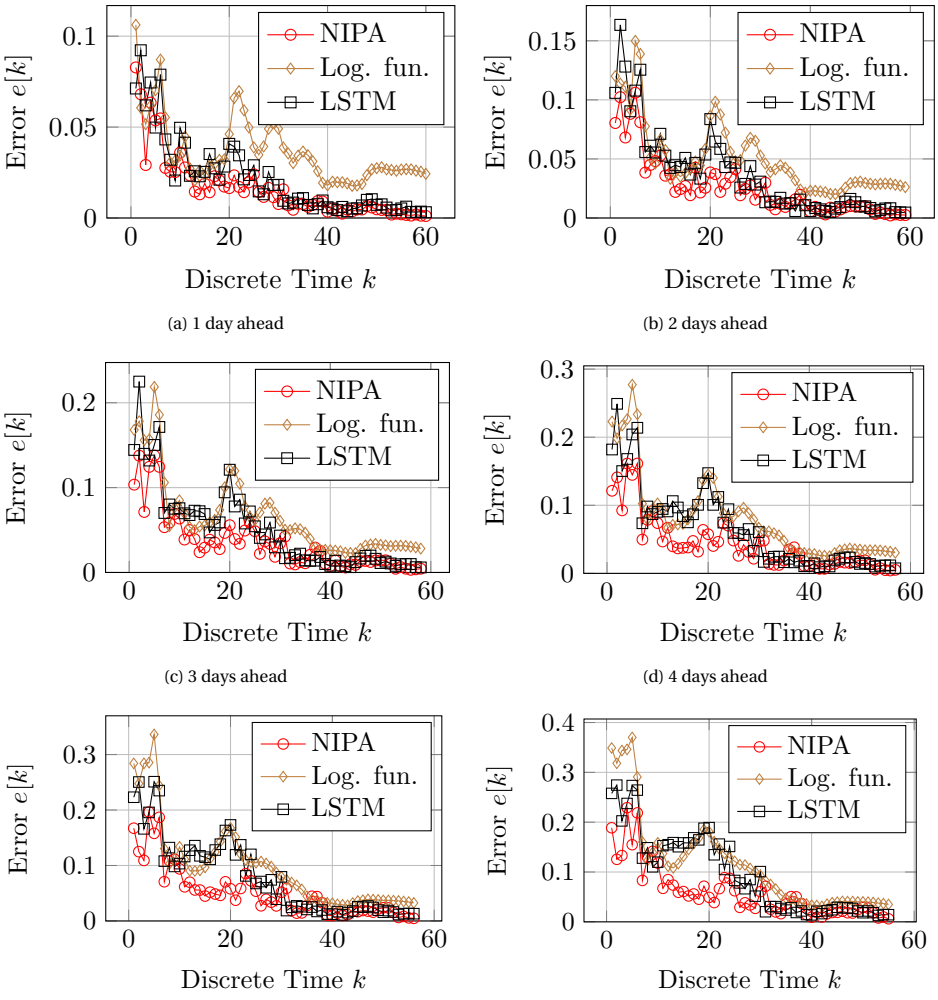

(a) 1 day ahead

(b) 2 days ahead

(c) 3 days ahead

(d) 4 days ahead

(e) 5 days ahead

(f) 6 days ahead

Figure 8.5: **Accuracy of predicting COVID-19 in the Netherlands versus time.** The subplots show the prediction accuracy for a forecast horizon from $m = 1$ day to $m = 6$ days. The initial time $k = 1$ corresponds to March 20, 2020.

8.4. CONCLUSIONS

We applied a network-based SIR epidemic model to predict the outbreak of the COVID-19 virus. The SIR epidemic model allows to explicitly specify the interactions of individuals of different geographical regions. However, the precise interactions between regions is unknown and must be inferred from observing the evolution of the outbreak.

We proposed the NIPA prediction method, which estimates the interactions between regions as an intermediate step. We applied NIPA to predict the number of SARS-CoV-2 infections for two scenarios: in the Chinese province Hubei and in the Netherlands. Our

Algorithm	Prediction error
NIPA	0.0381
Logistic function	0.0735
LSTM	0.0570

Table 8.2: **Average accuracy of predicting COVID-19 in the Netherlands.** The sMAPE prediction error $e[k]$ of NIPA, LSTM and logistic curve fitting, averaged over all nodes i and forecast horizons from $m = 1$ to $m = 6$ days.

results indicate that a network-based modelling and prediction approach is beneficial for accurate predictions of the COVID-19 outbreak.

Building upon the results in this chapter, we believe there are plenty of promising open research questions. In particular: the incorporation of a priori knowledge of the traffic flow to obtain more accurate predictions; generalising the NIPA prediction method from point forecasts to prediction intervals; account for *time-varying* lockdown measures; and adapting NIPA to epidemic models more general than the SIR model.

ACKNOWLEDGEMENTS

We are grateful to Fenghua Wang for helping with the collection of the data on the spread of COVID-19.

III

Spreading in Brain Networks: Relating Function and Structure

9

On the Series Expansion and the Eigenmode Approach

Functional brain networks are shaped and constrained by the underlying structural network. However, functional networks are not merely a one-to-one reflection of the structural network. Several theories have been put forward to understand the relationship between structural and functional networks, but it remains unclear how these theories can be unified. Here, we focus on two prominent methods for relating function and structure in the brain: the eigenmode approach *and the* series expansion approach. *Our contribution is fourfold. First, we show that the eigenmode approach can be written in terms of the series expansion approach. Second, for both the eigenmode and series expansion approach, we provide explicit expressions for the coefficients that result in the best fit. Third, we demonstrate that, regarding the goodness of fit to empirical functional data, the eigenmode approach always outperforms the series expansion approach. Fourth, we show that fitting the series expansion approach to empirical data is severely ill-conditioned. Thus, we argue that the eigenmode approach should be preferred over the series expansion approach. Our results provide an important step towards unification of existing theories for relating structure and function in brain networks.*

This chapter is based on P. Tewarie*, B. Prasse*, J. M. Meier, F. A. N. Santos, L. Douw, M. Schoonheim, C. J. Stam, P. Van Mieghem, and A. Hillebrand, *Mapping functional brain networks from the structural connectome: relating the series expansion and eigenmode approaches*, NeuroImage, **216**, 116805 (2020). (*P. Tewarie and B. Prasse contributed equally.)

9.1. INTRODUCTION

For many years, structural and functional brain networks have been studied independently [171, 172], revealing partly overlapping and partly divergent connectivity patterns. The last two decades have brought a wealth of studies that specifically aimed to elucidate the relationship between the functional and structural brain networks [173–177]. Structural networks are believed to shape and provide constraints for the dynamics of functional connectivity, which can be measured at different time-scales [178]. It has been widely acknowledged that, to some extent, functional networks can be predicted from the underlying structural connectome [179–181]. However, local neuronal dynamics can impact the emergence of functional connectivity, especially on shorter time scales [182, 183], rendering a direct mapping between structural and functional networks limited to the domain where functional connectivity is estimated at greater time scales.

A crucial observation is that functional networks are not merely a one-to-one mappings of the underlying structural network [176], which motivates the search for more sophisticated mappings of function and structure. Particular properties of the structural network were identified to shape the functional networks, including: the Euclidean distance between brain regions [184]; the outer product of the structural degree sequence [185, 186]; detours along the shortest paths in the structural network [187]; and diffusion properties of the structural network [188, 189]. Furthermore, approaches that rely on coupled neural mass models were successfully applied for explaining the emergence of resting-state functional networks from the underlying structural network. The prevalent view is that resting-state functional networks appear if the underlying system operates in a metastable regime [190–192] or in a multistable[1] regime [193–195].

Several studies aimed to formalise the mapping between structural and functional networks [196–200]. Since the seminal work by Robinson [200], several groups have independently demonstrated that functional connectivity can be represented in terms of the sum of all possible walks on the underlying structural network [199–205], which can also be understood in terms of flow equations or propagator theory on the network [200, 206]. The elegance of this approach is that it also incorporates other concepts, such as, for example, the importance of shortest paths and detours from these paths [187], as well as indirect paths of length two [207], for the formation of functional networks. One of the ways to describe this "mapping" approach between structure and function is to express the relationship as a series expansion [199].

Recent years have also seen a wealth of explorations by several independent groups of the eigenmode[2] approach, in which eigenvectors of the structural network are believed to form a basis-set to explain functional networks [208–213]. Several of these structural eigenmodes have been related to known functional subnetworks [212], and combinations of eigenmodes were able to explain the occurrence of frequency-specific functional networks [210]. This approach has also found its way to applications in neuroscience and was able to detect alterations in brain states during sleep [214]. Most of these studies extract the eigenmodes from the Laplacian[3] of the structural connectome

[1] Multistability refers to the co-existence of multiple attractors.
[2] An eigenmode refers to the eigenvalue and the corresponding eigenvector of a matrix.
[3] The Laplacian is defined as the diagonal matrix with the degrees on the diagonal minus the adjacency matrix.

[209, 212], or even from the Laplacian of structural connectivity along the cortical surface [213, 215], although eigenmodes of the weighted adjacency matrix itself have also been used [210]. We refer the reader to [216] for a theoretical underpinning of the eigenmode approach for the Laplacian.

Instead of exploring an abundance of unrelated or complementary theories simultaneously, we strive for unification of theories regarding the relationship between structural and functional brain networks. Given the robustness and generalizability of the series expansion and eigenmode approaches (which have been applied to different datasets by independent groups), we aim to understand the theoretical link between the eigenmode and series expansion approaches. Recently, Robinson [217] put forward the theoretical framework to prove the equivalence between the series expansion and eigenmode approach. More specifically, Robinson [217] demonstrated that the series approach can be formulated in terms of the spectral approach, and demonstrated the same mapping between structural and functional brain networks for the topological and spectral domain. Here, we take this notion further by relating the coefficients of the eigenmode and series expansion approach. Then, we analyse the strength of this relationship in empirical data from Diffusion Tensor Imaging (DTI) and resting-state functional Magnetic Resonance Imaging (fMRI). We analyse both approaches by comparing their goodness of fit analytically and numerically for empirical data.

9.2. THEORETICAL LINK BETWEEN THE SERIES EXPANSION APPROACH AND THE EIGENMODE APPROACH

We denote the structural connectivity matrix by $A \in \mathbb{R}^{N\times N}$ and the functional connectivity matrix by $W \in \mathbb{R}^{N\times N}$. Here, N denotes the number of nodes (brain regions) in both networks. Both matrices are symmetric with zeros along the diagonal. Here, we consider the eigenvector matrix X of A, where each column corresponds to one of the eigenvectors of A. In Section 9.7, we consider the eigenvectors of the Laplacian of the structural network [32]. The eigenmode approach assumes

$$W \approx XSX^T, \tag{9.1}$$

where S is a diagonal matrix. The elements s_i on the diagonal of S, $i = 1,...,N$, correspond to the weighting coefficients that can be estimated from empirical data [210] or can be derived analytically, see Section 9.3. Thus, the eigenmode approach assumes that the functional network W can be approximated by a weighted linear combination of the eigenvectors of the structural network A. Previous work has demonstrated that beyond a linear combination, a non-linear combination of the eigenvectors can significantly improve the prediction of functional networks [210]. However, a linear combination is explanatory for a large part of the explained variance of frequency-specific functional networks [210].

In the series approach, the functional connectivity matrix is expressed as a Taylor series expansion of the structural matrix, with unknown coefficients c_m, $m = 1,...,d$, and

can be reduced to [199, equation (4)]

$$W \approx \sum_{m=1}^{d} \frac{c_m}{\|A^m\|_2} A^m. \tag{9.2}$$

Here, d is the diameter (length of the longest shortest path) of the structural network. The coefficients c_m are divided by the 2-norm $\|\cdot\|_2$, since powers of A diverge quickly for increase in m. The series is truncated at $m = d$, since previous work [199] demonstrated that the fit with empirical fMRI or magnetoencephalography (MEG) data converges for $m = d$. However, the precise underlying phenomenon why the diameter seems a sufficient bound is a graph-theoretical, open question. An alternative normalisation to $\|A^m\|_2$ is $m!$, see [201], which would transform (9.2) into an expression of communicability if d is changed to infinity [218]. The powers A^m for unweighted matrices A correspond to configurations of walks in the structural network with length m. The Taylor series coefficients c_m can be estimated from the empirical data or analytically derived, see Section 9.3. Since the matrix A is symmetric, we can diagonalise A to obtain its real eigenvalues λ_i and eigenvectors x_i, where $i = 1, ..., N$. The eigenvectors are orthogonal, which implies that $A^m = XD^mX^T$. Thus, we can rewrite equation (9.2) as

$$W \approx \sum_{m=1}^{d} \frac{c_m}{\|A^m\|_2} XD^mX^T, \tag{9.3}$$

where $D = \mathrm{diag}(\lambda_1, ..., \lambda_N)$. Thus, the series approach states that for every addend in equation (9.3), there is a different weighting of the eigenvectors, which is determined by the powers of the eigenvalues λ_i and the Taylor coefficients c_m. Hence, the series approach and the eigenmode approach are equivalent (or strongly related) if the weighting coefficients on the diagonal of S for the eigenmodes are (approximately) equal to the series coefficients:

$$S \approx \sum_{m=1}^{d} \frac{c_m}{\|A^m\|_2} D^m. \tag{9.4}$$

Despite the fact that a relationship between the two approaches can be readily demonstrated, it is an open question if the coefficients, as estimated from empirical data, are indeed similar for both approaches.

9.3. FITTING COEFFICIENTS OF THE EIGENMODE AND SERIES EXPANSION APPROACHES TO EXPERIMENTAL DATA

The fitting error of the eigenmode approach depends on the eigenmode coefficients and follows from equation (9.1) as

$$\epsilon_{\mathrm{eigen}}(S) = \left\| W - XSX^T \right\|_F, \tag{9.5}$$

where $\|\cdot\|_F$ denotes the Frobenius matrix norm. The smaller the error $\epsilon_{\mathrm{eigen}}(S)$, the better the fit of the eigenmode approach. In other words, a smaller $\epsilon_{\mathrm{eigen}}(S)$ corresponds to a higher explanatory power of the eigenmode approach. Hence, to obtain the relationship

between the structural connectivity matrix A and the functional connectivity matrix W, we aim to find the diagonal matrix S that minimises the error $\epsilon_{\text{eigen}}(S)$. Note that W refers to the empirical or simulated functional connectivity matrix. Lemma 9.1 gives an explicit expression for the diagonal matrix S.

Lemma 9.1. *The diagonal matrix S that minimises the fitting error $\epsilon_{\text{eigen}}(S)$ equals*

$$S = \text{diag}\left(x_1^T W x_1, ..., x_N^T W x_N\right). \tag{9.6}$$

Proof. Appendix H.1. □

The fitting error of the series expansion approach depends on the coefficient vector c and follows from equation (9.3) as

$$\epsilon_{\text{series}}(c) = \left\| W - \sum_{m=1}^{d} \frac{c_m}{\|A^m\|_2} X D^m X^T \right\|_F.$$

Similarly as for the eigenmode approach, the smaller $\epsilon_{\text{series}}(c)$, the better the fit and the higher the explanatory power of the series expansion approach. We aim to find the coefficient vector c that minimises the error $\epsilon_{\text{series}}(c)$. Similarly to Lemma 9.1, we can derive an expression for the coefficient vector c of the series expansion approach:

Lemma 9.2. *Determining the coefficient vector c that minimises the fitting error $\epsilon_{\text{series}}(c)$ is equivalent to solving the linear least-squares problem*

$$\min_c \left\| v - c^T M \right\|_2^2. \tag{9.7}$$

Here, the $1 \times N$ vector v equals

$$v = \left(x_1^T W x_1, \quad ..., \quad x_N^T W x_N\right),$$

and the $d \times N$ matrix M is a Vandermonde matrix, given by

$$M = \begin{pmatrix} \frac{\lambda_1}{\lambda_1} & \frac{\lambda_2}{\lambda_1} & \cdots & \frac{\lambda_N}{\lambda_1} \\ \vdots & \vdots & \ddots & \vdots \\ \frac{\lambda_1^d}{\lambda_1^d} & \frac{\lambda_2^d}{\lambda_1^d} & \cdots & \frac{\lambda_N^d}{\lambda_1^d} \end{pmatrix}.$$

Proof. Appendix H.2. □

Provided that all eigenvalues λ_1, ..., λ_N are distinct, we obtain from equation (9.7) that the coefficient vector c is given by [219]

$$c = \left(MM^T\right)^{-1} M v^T. \tag{9.8}$$

To compute the coefficient vector c in practice, there are numerically stable methods, such as the Matlab command `mldivide`, that solve the least-squares problem in equation (9.7) without computing the inverse as in equation (9.8).

We stress that Lemma 9.1 and Lemma 9.2 follow rather straightforwardly and should not be considered as novel theoretical results. Here, we present these results within the context of mappings between structural and functional networks in the field of neuroimaging. In addition to $\epsilon_{\text{eigen}}(S)$ and $\epsilon_{\text{series}}(c)$ as a measure for the goodness of fit, we also use the Pearson correlation coefficient between predicted and actual functional connectivity matrices.

9.4. ILL-CONDITION OF THE SERIES EXPANSION APPROACH

Suppose the functional connectivity matrix W contains small estimation or measurement errors. Hence, we obtain the perturbed matrix $\tilde{W} = W + \Delta W$, for some $N \times N$ error matrix ΔW. Due to the perturbed matrix $\tilde{W}$, the coefficients that minimise equation (9.7) are also perturbed as $\tilde{c} = c + \Delta c$, where we denote the $d \times 1$ coefficient error vector by $\Delta c = (\Delta c_1, ..., \Delta c_d)^T$. We are interested in the sensitivity of the series approach to errors ΔW. More precisely: *How great is the impact of small errors ΔW on the error Δc of the series coefficients?* The *condition number* of the Vandermonde matrix M in Lemma 9.2 equals [133]

$$\kappa(M) = \frac{\sigma_1}{\sigma_d},$$

where σ_1 and σ_d denote the largest and smallest singular value of the matrix M, respectively. A small error ΔW results in an error Δc on the series coefficients that scales [133] with the square of the condition number $\kappa(M)$ as[4]

$$\frac{\|\Delta c\|_2}{\|c\|_2} \approx \kappa^2(M) \frac{\|\Delta W\|_2}{\|W\|_2} + \mathcal{O}\left(\frac{\left\|\Delta W^2\right\|_2}{\left\|W^2\right\|_2}\right). \tag{9.9}$$

Hence, the square of the condition number $\kappa(M)$ determines the sensitivity of the computed series coefficients c to errors ΔW. We emphasise that this sensitivity is an inherent property of the task of computing the coefficients c_1, ..., c_d and does not depend on the specific numerical method that is employed to solve equation (9.7).

Vandermonde matrices may have very large condition numbers [220]. The squared condition numbers $\kappa^2(M)$ for the structural connectivity matrices A used in the datasets 1 to 4, which are specified in Section 9.6, is given by Table 9.1. The value of $\kappa^2(M)$ is large for all datasets, which indicates that small errors in the functional connectivity matrix W can have very large impact on the error in c. Similarly, measurement errors ΔA on the structural connectivity matrix A can have a strong impact on the error of c. Furthermore, we emphasise that the structural and functional connectivity matrices A and W are digitally stored and processed with *finite-precision* arithmetic, which can result in large errors of c when $\kappa^2(M)$ is large - even if the matrices A and W had been measured with perfect accuracy.

[4] To be more precise [133], the left-hand side of Equation (9.9) is upper-bounded by some constant multiplied by the right-hand side of equation (9.9).

	Net. size N	Diam. d	Cond. numb. $\kappa^2(M)$	R^2 series vs. eigenm.
Dataset 1	78	6	$1.6 \cdot 10^5$	0.92
Dataset 2	188	5	$5.21 \cdot 10^4$	0.79
Dataset 3	264	6	$1.68 \cdot 10^5$	0.78
Dataset 4	78	5	$5.25 \cdot 10^4$	0.95

Table 9.1: **Ill-condition of the series expansion approach.** The condition numbers of the Vandermonde matrix M in Lemma 9.2 and the diameter (longest shortest path) d of the structural network A, whose elements have been discretised to either zero or one. For details on the datasets, see Section 9.6.

9.5. COMPARING THE EIGENMODE AND SERIES EXPANSION APPROACH

Similarity between the series and eigenmode approaches would entail that the eigenmode coefficients s_1, ..., s_N would be approximately equal to the series coefficients c_m multiplied by the powers of the eigenvalues of A, see (9.4). To quantify this similarity for empirical and simulated data, we computed the intraclass correlation coefficient between the diagonal of the left-hand and the diagonal of the right-hand side of Equation (9.4), i.e., the intraclass correlation between the respective coefficients. The intraclass correlation coefficient can be considered as a more rigorous method, compared to Pearson or Spearman correlations, to quantify whether the methods capture the same underlying link between structural and functional brain networks. Additionally, we quantify the similarity in estimated functional network connectivity between the two approaches in terms of the R^2 value. More precisely, we vectorised the upper triangle of the estimated functional connectivity matrix from both approaches and applied the linear least-squared regression to quantify the link-wise dependency between approaches, see Table 9.1.

The fitting error of the eigenmode approach is always smaller than or equal to the fit of the series approach:

Lemma 9.3. *For every structural connectivity matrix A and every functional connectivity matrix W, the optimal fit of the eigenmode approach is at least as good as the optimal fit of the series approach. More precisely, it holds that*

$$\min_S \epsilon_{\text{eigen}}(S) \leq \min_c \epsilon_{\text{series}}(c). \tag{9.10}$$

Proof. Appendix H.3. □

Furthermore, (9.10) holds true almost always with strict inequality, as shown in Appendix H.3. In other words, Lemma 9.3 states that the series approach never explains the experimental data better than the eigenmode approach. Thus, the eigenmode approach is a more accurate model for relating the structural connectivity matrix A and the functional connectivity matrix W.

9.6. APPLICATION OF BOTH APPROACHES TO EMPIRICAL AND SIMULATED NETWORKS

We used multimodal data (DTI and resting-state fMRI data) from four previously published empirical datasets. The first dataset (Dataset 1) consists of a literature-based structural network for 80 healthy subjects [221], combined with a group-averaged functional network based on fMRI data from 21 healthy adults. The first data set makes use of the automated anatomical labelling atlas (AAL) [222], with $N = 78$ nodes. We retrieved the second and third datasets from the University of California Los Angeles (UCLA) multimodal connectivity database [223]. The second dataset consists of a group-averaged structural network and a group-averaged resting-state fMRI network from 381 healthy adults from the Nathan Kline Institute (NKI)/Sample [224]. For the second dataset, we used the Craddock atlas [225] with $N = 188$ nodes. The third dataset consists of a group-averaged structural and the resting state-fMRI network is obtained from 79 typically-developing children from a UCLA autism dataset [223]. For the third dataset, the Power atlas [226] was used ($N = 264$). The fourth data set consists of a group-averaged structural and resting-state fMRI network ($N = 78$) from 10 healthy subjects from the human connectome data [227], using the AAL atlas. Processing pipelines for the structural connectome can be found in [210], and the processing pipeline for the resting-state fMRI network is given in Appendix H.4. We obtained the functional connectivity matrix W for all datasets by computing the Pearson correlation coefficient between the fMRI time-courses.

Figure 9.1 shows the empirical functional connectivity matrix and the estimated functional connectivity matrices using the series expansion and eigenmode approaches for all four empirical datasets. The estimates are obtained from the analytical expressions in (9.6) and (9.8), respectively. For every dataset, Figure 9.1 shows a scatter plot of the magnitude of the eigenmode coefficients s_i versus the aggregated coefficients for the series expansion approach, i.e., the sum of the powers of the eigenvalues of the structural network weighted by $c_m/\|A^m\|_2$, see (9.4). The number of points in the scatter plots correspond to the number of nodes N in the structural network. The intraclass correlation coefficients are shown in each scatter plot. For all datasets, with different network sizes N, there are strong and significant correlations between the coefficients from the eigenmode and the series approach. In agreement with Lemma 9.3, it holds that $\epsilon_{\text{eigen}}(S) < \epsilon_{\text{series}}(c)$ for all datasets.

9.7. EXTENSION TO THE EIGENMODES OF THE LAPLACIAN

So far, we have analysed the eigenmodes of the structural connectivity matrix A in relation to the series expansion approach. In contrast, other studies focused on the eigenmodes of the graph Laplacian [209, 212]. The analysis of the graph Laplacian is attractive due to well-behaved properties, such as the boundedness of its eigenvalues [32]. The graph Laplacian is defined as $Q_A = K_A - A$, where $K_A = \text{diag}(Au)$ refers to the degree matrix. We further normalised the graph Laplacian as $Q_{As} = K_A^{-1/2} Q_A K_A^{-1/2}$ to allow for comparison with [209]. Analogously, we computed the normalised graph Laplacian Q_{Ws} of the functional connectivity matrix W. The Laplacian Q_{As} can be diagonalised as $Q_{As} = Z\,\text{diag}(\mu_1, ..., \mu_N)Z^T$. Here, the columns z_i of the matrix Z are the eigenvec-

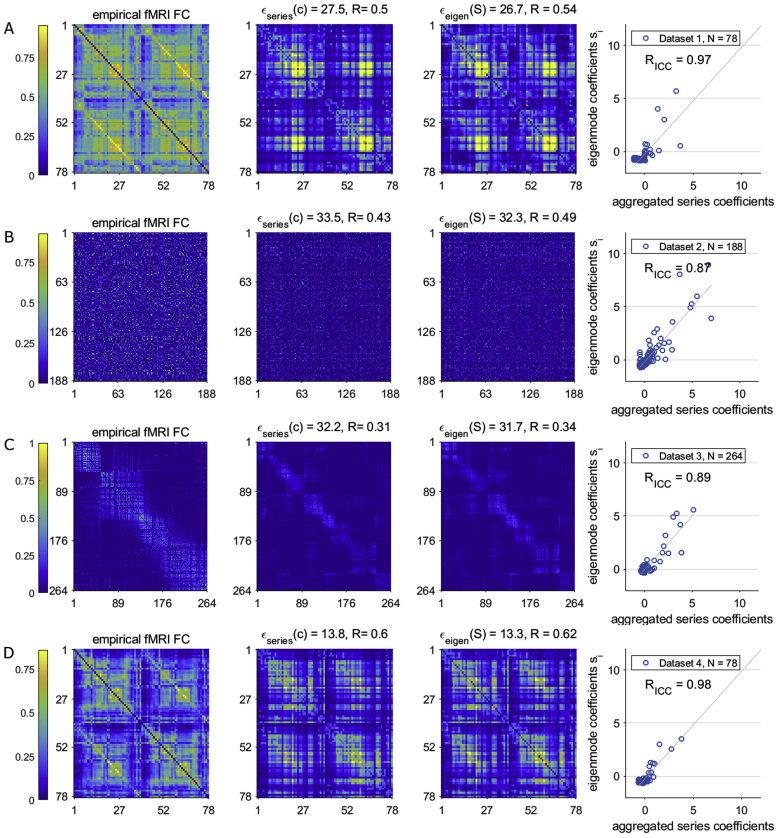

Figure 9.1: **Series expansion versus eigenmode approach (weighted adjacency matrix).** The first column depicts the empirical fMRI connectivity for all four independent datasets by the respective Panels A-D. The second and third column shows the estimated functional connectivity matrices for the series expansion and eigenmode approach, respectively, including the errors $\epsilon_{\text{eigen}}(S)$ and $\epsilon_{\text{series}}(c)$, and the Pearson correlation R between estimated and true functional connectivity matrices. The fourth column depicts the estimated coefficients s_i for the eigenmode approach and the *aggregated series coefficients*, which denote the diagonal elements of the right hand side of (9.4). A strong correlation was found for all datasets.

tors of the Laplacians Q_{As} to the eigenvalues μ_i. For the Laplacian Q_{As}, we computed the coefficients of the eigenmode approach in the same way as described in Section 9.3. Furthermore, we provide a comparison to the approach by Abdelnour *et al.* [209], which is based on an exponential relationship between eigenvalues of the structural and functional connectivity matrices.

First, we determine the fitting errors for series expansion and eigenmode approach when using the graph Laplacian. For the series expansion approach, since $A = K_A - Q_A$, we can rewrite (9.2) as

$$W \approx \sum_{m=1}^{d} \frac{c_m}{\|A^m\|_2} (K_A - Q_A)^m . \tag{9.11}$$

Since (9.2) and (9.11) are equivalent, the coefficients c_m and the fitting error $\epsilon_{\text{series}}(c)$ remain unaltered.

Similarly to (9.1), the eigenmode approach approximates the graph Laplacian Q_{Ws} of the functional connectivity matrix W by a linear combination of the eigenvectors X of the graph Laplacian of the structural network,

$$Q_{Ws} \approx ZPZ^T$$

for some diagonal matrix P. In the same way as for the eigenmode approach for the structural matrix A, we define the fitting error

$$\epsilon_Q(P) = \left\| Q_{Ws} - ZPZ^T \right\|_F. \tag{9.12}$$

By using the same reasoning as for the error $\epsilon_{\text{eigen}}(S)$ in Lemma 9.1, the diagonal matrix P that minimises the error $\epsilon_Q(P)$ equals

$$P = \text{diag}\left(z_1^T Q_{Ws} z_1, ..., z_N^T Q_{Ws} z_N\right).$$

By definition, $Q_W = K_W - W$, the estimated functional connectivity matrix W follows as

$$W \approx K_W - K_W^{\frac{1}{2}} ZPZ^T K_W^{\frac{1}{2}}, \tag{9.13}$$

where $K_W = \text{diag}(Wu)$. If there is a link between the series expansion and Laplacian eigenmode approaches, we can equate (9.11) and (9.13), which yields that

$$P \approx I - \sum_{m=1}^{d} \frac{c_m}{\|A^m\|_2} Z^T K_W^{-\frac{1}{2}} (K_A - Q_A)^m K_W^{-\frac{1}{2}} Z. \tag{9.14}$$

Unlike equation (9.4), the eigenvector matrix Z cannot be eliminated on the right-hand side of equation (9.14).

Additionally to (9.13), previous work has expressed the functional connectivity matrix W in terms of an exponential relationship between the eigenvalues of the structural graph Laplacian and the functional connectivity matrix [209],

$$W \approx \sum_{i=1}^{N} z_i z_i^T \left(ae^{-\alpha\mu_i} + b\right), \tag{9.15}$$

where the coefficients a, α and b are found using a non-linear minimisation method [209]. The fitting error for this methods equals

$$\epsilon_{\exp}(a, \alpha, b) = \left\| W - \sum_{i=1}^{N} z_i z_i^T \left(ae^{-\alpha\mu_i} + b\right) \right\|_F.$$

Figure 9.2 shows the actual and estimated functional connectivity matrices using the Laplacian eigenmode approaches for all four empirical datasets. The second column shows the estimated functional connectivity matrices based on (9.15), while the third column shows the estimated functional connectivity matrices based on (9.13). The Laplacian approaches are able to predict the true functional connectivity matrices. Correlations with the actual functional connectivity based on predictions from (9.13) seem to be the strongest. The diagonal elements of the right and left-hand side of equation (9.14) are depicted in the scatter plots in Figure 9.2. These scatter plots show strong correlations between the series expansion and graph Laplacian eigenmode approach.

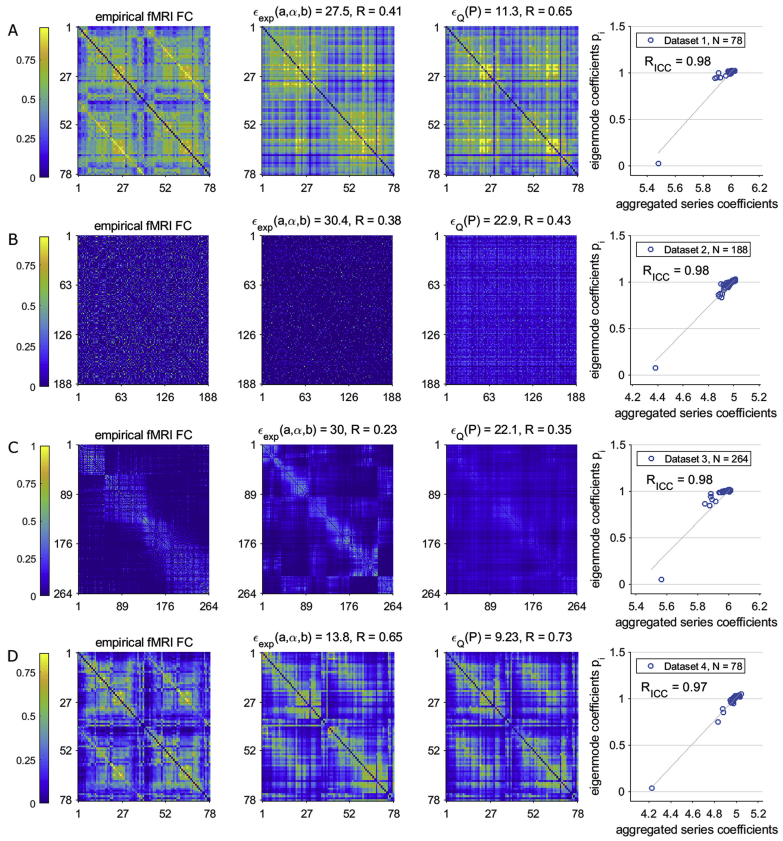

Figure 9.2: **Series expansion versus eigenmode approach (graph Laplacian).** Empirical fMRI connectivity for all four independent datasets are illustrated (A-D). The estimated functional connectivity matrices for the graph Laplacian approaches, i.e., based on an exponential mapping between eigenvalues (9.15) and based on minimising the fitting error (9.12), alongside the errors $\epsilon_{\exp}(a,\alpha,b)$ and $\epsilon_Q(P)$ and the Pearson correlation R between predicted and actual connectivity matrices. The scatter plot on the right shows the estimated coefficients p_i for the eigenmodes and the diagonal elements of the right hand side of (9.14), here called aggregated series coefficients. A strong and significant correlation was found for all datasets.

9.8. CONCLUSIONS

Recent years have seen a rise in studies that rely on understanding functional brain networks, in parts, in terms of the eigenmodes of the structural network [209–213]. Another existing theory is that functional networks emerge from the weighted sum of all possible walks in the structural network [200]. Here, we showed that the weighted sum of all possible walks corresponds to different weightings of the eigenmodes of the structural network. Hence, both approaches, the series expansion approach and the eigenmode approach, are strongly related. Our results apply to eigenmodes of the weighted adjacency matrix as well as eigenmodes based on the Laplacian. Furthermore, we derived expressions for the weighting coefficients for both the eigenmode approach and the series expansion approach. The theoretical correspondence between the two approaches

was verified by four independent empirical datasets. Both approaches identified very similar mappings between structural and functional networks, encouraging future research for unifying theories of structural-functional network relationships. However, we showed analytically that the fit of the eigenmode approach is always better than the fit of the series expansion approach. Furthermore, due to an ill-conditioned linear system, measurement and processing errors lead to large errors for the series approach. In summary, our findings advocate the use of the eigenmode approach instead of the series expansion approach.

10

CONNECTIVITY RECONSTRUCTION FOR MULTILAYER BRAIN NETWORKS

Large-scale neurophysiological networks are often reconstructed from band-pass filtered time series derived from magnetoencephalography (MEG) data. Common practice is to reconstruct, and analyse, these networks separately for different frequency bands. Recent evidence suggests that this separation may be inadequate, as there can be significant inter-layer coupling between frequency bands. However, the precise inter-layer interaction between frequency bands remains an open question. In this chapter, we propose a network reconstruction method, based on phase oscillator models, to estimate inter-layer connectivity from empirical data. We apply our method to empirical resting-state MEG data from healthy subjects and reconstruct the inter-layer coupling between the alpha and beta band, and the theta and gamma band. For both alpha-beta coupling and theta-gamma coupling, our results indicate that one-to-one interactions (multiplex structure) are dominant. Furthermore, for theta-gamma coupling, there are plenty inter-layer connections between distant brain regions, though weaker than the one-to-one connections. Our results form a stepping stone towards the identification of interdependencies across frequency-specific functional brain networks.

This chapter is based on P. Tewarie, B. Prasse, J. M. Meier, Á. Byrne, M. De Domenico, C. J. Stam, M. J. Brookes, A. Hillebrand, A. Daffertshofer, S. Coombes, and P. Van Mieghem, *Interlayer connectivity reconstruction for multilayer brain networks using phase oscillator models*, in preparation.

10.1. INTRODUCTION

Human brain functioning is widely believed to emerge from neuronal network activity operating at distinct spatio-temporal scales. At the macroscopic level, these functional brain networks may be derived from functional MRI (fMRI), electroencephalography (EEG) and magnetoencephalography (MEG) [171]. The topology of these networks can be characterised by *network science* metrics [228], which has been successful for obtaining new insights into temporal fluctuations of brain activity in different states (e.g., during cognitive tasks) and revealed common patterns in several neurological disorders [229, 230]. The application of network science to EEG and MEG data requires the reconstruction of several, frequency-specific functional networks. These distinct networks are usually analysed separately, even though oscillations in different frequency bands may have mutual neuronal sources and there may be functional interactions [231–234]. Thus, it is more appropriate to study the frequency-specific functional networks jointly [235, 236].

Several studies demonstrated the advantages of multilayer networks [237–239] in the context of neuroscience [235, 236, 240–249]. Here, functional networks have been considered as interconnected networks, where every frequency-specific network corresponds to one network layer. However, there is no consensus on the treatment of the connectivity between different network layers. This lack of consensus is unfortunate since the choice for inter-layer connectivity topology may have a significant impact on the properties of a multilayer network [216, 250]. In the case of encephalography, inter-layer connectivity can be regarded as a proxy for cross-frequency coupling [232, 233, 251–259]. Estimation of cross-frequency coupling with existing metrics remains difficult in practice [254, 260]. Recent studies support the existence of cross-frequency coupling in resting-state data [252, 256, 261]. In this chapter, we apply a novel data-driven approach for estimating cross-frequency coupling in a multilayer network setting. In particular, we consider both intra-layer and inter-layer functional connectivity within a single framework.

Our approach is based on applying a network reconstruction method to the inter-layer connectivity structure for empirical multilayer MEG networks. Thus, we do not require prior information about inter-layer connectivity. Since every network layer corresponds to one frequency band, inter-layer connectivity corresponds to cross-frequency phase synchronisation, similarly to [262]. Our approach is based on a multilayer phase oscillator model to describe MEG data.

10

10.2. INTER-LAYER NETWORK RECONSTRUCTION

We consider a network with $M = 2$ layers, both of which have N nodes and model respective frequency bands in MEG networks (for instance, the alpha and beta frequency band). The coupling between nodes *within* one layer is described by the $N \times N$ anatomical connectivity matrix A with elements a_{ij}, where $i, j = 1, ..., N$. Analogously, the symmetric $N \times N$ connectivity matrix B with elements b_{ij} describes the *inter-layer* (cross-frequency) coupling of nodes.

The evolution of the phase $\theta_i^L(t) \in [0, 2\pi)$ in layer $L \in \{1, 2\}$ of every node i is described

by a multilayer phase oscillator model as

$$\frac{d\theta_i^L(t)}{dt} = \omega_i^L + \frac{c}{N}\sum_{j=1}^{N} a_{ij} H\left(\theta_j^L(t) - \theta_i^L(t)\right) + \sum_{j=1}^{N} b_{ij} H\left(f_1\theta_j^{L'}(t) - f_2\theta_i^L(t)\right). \tag{10.1}$$

Here, H denotes to the phase-interaction function between nodes, $L' = 1$ if $L = 2$ and $L' = 2$ if $L = 1$, the integers f_1 and f_2 represent the frequency ratio between different layers, and c denotes the global coupling strength. Thus, we assume that H is the same for the coupling within and the coupling between layers. We refer the reader to [262] for an extensive overview of candidates for the phase interaction function H. The two layers $L = 1, 2$ differ in their mean and standard deviation of the respective distributions of natural frequencies ω_i^L, which we both consider to be Gaussian. For a small sampling time Δt, we approximate the derivative in (10.1) by a finite difference, which yields that

$$\begin{aligned}\Delta t \sum_{j=1}^{N} b_{ij} H\left(f_1\theta_j^{L'}[k] - f_2\theta_i^L[k]\right) =& \theta_i^L[k+1] - \theta_i^L[k] - \Delta t\omega_i^L \\ &- \frac{c\Delta t}{N}\sum_{j=1}^{N} a_{ij} H\left(\theta_j^L[k] - \theta_i^L[k]\right),\end{aligned} \tag{10.2}$$

where k denotes the discrete time step and we denote $\theta_i^L[k] = \theta_i^L(k\Delta t)$. At every time k, we define the $1 \times N$ vector

$$\Upsilon_i^L[k] = \Delta t\left(H\left(f_1\theta_1^{L'}[k] - f_2\theta_i^L[k]\right), \quad ..., \quad H\left(f_1\theta_N^{L'}[k] - f_2\theta_i^L[k]\right)\right), \tag{10.3}$$

and we denote the right side of (10.2) as

$$\alpha_i^L[k] = \theta_i^L[k+1] - \theta_i^L[k] - \Delta t\omega_i^L - \frac{c\Delta t}{N}\sum_{j=1}^{N} a_{ij} H\left(\theta_j^L[k] - \theta_i^L[k]\right).$$

We denote the number of observations by n and stack (10.3) for different times k to obtain the $n \times N$ matrix

$$\Upsilon_i = \begin{pmatrix} \Upsilon_i^1[1] \\ \vdots \\ \Upsilon_i^1[n] \end{pmatrix}.$$

Furthermore, we define the $n \times 1$ vector $\alpha_i = \left(\alpha_i^1[1], ..., \alpha_i^1[n]\right)^T$. Then, the i-th column B_i of the inter-layer connectivity matrix B satisfies

$$\Upsilon_i B_i = \alpha_i. \tag{10.4}$$

Thus, the inter-layer connectivity matrix B could be estimated based on solving the set of linear equations (10.4). However, to reduce the impact of model and measurement errors, we do not solve (10.4) directly. Instead, we employ a similar network reconstruction

approach as in Chapter 7. For every node i, we estimate the column B_i of the inter-layer connectivity matrix by the LASSO [141, 148]

$$\begin{aligned} \min_{B_i} \quad & \|\Upsilon_i B_i - \alpha_i\|_2^2 + \rho_i \|B_i\|_1 \\ \text{s.t.} \quad & 0 \le B_i \le u. \end{aligned} \tag{10.5}$$

We emphasise that (10.5) includes the estimation of the diagonal entries of the inter-layer connectivity matrix B. Hence, we explicitly take potential one-to-one inter-layer coupling into account. Algorithm 10.1 describes the network reconstruction method in pseudocode. For more details, we refer to Chapter 7.

Algorithm 10.1 Network Reconstruction for the multilayer phase oscillator model

Input: phases $\theta_i^L[1],...,\theta_i^L[n]$ for all nodes i and layer $L = 1,2$; link threshold ϵ
Output: inter-layer matrix estimate $\hat{B}$
for $i = 1,...,N$ **do**
  $\rho_{\max,i} \leftarrow \|2\Upsilon_i^T \alpha_i\|_\infty$
  $\rho_{\min,i} \leftarrow 10^{-6}\rho_{\max,i}$
  $S_i \leftarrow$ 100 logarithmically equidistant values from $\rho_{\min,i}$ to $\rho_{\max,i}$
  for $\rho_i \in S_i$ **do**
    estimate MSE$(\hat{B}_i(\rho_i))$ by 10-fold cross validation on Υ_i, α_i
  end for
  $\rho_{\text{opt}} \leftarrow$ minimiser of the estimates of MSE$(\hat{B}_i(\rho_i))$
  $\hat{B}_i \leftarrow$ the solution $\hat{B}_i(\rho_{\text{opt}})$ to (10.5) on the whole data set Υ_i, α_i
end for
$\hat{B} \leftarrow (\hat{B}_1,...,\hat{B}_N)$
$\hat{B} \leftarrow (\hat{B} + \hat{B}^T)/2$
$\hat{b}_{ij} \leftarrow 0$ for all (i,j) with $\hat{b}_{ij} < \epsilon$

10.3. EVALUATION ON SYNTHETIC DATA

In the following, we consider a multilayer Kuramoto model [263–266] for the phase interactions (10.1), for which the function H becomes

$$H(\theta) = \sin(\theta). \tag{10.6}$$

However, we emphasise that our approach can be adapted to general phase-interaction functions H.

Figure 10.1 provides an overview of our analysis. We evaluated the inter-layer network reconstruction by providing input from simulations with ground truth for inter-layer connectivity. We generated phase time series using the network dynamics (10.1) with the phase interaction function given by (10.6). For all nodes i at every time k, we added uncorrelated white Gaussian errors $w_i^L[k]$. Thus, we generated the phases $\theta_i^L[k]$ as

$$\theta_i^L[k+1] = \theta_i^L[k] + \Delta t f_{\text{phase}}(\theta^L[k], \theta^{L'}[k]) + w_i^L[k]. \tag{10.7}$$

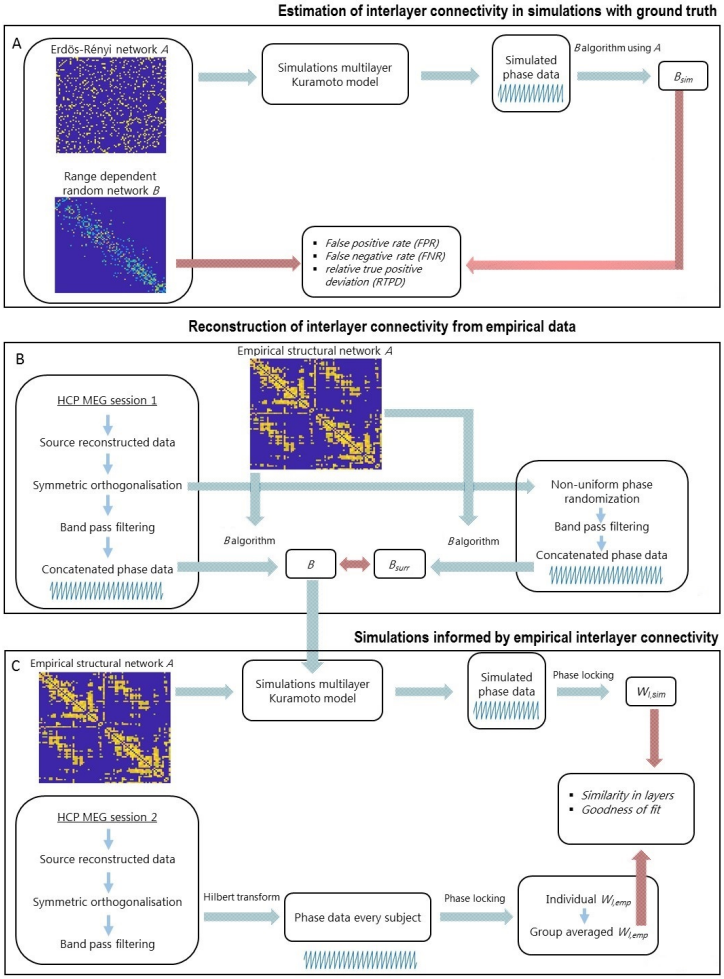

Figure 10.1: **Overview of the data analysis steps.** Panel A illustrates the extraction of inter-layer connectivity matrix B in simulations of the multilayer phase oscillation model (10.7) with known ground truth for the matrix B. The step "B Algorithm using A"refers to the network reconstruction method, which relies on the known structural connectivity matrix A. In Panel A, the subscript "sim" emphasises that the matrix B_{sim} is generated by a random graph model. Panel B depicts the network reconstruction of the inter-layer connectivity matrix B from empirical MEG phase data, where B_{surr} is a surrogate inter-layer connectivity matrix. Panel C illustrates the simulations, which are based on the reconstructed empirical inter-layer connectivity matrix B and compare the simulated intra-layer functional connectivity matrix W_{sim} to the empirical functional connectivity matrix W_{emp}. Red arrows correspond to final analysis steps in each panel.

where $f_{\text{phase}}(\theta^L[k],\theta^{L'}[k])$ denotes the right side of (10.1), and we set the sampling time to $\Delta t = 0.01$. We generated the natural frequencies ω_i^L for all nodes i and layers L by a Gaussian distribution, with mean $\omega_0^1 = 1$ and $\omega_0^2 = 2$ for the respective layers.

First, we evaluate the network reconstruction accuracy versus the link sparsity. We

generate an unweighted and connected structural connectivity matrix A by the Erdős-Rényi random graph model [74] with link probability $p_{\mathrm{ER}} = 0.2$ and $N = 78$ nodes. We only considered realisations of the structural connectivity matrix A that were irreducible. We generated the matrix B by a range-dependent random graph model [267] using the Contest toolbox for Matlab [268]. The probability of an inter-layer link between two nodes i and j, i.e., $b_{ij} = 1$, is given by $\alpha 0.9^{|i-j|-1}$. The parameter α was varied over the interval $[0.5, 1.75]$, resulting in networks with different link densities. Furthermore, we only considered symmetric inter-layer coupling matrix, by setting $B \leftarrow (B + B^T)/2$. Second, we evaluated the network reconstruction accuracy versus the variance σ^2 of the model errors $w_i^L[k]$ in (10.7). We varied the variance σ^2 in the interval $[0.05, 0.5]$. The other parameters were set to: coupling $c = 1$, frequency ratios $f_1 = 1$ and $f_2 = 2$, sampling time $\Delta t = 0.01$, and the number of observations $n = 10N^2$.

We quantified the inter-layer network reconstruction accuracy with respect to three error metrics. First, the false positive rate (FPR), which is given by the fraction of node pairs (i, j) for which $b_{ij} = 0$ but $\hat{b}_{ij} > 0$. Here, $\hat{b}_{ij}$ denote the elements of the estimated inter-layer connectivity matrix $\hat{B}$. Second, the false negative rate (FNR), which equals to the fraction of node pairs (i, j) for which $b_{ij} > 0$ but $\hat{b}_{ij} = 0$. We normalised both FPR and FNR metrics by the link density of the ground-truth inter-layer connectivity matrix B. Third, the relative true positive deviation (RTPD), which is given by $|b_{ij} - \hat{b}_{ij}|/b_{ij}$, averaged over all node pairs (i, j) for which both $b_{ij} > 0$ and $\hat{b}_{ij} > 0$. Thus, the RTPD quantifies the estimation accuracy of the reconstructed link *weights*.

Figure 10.2 shows the impact of link sparsity in the matrix B on the error metrics FPR and FNR. The greater the link density, the greater the estimation errors FPR, whereas the link sparsity has little impact on the FNR error. In contrast, the link weight error metric RTPD remains unaffected as the link density was varied. Furthermore, the FPR error slightly increases for larger model errors $w_i^L[k]$, and the link weight error metric RTPD remains largely unaffected for larger model errors $w_i^L[k]$.

10.4. INTER-LAYER CONNECTIVITY RECONSTRUCTION FOR EMPIRICAL MEG DATA

10.4.1. EMPIRICAL MEG AND DIFFUSION WEIGHTED IMAGING DATA

We consider resting-state magnetoencephalography (MEG) data from 89 healthy subjects from the Human Connectome Project [227, 269]. Every subject underwent three separate recording sessions, which were used as training and validation datasets for separate analysis steps (see Figure 10.1). The resting-state data for each session and subject is given as separate input to an atlas-based scalar beamforming approach [270, 271], by using the automated anatomical labelling atlas (AAL) which results in time courses at $N = 78$ cortical regions [222]. We refer to [272] for further details on the pre-processing steps. To reduce signal leakage, we applied symmetric multivariate orthogonalisation [273]. The theta (4-8 Hz), alpha (8-13 Hz), beta (13-30 Hz), and low gamma (30-48 Hz) frequency bands were obtained by bandpass filtering. We applied the Hilbert transform to obtained the instantaneous phases and concatenated the signals of all subjects (from session one) to obtain the phase input $\theta_i^L[k]$ to the network reconstruction method (10.5), see Figure 10.1, Panel B.

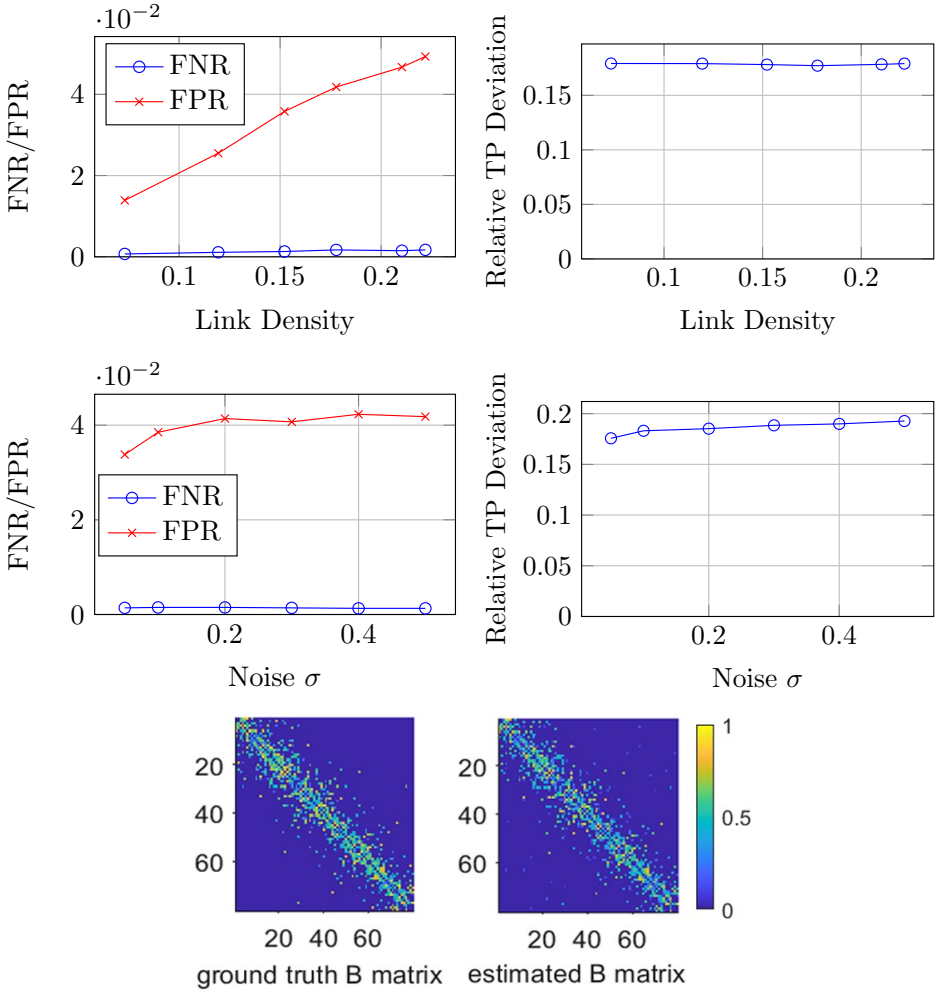

Figure 10.2: **Simulations with ground truth inter-layer connectivity.** Performance of the inter-layer network reconstruction algorithm in simulations with ground truth for inter-layer connectivity matrix B. The results in the first two rows are averaged over 20 realisations. The top left subplot shows the false positive rate (FPR) and the false negative rate (FNR) for reconstructed networks. The simulations are based on (10.7) with known ground-truth inter-layer networks B, which were generated by a range dependent random graph model with varying link density. The top right subplot shows the corresponding relative true positive deviation (RTPD). The second row shows the effect of increasing levels of model errors on the reconstruction accuracy, with respect to the error metrics FPR, FPN and RTPD, where the link density of the matrix B equals 0.14. The third row compares an exemplary ground-truth matrix B, with link density 0.14 and noise level of 0.05, to the estimated inter-layer network.

Furthermore, we estimated *intra*-layer phase connectivity by the phase locking value (PLV), after leakage reduction and band-pass filtering based on data from session two for the alpha and beta band (Figure 10.1, Panel C). For windows of 13 seconds, the PLV [274]

between two nodes i, j is given by

$$PLV_{ij} = \left| \frac{1}{U} \sum_{k=1}^{U} e^{-\mathrm{i}\Delta\theta_{ij}[k]} \right|.$$

Here, U corresponds to the window width (in samples), $\Delta\theta_{ij}[k]$ denotes the instantaneous phase difference between node i and j at time k, and i is the imaginary unit. The phase connectivity matrices PLV with elements PLV_{ij} were averaged across windows (on average 22 windows per subject) and subjects to obtain one $N \times N$ group-averaged intra-layer connectivity matrix $W_{L,emp}$ for every layer L. We obtained the data on the structural connectome from the Human Connectome Project, as described in [210].

10.4.2. RECONSTRUCTION OF INTER-LAYER CONNECTIVITY FROM EMPIRICAL DATA

An overview of the analysis in this section is given by Figure 10.1, Panel B. First, we focussed on the inter-layer connectivity between the alpha and beta band. We reconstructed the inter-layer connectivity matrix B by the LASSO (10.5), where we used the concatenated phase data from all subjects from session with the empirical connectome A as input. The parameters of the model (10.1) were set to $c = 1$, $f_1 = 1$ and $f_2 = 2$.

Furthermore, we used surrogate phase data to evaluate the network reconstruction method if there is no genuine underlying phase synchronisation. More specifically, we generated surrogate time series by adding white Gaussian errors to the phases of every node i. After obtaining the instantaneous phases, we applied the network reconstruction method (10.5) to the surrogate data.

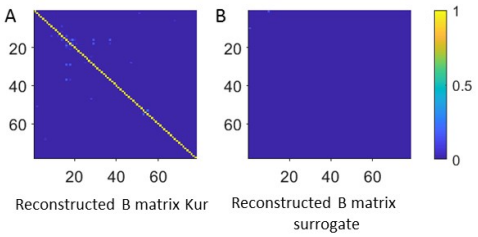

Figure 10.3: **Reconstructed inter-layer connectivity for two-layered alpha and beta band network.** Panel A shows the reconstructed inter-layer connectivity matrix B based on the multilayer phase oscillation model (10.1) for empirical data. Panel B shows the reconstructed inter-layer connectivity matrix B for surrogate data.

Figure 10.3 shows the network reconstruction results for both the empirical phase data and surrogate data. The reconstructed inter-layer connectivity matrix B for empirical phase data is very sparse: predominantly, there are strong one-to-one connections and only few, weak connections between distant nodes. For the surrogate data, the reconstructed inter-layer connectivity matrix B is almost zero, in stark contrast to the reconstructed network for genuine experimental data. The resulting reconstructed network for surrogate data indicates that one-to-one coupling as inter-layer connectivity is not necessarily the minimal solution of the inter-layer network reconstruction problem.

Thus, the reconstructed inter-layer connectivity for empirical data could not have been obtained from a system without any underlying inter-layer connectivity.

10.5. SIMULATIONS ON RECONSTRUCTED NETWORKS

Figure 10.1, Panel C, provides an overview of the analysis steps for this section, where we focus on the question: *How well does the reconstructed inter-layer connectivity network and the phase oscillator model (10.1) explain the empirical MEG data?* Thus, we *generate* phases $\theta_i^L[k]$ according to the dynamics (10.1) on the reconstructed inter-layer connectivity B, given in Section 10.4.2, and the empirical connectome A. We considered a range of values for the coupling c. For every value of the coupling c, we computed: (i) the Kuramoto order parameter for each layer L, $r_L[k] = \left|1/N \sum_{i=1}^{N} e^{i\theta_i^L[k]}\right|$, averaged over time k; (ii) the R^2 value between simulated functional connectivity $W_{L,sim}$ and empirical functional connectivity $W_{L,emp}$ for every layer L; (iii) the Spearman correlation coefficient $\rho = \text{corr}\left(W_{1,sim}, W_{2,sim}\right)$ of the upper-triangular part of the symmetric matrices $W_{1,sim}$, $W_{2,sim}$, to quantify the inter-layer correlation of the functional connectivity.

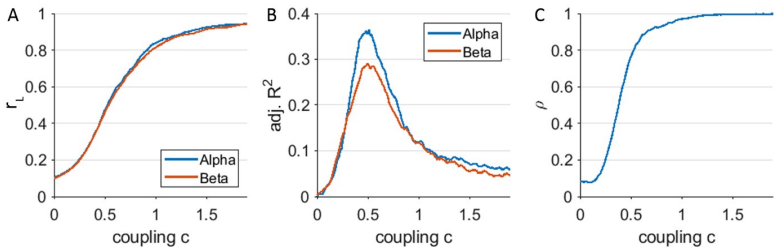

Figure 10.4: **Simulations and fit with empirical data.** Panel A shows the Kuramoto order parameter r_L for both layers $L = 1,2$ for a range of coupling values c. Panel B shows the adjusted R^2, which quantifies the fit of simulated intra-layer functional connectivity $W_{L,sim}$ to the empirical functional connectivity matrices $W_{L,emp}$, for a range of coupling values c. Panel C displays the (simulated) inter-layer correlation for a range of coupling values c. The results were averaged over 20 realisations and subsequently smoothed by a moving average filter.

Figure 10.4, Panel A, shows that there is a rapid transition for the Kuramoto order parameter from weak to strong phase synchronisation, without a clear plateau for lower coupling values c. Figure 10.4, Panel B, shows that the best fit of simulated PLV connectivity matrices with group-averaged empirical PLV connectivity matrices occurs at intermediate coupling values around $c = 0.5$. An adjusted R^2 value of around 0.3-0.4 indicates that, to some extent, the multilayer Kuramoto network model (10.1) is explanatory for the observed functional connectivity in empirical MEG data. Furthermore, the fit of the intra-layer network for the alpha band is slightly better than for the beta band. For empirical data, the inter-layer correlation between alpha and beta band equals $\rho = 0.62$. Figure 10.4, Panel C, shows that the best match of simulated and empirical inter-layer correlation ρ occurs for coupling value around $c \approx 0.5$.

10.6. INTER-LAYER CONNECTIVITY RECONSTRUCTION FOR THE THETA AND GAMMA BAND

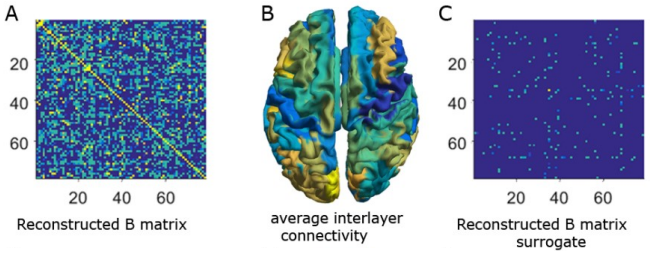

Figure 10.5: **Reconstructed inter-layer connectivity for two-layered theta and gamma band network.** Panel A shows the reconstructed inter-layer connectivity matrix B based on the multilayer phase oscillation model (10.1) for empirical data. Panel B displays the mean inter-layer connectivity matrix B on a template brain viewed from the top. Panel C shows the reconstructed inter-layer connectivity matrix B for surrogate data.

In Section 10.4, we considered the inter-layer connectivity between the alpha and beta band. Previous work [252] demonstrated cross-frequency coupling also between the theta and gamma band. Similar to the results in Figure 10.3, we reconstructed the inter-layer connectivity matrix B for the theta and gamma band. We used the empirical data of all subjects from session one and set the parameters $c = 1$, $f_1 = 1$ and $f_2 = 6$. Analogously to Section 10.4, we also used surrogate phase data to test the outcome in the absence of genuine underlying phase synchronisation in the data. Figure 10.5 shows that the estimated inter-layer connectivity matrix between theta and gamma band shows many more off-diagonal elements compared to the alpha-beta band, as well as in comparison to surrogate data (Figure 10.5, Panel C). The results indicate the presence of long-range inter-layer connections between brain regions.

10.7. CONCLUSIONS

We proposed a network reconstruction method, which is based on the LASSO, to estimate the inter-layer connectivity for MEG networks. We considered a multilayer Kuramoto phase oscillator model, but our approach is applicable to more general phase interaction functions H. For simulated phase oscillation data, our method accurately reconstructs the inter-layer connectivity, also in the presence of the model errors. For empirical MEG data, we considered the reconstruction of the interconnectivity of two pairs of frequency bands. First, for the alpha and beta frequency band, our network reconstruction method indicates that the empirical inter-layer connectivity is dominated by one-to-one connectivity between the two frequency bands. Second, for the theta and gamma frequency band, our method revealed widespread, long-distance connections between brain regions.

Thus, our main conclusion is that the topology of inter-layer coupling strongly depends on the combination of frequency bands, which advances the relatively young field of multilayer functional brain networks [235, 236, 242, 247, 275, 276]. While challenging, promising directions for future research include the generalisation of our work to: (i)

multilayer networks with more than two layers; (ii) phase-amplitude coupling [231, 277–280] and amplitude-amplitude coupling [235, 236]; (iii) different phase interaction functions H.

11

CONCLUSIONS

11.1. ANALYSIS OF EPIDEMICS ON NETWORKS

In the first part of this thesis, we provided an in-depth analysis of the NIMFA epidemic model (1.1). In particular, we focussed on obtaining a detailed description of the evolution of the $N \times 1$ viral state vector $v(t)$. The aim of Chapter 2 was to reduce the complexity of the set of N nonlinear NIMFA differential equations (1.1). More specifically, we gave a complete characterisation of contact networks for which the viral state $v(t)$ is governed by only $m \ll N$ differential equations. Our main result in Theorem 2.14 reveals a duality of function and structure: the viral state $v(t)$ is described by $m \ll N$ differential equations *if and only if* the contact network has an equitable partition with m cells. Thus, reducing the complexity of the NIMFA (1.1) translates to searching for structures that resemble equitable partitions. If the nodes can be clustered into an *approximate* equitable partition, then the viral state $v(t)$ is approximated, and bounded, by $m \ll N$ differential equations. Our results are an important step towards understanding epidemic outbreaks in large populations with a community structure.

In Chapter 3, we derived the closed-form solution of the NIMFA differential equations (1.1) around the epidemic threshold, i.e., as $R_0 \downarrow 1$. The solution approach is based on a surprising observation: for arbitrarily large and heterogeneous, undirected contact networks B, the viral dynamics lie (approximately) in a one-dimensional subspace of $\mathbb{R}^N$. Thus, compared to the *exact* reduction of the viral dynamics to $m \ll N$ differential equations in Chapter 2, which is only possible for equitable partitions, an *approximate* reduction to $m = 1$ differential equations is possible for *every* network, provided that $R_0 \approx 1$. As an important consequence, the structure of the contact network B only has a small impact on the viral dynamics when $R_0 \approx 1$. More specifically, the viral dynamics on arbitrary contact graphs can be reduced to the viral spread on a complete graph as $R_0 \downarrow 1$. Thus, our results prove that, even on a complicated contact network, the evolution of an epidemic outbreak can be astonishingly simple.

In Chapter 4, we study the NIMFA epidemic model (1.1) in discrete time $k \in \mathbb{N}$. In particular, for a small initial state $v[1]$, we show that the viral state $v[k]$ is (almost always)

monotonically increasing, the steady state v_∞ is exponentially stable. Furthermore, we provide linear systems that bound the viral state $v[k]$ at every time k. Thus, we provided the foundation for applying the NIMFA epidemic model to real-world, discrete-time epidemic data.

11.2. NETWORK RECONSTRUCTION AND PREDICTION OF EPIDEMICS

The second part of this thesis focusses on the prediction of epidemic outbreaks. The contact network is essential for predicting epidemic outbreaks. However, in most applications, the contact network is not known. Hence, to predict epidemic outbreaks, one resorts to reconstructing the network from past observations of the epidemic. In Chapter 5, we consider the network reconstruction for the stochastic SIS process on individual level, and our contribution is twofold. First, we prove that the maximum-likelihood SIS network reconstruction problem is NP-hard. The NP-hardness holds for any contact graph that generated the SIS viral state observations. Hence, there are no efficient algorithms for solving the general maximum-likelihood SIS network reconstruction problem. Second, we propose an polynomial-time heuristic network reconstruction method. Numerical simulations on small networks, which allow for solving the SIS network reconstruction problem optimally, show that our heuristic performs almost optimally. By applying our method to larger networks, we find that a tremendous number of observations is required for an accurate SIS network reconstruction. Thus, obtaining the contact network between individuals from SIS viral state observations seems infeasible in practice, which is a motivation to consider epidemic outbreak on a coarser level, between groups of individuals.

Before developing prediction methods for epidemic outbreaks between groups of individuals, it is imperative to be aware of fundamental prediction limits. Thus, we studied the predictability of epidemic outbreaks in Chapter 6. In particular, we focussed on the logistic function, which is central to both the SIS and SIR epidemic model (see Theorem 3.7). We showed that predicting a logistic function from past observations is severely ill-conditioned, regardless of the specific prediction method. Importantly, even under idealised conditions, an accurate fit of the logistic function to past data of an epidemic outbreak does not imply an accurate prediction. In summary, an epidemic outbreak can be predicted accurately only in the short term.

In Chapter 7, we developed a prediction method for a general class of epidemic models on networks. Our contribution was twofold. First, we proposed the general GEMF model which unifies a diverse class of models for epidemics on networks. We considered the GEMF epidemic model in discrete time, which is more amenable to describing and predicting real epidemics. In particular, the discrete-time NIMFA epidemic model in Chapter 4 is a special case of the discrete-time GEMF model. Second, based on the GEMF model, we proposed a prediction method for epidemic outbreaks, which infers the contact network as an intermediate step. Complementing the results in Chapter 2 and Chapter 3, we found that the viral state for general GEMF models (with high accuracy) equals the linear combination of only $m \ll N$ agitation modes, also when $R_0 \gg 1$. Since the viral state is barely agitated, there are infinitely many, greatly diverse contact

networks that are consistent with past observations of an epidemic outbreak. Thus, it is not possible to reconstruct the contact network, unless many epidemic outbreaks on the same network are observed. On the positive side, we made the decisive observation that an epidemic outbreak can be predicted without the contact network.

In Chapter 8, we adjusted the network-inference based prediction method of Chapter 7 to forecast the spread of COVID-19. Particularly, we focussed on the prediction of COVID-19 in the Netherlands and in the Chinese province Hubei. The network-inference based prediction method outperforms several other approaches. Hence, our results indicate that the network-based modelling is a promising approach for predicting epidemic outbreaks.

11.3. SPREADING IN BRAIN NETWORKS: RELATING FUNCTION AND STRUCTURE

A central challenge in neuroscience is the description of how the structural brain network shapes the functional brain network. In Chapter 9, we analyse two prominent approaches for relating function and structure in the brain: the *eigenmode approach*, which describes the functional brain network as the weighted sum of outer products of the structural eigenvectors; and the *series expansion approach*, which describes the functional brain network as a polynomial of the structural network. By deriving explicit expressions for the best-fit coefficients for both approaches, we show that the approaches are strongly related. Furthermore, we show that the eigenmode approach is more accurate and, in contrast to the series expansion approach, numerically well-conditioned. Thus, we conclude that the eigenmode approach is preferable over the series expansion approach. Our results constitute an important step towards a unification of theories that relate function and structure in the brain.

Most studies analyse different frequency-specific functional brain networks (e.g., alpha and beta band) separately, although these networks originate from the same empirical data source. Only recently, cross-frequency dependencies are taken into account. In Chapter 10, we reconstruct cross-frequency coupling between different brain regions. Our reconstruction method is based on a multilayer phase oscillator model in which the layers correspond to different frequency bands. We found that cross-frequency coupling is dominated by one-to-one interactions between the brain regions. Furthermore, in contrast to alpha-beta band coupling, there are significant theta-gamma band couplings between several distinct brain regions. Our findings advance the understanding of functional dependencies between brain regions, beyond the restriction to single frequency bands.

11.4. DIRECTIONS FOR FUTURE WORK

The proper orthogonal decomposition (POD), given by (2.1), was an overarching method in this thesis, with applications in Chapters 2 and 3 and Chapters 7 and 8. The POD (2.1) reveals a stark contrast: the contact network is *complicated* and *large*, but the viral dynamics follow a *simple* linear combination of *only few* agitation modes y_1, ..., y_m. The POD is a powerful means of complexity reduction, based on which we derived the

closed-form solution of NIMFA in Chapter 2 and predicted epidemics without the contact network in Chapter 7. To the best of our knowledge, the application of the POD to dynamics on networks is novel. Thus, the application of the POD to network dynamics other than epidemics seems to be a promising research direction, as already demonstrated by [53, 57].

While we have considered the fairly general setting of heterogeneous spreading rates δ_i and β_{ij}, we assumed a symmetric infection rate matrix B to derive the results in Chapter 2 and Chapter 3. The generalisation of our results to asymmetric matrices B, i.e., directed contact graphs, is an open challenge.

Throughout this thesis, we assumed time-invariant contact networks. However, the contact network may not be constant, particularly for time-varying lockdown measures. Initial work [159] suggests that the prediction accuracy of the prediction method in Chapter 7 may significantly improve, when time-varying lockdown measures are considered. The generalisation of our results to time-varying spreading rates $\beta_{ij}(t)$ and $\delta_i(t)$ stands on the agenda of future research.

APPENDICES

A

APPENDIX TO CHAPTER 2

A.1. PROOF OF LEMMA 2.11

Let w denote a vector in the orthogonal complement $\mathcal{V}^\perp$ of the invariant set $\mathcal{V}$. Hence, it must hold that $w^T v(t) = 0$ for every time $t \geq 0$ if $v(0) \in \mathcal{V}$, which is equivalent to both $w^T v(0) = 0$ and

$$\frac{d(w^T v(t))}{dt} = 0 \quad \forall v(t) \in \mathcal{V}, w \in \mathcal{V}^\perp. \tag{A.1}$$

We replace the notation $v(t) \in \mathcal{V}$ by $v \in \mathcal{V}$. Then, we obtain from the NIMFA equations (1.2) that (A.1) is equivalent to

$$w^T \left(-Sv + \operatorname{diag}(u - v)Bv\right) = 0 \quad \forall v \in \mathcal{V}, w \in \mathcal{V}^\perp.$$

Under Assumption 2.7, it holds that $Sv \in \mathcal{V}$. Hence, the vector $w \in \mathcal{V}^\perp$ is orthogonal to the vector Sv, which yields that

$$w^T \operatorname{diag}(u - v)Bv = 0.$$

Since $\operatorname{diag}(u)$ is the identity matrix, we obtain that

$$w^T Bv = w^T \operatorname{diag}(v)Bv. \tag{A.2}$$

Since the invariant set $\mathcal{V}$ is a subspace of $\mathbb{R}^N$, $v \in \mathcal{V}$ implies that $\sigma v \in \mathcal{V}$ for any scalar $\sigma \in \mathbb{R}$. For the vector σv, where we consider $\sigma > 0$, it follows from (A.2) that

$$\sigma w^T Bv = \sigma^2 w^T \operatorname{diag}(v)Bv,$$

which is equivalent to

$$w^T Bv = \sigma w^T \operatorname{diag}(v)Bv.$$

A

Thus, we obtain with (A.2) for every scalar $\sigma > 0$ that

$$w^T \operatorname{diag}(v) B v = \sigma w^T \operatorname{diag}(v) B v,$$

which implies that

$$w^T \operatorname{diag}(v) B v = 0. \tag{A.3}$$

Then, from (A.2), it follows that

$$w^T B v = 0$$

for all vectors $w \in \mathcal{V}^\perp$, $v \in \mathcal{V}$. The vector Bv is orthogonal to all vectors $w \in \mathcal{V}^\perp$, only if $Bv \in \mathcal{V}$. Thus, the set $\mathcal{V}$ is an invariant subspace [281] of the infection rate matrix B. The sets of vectors $y_1, ..., y_m$ and $y_{m+1}, ..., y_N$ span the invariant set $\mathcal{V}$ and the orthogonal complement $\mathcal{V}^\perp$, respectively, see (2.2) and (2.14). Thus, we can express the symmetric matrix B as

$$B = \begin{pmatrix} y_1 & \dots & y_N \end{pmatrix} \begin{pmatrix} M_1 & M_{12} \\ 0 & M_2 \end{pmatrix} \begin{pmatrix} y_1^T \\ \vdots \\ y_N^T \end{pmatrix} \tag{A.4}$$

for some $m \times m$ symmetric matrix M_1 and some $(N-m) \times (N-m)$ symmetric matrix M_2. The $m \times (N-m)$ matrix M_{12} describes the mapping from the subspace $\mathcal{V}^\perp$ to the subspace $\mathcal{V}$. Since the matrix B is symmetric, it holds that $M_{12} = 0$, and (A.4) becomes

$$B = \begin{pmatrix} y_1 & \dots & y_N \end{pmatrix} \begin{pmatrix} M_1 & 0 \\ 0 & M_2 \end{pmatrix} \begin{pmatrix} y_1^T \\ \vdots \\ y_N^T \end{pmatrix}.$$

Furthermore, since the matrix B is diagonalisable as (2.16), the matrices M_1 and M_2 are diagonalisable [281, Exercise 24, Section 5.4]. Thus, there is some orthogonal $m \times m$ matrix C_1 and some orthogonal $(N-m) \times (N-m)$ matrix C_2 such that

$$B = \begin{pmatrix} y_1 & \dots & y_N \end{pmatrix} \begin{pmatrix} C_1 & 0 \\ 0 & C_2 \end{pmatrix} \begin{pmatrix} \Lambda_1 & 0 \\ 0 & \Lambda_2 \end{pmatrix} \begin{pmatrix} C_1^T & 0 \\ 0 & C_2^T \end{pmatrix} \begin{pmatrix} y_1^T \\ \vdots \\ y_N^T \end{pmatrix}. \tag{A.5}$$

where the $m \times m$ diagonal matrix Λ_1 and the $(N-m) \times (N-m)$ diagonal matrix Λ_2 contain the eigenvalues of B. In contrast to the $N \times N$ matrix Λ in (2.16), the diagonal entries of the matrices Λ_1 and Λ_2 may not be ordered with respect to their magnitude. Hence, there is some permutation $\phi : \{1, ..., N\} \to \{1, ..., N\}$ of the eigenvalues $\lambda_1, ..., \lambda_N$ such that

$$\Lambda_1 = \operatorname{diag}\left(\lambda_{\phi(1)}, ..., \lambda_{\phi(m)}\right)$$

and

$$\Lambda_2 = \operatorname{diag}\left(\lambda_{\phi(m+1)}, ..., \lambda_{\phi(N)}\right).$$

We define the $N \times m$ matrix $E_{\mathcal{V}}$ and the $N \times (N-m)$ matrix $E_{\mathcal{V}^\perp}$ as

$$E_{\mathcal{V}} = \begin{pmatrix} y_1 & \dots & y_m \end{pmatrix} C_1$$

and

$$E_{\mathcal{V}^\perp} = \begin{pmatrix} y_{N-m} & \dots & y_N \end{pmatrix} C_2.$$

Since the matrices C_1 and C_2 are nonsingular, the columns of the matrices $E_{\mathcal{V}}$ and $E_{\mathcal{V}^\perp}$ span the subspaces $\mathcal{V}$ and $\mathcal{V}^\perp$, respectively. We obtain that

$$B = \begin{pmatrix} E_{\mathcal{V}} & E_{\mathcal{V}^\perp} \end{pmatrix} \operatorname{diag}\left(\lambda_{\phi(1)}, \dots, \lambda_{\phi(N)}\right) \begin{pmatrix} E_{\mathcal{V}}^T \\ E_{\mathcal{V}^\perp}^T \end{pmatrix}.$$

Thus, the matrices $E_{\mathcal{V}}, E_{\mathcal{V}^\perp}$ equal to

$$E_{\mathcal{V}} = \begin{pmatrix} x_{\phi(1)} & \dots & x_{\phi(m)} \end{pmatrix} \tag{A.6}$$

and

$$E_{\mathcal{V}^\perp} = \begin{pmatrix} x_{\phi(N-m)} & \dots & x_{\phi(N)} \end{pmatrix},$$

where the columns $x_{\phi(1)}, \dots, x_{\phi(N)}$ are eigenvectors to the eigenvalues $\lambda_{\phi(1)}, \dots, \lambda_{\phi(N)}$ of the matrix B, which completes the proof.

A.2. PROOF OF LEMMA 2.12

From (A.5), it follows that

$$B = \begin{pmatrix} y_1 & \dots & y_m \end{pmatrix} C_1 \Lambda_1 C_1^T \begin{pmatrix} y_1^T \\ \vdots \\ y_m^T \end{pmatrix} + \begin{pmatrix} y_{m+1} & \dots & y_N \end{pmatrix} C_2 \Lambda_2 C_2^T \begin{pmatrix} y_{m+1}^T \\ \vdots \\ y_N^T \end{pmatrix}.$$

We complete the proof by identifying the $m \times m$ matrix $\tilde{B}_{\mathcal{V}} = C_1 \Lambda_1 C_1^T$ and the $(N-m) \times (N-m)$ matrix $\tilde{B}_{\mathcal{V}^\perp} = C_2 \Lambda_2 C_2^T$.

A.3. PROOF OF THEOREM 2.14

The proof of Theorem 2.14 is based on four lemmas. First, Lemma A.1 relates the product $\operatorname{diag}(w)v$ to the subspaces $\mathcal{V}_{\neq 0}$ and $\mathcal{V}^\perp$:

Lemma A.1. *For all vectors $v \in \mathcal{V}_{\neq 0}$ and $w \in \mathcal{V}^\perp$, it holds that* $\operatorname{diag}(w)v \in \mathcal{V}^\perp$.

Proof. Since $w^T \operatorname{diag}(v) = (w_1 v_1, \dots, w_N v_N) = v^T \operatorname{diag}(w)$, we obtain from (A.3) that

$$v^T \operatorname{diag}(w) B v = 0.$$

Equivalently, by taking the transpose, it holds that

$$v^T B \operatorname{diag}(w) v = 0. \tag{A.7}$$

The invariant set $\mathcal{V}$ is given by the span of some orthogonal vectors $y_1, ..., y_m$. Lemma 2.11 states that $\mathcal{V} = \text{span}\{x_{\phi(1)}, ..., x_{\phi(m)}\}$, where $x_{\phi(l)}$ is an eigenvector of the matrix B to the eigenvalue $\lambda_{\phi(l)}$ for some permutation ϕ. Thus, every vector $v \in \mathcal{V}$ can be written as

$$v = \begin{pmatrix} x_{\phi(1)} & ... & x_{\phi(m)} \end{pmatrix} z \tag{A.8}$$

for some $m \times 1$ vector $z = (z_1, ..., z_m)^T$, and the subspace $\mathcal{V}$ equals

$$\mathcal{V} = \left\{ \begin{pmatrix} x_{\phi(1)} & ... & x_{\phi(m)} \end{pmatrix} z \middle| z \in \mathbb{R}^m \right\}.$$

With (A.8), we can rewrite (A.7) as

$$z^T \Lambda_1 \begin{pmatrix} x_{\phi(1)}^T \\ \vdots \\ x_{\phi(m)}^T \end{pmatrix} \text{diag}(w) \begin{pmatrix} x_{\phi(1)} & ... & x_{\phi(m)} \end{pmatrix} z = 0, \tag{A.9}$$

with the $m \times m$ diagonal matrix $\Lambda_1 = \text{diag}(\lambda_{\phi(1)}, ..., \lambda_{\phi(m)})$. The quadratic form (A.9) equals zero for all vectors $cz \in \mathbb{R}^m$ if and only if

$$\Lambda_1 \begin{pmatrix} x_{\phi(1)}^T \\ \vdots \\ x_{\phi(m)}^T \end{pmatrix} \text{diag}(w) \begin{pmatrix} x_{\phi(1)} & ... & x_{\phi(m)} \end{pmatrix} = 0,$$

which implies, with (A.8), that

$$\Lambda_1 \begin{pmatrix} x_{\phi(1)}^T \\ \vdots \\ x_{\phi(m)}^T \end{pmatrix} \text{diag}(w) v = 0$$

for all vectors $v \in \mathcal{V}$. Componentwise, we obtain that

$$\lambda_{\phi(l)} x_{\phi(l)}^T \text{diag}(w) v = 0 \tag{A.10}$$

for all rows $l = 1, ..., m$ and all vectors $v \in \mathcal{V}$. Equation (A.10) is satisfied if and only if $\lambda_{\phi(l)} = 0$ or $x_{\phi(l)}^T \text{diag}(w) v = 0$ for all rows $l = 1, ..., m$. The subspace $\mathcal{V}_0$ contains the vectors $x_{\phi(l)}$ for which $\lambda_{\phi(l)} = 0$, and the subspace $\mathcal{V}^\perp$ contains the vectors $x_{\phi(m+1)}, ..., x_{\phi(N)}$ which are orthogonal to the vectors $x_{\phi(1)}, ..., x_{\phi(m)}$. Thus, the vector $\text{diag}(w) v$ must be element of the subspaces $\mathcal{V}_0$ or $\mathcal{V}^\perp$, or the vector $\text{diag}(w) v$ must equal to the sum of two vectors in the subspaces $\mathcal{V}_0$ and $\mathcal{V}$. Hence, with the direct sum (2.15), we can reformulate (A.10) as

$$\text{diag}(w) v \in \mathcal{V}^\perp \oplus \mathcal{V}_0 \tag{A.11}$$

for all vectors $v \in \mathcal{V}$. We define the $N \times m_1$ matrix $E_{\mathcal{V}_{\neq 0}}$ as

$$E_{\mathcal{V}_{\neq 0}} = \begin{pmatrix} x_{\phi(1)} & ... & x_{\phi(m_1)} \end{pmatrix}$$

and the $N \times (m - m_1)$ matrix $E_{\mathcal{V}_0}$ as

$$E_{\mathcal{V}_0} = \begin{pmatrix} x_{\phi(m_1+1)} & \dots & x_{\phi(m)} \end{pmatrix}.$$

Thus, the definition of the matrix $E_{\mathcal{V}}$ in (A.6) implies that $E_{\mathcal{V}} = \begin{pmatrix} E_{\mathcal{V}_{\neq 0}} & E_{\mathcal{V}_0} \end{pmatrix}$, and the matrix $\operatorname{diag}(w)$ can be written as

$$\operatorname{diag}(w) = \begin{pmatrix} E_{\mathcal{V}_{\neq 0}} & E_{\mathcal{V}_0} & E_{\mathcal{V}^\perp} \end{pmatrix} \begin{pmatrix} M_{11} & M_{12} & M_{13} \\ M_{21} & M_{22} & M_{23} \\ M_{31} & M_{32} & M_{33} \end{pmatrix} \begin{pmatrix} E_{\mathcal{V}_{\neq 0}}^T \\ E_{\mathcal{V}_0}^T \\ E_{\mathcal{V}^\perp}^T \end{pmatrix}$$

for some matrices M_{ij}, where $i, j = 1, 2, 3$, whose dimensions follow from the dimension of the matrices $E_{\mathcal{V}_{\neq 0}}$, $E_{\mathcal{V}_0}$ and $E_{\mathcal{V}^\perp}$. The matrices M_{11} and M_{12} describe the mapping of the matrix $\operatorname{diag}(w)$ from the subspaces $\mathcal{V}_{\neq 0}$ and $\mathcal{V}_0$, respectively, to the subspace $\mathcal{V}_{\neq 0}$. From (A.11), we obtain that $M_{11} = 0$ and $M_{12} = 0$. Furthermore, since the matrix $\operatorname{diag}(w)$ is symmetric, it holds that $M_{21} = M_{12}^T = 0$. Hence, to satisfy (A.11), the matrix $\operatorname{diag}(w)$ must equal to

$$\operatorname{diag}(w) = \begin{pmatrix} E_{\mathcal{V}_{\neq 0}} & E_{\mathcal{V}_0} & E_{\mathcal{V}^\perp} \end{pmatrix} \begin{pmatrix} 0 & 0 & M_{13} \\ 0 & M_{22} & M_{23} \\ M_{31} & M_{32} & M_{33} \end{pmatrix} \begin{pmatrix} E_{\mathcal{V}_{\neq 0}}^T \\ E_{\mathcal{V}_0}^T \\ E_{\mathcal{V}^\perp}^T \end{pmatrix},$$

which implies for all vectors $v \in \mathcal{V}_{\neq 0}$ that $\operatorname{diag}(w)v \in \mathcal{V}^\perp$. □

Lemma A.1 states that for all vectors $v \in \mathcal{V}_{\neq 0}$ and $w \in \mathcal{V}^\perp$, there must be some vector $\tilde{w} \in \mathcal{V}^\perp$ such that

$$\operatorname{diag}(w)v = \tilde{w}. \tag{A.12}$$

We aim to find *all* subspaces $\mathcal{V}_{\neq 0}$ and $\mathcal{V}^\perp$ whose elements v and w, $\tilde{w}$, respectively, satisfy (A.12). From Lemma 2.11 it follows that a basis of the $N - m$ dimensional subspace $\mathcal{V}^\perp$ is given by the columns of the matrix

$$E_{\mathcal{V}^\perp} = \begin{pmatrix} \left(x_{\phi(m+1)}\right)_1 & \dots & \left(x_{\phi(N)}\right)_1 \\ \vdots & \ddots & \vdots \\ \left(x_{\phi(m+1)}\right)_N & \dots & \left(x_{\phi(N)}\right)_N \end{pmatrix}. \tag{A.13}$$

For every matrix, the column rank equals the row rank. Since the columns of the matrix $E_{\mathcal{V}^\perp}$ are linearly independent, there are $N - m$ linearly independent rows of the matrix $E_{\mathcal{V}^\perp}$. Without loss of generality[1], we assume that the *first* $N - m$ rows of the matrix $E_{\mathcal{V}^\perp}$ are linearly independent. Hence, the first $N - m$ rows span the Euclidean space $\mathbb{R}^{N-m}$,

$$\operatorname{span}\left\{ \begin{pmatrix} \left(x_{\phi(m+1)}\right)_1 \\ \vdots \\ \left(x_{\phi(N)}\right)_1 \end{pmatrix}, \begin{pmatrix} \left(x_{\phi(m+1)}\right)_2 \\ \vdots \\ \left(x_{\phi(N)}\right)_2 \end{pmatrix}, \dots, \begin{pmatrix} \left(x_{\phi(m+1)}\right)_{N-m} \\ \vdots \\ \left(x_{\phi(N)}\right)_{N-m} \end{pmatrix} \right\} = \mathbb{R}^{N-m}. \tag{A.14}$$

[1] Otherwise, consider a permutation of the rows, which is equivalent to a relabelling of the nodes.

Thus, for *all* vectors $w \in \mathcal{V}^{\perp}$ and $v \in \mathcal{V}_{\neq 0}$, there is a vector $\tilde{w} \in \mathcal{V}^{\perp}$ whose first $N-m$ entries satisfy (A.12), i.e.,

$$\tilde{w}_i = w_i v_i, \quad i = 1, ..., N-m. \tag{A.15}$$

The last m entries of the vector $\tilde{w} \in \mathcal{V}^{\perp}$ are determined by the first $(N-m)$ entries of the vector w, as shown by Lemma A.2. (Lemma A.2 is not a novel contribution, but we include Lemma A.2 for completeness.)

Lemma A.2. *Suppose that that the first $N-m$ rows of the matrix $E_{\mathcal{V}^{\perp}}$ are linearly independent. Then, there are some $(N-m)\times 1$ vectors $\chi_{N-m}, ..., \chi_N$ such that the last m entries of any vector $w \in \mathcal{V}^{\perp}$ follow from the first $(N-m)$ entries as*

$$w_i = \chi_i^T \begin{pmatrix} w_1 \\ \vdots \\ w_{N-m} \end{pmatrix}, \quad i = N-m+1, ..., N.$$

Proof. With the definition of the matrix $E_{\mathcal{V}^{\perp}}$ in (A.13), every vector $w \in \mathcal{V}^{\perp}$ can be written as

$$w = \begin{pmatrix} x_{\phi(m+1)} & ... & x_{\phi(N)} \end{pmatrix} \begin{pmatrix} z_{m+1} \\ \vdots \\ z_N \end{pmatrix} \tag{A.16}$$

for some scalars $z_{m+1}, ..., z_N \in \mathbb{R}$. Thus, the first $N-m$ entries of the vector w follow as

$$\begin{pmatrix} w_1 \\ \vdots \\ w_{N-m} \end{pmatrix} = M \begin{pmatrix} z_{m+1} \\ \vdots \\ z_N \end{pmatrix}, \tag{A.17}$$

where the $(N-m)\times(N-m)$ matrix M equals to the first $N-m$ rows of the matrix $E_{\mathcal{V}^{\perp}}$,

$$M = \begin{pmatrix} \left(x_{\phi(m+1)}\right)_1 & ... & \left(x_{\phi(N)}\right)_1 \\ \vdots & \ddots & \vdots \\ \left(x_{\phi(m+1)}\right)_{N-m} & ... & \left(x_{\phi(N)}\right)_{N-m} \end{pmatrix}.$$

By assumption, the first $N-m$ rows of the matrix $E_{\mathcal{V}^{\perp}}$ are linearly independent. Hence, the matrix M is nonsingular, and the scalars $z_{m+1}, ..., z_N$ follow from (A.17) as

$$\begin{pmatrix} z_{m+1} \\ \vdots \\ z_N \end{pmatrix} = M^{-1} \begin{pmatrix} w_1 \\ \vdots \\ w_{N-m} \end{pmatrix}.$$

Thus, we obtain the last m entries of the vector w with (A.16) as

$$\begin{pmatrix} w_{N-m+1} \\ \vdots \\ w_N \end{pmatrix} = \begin{pmatrix} \left(x_{\phi(m+1)}\right)_{N-m+1} & \dots & \left(x_{\phi(N)}\right)_{N-m+1} \\ \vdots & \ddots & \vdots \\ \left(x_{\phi(m+1)}\right)_N & \dots & \left(x_{\phi(N)}\right)_N \end{pmatrix} \begin{pmatrix} z_{m+1} \\ \vdots \\ z_N \end{pmatrix}$$
$$= \begin{pmatrix} \left(x_{\phi(m+1)}\right)_{N-m+1} & \dots & \left(x_{\phi(N)}\right)_{N-m+1} \\ \vdots & \ddots & \vdots \\ \left(x_{\phi(m+1)}\right)_N & \dots & \left(x_{\phi(N)}\right)_N \end{pmatrix} M^{-1} \begin{pmatrix} w_1 \\ \vdots \\ w_{N-m} \end{pmatrix}.$$

To complete the proof, we define the vectors $\chi_{N-m+1}, \dots, \chi_N$ as

$$\begin{pmatrix} \chi_{N-m+1}^T \\ \vdots \\ \chi_N^T \end{pmatrix} = \begin{pmatrix} \left(x_{\phi(m+1)}\right)_{N-m+1} & \dots & \left(x_{\phi(N)}\right)_{N-m+1} \\ \vdots & \ddots & \vdots \\ \left(x_{\phi(m+1)}\right)_N & \dots & \left(x_{\phi(N)}\right)_N \end{pmatrix} M^{-1}.$$

□

We combine Lemma A.2 and (A.15), which yields for the last $(N-m)$ entries of the vector $\tilde{w} \in \mathcal{V}^\perp$ that

$$\begin{aligned} \tilde{w}_i &= \sum_{j=1}^{N-m} \chi_{ij} \tilde{w}_j \\ &= \sum_{j=1}^{N-m} \chi_{ij} w_j v_j, \end{aligned}$$

where $i = N-m+1, \dots, N$. Furthermore, (A.12) states that $\tilde{w}_i = v_i w_i$. Thus, it must hold that

$$w_i v_i = \sum_{j=1}^{N-m} \chi_{ij} w_j v_j$$

for the entries $i = N-m+1, \dots, N$. Since the vector w is element of the subspace $\mathcal{V}^\perp$, we apply Lemma A.2 again and obtain that

$$\left(\sum_{j=1}^{N-m} \chi_{ij} w_j \right) v_i = \sum_{j=1}^{N-m} \chi_{ij} w_j v_j.$$

Thus, for all entries $i = N-m+1, \dots, N$, it must hold that

$$\sum_{j=1}^{N-m} \chi_{ij} w_j (v_i - v_j) = 0 \tag{A.18}$$

for all vectors $w \in \mathcal{V}^\perp$ and $v \in \mathcal{V}_{\neq 0}$. Since the first $N-m$ rows of the matrix $E_{\mathcal{V}^\perp}$ are linearly independent, see (A.14), it follows that (A.18) must be satisfied for *all* scalars w_1, ..., w_{N-m} in $\mathbb{R}$. Hence, for all vectors $v \in \mathcal{V}_{\neq 0}$, it must hold that $\chi_{ij}(v_i - v_j) = 0$ for all indices $j = 1, \dots, N-m$, which is equivalent to $\chi_{ij} = 0$ or $v_j = v_i$. Thus, the non-zero entries of the vectors χ_i indicate which nodes j have the same viral state as node i.

A

Example A.3. *Consider a network of $N = 5$ nodes with an invariant set $\mathcal{V}$ of dimension $m = 3$. Furthermore, consider that $\mathcal{V}_0 = \emptyset$, which implies with (2.18) that $\mathcal{V} = \mathcal{V}_{\neq 0}$. Thus, there are $N - m = 2$ vectors χ_4, χ_5. Suppose that the vectors χ_4, χ_5 equal to $\chi_4 = (\chi_{41}, 0)^T$ and $\chi_5 = (0, \chi_{52})^T$, where $\chi_{41}, \chi_{52} \neq 0$. Then, (A.18) implies that $v_1 = v_4$ and $v_2 = v_5$ for every viral state $v \in \mathcal{V}$. Hence, the subspace $\mathcal{V} = \text{span}\{y_1, y_2, y_3\}$ is given by the basis vectors*

$$y_1 = \frac{1}{\sqrt{2}} \begin{pmatrix} 1 \\ 0 \\ 0 \\ 1 \\ 0 \end{pmatrix}, \quad y_2 = \frac{1}{\sqrt{2}} \begin{pmatrix} 0 \\ 1 \\ 0 \\ 0 \\ 1 \end{pmatrix}, \quad y_3 = \begin{pmatrix} 0 \\ 0 \\ 1 \\ 0 \\ 0 \end{pmatrix}.$$

For $l = 1, 2, 3$, the eigenvector $x_{\phi(l)}$ of the infection rate matrix B equals to a linear combination of the basis vectors y_1, y_2, y_3.

From (A.18), we can determine disjoint subsets $\mathcal{N}_1, \mathcal{N}_2, \ldots$ of the set of all nodes $\mathcal{N} = \{1, \ldots, N\}$ as follows: If two nodes i, j are element of the same subset $\mathcal{N}_l \subseteq \mathcal{N}$, then the viral states are equal, $v_i = v_j$, for every viral state $v \in \mathcal{V}_{\neq 0}$. If a subset contains only one node, $\mathcal{N}_l = \{i\}$, then the viral state can be arbitrary $v_i \in \mathbb{R}$, independently of the viral state v_j of other nodes $j \neq i$. Every subset defines a basis vector y_l of the subspace $\mathcal{V}_{\neq 0}$ as

$$(y_l)_i = \begin{cases} \frac{1}{\sqrt{|\mathcal{N}_l|}} & \text{if} \quad i \in \mathcal{N}_l, \\ 0 & \text{if} \quad i \notin \mathcal{N}_l. \end{cases} \tag{A.19}$$

Then, the subspace $\mathcal{V}_{\neq 0}$ equals to the span of the vectors y_l of all subsets $\mathcal{N}_l$. Since the dimension of the subspace $\mathcal{V}_{\neq 0}$ is m_1, there must be m_1 subsets $\mathcal{N}_1, \ldots, \mathcal{N}_{m_1}$. Every node i is element of at most one subset $\mathcal{N}_l$. Hence, the vectors $y_l, y_{\tilde{l}}$ are orthogonal for $l \neq \tilde{l}$.

Furthermore, some nodes i might not be element of any subset $\mathcal{N}_1, \ldots, \mathcal{N}_{m_1}$, which would imply that $(y_l)_i = 0$ for all basis vectors y_l of $\mathcal{V}_{\neq 0}$. We define the subset $\mathcal{N}_{m_1+1}$, whose elements are the nodes i that are not in any other subset $\mathcal{N}_1, \ldots, \mathcal{N}_{m_1}$. As shown by Lemma A.4, the set $\mathcal{N}_{m_1+1}$ is empty:

Lemma A.4. *Under Assumptions 2.7 to 2.10, it holds that $\mathcal{N}_{m_1+1} = \emptyset$.*

Proof. Under Assumption 2.8, there is a viral state vector $v \in \mathcal{V}$ with positive entries. The positive viral state vector v satisfies

$$v = \sum_{l=1}^{m_1} z_l y_l + \sum_{l=m_1+1}^{m} z_l y_l \tag{A.20}$$

for some scalars $z_1, \ldots, z_m \in \mathbb{R}$. We denote the projection of the viral state v onto the subspace $\mathcal{V}_0$ as

$$v_{\text{ker}} = \sum_{l=m_1+1}^{m} z_l y_l$$

Every basis vector y_l of the subspace $\mathcal{V}_{\neq 0}$ satisfies $(y_l)_i = 0$ for all nodes $i \in \mathcal{N}_{m_1+1}$. Thus, we obtain with (A.20) that

$$(v_{\text{ker}})_i = v_i > 0 \tag{A.21}$$

for all nodes $i \in \mathcal{N}_{m_1+1}$. Any vector $\tilde{v} \in \mathcal{V}_{\neq 0}$ is orthogonal to the vector $v_{\text{ker}} \in \mathcal{V}_0$. Hence, it holds that

$$\sum_{i=1}^{N} (\tilde{v})_i \, (v_{\text{ker}})_i = 0.$$

We split the sum

$$\sum_{l=1}^{m_1} \sum_{i \in \mathcal{N}_l} (\tilde{v})_i \, (v_{\text{ker}})_i + \sum_{i \in \mathcal{N}_{m_1+1}} (\tilde{v})_i \, (v_{\text{ker}})_i = 0.$$

Since $(\tilde{v})_i = 0$ for all nodes $i \in \mathcal{N}_{m_1+1}$, we obtain that

$$\sum_{l=1}^{m_1} \sum_{i \in \mathcal{N}_l} (\tilde{v})_i \, (v_{\text{ker}})_i = 0 \quad \forall \tilde{v} \in \mathcal{V}_{\neq 0}. \tag{A.22}$$

Furthermore, we define the $N \times 1$ vector u_a with the entries

$$(u_a)_i = \begin{cases} 1 & \text{if } i \notin \mathcal{N}_{m_1+1}, \\ 0 & \text{if } i \in \mathcal{N}_{m_1+1}. \end{cases}$$

From the definition of the basis vectors y_l in (A.19), it follows that the vector u_a equals

$$u_a = \sum_{l=1}^{m_1} \sqrt{|\mathcal{N}_l|} y_l.$$

Thus, vector u_a is element of $\mathcal{V}_{\neq 0}$. Since the vector v_{ker} is in the kernel of the matrix B, it holds that $B v_{\text{ker}} = 0$, which implies that

$$u_a^T B v_{\text{ker}} = 0. \tag{A.23}$$

We decompose the vector v_{ker} as $v_{\text{ker}} = v_{\text{ker},a} + v_{\text{ker},b}$, where the first addend equals

$$\left(v_{\text{ker},a}\right)_i = \begin{cases} (v_{\text{ker}})_i & \text{if } i \notin \mathcal{N}_{m_1+1}, \\ 0 & \text{if } i \in \mathcal{N}_{m_1+1}, \end{cases}$$

and the second addend equals

$$\left(v_{\text{ker},b}\right)_i = \begin{cases} 0 & \text{if } i \notin \mathcal{N}_{m_1+1} \\ (v_{\text{ker}})_i & \text{if } i \in \mathcal{N}_{m_1+1}. \end{cases} \tag{A.24}$$

Then, (A.23) becomes

$$u_a^T B v_{\text{ker},a} + u_a^T B v_{\text{ker},b} = 0.$$

Since $u_a \in \mathcal{V}_{\neq 0}$ and $\mathcal{V}_{\neq 0}$ is an invariant subspace of the matrix B, it holds that $Bu_a \in \mathcal{V}_{\neq 0}$. Thus, (A.22) implies that $u_a^T B v_{\text{ker},a} = 0$, and we obtain that

$$u_a^T B v_{\text{ker},b} = 0,$$

which is equivalent to

$$\sum_{l=1}^{m_1} \sum_{i \in \mathcal{N}_l} \sum_{j=1}^{N} \beta_{ij} \left(v_{\text{ker},b}\right)_j = 0.$$

With the definition of the vector $v_{\text{ker},b}$ in (A.24), we obtain that

$$\sum_{l=1}^{m_1} \sum_{i \in \mathcal{N}_l} \sum_{j \in \mathcal{N}_{m_1+1}} \beta_{ij} \left(v_{\text{ker}}\right)_j = 0. \tag{A.25}$$

As stated by (A.21), the entries $\left(v_{\text{ker}}\right)_j$ are positive for all nodes $j \in \mathcal{N}_{m_1+1}$. Furthermore, the infection rates β_{ij} are non-negative under Assumption 2.9. Hence, (A.25) is satisfied only if $\beta_{ij} = 0$ for all nodes $j \in \mathcal{N}_{m_1+1}$ and $i \in \mathcal{N}_l$ for all subsets $l = 1, ..., m_1$. In other words, the nodes in $\mathcal{N}_{m_1+1}$ are not connected to any nodes in $\mathcal{N}_1, ..., \mathcal{N}_{m_1}$, which contradicts the irreducibility of the matrix B under Assumption 2.10. Hence, it must hold that $\mathcal{N}_{m_1+1} = \emptyset$. □

Since $\mathcal{N}_{m_1+1} = \emptyset$, it holds that $\mathcal{N}_1 \cup ... \cup \mathcal{N}_{m_1} = \mathcal{N}$. Hence, the disjoint subsets $\mathcal{N}_1$, ..., $\mathcal{N}_{m_1}$ define a partition of the set of all nodes $\mathcal{N} = \{1, ..., N\}$. To complete the proof of Theorem 2.14, we must show that the subsets $\mathcal{N}_1$, ..., $\mathcal{N}_{m_1}$ are an *equitable* partition of the infection rate matrix B. Hence, we must show that the sum of the infection rates β_{ij},

$$\sum_{j \in \mathcal{N}_l} \beta_{ij}, \tag{A.26}$$

is the same for all nodes $i \in \mathcal{N}_p$ and all cells $l, p = 1, ..., m_1$. Lemma 2.11 states that

$$\begin{aligned} \mathcal{V}_{\neq 0} &= \text{span}\left\{y_1, ..., y_{m_1}\right\} \\ &= \text{span}\left\{x_{\phi(1)}, ..., x_{\phi(m_1)}\right\}. \end{aligned}$$

Thus, there must be some nonsingular $m_1 \times m_1$ matrix H such that

$$\begin{pmatrix} x_{\phi(1)} & ... & x_{\phi(m_1)} \end{pmatrix} = \begin{pmatrix} y_1 & ... & y_{m_1} \end{pmatrix} H. \tag{A.27}$$

Since the set eigenvectors x_i and the set of vectors y_l are orthonormal, the matrix H is

orthogonal[2]. The eigendecomposition of the matrix B reads

$$\begin{aligned} B = &\begin{pmatrix} x_{\phi(1)} & \dots & x_{\phi(m_1)} \end{pmatrix} \operatorname{diag}\left(\lambda_{\phi(1)}, \dots, \lambda_{\phi(m_1)}\right) \begin{pmatrix} x_{\phi(1)}^T \\ \vdots \\ x_{\phi(m_1)}^T \end{pmatrix} \\ &+ \begin{pmatrix} x_{\phi(m_1+1)} & \dots & x_{\phi(m)} \end{pmatrix} \operatorname{diag}\left(\lambda_{\phi(m_1+1)}, \dots, \lambda_{\phi(m)}\right) \begin{pmatrix} x_{\phi(m_1+1)}^T \\ \vdots \\ x_{\phi(m)}^T \end{pmatrix} \\ &+ \begin{pmatrix} x_{\phi(m+1)} & \dots & x_{\phi(N)} \end{pmatrix} \operatorname{diag}\left(\lambda_{\phi(m+1)}, \dots, \lambda_{\phi(N)}\right) \begin{pmatrix} x_{\phi(m+1)}^T \\ \vdots \\ x_{\phi(N)}^T \end{pmatrix}. \end{aligned}$$

With (A.27), and since the eigenvalues $\lambda_{\phi(l)} = 0$ for $l = m_1 + 1, \dots, m$, we obtain that

$$\begin{aligned} B = &\begin{pmatrix} y_1 & \dots & y_{m_1} \end{pmatrix} H \operatorname{diag}\left(\lambda_{\phi(1)}, \dots, \lambda_{\phi(m_1)}\right) H^T \begin{pmatrix} y_1^T \\ \vdots \\ y_{m_1}^T \end{pmatrix} \\ &+ \begin{pmatrix} x_{\phi(m+1)} & \dots & x_{\phi(N)} \end{pmatrix} \operatorname{diag}\left(\lambda_{\phi(m+1)}, \dots, \lambda_{\phi(N)}\right) \begin{pmatrix} x_{\phi(m+1)}^T \\ \vdots \\ x_{\phi(N)}^T \end{pmatrix}. \end{aligned} \tag{A.28}$$

Consider two nodes $i \in \mathcal{N}_p$ and a subset $\mathcal{N}_l$ for some $l = 1, \dots, m_1$. Since

$$(y_l)_j = \begin{cases} \frac{1}{\sqrt{|\mathcal{N}_l|}} & \text{if } j \in \mathcal{N}_l, \\ 0 & \text{if } j \notin \mathcal{N}_l, \end{cases}$$

we can express the sum (A.26) as

$$\sum_{j \in \mathcal{N}_l} \beta_{ij} = \sqrt{|\mathcal{N}_l|} \begin{pmatrix} \beta_{i1} & \dots & \beta_{iN} \end{pmatrix} y_l.$$

Thus, with the $N \times 1$ basic vector e_i, it holds that

$$\sum_{j \in \mathcal{N}_l} \beta_{ij} = \sqrt{|\mathcal{N}_l|} e_i^T B y_l.$$

From the orthogonality of the vectors $y_1, \dots, y_{m_1}$ and from $x_{\phi(k)}^T y_l = 0$ for $k = m+1, \dots, N$, we obtain with (A.28) that

$$\sum_{j \in \mathcal{N}_l} \beta_{ij} = \sqrt{|\mathcal{N}_l|} e_i^T \begin{pmatrix} y_1 & \dots & y_{m_1} \end{pmatrix} H \operatorname{diag}\left(\lambda_{\phi(1)}, \dots, \lambda_{\phi(m_1)}\right) H^T e_{m_1 \times 1, l}, \tag{A.29}$$

[2] Since $x_i^T x_j = 1$ if $i = j$ and $x_i^T x_j = 0$ if $i \neq j$ and analogously for the vectors y_i, y_j, it follows from $x_i^T x_j = y_i^T H^T H y_j$ that the matrix H is orthogonal.

where the l-th entry of the $m_1 \times 1$ vector $e_{m_1\times 1,l}$ equals one, and the other entries of $e_{m_1\times 1,l}$ equal zero. Since node i is element of exactly one subset $\mathcal{N}_p$, it holds that

$$e_i^T \begin{pmatrix} y_1 & \dots & y_{m_1} \end{pmatrix} = \frac{1}{\sqrt{|\mathcal{N}_p|}} \tilde{e}_{m_1\times 1,p}^T.$$

Then, (A.29) becomes

$$\sum_{j\in\mathcal{N}_l} \beta_{ij} = d_{il},$$

where

$$d_{il} = \frac{\sqrt{|\mathcal{N}_l|}}{\sqrt{|\mathcal{N}_p|}} e_{m_1\times 1,p}^T H \operatorname{diag}\left(\lambda_{\phi(1)},\dots,\lambda_{\phi(m_1)}\right) H^T e_{m_1\times 1,l}$$

is the same for all nodes $i \in \mathcal{N}_p$, which completes the proof.

A.4. PROOF OF THEOREM 2.16

By assumption, the infection rates $\beta_{i,j}$ are the same for all nodes i in any cell $\mathcal{N}_l$ and all nodes j in any cell $\mathcal{N}_p$. Thus, with the definition of the vectors y_1, ..., y_r in (2.19), the symmetric infection rate matrix equals

$$B = \begin{pmatrix} y_1 & \dots & y_r \end{pmatrix} \tilde{B}_{\mathcal{V}_{\neq 0}} \begin{pmatrix} y_1^T \\ \vdots \\ y_r^T \end{pmatrix} \tag{A.30}$$

for some symmetric $r \times r$ matrix $\tilde{B}_{\mathcal{V}_{\neq 0}}$. Since the kernel $\ker(B)$ is the orthogonal complement of the subspace $\mathcal{V}_{\neq 0}$, it holds that $\mathbb{R}^N = \mathcal{V}_{\neq 0} \oplus \ker(B)$. Thus, any viral state vector $v(t) \in [0,1]^N$ can be decomposed as $v(t) = \tilde{v}(t) + v_{\ker}(t)$, where $\tilde{v}(t) \in \mathcal{V}_{\neq 0}$ and $v_{\ker}(t) \in \ker(B)$. With the decomposition $v(t) = \tilde{v}(t) + v_{\ker}(t)$, NIMFA (1.2) becomes

$$\begin{aligned} \frac{dv(t)}{dt} &= -S\left(\tilde{v}(t) + v_{\ker}(t)\right) + \operatorname{diag}\left(u - \tilde{v}(t) - v_{\ker}(t)\right) B\left(\tilde{v}(t) + v_{\ker}(t)\right) \\ &= -S\tilde{v}(t) - Sv_{\ker}(t) + \operatorname{diag}\left(u - \tilde{v}(t) - v_{\ker}(t)\right) B\tilde{v}(t), \end{aligned}$$

where the second equality follows from $Bv_{\ker}(t) = 0$. Further rearrangement yields that

$$\frac{dv(t)}{dt} = (B - S)\,\tilde{v}(t) - \operatorname{diag}\left(\tilde{v}(t)\right) B\tilde{v}(t) - Sv_{\ker}(t) - \operatorname{diag}\left(v_{\ker}(t)\right) B\tilde{v}(t). \tag{A.31}$$

We decompose the derivative $dv(t)/dt$ into two addends, by making use of two lemmas:

Lemma A.5. *Suppose that the assumptions in Theorem 2.16 hold true. Then, if $\tilde{v} \in \mathcal{V}_{\neq 0}$, the vector*

$$B\tilde{v} - S\tilde{v} - \operatorname{diag}\left(\tilde{v}\right) B\tilde{v} \tag{A.32}$$

is element of $\mathcal{V}_{\neq 0}$.

Proof. We consider the three addends of the vector (A.32) separately. First, (A.30) shows that the addend $B\tilde{v}$ is element of $\mathcal{V}_{\neq 0}$ if $\tilde{v} \in \mathcal{V}_{\neq 0}$. Second, we consider the addend $S\tilde{v}$. By assumption, the curing rates δ_i are the same for all nodes i in the same cell $\mathcal{N}_l$. Thus, we obtain from the definition of the agitation modes y_l in (2.19) that

$$Sy_l = \delta_i y_l \tag{A.33}$$

for $l = 1, ..., r$, where i denotes an arbitrary node in cell $\mathcal{N}_l$. Since the agitation modes y_1, ..., y_r span the subspace $\mathcal{V}_{\neq 0}$, (A.33) implies that $S\tilde{v}$ if $\tilde{v} \in \mathcal{V}_{\neq 0}$.

Third, we consider the addend $\operatorname{diag}(\tilde{v})\, B\tilde{v}$. Since $\tilde{v} \in \mathcal{V}_{\neq 0}$, it holds that

$$\tilde{v} = \sum_{l=1}^{r} \left(y_l^T \tilde{v}\right) y_l.$$

Similarly, since $B\tilde{v} \in \mathcal{V}_{\neq 0}$, it holds that

$$B\tilde{v} = \sum_{l=1}^{r} \left(y_l^T B\tilde{v}\right) y_l. \tag{A.34}$$

Thus, we obtain that

$$\operatorname{diag}(\tilde{v})\, B\tilde{v} = \sum_{l=1}^{r} \sum_{p=1}^{r} \left(y_l^T \tilde{v}\right) \left(y_p^T B\tilde{v}\right) \operatorname{diag}(y_l)\, y_p. \tag{A.35}$$

From the definition of the vectors y_l in (2.19) it follows that

$$\operatorname{diag}\left(y_l\right) y_p = \begin{cases} y_l^2 & \text{if} \quad l = p, \\ 0 & \text{if} \quad l \neq p, \end{cases}$$

where the $N \times 1$ vector $y_l^2 = \left((y_l)_1^2, ..., (y_l)_N^2\right)^T$ denotes Hadamard product of the vector y_l with itself. Thus, (A.35) becomes

$$\operatorname{diag}(\tilde{v})\, B\tilde{v} = \sum_{l=1}^{r} \left(y_l^T \tilde{v}\right) \left(y_l^T B\tilde{v}\right) y_l^2. \tag{A.36}$$

With (2.19), the Hadamard product y_l^2 equals

$$(y_l)_i^2 = \begin{cases} \frac{1}{|\mathcal{N}_l|} & \text{if} \quad i \in \mathcal{N}_l, \\ 0 & \text{if} \quad i \notin \mathcal{N}_l, \end{cases}$$

which implies that $(y_l)^2 = y_l / \sqrt{|\mathcal{N}_l|}$ and yields with (A.36) that

$$\operatorname{diag}(\tilde{v})\, B\tilde{v} = \sum_{l=1}^{r} \frac{\left(y_l^T \tilde{v}\right) \left(y_l^T B\tilde{v}\right)}{\sqrt{|\mathcal{N}_l|}} y_l.$$

Thus, the vector $\operatorname{diag}(\tilde{v})\, B\tilde{v}$ is a linear combination of the vectors $y_1, ..., y_r$, which implies that $\operatorname{diag}(\tilde{v})\, B\tilde{v}\mathcal{V}_{\neq 0}$. Hence, we have shown that all three addends of the vector (A.32) are in $\mathcal{V}_{\neq 0}$, which completes the proof. □

A

Lemma A.6. *Suppose that the assumptions in Theorem 2.16 hold true. Then, if* $\tilde{v} \in \mathcal{V}_{\neq 0}$ *and* $v_{\ker} \in \ker(B)$*, the vector*

$$S v_{\ker} + \operatorname{diag}(v_{\ker}) B \tilde{v} \tag{A.37}$$

is element of $\ker(B)$.

Proof. The kernel $\ker(B)$ is the orthogonal complement of the subspace $\mathcal{V}_{\neq 0}$. Thus, the vector (A.37) is element of $\ker(B)$ if $S v_{\ker}$ is orthogonal to every basis vector $y_1, \ldots, y_r$ of the subspace $\mathcal{V}_{\neq 0}$. We show separately that both addends of the vector (A.37) are orthogonal to every vector $y_1, \ldots, y_r$. First, for any $l = 1, \ldots, r$, we obtain for the first addend in (A.37) that

$$y_l^T S v_{\ker} = \left(S y_l\right)^T v_{\ker},$$

since the matrix S is symmetric. With (A.33), we obtain for an arbitrary node $i \in \mathcal{N}_l$ that

$$y_l^T S v_{\ker} = \delta_i y_l^T v_{\ker} = 0.$$

Thus, the addend $S v_{\ker}$ is element of $\ker(B)$.

Second, for any $l = 1, \ldots, r$, we obtain for the second addend in (A.37) with (A.34) that

$$\begin{aligned} y_l^T \operatorname{diag}(v_{\ker}) B \tilde{v} &= \sum_{q=1}^{r} \left(y_l^T B \tilde{v}\right) y_l^T \operatorname{diag}(v_{\ker}) y_q \\ &= \sum_{q=1}^{r} \left(y_q^T B \tilde{v}\right) v_{\ker}^T \operatorname{diag}\left(y_l\right) y_q. \end{aligned}$$

Analogous steps as in the proof of Lemma A.5 yield that

$$y_l^T \operatorname{diag}(v_{\ker}) B \tilde{v} = \frac{\left(y_l^T B \tilde{v}\right)}{\sqrt{|\mathcal{N}_l|}} v_{\ker}^T y_l.$$

Thus, by the orthogonality of the vectors $v_{\ker}$ and y_l,

$$y_l^T \operatorname{diag}(v_{\ker}) B \tilde{v} = 0,$$

which completes the proof. □

With Lemma A.5 and Lemma A.6, we obtain from (A.31) that

$$\frac{d v(t)}{dt} = \frac{d \tilde{v}(t)}{dt} + \frac{d v_{\ker}(t)}{dt},$$

where

$$\frac{d \tilde{v}(t)}{dt} = -S \tilde{v}(t) + \operatorname{diag}(u - \tilde{v}(t)) B \tilde{v}(t)$$

and

$$\frac{d v_{\ker}(t)}{dt} = -S v_{\ker}(t) - \operatorname{diag}(v_{\ker}(t)) B \tilde{v}(t),$$

which completes the proof, since

$$\operatorname{diag}(v_{\ker}(t)) B \tilde{v}(t) = \operatorname{diag}(B \tilde{v}(t)) v_{\ker}(t).$$

A.5. PROOF OF THEOREM 2.17

Since the spreading rates are homogeneous, $\beta_{ij} = \beta$ and $\delta_i = \delta$, the infection rate matrix equals

$$B = \beta u u^T, \tag{A.38}$$

and the curing rate matrix equals

$$S = \delta I. \tag{A.39}$$

Thus, with $r = 1$ cell $\mathcal{N}_1 = \{1, ..., N\}$, Theorem 2.16 yields that the viral state $v(t)$ can be decomposed as $v(t) = \tilde{v}(t) + v_{\ker}(t)$. We prove Theorem 2.17 in two steps. First, we show that the projection $\tilde{v}(t)$ equals $c_1(t)v_\infty$ at every time t. Second, we prove that the projection $v_{\ker}(t)$ equals $c_2(t)y_2$ at every time t.

A.5.1. PROJECTION ON THE SUBSPACE $\mathcal{V}_{\neq 0}$

With the reduced-size curing rate matrix $S^\pi = \delta$ and the quotient matrix $B^\pi = N\beta$, Theorem 2.4 yields that the projection on the subspace $\mathcal{V}_{\neq 0}$ satisfies $\tilde{v}(t) = v^\pi(t)u$. The evolution (2.12) of the reduced-size, scalar viral state $v^\pi(t)$ becomes

$$\frac{dv^\pi(t)}{dt} = -\delta v^\pi(t) + \big(1 - v^\pi(t)\big) N\beta v^\pi(t). \tag{A.40}$$

We consider two cases for the value of the spreading parameters β and δ.

1. If $\delta \neq \beta N$, then the solution of (A.40) equals [59]

   $$v^\pi(t) = \frac{v^\pi_\infty}{2}\left(1 + \tanh\left(\frac{w}{2}t + \Upsilon_1(0)\right)\right)$$

   with the reduced-size steady state $v^\pi_\infty = 1 - \frac{\delta}{\beta N}$, the viral slope $w = \beta N - \delta$ and the constant

   $$\Upsilon_1(0) = \operatorname{arctanh}\left(2\frac{v(0)}{v^\pi_\infty} - 1\right).$$

   Thus, the projection $\tilde{v}(t) = v^\pi(t)u$ is equal to $c_1(t)y_1$ at every time t.

2. If $\delta = \beta N$, then the differential equation (A.40) reduces to

   $$\frac{dv^\pi(t)}{dt} = -\delta\left(v^\pi(t)\right)^2,$$

   whose solution equals

   $$v^\pi(t) = \left(\delta t + \frac{1}{v^\pi(0)}\right)^{-1}.$$

   With $v^\pi(0) = y_1^T v(0)/\sqrt{N}$, we arrive at the closed-form expression (2.25) for the function $c_1(t)$.

A

A.5.2. PROJECTION ON THE KERNEL $\ker(B)$

With (A.38) and (A.39), Theorem 2.16 yields that the projection $v_{\ker}(t)$ obeys

$$\frac{dv_{\ker}(t)}{dt} = -\left(\delta I + \beta \operatorname{diag}\left(uu^T \tilde{v}(t)\right)\right) v_{\ker}(t).$$

Since $\tilde{v}(t) = c_1(t)y_1$ and $(y_1)_i = 1/\sqrt{N}$ for all nodes i, we obtain that

$$\begin{aligned}\frac{dv_{\ker}(t)}{dt} &= -\left(\delta I + \beta\sqrt{N}c_1(t) I\right) v_{\ker}(t) \\ &= -\left(\delta + \beta\sqrt{N}c_1(t)\right) v_{\ker}(t). \end{aligned} \tag{A.41}$$

For any initial condition $v_{\ker}(0) \in \ker(B)$, the right side of (A.41) is in the one-dimensional subspace $\operatorname{span}\{v_{\ker}(0)\}$. Thus, the projection $v_{\ker}(t)$ obeys $v_{\ker}(t) = c_2(t)\, v_{\ker}(0)$. We solve (A.41) in two steps. First, we compute the initial condition $v_{\ker}(0)$. Since $v(0) = v_{\ker}(0) + c_1(0)y_1$, the initial condition $v_{\ker}(0)$ is obtained as

$$\begin{aligned} v_{\ker}(0) &= v(0) - c_1(0)y_1 \\ &= v(0) - \left(y_1^T v(0)\right) y_1. \end{aligned}$$

Hence, it follows that

$$v_{\ker}(0) = \left(I - y_1 y_1^T\right) v(0).$$

Second, using $v_{\ker}(t) = c_2(t)\, v_{\ker}(0)$, we project (A.41) on the initial condition $v_{\ker}(0)$ to obtain that the scalar function $c_2(t)$ obeys the linear differential equation

$$\frac{dc_2(t)}{dt} = -\delta c_2(t) - \beta\sqrt{N}c_1(t)c_2(t). \tag{A.42}$$

Again, we consider two cases for the value of the spreading parameters β and δ.

1. If $\delta \neq \beta N$, then we obtain with the function $c_1(t)$ given by (2.22) that

   $$\frac{dc_2(t)}{dt} = -\delta c_2(t) - \frac{w}{2}\left(1 + \tanh\left(\frac{w}{2}t + \Upsilon_1(0)\right)\right) c_2(t).$$

   Hence, with the constant $\Phi = w/2 + \delta$, it follows that

   $$\log(c_2(t)) = -\int_0^t \left(\Phi + \frac{w}{2}\tanh\left(\frac{w}{2}\xi + \Upsilon_1(0)\right)\right) d\xi.$$

   The integral of the hyperbolic tangent equals to the logarithm of the hyperbolic cosine [282],

   $$\int \tanh(\xi)\, d\xi = \log(\cosh(\xi)),$$

   which yields that

   $$\begin{aligned}\log(c_2(t)) &= -\Phi t - \frac{w}{2}\frac{2}{w}\log\left(\cosh\left(\frac{w}{2}t + \Upsilon_1(0)\right)\right) + K(0) \\ &= -\Phi t - \log\left(\cosh\left(\frac{w}{2}t + \Upsilon_1(0)\right)\right) + K(0)\end{aligned}$$

for some constant $K(0)$, which is equivalent to

$$\log(c_2(t)) = -\Phi t + \log\left(\cosh\left(\frac{w}{2}t + \Upsilon_1(0)\right)^{-1}\right) + K(0).$$

With the hyperbolic secant $\operatorname{sech}(x) = \cosh(x)^{-1}$, we obtain that

$$c_2(t) = \Upsilon_2(0)e^{-\Phi t}\operatorname{sech}\left(\frac{w}{2}t + \Upsilon_1(0)\right), \tag{A.43}$$

where $\Upsilon_2(0) = \exp(K(0))$. At the initial time $t = 0$, (A.43) becomes

$$c_2(0) = \Upsilon_2(0)\operatorname{sech}(\Upsilon_1(0)),$$

and it holds that

$$c_2(0) = \frac{v_{\text{ker}}^T(0)v(0)}{\|v_{\text{ker}}(0)\|_2^2}. \tag{A.44}$$

Thus, with $\operatorname{sech}(x) = \cosh(x)^{-1}$, we obtain the constant $\Upsilon_2(0)$ as (2.24), which completes the proof.

2. If $\delta = \beta N$, then the function $c_1(t)$ is given by (2.25). Thus, the differential equation (A.42) for the function $c_2(t)$ becomes

$$\frac{dc_2(t)}{dt} = -\delta c_2(t) - \beta N\left(\delta t + \frac{\sqrt{N}}{y_1^T v(0)}\right)^{-1} c_2(t).$$

Thus, it holds that

$$\log(c_2(t)) = -\int_0^t \delta + \beta N\left(\delta\xi + \frac{\sqrt{N}}{y_1^T v(0)}\right)^{-1} d\xi.$$

Since

$$\int\left(\delta\xi + \frac{\sqrt{N}}{y_1^T v(0)}\right)^{-1} d\xi = \frac{1}{\delta}\log\left(\delta\xi + \frac{\sqrt{N}}{y_1^T v(0)}\right),$$

we obtain for some constant $K_2(0)$ that

$$\begin{aligned}\log(c_2(t)) &= -\delta t - \frac{\beta N}{\delta}\log\left(\delta t + \frac{\sqrt{N}}{y_1^T v(0)}\right) + K_2(0)\\ &= -\delta t + \log\left(\left(\delta t + \frac{\sqrt{N}}{y_1^T v(0)}\right)^{-\frac{\beta N}{\delta}}\right) + K_2(0).\end{aligned}$$

Hence, the function $c_2(t)$ equals

$$c_2(t) = \tilde{\Upsilon}_2(0)e^{-\delta t}\left(\delta t + \frac{\sqrt{N}}{y_1^T v(0)}\right)^{-\frac{\beta N}{\delta}},$$

where $\tilde{\Upsilon}_2(0) = e^{K_2(0)}$. At the initial time $t = 0$, we obtain that

$$c_2(0) = \tilde{\Upsilon}_2(0) \left(\frac{\sqrt{N}}{y_1^T v(0)} \right)^{-\frac{\beta N}{\delta}}.$$

Thus, it holds that

$$\begin{aligned} \tilde{\Upsilon}_2(0) &= c_2(0) \left(\frac{\sqrt{N}}{y_1^T v(0)} \right)^{\frac{\beta N}{\delta}} \\ &= \frac{v_{\ker}^T(0) v(0)}{\| v_{\ker}(0) \|_2^2} \left(\frac{\sqrt{N}}{y_1^T v(0)} \right)^{\frac{\beta N}{\delta}}, \end{aligned}$$

where the second equality follows from (A.44).

A.6. PROOF OF THEOREM 2.18

The viral state $\tilde{v}_i(t)$ evolves as

$$\frac{d\tilde{v}_i(t)}{dt} = \tilde{f}_{\text{NIMFA},i}(\tilde{v}(t)),$$

where we define, for every node i,

$$\tilde{f}_{\text{NIMFA},i}(\tilde{v}(t)) = -\tilde{\delta}_i \tilde{v}_i(t) + (1 - \tilde{v}_i(t)) \sum_{j=1}^{N} \tilde{\beta}_{ij} \tilde{v}_j(t). \tag{A.45}$$

Since $\tilde{\beta}_{ij} \geq \beta_{ij}$ and $\tilde{\delta}_i \leq \delta_i$ for all nodes i, we obtain an upper bound on NIMFA (1.1) as

$$\begin{aligned} \frac{dv_i(t)}{dt} &\leq -\tilde{\delta}_i v_i(t) + (1 - v_i(t)) \sum_{j=1}^{N} \tilde{\beta}_{ij} v_j(t) \\ &= \tilde{f}_{\text{NIMFA},i}(v(t)). \end{aligned}$$

Since $dv_i(t)/dt \leq \tilde{f}_{\text{NIMFA},i}(v(t))$, we can apply the *Kamke-Müller condition* [283, 284], see also [7]: If $v \leq \tilde{v}$ and $v_i = \tilde{v}_i$ implies that $\tilde{f}_{\text{NIMFA},i}(v) \leq \tilde{f}_{\text{NIMFA},i}(\tilde{v})$ for all nodes i, then $v(0) \leq \tilde{v}(0)$ implies that $v(t) \leq \tilde{v}(t)$ at every time $t \geq 0$.

Thus, it remains to show that $v \leq \tilde{v}$ and $v_i = \tilde{v}_i$ implies that $\tilde{f}_{\text{NIMFA},i}(v) \leq \tilde{f}_{\text{NIMFA},i}(\tilde{v})$. From (A.45), we obtain that

$$\tilde{f}_{\text{NIMFA},i}(v) - \tilde{f}_{\text{NIMFA},i}(\tilde{v}) = -\tilde{\delta}_i (v_i - \tilde{v}_i) + (1 - v_i) \sum_{j=1}^{N} \tilde{\beta}_{ij} v_j - (1 - \tilde{v}_i) \sum_{j=1}^{N} \tilde{\beta}_{ij} \tilde{v}_j.$$

From $v_i = \tilde{v}_i$, it follows that

$$\tilde{f}_{\text{NIMFA},i}(v) - \tilde{f}_{\text{NIMFA},i}(\tilde{v}) = (1 - v_i) \sum_{j=1}^{N} \tilde{\beta}_{ij} v_j - (1 - v_i) \sum_{j=1}^{N} \tilde{\beta}_{ij} \tilde{v}_j,$$

which yields that

$$\begin{aligned}\tilde{f}_{\text{NIMFA},i}(v) - \tilde{f}_{\text{NIMFA},i}(\tilde{v}) &= \sum_{j=1}^{N} \tilde{\beta}_{ij}\left(v_j - v_i v_j - \tilde{v}_j + v_i \tilde{v}_j\right) \\ &= \sum_{j=1}^{N} \tilde{\beta}_{ij}(1 - v_i)\left(v_j - \tilde{v}_j\right).\end{aligned}$$

Since $\left(v_j - \tilde{v}_j\right) \leq 0$, we obtain that $\tilde{f}_{\text{NIMFA},i}(v) \leq \tilde{f}_{\text{NIMFA},i}(\tilde{v})$, which completes the proof.

A.7. PROOF OF THEOREM 2.19

Here, we prove that $v_i(t) \geq v_{\text{lb},l}(t)$ for all nodes i in any cell $\mathcal{N}_l$. The proof of $v_i(t) \leq v_{\text{ub},l}(t)$ follows analogously. First, we define the curing rates $\tilde{\delta}_{\text{max},i}$ by

$$\tilde{\delta}_{\text{max},i} = \delta_{\text{max},l}$$

for all nodes i in any cell $\mathcal{N}_p$. Thus, (2.28) implies that $\tilde{\delta}_{\text{max},i} \geq \delta_i$ for all nodes $i = 1, \ldots, N$.

Lemma A.7. *For all nodes i, j, there are infection rates $\tilde{\beta}_{ij}$, which satisfy $\tilde{\beta}_{ij} \leq \beta_{ij}$ and*

$$\sum_{j \in \mathcal{N}_l} \tilde{\beta}_{ij} = d_{\text{min},pl} \tag{A.46}$$

for all nodes i in any cell $\mathcal{N}_p$ and all cells $\mathcal{N}_l$.

Proof. With the definition of the lower bound $d_{\text{min},pl}$ in (2.26), we obtain that (A.46) is satisfied if

$$\sum_{j \in \mathcal{N}_l} \tilde{\beta}_{ij} = \min_{i \in \mathcal{N}_p} \sum_{k \in \mathcal{N}_l} \beta_{ik}. \tag{A.47}$$

Denote the difference of the infection rates by $\varepsilon_{ij} = \beta_{ij} - \tilde{\beta}_{ij}$. Thus, $\tilde{\beta}_{ij} \leq \beta_{ij}$ and $\tilde{\beta}_{ij} \geq 0$ holds if and only if $0 \leq \varepsilon_{ij} \leq \beta_{ij}$. We obtain from (A.47) that the differences ε_{ij} must satisfy

$$\sum_{j \in \mathcal{N}_l} \beta_{ij} - \sum_{j \in \mathcal{N}_l} \varepsilon_{ij} = \min_{i \in \mathcal{N}_p} \sum_{k \in \mathcal{N}_l} \beta_{ik},$$

which yields that

$$\sum_{j \in \mathcal{N}_l} \varepsilon_{ij} = \sum_{j \in \mathcal{N}_l} \beta_{ij} - \min_{i \in \mathcal{N}_p} \sum_{k \in \mathcal{N}_l} \beta_{ik}. \tag{A.48}$$

To complete the proof, we must show that there exist some $\varepsilon_{ij} \in [0, \beta_{ij}]$ that solve (A.48). Since

$$\sum_{j \in \mathcal{N}_l} \beta_{ij} \geq \min_{i \in \mathcal{N}_p} \sum_{k \in \mathcal{N}_l} \beta_{ik}$$

and $\beta_{ij} \geq 0$, the right side of (A.48) is some value in $[0, \sum_{j \in \mathcal{N}_l} \beta_{ij}]$. Since the feasible values of the infection rate differences ε_{ij} are in the interval $[0, \beta_{ij}]$, the left side of (A.48) may attain an arbitrary value in $[0, \sum_{j \in \mathcal{N}_l} \beta_{ij}]$. Thus, there are some infection rate differences $\varepsilon_{ij} \in [0, \beta_{ij}]$ that solve (A.48), which completes the proof. □

Lemma A.7 states the existence of an $N \times N$ matrix $\tilde{B}_{\min}$ whose elements $\tilde{\beta}_{\min,ij}$ satisfy $\tilde{\beta}_{ij} \leq \beta_{ij}$ and (A.46). Thus, π is an equitable partition of the matrix $\tilde{B}_{\min}$. We define the $N \times 1$ viral state $\tilde{v}_{\mathrm{lb}}(t)$ as

$$\frac{d\tilde{v}_{\mathrm{lb}}(t)}{dt} = -\operatorname{diag}\left(\tilde{\delta}_{\max,1},\ldots,\tilde{\delta}_{\max,N}\right)\tilde{v}_{\mathrm{lb}}(t) + \operatorname{diag}\left(u - \tilde{v}_{\mathrm{lb}}(t)\right)\tilde{B}_{\min}\tilde{v}_{\mathrm{lb}}(t) \tag{A.49}$$

with the initial viral state

$$\tilde{v}_{\mathrm{lb},i}(0) = \min_{j\in\mathcal{N}_p} v_j(0)$$

for all nodes i in any cell $\mathcal{N}_p$. Since $\tilde{v}_{\mathrm{lb},i}(0) \leq v_i(0)$, $\tilde{\delta}_{\max,i} \geq \delta_i$ and $\tilde{\beta}_{\min,ij} \leq \beta_{ij}$ for all nodes i, j, Theorem 2.18 yields that $\tilde{v}_{\mathrm{lb},i}(t) \leq v_i(t)$ for every node i at every time t. Furthermore, Theorem 2.4 yields that the N-dimensional dynamics of the viral state $\tilde{v}_{\mathrm{lb}}(t)$ in (A.49) can be reduced to the r-dimensional dynamics of the reduced-size viral state $v_{\mathrm{lb}}(t)$ in (2.29), which completes the proof.

B

APPENDIX TO CHAPTER 3

B.1. NOMENCLATURE

The following nomenclature is confined to the derivations in this appendix. The eigenvalues of the effective infection rate matrix W are denoted, in decreasing order, by $|\lambda_1| \geq \ldots \geq |\lambda_N|$. The principal eigenvector of unit length of the matrix W is denoted by x_1 and satisfies $Wx_1 = \lambda_1 x_1$. The largest and smallest curing rate of δ_1, ..., δ_N are denoted by $\delta_{\max}$ and $\delta_{\min}$, respectively. The numerical radius $r(M)$ for an $N \times N$ matrix M is defined as [285]

$$r(M) = \max_{z \in \mathbb{C}^N} \left| \frac{z^H M z}{z^H z} \right|,$$

where z^H is the conjugate transpose of a complex $N \times 1$ vector z. For a square matrix M, we denote the 2-norm by $\|M\|_2$, which equals the largest singular value of M. In particular, it holds that the 2-norm of the curing rate matrix S equals $\|S\|_2 = \delta_{\max}$.

B.2. PROOF OF THEOREM 3.4

The steady-state v_∞ solely depends on the effective infection rate matrix W: By left-multiplication of (1.5) with the diagonal matrix S^{-1}, we obtain that

$$(W - I)\, v_\infty = \operatorname{diag}(v_\infty)\, W v_\infty. \tag{B.1}$$

In general, the effective infection rate matrix W, defined in (3.1) as $W = S^{-1}B$, is asymmetric, which prevents a straightforward adaptation of the proof in [70, Lemma 4]. However, the matrix W is similar to the matrix

$$\begin{aligned} \tilde{W} &= S^{-\frac{1}{2}} B S^{-\frac{1}{2}} \\ &= S^{\frac{1}{2}} W S^{-\frac{1}{2}}. \end{aligned} \tag{B.2}$$

Since the infection rate matrix B is symmetric under Assumption 3.3, the matrix $\tilde{W}$ is symmetric. Hence, the matrix $\tilde{W}$, and also the effective infection rate matrix W, are

diagonalisable. With (B.2), we write the steady-state (B.1) with respect to the symmetric matrix $\tilde{W}$ as

$$\left(\tilde{W} - I\right) S^{\frac{1}{2}} v_\infty = \operatorname{diag}(v_\infty)\, \tilde{W} S^{\frac{1}{2}} v_\infty. \tag{B.3}$$

We decompose the matrix $\tilde{W}$ as

$$\tilde{W} = \lambda_1 \tilde{x}_1^T \tilde{x}_1 + \sum_{k=2}^{N} \lambda_k \tilde{x}_k^T \tilde{x}_k, \tag{B.4}$$

where the eigenvalues of $\tilde{W}$ are real and equal to $\lambda_1 > \lambda_2 \geq ... \geq \lambda_N$ with the corresponding normalized eigenvectors denoted by $\tilde{x}_1, ..., \tilde{x}_N$. Then, the steady-state vector v_∞ can be expressed as linear combination

$$v_\infty = \sum_{l=1}^{N} \psi_l \tilde{x}_l,$$

where the coefficients equal $\psi_l = v_\infty^T \tilde{x}_l$. To prove Theorem 3.4, we would like to express the coefficients $\psi_1, ..., \psi_N$ as a power series around $R_0 = 1$. However, in the limit process $(B, S) \to (B^*, S^*)$, the eigenvectors $\tilde{x}_1, ..., \tilde{x}_N$ of the matrix $\tilde{W}$ are not necessarily constant. Hence, the coefficients ψ_l depend on the full matrix $\tilde{W}$ and not only on the basic reproduction number R_0. To overcome the challenge of non-constant eigenvectors $\tilde{x}_1, ..., \tilde{x}_N$ in the limit process $(B, S) \to (B^*, S^*)$, we define the $N \times N$ symmetric auxiliary matrix

$$M(z) = z \tilde{x}_1^T \tilde{x}_1 + \sum_{k=2}^{N} \lambda_k \tilde{x}_k^T \tilde{x}_k \tag{B.5}$$

for a scalar $z \geq 1$. Thus, the matrix $M(z)$ is obtained from the matrix $\tilde{W}$ by replacing the largest eigenvalue λ_1 of $\tilde{W}$ by z. In particular, the definition of the matrix $M(z)$ in (B.5) and (B.4) imply that $M(\lambda_1) = \tilde{W}$. When the matrix $\tilde{W}$ is formally replaced by the matrix $M(z)$, the steady-state equation (B.3) becomes

$$(M(z) - I)\, S^{\frac{1}{2}} \tilde{v}(z) = \operatorname{diag}(\tilde{v}(z))\, M(z) S^{\frac{1}{2}} \tilde{v}(z) \tag{B.6}$$

where the $N \times 1$ vector $\tilde{v}(z)$ denotes the solution of (B.6). Since $M(R_0) = \tilde{W}$, the solution of (B.6) at $z = R_0$ and the solution to (B.3) coincide, i.e., $\tilde{v}(R_0) = v_\infty$. Lemma B.1 expresses the solution of the equation (B.6) as a power series.

Lemma B.1. *Suppose that Assumptions 3.1 and 3.3 hold. If (B, S) is sufficiently close to (B^*, S^*), then the $N \times 1$ vector $\tilde{v}(z)$ which satisfies (B.6) equals*

$$\tilde{v}(z) = (z-1) \left(\sum_{l=1}^{N} \frac{1}{\sqrt{\delta_l}} (\tilde{x}_1)_l^3 \right)^{-1} S^{-\frac{1}{2}} \tilde{x}_1 + \phi(z), \tag{B.7}$$

where the $N \times 1$ vector $\phi(z)$ satisfies $\|\phi(z)\|_2 \leq \sigma(B, S)(z-1)^2$ for some scalar $\sigma(B, S)$ when z approaches 1 from above.

Proof. The proof is an adaptation of the proof [70, Lemma 4]. We express the solution $\tilde{v}(z)$ of (B.6) as linear combination of the vectors $S^{-\frac{1}{2}}\tilde{x}_1, ..., S^{-\frac{1}{2}}\tilde{x}_N$, i.e.,

$$\tilde{v}(z) = \sum_{k=1}^{N} \psi_k(z) S^{-\frac{1}{2}} \tilde{x}_k. \tag{B.8}$$

Since the diagonal matrix $S^{-\frac{1}{2}}$ is full rank, the vectors $\left(S^{-\frac{1}{2}}\tilde{x}_k\right)$, where $k = 1, ..., N$, are linearly independent. Furthermore, we express the coefficients $\psi_k(z)$ as a power series

$$\psi_k(z) = \sum_{j=0}^{\infty} g_j(k)\,(z-1)^j, \tag{B.9}$$

where $g_0(k) = 0$ for every $k = 1, ..., N$, since [18] it holds that $\tilde{v}(z) = 0$ when $z = 1$. We denote the eigenvalues of the matrix $M(z)$ by

$$\lambda_k(z) = \begin{cases} z & \text{if} \quad k = 1, \\ \lambda_k & \text{if} \quad k \geq 2. \end{cases} \tag{B.10}$$

By substituting (B.8) into (B.6), we obtain that

$$\sum_{k=1}^{N} (\lambda_k(z) - 1)\,\psi_k(z)\tilde{x}_k = \operatorname{diag}\left(\sum_{l=1}^{N} \psi_l(z)\tilde{x}_l\right) S^{-\frac{1}{2}} \sum_{k=1}^{N} \lambda_k(z)\psi_k(z)\tilde{x}_k$$

and left-multiplying with the eigenvector $\tilde{x}_m^T$, for any $m = 1, ..., N$, yields that

$$(\lambda_m(z) - 1)\,\psi_m(z) = \sum_{n=1}^{N} (\tilde{x}_m)_n \sum_{l=1}^{N} \psi_l(z)\,(\tilde{x}_l)_n \frac{1}{\sqrt{\delta_n}} \sum_{k=1}^{N} \psi_k(z)\lambda_k(z)\,(\tilde{x}_k)_n. \tag{B.11}$$

We define

$$X(m,l,k) = \sum_{n=1}^{N} \frac{1}{\sqrt{\delta_n}} (\tilde{x}_m)_n\,(\tilde{x}_l)_n\,(\tilde{x}_k)_n.$$

Then, we rewrite (B.11) as

$$(\lambda_m(z) - 1)\,\psi_m(z) = \sum_{l=1}^{N}\sum_{k=1}^{N} \psi_l(z)\psi_k(z)\lambda_k(z)X(m,l,k). \tag{B.12}$$

First, we focus on the left-hand side of (B.12), which we denote by

$$\theta_m(z) = (\lambda_m(z) - 1)\,\psi_m(z).$$

With the power series (B.9), we obtain that

$$\theta_m(z) = (\lambda_m(z) - 1) \sum_{j=1}^{\infty} g_j(m)\,(z-1)^j.$$

B

Further rewriting yields that

$$\begin{aligned}\theta_m(z) &= (\lambda_m(z) - z + z - 1) \sum_{j=1}^{\infty} g_j(m)\,(z-1)^j \\ &= (\lambda_m(z) - z) \sum_{j=1}^{\infty} g_j(m)\,(z-1)^j + \sum_{j=1}^{\infty} g_j(m)\,(z-1)^{j+1} \\ &= \sum_{j=1}^{\infty} (\lambda_m(z) - z)\, g_j(m)\,(z-1)^j + \sum_{j=2}^{\infty} g_{j-1}(m)\,(z-1)^j . \end{aligned} \tag{B.13}$$

Second, we rearrange the right-hand side of (B.12) as

$$\theta_m(z) = \lambda_1(z) \sum_{l=1}^{N} \psi_l(z)\psi_1(z)X(m,l,1) + \sum_{l=1}^{N}\sum_{k=2}^{N} \psi_l(z)\psi_k(z)\lambda_k(z)X(m,l,k).$$

By the definition of $\lambda_k(z)$ in (B.10) it holds that $\lambda_1(z) = z$, and we obtain that

$$\theta_m(z) = (z-1) \sum_{l=1}^{N} \psi_l(z)\psi_1(z)X(m,l,1) + \sum_{l=1}^{N}\sum_{k=1}^{N} \psi_l(z)\psi_k(z)\tilde{\lambda}_k X(m,l,k), \tag{B.14}$$

where

$$\tilde{\lambda}_k = \begin{cases} 1 & \text{if} \quad k = 1, \\ \lambda_k & \text{if} \quad k \geq 2. \end{cases}$$

Introducing the power series (B.9) into (B.14) and executing the Cauchy product for $\psi_l(z)\psi_k(z)$ yields that

$$\begin{aligned}\theta_m(z) = &\sum_{j=1}^{\infty} \left(\sum_{n=1}^{j-1} \sum_{l=1}^{N} g_{j-n}(1) g_n(l) X(m,l,1) \right) (z-1)^{j+1} \\ &+ \sum_{j=1}^{\infty} \left(\sum_{n=1}^{j-1} \sum_{l=1}^{N} \sum_{k=1}^{N} g_{j-n}(l) g_n(k) \tilde{\lambda}_k X(m,l,k) \right) (z-1)^j .\end{aligned}$$

We shift the index j in the first term and obtain that

$$\begin{aligned}\theta_m(z) = &\sum_{j=2}^{\infty} \left(\sum_{n=1}^{j-2} \sum_{l=1}^{N} g_{j-1-n}(1) g_n(l) X(m,l,1) \right) (z-1)^j \\ &+ \sum_{j=1}^{\infty} \left(\sum_{n=1}^{j-1} \sum_{l=1}^{N} \sum_{k=1}^{N} g_{j-n}(l) g_n(k) \tilde{\lambda}_k X(m,l,k) \right) (z-1)^j .\end{aligned} \tag{B.15}$$

Finally, we equate powers in $(z-1)^j$ in (B.13) and (B.15), which yields for $j = 1$ that

$$(\lambda_m(z) - z)\, g_1(m) = 0 \tag{B.16}$$

for every $m = 1, \ldots, N$. The spectral radius of the limit W^* of the effective infection rate matrix W equals 1. Furthermore, the limit W^* is a non-negative and irreducible matrix.

Thus, the eigenvalues of the limit W^* obey $\lambda_1^* = 1 > |\lambda_m^*|$ for every $m \geq 2$, which implies that $|\lambda_m| < 1$ for every $m \geq 2$ provided that (B, S) is sufficiently close to (B^*, S^*). With the definition of $\lambda_m(z)$ in (B.10), we obtain from (B.16) that $g_1(m) = 0$ when $m \geq 2$ provided that (B, S) is sufficiently close to (B^*, S^*), since $z \geq 1$.

For $j \geq 2$, equating powers in (B.15) yields that

$$(\lambda_m(z) - z)\, g_j(m) + g_{j-1}(m) = \sum_{n=1}^{j-2} \sum_{l=1}^{N} g_{j-1-n}(1) g_n(l) X(m,l,1) + \sum_{n=1}^{j-1} \sum_{l=1}^{N} \sum_{k=1}^{N} g_{j-n}(l) g_n(k) \tilde{\lambda}_k X(m,l,k). \tag{B.17}$$

In particular, for the case $j = 2$, we obtain that

$$\begin{aligned}(\lambda_m(z) - z)\, g_2(m) + g_1(m) &= \sum_{l=1}^{N} \sum_{k=1}^{N} g_1(l) g_1(k) \tilde{\lambda}_k X(m,l,k) \\ &= g_1(1) g_1(1) X(m,1,1),\end{aligned} \tag{B.18}$$

since $g_1(l) = 0$ for all $l \geq 2$ and $\tilde{\lambda}_1 = 1$. Since $\lambda_1(z) = z$, we obtain for $m = 1$ from (B.18) that

$$g_1(1) = g_1(1)^2 X(1,1,1)$$

and, hence,

$$g_1(1) = \frac{1}{X(1,1,1)} = \left(\sum_{l=1}^{N} \frac{1}{\sqrt{\delta_l}} (\tilde{x}_1)_l^3 \right)^{-1}.$$

Since $g_1(m) = 0$ for $m \geq 2$, we obtain that the power series (B.8) for the solution $\tilde{v}(z)$ of (B.6) becomes

$$\tilde{v}(z) = (z-1) g_1(1) S^{-\frac{1}{2}} \tilde{x}_1 + \phi(z), \tag{B.19}$$

where the $N \times 1$ vector $\phi(z)$ equals

$$\phi(z) = \sum_{k=1}^{N} \left(\sum_{j=2}^{\infty} g_j(k) (z-1)^j \right) S^{-\frac{1}{2}} \tilde{x}_k.$$

Thus, it holds $\|\phi(z)\|_2 = \mathcal{O}\left((z-1)^2\right)$ when z approaches 1 from above, which proves Lemma B.1. □

We believe that, based on (B.17), a recursion for the coefficients $g_j(k)$ can be obtained for powers $j \geq 2$, similar to the proof of [70, Lemma 4]. The radius of convergence of the power series (B.19) is an open problem, see also [286]. To express the solution $\tilde{v}(z)$ in (B.7) in terms of the principal eigenvector x_1 of the effective infection rate matrix W, we propose Lemma B.2.

B

Lemma B.2. *Under Assumptions 3.1 and 3.3, it holds that*

$$\left(\sum_{l=1}^{N} \frac{1}{\sqrt{\delta_l}} (\tilde{x}_1)_l^3\right)^{-1} S^{-\frac{1}{2}} \tilde{x}_1 = \frac{\sum_{l=1}^{N} \delta_l (x_1)_l^2}{\sum_{l=1}^{N} \delta_l (x_1)_l^3} x_1. \tag{B.20}$$

Proof. From (B.2), it follows that the principal eigenvector $\tilde{x}_1$ of the matrix $\tilde{W}$ and the principal eigenvector x_1 of the effective infection rate matrix W are related via

$$\tilde{x}_1 = \frac{1}{\left\| S^{\frac{1}{2}} x_1 \right\|_2} S^{\frac{1}{2}} x_1,$$

or, component-wise,

$$(\tilde{x}_1)_l = \frac{1}{\left\| S^{\frac{1}{2}} x_1 \right\|_2} \sqrt{\delta_l}\, (x_1)_l.$$

Then, we rewrite the left-hand side of (B.20) as

$$\left(\sum_{l=1}^{N} \frac{1}{\sqrt{\delta_l}} (\tilde{x}_1)_l^3\right)^{-1} S^{-\frac{1}{2}} \tilde{x}_1 = \left(\sum_{l=1}^{N} \delta_l (x_1)_l^3\right)^{-1} \left\| S^{\frac{1}{2}} x_1 \right\|_2^2 x_1,$$

which simplifies to

$$\left(\sum_{l=1}^{N} \frac{1}{\sqrt{\delta_l}} (\tilde{x}_1)_l^3\right)^{-1} S^{-\frac{1}{2}} \tilde{x}_1 = \frac{x_1^T S x_1}{\sum_{l=1}^{N} \delta_l (x_1)_l^3} x_1.$$

Writing out the quadratic form in the numerator completes the proof. □

The basic reproduction number R_0 converges to 1 when $(B,S) \to (B^*,S^*)$. Hence, if (B,S) is sufficiently close to (B^*,S^*), then the basic reproduction number R_0 is smaller than the radius of convergence of the power series (B.8). Thus, if (B,S) is sufficiently close to (B^*,S^*), then the solution $\tilde{v}(R_0)$ to (B.6) at $z = R_0$ follows with Lemma B.1 as

$$\begin{aligned} \tilde{v}(R_0) &= (R_0 - 1) \left(\sum_{l=1}^{N} \frac{1}{\sqrt{\delta_l}} (\tilde{x}_1)_l^3\right)^{-1} S^{-\frac{1}{2}} \tilde{x}_1 + \phi(R_0) \\ &= \gamma x_1 + \phi(R_0), \end{aligned}$$

where the last equality follows from Lemma B.2 and the definition of the scalar γ in (3.3). We emphasise that Lemma B.1 implies that $\gamma = \mathcal{O}(R_0 - 1)$ and, hence, $\| \tilde{v}(R_0) \|_2 = \mathcal{O}(R_0 - 1)$ as $(B,S) \to (B^*,S^*)$. Since $M(R_0) = \tilde{W}$, the solution of (B.6) at $z = R_0$ and the solution to (B.3) coincide, i.e., $\tilde{v}(R_0) = v_\infty$. Thus, from the definition of the vector η in (3.2), we obtain that

$$\begin{aligned} \|\eta\|_2 &= \| v_\infty - \gamma x_1 \|_2 \\ &= \| \phi(R_0) \|_2 \end{aligned} \tag{B.21}$$

when $(B,S) \to (B^*,S^*)$. Lemma B.1 states that $\|\phi(z)\|_2 = \mathcal{O}\left((z-1)^2\right)$ as $z \downarrow 1$. Hence, we obtain from (B.21) that

$$\|\eta\|_2 \leq \sigma(B,S)(R_0-1)^2 \tag{B.22}$$

for some scalar $\sigma(B,S)$ when $(B,S) \to (B^*,S^*)$.

Furthermore, when (B,S) converges to the limit (B^*,S^*), the scalar $\sigma(B,S)$ converges to some limit $\sigma(B^*,S^*)$. Hence, by defining the constant

$$\sigma = \sigma(B^*,S^*) + \epsilon_\sigma$$

for some $\epsilon_\sigma > 0$, it holds that

$$\sigma(B,S) < \sigma,$$

for all (B,S) which are sufficiently close to (B^*,S^*). Finally, we obtain from (B.22) that

$$\|\eta\|_2 \leq \sigma(R_0-1)^2$$

when (B,S) approaches (B^*,S^*).

B.3. PROOF OF LEMMA 3.5

We divide Lemma 3.5 into two parts. In Subsection B.3.1, we prove that the viral state $v(t)$ does not overshoot the steady-state v_∞. In Subsection B.3.2, we show that the function $c(t)$ lies in the interval $[0,1]$.

B.3.1. ABSENCE OF OVERSHOOT

Suppose that at some time t_0 it holds $v_i(t_0) = v_{\infty,i}$ for some node i and that $v_j(t_0) \leq v_{\infty,j}$ for every node j. Since $v_i(t_0) = v_{\infty,i}$, the NIMFA equation (1.1) yields that

$$\left.\frac{dv_i(t)}{dt}\right|_{t=t_0} = -\delta_i v_{\infty,i} + (1-v_{\infty,i}) \sum_{j=1}^{N} \beta_{ij} v_j(t_0).$$

Since $v_j(t_0) \leq v_{\infty,j}$ for every node j, we obtain that

$$\left.\frac{dv_i(t)}{dt}\right|_{t=t_0} \leq -\delta_i v_{\infty,i} + (1-v_{\infty,i}) \sum_{j=1}^{N} \beta_{ij} v_{\infty,j} = 0,$$

where the last equality follows from the steady-state equation (1.5). Thus, $v_i(t_0) = v_{\infty,i}$ implies that $\left.\frac{dv_i(t)}{dt}\right|_{t=t_0} \leq 0$, which means that, at time t_0, the viral state $v_i(t_0)$ does not increase. Hence, the viral state $v_i(t_0)$ cannot exceed the steady-state $v_{\infty,i}$ at any time $t \geq 0$.

B.3.2. BOUNDEDNESS OF THE FUNCTION $c(t)$

Relation (3.12) indicates that

$$c(t) = \frac{1}{\|v_\infty\|_2^2} v_\infty^T v(t) = \frac{1}{\|v_\infty\|_2^2} \left(v_{\infty,1} v_1(t) + \ldots + v_{\infty,N} v_N(t)\right) \tag{B.23}$$

Subsection B.3.1 shows that Assumption 3.2 implies that $v_i(t) \leq v_{\infty,i}$ for all nodes i and every time t. Thus, we obtain from (B.23) that

$$c(t) \leq \frac{1}{\|v_\infty\|_2^2} \left(v_{\infty,1} v_{\infty,1} + \ldots + v_{\infty,N} v_{\infty,N} \right) = 1$$

Analogously, since $v_i(t) \geq 0$ for all nodes i and every time t, we obtain from (B.23) that $c(t) \geq 0$.

B.4. PROOF OF THEOREM 3.6

By inserting the ansatz (3.11) into the NIMFA equations (1.2), we obtain that

$$\frac{dc(t)}{dt} v_\infty + \frac{d\xi(t)}{dt} = \Lambda_1(t) + \Lambda_2(t). \tag{B.24}$$

Here, the function $\Lambda_1(t)$ is given by

$$\Lambda_1(t) = (B - S)\, c(t)\, v_\infty - c^2(t) \mathrm{diag}(v_\infty) B v_\infty,$$

which simplifies, with the steady-state equation (1.5), to

$$\Lambda_1(t) = \left(c(t) - c^2(t) \right) (B - S)\, v_\infty. \tag{B.25}$$

The function $\Lambda_2(t)$ is given by

$$\Lambda_2(t) = (B - S)\, \xi(t) - c(t) \mathrm{diag}(\xi(t)) B v_\infty - c(t) \mathrm{diag}(v_\infty) B \xi(t) - \mathrm{diag}(\xi(t)) B \xi(t).$$

With $\mathrm{diag}(\xi(t)) B v_\infty = \mathrm{diag}(B v_\infty) \xi(t)$, we obtain that

$$\Lambda_2(t) = \left(B - S - c(t) \mathrm{diag}(B v_\infty) - c(t) \mathrm{diag}(v_\infty) B \right) \xi(t) - \mathrm{diag}(\xi(t)) B \xi(t). \tag{B.26}$$

To show that the error term $\xi(t)$ converges to zero at every time t when $(B, S) \to (B^*, S^*)$, we consider the squared Euclidean norm $\|\xi(t)\|_2^2$. The convergence of the squared norm $\|\xi(t)\|_2^2$ to zero implies the convergence of the error term $\xi(t)$ to zero. The derivative of the squared norm $\|\xi(t)\|_2^2$ is given by

$$\frac{d\|\xi(t)\|_2^2}{dt} = 2 \xi^T(t) \frac{d\xi(t)}{dt}.$$

Thus, we obtain from (B.24) that

$$\frac{1}{2} \frac{d\|\xi(t)\|_2^2}{dt} = \xi^T(t) \Lambda_1(t) + \xi^T(t) \Lambda_2(t), \tag{B.27}$$

since $\xi^T(t) v_\infty = 0$ by definition of $\xi(t)$. We do not know how to solve (B.27) exactly, and we resort to bounding the two addends on the right-hand side of (B.27) in Subsection B.4.1 and Subsection B.4.2, respectively. In Subsection B.4.3 we complete the proof of Theorem 3.6 by deriving an upper bound on the squared norm $\|\xi(t)\|_2^2$.

B.4.1. UPPER BOUND ON $\xi^T(t)\Lambda_1(t)$

We obtain an upper bound on the projection of the function $\Lambda_1(t)$ onto the error vector $\xi(t)$, which is linear with respect to the norm $\|\xi(t)\|_2$:

Lemma B.3. *Under Assumptions 3.1 to 3.3, it holds at every time $t \geq 0$ that*

$$\left|\xi^T(t)\Lambda_1(t)\right| \leq \frac{1}{4}\delta_{\max}\left(\gamma(R_0-1)+(R_0+1)\|\eta\|_2\right)\|\xi(t)\|_2.$$

Proof. From (B.25) and the definition of the matrix W in (3.1) it follows that

$$\xi^T(t)\Lambda_1(t) = \left(c(t)-c^2(t)\right)\xi^T(t)S(W-I)\,v_\infty.$$

With Theorem 3.4, we obtain that

$$\xi^T(t)\Lambda_1(t) = \left(c(t)-c^2(t)\right)\left(\gamma(R_0-1)\xi^T(t)Sx_1+\xi^T(t)S(W-I)\eta\right).$$

The triangle inequality yields that

$$\left|\xi^T(t)\Lambda_1(t)\right| \leq \left|c(t)-c^2(t)\right|\left(|\gamma(R_0-1)|\left|\xi^T(t)Sx_1\right|+\left|\xi^T(t)S(W-I)\eta\right|\right). \tag{B.28}$$

With the Cauchy-Schwarz inequality, the first addend in (B.28) is bounded by

$$\begin{aligned}\left|\xi^T(t)Sx_1\right| &\leq \|S^T\xi(t)\|_2\|x_1\|_2\\ &= \|S\xi(t)\|_2,\end{aligned}$$

since $\|x_1\|_2 = 1$ and the matrix S is symmetric. The matrix 2-norm is sub-multiplicative, which yields that

$$\begin{aligned}\left|\xi^T(t)Sx_1\right| &\leq \|S\|_2\|\xi(t)\|_2\\ &= \delta_{\max}\|\xi(t)\|_2.\end{aligned}$$

Thus, (B.28) gives that

$$\left|\xi^T(t)\Lambda_1(t)\right| \leq \left|c(t)-c^2(t)\right|\left(\gamma(R_0-1)\delta_{\max}\|\xi(t)\|_2+\left|\xi^T(t)S(W-I)\eta\right|\right), \tag{B.29}$$

since $\gamma > 0$ and $R_0 > 1$. We consider the second addend in (B.29), which we write with (B.2) as

$$\left|\xi^T(t)S(W-I)\eta\right| = \left|\xi^T(t)S^{\frac{1}{2}}(\tilde{W}-I)S^{\frac{1}{2}}\eta\right|.$$

From the Cauchy-Schwarz inequality and the sub-multiplicativity of the matrix norm we obtain that

$$\left|\xi^T(t)S(W-I)\eta\right| \leq \|\xi(t)\|_2\|S^{\frac{1}{2}}\|_2\|\tilde{W}-I\|_2\|S^{\frac{1}{2}}\|_2\|\eta\|_2.$$

The triangle inequality and the symmetry of the matrix $\tilde{W}$ imply that

$$\|\tilde{W}-I\|_2 \leq \|\tilde{W}\|_2+\|I\|_2 = R_0+1.$$

Thus, we can bound the second added in (B.29) by

$$\left|\xi^T(t)S(W-I)\eta\right| \leq \delta_{\max}(R_0+1)\|\xi(t)\|_2\|\eta\|_2,$$

since $\|S^{\frac{1}{2}}\|_2 = \sqrt{\delta_{\max}}$. Hence, (B.29) yields the upper bound

$$\left|\xi^T(t)\Lambda_1(t)\right| \leq \left|c(t)-c^2(t)\right|\delta_{\max}\left(\gamma(R_0-1)+(R_0+1)\|\eta\|_2\right)\|\xi(t)\|_2.$$

Finally, Lemma 3.5 states that $0 \leq c(t) \leq 1$, which implies that

$$\left|c(t)-c^2(t)\right| \leq 1/4$$

and completes the proof. □

B.4.2. UPPER BOUND ON $\xi^T(t)\Lambda_2(t)$

Lemma B.4 states an intermediate result, which we will use to bound the projection of the function $\Lambda_2(t)$ onto the error vector $\xi(t)$.

Lemma B.4. *Suppose that Assumptions 3.1 to 3.3 hold. Then, at every time $t \geq 0$, it holds that*

$$\xi^T(t)\Lambda_2(t) \leq -\|S^{\frac{1}{2}}\xi(t)\|_2^2 + \xi^T(t)\mathrm{diag}(u-c(t)v_\infty)B\xi(t).$$

Proof. From (B.26) it follows that

$$\begin{aligned}\xi^T(t)\Lambda_2(t) =& \xi^T(t)\left(B-S-c(t)\mathrm{diag}(Bv_\infty)-c(t)\mathrm{diag}(v_\infty)B\right)\xi(t)\\ &-\xi^T(t)\mathrm{diag}(\xi(t))B\xi(t).\end{aligned} \tag{B.30}$$

To simplify (B.30), we aim to bound the last addend of (B.30) by an expression that is quadratic in the error vector $\xi(t)$. The last addend equals

$$-\xi^T(t)\mathrm{diag}(\xi(t))B\xi(t) = \sum_{l=1}^{N}\xi_l^2(t)\sum_{j=1}^{N}\beta_{lj}\left(-\xi_j(t)\right). \tag{B.31}$$

Since $v(t) = c(t)v_\infty + \xi(t)$ and $v_i(t) \geq 0$ for every node i at every time t, it holds that

$$-\xi_i(t) \leq c(t)v_{\infty,i}, \quad i = 1,\ldots,N. \tag{B.32}$$

By inserting (B.32) in (B.31), the last addend of (B.30) is bounded by

$$-\xi^T(t)\mathrm{diag}(\xi(t))B\xi(t) \leq \sum_{l=1}^{N}\xi_l^2(t)\sum_{j=1}^{N}\beta_{lj}c(t)v_{\infty,j},$$

which simplifies to

$$-\xi^T(t)\mathrm{diag}(\xi(t))B\xi(t) \leq c(t)\xi^T(t)\mathrm{diag}(Bv_\infty)\xi(t). \tag{B.33}$$

By applying the upper bound (B.33) to (B.30), we obtain that

$$\xi^T(t)\Lambda_2(t) \leq \xi^T(t)\left(B-S-c(t)\mathrm{diag}(v_\infty)B\right)\xi(t).$$

With the definition of the matrix $\tilde{W}$ in (B.2), we obtain that

$$\xi^T(t)\Lambda_2(t) \leq \xi^T(t)S^{\frac{1}{2}}\left(\tilde{W}-I-c(t)\mathrm{diag}(v_\infty)\tilde{W}\right)S^{\frac{1}{2}}\xi(t),$$

and further rearranging completes the proof. □

For any scalar $\varsigma \in [0,1]$ and any vector $v \in \mathbb{R}^N$, we define

$$\Theta(\varsigma, v, B, S) = \frac{\left|v^T \operatorname{diag}(u - \varsigma v_\infty) B v\right|}{\|S^{\frac{1}{2}} v\|_2^2}.$$

Then, we obtain from Lemma B.4 that

$$\xi^T(t)\Lambda_2(t) \leq (\Theta(c(t), \xi(t), B, S) - 1)\, \|S^{\frac{1}{2}}\xi(t)\|_2^2. \tag{B.34}$$

To bound the term $\Theta(c(t), \xi(t), B, S)$, we make use of (parts of) the results of Issos [287], which are analogues of the Perron-Frobenius Theorem for the numerical radius of a non-negative, irreducible matrix:

Theorem B.5 ([287])**.** *Let M be a real irreducible and non-negative $N \times N$ matrix. Then, there is a positive vector $z \in \mathbb{R}^N$ of length $z^T z = 1$ such that $z^T M z = r(M)$. Furthermore, if $\tilde{z}^T M \tilde{z} = r(M)$ holds for a vector $\tilde{z} \in \mathbb{R}^N$ of length $\tilde{z}^T \tilde{z} = 1$, then either $\tilde{z} = z$ or $\tilde{z} = -z$.*

We refer the reader to [287–289] for further results on the numerical radius of non-negative matrices. We apply Theorem B.5 to obtain:

Lemma B.6. *Denote the set of $N \times 1$ vectors with at least one positive and at least one negative component as*

$$\mathcal{Q} = \left\{ v \in \mathbb{R}^N \middle| \exists i, j : v_j > 0 > v_i \right\}.$$

Then, it holds that $\Theta(\varsigma, v, B, S) < R_0$ for every scalar $\varsigma \in [0,1]$ and for every vector $v \in \mathcal{Q}$.

Proof. By introducing the $N \times 1$ vector $\tilde{v} = S^{\frac{1}{2}} v$ and by using (B.2), we rewrite the term $\Theta(\varsigma, v, B, S)$ as

$$\Theta(\varsigma, v, B, S) = \frac{\left|\tilde{v}^T \operatorname{diag}(u - \varsigma v_\infty) \tilde{W} \tilde{v}\right|}{\|\tilde{v}\|_2^2}. \tag{B.35}$$

For every scalar $\varsigma \in [0,1]$ the matrix $(\operatorname{diag}(u - \varsigma v_\infty)\tilde{W})$ is irreducible and non-negative. Since $v \in \mathcal{Q}$ and the matrix S is a diagonal matrix with non-negative entries, it holds that $\tilde{v}_i < 0$ and $\tilde{v}_j > 0$ for some i, j. Hence, at least two components of the vector $\tilde{v}$ have different signs, and Theorem B.5 implies that (B.35) is bounded by

$$\Theta(\varsigma, v, B, S) < r\left(\operatorname{diag}(u - \varsigma v_\infty)\tilde{W}\right).$$

Since the matrix $\tilde{W}$ is irreducible and $\operatorname{diag}(u - \varsigma v_\infty)\tilde{W} \leq \tilde{W}$ for every $\varsigma \in [0,1]$, where the inequality holds element-wise, it holds [289, Corollary 3.6.] that

$$\Theta(\varsigma, v, B, S) < r\left(\tilde{W}\right).$$

The matrix $\tilde{W}$ is symmetric, and, hence, the numerical radius $r\left(\tilde{W}\right)$ equals the spectral radius $\rho\left(\tilde{W}\right) = R_0$, which yields that

$$\Theta(\varsigma, v, B, S) < R_0.$$

□

Finally, we obtain a bound on the projection of the function $\Lambda_2(t)$ onto the error vector $\xi(t)$ as:

Lemma B.7. *Under Assumptions 3.1 to 3.3, there is some constant $\omega > 0$ such that*

$$\xi^T(t)\Lambda_2(t) \leq -\omega\delta_{\max}\|\xi(t)\|_2^2$$

holds at every time $t \geq 0$ when (B,S) approaches (B^*,S^*).

Proof. We denote the maximum of the function $\Theta(\varsigma,\upsilon,B,S)$ with respect to $\varsigma \in [0,1]$ and $\upsilon \in \mathcal{Q}$ by

$$\Theta_{\max}(B,S) = \max_{\varsigma\in[0,1],\upsilon\in\mathcal{Q}} \Theta(\varsigma,\upsilon,B,S). \tag{B.36}$$

As a first step, we consider the value of $\Theta_{\max}(B^*,S^*)$ at the limit (B^*,S^*). Since the steady-state υ_∞ equals to zero at the limit (B^*,S^*), we obtain from (B.35) that

$$\Theta(\varsigma,\upsilon,B^*,S^*) = \frac{1}{\|\tilde{\upsilon}\|_2^2}\left|\tilde{\upsilon}^T\tilde{W}^*\tilde{\upsilon}\right|, \tag{B.37}$$

where we denote $\tilde{W}^* = (S^*)^{-\frac{1}{2}}B^*(S^*)^{-\frac{1}{2}}$. Since $R_0 = 1$ at the limit (B^*,S^*), Lemma B.6 implies that

$$\Theta_{\max}(B^*,S^*) < 1. \tag{B.38}$$

As a second step, we consider that the infection rate matrix B and the curing rate matrix S do not equal the respective limit B^* and S^*. Thus, there are non-zero $N\times N$ matrices $\Delta B, \Delta S$ and $\Delta\tilde{W}$ such that $B = B^* + \Delta B$, $S = S^* + \Delta S$, and $\tilde{W} = \tilde{W}^* + \Delta\tilde{W}$. Then, we obtain from (B.35) that

$$\Theta(\varsigma,\upsilon,B,S) = \frac{1}{\|\tilde{\upsilon}\|_2^2}\left|\tilde{\upsilon}^T\left(\tilde{W}^* - \varsigma\,\mathrm{diag}(\upsilon_\infty)\tilde{W}^* + \mathrm{diag}(u-\varsigma\upsilon_\infty)\Delta\tilde{W}\right)\tilde{\upsilon}\right|,$$

which is bounded by

$$\begin{aligned}\Theta(\varsigma,\upsilon,B,S) \leq{}& \frac{1}{\|\tilde{\upsilon}\|_2^2}\left|\tilde{\upsilon}^T\tilde{W}^*\tilde{\upsilon}\right| + \frac{1}{\|\tilde{\upsilon}\|_2^2}\left|\tilde{\upsilon}^T\varsigma\,\mathrm{diag}(\upsilon_\infty)\tilde{W}^*\tilde{\upsilon}\right| \\ &+ \frac{1}{\|\tilde{\upsilon}\|_2^2}\left|\tilde{\upsilon}^T\mathrm{diag}(u-\varsigma\upsilon_\infty)\Delta\tilde{W}\tilde{\upsilon}\right|.\end{aligned} \tag{B.39}$$

Maximising every addend in (B.39) independently yields an upper bound on $\Theta_{\max}(B,S)$ as

$$\begin{aligned}\Theta_{\max}(B,S) \leq{}& \max_{\varsigma\in[0,1],\upsilon\in\mathcal{Q}} \frac{1}{\|\tilde{\upsilon}\|_2^2}\left|\tilde{\upsilon}^T\tilde{W}^*\tilde{\upsilon}\right| \\ &+ \max_{\varsigma\in[0,1],\upsilon\in\mathcal{Q}} \frac{1}{\|\tilde{\upsilon}\|_2^2}\left|\tilde{\upsilon}^T\varsigma\,\mathrm{diag}(\upsilon_\infty)\tilde{W}^*\tilde{\upsilon}\right| \\ &+ \max_{\varsigma\in[0,1],\upsilon\in\mathcal{Q}} \frac{1}{\|\tilde{\upsilon}\|_2^2}\left|\tilde{\upsilon}^T\mathrm{diag}(u-\varsigma\upsilon_\infty)\Delta\tilde{W}\tilde{\upsilon}\right|.\end{aligned} \tag{B.40}$$

In the following, we state upper bounds for each of the three addends in (B.37) separately. With (B.37), we write the first addend in (B.40) as

$$\begin{aligned}\max_{\varsigma\in[0,1],\upsilon\in\mathcal{Q}} \frac{1}{\|\tilde{v}\|_2^2}\left|\tilde{v}^T\tilde{W}^*\tilde{v}\right| &= \max_{\varsigma\in[0,1],\upsilon\in\mathcal{Q}} \Theta(\varsigma,\upsilon,B^*,S^*) \\ &= \Theta_{\max}(B^*,S^*),\end{aligned} \tag{B.41}$$

where the last equality follows from the definition of $\Theta_{\max}(B^*,S^*)$ in (B.36). Regarding the second addend in (B.40), it holds that

$$\begin{aligned}\max_{\varsigma\in[0,1],\upsilon\in\mathcal{Q}} \frac{1}{\|\tilde{v}\|_2^2}\left|\tilde{v}^T\varsigma\operatorname{diag}(\upsilon_\infty)\tilde{W}^*\tilde{v}\right| &\le \max_{\varsigma\in[0,1]}\max_{\upsilon\in\mathbb{R}^N} \frac{1}{\|\tilde{v}\|_2^2}\left|\tilde{v}^T\varsigma\operatorname{diag}(\upsilon_\infty)\tilde{W}^*\tilde{v}\right| \\ &= \max_{\varsigma\in[0,1]} r\left(\varsigma\operatorname{diag}(\upsilon_\infty)\tilde{W}^*\right),\end{aligned}$$

where the last equality follows from the definition the numerical radius. Hence, the second addend in (B.40) is bounded by

$$\max_{\varsigma\in[0,1],\upsilon\in\mathcal{Q}} \frac{1}{\|\tilde{v}\|_2^2}\left|\tilde{v}^T\varsigma\operatorname{diag}(\upsilon_\infty)\tilde{W}^*\tilde{v}\right| \le r\left(\varsigma_{\text{opt}}^{(1)}\operatorname{diag}(\upsilon_\infty)\tilde{W}^*\right) \tag{B.42}$$

for some $\varsigma_{\text{opt}}^{(1)}\in[0,1]$. Similarly, we obtain an upper bound on the third addend in (B.40) as

$$\max_{\varsigma\in[0,1],\upsilon\in\mathcal{Q}} \frac{1}{\|\tilde{v}\|_2^2}\left|\tilde{v}^T\operatorname{diag}(u-\varsigma\upsilon_\infty)\Delta\tilde{W}\tilde{v}\right| \le r\left(\operatorname{diag}(u-\varsigma_{\text{opt}}^{(2)}\upsilon_\infty)\Delta\tilde{W}\right) \tag{B.43}$$

for some $\varsigma_{\text{opt}}^{(2)}\in[0,1]$. With (B.41), (B.42) and (B.43), we obtain from (B.40) that

$$\Theta_{\max}(B,S) \le \Theta_{\max}(B^*,S^*) + r\left(\varsigma_{\text{opt}}^{(1)}\operatorname{diag}(\upsilon_\infty)\tilde{W}^*\right) + r\left(\operatorname{diag}(u-\varsigma_{\text{opt}}^{(2)}\upsilon_\infty)\Delta\tilde{W}\right). \tag{B.44}$$

The numerical radius $r(M)$ is a vector[1] norm [285] on the space of $N\times N$ matrices M. Thus, the numerical radius $r(M)$ converges to zero if the matrix M converges to zero. Since $\upsilon_\infty\to 0$ and $\Delta\tilde{W}\to 0$ as $(B,S)\to(B^*,S^*)$ and $\varsigma_{\text{opt}}^{(1)},\varsigma_{\text{opt}}^{(2)}$ are bounded, the last two addends in (B.44) converge to zero as $(B,S)\to(B^*,S^*)$. Hence, for every scalar $\omega>0$ there is a $\vartheta(\omega)$ such that $\|B-B^*\|_2<\vartheta(\omega)$ and $\|S-S^*\|_2<\vartheta(\omega)$ implies that

$$\Theta_{\max}(B,S) \le \Theta_{\max}(B^*,S^*) + \omega. \tag{B.45}$$

We choose the scalar $\omega=(1-\Theta_{\max}(B^*,S^*))/2$, which is positive due to (B.38). Then, the right-hand side of (B.45) becomes

$$\begin{aligned}\Theta_{\max}(B^*,S^*)+\omega &= \frac{1}{2}+\frac{1}{2}\Theta_{\max}(B^*,S^*) \\ &= 1-\omega.\end{aligned}$$

[1] The numerical radius is not a *matrix* norm, since the numerical radius is not sub-multiplicative.

Thus, we obtain from (B.45) that

$$\Theta_{\max}(B,S) \leq 1-\omega \tag{B.46}$$

holds for all (B,S) which are sufficiently close to the limit (B^*,S^*).

By definition, the error vector $\xi(t)$ at any time $t \geq 0$ is orthogonal to the steady-state vector v_∞. Since the steady-state v_∞ is positive, the error vector $\xi(t)$ has at least one positive and one negative element, and, hence, it holds that $\xi(t) \in \mathcal{Q}$. Thus, we obtain from the definition of the term $\Theta_{\max}(B,S)$ in (B.36) that

$$\Theta(c(t),\xi(t),B,S) \leq \Theta_{\max}(B,S).$$

With (B.46), we obtain from (B.34) that

$$\xi^T(t)\Lambda_2(t) \leq -\omega \|S^{\frac{1}{2}}\xi(t)\|_2^2.$$

From the sub-multiplicativity of the matrix norm, we obtain that

$$\xi^T(t)\Lambda_2(t) \leq -\omega \|S^{\frac{1}{2}}\|_2^2 \|\xi(t)\|_2^2,$$

which completes the proof, since $\|S^{\frac{1}{2}}\|_2^2 = \delta_{\max}$. □

B.4.3. BOUND ON THE ERROR VECTOR $\xi(t)$

With Lemma B.3 and Lemma B.7, we upper-bound (B.27) by

$$\frac{1}{2}\frac{d\|\xi(t)\|_2^2}{dt} \leq \frac{1}{4}\delta_{\max}\left(\gamma(R_0-1)+(R_0+1)\|\eta\|_2\right)\|\xi(t)\|_2 - \omega\delta_{\max}\|\xi(t)\|_2^2.$$

From

$$\frac{d\|\xi(t)\|_2}{dt} = \frac{1}{2\|\xi(t)\|_2}\frac{d\|\xi(t)\|_2^2}{dt},$$

it follows that

$$\frac{d\|\xi(t)\|_2}{dt} \leq \frac{1}{4}\delta_{\max}\left(\gamma(R_0-1)+(R_0+1)\|\eta\|_2\right) - \omega\delta_{\max}\|\xi(t)\|_2.$$

We denote

$$\varphi(B,S) = \frac{1}{4}\left(\gamma(R_0-1)+(R_0+1)\|\eta\|_2\right), \tag{B.47}$$

and we obtain that

$$\frac{d\|\xi(t)\|_2}{dt} \leq \varphi(B,S)\,\delta_{\max} - \omega\delta_{\max}\|\xi(t)\|_2. \tag{B.48}$$

The upper bound (B.48) is a linear first-order ordinary differential inequality, which is solved by [290]

$$\|\xi(t)\|_2 \leq e^{-\omega\delta_{\max}t}\left(\|\xi(0)\|_2 + \int_0^t \varphi(B,S)\,\delta_{\max}e^{\omega\delta_{\max}\tilde{t}}\,d\tilde{t}\right),$$

which simplifies to

$$\|\xi(t)\|_2 \leq \left(\|\xi(0)\|_2 - \frac{\varphi(B,S)}{\omega}\right) e^{-\omega\delta_{\max} t} + \frac{\varphi(B,S)}{\omega}.$$

The triangle inequality yields that

$$\|\xi(t)\|_2 \leq \|\xi(0)\|_2 e^{-\omega\delta_{\max} t} + \frac{\varphi(B,S)}{\omega}\left(1 + e^{-\omega\delta_{\max} t}\right). \tag{B.49}$$

Furthermore, since $e^{-\omega\delta_{\max} t} \leq 1$ at every time $t \geq 0$, we obtain from (B.49) that

$$\|\xi(t)\|_2 \leq \|\xi(0)\|_2 e^{-\omega\delta_{\max} t} + 2\frac{\varphi(B,S)}{\omega}. \tag{B.50}$$

The maximum $\delta_{\max}$ of the curing rates converges to some limit $\delta^*_{\max}$ when $(B,S) \to (B^*,S^*)$. Hence, for any $\epsilon > 0$ it holds that $\delta^*_{\max} - \epsilon < \delta_{\max}$ when (B,S) approaches (B^*,S^*). For some $\epsilon \in (0, \delta^*_{\max})$, we set the constant

$$\sigma_1 = \omega(\delta^*_{\max} - \epsilon).$$

Then, it holds that $\sigma_1 < \omega\delta_{\max}$ when (B,S) approaches (B^*,S^*), and we obtain from (B.50) that

$$\|\xi(t)\|_2 \leq \|\xi(0)\|_2 e^{-\sigma_1 t} + 2\frac{\varphi(B,S)}{\omega}. \tag{B.51}$$

Theorem 3.4 states that $\gamma = \mathcal{O}(R_0 - 1)$ and $\|\eta\|_2 = \mathcal{O}\left((R_0-1)^2\right)$ when (B,S) approaches (B^*,S^*). Thus, it follows from the definition of the term $\varphi(B,S)$ in (B.47) that $\varphi(B,S) = \mathcal{O}\left((R_0-1)^2\right)$. Hence, there is a constant $\sigma_2 > 0$ such that (B.51) yields that

$$\|\xi(t)\|_2 \leq \|\xi(0)\|_2 e^{-\sigma_1 t} + \sigma_2 (R_0 - 1)^2$$

when (B,S) approaches (B^*,S^*).

B.5. PROOF OF THEOREM 3.7

By projecting the differential equation (B.24) onto the steady-state vector v_∞, we obtain that

$$\frac{dc(t)}{dt} v_\infty^T v_\infty = v_\infty^T \Lambda_1(t) + v_\infty^T \Lambda_2(t),$$

since $v_\infty^T \xi(t) = 0$ by definition of the error term $\xi(t)$. We divide by $\|v_\infty\|_2^2$ and obtain with (B.25) that

$$\frac{dc(t)}{dt} = \left(c(t) - c^2(t)\right) \frac{v_\infty^T (B-S) v_\infty}{\|v_\infty\|_2^2} + \frac{v_\infty^T \Lambda_2(t)}{\|v_\infty\|_2^2}. \tag{B.52}$$

The first addend in the differential equation (B.52) can be expressed in a simpler manner when (B,S) approaches (B^*,S^*):

Lemma B.8. *Under Assumptions 3.1 and 3.3, it holds that*

$$\frac{v_\infty^T (B-S)\, v_\infty}{v_\infty^T v_\infty} = (R_0-1)\, x_1^T S x_1 + \zeta, \tag{B.53}$$

where $\zeta = \mathcal{O}\left((R_0-1)^2\right)$ *when* (B,S) *approaches* (B^*,S^*).

Proof. With Theorem 3.4 and the definition of the matrix W in (3.1), the numerator of the left-hand side of (B.53) becomes

$$\begin{aligned} v_\infty^T (B-S)\, v_\infty &= (\gamma x_1 + \eta)^T \left(S(W-I)\gamma x_1 + (B-S)\eta\right) \\ &= (\gamma x_1 + \eta)^T (\gamma(R_0-1) S x_1 + (B-S)\eta), \end{aligned}$$

where the last equality follows from $W x_1 = R_0 x_1$. Thus, it holds that

$$v_\infty^T (B-S)\, v_\infty = \gamma^2 (R_0-1) x_1^T S x_1 + \gamma x_1^T (B-S)\eta + \gamma(R_0-1)\eta^T S x_1 + \eta^T (B-S)\eta. \tag{B.54}$$

Under Assumption 3.3, both matrices B and S are symmetric, which implies that

$$\begin{aligned} \left(x_1^T (B-S)\right)^T &= (B-S) x_1 \\ &= S(R_0-1) x_1. \end{aligned}$$

Hence, we obtain from (B.54) that

$$v_\infty^T (B-S)\, v_\infty = \gamma^2 (R_0-1) x_1^T S x_1 + \gamma(R_0-1) x_1^T S\eta + \gamma(R_0-1)\eta^T S x_1 + \eta^T (B-S)\eta.$$

Since $\gamma = \mathcal{O}(R_0-1)$ and $\|\eta\|_2 = \mathcal{O}\left((R_0-1)^2\right)$, we finally rewrite the numerator of the left-hand side of (B.53) as

$$v_\infty^T (B-S)\, v_\infty = \gamma^2 (R_0-1) x_1^T S x_1 + \mathcal{O}\left((R_0-1)^4\right). \tag{B.55}$$

With Theorem 3.4, the denominator of the left-hand side of (B.53) equals

$$\begin{aligned} v_\infty^T v_\infty &= \gamma^2 + 2\gamma\eta^T x_1 + \|\eta\|_2^2 \\ &= \gamma^2 + \mathcal{O}\left((R_0-1)^3\right). \end{aligned} \tag{B.56}$$

Combining the approximate expressions for the numerator (B.55) and the denominator (B.56) completes the proof. □

We define the *viral slope* $\bar{\omega}$ as

$$\bar{\omega} = (R_0-1)\, x_1^T S x_1 \tag{B.57}$$

and the function $n(t)$ as

$$n(t) = \left(c(t) - c^2(t)\right)\zeta + \frac{v_\infty^T \Lambda_2(t)}{\|v_\infty\|_2^2}. \tag{B.58}$$

Then, we obtain from (B.52) that

$$\frac{dc(t)}{dt} = \big(c(t) - c^2(t)\big)\,\varpi + n(t). \tag{B.59}$$

The function $n(t)$ is complicated and depends on the error vector $\xi(t)$. Hence, we cannot solve the differential equation (B.59) for the function $c(t)$ without knowing the solution for the error vector $\xi(t)$. However, as $(B,S) \to (B^*,S^*)$, the function $n(t)$ converges to zero uniformly in time t as stated by the bound in Lemma B.9.

Lemma B.9. *Under Assumptions 3.1 to 3.3, it holds at every time $t \geq 0$ that*

$$|n(t)| \leq \sigma_1 \|\xi(0)\|_2 e^{-\sigma_2 t} + \sigma_3 (R_0 - 1)^2$$

for some constants $\sigma_1, \sigma_2, \sigma_3 > 0$ when (B,S) approaches (B^*,S^*).

Proof. Regarding the first addend in the definition of the function $n(t)$ in (B.58), Lemma 3.5 implies that $0 \leq c(t) - c^2(t) \leq 1/4$ at every time t. Hence, Lemma B.8 yields that there is a constant $\tilde{\sigma}_0$ such that

$$\big|\big(c(t) - c^2(t)\big)\zeta\big| \leq \tilde{\sigma}_0 (R_0 - 1)^2$$

at every time t when (B,S) approaches (B^*,S^*). Regarding the second addend of the function $n(t)$ defined in (B.58), it follows from the definition of the function $\Lambda_2(t)$ in (B.26) that

$$\frac{v_\infty^T \Lambda_2(t)}{\|v_\infty\|_2^2} = \frac{1}{\|v_\infty\|_2^2} v_\infty^T \big(B - S - c(t)\mathrm{diag}(Bv_\infty) - \mathrm{diag}(v(t))B\big)\xi(t),$$

since $v(t) = c(t)v_\infty + \xi(t)$. Thus, it holds that

$$\frac{v_\infty^T \Lambda_2(t)}{\|v_\infty\|_2^2} = \frac{1}{\|v_\infty\|_2^2} v_\infty^T \big(-S + \mathrm{diag}(u - v(t))B - c(t)\mathrm{diag}(Bv_\infty)\big)\xi(t).$$

With the definition of the matrix $\tilde{W}$ in (B.2), we obtain that

$$\frac{v_\infty^T \Lambda_2(t)}{\|v_\infty\|_2^2} = \frac{1}{\|v_\infty\|_2^2} v_\infty^T S^{\frac{1}{2}} \Big(-I + \mathrm{diag}(u - v(t))\tilde{W} - c(t) S^{-\frac{1}{2}} \mathrm{diag}(Bv_\infty) S^{-\frac{1}{2}}\Big) S^{\frac{1}{2}} \xi(t).$$

The Cauchy-Schwarz inequality yields an upper bound as

$$\left|\frac{v_\infty^T \Lambda_2(t)}{\|v_\infty\|_2^2}\right| \leq \frac{1}{\|v_\infty\|_2^2} \left\|S^{\frac{1}{2}}\xi(t)\right\|_2 \left\|\Big(-I + \mathrm{diag}(u - v(t))\tilde{W} - c(t) S^{-\frac{1}{2}} \mathrm{diag}(Bv_\infty) S^{-\frac{1}{2}}\Big) S^{\frac{1}{2}} v_\infty\right\|_2.$$

With $\left\|S^{\frac{1}{2}}\xi(t)\right\|_2 \leq \sqrt{\delta_{\max}}\,\|\xi(t)\|_2$ and the triangle inequality, we obtain that

$$\begin{aligned}\left|\frac{v_\infty^T \Lambda_2(t)}{\|v_\infty\|_2^2}\right| \leq{}& \sqrt{\delta_{\max}} \frac{\|\xi(t)\|_2}{\|v_\infty\|_2^2} \left\|\big(\tilde{W} - I\big) S^{\frac{1}{2}} v_\infty\right\|_2 \\ &+ \sqrt{\delta_{\max}} \frac{\|\xi(t)\|_2}{\|v_\infty\|_2^2} \left\|\mathrm{diag}(v(t))\tilde{W}\right\|_2 \left\|S^{\frac{1}{2}} v_\infty\right\|_2 \\ &+ \sqrt{\delta_{\max}} \frac{\|\xi(t)\|_2}{\|v_\infty\|_2^2} \left\|c(t) S^{-\frac{1}{2}} \mathrm{diag}(Bv_\infty) S^{-\frac{1}{2}}\right\|_2 \left\|S^{\frac{1}{2}} v_\infty\right\|_2.\end{aligned} \tag{B.60}$$

B

In the following, we consider the three addends in (B.60) separately. Regarding the first addend, we obtain with the definition of the matrix $\tilde{W}$ in (B.2) that

$$\begin{aligned}\left(\tilde{W}-I\right)S^{\frac{1}{2}}v_\infty &= S^{\frac{1}{2}}(W-I)\,v_\infty \\ &= \gamma(R_0-1)S^{\frac{1}{2}}x_1 + S^{\frac{1}{2}}(W-I)\,\eta,\end{aligned}$$

where the last equality follows from Theorem 3.4. Thus, the triangle inequality yields that

$$\left\|\left(\tilde{W}-I\right)S^{\frac{1}{2}}v_\infty\right\|_2 \leq \gamma(R_0-1)\left\|S^{\frac{1}{2}}x_1\right\|_2 + \left\|S^{\frac{1}{2}}(W-I)\,\eta\right\|_2.$$

With the sub-multiplicativity of the matrix 2-norm, we obtain that

$$\left\|\left(\tilde{W}-I\right)S^{\frac{1}{2}}v_\infty\right\|_2 \leq \sqrt{\delta_{\max}}\left(\gamma(R_0-1)+(R_0+1)\left\|\eta\right\|_2\right),$$

since $\|(W-I)\|_2 \leq R_0+1$. Since $\gamma = \mathcal{O}(R_0-1)$ and $\left\|\eta\right\|_2 = \mathcal{O}((R_0-1)^2)$ when $(B,S)\to(B^*,S^*)$, there is a constant $\tilde{\sigma}_1$ such that

$$\left\|\left(\tilde{W}-I\right)S^{\frac{1}{2}}v_\infty\right\|_2 \leq \tilde{\sigma}_1(R_0-1)^2 \tag{B.61}$$

when (B,S) approaches (B^*,S^*). Regarding the second addend in (B.60), it holds that

$$\begin{aligned}\left\|\operatorname{diag}(v(t))\tilde{W}\right\|_2 &\leq \left\|\operatorname{diag}(v(t))\right\|_2\left\|\tilde{W}\right\|_2 \\ &= R_0 \max_{l=1,\dots,N} v_{\infty,l}.\end{aligned}$$

Since $\|v_\infty\|_2 = \mathcal{O}(R_0-1)$ when $(B,S)\to(B^*,S^*)$, it follows that there is a constant $\tilde{\sigma}_2$ such that

$$\left\|\operatorname{diag}(v(t))\tilde{W}\right\|_2\left\|S^{\frac{1}{2}}v_\infty\right\|_2 \leq \tilde{\sigma}_2(R_0-1)^2 \tag{B.62}$$

when (B,S) approaches (B^*,S^*). Regarding the third addend in (B.60), it holds per definition of the matrix 2-norm that

$$\begin{aligned}\left\|c(t)S^{-\frac{1}{2}}\operatorname{diag}(Bv_\infty)S^{-\frac{1}{2}}\right\|_2 &= c(t)\max_{l=1,\dots,N}\sum_{j=1}^{N}\frac{\beta_{jl}}{\delta_l}v_{\infty,j} \\ &\leq \max_{l=1,\dots,N}(Wv_\infty)_l,\end{aligned}$$

where the last inequality follows from $c(t)\leq 1$, as stated by Lemma 3.5, and the definition of the effective infection rate matrix W in (3.1). Hence, we obtain the upper-bound

$$\left\|c(t)S^{-\frac{1}{2}}\operatorname{diag}(Bv_\infty)S^{-\frac{1}{2}}\right\|_2\left\|S^{\frac{1}{2}}v_\infty\right\|_2 \leq \tilde{\sigma}_3(R_0-1)^2 \tag{B.63}$$

for some constant $\tilde{\sigma}_3$ when (B,S) approaches (B^*,S^*). We apply the three upper bounds (B.61), (B.62) and (B.63) to (B.60) and obtain that

$$\left|\frac{v_\infty^T\Lambda_2(t)}{\|v_\infty\|_2^2}\right| \leq \sqrt{\delta_{\max}}\,(\tilde{\sigma}_1+\tilde{\sigma}_2+\tilde{\sigma}_3)\,\frac{(R_0-1)^2}{\|v_\infty\|_2^2}\,\|\xi(t)\|_2$$

when (B,S) approaches (B^*,S^*). Since $\|v_\infty\|_2^2 = \mathcal{O}((R_0-1)^2)$ when $(B,S)\to(B^*,S^*)$, there is a constant $\tilde{\sigma}_4$ such that, as (B,S) approaches (B^*,S^*), it holds

$$\left|\frac{v_\infty^T \Lambda_2(t)}{\|v_\infty\|_2^2}\right| \leq \tilde{\sigma}_4 \|\xi(t)\|_2$$

at every time t. Thus, we have obtained an upper bound, which is proportional to the norm of the error vector $\xi(t)$. Finally, we apply Theorem 3.6 to bound the norm $\|\xi(t)\|_2$, which completes the proof. □

Lemma B.9 suggests that, since $n(t)\to 0$ when $(B,S)\to(B^*,S^*)$, the differential equation (B.59) for the function $c(t)$ is approximated by the logistic differential equation

$$\frac{dc(t)}{dt} \approx \left(c(t)-c^2(t)\right)\varpi. \tag{B.64}$$

To make the statement (B.64) precise, we define the function $c_b(t,x)$, for any scalar x with $|x|<\varpi$, as

$$c_b(t,x) = \frac{1}{2} + \frac{1}{2}\sqrt{1+\frac{x}{\varpi}}\tanh\left(\frac{\sqrt{\varpi(\varpi+x)}}{2}t + \Upsilon(x)\right), \tag{B.65}$$

where the constant $\Upsilon(x)$ is set such that $c_b(0,x)=c(0)$, i.e.,

$$\Upsilon(x) = \operatorname{artanh}\left(\frac{2w}{\sqrt{\varpi(\varpi+x)}}\left(c(0)-\frac{1}{2}\right)\right).$$

Lemma B.10 states an upper and a lower bound on the function $c(t)$.

Lemma B.10. *Suppose that Assumptions 3.1 to 3.3 hold and that*

$$\|\xi(0)\|_2 \leq \sigma_1 (R_0-1)^p \tag{B.66}$$

for some constants $\sigma_1>0$ and $p>1$ when (B,S) approaches (B^*,S^*). Then, the function $c(t)$ is bounded by

$$c_b(t,-\kappa) \leq c(t) \leq c_b(t,\kappa) \quad \forall\ t\geq 0,$$

where the scalar κ equals $\kappa=\sigma_2(R_0-1)^s$ with $s=\min\{p,2\}$ and some constant $\sigma_2>0$ as (B,S) approaches (B^*,S^*).

Proof. With (B.66), Lemma B.9 implies that it holds that

$$|n(t)| \leq \tilde{\sigma}_1 (R_0-1)^p e^{-\tilde{\sigma}_2 t} + \tilde{\sigma}_3 (R_0-1)^2$$

for some constants $\tilde{\sigma}_1,\tilde{\sigma}_2,\tilde{\sigma}_3>0$. Since $e^{-\tilde{\sigma}_2 t}\leq 1$, we obtain that $|n(t)|\leq\kappa$ at every time t, where we define the scalar

$$\kappa = \tilde{\sigma}_4 (R_0-1)^s$$

with the constants $s = \min\{p,2\}$ and $\tilde{\sigma}_4 = \tilde{\sigma}_1 + \tilde{\sigma}_3$. With $|n(t)| \leq \kappa$, we obtain from the differential equation (B.59) for the function $c(t)$ that

$$\big(c(t) - c^2(t)\big)\,\varpi - \kappa \leq \frac{dc(t)}{dt} \leq \big(c(t) - c^2(t)\big)\,\varpi + \kappa \quad \forall\ t \geq 0. \tag{B.67}$$

The upper and lower bound (B.67) give rise to a Riccati differential equation, which can be solved exactly, and we obtain that the function $c(t)$ is bounded by

$$c(t) \geq \frac{1}{2} + \frac{1}{2}\sqrt{1 - \frac{\kappa}{\varpi}}\,\tanh\left(\frac{\sqrt{\varpi(\varpi-\kappa)}}{2}\,t + \Upsilon(-\kappa)\right)$$

and

$$c(t) \leq \frac{1}{2} + \frac{1}{2}\sqrt{1 + \frac{\kappa}{\varpi}}\,\tanh\left(\frac{\sqrt{\varpi(\varpi+\kappa)}}{2}\,t + \Upsilon(\kappa)\right).$$

at every time $t \geq 0$. □

When (B,S) approaches (B^*,S^*), Theorem 3.6 states that the error term $\xi(t)$ is negligible and, furthermore, Lemma B.10 states that the function $c(t)$ converges to $c_b(t,0)$. Thus, based on the ansatz (3.11), we approximate the viral state $v(t)$ by

$$v_{\mathrm{apx}}(t) = c_b(t,0)\,v_\infty.$$

With the definition of the function $c_b(t,x)$ in (B.65), it holds that

$$v_{\mathrm{apx}}(t) = \frac{1}{2}\left(1 + \tanh\left(\frac{\varpi}{2} + \Upsilon(0)\right)\right) v_\infty.$$

Then, it follows from the ansatz (3.11) that the difference of the exact viral state $v(t)$ to the approximation $v_{\mathrm{apx}}(t)$ equals

$$\|v(t) - v_{\mathrm{apx}}(t)\|_2 = |c(t) - c_b(t,0)|\,\|v_\infty\|_2 + \|\xi(t)\|_2. \tag{B.68}$$

The norm $\|\xi(t)\|_2$ of the error term $\xi(t)$ is bounded by Theorem 3.6. Thus, it remains to bound the first addend of (B.68). With Lemma B.10, the difference of the function $c(t)$ to $c_b(t,0)$ is bounded by

$$|c(t) - c_b(t,0)| \leq c_b(t,\kappa) - c_b(t,-\kappa). \tag{B.69}$$

Furthermore, the scalar κ converges to zero when (B,S) approaches (B^*,S^*). Hence, if we show that, as the scalar κ converges to zero, the upper bound $c_b(t,\kappa)$ converges to the lower bound $c_b(t,-\kappa)$ then (B.69) implies that the function $c(t)$ converges to $c_b(t,0)$. Furthermore, we must show that the upper bound $c_b(t,\kappa)$ converges to the lower bound $c_b(t,-\kappa)$ *uniformly in time* t, since the upper bound on the approximation error $\|v(t) - v_{\mathrm{apx}}(t)\|_2$ in Theorem 3.7 does not depend on time t. From the definition of the function $c_b(t,x)$ in (B.65) we obtain that

$$|c(t) - c_b(t,0)| \leq \frac{1}{2}\sqrt{1 + \frac{\kappa}{\varpi}}\,g(t,\kappa) - \frac{1}{2}\sqrt{1 - \frac{\kappa}{\varpi}}\,g(t,-\kappa), \tag{B.70}$$

where we denote

$$g(t,\kappa) = \tanh\left(\frac{\sqrt{\varpi\,(\varpi+\kappa)}}{2}\,t + \Upsilon\,(\kappa)\right). \tag{B.71}$$

Lemma B.10 states that $\kappa = \mathcal{O}((R_0-1)^s)$ for some $s>1$ when (B,S) approaches (B^*,S^*). Furthermore, Lemma B.8 states that $\varpi = \mathcal{O}(R_0-1)$. Hence, it holds that $\kappa/\varpi = \mathcal{O}((R_0-1)^{s-1})$ when (B,S) approaches (B^*,S^*). For small x, the series expansion of the square root yields that

$$\frac{1}{2}\sqrt{1+x} = \frac{1}{2} + \frac{1}{4}x + \mathcal{O}(x^2).$$

Thus, for small values of κ/ϖ, we obtain from (B.70) that

$$\begin{aligned}|c(t) - c_b(t,0)| \leq& \frac{1}{2}\big(g(t,\kappa) - g(t,-\kappa)\big) + \frac{1}{4\varpi}\kappa\big(g(t,\kappa) + g(t,-\kappa)\big)\\ &+ \big(g(t,\kappa) - g(t,-\kappa)\big)\cdot\mathcal{O}\left(\frac{\kappa^2}{\varpi^2}\right).\end{aligned}$$

Since the magnitude of the hyperbolic tangent is bounded by 1, it follows from the definition of the function $g(t,\kappa)$ in (B.71) that

$$\big|g(t,\kappa) - g(t,-\kappa)\big| \leq \big|g(t,\kappa)\big| + \big|g(t,-\kappa)\big| \leq 2,$$

which yields that

$$|c(t) - c_b(t,0)| \leq \frac{1}{2}\big(g(t,\kappa) - g(t,-\kappa)\big) + \frac{1}{2\varpi}\kappa + \mathcal{O}\left((R_0-1)^{2(s-1)}\right), \tag{B.72}$$

since $\kappa/\varpi = \mathcal{O}((R_0-1)^{s-1})$. The last two addends of (B.72) are independent of time t. Thus, it remains to show that first addend, i.e., the difference $(g(t,\kappa) - g(t,-\kappa))$, converges to zero *uniformly in time* t as $\kappa \to 0$.

Lemma B.11. *Under Assumptions 3.1 to 3.3, there is some constant $\sigma_1 > 0$ such that*

$$\big|g(t,\kappa) - g(t,-\kappa)\big| \leq 2\sigma_1\kappa$$

at every time $t \geq 0$ when the scalar κ approaches zero from above.

Proof. The mean value theorem gives that

$$g(t,\kappa) = g(t,0) + \partial_\kappa g(t,\kappa)\big|_{\kappa=z(t)}\,\kappa$$

for some $z(t) \in (0,\kappa)$. Thus, it holds that

$$g(t,\kappa) - g(t,-\kappa) = \partial_\kappa g(t,\kappa)\big|_{\kappa=z_1(t)}\,\kappa + \partial_\kappa g(t,\kappa)\big|_{\kappa=z_2(t)}\,\kappa$$

for some $z_1(t) \in (0,\kappa)$ and $z_2(t) \in (-\kappa,0)$, which yields that

$$\big|g(t,\kappa) - g(t,-\kappa)\big| = \Big|\partial_\kappa g(t,\kappa)\big|_{\kappa=z_1(t)}\Big|\,\kappa + \Big|\partial_\kappa g(t,\kappa)\big|_{\kappa=z_2(t)}\Big|\,\kappa. \tag{B.73}$$

B

To express the derivative of the function $g(t,\kappa)$, we write the function $g(t,x)$ as

$$g(t,\kappa) = \tanh(h(t,\kappa)),$$

where we define the function $h(t,\kappa)$ as

$$h(t,\kappa) = \frac{\sqrt{\varpi\,(\varpi+\kappa)}}{2}\,t + \Upsilon\,(\kappa)\,.$$

Then, the derivative of the function $g(t,\kappa)$ with respect to the scalar κ is given by

$$\partial_\kappa g(t,\kappa) = \frac{4}{\left(e^{-h(t,\kappa)} + e^{h(t,\kappa)}\right)^2}\partial_\kappa h(t,\kappa),$$

which is bounded by

$$\left|\partial_\kappa g(t,\kappa)\right| \leq 4e^{-2h(t,\kappa)}\left|\partial_\kappa h(t,\kappa)\right|. \tag{B.74}$$

With the derivative of the function $h(t,\kappa)$, i.e.,

$$\partial_\kappa h(t,\kappa) = \frac{\varpi}{4\sqrt{\varpi\,(\varpi+\kappa)}}\,t + \partial_\kappa \Upsilon\,(\kappa)\,,$$

we obtain from (B.74) that

$$\left|\partial_\kappa g(t,\kappa)\right| \leq 4e^{-\sqrt{\varpi(\varpi+\kappa)}t - 2\Upsilon(\kappa)}\left|\frac{\varpi}{4\sqrt{\varpi\,(\varpi+\kappa)}}\,t + \partial_\kappa \Upsilon\,(\kappa)\right|.$$

The right-hand side of (B.74) is finite at every time $t \geq 0$. Furthermore, for every scalar κ, the right-hand side of (B.74) converges to zero when $t \to \infty$. Hence, we can upper-bound the derivative $\left|\partial_\kappa g(t,\kappa)\right|$ by some constant $\sigma_1 > 0$ for every time t. Thus, we obtain from (B.73) that

$$\left|g(t,\kappa) - g(t,-\kappa)\right| = 2\sigma_1\kappa \quad \forall\ t \geq 0.$$

□

With Lemma B.11, we obtain from (B.72) that there is a constant $\sigma_1 > 0$ such that

$$|c(t) - c_b(t,0)| \leq \sigma_1\kappa + \frac{1}{2}\frac{\kappa}{\varpi} + \mathcal{O}\left((R_0-1)^{2(s-1)}\right) \quad \forall\ t \geq 0.$$

Since $\kappa = \mathcal{O}((R_0-1)^s)$ and $\varpi = \mathcal{O}(R_0-1)$ when (B,S) approaches (B^*,S^*), we obtain that there exists some constant $\sigma_2 > 0$ such that

$$|c(t) - c_b(t,0)| \leq \sigma_2(R_0-1)^{s-1}.$$

Thus, it follows from (B.68) that

$$\|v(t) - v_{\text{apx}}(t)\|_2 \leq \sigma_2(R_0-1)^{s-1}\|v_\infty\|_2 + \|\xi(t)\|_2, \quad \forall\, t \geq 0.$$

Hence, we obtain an upper bound as

$$\frac{\|v(t)-v_{\text{apx}}(t)\|_2}{\|v_\infty\|_2} \leq \sigma_2(R_0-1)^{s-1} + \frac{\|\xi(t)\|_2}{\|v_\infty\|_2}.$$

Then, the upper bound on the error vector $\xi(t)$ in Theorem 3.6 implies that there are constants σ_3, σ_4 such that

$$\frac{\|v(t)-v_{\text{apx}}(t)\|_2}{\|v_\infty\|_2} \leq \sigma_2(R_0-1)^{s-1} + \frac{\|\xi(0)\|_2}{\|v_\infty\|_2} e^{-\sigma_3 t} + \sigma_4 \frac{(R_0-1)^2}{\|v_\infty\|_2}.$$

By assumption it holds that $\|\xi(0)\|_2 = \mathcal{O}((R_0-1)^p)$ for some constant $p>1$, and it holds that $\|v_\infty\|_2 = \mathcal{O}(R_0-1)$ as stated by Theorem 3.4. Thus, we obtain that

$$\frac{\|v(t)-v_{\text{apx}}(t)\|_2}{\|v_\infty\|_2} \leq \sigma_2(R_0-1)^{s-1} + \sigma_5(R_0-1)^{p-1} + \sigma_6(R_0-1)$$

for some constants $\sigma_5, \sigma_6 > 0$, since $e^{-\sigma_3 t} \leq 1$. By using the definition $s = \min\{p, 2\}$ of the scalar s, we complete the proof.

B.6. PROOF OF COROLLARY 3.8

By assumption, it holds that $v(0) = r_0 v_\infty$, which implies that $\xi(0) = 0$. Thus, we obtain from (3.17) that

$$\frac{\|v(t)-v_{\text{apx}}(t)\|_2}{\|v_\infty\|_2} \leq \sigma_1(R_0-1) \quad \forall\, t \geq 0$$

when (B,S) approaches (B^*,S^*). From the definition of the approximation $v_{\text{apx}}(t)$ in (3.15), we obtain that $v_{\text{apx},i}(t_{01}) = r_1 v_{\infty,i}$ for every node i is equivalent to

$$\tanh\left(\frac{\varpi}{2} t_{01} + \Upsilon(0)\right) = 2r_1 - 1$$

With the definition of the term $\Upsilon(0)$ in (3.14), it follows that

$$\frac{\varpi}{2} t_{01} = \operatorname{artanh}(2r_1-1) - \operatorname{artanh}\left(2\frac{v_\infty^T v(0)}{\|v_\infty\|_2^2} - 1\right).$$

From $v(0) = r_0 v_\infty$, we obtain that

$$t_{01} = \frac{2}{\varpi}\left(\operatorname{artanh}(2r_1-1) - \operatorname{artanh}(2r_0-1)\right).$$

The inverse hyperbolic tangent equals

$$\operatorname{artanh}(x) = \frac{1}{2}\left(\log(1+x) - \log(1-x)\right),$$

which completes the proof.

B

B.7. PROOF OF COROLLARY 3.10

For NIMFA (1.3) with homogeneous spreading parameters β, δ, the effective infection rate matrix reduces to $W = \frac{\beta}{\delta} A$. Hence, the basic reproduction number reproduction becomes

$$R_0 = \frac{\beta}{\delta} \rho(A) = \frac{\tau}{\tau_c},$$

where the last equation follows from the definition of the effective infection rate $\tau = \beta/\delta$ and the epidemic threshold $\tau_c = 1/\rho(A)$. Furthermore, it holds that $\delta_l = \delta$ for every node l and $\sum_{l=1}^{N} (x_1)_l^2 = 1$, since the principal eigenvector x_1 is of unit length. Thus, the definition of the approximation $v_{\text{apx}}(t)$ in (3.15) yields that

$$v_{\text{apx}}(t) = \frac{1}{2} \left(1 + \tanh \left(\frac{(\tau - \tau_c)\delta}{2\tau_c} t + \Upsilon(0) \right) \right) v_\infty.$$

B.8. PROOF OF COROLLARY 3.11

Since $R_0 > 1$, the viral state $v(t)$ converges to a positive steady state v_∞ as $t \to \infty$. Thus, the steady state v_∞ must be element of the $m = 1$ dimensional invariant set $\mathcal{V} = \text{span}\{y_1\}$, which implies that $v_\infty = \tilde{c} y_1$ for some scalar c. Hence, the unit-length agitation mode equals either $y_1 = v_\infty / \| v_\infty \|_2$ or $y_1 = -v_\infty / \| v_\infty \|_2$. Without loss of generality assume that $y_1 = v_\infty / \| v_\infty \|_2$. Then, under Assumption 3.3, the matrix B is connected, which implies that $B y_1 \neq 0$ since the vector y_1 is positive. Thus, the subspace $\mathcal{V}_0$ must be empty.

To prove Corollary 3.11, we must show two directions. **"If" direction**: Suppose the infection rate matrix B is regular. Then, the viral state $v_{\infty,i}$ is the same for all nodes i, and $v(0) \in \mathcal{V}$ implies that $v_i(0) = v_j(0)$ for all nodes i, j. Since the matrix B is regular and the initial viral state $v_i(0)$ is the same for every node i, the approximation $v_{\text{apx}}(t) = c(t) v_\infty$ is exact. Since $v(t) = c(t) v_\infty$ at every time t, the invariant set $\mathcal{V} = \text{span}\{y_1\}$ is indeed a one-dimensional invariant set of NIMFA.

"Only if" direction: Suppose the one-dimensional subspace $\mathcal{V} = \text{span}\{y_1\}$ is an invariant set of NIMFA. Then, Theorem 2.14 yields that the infection rate matrix B has the equitable partition $\pi = \{\mathcal{N}_1\}$, where the cell $\mathcal{N}_1 = \{1, \ldots, N\}$ contains all nodes. Thus, (2.10) yields, for some degree d_{11}, that

$$d_{11} = \sum_{k \in \mathcal{N}_1} \beta_{ik} = \sum_{k=1}^{N} \beta_{ik}$$

for all nodes i. Thus, we obtain with definition (3.21) that the matrix B is regular.

B.9. PROOF OF THEOREM 3.12

We acknowledge the help of Karel Devriendt, who constructed an effective infection rate matrix of homogeneous NIMFA with a given principal eigenvector x_1. The idea of proving Theorem 3.12 is based on Corollary 3.9: When $R_0 \downarrow 1$, the viral state dynamics of heterogeneous NIMFA (1.1) are determined by the four variables $x_1, \varpi, \gamma, \Upsilon(0)$. Thus, we aim to show that the corresponding four variables of the homogeneous NIMFA system

(3.22), which we denote by $x_{1,\text{hom}}, \varpi_{\text{hom}}, \gamma_{\text{hom}}$ and $\Upsilon_{\text{hom}}(0)$, are the same as the variables $x_1, \varpi, \gamma, \Upsilon(0)$ of heterogeneous NIMFA (1.1).

Lemma B.12. *The homogeneous NIMFA system (3.22) and heterogeneous NIMFA (1.1) have the same principal eigenvector $x_{1,\text{hom}} = x_1$, the variable $\gamma_{\text{hom}} = \gamma$ and viral slope $\varpi_{\text{hom}} = \varpi$.*

Proof. First, we consider the principal eigenvector x_1. The effective infection rate matrix of the homogeneous NIMFA system (3.22) equals

$$W_{\text{hom}} = \frac{\beta_{\text{hom}}}{\delta_{\text{hom}}} u u^T + \frac{\beta_{\text{hom}}}{\delta_{\text{hom}}} \frac{1}{\min\limits_{l=1,\dots,N} (x_1)_l} \sum_{j=1}^{N} (x_1)_j I - \frac{\beta_{\text{hom}}}{\delta_{\text{hom}}} \sum_{j=1}^{N} (x_1)_j \operatorname{diag}\left(\frac{1}{(x_1)_1}, \dots, \frac{1}{(x_1)_N}\right). \tag{B.75}$$

We show that the principal eigenvector x_1 of heterogeneous NIMFA (1.1) is also the principal eigenvector $x_{1,\text{hom}}$ of the matrix W_{hom}. Indeed,

$$\begin{aligned} W_{\text{hom}} x_1 &= \frac{\beta_{\text{hom}}}{\delta_{\text{hom}}} \sum_{j=1}^{N} (x_1)_j u + \frac{\beta_{\text{hom}}}{\delta_{\text{hom}}} \frac{1}{\min\limits_{l=1,\dots,N} (x_1)_l} \sum_{j=1}^{N} (x_1)_j x_1 - \frac{\beta_{\text{hom}}}{\delta_{\text{hom}}} \sum_{j=1}^{N} (x_1)_j u \\ &= \frac{\beta_{\text{hom}}}{\delta_{\text{hom}}} \frac{1}{\min\limits_{l=1,\dots,N} (x_1)_l} \sum_{j=1}^{N} (x_1)_j x_1. \end{aligned}$$

Thus, x_1 is an eigenvector of the effective infection rate matrix W_{hom} of the homogeneous NIMFA system (3.22). The corresponding eigenvalue equals

$$\lambda_{1,\text{hom}} = \frac{\beta_{\text{hom}}}{\delta_{\text{hom}}} \frac{1}{\min\limits_{l=1,\dots,N} (x_1)_l} \sum_{j=1}^{N} (x_1)_j. \tag{B.76}$$

The effective infection rate matrix W_{hom} is non-negative and irreducible, by definition (B.75). Thus, the Perron-Frobenius Theorem [32] yields that the eigenvalue $\lambda_{1,\text{hom}}$ to the positive eigenvector x_1 equals the spectral radius $\rho(W_{\text{hom}}) = \lambda_{1,\text{hom}}$ and that $x_{1,\text{hom}} = x_1$. Second, we consider the variables $\gamma, \gamma_{\text{hom}}$ in Theorem 3.4. By definition (3.3) and since x_1 is a vector of length 1, it holds that

$$\begin{aligned} \gamma_{\text{hom}} &= (\lambda_{1,\text{hom}} - 1) \frac{1}{\sum_{l=1}^{N} (x_1)_l^3} \\ &= \left(\frac{\beta_{\text{hom}}}{\delta_{\text{hom}}} \frac{1}{\min\limits_{l=1,\dots,N} (x_1)_l} \sum_{j=1}^{N} (x_1)_j - 1 \right) \frac{1}{\sum_{p=1}^{N} (x_1)_p^3}, \end{aligned}$$

where the last equality follows from (B.76). With (3.24), we obtain further that

$$\gamma_{\text{hom}} = \left(\left(1 + \gamma \sum_{l=1}^{N} (x_1)_l^3 \right) - 1 \right) \frac{1}{\sum_{p=1}^{N} (x_1)_p^3} = \gamma.$$

Third, we show that the viral slope ϖ_{hom} of the homogeneous NIMFA (3.22) equals the viral slope ϖ of heterogeneous NIMFA (1.1). From the definition (B.57), the variable ϖ_{hom} of the homogeneous NIMFA system (3.22) follows as

$$\varpi_{\text{hom}} = \left(\lambda_{1,\text{hom}} - 1\right)\delta_{\text{hom}}.$$

With (B.76), we obtain that

$$\varpi_{\text{hom}} = \beta_{\text{hom}} \frac{1}{\min\limits_{l=1,\dots,N} (x_1)_l} \sum_{j=1}^{N} (x_1)_j - \delta_{\text{hom}}.$$

Then, the definition of the infection rate β_{hom} in (3.24) yields that

$$\begin{aligned}\varpi_{\text{hom}} &= \delta_{\text{hom}} \left(1 + \gamma \sum_{l=1}^{N} (x_1)_l^3\right) - \delta_{\text{hom}} \\ &= \delta_{\text{hom}} \gamma \sum_{l=1}^{N} (x_1)_l^3,\end{aligned}$$

which simplifies with the definition of δ_{hom} in (3.23) to

$$\varpi_{\text{hom}} = \gamma \sum_{l=1}^{N} \delta_l (x_1)_l^3.$$

Then, the definition of γ in (3.3) yields that

$$\varpi_{\text{hom}} = (R_0 - 1) \sum_{l=1}^{N} \delta_l (x_1)_l^2.$$

Thus, the viral slope ϖ_{hom} of the homogeneous NIMFA system (3.22) equals the viral slope ϖ of heterogeneous NIMFA (1.1), which completes the proof. □

In contrast to the variables x_1, γ, ϖ in Lemma B.12, the two variables $\Upsilon_{\text{hom}}(0)$ and $\Upsilon(0)$, given by definition (3.14), are not necessarily equal, since the steady states v_∞ and $v_{\infty,\text{hom}}$ might be different. For the homogeneous NIMFA system (3.22) and heterogeneous NIMFA (1.1), we denote the viral state approximations of Corollary 3.9 by $\tilde{v}_{\text{apx}}(t)$ and $\tilde{v}_{\text{apx,hom}}(t)$, respectively. The difference of the viral state vectors $v(t)$ and $v_{\text{hom}}(t)$ can be written as

$$v(t) - v_{\text{hom}}(t) = \tilde{v}_{\text{apx}}(t) - \tilde{v}_{\text{apx,hom}}(t) + \left(v(t) - \tilde{v}_{\text{apx}}(t)\right) - \left(v_{\text{hom}}(t) - \tilde{v}_{\text{apx,hom}}(t)\right).$$

With the triangle inequality, we obtain that

$$\|v(t) - v_{\text{hom}}(t)\|_2 \leq \left\|\tilde{v}_{\text{apx}}(t) - \tilde{v}_{\text{apx,hom}}(t)\right\|_2 + \left\|v(t) - \tilde{v}_{\text{apx}}(t)\right\|_2 + \left\|v_{\text{hom}}(t) - \tilde{v}_{\text{apx,hom}}(t)\right\|_2. \tag{B.77}$$

Corollary 3.9 states that there is some constant σ, such that, at every time $t \geq 0$, it holds that

$$\|v(t) - \tilde{v}_{\text{apx}}(t)\|_2 \leq \sigma \|v_\infty\|_2 (R_0 - 1)^{s-1} = \mathcal{O}\left((R_0 - 1)^s\right)$$

as $R_0 \downarrow 1$, since $\|v_\infty\|_2 = \mathcal{O}(R_0 - 1)$ by Theorem 3.4. Similarly, Corollary 3.9 implies that $\|v_{\text{hom}}(t) - \tilde{v}_{\text{apx, hom}}(t)\|_2 = \mathcal{O}((R_0-1)^s)$ as $R_0 \downarrow 1$. Thus, (B.77) yields that

$$\|v(t) - v_{\text{hom}}(t)\|_2 \leq \left\| v_{\text{apx}}(t) - v_{\text{apx,hom}}(t) \right\|_2 + \mathcal{O}\left((R_0-1)^s\right). \tag{B.78}$$

In the following, we bound the first addend on the right side of (B.78). We insert the expression (3.18) for the approximations $v_{\text{apx}}(t)$ and $v_{\text{apx,hom}}(t)$ to obtain that

$$\begin{aligned} v_{\text{apx}}(t) - v_{\text{apx,hom}}(t) &= \left(1 + \tanh\left(\frac{\varpi}{2}t + \Upsilon(0)\right)\right)\frac{\gamma}{2}x_1 \\ &\quad - \left(1 + \tanh\left(\frac{\varpi_{\text{hom}}}{2}t + \Upsilon_{\text{hom}}(0)\right)\right)\frac{\gamma_{\text{hom}}}{2}x_{1,\text{hom}} \\ &= \left(\tanh\left(\frac{\varpi}{2}t + \Upsilon(0)\right) - \tanh\left(\frac{\varpi}{2}t + \Upsilon_{\text{hom}}(0)\right)\right)\frac{\gamma}{2}x_1, \end{aligned}$$

where the second equality follows from Lemma B.12. From [282, 4.5.45], it follows that

$$v_{\text{apx}}(t) - v_{\text{apx,hom}}(t) = \operatorname{sech}\left(\frac{\varpi}{2}t + \Upsilon(0)\right)\operatorname{sech}\left(\frac{\varpi}{2}t + \Upsilon_{\text{hom}}(0)\right)\sinh\left(\Upsilon(0) - \Upsilon_{\text{hom}}(0)\right)\frac{\gamma}{2}x_1.$$

Since $0 < \operatorname{sech}(t) \leq 1$ for every time t and the eigenvector x_1 has length 1, we obtain that

$$\left\| v_{\text{apx}}(t) - v_{\text{apx,hom}}(t) \right\|_2 \leq \frac{\gamma}{2}\left|\sinh\left(\Upsilon(0) - \Upsilon_{\text{hom}}(0)\right)\right|.$$

Thus, the difference of the viral states $v(t)$ and $v_{\text{hom}}(t)$ in (B.78) is bounded by

$$\|v(t) - v_{\text{hom}}(t)\|_2 \leq \frac{\gamma}{2}\left|\sinh\left(\Upsilon(0) - \Upsilon_{\text{hom}}(0)\right)\right| + \mathcal{O}\left((R_0-1)^s\right). \tag{B.79}$$

To bound the hyperbolic sine on the right side of (B.79), we introduce:

Lemma B.13. *Suppose that Assumptions 3.1 to 3.3 hold. Furthermore, assume that the initial viral states of the homogeneous NIMFA system (3.22) and heterogeneous NIMFA (1.1) are the same, i.e., $v(0) = v_{\text{hom}}(0)$. Then, as $R_0 \downarrow 1$, it holds that*

$$\left|\sinh\left(\Upsilon(0) - \Upsilon_{\text{hom}}(0)\right)\right| = \mathcal{O}(R_0 - 1).$$

Proof. The series expansion [282, 4.5.62] of the hyperbolic sine yields that

$$\sinh\left(\Upsilon(0) - \Upsilon_{\text{hom}}(0)\right) = \Upsilon(0) - \Upsilon_{\text{hom}}(0) + \mathcal{O}\left(\left(\Upsilon(0) - \Upsilon_{\text{hom}}(0)\right)^3\right). \tag{B.80}$$

In the following, we consider the difference $\Upsilon(0) - \Upsilon_{\text{hom}}(0)$. Since $v(0) = v_{\text{hom}}(0)$ by the assumption, it follows from the definition of the variable $\Upsilon(0)$ in (3.14) that

$$\begin{aligned} \Upsilon(0) - \Upsilon_{\text{hom}}(0) &= \operatorname{artanh}\left(2\frac{v_\infty^T v(0)}{\|v_\infty\|_2^2} - 1\right) - \operatorname{artanh}\left(2\frac{v_{\infty,\text{hom}}^T v(0)}{\|v_{\infty,\text{hom}}\|_2^2} - 1\right) \\ &= \operatorname{artanh}(\varrho) - \operatorname{artanh}(\varrho + \Theta), \end{aligned} \tag{B.81}$$

where we define

$$\varrho = 2\frac{v_\infty^T v(0)}{\|v_\infty\|_2^2} - 1 \tag{B.82}$$

and

$$\Theta = 2\frac{v_{\infty,\mathrm{hom}}^T v(0)}{\|v_{\infty,\mathrm{hom}}\|_2^2} - 1 - \varrho. \tag{B.83}$$

The Taylor series of $\operatorname{artanh}(\varrho+\Theta)$ around $\Theta = 0$ reads

$$\operatorname{artanh}(\varrho+\Theta) = \operatorname{artanh}(\varrho) + \frac{1}{1-\varrho^2}\Theta + \mathcal{O}(\Theta^2).$$

Thus, we obtain from (B.81) that

$$\Upsilon(0) - \Upsilon_{\mathrm{hom}}(0) = \frac{1}{\varrho^2-1}\Theta + \mathcal{O}(\Theta^2). \tag{B.84}$$

Hence, to bound the difference $\Upsilon(0) - \Upsilon_{\mathrm{hom}}(0)$, we aim to bound the variable Θ. The definition of Θ in (B.83) yields with (B.82) that

$$\begin{aligned}\Theta &= 2\frac{v_{\infty,\mathrm{hom}}^T v(0)}{\|v_{\infty,\mathrm{hom}}\|_2^2} - 2\frac{v_\infty^T v(0)}{\|v_\infty\|_2^2} \\ &= 2\left(\frac{v_{\infty,\mathrm{hom}}^T}{\|v_{\infty,\mathrm{hom}}\|_2^2} - \frac{v_\infty^T}{\|v_\infty\|_2^2}\right) v(0).\end{aligned}$$

The Cauchy-Schwarz inequality gives that

$$\begin{aligned}|\Theta| &\le 2\|v(0)\|_2 \left\| \frac{v_{\infty,\mathrm{hom}}}{\|v_{\infty,\mathrm{hom}}\|_2^2} - \frac{v_\infty}{\|v_\infty\|_2^2} \right\|_2 \\ &= 2\frac{\|v(0)\|_2}{\|v_\infty\|_2^2} \left\| \frac{\|v_\infty\|_2^2}{\|v_{\infty,\mathrm{hom}}\|_2^2} v_{\infty,\mathrm{hom}} - v_\infty \right\|_2.\end{aligned}$$

Under Assumption 3.2, it holds that $\|v(0)\|_2 \le \|v_\infty\|_2$, and hence

$$|\Theta| \le 2\frac{1}{\|v_\infty\|_2} \left\| \frac{\|v_\infty\|_2^2}{\|v_{\infty,\mathrm{hom}}\|_2^2} v_{\infty,\mathrm{hom}} - v_\infty \right\|_2,$$

which can be rewritten as

$$|\Theta| \le 2\frac{1}{\|v_\infty\|_2} \left\| v_{\infty,\mathrm{hom}} - v_\infty + \left(\frac{\|v_\infty\|_2^2}{\|v_{\infty,\mathrm{hom}}\|_2^2} - 1 \right) v_{\infty,\mathrm{hom}} \right\|_2.$$

The triangle inequality yields that

$$|\Theta| \le 2\frac{\|v_{\infty,\mathrm{hom}} - v_\infty\|_2}{\|v_\infty\|_2} + 2\frac{1}{\|v_\infty\|_2} \left\| \left(\frac{\|v_\infty\|_2^2}{\|v_{\infty,\mathrm{hom}}\|_2^2} - 1 \right) v_{\infty,\mathrm{hom}} \right\|_2,$$

which becomes

$$|\Theta| \leq 2\frac{\left\|v_{\infty,\text{hom}} - v_\infty\right\|_2}{\|v_\infty\|_2} + 2\frac{\left\|v_{\infty,\text{hom}}\right\|_2}{\|v_\infty\|_2}\left|\frac{\|v_\infty\|_2^2}{\|v_{\infty,\text{hom}}\|_2^2} - 1\right|$$
$$= 2\frac{\left\|v_{\infty,\text{hom}} - v_\infty\right\|_2}{\|v_\infty\|_2} + 2\frac{\left|\|v_\infty\|_2^2 - \|v_{\infty,\text{hom}}\|_2^2\right|}{\|v_\infty\|_2\left\|v_{\infty,\text{hom}}\right\|_2}. \tag{B.85}$$

Since, by Lemma B.12, $\gamma_{\text{hom}} = \gamma$ and $x_{1,\text{hom}} = x_1$, Theorem 3.4 implies that

$$v_{\infty,\text{hom}} = \gamma x_1 + \eta_{\text{hom}} \tag{B.86}$$

for some $N \times 1$ vector η_{hom} that satisfies $\|\eta_{\text{hom}}\|_2 = \mathcal{O}\left((R_0-1)^2\right)$ as $R_0 \downarrow 1$. Thus, with (3.2) and (B.86), we obtain from (B.85) that

$$|\Theta| \leq 2\frac{\left\|\eta - \eta_{\text{hom}}\right\|_2}{\|v_\infty\|_2} + 2\frac{\left|2\gamma x_1^T\left(\eta - \eta_{\text{hom}}\right) + \|\eta\|_2^2 - \|\eta_{\text{hom}}\|_2^2\right|}{\|v_\infty\|_2\left\|v_{\infty,\text{hom}}\right\|_2}.$$

Finally, it holds that $\|\eta\|_2 = \mathcal{O}\left((R_0-1)^2\right)$, $\|\eta_{\text{hom}}\|_2 = \mathcal{O}\left((R_0-1)^2\right)$, $\gamma = \mathcal{O}(R_0-1)$, $\|v_\infty\|_2 = \mathcal{O}(R_0-1)$ and $\|v_{\infty,\text{hom}}\|_2 = \mathcal{O}(R_0-1)$. Thus, we obtain that $|\Theta| = \mathcal{O}(R_0-1)$ as $R_0 \downarrow 1$, which completes the proof in combination with (B.80) and (B.84). □

With Lemma B.13 and $\gamma = \mathcal{O}(R_0-1)$, we obtain from (B.79) that

$$\begin{aligned}\|v(t) - v_{\text{hom}}(t)\|_2 =& \mathcal{O}\left((R_0-1)^2\right) + \mathcal{O}\left((R_0-1)^s\right)\\ =& \mathcal{O}\left((R_0-1)^s\right),\end{aligned}$$

since, by definition, $s = \min\{p,2\} \leq 2$. Since $\|v_\infty\|_2 = \mathcal{O}(R_0-1)$ by Theorem 3.4, it holds that

$$\frac{\|v(t) - v_{\text{hom}}(t)\|_2}{\|v_\infty\|_2} = \mathcal{O}\left((R_0-1)^{s-1}\right)$$

as $R_0 \downarrow 1$, which completes the proof.

C

Appendix to Chapter 4

C.1. Proof of Lemma 4.8

The elements of the matrix R, defined by (4.4), equal

$$R_{ij} = \begin{cases} 1 - \delta_{\Delta t,i} + \beta_{\Delta t,ii} & \text{if} \quad i = j, \\ \beta_{\Delta t,ij} & \text{if} \quad i \neq j. \end{cases}$$

Under Assumption 4.2, it holds $\beta_{\Delta t,ij} \geq 0$ for all nodes i, j. Thus, the off-diagonal entries of the matrix R are non-negative. For the diagonal entries of the matrix R, it holds

$$R_{ii} = 1 - \delta_{\Delta t,i} + \beta_{\Delta t,ii} \geq 1 - \delta_i \Delta t,$$

since $\beta_{\Delta t,ii} \geq 0$ and $\delta_{\Delta t,i} = \delta_i \Delta t$. From Assumption 4.3, we further obtain that

$$R_{ii} \geq 1 - \delta_i \frac{1}{\delta_i + \sum_{j=1}^{N} \beta_{ij}} \geq 0.$$

Hence, the matrix R is non-negative. Furthermore, the matrix R is irreducible, which follows from the irreducibility of the matrix $B_{\Delta t}$ under Assumption 4.5.

C.2. Proof of Lemma 4.9

The proof is analogous to the proof in [20, Theorem 5 and Lemma 9]. From the steady-state equation (4.3), we obtain that

$$v_{\infty,i} \left(\delta_{\Delta t,i} + \sum_{j=1}^{N} \beta_{\Delta t,ij} v_{\infty,j} \right) = \sum_{j=1}^{N} \beta_{\Delta t,ij} v_{\infty,j}.$$

Hence, it holds that

$$v_{\infty,i} = \frac{\sum_{j=1}^{N} \beta_{\Delta t,ij} v_{\infty,j}}{\delta_{\Delta t,i} + \sum_{j=1}^{N} \beta_{\Delta t,ij} v_{\infty,j}},$$

which equals

$$v_{\infty,i} = 1 - \frac{\delta_{\Delta t,i}}{\delta_{\Delta t,i} + \sum_{j=1}^{N} \beta_{\Delta t,ij} v_{\infty,j}}. \tag{C.1}$$

Since $v_{\infty,j} \leq 1$ for every node j, we obtain an upper bound on the steady-state $v_{\infty,i}$ of node i as

$$v_{\infty,i} \leq 1 - \frac{\delta_{\Delta t,i}}{\delta_{\Delta t,i} + \sum_{j=1}^{N} \beta_{\Delta t,ij}}.$$

We denote the minimum of the steady-state vector by

$$v_{\infty,\min} = \min\{v_{\infty,1}, ..., v_{\infty,N}\}.$$

Theorem 4.7 implies that $v_{\infty,\min} > 0$. Assuming that the minimum $v_{\infty,\min}$ occurs at node i, we obtain from (C.1) that

$$\begin{aligned} v_{\infty,\min} &= 1 - \frac{\delta_{\Delta t,i}}{\delta_{\Delta t,i} + \sum_{j=1}^{N} \beta_{\Delta t,ij} v_{\infty,j}} \\ &\geq 1 - \frac{\delta_{\Delta t,i}}{\delta_{\Delta t,i} + v_{\infty,\min} \sum_{j=1}^{N} \beta_{\Delta t,ij}}. \end{aligned}$$

Hence, it holds that

$$v_{\infty,\min} \geq \frac{v_{\infty,\min} \sum_{j=1}^{N} \beta_{\Delta t,ij}}{\delta_{\Delta t,i} + v_{\infty,\min} \sum_{j=1}^{N} \beta_{\Delta t,ij}},$$

from which we obtain that

$$v_{\infty,\min} \geq 1 - \frac{\delta_{\Delta t,i}}{\sum_{j=1}^{N} \beta_{\Delta t,ij}}.$$

C.3. PROOF OF PROPOSITION 4.10

Since $\Delta v_i[k+1] = v_i[k+1] - v_{\infty,i}$, the evolution of the difference $\Delta v_i[k]$ over time k can be stated with the NIMFA equations (4.1) as

$$\Delta v_i[k+1] = (1 - \delta_{\Delta t,i}) v_i[k] + \sum_{j=1}^{N} \beta_{\Delta t,ij} v_j[k] - v_i[k] \sum_{j=1}^{N} \beta_{\Delta t,ij} v_j[k] - v_{\infty,i}. \tag{C.2}$$

We would like to express the difference $\Delta v_i[k+1]$ at the next time $k+1$ only in dependency of the difference $\Delta v[k]$ at the current time k and the constant steady state v_∞. The steady state v_∞ is given by (4.3) and satisfies

$$v_{\infty,i} = (1 - \delta_{\Delta t,i}) v_{\infty,i} + (1 - v_{\infty,i}) \sum_{j=1}^{N} \beta_{\Delta t,ij} v_{\infty,j}, \tag{C.3}$$

for all nodes i. We insert (C.3) in (C.2) and obtain that

$$\begin{aligned}\Delta v_i[k+1] =&(1-\delta_{\Delta t,i})\,v_i[k] + \sum_{j=1}^{N}\beta_{\Delta t,ij}\,v_j[k] - v_i[k]\sum_{j=1}^{N}\beta_{\Delta t,ij}\,v_j[k]\\ &-(1-\delta_{\Delta t,i})\,v_{\infty,i} - \sum_{j=1}^{N}\beta_{\Delta t,ij}\,v_{\infty,j} + v_{\infty,i}\sum_{j=1}^{N}\beta_{\Delta t,ij}\,v_{\infty,j}.\end{aligned} \tag{C.4}$$

Since $\Delta v_i[k] = v_i[k] - v_{\infty,i}$, we can express (C.4) more compactly as

$$\begin{aligned}\Delta v_i[k+1] =&(1-\delta_{\Delta t,i})\Delta v_i[k] + \sum_{j=1}^{N}\beta_{\Delta t,ij}\Delta v_j[k]\\ &-\sum_{j=1}^{N}\beta_{\Delta t,ij}\left(v_i[k]\,v_j[k] - v_{\infty,i}\,v_{\infty,j}\right).\end{aligned} \tag{C.5}$$

The first two terms in (C.5) are already in the desired form: they depend on the difference $\Delta v[k]$ but not on the viral state $v[k]$ at time k. To replace the viral state $v[k]$ in the last term of (C.5) by an expression of the difference $\Delta v[k]$, we observe that

$$v_i[k]\,v_j[k] - v_{\infty,i}\,v_{\infty,j} = \Delta v_i[k]\Delta v_j[k] + \Delta v_i[k]\,v_{\infty,j} + v_{\infty,i}\Delta v_j[k], \tag{C.6}$$

since $v_i[k] = \Delta v_i[k] + v_{\infty,i}$. Inserting (C.6) in (C.5) yields that

$$\begin{aligned}\Delta v_i[k+1] =&\left(1-\delta_{\Delta t,i} - \sum_{j=1}^{N}\beta_{\Delta t,ij}\,v_{\infty,j}\right)\Delta v_i[k]\\ &+(1-v_{\infty,i})\sum_{j=1}^{N}\beta_{\Delta t,ij}\Delta v_j[k] - \Delta v_i[k]\sum_{j=1}^{N}\beta_{\Delta t,ij}\Delta v_j[k].\end{aligned} \tag{C.7}$$

The expression (C.7) can be further simplified. The steady-state equation (4.3) is equivalent to

$$\sum_{j=1}^{N}\beta_{\Delta t,ij}\,v_{\infty,j} = \delta_{\Delta t,i}\left(\frac{1}{1-v_{\infty,i}} - 1\right). \tag{C.8}$$

From (C.8), it follows that (C.7) is equivalent to

$$\begin{aligned}\Delta v_i[k+1] =&\left(1+\frac{\delta_{\Delta t,i}}{v_{\infty,i}-1}\right)\Delta v_i[k] + (1-v_{\infty,i})\sum_{j=1}^{N}\beta_{\Delta t,ij}\Delta v_j[k]\\ &-\Delta v_i[k]\sum_{j=1}^{N}\beta_{\Delta t,ij}\Delta v_j[k].\end{aligned} \tag{C.9}$$

Stacking equation (C.9) for all nodes $i = 1,\ldots,N$ completes the proof.

C.4. PROOF OF LEMMA 4.11

We consider the elements of the matrix F. For $i \neq j$ it holds that

$$F_{ij} = \left(1 - v_{\infty,i}\right) \beta_{\Delta t,ij} \geq 0,$$

since $v_{\infty,i} \leq 1$ and $\beta_{\Delta t,ij} \geq 0$. The diagonal elements of the matrix F equal

$$F_{ii} = 1 + \frac{\delta_{\Delta t,i}}{v_{\infty,i} - 1} + \left(1 - v_{\infty,i}\right) \beta_{\Delta t,ii}, \quad i = 1, ..., N.$$

Since $\beta_{\Delta t,ii} \geq 0$, we obtain that

$$F_{ii} \geq 1 + \frac{\delta_{\Delta t,i}}{v_{\infty,i} - 1}. \tag{C.10}$$

We proceed the proof by showing that the right hand side of (C.10) is non-negative, i.e.,

$$1 + \frac{\delta_{\Delta t,i}}{v_{\infty,i} - 1} \geq 0,$$

which is equivalent to

$$v_{\infty,i} \leq 1 - \delta_{\Delta t,i}. \tag{C.11}$$

With the upper bound on the viral state $v_{\infty,i}$ provided by Lemma 4.9, we obtain that a sufficient condition for (C.11) is

$$1 - \frac{\delta_{\Delta t,i}}{\delta_{\Delta t,i} + \sum_{j=1}^{N} \beta_{\Delta t,ij}} \leq 1 - \delta_{\Delta t,i},$$

which is equivalent to

$$\delta_{\Delta t,i} + \sum_{j=1}^{N} \beta_{\Delta t,ij} \leq 1.$$

From $\delta_{\Delta t,i} = \delta_i \Delta t$ and $\beta_{\Delta t,ij} = \beta_{ij} \Delta t$, we finally obtain that

$$\Delta t \leq \frac{1}{\delta_i + \sum_{j=1}^{N} \beta_{ij}},$$

is a sufficient condition for $F_{ii} \geq 0$, which is satisfied under Assumption 4.3.

C.5. PROOF OF COROLLARY 4.12

We rewrite equation (C.7) to obtain that

$$\Delta v_i[k+1] = g_i[k] + h_i[k] \Delta v_i[k], \tag{C.12}$$

where the terms $g_i[k]$ and $h_i[k]$ are given by

$$g_i[k] = (1 - v_{\infty,i}) \sum_{j=1}^{N} \beta_{\Delta t,ij} \Delta v_j[k] \tag{C.13}$$

and

$$h_i[k] = 1 - \delta_{\Delta t,i} - \sum_{j=1}^{N} \beta_{\Delta t,ij} \left(v_{\infty,j} + \Delta v_j[k] \right)$$

for every node i. Since $\beta_{\Delta t,ij} \geq 0$ and $(1 - v_{\infty,i}) \geq 0$, the definition (C.13) of $g_i[k]$ shows that

$$\Delta v_j[k] \leq 0 \; \forall j = 1, ..., N \Rightarrow g_i[k] \leq 0.$$

Furthermore, by the definition of $\Delta v_j[k] = v_j[k] - v_{\infty,j}$ and since $v_j[k] \leq 1$, it holds that

$$h_i[k] = 1 - \delta_{\Delta t,i} - \sum_{j=1}^{N} \beta_{\Delta t,ij} v_j[k] \geq 1 - \delta_{\Delta t,i} - \sum_{j=1}^{N} \beta_{\Delta t,ij}. \tag{C.14}$$

Assumption 4.3 states that $\delta_{\Delta t,i} + \sum_{j=1}^{N} \beta_{\Delta t,ij} \leq 1$. Hence, (C.14) implies that $h_i[k] \geq 0$. From $g_i[k] \leq 0$ if $\Delta v_i[k] \leq 0$ for all nodes i, $h_i[k] \geq 0$ and (C.12) it follows that: $\Delta v_i[k] \leq 0$ for all nodes i implies that $\Delta v_i[k+1] \leq 0$ for all nodes i. Hence, we obtain by induction that $\Delta v_i[1] \leq 0$ for all nodes i implies $\Delta v_i[k] \leq 0$ for all nodes i at every time $k \geq 1$, which proves Corollary 4.12. (Analogously, we can prove that $\Delta v_i[1] \geq 0$ for all nodes i implies $\Delta v_i[k] \geq 0$ for all nodes i at every time $k \geq 1$.)

C.6. PROOF OF THEOREM 4.13

The discrete-time NIMFA system (4.2) is asymptotically stable at the steady-state v_∞ if the linearisation (4.9) at $\Delta v[k] = 0$ is stable [42]. The LTI system (4.9) is stable if the magnitudes of all the eigenvalues of its $N \times N$ system matrix F are smaller than one, which is equivalent to $\rho(F) < 1$ by the definition of the spectral radius. Lemma 4.11 states that the matrix F is non-negative. Hence, the spectral radius $\rho(F)$ is bounded by [285, Theorem 8.1.26.]

$$\rho(F) \leq \max_{i=1,...,N} \frac{1}{y_i} \sum_{j=1}^{N} F_{ij} y_j$$

for any $N \times 1$ vector $y > 0$. It holds $v_\infty > 0$ and by setting $y = v_\infty$, we obtain that

$$\rho(F) \leq \max_{i=1,...,N} \frac{1}{v_{\infty,i}} \sum_{j=1}^{N} F_{ij} v_{\infty,j}. \tag{C.15}$$

From the definition of the matrix F in (4.7) it follows that

$$\begin{aligned} \sum_{j=1}^{N} F_{ij} v_{\infty,j} &= v_{\infty,i} - \delta_{\Delta t,i} \frac{v_{\infty,i}}{1 - v_{\infty,i}} + \left(1 - v_{\infty,i}\right) \sum_{j=1}^{N} \beta_{\Delta t,ij} v_{\infty,j} \\ &= v_{\infty,i} - \delta_{\Delta t,i} \frac{v_{\infty,i}}{1 - v_{\infty,i}} + \delta_{\Delta t,i} v_{\infty,i}, \end{aligned}$$

where the last equality follows from the steady-state equation (4.3). Thus, the upper bound (C.15) on the spectral radius $\rho(F)$ becomes

$$\rho(F) \leq \max_{i=1,\dots,N} \quad 1 - \delta_{\Delta t,i} \frac{\nu_{\infty,i}}{1-\nu_{\infty,i}} < 1,$$

since $\delta_{\Delta t,i} > 0$ and $\nu_{\infty,i} > 0$ for every node i. From $\rho(F) < 1$ it follows that the linearisation (4.9) is stable. Thus, the discrete-time NIMFA system (4.1) is asymptotically stable at the steady-state ν_∞.

C

C.7. PROOF OF LEMMA 4.15

Since $\Delta\nu[k] = \nu[k] - \nu_\infty$, the viral state $\nu[k]$ is strictly increasing at time k if and only if the difference $\Delta\nu[k]$ is strictly increasing at time k. Thus, it holds that

$$\Delta\nu_j[k] > \Delta\nu_j[k-1], \quad j = 1,\dots,N, \tag{C.16}$$

since the viral state $\nu[k-1]$ is assumed to be strictly increasing at time $k-1$. From Proposition 4.10 it follows that

$$\begin{aligned}\Delta\nu_i[k+1] - \Delta\nu_i[k] = &\sum_{j=1}^{N} F_{ij}\left(\Delta\nu_j[k] - \Delta\nu_j[k-1]\right) \\ &+ \sum_{j=1}^{N} \beta_{\Delta t,ij}\left(\Delta\nu_i[k-1]\Delta\nu_j[k-1] - \Delta\nu_i[k]\Delta\nu_j[k]\right).\end{aligned} \tag{C.17}$$

As stated by Lemma 4.11, the matrix F is non-negative under Assumption 4.3. Thus, we obtain from $F_{ij} \geq 0$ and (C.16) that the first sum in (C.17) is positive. Regarding the second sum in (C.17), we observe that

$$\Delta\nu_i[k-1]\Delta\nu_j[k-1] - \Delta\nu_i[k]\Delta\nu_j[k] > \Delta\nu_i[k-1]\Delta\nu_j[k-1] - \Delta\nu_i[k]\Delta\nu_j[k-1] \tag{C.18}$$

due to (C.16) and since $\Delta\nu_i[k] \leq 0$ holds for every node i under Assumption 4.4 as stated by Corollary 4.12. With (C.16) and $\Delta\nu_i[k] \leq 0$ for every node i, we obtain from (C.18) that

$$\Delta\nu_i[k-1]\Delta\nu_j[k-1] - \Delta\nu_i[k]\Delta\nu_j[k] > 0.$$

Hence, since $\beta_{\Delta t,ij} \geq 0$ for every nodes i, j, both sums in (C.17) are positive, which implies that $\Delta\nu_i[k+1] > \Delta\nu_i[k]$ for every node i.

C.8. PROOF OF THEOREM 4.16

Lemma 4.15 states that $\nu[k+1] > \nu[k]$ implies that $\nu[k+2] > \nu[k+1]$ for any time $k \geq 1$. Thus, $\nu[2] > \nu[1]$ implies by induction that the viral state $\nu[k]$ is globally strictly increasing. Furthermore, if the viral state $\nu[k]$ is globally strictly increasing then it holds $\nu[2] > \nu[1]$ by Definition 4.14. Hence, the viral state $\nu[k]$ is globally strictly increasing if and only if $\nu[2] > \nu[1]$. We prove the two statements of Theorem 4.16 in Subsection C.8.1 and Subsection C.8.2, respectively, by stating equivalent conditions to $\nu[2] > \nu[1]$.

C.8.1. FIRST STATEMENT

From the NIMFA equations (4.1), it follows that

$$v_i[2] - v_i[1] = -\delta_{\Delta t,i} v_i[1] + (1 - v_i[1]) \sum_{j=1}^{N} \beta_{\Delta t,ij} v_j[1].$$

Lemma 4.9 and Assumption 4.2 imply that $v_{\infty,i} < 1$ for every node i. Thus, it holds that $v_i[1] < 1$ for every node i under Assumption 4.4. Hence, $v[2] > v[1]$ is equivalent to

$$\sum_{j=1}^{N} \beta_{\Delta t,ij} v_j[1] > \delta_{\Delta t,i} \frac{v_i[1]}{1 - v_i[1]}, \quad \forall i = 1, ..., N. \tag{C.19}$$

The geometric series yields that

$$\frac{v_i[1]}{1 - v_i[1]} = \sum_{l=1}^{\infty} v_i^l[1],$$

which converges since $v_i[1] < 1$ for every node i. Thus, (C.19) is equivalent to

$$\sum_{j=1}^{N} \beta_{\Delta t,ij} v_j[1] > \delta_{\Delta t,i} \sum_{l=1}^{\infty} v_i^l[1], \quad \forall i = 1, ..., N. \tag{C.20}$$

We stack (C.20) and obtain that

$$B_{\Delta t} v[1] > \operatorname{diag}(\delta_{\Delta t}) \sum_{l=1}^{\infty} v^l[1], \tag{C.21}$$

where we denote $v^l[1] = (v_1^l[1], ..., v_N^l[1])^T$. By subtracting $\operatorname{diag}(\delta_{\Delta t}) v[1]$ on both sides of (C.21), we obtain the first statement of Theorem 4.16. We derived the statement (C.21) from $v[2] > v[1]$ by equivalent transformations. Hence, $v[2] > v[1]$ holds if and only if (C.21) holds true.

C.8.2. SECOND STATEMENT

We obtain the second statement of Theorem 4.16 by considering when $\Delta v[2] > \Delta v[1]$ holds, which is equivalent to $v[2] > v[1]$. With Proposition 4.10, it holds for node i that

$$\begin{aligned} \Delta v_i[2] - \Delta v_i[1] = &\frac{\delta_{\Delta t,i}}{v_{\infty,i} - 1} \Delta v_i[1] + (1 - v_{\infty,i}) \sum_{j=1}^{N} \beta_{\Delta t,ij} \Delta v_j[1] \\ &- \Delta v_i[1] \sum_{j=1}^{N} \beta_{\Delta t,ij} \Delta v_j[1]. \end{aligned}$$

Thus, $\Delta v[2] > \Delta v[1]$ holds if and only if, for every node i,

$$(1 - v_{\infty,i} - \Delta v_i[1]) \sum_{j=1}^{N} \beta_{\Delta t,ij} \Delta v_j[1] > \frac{\delta_{\Delta t,i}}{1 - v_{\infty,i}} \Delta v_i[1]. \tag{C.22}$$

Following the arguments before (C.19), it holds that $v_i[1] < 1$ for every node i. Hence, it holds that $\Delta v_i[1] < 1 - v_{\infty,i}$ for every node i. Thus, the inequality (C.22) is equivalent to

$$\sum_{j=1}^{N} \beta_{\Delta t,ij} \Delta v_j[1] > \frac{\delta_{\Delta t,i}}{1 - v_{\infty,i}} \frac{\Delta v_i[1]}{1 - v_{\infty,i} - \Delta v_i[1]}. \tag{C.23}$$

We rewrite the right-hand side of (C.23) to obtain the equivalent inequality

$$\begin{aligned} \sum_{j=1}^{N} \beta_{\Delta t,ij} \Delta v_j[1] &> \frac{\delta_{\Delta t,i}}{1 - v_{\infty,i}} \frac{\dfrac{\Delta v_i[1]}{1 - v_{\infty,i}}}{1 - \dfrac{\Delta v_i[1]}{1 - v_{\infty,i}}} \\ &= \frac{\delta_{\Delta t,i}}{1 - v_{\infty,i}} \sum_{l=1}^{\infty} \left(\frac{\Delta v_i[1]}{1 - v_{\infty,i}} \right)^l, \end{aligned} \tag{C.24}$$

where the equality follows from the geometric series, which converges since $\Delta v_i[1] < 1 - v_{\infty,i}$ for every node i. We introduce $z_i = \Delta v_i[1] / (1 - v_{\infty,i})$ for every node i and we obtain from (C.24) that $v[2] > v[1]$ is equivalent to

$$\sum_{j=1}^{N} \beta_{\Delta t,ij} (1 - v_{\infty,j}) z_j > \frac{\delta_{\Delta t,i}}{1 - v_{\infty,i}} \sum_{l=1}^{\infty} z_i^l, \quad \forall i = 1, \ldots, N.$$

We bring the first-order terms on the left-hand side to obtain the equivalent statement

$$(1 - v_{\infty,i}) \sum_{j=1}^{N} \beta_{\Delta t,ij} (1 - v_{\infty,j}) z_j - \delta_{\Delta t,i} z_i > \delta_{\Delta t,i} \sum_{l=2}^{\infty} z_i^l \tag{C.25}$$

for all align $i = 1, \ldots, N$. Stacking (C.25) yields that $v[2] > v[1]$ implies that

$$\left(\operatorname{diag}(u - v_\infty) B_{\Delta t} \operatorname{diag}(u - v_\infty) - \operatorname{diag}(\delta_{\Delta t}) \right) z > \operatorname{diag}(\delta_{\Delta t}) \sum_{l=2}^{\infty} z^l. \tag{C.26}$$

We obtained the statement (C.26) from $v[2] > v[1]$ by equivalent transformations. Hence, $v[2] > v[1]$ holds if and only if (C.26) holds true, which completes the proof of the second statement of Theorem 4.16.

C.9. PROOF OF COROLLARY 4.17

We prove Corollary 4.17 for the two different initial viral states $v[1]$ in Subsection C.9.1 and Subsection C.9.2, respectively.

C.9.1. FIRST STATEMENT

The initial state is given by $v[1] = \epsilon x_1 + \eta$, where the $N \times 1$ vector η satisfies $\|\eta\|_2 = \mathcal{O}(\epsilon^p)$ with $p > 1$. By the definition of the principal eigenvector x_1, we obtain that

$$Rv[1] = \rho(R)\epsilon x_1 + R\eta.$$

Thus, we obtain that

$$Rv[1] = \rho(R)v[1] + \big(R - \rho(R)I\big)\eta. \tag{C.27}$$

We add $v[1]$ on both sides of the inequality of the first statement of Theorem 4.16, which yields that the viral state $v[k]$ is globally strictly increasing if and only if

$$\big(I + B_{\Delta t} - \mathrm{diag}\,(\delta_{\Delta t})\big)\, v[1] > v[1] + \mathrm{diag}\,(\delta_{\Delta t}) \sum_{l=2}^{\infty} v^l[1],$$

which simplifies to

$$Rv[1] > v[1] + \mathrm{diag}\,(\delta_{\Delta t}) \sum_{l=2}^{\infty} v^l[1]. \tag{C.28}$$

With (C.27), we obtain from (C.28) that the viral state $v[k]$ is globally strictly increasing if

$$\rho(R)v[1] + \big(R - \rho(R)I\big)\eta > v[1] + \mathrm{diag}\,(\delta_{\Delta t}) \sum_{l=2}^{\infty} v^l[1],$$

which is equivalent to

$$\big(\rho(R) - 1\big)\, v[1] > \big(\rho(R)I - R\big)\eta + \mathrm{diag}\,(\delta_{\Delta t}) \sum_{l=2}^{\infty} v^l[1]. \tag{C.29}$$

Since $\rho(R) > 1$ and $v[1] > 0$, the left-hand side of (C.29) is positive and in $\mathcal{O}(\epsilon)$ and the right-hand side of (C.29) is in $\mathcal{O}(\epsilon^p)$ with $p > 1$. Hence, there is an $\epsilon > 0$ such that (C.29) holds true.

C.9.2. SECOND STATEMENT

The initial state is given by

$$v[1] = (1 - \epsilon)\, v_\infty + \eta, \tag{C.30}$$

where the $N \times 1$ vector η satisfies $\|\eta\|_2 = \mathcal{O}(\epsilon^p)$ with $p > 1$. With (C.30), we obtain the i-th component of the vector z in Theorem 4.16 as

$$z_i = \frac{-\epsilon v_{\infty,i} + \eta_i}{1 - v_{\infty,i}}. \tag{C.31}$$

Then, with (C.31), the inequality in the second statement of Theorem 4.16 becomes

$$\big(1 - v_{\infty,i}\big) \sum_{j=1}^{N} \beta_{\Delta t,ij} \big(-\epsilon v_{\infty,j} + \eta_j\big) - \delta_{\Delta t,i} \frac{-\epsilon v_{\infty,i} + \eta_i}{1 - v_{\infty,i}} > \delta_{\Delta t,i} \sum_{l=2}^{\infty} z_i^l$$

for every node $i = 1, \ldots, N$. We rearrange and obtain that

$$\begin{aligned} -\epsilon \big(1 - v_{\infty,i}\big) \sum_{j=1}^{N} \beta_{\Delta t,ij} v_{\infty,j} + \epsilon \delta_{\Delta t,i} \frac{v_{\infty,i}}{1 - v_{\infty,i}} > &- \big(1 - v_{\infty,i}\big) \sum_{j=1}^{N} \beta_{\Delta t,ij} \eta_j \\ &+ \delta_{\Delta t,i} \frac{\eta_i}{1 - v_{\infty,i}} + \delta_{\Delta t,i} \sum_{l=2}^{\infty} z_i^l, \end{aligned} \tag{C.32}$$

for every node i. We rewrite the sum on the left-hand side of (C.32) by using the steady-state equation (4.3), which yields that

$$-\epsilon\delta_{\Delta t,i}\nu_{\infty,i}+\epsilon\delta_{\Delta t,i}\frac{\nu_{\infty,i}}{1-\nu_{\infty,i}}>-\left(1-\nu_{\infty,i}\right)\sum_{j=1}^{N}\beta_{\Delta t,ij}\eta_j+\delta_{\Delta t,i}\frac{\eta_i}{1-\nu_{\infty,i}}+\delta_{\Delta t,i}\sum_{l=2}^{\infty}z_i^l,$$

which simplifies to

$$\epsilon\delta_{\Delta t,i}\frac{\nu_{\infty,i}^2}{1-\nu_{\infty,i}}>-\left(1-\nu_{\infty,i}\right)\sum_{j=1}^{N}\beta_{\Delta t,ij}\eta_j+\delta_{\Delta t,i}\frac{\eta_i}{1-\nu_{\infty,i}}+\delta_{\Delta t,i}\sum_{l=2}^{\infty}z_i^l. \tag{C.33}$$

The left-hand side of (C.33) is positive and in $\mathcal{O}(\epsilon)$ and the right-hand side of (C.33) is in $\mathcal{O}(\epsilon^p)$. Hence, there is an $\epsilon>0$ such that the inequality (C.33) holds true.

C.10. PROOF OF THEOREM 4.19

Before giving a rigorous proof of the statement of Theorem 4.19, we give an intuitive explanation:

Intuitive Explanation. *If the initial viral state $v[1]$ is close to zero, then the NIMFA model (4.2) is accurately described by its linearisation (4.8) around the origin. The viral state $v[k]$ of the LTI system (4.8) converges quickly to the principal eigenvector x_1 of the system matrix R. If the viral state $v[k^*]$ at some time $k^*\geq 1$ is small and almost parallel to the principal eigenvector x_1, then it follows from Corollary 4.17 that $v[k]$ is strictly increasing at every time $k\geq k^*$.*

In the following, we give a rigorous proof of Theorem 4.19. If existent, k^* denotes the time when the viral state $v[k]$ begins to be strictly increasing, i.e., $v[k+1]>v[k]$ for every time $k\geq k^*$. To find an expression for the time k^*, we obtain from Theorem 4.16 that the viral state $v[k]$ is increasing at every time $k\geq k^*$ if and only if

$$Rv[k^*]>v[k^*]+\operatorname{diag}(\delta_{\Delta t})\sum_{l=2}^{\infty}v^l[k^*], \tag{C.34}$$

which follows from adding the viral state $v[k^*]$ at time k^* on both sides of (4.10). We obtain an approximation the viral state $v[k^*]$ at time k^* from the linearisation (4.8) of the NIMFA model (4.2) around the origin. First, we decompose the matrix R into two addends

$$R=\rho(R)x_1x_1^T+\tilde{R}.$$

Here, the $N\times N$ matrix $\tilde{R}$ is given by

$$\tilde{R}=R-\rho(R)x_1x_1^T,$$

and it holds that $\tilde{R}x_1=0$. Then, the linearisation (4.8) yields that

$$v[k+1]\approx Rv[k]=\rho(R)x_1x_1^Tv[k]+\tilde{R}v[k]. \tag{C.35}$$

After iterating (C.35), the viral state $v[k^*]$ at time $k^* \geq 1$ follows as

$$v[k^*] = R^{k^*-1} v[1] + \eta[k^*], \tag{C.36}$$

where the linearisation error vector $\eta[k^*]$ is in $\|\eta[k^*]\|_2 = \mathcal{O}\left(\|v[1]\|_2^2\right)$ for any fixed time k^* when $v[1] \to 0$. We rewrite (C.36) as

$$v[k^*] = \rho(R)^{k^*-1} \left(x_1^T v[1]\right) x_1 + \tilde{R}^{k^*-1} v[1] + \eta[k^*]. \tag{C.37}$$

By inserting (C.37) in (C.34), we obtain that the viral state $v[k]$ is strictly increasing at every time $k \geq k^*$ if

$$\rho(R)^{k^*} x_1 \left(x_1^T v[1]\right) + \tilde{R}^{k^*} v[1] > \rho(R)^{k^*-1} x_1 \left(x_1^T v[1]\right) + \tilde{R}^{k^*-1} v[1] + \Upsilon[k^*]. \tag{C.38}$$

Here, the $N \times 1$ vector $\Upsilon[k^*]$ equals

$$\Upsilon[k^*] = \operatorname{diag}(\delta_{\Delta t}) \sum_{l=2}^{\infty} v^l[k^*] + (I - R)\eta[k^*].$$

It holds that $\|\Upsilon[k^*]\|_2 = \mathcal{O}\left(\|v[1]\|_2^2\right)$ for any fixed time k^* when $v[1] \to 0$. We rearrange (C.38), which yields that

$$\rho(R)^{k^*-1} \left(\rho(R) - 1\right) \left(x_1^T v[1]\right) x_1 > \tilde{R}^{k^*-1} \left(I - \tilde{R}\right) v[1] + \Upsilon[k^*]. \tag{C.39}$$

To obtain a bound on the time k^* from (C.39), we state Lemma C.1 and Lemma C.3, which bound the left and right side of (C.39), respectively.

Lemma C.1. *Suppose that Assumption 4.2–4.6 hold. Then, it holds that*

$$\left(\rho(R)^{k^*-1} \left(\rho(R) - 1\right) \left(x_1^T v[1]\right) x_1\right)_i \geq \rho(R)^{k^*-1} \left(\rho(R) - 1\right) x_{1,\min}^2 \|v[1]\|_1$$

for every $i = 1, \ldots, N$, where $x_{1,\min} = \min\{(x_1)_1, \ldots, (x_1)_N\}$.

Proof. It holds that

$$x_1^T v[1] \geq x_{1,\min} \sum_{i=1}^{N} v_i[1] = x_{1,\min} \|v[1]\|_1,$$

since $v[1] \geq 0$ and $x_{1,\min} > 0$. Then, the i-th component of the left-hand side of (C.39) becomes

$$\left(\rho(R)^{k^*-1} \left(\rho(R) - 1\right) \left(x_1^T v[1]\right) x_1\right)_i \geq \rho(R)^{k^*-1} \left(\rho(R) - 1\right) x_{1,\min} \|v[1]\|_1 (x_1)_i.$$

since $\left(\rho(R) - 1\right) > 0$. We employ the lower bound $(x_1)_i \geq x_{1,\min}$ to complete the proof. □

For completeness, we introduce Lemma C.2, which is from [285, Corollary 5.6.13.] and applied in the proof of Lemma C.3.

Lemma C.2 ([285]). *Let an $N \times N$ matrix M and an $\varepsilon > 0$ be given. Then, there is a constant $c(M,\varepsilon)$ such that*

$$\left(M^k\right)_{ij} \leq c(M,\varepsilon)\left(\rho(M)+\varepsilon\right)^k$$

for all $k = 1,2,\ldots$ and all $i, j = 1,\ldots,N$.

For any $N \times 1$ vector z, the maximum vector norm is given by

$$\|z\|_\infty = \max\{|z_1|,\ldots,|z_N|\}.$$

For any $N \times N$ matrix M with elements m_{ij}, we denote the matrix norm which is induced the maximum vector norm by

$$\|M\|_\infty = \max_{i=1,\ldots,N} \sum_{j=1}^{N} |m_{ij}|. \tag{C.40}$$

Lemma C.3. *Suppose that Assumption 4.2–4.6 hold and let $\varepsilon > 0$ be given. Then, there is a constant $\sigma(\tilde{R},\varepsilon)$ such that*

$$\left(\tilde{R}^{k^*-1}\left(I-\tilde{R}\right)v[1]\right)_i \leq \sigma(\tilde{R},\varepsilon)\left(\rho(\tilde{R})+\varepsilon\right)^{k^*-1}\left\|I-\tilde{R}\right\|_\infty \|v[1]\|_1$$

holds for every integer $k^* \geq 2$ and every $i = 1,\ldots,N$.

Proof. For any $N \times 1$ vector z and any $N \times N$ matrix M, it holds that

$$(Mz)_i = \sum_{j=1}^{N} m_{ij} z_j \leq \sum_{l=1}^{N} |m_{il}| \sum_{j=1}^{N} |z_j|.$$

From (C.40) and $\|z\|_1 = \sum_{j=1}^{N} |z_j|$, we obtain that

$$(Mz)_i \leq \|M\|_\infty \|z\|_1, \quad i = 1,\ldots,N, \tag{C.41}$$

for any vector z and any square matrix M. By setting the matrix M to $M = \left(\tilde{R}^{k^*-1}\left(I-\tilde{R}\right)\right)$ and the vector z to $z = v[1]$, we obtain from (C.41) that

$$\left(\tilde{R}^{k^*-1}\left(I-\tilde{R}\right)v[1]\right)_i \leq \left\|\tilde{R}^{k^*-1}\left(I-\tilde{R}\right)\right\|_\infty \|v[1]\|_1$$

for every $i = 1,\ldots,N$. Since the matrix norm is sub-multiplicative[1], it holds that

$$\left(\tilde{R}^{k^*-1}\left(I-\tilde{R}\right)v[1]\right)_i \leq \left\|\tilde{R}^{k^*-1}\right\|_\infty \left\|I-\tilde{R}\right\|_\infty \|v[1]\|_1. \tag{C.42}$$

For a given square matrix M and a given $\varepsilon > 0$, there is a constant $\sigma(M,\varepsilon)$ such that

$$\|M^k\|_\infty \leq \sigma(M,\varepsilon)\left(\rho(M)+\varepsilon\right)^k \tag{C.43}$$

[1] A matrix norm $\|\cdot\|$ is sub-multiplicative if $\|AB\| \leq \|A\|\|B\|$ holds for any matrices A, B.

for all integers $k \geq 1$, which follows from applying Lemma C.2 to every addend of the sum

$$\|M^k\|_\infty = \max_{i=1,\dots,N} \sum_{j=1}^{N} \left| \left(M^k\right)_{ij} \right|.$$

We combine (C.43) and (C.42) and obtain that, for any $\varepsilon > 0$, there is a constant $\sigma(\tilde{R},\varepsilon)$ such that

$$\left(\tilde{R}^{k^*-1}\left(I-\tilde{R}\right)v[1]\right)_i \leq \sigma(\tilde{R},\varepsilon)\left(\rho(\tilde{R})+\varepsilon\right)^{k^*-1}\left\|I-\tilde{R}\right\|_\infty \|v[1]\|_1$$

holds for every integer $k^* \geq 2$ and every node $i = 1,\dots,N$. □

By applying the bounds of Lemma C.1 and Lemma C.3 to (C.39), we obtain that the viral state $v[k]$ is strictly increasing at every time $k \geq k^*$ if

$$\rho(R)^{k^*-1}\left(\rho(R)-1\right)x_{1,\min}^2\|v[1]\|_1 > \sigma(\tilde{R},\varepsilon)\left(\rho(\tilde{R})+\varepsilon\right)^{k^*-1}\left\|I-\tilde{R}\right\|_\infty \|v[1]\|_1 + \Upsilon[k^*]. \tag{C.44}$$

In the limit $v[1] \to 0$, it holds $\Upsilon[k^*] = \mathcal{O}(\|v[1]\|_2^2)$ for k^* fixed and the inequality (C.44) converges to

$$\rho(R)^{k^*-1}\left(\rho(R)-1\right)x_{1,\min}^2 > \sigma(\tilde{R},\varepsilon)\left(\rho(\tilde{R})+\varepsilon\right)^{k^*-1}\left\|I-\tilde{R}\right\|_\infty.$$

We take the logarithm and obtain that

$$\log\left(\left(\rho(R)-1\right)x_{1,\min}^2\right) > \log\left(\sigma(\tilde{R},\varepsilon)\left\|I-\tilde{R}\right\|_\infty\right) + \left(k^*-1\right)\log\left(\frac{\rho(\tilde{R})+\varepsilon}{\rho(R)}\right). \tag{C.45}$$

We choose ε such that $\rho(\tilde{R})+\varepsilon < \rho(R)$ and find that (C.45) is satisfied if

$$k^* > \frac{\log\left(\dfrac{\left(\rho(R)-1\right)x_{1,\min}^2}{\sigma(\tilde{R},\varepsilon)\left\|I-\tilde{R}\right\|_\infty}\right)}{\log\left(\rho(\tilde{R})+\varepsilon\right)-\log\left(\rho(R)\right)} + 1. \tag{C.46}$$

Hence, in the limit $v[1] \to 0$, the viral state $v[k]$ is strictly increasing at every time $k \geq k^*$ if k^* satisfies (C.46) and we emphasise that (C.46) is independent of $v[1]$. Thus, when $v[1] \to 0$, the set S_- of time instants k, for which the viral state $v[k]$ is not strictly increasing, is a subset of $\{1,\dots,k^*-1\}$. Hence, the set S_- is finite when $v[1] \to 0$, which is the first requirement for a quasi-increasing viral state evolution by Definition 4.18. It remains to show that, for any ϵ-stringency,

$$\|v[k+1]-v[k]\|_2 \leq \epsilon \quad \forall k \in S_-, \tag{C.47}$$

if $\|v[1]\|_2 \leq \vartheta(\epsilon)$ for a sufficiently small $\vartheta(\epsilon)$. With the triangle inequality it holds that

$$\|v[k+1]-v[k]\|_2 \leq \|v[k+1]\|_2 + \|v[k]\|_2, \quad \forall k \in S_-.$$

Since $v[1] \to 0$ implies that $v[k] \to 0$ for every time $k \leq k^*+1$, we obtain that, for any ϵ-stringency, there is a $\vartheta(\epsilon)$ such that $\|v[1]\|_2 \leq \vartheta(\epsilon)$ implies (C.47).

C.11. PROOF OF PROPOSITION 4.20

We prove Proposition 4.20 by induction. More precisely, we show that if the base case at time $k = 1$ is satisfied, i.e. $v_{\mathrm{ub}}^{(1)}[1] \geq v[1]$, then it holds $v_{\mathrm{ub}}^{(1)}[k] \geq v[k]$ at every time $k \geq 1$. For the inductive step from time $k \geq 1$ to time $k+1$, we obtain from (4.1) and (4.12) that

$$\begin{aligned} v_{\mathrm{ub},i}^{(1)}[k+1] - v_i[k+1] =& (1-\delta_{\Delta t,i})\left(v_{\mathrm{ub},i}^{(1)}[k] - v_i[k]\right) \\ &+ \sum_{j=1}^{N} \beta_{\Delta t,ij}\left(v_{\mathrm{ub},j}^{(1)}[k] - v_j[k]\right) + v_i[k]\sum_{j=1}^{N}\beta_{\Delta t,ij} v_j[k]. \end{aligned} \tag{C.48}$$

Hence, $v_{\mathrm{ub},j}^{(1)}[k] \geq v_j[k]$ for every node j and $(1-\delta_{\Delta t,i}) \geq 0$ by Assumption 4.3 implies that the first term and the first sum of (C.48) are non-negative. Since the second sum in (C.48) is positive, it follows from (C.48) that $v_{\mathrm{ub},i}^{(1)}[k+1] > v_i[k+1]$ if $v_{\mathrm{ub},j}^{(1)}[k] \geq v_j[k]$ for every node j. Thus, it follows by induction, that the base case at time $k = 1$, i.e., $v_{\mathrm{ub}}^{(1)}[1] \geq v[1]$, implies that $v_{\mathrm{ub}}^{(1)}[k] \geq v[k]$ at every time $k \geq 1$. The LTI system (4.12) is asymptotically stable if and only if the spectral radius $\rho(R)$ satisfies $\rho(R) < 1$.

C.12. PROOF OF PROPOSITION 4.21

C.12.1. FIRST STATEMENT

We prove that $\Delta v_{\mathrm{ub},i}[k]$, given by (4.13), is an upper bound of $\Delta v_i[k]$ for all nodes i at every time $k \geq 1$ by induction. For the initial time $k = 1$, it holds that $\Delta v_{\mathrm{ub},i}[1] \geq \Delta v_i[1]$ by assumption. In the following, we show that $\Delta v_{\mathrm{ub},i}[k] \geq \Delta v_i[k]$ for all nodes i implies that $\Delta v_{\mathrm{ub},i}[k+1] \geq \Delta v_i[k+1]$ for all nodes i. From (4.13) and (4.6) it follows that the difference of the bound $\Delta v_{\mathrm{ub},i}[k+1]$ to the true value $\Delta v_i[k+1]$ at time $k+1$ can be stated as

$$\Delta v_{\mathrm{ub}}[k+1] - \Delta v[k+1] = F\left(\Delta v_{\mathrm{ub}}[k] - \Delta v[k]\right) + \mathrm{diag}\left(\Delta v[k]\right) B_{\Delta t} \Delta v[k]. \tag{C.49}$$

For the first term it holds that $F\left(\Delta v_{\mathrm{ub}}[k] - \Delta v[k]\right) \geq 0$, because $\Delta v_{\mathrm{ub}}[k] - \Delta v[k] \geq 0$ and the matrix F is non-negative by Lemma 4.11. Under Assumption 4.4, Corollary 4.12 implies that $\Delta v_i[k] \leq 0$ for every node i at every time $k \geq 1$. Thus, we obtain for the second term in (C.49) that

$$\sum_{j=1}^{N} \beta_{\Delta t,ij} \Delta v_j[k] \Delta v_i[k] \geq 0, \quad i = 1, \ldots, N,$$

since $\beta_{\Delta t,ij} \geq 0$ for every $i, j = 1, \ldots, N$ under Assumption 4.2. Thus, both addends of (C.49) are non-negative, which implies that $\Delta v_{\mathrm{ub}}[k+1] \geq \Delta v[k+1]$.

C.12.2. SECOND STATEMENT

We prove the second statement of Proposition 4.21 by induction. More precisely, we show that if the base case at time $k = 1$ is satisfied, i.e. $\Delta v_{\mathrm{ub}}[1] \leq 0$, then it holds that $\Delta v_{\mathrm{ub}}[k] \leq 0$ at every time $k \geq 1$. For the inductive step from time $k \geq 1$ to time $k+1$, we make use of the fact that, under Assumption 4.3, the matrix F is non-negative as stated

by Lemma 4.11. Hence, we obtain from

$$\Delta v_{\mathrm{ub},i}[k+1] = \sum_{j=1}^{N} F_{ij} \Delta v_{\mathrm{ub},j}[k]$$

that $\Delta v_{\mathrm{ub},i}[k] \leq 0$ for every node i implies $\Delta v_{\mathrm{ub},i}[k+1] \leq 0$ for every node i. Thus, it follows by induction, that the base case at time $k = 1$, $\Delta v_{\mathrm{ub}}[1] \leq 0$, implies that $\Delta v_{\mathrm{ub}}[k] \leq 0$ at every time $k \geq 1$.

C.13. PROOF OF PROPOSITION 4.22

C.13.1. FIRST STATEMENT

Since $F_{\mathrm{lb}} = F - \mathrm{diag}\,(v_{\min} - v_\infty)\, B_{\Delta t}$, we can rewrite the lower bound $\Delta v_{\mathrm{lb}}[k+1]$ at time $k+1$ with (4.15) as

$$\Delta v_{\mathrm{lb}}[k+1] = F \Delta v_{\mathrm{lb}}[k] - \mathrm{diag}\,(v_{\min} - v_\infty)\, B_{\Delta t} \Delta v_{\mathrm{lb}}[k]. \tag{C.50}$$

We prove that $\Delta v_{\mathrm{lb}}[k]$ given by (C.50) is indeed a lower bound of $\Delta v[k]$ at every time $k \geq 1$ by induction. At the initial time $k = 1$, it holds that $\Delta v_{\mathrm{lb}}[1] \leq \Delta v[1]$ by assumption. In the following, we show that $\Delta v_{\mathrm{lb}}[k] \leq \Delta v[k]$ implies that $\Delta v_{\mathrm{lb}}[k+1] \leq \Delta v[k+1]$ for any time $k \geq 1$. We obtain from (4.6) and (C.50) that

$$\begin{aligned} \Delta v[k+1] - \Delta v_{\mathrm{lb}}[k+1] =& F(\Delta v[k] - \Delta v_{\mathrm{lb}}[k]) + \mathrm{diag}\,(v_{\min} - v_\infty)\, B_{\Delta t} \Delta v_{\mathrm{lb}}[k] \\ & - \mathrm{diag}\,(\Delta v[k])\, B_{\Delta t} \Delta v[k]. \end{aligned} \tag{C.51}$$

Under Assumption 4.3, Lemma 4.11 implies that the matrix F is non-negative. From the non-negativity of the matrix F and from $\Delta v[k] \geq \Delta v_{\mathrm{lb}}[k]$ it follows that the first term of (C.51) is non-negative, $F(\Delta v[k] - \Delta v_{\mathrm{lb}}[k]) \geq 0$. We denote the i-th component of the second and third terms in (C.51) by

$$\varsigma_i = \sum_{j=1}^{N} \beta_{\Delta t,ij} \left((v_{\min,i} - v_{\infty,i})\, \Delta v_{\mathrm{lb},j}[k] - \Delta v_i[k] \Delta v_j[k] \right).$$

Under Assumption 4.4 it holds that $\Delta v_i[k] \leq 0$ as stated by Corollary 4.12. Furthermore, since $\Delta v_j[k] \geq \Delta v_{\mathrm{lb},j}[k]$, we obtain that

$$\varsigma_i \geq \sum_{j=1}^{N} \beta_{\Delta t,ij} \left((v_{\min,i} - v_{\infty,i})\, \Delta v_{\mathrm{lb},j}[k] - \Delta v_i[k] \Delta v_{\mathrm{lb},j}[k] \right).$$

Since we assumed that $v[k] \geq v_{\min}$ holds at every time k, we obtain that $\Delta v[k] \geq v_{\min} - v_\infty$ at every time k. Hence, we can bound the term ς_i by

$$\varsigma_i \geq \sum_{j=1}^{N} \beta_{\Delta t,ij} \left((v_{\min,i} - v_{\infty,i})\, \Delta v_{\mathrm{lb},j}[k] - (v_{\min,i} - v_{\infty,i})\, \Delta v_{\mathrm{lb},j}[k] \right) = 0.$$

Thus, (C.51) is non-negative, which implies that $\Delta v[k+1] \geq \Delta v_{\mathrm{lb}}[k+1]$ if $\Delta v[k] \geq \Delta v_{\mathrm{lb}}[k]$.

C.13.2. SECOND STATEMENT

Parts of the proof are inspired by the proof of Ahn and Hassibi [78, Theorem 5.1] and based on two lemmas.

Lemma C.4. *For any two vectors $z, \tilde{z}$ with $z \geq \tilde{z}$ it holds that $F_{\text{lb}} z \geq F_{\text{lb}} \tilde{z}$.*

Proof. First, we show that the matrix F_{lb} is non-negative. The elements of the matrix F_{lb} are given by

$$(F_{\text{lb}})_{ij} = \begin{cases} 1 + \dfrac{\delta_{\Delta t,i}}{v_{\infty,i} - 1} + \left(1 - v_{\min,i}\right) \beta_{\Delta t,ii} & \text{if } i = j, \\ \left(1 - v_{\min,i}\right) \beta_{\Delta t,ij} & \text{if } i \neq j. \end{cases} \tag{C.52}$$

For every node i, we have $(F_{\text{lb}})_{ii} \geq F_{ii} \geq 0$ under Assumption 4.3 as stated by Lemma 4.11. Since $v_{\min,i} < 1$ and $\beta_{\Delta t,ij} \geq 0$ for every nodes i, j, the matrix F_{lb} is non-negative. Hence, $z \geq \tilde{z}$ implies that

$$(F_{\text{lb}} z - F_{\text{lb}} \tilde{z})_i = \sum_{j=1}^{N} (F_{\text{lb}})_{ij} \left(z_j - \tilde{z}_j\right) \geq 0, \quad \forall i = 1, ..., N.$$

□

Lemma C.5. *Define the $N \times 1$ vector $z^{(1)}$ as $z^{(1)} = -v_\infty$ and the $N \times 1$ vectors $z^{(k+1)}$ as $z^{(k+1)} = F_{\text{lb}} z^{(k)}$ for all $k \geq 1$. Then, the vector $z^{(k)}$ at iteration k is bounded by*

$$z^{(k)} \geq -\left(1 - \delta_{\Delta t,\min} \frac{\gamma}{1-\gamma}\right)^k v_\infty. \tag{C.53}$$

Proof. The right-hand side of (C.53) is proportional to the steady-state vector v_∞ and, as a first step, we consider the product $(-F_{\text{lb}} v_\infty)$. With (C.52), we obtain for every $i = 1, ..., N$ that

$$\begin{aligned} (-F_{\text{lb}} v_\infty)_i &= -\sum_{j=1}^{N} (F_{\text{lb}})_{ij} v_{\infty,j} \\ &= -v_{\infty,i} + \delta_{\Delta t,i} \frac{v_{\infty,i}}{1 - v_{\infty,i}} - \left(1 - v_{\min,i}\right) \sum_{j=1}^{N} \beta_{\Delta t,ij} v_{\infty,j}. \end{aligned}$$

The steady-state equation (4.3) yields that

$$-\sum_{j=1}^{N} (F_{\text{lb}})_{ij} v_{\infty,j} = -v_{\infty,i} + \delta_{\Delta t,i} \frac{v_{\infty,i}}{1 - v_{\infty,i}} - \left(1 - v_{\min,i}\right) \delta_{\Delta t,i} \frac{v_{\infty,i}}{1 - v_{\infty,i}}. \tag{C.54}$$

We simplify (C.54) and obtain that

$$-\sum_{j=1}^{N} (F_{\text{lb}})_{ij} v_{\infty,j} = -v_{\infty,i} \left(1 - \delta_{\Delta t,i} \frac{v_{\min,i}}{1 - v_{\infty,i}}\right). \tag{C.55}$$

We stack (C.55), which yields that

$$-F_{\mathrm{lb}}\, v_\infty \geq -v_\infty \left(1-\delta_{\Delta t,\min}\frac{\gamma}{1-\gamma}\right), \tag{C.56}$$

since $\delta_{\Delta t,i} \geq \delta_{\Delta t,\min}$ and $v_{\infty,i} \geq v_{\min,i} \geq \gamma$ for every node i. As a second step, we obtain the inequality (C.53) from (C.56) by induction. At $k=1$, (C.53) holds true with equality. Consider that (C.53) holds at time $k \geq 1$, then we obtain that

$$z^{(k+1)} = F_{\mathrm{lb}}\, z^{(k)} \geq F_{\mathrm{lb}} \left(-\left(1-\delta_{\Delta t,\min}\frac{\gamma}{1-\gamma}\right)^k v_\infty\right),$$

where the inequality follows from Lemma C.4. Finally, with (C.56), we obtain that

$$z^{(k+1)} \geq -\left(1-\delta_{\Delta t,\min}\frac{\gamma}{1-\gamma}\right)^{k+1} v_\infty.$$

□

Since $\Delta v_{\mathrm{lb}}[1] = \Delta v[1]$ and $\Delta v[1] = v[1] - v_\infty$, it holds that $\Delta v_{\mathrm{lb}}[1] \geq -v_\infty = z^{(1)}$. Hence, Lemma C.4 and Lemma C.5 yield, by induction, that

$$\Delta v_{\mathrm{lb}}[k] \geq z^{(k)} \geq -\left(1-\delta_{\Delta t,\min}\frac{\gamma}{1-\gamma}\right)^k v_\infty$$

at every time $k \geq 1$.

C.14. PROOF OF LEMMA 4.23

In Subsection C.14.1, we consider that the initial viral state $v[1]$ satisfies $v[1] > 0$. In Subsection C.14.2, we consider that the initial viral state $v[1]$ satisfies $v[1] \neq 0$ but not $v[1] > 0$.

C.14.1. POSITIVE INITIAL VIRAL STATE

We consider that the initial viral state $v[1]$ satisfies $v[1] > 0$. The proof consists of three steps:

1. It follows from the NIMFA equations (4.1) that $v_i[k] > 0$ implies that $v_i[k+1] > 0$ since $(1-\delta_{\Delta t,i}) > 0$ and $\beta_{\Delta t,ij} \geq 0$ for all nodes i, j. Hence, it holds that $v[k] > 0$ at every time $k \geq 1$.

2. The viral state vector $v[k]$ does not approach zero arbitrarily close: Under Assumption 4.6, the origin is an unstable equilibrium of the NIMFA equations (4.2). From $v_i[k] > 0$ for every node i we obtain that $x_1^T v[k] > 0$, where $x_1 > 0$ is the eigenvector to the unstable eigenvalue $\rho(R) > 1$ of the linearisation (4.8) of the NIMFA model (4.2) around the origin. Hence, there is an $\epsilon > 0$ such that $\|v[k]\|_2 > \epsilon$ at every time $k \geq 1$.

3. The viral state $v_i[k]$ of any *single* node i does not approach zero arbitrarily close. (This is a stronger statement than the second statement.) Since the viral state vector $v[k]$ does not approach zero arbitrarily close, there is at least one node i such that $v_i[k] \geq v_{\min,i}$ for some $v_{\min,i} > 0$ at every time $k \geq 1$. Under Assumption 4.5, node i has at least one neighbour $l \neq i$, for which the NIMFA equations (4.1) are given by

$$v_l[k+1] = \sum_{j=1}^{N} \beta_{\Delta t,lj} v_j[k] + v_l[k] \left(1 - \delta_{\Delta t,l} - \sum_{j=1}^{N} \beta_{\Delta t,lj} v_j[k]\right). \tag{C.57}$$

With $v_j[k] \leq 1$ for every node j we obtain that

$$1 - \delta_{\Delta t,l} - \sum_{j=1}^{N} \beta_{\Delta t,lj} v_j[k] \geq 1 - \delta_{\Delta t,l} - \sum_{j=1}^{N} \beta_{\Delta t,lj} \geq 0,$$

where the last inequality follows from Assumption 4.3. Thus, (C.57) yields that

$$v_l[k+1] \geq \sum_{j=1}^{N} \beta_{\Delta t,lj} v_j[k] \geq \beta_{\Delta t,lj} v_i[k] \geq v_{\min,l} > 0,$$

where we define $v_{\min,l} \beta_{\Delta t,li} v_{\min,i}$. Hence, if there is a $v_{\min,i} > 0$ for some node i such that $v_i[k] \geq v_{\min,i}$ at every time $k \geq 1$, then it holds $v_l[k] \geq v_{\min,l}$ at every time $k \geq 1$ for every node l which is adjacent to node i. By repeating this argument for every node in the connected graph, we find that there is a positive vector $v_{\min} > 0$ such that $v[k] \geq v_{\min}$ holds at every time $k \geq 1$ provided that $v[1] > 0$.

C.14.2. NON-ZERO INITIAL VIRAL STATE

We consider that the initial viral state $v[1]$ does not satisfy $v[1] > 0$, but only $v[1] \neq 0$. Since the graph given by the infection probability matrix $B_{\Delta t}$ is strongly connected, there is a pair of adjacent nodes i, l such that the initial viral state $v[1]$ satisfies $v_i[1] > 0$ and $v_l[1] = 0$. It follows from the NIMFA equations (4.1) that node i infects its neighbour l and, hence, it holds that $v_l[2] > 0$. Furthermore, it holds $v_i[2] > 0$ as argued in the first point of Subsection C.14.1. The more time k evolves, the more nodes l become infected. At some time $k^* \leq N-1$ all nodes are infected, and the viral state satisfies $v[k^*] > 0$. We apply the three arguments in Subsection C.14.1 to the viral state $v[k^*]$ at time k^* to establish that there is a vector $v_{\min} > 0$ such that the viral state satisfies $v[k] > v_{\min}$ for every time $k \geq k^*$.

C.15. PROOF OF COROLLARY 4.24

If the initial viral state $v[1]$ satisfies $v[1] > 0$, then Lemma 4.23 states that there exists some vector $v_{\min} > 0$ such that $v[k] \geq v_{\min}$ at every time $k \geq 1$. Since

$$\Delta v_{\mathrm{lb}}[k] \leq \Delta v[k] \leq 0 \Rightarrow \|\Delta v[k]\|_2 \leq \|\Delta v_{\mathrm{lb}}[k]\|_2,$$

Proposition 4.22 yields that

$$\|\Delta v[k]\|_2 \leq \left(1 - \delta_{\Delta t,\min} \frac{\gamma}{1-\gamma}\right)^{k-1} \|v_\infty\|_2 \quad \forall k \geq 1, \tag{C.58}$$

where $\gamma = \min\{v_{\min,1}, ..., v_{\min,N}\} > 0$. If the initial viral state $v[1]$ satisfies $v[1] \neq 0$ but not $v[1] > 0$, then Lemma 4.23 yields an analogous statement to (C.58) by formally replacing $k \geq 1$ by $k \geq k^*$.

If the viral state $v[k]$ is globally strictly increasing and $v[1] > 0$, then we can set $v_{\min} = v[1]$, which yields that

$$\|\Delta v[k]\|_2 \leq \alpha^{k-1} \|v_\infty\|_2 \quad \forall k \geq 1,$$

where

$$\alpha = 1 - \delta_{\Delta t,\min} \frac{\gamma}{1-\gamma}$$

and $\gamma = \min\{v_1[1], ..., v_N[1]\} > 0$.

D

APPENDIX TO CHAPTER 5

D.1. PROOF OF LEMMA 5.1

Section 5.3 states three kind of transitions for the sampled-time ϵ-SIS process. We prove that the bound (5.4) on the sampling time Δt ensures that all three kinds of transitions are well-defined.

1. A single node i changes from the infected state at discrete time k to the susceptible state at discrete time $k+1$. The probability of this transition is

$$\Pr\Big[x_i[k+1]=0|x_i[k]=1,x[k],\theta\Big]=\delta\Delta t,$$

which needs to be smaller than one. Thus, the sampling time Δt must obey

$$\Delta t \leq \frac{1}{\delta}. \tag{D.1}$$

2. A single node i changes from the susceptible state at time instant k to the infected state at time instant $k+1$ with the probability (5.2). Since the number of infectious neighbours $N_i(A,k)$ is bounded by the number of nodes, $N_i(A,k) \leq N$, we can bound (5.2) as

$$\Pr\Big[x_i[k+1]=1\Big|x_i[k]=0,x[k],\theta\Big] \leq \epsilon_{\Delta t}+\beta_{\Delta t}N. \tag{D.2}$$

Since by definition $\epsilon_{\Delta t}=\epsilon\Delta t$ and $\beta_{\Delta t}=\beta\Delta t$, we obtain that (D.2) is bounded by 1, if

$$\Delta t \leq \frac{1}{\epsilon+N\beta}. \tag{D.3}$$

3. The state of no node changes from time k to time $k+1$. Denote the susceptible and infected nodes, respectively, at time instant k by

$$M_0[k]=\{j\in\mathbb{N}_N|x_j[k]=0\}$$

and

$$M_1[k] = \{j \in \mathbb{N}_N | x_j[k] = 1\}.$$

With the $N \times 1$ all-one vector as $u = (1, ..., 1)^T$, we obtain that

$$|M_0[k]| = u^T(u - x[k]), \tag{D.4}$$
$$|M_1[k]| = u^T x[k]. \tag{D.5}$$

We rewrite the probability of no change from time k to $k+1$ as

$$\Pr\Big[x[k+1] = x[k]\Big|x[k],\theta\Big] = 1 - \sum_{j\in M_1[k]} \delta_{\Delta t} - \sum_{i\in M_0[k]} (\beta_{\Delta t} N_i(A,k) + \epsilon_{\Delta t})$$

D

With (D.5), we obtain that

$$\Pr\Big[x[k+1] = x[k]\Big|x[k],\theta\Big] = 1 - \delta_{\Delta t} u^T x[k] - \sum_{i\in M_0[k]} \left(\epsilon_{\Delta t} + \beta_{\Delta t} \sum_{j=1}^{N} a_{ij} x_j[k]\right).$$

Furthermore, from (D.4) it follows that

$$\begin{aligned}\Pr\Big[x[k+1] = x[k]\Big|x[k],\theta\Big] =& 1 - \delta_{\Delta t} u^T x[k] - u^T(u - x[k])\epsilon_{\Delta t} \\ &- \sum_{i\in M_0[k]} \sum_{j=1}^{N} \beta_{\Delta t} a_{ij} x_j[k].\end{aligned}$$

Since

$$\sum_{i\in M_0[k]} a_{ij} = \sum_{i=1}^{N} (1 - x_i[k]) a_{ij}$$

and $u^T u = N$, it holds that

$$\begin{aligned}\Pr\Big[x[k+1] = x[k]\Big|x[k],\theta\Big] =& 1 - N\epsilon_{\Delta t} + (\epsilon_{\Delta t} - \delta_{\Delta t}) u^T x[k] \\ &- \sum_{j=1}^{N} \beta_{\Delta t} x_j[k] \sum_{i=1}^{N} (1 - x_i[k]) a_{ij}.\end{aligned} \tag{D.6}$$

The right side of (D.6) is bounded by

$$\Pr\Big[x[k+1] = x[k]\Big|x[k],\theta\Big] \leq 1 - N\epsilon_{\Delta t} + (\epsilon_{\Delta t} - \delta_{\Delta t}) u^T x[k], \tag{D.7}$$

since the sum in (D.6) is non-negative. If the upper bound (D.7) does not exceed one, then also the transition probability $\Pr\Big[x[k+1] = x[k]\Big|x[k],\theta\Big]$ is bounded by one. We consider two cases, depending on the values the self-infection rate $\epsilon_{\Delta t}$ and the curing rate $\delta_{\Delta t}$. First, if $\epsilon_{\Delta t} \geq \delta_{\Delta t}$, then we apply $u^T x[k] \leq N$ and obtain that

$$\Pr\Big[x[k+1] = x[k]\Big|x[k],\theta\Big] \leq 1 - \delta_{\Delta t} N. \tag{D.8}$$

Second, if $\epsilon_{\Delta t} < \delta_{\Delta t}$, then we obtain that

$$\Pr\Big[x[k+1] = x[k]\Big|x[k],\theta\Big] \leq 1 - N\epsilon_{\Delta t}, \tag{D.9}$$

since $u^T x[k] \geq 0$. The curing rate $\delta_{\Delta t}$ and self-infection rate $\epsilon_{\Delta t}$ are non-negative. Thus, both upper bounds (D.8) and (D.9) do not exceed one. Thus, also the transition probability $\Pr\Big[x[k+1] = x[k]\Big|x[k],\theta\Big]$ does not exceed one.

Lastly, we must ensure that the expression for $\Pr[x[k+1] = x[k]|x[k],\theta]$ is not negative. We obtain from (D.6) that

$$\begin{aligned}\Pr\Big[x[k+1] = x[k]\Big|x[k],\theta\Big] \geq & 1 - N\epsilon_{\Delta t} + (\epsilon_{\Delta t} - \delta_{\Delta t})u^T x[k] \\ & - \beta_{\Delta t}\sum_{j=1}^{N} x_j[k]\sum_{i=1}^{N}(1 - x_i[k]),\end{aligned}$$

since $a_{ij} \geq 0$. Furthermore, it holds that

$$\Pr\Big[x[k+1] = x[k]\Big|x[k],\theta\Big] \geq 1 - N\epsilon_{\Delta t} + (\epsilon_{\Delta t} - \delta_{\Delta t})u^T x[k] - \beta_{\Delta t}\frac{N^2}{4},$$

which follows after minimisation with respect to $\xi = \sum_{j=1}^{N} x_j[k]$, where the minimum is attained at $\xi = \frac{N}{2}$. Thus, the transition probability $\Pr\Big[x[k+1] = x[k]\Big|x[k],\theta\Big]$ is not negative if the sampling time Δt satisfies

$$\Delta t \leq \frac{4}{N^2\beta + 4N\max\{\epsilon,\delta\}}. \tag{D.10}$$

The upper bound on Δt in (D.10) is smaller than both bounds in (D.1) and (D.3). Hence, the bound (D.10) is a sufficient condition for all transition probabilities of the sampled-time Markov chain to lie in the interval $[0,1]$.

D.2. PROOF OF LEMMA 5.11

The objective function of (5.17) equals

$$\begin{aligned}f_n(\hat{a}_{13},\ldots,\hat{a}_{1N}) &= \log\Big(\Pr\Big[x[1],\ldots,x[n]\Big|\hat{a}_{13},\ldots,\hat{a}_{1N}\Big]\Big) \\ &= \sum_{k=1}^{n-1}\log\Big(\Pr\Big[x[k+1]\Big|x[k],\hat{a}_{13},\ldots,\hat{a}_{1N}\Big]\Big),\end{aligned} \tag{D.11}$$

where the last equality follows from the Markov property of the sampled-time SIS process. To reduce the zero-one UQP (5.12) to the reduced-size SIS network reconstruction problem (5.17), we show below that it is possible to construct a series of viral state transitions $x[k] \to x[k+1]$ for the time points $k = 1,\ldots,n-1$ for all adjacency matrices $A \in \mathcal{A}$, such that the objective function f_n of the latter problem is of the form

$$f_n(\hat{a}_{13},\ldots,\hat{a}_{1N}) = \sum_{i=3}^{N}\sum_{j=i+1}^{N} g_{ij}\hat{a}_{1i}\hat{a}_{1j} + \sum_{l=3}^{N} g_l\hat{a}_{1l} + g_{\text{const}}, \tag{D.12}$$

with the coefficients g_{ij} and g_l and an additive term g_{const} which is constant with respect to the links $\hat{a}_{13}, ..., \hat{a}_{1N}$ and, hence, can be omitted in the optimisation problem (5.17). We prove Lemma 5.11 in five steps, on which we elaborate in detail in the respective Subsections D.2.1 to D.2.5.

1. We design a viral state transition $\mathfrak{I}_{ij} : x[k] \to x[k+1]$ which results in setting the *quadratic costs* g_{ij} of (D.12) to a value. In Subsection D.2.5, we show that if the viral state transition $\mathfrak{I}_{ij}$ occurs, then we obtain $g_{ij} = -2$, and if it does not occur, then we obtain $g_{ij} = 0$.

2. We design a viral state transition $\mathfrak{I}_l : x[k] \to x[k+1]$ which results in setting the *linear costs* g_l of (D.12) to a *positive* value $g_l > 0$.

3. We design a viral state transition $\mathfrak{C}_l : x[k] \to x[k+1]$ which results in setting the linear cost g_l of (D.12) to a *negative* value $g_l < 0$.

4. We show how two transitions of the kind $\mathfrak{I}_{ij}, \mathfrak{I}_l$ and $\mathfrak{C}_l$ can be connected by constructing a suitable transition sequence.

5. We show that it is possible to construct a viral state sequence $x[1], ..., x[n]$ which is composed of several of the three kinds of viral state transitions $\mathfrak{I}_{ij}, \mathfrak{I}_l$ and $\mathfrak{C}_l$. If the viral state transition $\mathfrak{I}_l$ occurs multiple times, then the value of the coefficient g_l increases. On the other hand, if the viral state transition $\mathfrak{C}_l$ occurs multiple times, then the value of the coefficient g_l decreases[1]. By choosing the multiplicity of the occurrence of viral state transitions $\mathfrak{I}_{ij}$, $\mathfrak{I}_l$ and $\mathfrak{C}_l$, we show that the reduced-size SIS network reconstruction (5.17) becomes a zero-one UQP of the form (5.20).

D.2.1. SETTING THE QUADRATIC COSTS

In order to set the coefficients g_{ij} for $i \geq 3$ and $j \geq i+1$, corresponding to the terms $g_{ij}\hat{a}_{1i}\hat{a}_{1j}$ in the objective function (D.12), we construct the following special case of an infectious transition (5.2). The links $\hat{a}_{1i}$ and $\hat{a}_{1j}$ appear simultaneously in the probability for the infectious transition (5.2) if both node i and node j are infected at time k, i.e. $x_i[k] = x_j[k] = 1$, and node 1 becomes infected at time $k+1$, i.e. $x_1[k] = 0 \to x_1[k+1] = 1$. We choose the viral state of node 2 as[2] $x_2[k] = 1$ and define the transition

$$\mathfrak{I}_{ij} = \left\{ x[k+1] = e_1 + e_2 + e_i + e_j \middle| x[k] = e_2 + e_i + e_j \right\}.$$

The elements of the vector $e_i \in \mathbb{R}^N$ are given by $(e_i)_m = \delta_{mi}$, where δ_{mi} is the Kronecker delta. The transition $\mathfrak{I}_{ij}$ is a special case of an infectious transition (5.2) and, since $\hat{a}_{12} = a_{12} = 1$ in the reduced-size SIS network reconstruction (5.17), its transition probability is

[1] In the following Lemma 5.12, we show that the coefficient g_l can be set (arbitrarily close) to any value in $\mathbb{R}$ by adjusting the number of occurrences of the transitions $\mathfrak{I}_l$ and $\mathfrak{C}_l$.

[2] If node i and j were the only infected nodes at time k, then the transition probability (D.13) would equal zero if both elements $\hat{a}_{1i} = 0$ and $\hat{a}_{1j} = 0$. In that case, we would not be able to express the logarithm of the transition probability in the form (D.14) for all values of the elements $\hat{a}_{1i}, \hat{a}_{1j} \in \{0, 1\}$.

given by

$$\Pr\left[\mathfrak{I}_{ij}\middle|\hat{a}_{13},\dots,\hat{a}_{1N}\right]=\begin{cases}\beta_{\Delta t} & \text{if} \quad \hat{a}_{1i}=0\wedge\hat{a}_{1j}=0,\\ 2\beta_{\Delta t} & \text{if} \quad (\hat{a}_{1i}=0\wedge\hat{a}_{1j}=1)\vee(\hat{a}_{1i}=1\wedge\hat{a}_{1j}=0),\\ 3\beta_{\Delta t} & \text{if} \quad \hat{a}_{1i}=1\wedge\hat{a}_{1j}=1.\end{cases} \tag{D.13}$$

To compute the objective function f_n according to (D.11), we express the logarithm of the above transition probability (D.13) more compactly as

$$\begin{aligned}\log\left(\Pr\left[\mathfrak{I}_{ij}\middle|\hat{a}_{13},\dots,\hat{a}_{1N}\right]\right)&=(1-\hat{a}_{1i})(1-\hat{a}_{1j})\log(\beta_{\Delta t})+\hat{a}_{1i}(1-\hat{a}_{1j})\log(2\beta_{\Delta t})\\&\quad+(1-\hat{a}_{1i})\hat{a}_{1j}\log(2\beta_{\Delta t})+\hat{a}_{1i}\hat{a}_{1j}\log(3\beta_{\Delta t})\\&=\log(\beta_{\Delta t})+\hat{a}_{1i}\log(2)+\hat{a}_{1j}\log(2)+\hat{a}_{1i}\hat{a}_{1j}\log\left(\frac{3}{4}\right)\end{aligned} \tag{D.14}$$

If solely the transition $\mathfrak{I}_{ij}$ occurred once, then it follows from (D.14) that the quadratic cost of (D.12) would equal $g_{ij}=\log\left(\frac{3}{4}\right)<0$. We emphasise that the transitions $\mathfrak{I}_{ij}$ only need to occur for $i\geq 3$ and $j\geq i+1$ since the quadratic coefficients g_{ij} in the objective function (D.12) only occur for those values of i and j.

D.2.2. SETTING THE LINEAR COSTS TO A POSITIVE VALUE

In order to set the coefficients g_l, corresponding to the terms $g_l\hat{a}_{1l}$ in the objective function of (D.12), to a positive value $g_l>0$, we construct the following special case of an infectious transition (5.2). The link $\hat{a}_{1l}$ appears in the probability for the infectious transition (5.2) if node l is infected at time k, i.e. $x_l[k]=1$, and node 1 becomes infected at time $k+1$, i.e. $x_1[k]=0\rightarrow x_1[k+1]=1$. Analogously to Subsection D.2.1, we choose the viral state of node 2 as $x_2[k]=1$ and define the transition

$$\mathfrak{I}_l=\left\{x[k+1]=e_1+e_2+e_l\middle|x[k]=e_2+e_l\right\}.$$

The transition $\mathfrak{I}_l$ is a special case of an infectious transition (5.2). Since $\hat{a}_{12}=a_{12}=1$ in the reduced-size SIS network reconstruction (5.17), the transition probability of $\mathfrak{I}_l$ is given by

$$\Pr\left[\mathfrak{I}_l\middle|\hat{a}_{13},\dots,\hat{a}_{1N}\right]=\begin{cases}\beta_{\Delta t} & \text{if} \quad \hat{a}_{1l}=0,\\ 2\beta_{\Delta t} & \text{if} \quad \hat{a}_{1l}=1.\end{cases} \tag{D.15}$$

To compute the objective function f_n according to (D.11), we obtain the logarithm of the above transition probability (D.15) as

$$\begin{aligned}\log\left(\Pr\left[\mathfrak{I}_l\middle|\hat{a}_{13},\dots,\hat{a}_{1N}\right]\right)&=(1-\hat{a}_{1l})\log(\beta_{\Delta t})+\hat{a}_{1l}\log(2\beta_{\Delta t})\\&=\log(\beta_{\Delta t})+\hat{a}_{1l}\log(2).\end{aligned} \tag{D.16}$$

If solely the transition $\mathfrak{I}_l$ occurred once, then it follows from (D.16) that the linear cost of (D.12) would equal $g_l=\log(2)>0$.

D.2.3. SETTING THE LINEAR COSTS TO A NEGATIVE VALUE

In order to set the coefficients g_l, corresponding to the terms $g_l \hat{a}_{1l}$ in the objective function of (D.12), to a negative value $g_l < 0$, we construct the following special case of a constant transition (5.3). The link $\hat{a}_{1l}$ appears in the probability for the constant transition (5.3) if node 1 is susceptible and node l is infected ($x_1[k] = 0$ and $x_l[k] = 1$). Hence, we define the transition

$$\mathfrak{C}_l = \left\{ x[k+1] = e_l \middle| x[k] = e_l \right\}. \tag{D.17}$$

The transition $\mathfrak{C}_l$ is a special case of a constant transition (5.3) and its transition probability can be calculated as follows. From time k to time $k+1$, the probability of the infection of a node $m \neq l$ is

$$\Pr\left[\text{Node } m \text{ gets infected at } k+1 \middle| x[k] = e_l, \hat{a}_{13}, ..., \hat{a}_{1N} \right] = \beta_{\Delta t} \hat{a}_{ml}$$

The probability of an infection of a node at the time $k+1$ is hence

$$\begin{aligned} \Pr\left[\text{A node gets infected at } k+1 \middle| x[k] = e_l, \hat{a}_{13}, ..., \hat{a}_{1N} \right] &= \sum_{m=1, m\neq l}^{N} \beta_{\Delta t} \hat{a}_{ml} \\ &= \beta_{\Delta t} \hat{a}_{1l} + \beta_{\Delta t} + \beta_{\Delta t} \sum_{m=3, m\neq l}^{N} \hat{a}_{ml}, \end{aligned}$$

since $\hat{a}_{12} = a_{12} = 1$ in the reduced-size SIS network reconstruction (5.17). The probability of the curing (5.1) of node l equals $\delta_{\Delta t}$. Thus, the probability for the constant transition (D.17) becomes

$$\begin{aligned} \Pr\left[\mathfrak{C}_l \middle| \hat{a}_{13}, ..., \hat{a}_{1N} \right] &= 1 - \delta_{\Delta t} - \beta_{\Delta t} \hat{a}_{1l} - \beta_{\Delta t} - \beta_{\Delta t} \sum_{m=3, m\neq l}^{N} \hat{a}_{ml} \\ &= \xi - \beta_{\Delta t} \hat{a}_{1l}, \end{aligned} \tag{D.18}$$

where

$$\xi = 1 - \delta_{\Delta t} - \beta_{\Delta t} - \beta_{\Delta t} \sum_{m=3, m\neq l}^{N} \hat{a}_{ml}$$

is constant with respect to the links $\hat{a}_{13}, ..., \hat{a}_{1N}$ and does not have to be considered in the optimisation problem (5.17). It holds that $\Pr\left[\mathfrak{C}_l \middle| \hat{a}_{13}, ..., \hat{a}_{1N} \right]$ is in $[0, 1]$ for all link estimates $\hat{a}_{13}, ..., \hat{a}_{1N}$, which implies that $\xi > 0$. To compute the objective function f_n according to (D.11), we obtain the logarithm of the transition probability (D.18) as

$$\begin{aligned} \log\left(\Pr\left[\mathfrak{C}_l \middle| \hat{a}_{13}, ..., \hat{a}_{1N} \right] \right) &= (1 - \hat{a}_{1l}) \log(\xi) + \hat{a}_{1l} \log(\xi - \beta_{\Delta t}) \\ &= \log(\xi) + \hat{a}_{1l} \log\left(1 - \frac{\beta_{\Delta t}}{\xi} \right). \end{aligned} \tag{D.19}$$

If solely the transition $\mathfrak{C}_l$ occurred once, then it follows from (D.19) that the linear cost of (D.12) would equal $g_l = \log\left(1 - \frac{\beta_{\Delta t}}{\xi}\right) < 0$.

D.2.4. CONNECTING VIRAL STATE TRANSITIONS

In order to set the coefficients g_l and g_{ij} for more than one node l (or for more than one pair of nodes i and j), the transitions $\mathfrak{I}_{ij}$, $\mathfrak{I}_l$ and $\mathfrak{C}_l$ must occur multiple times in the viral state sequence $x[1], ..., x[n]$ for different values of l, i and j. Consider that one of the transitions $\mathfrak{I}_{ij}$, $\mathfrak{I}_l$ or $\mathfrak{C}_l$ occurs from time k_0 to k_0+1 and that another (not necessarily different) of the transitions $\mathfrak{I}_{ij}$, $\mathfrak{I}_l$ or $\mathfrak{C}_l$ shall occur from time $k_0+\Delta k$ to $k_0+\Delta k+1$ for some $\Delta k \geq 1$. For *any* connected adjacency matrix $A \in \mathcal{A}$, there is a viral state sequence which transform the viral state $x[k_0+1]$ at the end of one transition to the viral state $x[k_0+\Delta k]$ at the beginning of another transition, as we show in the three steps below.

1. If the transition $x[k_0] \to x[k_0+1]$ is one of the infectious transition $\mathfrak{I}_{ij}$ or $\mathfrak{I}_l$, then node 1 is infected at time k_0+1. In that case, we consider that node 1 cures from time k_0+1 to k_0+2. In the two steps below, replace formally time k_0+1 by k_0+2.

2. The expressions (D.14), (D.16) and (D.19) influence the values of the coefficients g_l and g_{ij} in the objective function (D.12). In order to give explicit expressions for coefficients g_l and g_{ij}, we would like to achieve that the viral state transitions from time k_0+1 to $k_0+\Delta k$ do not have an influence on the values of any of the coefficients g_l and g_{ij}, such that their value is solely determined by the expressions (D.14), (D.16) and (D.19).

   The coefficients g_l and g_{ij} correspond to addends in the objective function (D.12), which include the links $\hat{a}_{1l}$, $\hat{a}_{1i}$ and $\hat{a}_{1j}$, which are incident to node 1. A link $\hat{a}_{1l}$, which is incident to node 1, appears in the expressions for the probability of a viral state transition $x[k] \to x[k+1]$ of the sampled-time SIS process for exactly two cases. Firstly, in the probability of an infectious transition (5.2) from time k to $k+1$ only if node 1 is infected before or afterwards ($x_1[k]=1$ or $x_1[k+1]=1$). Secondly, the link $\hat{a}_{1l}$ may appear in the probability of a constant transition (5.3) from time k to $k+1$. We thus would like to exclude these two kinds of transitions from time k_0+1 to $k_0+\Delta k$.

   Hence, we want to construct the viral state transitions from time k_0+1 to $k_0+\Delta k$ such that the first node is constantly susceptible ($x_1[k]=0$ for $k=k_0+1, ..., k_0+\Delta k$) and additionally, such that there is no constant transition (5.3) from time k_0+1 to $k_0+\Delta k$. Then, the coefficients g_l and g_{ij} in the objective function (D.12) are not affected by any of the viral state transitions from time k_0+1 to $k_0+\Delta k$ and are solely determined by the expressions (D.14), (D.16) and (D.19).

3. The graph given by an adjacency matrix $A \in \mathcal{A}$ remains connected if node 1 is removed as stated above Definition 5.10. Thus, there exists a time $k_0+\Delta k \geq k_0+1$ and a finite sequence of non-constant transitions of the SIS process which transforms the viral state $x[k_0+1]$ to any other viral state $x[k_1] \in \{0,1\}^{N-1}$ under the constraint that node 1 is susceptible $x_1[k]=0$ for time $k=k_0+1$ to k_1: The simplest of such transition sequences would be successive infections (5.2), resulting in all nodes $2, ..., N$ being infected, with a subsequent curing (5.1) of those nodes i for which $x_i[k_0+\Delta k]=0$ shall hold.

For a network of six nodes, Figure D.1 gives an illustration on how two infectious

transitions, namely $\mathfrak{I}_{34}$ and $\mathfrak{I}_6$, can be connected by the viral state sequence described in the three steps above.

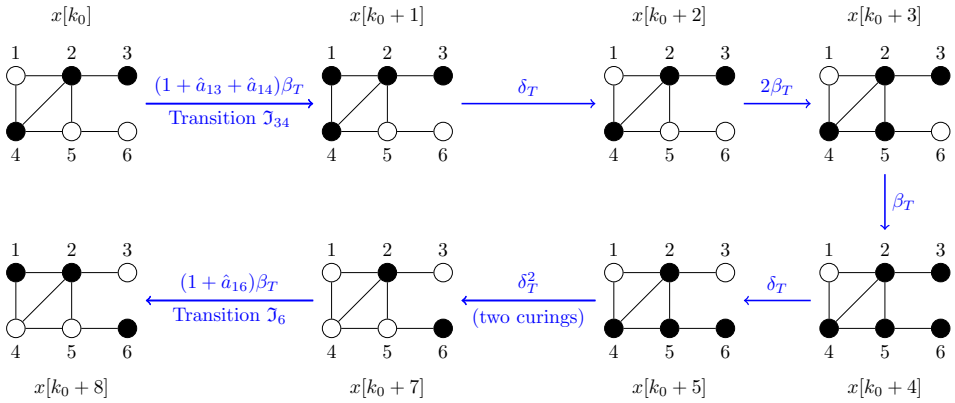

Figure D.1: An illustration of connecting two viral transitions, namely $\mathfrak{I}_{34}$ from time k_0 to k_0+1 and $\mathfrak{I}_6$ from time k_0+7 to k_0+8, for a connected network of six nodes by the procedure described in Subsection D.2.4. Above the blue arrows, the respective transition probabilities are stated. It holds $\hat{a}_{12}=a_{12}=1$ and $\hat{a}_{ij}=a_{ij}$ for $i,j\geq 2$ in the optimisation problem (5.17), and thus the transition probabilities from time k_0+1 to k_0+7 can be stated without the dependency on $\hat{a}_{ij}$. On the other hand, both transitions $\mathfrak{I}_{34}$ and $\mathfrak{I}_6$ do depend on the elements $\hat{a}_{ij}$. Since the transition $\mathfrak{I}_{34}$ from time k_0 to k_0+1 is an infectious transition, we consider that node 1 cures from time k_0+1 to k_0+2 according to step one in Subsection D.2.4. Then, following the description in step two and three of Subsection D.2.4, every node except node 1 becomes infected from time k_0+1 to k_0+4. Subsequently, the nodes 3, 4 and 5 cure from time k_0+4 to k_0+7 as required for the first state of the transition $\mathfrak{I}_6$. In Subsection D.2.5, the viral state sequence from time k_0+1 to k_0+7 is also denoted by $\mathfrak{F}(x[k_0+1],\mathfrak{I}_6)$, and its length is given by $\tau\left(\mathfrak{F}(x[k_0+1],\mathfrak{I}_6)\right)=6$.

D.2.5. CONSTRUCTING THE COMPLETE VIRAL STATE SEQUENCE

We consider that each of the viral state transitions $\mathfrak{I}_{ij}$, $\mathfrak{I}_l$ and $\mathfrak{C}_l$ may occur multiple times, and denote the multiplicities by m_{ij}, m_{1l} and m_{2l}, respectively. By $\mathfrak{T}$ we denote a viral state transition that is of the kind $\mathfrak{I}_{ij}$, $\mathfrak{I}_l$ or $\mathfrak{C}_l$. Furthermore, we denote by $\mathfrak{F}(x[k],\mathfrak{T})$ the viral state sequence which transforms the viral state $x[k]$ at time k to the first state of the transition $\mathfrak{T}$ (see also Figure D.1 for an example), following the description in Subsection D.2.4. The length (number of discrete time steps) of the viral state sequence $\mathfrak{F}(x[k],\mathfrak{T})$ is denoted by $\tau\left(\mathfrak{F}(x[k],\mathfrak{T})\right)$. The construction of the whole viral state sequence, which includes the viral state transitions $\mathfrak{I}_{ij}$, $\mathfrak{I}_l$ and $\mathfrak{C}_l$ with the multiplicities m_{ij}, m_{1l} and m_{2l}, is given in pseudo-code by Algorithm D.1. We emphasise that if a non-zero multiplicity of a viral state transition is increased, then only the respective for-loop (e.g. line 18 to line 21 for the transition $\mathfrak{I}_l$ if its multiplicity $m_{1l}=c\neq 0$ is increased to $m_{1l}=2c$ for some $c\in\mathbb{N}$) in Algorithm D.1 is run more often. In particular, line 9 is not executed more often when the multiplicities of the viral state transitions are increased.

In the following, we show how the multiplicities m_{ij}, m_{1l} and m_{2l} of the viral state transitions can be adjusted such that the reduced-size SIS network reconstruction (5.20) attains the form (5.17). For the viral state sequence $x[1],\ldots,x[n]$ given by the output of Algorithm D.1, the coefficients g_{ij} of the objective function (D.12) follow from the ex-

Algorithm D.1 Construction of Viral State Sequence for Reduced-Size SIS Network Reconstruction

Input: graph $G = (\mathcal{N}, \mathcal{L})$, initial state $x[0]$, multiplicities m_{1l}, m_{2l}, m_{ij}
Output: viral state sequence $x[1], ..., x[n]$
$\mathcal{Q} \leftarrow \{\mathfrak{I}_{ij} | r_{ij} = 1\} \cup \{\mathfrak{I}_l | m_{1l} \geq 1\} \cup \{\mathfrak{C}_l | m_{2l} \geq 1\}$ ▷ initialise the queue $\mathcal{Q}$
$k \leftarrow 1$
while $\mathcal{Q} \neq \emptyset$ **do**
    $\mathfrak{T} \leftarrow$ some element of $\mathcal{Q}$ ▷ dequeue a transition $\mathfrak{T}$ from $\mathcal{Q}$
    $\mathcal{Q} \leftarrow \mathcal{Q} \setminus \{\mathfrak{T}\}$
    $\Delta k \leftarrow \tau(\mathfrak{F}(x[k-1], \mathfrak{T}))$ ▷ length of transition from $x[k-1]$ to first state of $\mathfrak{T}$
    $(x[k], ..., x[k+\Delta k-1]) \leftarrow \mathfrak{F}(x[k-1], \mathfrak{T})$
    $k \leftarrow k + \Delta k$
    if $\mathfrak{T} = \mathfrak{I}_{ij}$ for some (i, j) **then**
        for $c = 1, ..., , m_{ij}$ **do**
            $(x[k], x[k+1]) \leftarrow (e_2 + e_i + e_j, e_1 + e_2 + e_i + e_j)$ ▷ transition $\mathfrak{I}_{ij}$
            $k \leftarrow k + 2$
        end for
    end if
    if $\mathfrak{T} = \mathfrak{I}_l$ for some l **then**
        for $c = 1, ..., , m_{1l}$ **do**
            $(x[k], x[k+1]) \leftarrow (e_2 + e_l, e_1 + e_2 + e_l)$ ▷ transition $\mathfrak{I}_l$
            $k \leftarrow k + 2$
        end for
    end if
    if $\mathfrak{T} = \mathfrak{C}_l$ for some l **then**
        for $c = 1, ..., , m_{2l}$ **do**
            $x[k] \leftarrow e_l$ ▷ transition $\mathfrak{C}_l$
            $k \leftarrow k + 1$
        end for
    end if
end while
$n \leftarrow k - 1$

pression (D.14) for the probability of the viral state transition $\mathfrak{I}_{ij}$ as

$$g_{ij} = \log\left(\frac{3}{4}\right) m_{ij}. \tag{D.20}$$

Furthermore, the expressions (D.14), (D.16) and (D.19) for the viral state transitions $\mathfrak{I}_{ij}$ (for $i \geq 3$ and $j \geq i+1$), $\mathfrak{I}_l$ and $\mathfrak{C}_l$, respectively, yield the coefficients g_l as

$$g_l = \log(2)\, m_{1l} + \log\left(1 - \frac{\beta_{\Delta t}}{\xi}\right) m_{2l} + \log(2) \left(\sum_{i=3}^{l-1} m_{il} + \sum_{i=l+1}^{N} m_{li} \right).$$

From (D.20) follows that

$$g_l = \log(2)\, m_{1l} + \log\left(1 - \frac{\beta_{\Delta t}}{\xi}\right) m_{2l} + \frac{\log(2)}{\log\left(\frac{3}{4}\right)} \left(\sum_{i=3}^{l-1} g_{il} + \sum_{i=l+1}^{N} g_{li} \right). \tag{D.21}$$

The values of the coefficients g_{ij} of the zero-one UQP (5.20) have to be either -2 or 0, which we obtain from (D.20) by the two steps below.

1. We choose that the transition $\mathfrak{I}_{ij}$ either occurs never or, independently of the nodes i and j, m_0 times. Thus

   $$m_{ij} = m_0 r_{ij}, \tag{D.22}$$

   where the binary variable r_{ij} denotes whether the transition $\mathfrak{I}_{ij}$ occurs either never ($r_{ij} = 0$) or m_0 times ($r_{ij} = 1$). Then, the coefficients g_{ij}, given by (D.20), become

   $$g_{ij} = \log\left(\frac{3}{4}\right) m_0 r_{ij}.$$

2. We multiply the objective function (D.12) with a constant factor $\mu = -2/\log\left(\frac{3}{4}\right) > 0$ and divide by m_0, which yields the new objective function

   $$\begin{aligned} \tilde{f}_n(\hat{a}_{13}, \ldots, \hat{a}_{1N}) &= \frac{\mu}{m_0} f_n(\hat{a}_{13}, \ldots, \hat{a}_{1N}) \\ &= \sum_{i=3}^{N} \sum_{j=i+1}^{N-1} c_{ij} \hat{a}_{1i} \hat{a}_{1j} + \sum_{l=3}^{N} c_l \hat{a}_{1l} + c_{\text{const}}, \end{aligned} \tag{D.23}$$

   with the coefficients $c_{ij} = \mu g_{ij}/m_0$, $c_l = \mu g_l/m_0$ and $c_{\text{const}} = \mu g_{\text{const}}/m_0$. The maximisation of $f_n(\hat{a}_{13}, \ldots, \hat{a}_{1N})$ is equivalent to the maximisation of $\tilde{f}_n(\hat{a}_{13}, \ldots, \hat{a}_{1N})$. As desired, the coefficients c_{ij} attain the values -2 and 0 for $r_{ij} = 1$ and $r_{ij} = 0$, respectively.

From (D.21), (D.22) and (D.23), we obtain the coefficients c_l of the new objective function $\tilde{f}_n(\hat{a}_{13}, \ldots, \hat{a}_{1N})$ as

$$c_l = \frac{\mu}{m_0} \log(2)\, m_{1l} + \frac{\mu}{m_0} m_{2l} \log\left(1 - \frac{\beta_{\Delta t}}{\xi}\right) + \frac{\mu}{m_0} \frac{\log(2)}{\log\left(\frac{3}{4}\right)} \left(\sum_{i=3}^{l-1} g_{il} + \sum_{i=l+1}^{N} g_{li} \right). \tag{D.24}$$

Since $g_{il} = m_0 c_{il}/\mu$, equation (D.24) is equivalent to

$$c_l = \frac{m_{1l}}{m_0}\mu\log(2) + \frac{m_{2l}}{m_0}\mu\log\left(1-\frac{\beta_{\Delta t}}{\xi}\right) + \frac{\log(2)}{\log\left(\frac{3}{4}\right)}\left(\sum_{i=3}^{l-1} c_{il} + \sum_{i=l+1}^{N} c_{li}\right). \tag{D.25}$$

By defining

$$\lambda_+ = \mu\log(2) > 0 \tag{D.26}$$

$$\lambda_- = \mu\log\left(1-\frac{\beta_{\Delta t}}{\xi}\right) < 0 \tag{D.27}$$

$$\eta_l = \frac{\log(2)}{\log\left(\frac{3}{4}\right)}\left(\sum_{i=3}^{l-1} c_{il} + \sum_{i=l+1}^{N} c_{li}\right) \geq 0, \tag{D.28}$$

it follows that (D.25) is equivalent to (5.19). Hence, we have proved Lemma 5.11.

D.3. PROOF OF LEMMA 5.12

Equation (5.19) shows that the coefficients c_l are determined by the numbers m_0 and m_{1l} of infectious transitions $\mathfrak{I}_{ij}$ and $\mathfrak{I}_l$ and by the number m_{2l} of constant transitions $\mathfrak{C}_l$. The third addend η_l in (5.19) is constant with respect to the number m_{1l}, m_{2l} and m_0 of occurrences of the viral state transitions $\mathfrak{I}_{ij}$, $\mathfrak{I}_l$ and $\mathfrak{C}_l$. We consider the two terms with which the coefficients m_{1l} and m_{2l} in equation (5.19) are multiplied and denote them by $q_0 = \lambda_+/m_0$ and $q_1 = \lambda_-/m_0$. It holds that $q_0 > 0$ and $q_1 < 0$. Furthermore, if m_0 grows to infinity, then the absolute value of the two coefficients q_0 and q_1 becomes arbitrarily small. Thus, for a sufficiently large number m_0 of infectious transitions $\mathfrak{I}_{ij}$, we can choose the number m_{1l} of infectious transitions $\mathfrak{I}_l$ and the number m_{2l} of constant transitions $\mathfrak{C}_l$, such that the coefficient c_l, given by (5.19), is arbitrarily close to any real number $b_l \in \mathbb{R}$.

D.4. PROOF OF LEMMA 5.13

We define the vector, which is composed of the optimisation variables of the zero-one UQP (5.12), as

$$y = (y_1, ..., y_N) \in \{0,1\}^N.$$

Furthermore, we denote the objective function of the zero-one UQP (5.12) by

$$f_{\text{obj}}(y) = \sum_{i=1}^{N}\sum_{j=i+1}^{N} b_{ij} y_i y_j + \sum_{l=1}^{N} b_l y_l. \tag{D.29}$$

The coefficients c_l given by (5.19) do not precisely equal the coefficients b_l for any finite numbers of transitions m_0, m_{1l}, m_{2l}. Instead, we have

$$c_l = b_l + \varepsilon_{\text{th},l}, \tag{D.30}$$

with the error $\varepsilon_{\text{th},l}$ on the l-th coefficient. The statement (5.21) implies that there is a finite number of transitions m_0, m_{1l}, m_{2l}, such that the error terms $\varepsilon_{\text{th},l}$ are bounded by an arbitrarily small $\varepsilon_{\max} \in \mathbb{R}^+$ and may be chosen to be non-negative:

$$0 \leq \varepsilon_{\text{th},l} \leq \varepsilon_{\max}, \quad l = 1, ..., N. \tag{D.31}$$

Thus, when the coefficients b_l in (D.29) are replaced by the distorted coefficients c_l in (D.30), the objective function f_{obj}, given by (D.29), is replaced by

$$\begin{aligned}\tilde{f}_{\text{obj}}(y) &= \sum_{i=1}^{N} \sum_{j=i+1}^{N} b_{ij} y_i y_j + \sum_{l=1}^{N} c_l y_l \\ &= \sum_{i=1}^{N} \sum_{j=i+1}^{N} b_{ij} y_i y_j + \sum_{l=1}^{N} b_l y_l + \sum_{l=1}^{N} \varepsilon_{\text{th},l} y_l.\end{aligned}$$

More compactly, we obtain

$$\tilde{f}_{\text{obj}}(y) = f_{\text{obj}}(y) + \varepsilon^T y, \tag{D.32}$$

with the error vector $\varepsilon = (\varepsilon_1, ..., \varepsilon_N)^T$.

Our aim is to show that the solution $\tilde{y}_{\text{opt}}$, or one of the solutions, to the zero-one UQP (5.12), with the objective function $\tilde{f}_{\text{obj}}$ given by (D.32), is also a solution to the original zero-one UQP (5.12) with the objective function f_{obj} given by (D.29). Hence, the solution $\tilde{y}_{\text{opt}}$ would also be a solution to the maximum cut problem. More precisely, we want to show that

$$\exists \tilde{y}_{\text{opt}} \in S_{\text{opt}} : \quad \tilde{f}_{\text{obj}}(\tilde{y}_{\text{opt}}) > \tilde{f}_{\text{obj}}(y) \quad \forall y \notin S_{\text{opt}}, \tag{D.33}$$

where the set of solutions to the zero-one UQP (5.12) with the objective function f_{obj}, given by (D.29), is denoted as S_{opt}. We denote the value of the objective function f_{obj}, given by (D.29), evaluated at one of the elements in S_{opt} as

$$f_{\text{opt}} = f_{\text{obj}}(y), \quad y \in S_{\text{opt}}. \tag{D.34}$$

Furthermore, we define the gap from the optimal value f_{opt} to the next largest value, that the objective function f_{obj} attains, as

$$\begin{aligned}\Delta f = \min_{y} \quad & f_{\text{opt}} - f_{\text{obj}}(y) \\ \text{s.t.} \quad & y \notin S_{\text{opt}}.\end{aligned} \tag{D.35}$$

It holds $\Delta f \geq 1$, since the maximum cuts, given by the elements in S_{opt}, contain at least one more link than any suboptimal cut.

With the definitions above, we can show the statement (D.33) as follows. The equations (D.32) and (D.34) yield, for any $\tilde{y}_{\text{opt}} \in S_{\text{opt}}$ and any $y \notin S_{\text{opt}}$, that

$$\begin{aligned}\tilde{f}_{\text{obj}}(\tilde{y}_{\text{opt}}) - \tilde{f}_{\text{obj}}(y) &= f_{\text{opt}} - f_{\text{obj}}(y) + \varepsilon^T (\tilde{y}_{\text{opt}} - y) \\ &\geq \Delta f + \varepsilon^T (\tilde{y}_{\text{opt}} - y),\end{aligned}$$

where the inequality follows from (D.35). Since the optimisation variables y_l are either 0 or 1, we have $\tilde{y}_{\text{opt}} - y \geq -u$, where the inequality holds component-wise and $u = (1,...,1)^T \in \mathbb{R}^N$ denotes the all-one vector. As stated by (D.31), the error terms $\varepsilon_{\text{th},l}$ are positive. Hence, we obtain

$$\begin{aligned} \tilde{f}_{\text{obj}}(\tilde{y}_{\text{opt}}) - \tilde{f}_{\text{obj}}(y) &\geq \Delta f - \varepsilon^T u \\ &\geq \Delta f - N\varepsilon_{\max}, \end{aligned} \tag{D.36}$$

where the last inequality follows from (D.31). From the inequality (D.36) we obtain

$$\tilde{f}_{\text{obj}}(\tilde{y}_{\text{opt}}) > \tilde{f}_{\text{obj}}(y)$$

if

$$\varepsilon_{\max} < \frac{1}{N} \leq \frac{\Delta f}{N}.$$

D

D.5. PROOF OF LEMMA 5.14

The objective function of the full-size SIS network reconstruction (5.10) at time $n_2 > n_1$ satisfies

$$\begin{aligned} f_{n_2}(\hat{A}) &= \log\left(\Pr\left[x[1],...,x[n_2]\middle|\hat{A}\right]\right) \\ &= \log\left(\Pr\left[x[1],...,x[n_1]\middle|\hat{A}\right]\right) + \sum_{k=n_1}^{n_2-1} \log\left(\Pr\left[x[k+1]\middle|x[k],\hat{A}\right]\right), \end{aligned} \tag{D.37}$$

which follows from the Markov property of the SIS process. We adjust the second addend of (D.37) by constructing the viral state sequence $x[n_1+1],...,x[n_2]$, such that the objective function f_{n_2} at time n_2 attains the form (5.22) in the second statement of Lemma 5.14.

We divide the first statement of Lemma 5.14 into two parts: Firstly, we show in Subsection D.5.1 how to construct a viral state sequence $x[n_1+1],...,x[n_2]$, such that $(A_{\text{ML}})_{ij} = a_{ij}$ if $a_{ij} = 1$. Secondly, we show in Subsection D.5.2 how to construct a viral state sequence $x[n_1+1],...,x[n_2]$, such that $(A_{\text{ML}})_{ij} = a_{ij}$ if $a_{ij} = 0$. The second statement of Lemma 5.14 is proved in Subsection D.5.3.

D.5.1. ENFORCE EXISTENCE OF LINKS

We denote the set of links $(i,j) \in \mathcal{L}$ in the first statement of Lemma 5.14 by

$$\bar{\mathcal{L}} = \left\{(i,j) \in \mathcal{L}\middle|(i,j) = (1,2) \vee (i \geq 2 \wedge j \geq 2)\right\}.$$

We aim to construct a viral state sequence such that the ML estimate (5.10) satisfies $(A_{\text{ML}})_{ij} = a_{ij}$ if the element of the true adjacency matrix is $a_{ij} = 1$ for all links $(i,j) \in \bar{\mathcal{L}}$. We make use of the following transition: If a node j gets infected at time $k+1$ and only node i has been infected at time k, then there must be a link between node i and j. We define the infectious transition, followed by a curing of node i, as

$$\mathfrak{E}_{ij} = \left\{x[k+2] = e_j, x[k+1] = e_i + e_j \middle| x[k] = e_i\right\}. \tag{D.38}$$

The probability of the transition $\mathfrak{E}_{ij}$ follows from (5.2) and (5.1) as

$$\Pr\left[\mathfrak{E}_{ij}\middle|\hat{A}\right] = \begin{cases} \beta_{\Delta t}\delta_{\Delta t} & \text{if} \quad \hat{a}_{ij} = 1, \\ 0 & \text{if} \quad \hat{a}_{ij} = 0. \end{cases} \tag{D.39}$$

We construct the viral state sequence $x[n_1+1],...,x[n_2]$ such that it contains $\mathfrak{E}_{ij}$ at least once for all links $(i,j) \in \bar{\mathcal{L}}$. Then, it follows from (D.39) that if the underlying matrix has the element $a_{ij} = 1$ but the solution candidate $\hat{A}$ contains a zero element $\hat{a}_{ij} = 0$ for any link $(i,j) \in \bar{\mathcal{L}}$, then the objective function of (5.10) becomes zero: $\Pr\left[x[1],...,x[n_2]\middle|\hat{A}\right] = 0$. Thus, the solution A_{ML} to the full-size SIS network reconstruction (5.10) with the objective function (D.37) has to satisfy

$$(A_{\mathrm{ML}})_{ij} = 1 \quad \text{if} \quad a_{ij} = 1, \quad \forall (i,j) \in \bar{\mathcal{L}} \tag{D.40}$$

D.5.2. ENFORCE ABSENCE OF LINKS

We aim to construct a viral state sequence such that the ML estimate (5.10) satisfies $(A_{\mathrm{ML}})_{ij} = a_{ij}$ if the element of the true adjacency matrix is $a_{ij} = 0$. We observe the following: If solely a node l is infected at time k and the viral state $x[k]$ does not change from time k to $k+1$, then the existence of a link from node l to another node m becomes *less probable*, which follows from (5.3). For a node $l \geq 2$, we define the constant viral state transition

$$\mathfrak{A}_l = \left\{x[k+1] = e_l \middle| x[k] = e_l\right\}. \tag{D.41}$$

The probability of the transition above follows from (5.3) as

$$\Pr\left[\mathfrak{A}_l\middle|\hat{A}\right] = 1 - \delta_{\Delta t} - \sum_{m=1}^{N} \beta_{\Delta t}\hat{a}_{ml}. \tag{D.42}$$

We consider that the transition $\mathfrak{A}_l$ successively occurs κ_l times from some time $k_0 \in \{n_1+1,...,n_2\}$ to time $k_0+\kappa_l$. For ease of exposition and without loss of generality, we assume that $k_0 = n_1+1$. Hence, the transition $\mathfrak{A}_l$ multiply occurs from time n_1+1 to time $n_1+\kappa_l+1$. Then, the probability of the transition sequence from time n_1+1 to $n_1+\kappa_l+1$ follows from (D.42) as

$$\log\left(\Pr\left[x[n_1+\kappa_l+1] = x[n_1+\kappa_l] = ... = x[n_1+2] = e_l \middle| x[n_1+1] = e_l, \hat{A}\right]\right) = \kappa_l \log\left(\Pr\left[\mathfrak{A}_l\middle|\hat{A}\right]\right). \tag{D.43}$$

The objective function of the full-size SIS network reconstruction (5.10) at time $n_1+\kappa_l+1$ becomes

$$\begin{aligned} f_{n_1+\kappa_l+1}(\hat{A}) &= f_{n_1}(\hat{A}) + \kappa_l \log\left(\Pr\left[\mathfrak{A}_l\middle|\hat{A}\right]\right) \\ &= f_{n_1}(\hat{A}) + \kappa_l \log\left(1 - \delta_{\Delta t} - \beta_{\Delta t}\sum_{m=1}^{N}\hat{a}_{ml}\right), \end{aligned}$$

where the last equality follows from (D.42) and (D.43). By defining the degree of node l minus the element $\hat{a}_{1l}$ as

$$d_l(\hat{A}) = \sum_{m=2}^{N} \hat{a}_{ml}, \tag{D.44}$$

we finally formulate the objective function of the SIS network reconstruction (5.10) at time $n_1 + \kappa_l + 1$ as

$$f_{n_1+\kappa_l+1}(\hat{A}) = f_{n_1}(\hat{A}) + \kappa_l \log\left(1 - \delta_{\Delta t} - \beta_{\Delta t} d_l(\hat{A}) - \beta_{\Delta t} \hat{a}_{1l}\right). \tag{D.45}$$

Based on the above formulation of the objective function (D.45), we will show that if the number κ_l of occurrences of the transition $\mathfrak{A}_l$ is great enough, then the solution A_{ML} to the SIS network reconstruction (5.10) satisfies $(A_{\mathrm{ML}})_{ml} = a_{ml}$ for all nodes $m \geq 2$.

Due to $a_{ij} = 1 \Rightarrow \hat{a}_{ij} = 1$ for $i, j \geq 2$ as stated by (D.40), the ML estimate A_{ML} has at least as many links between the nodes $i, j \geq 2$ as the true adjacency matrix A. Thus, the degree $d_l(A)$ of node l of the true adjacency matrix A, given by (D.44) when replacing $\hat{a}_{ml}$ by a_{ml}, is upper bounded by

$$d_l(A_{\mathrm{ML}}) \geq d_l(A). \tag{D.46}$$

Furthermore, since $(A_{\mathrm{ML}})_{ij} = a_{ij}$ for $i, j \geq 2$, we obtain

$$d_l(A_{\mathrm{ML}}) = d_l(A) \Leftrightarrow (A_{\mathrm{ML}})_{ml} = a_{ml} \quad \forall m = 2, \ldots, N. \tag{D.47}$$

Hence, it is sufficient to show that the ML estimate A_{ML} satisfies $d_l(A_{\mathrm{ML}}) = d_l(A)$ in order to prove the second statement of Lemma 5.14.

In the following, we consider two solution candidates to the full-size SIS network reconstruction (5.10): two matrices $\hat{A}_1$ and $\hat{A}_2$. We assume that the first row (and column) of the two solution candidates are equal, i.e.

$$(\hat{A}_1)_{1m} = (\hat{A}_2)_{1m}, \quad m = 1, \ldots, N. \tag{D.48}$$

From (D.48) follows that the matrices $\hat{A}_1$ and $\hat{A}_2$ result in the same objective value for the *reduced-size* SIS network reconstruction (5.17), since the optimisation is only with respect to the matrix elements $\hat{a}_{1m}$ for $m = 3, \ldots, N$. We consider that the two matrices $\hat{A}_1$ and $\hat{A}_2$ differ as follows. On the one hand, the first solution candidate $\hat{A}_1$ is a matrix that satisfies (D.46) with equality:

$$d_l(\hat{A}_1) = d_l(A). \tag{D.49}$$

On the other hand, the second solution candidate $\hat{A}_2$ is a matrix that does not satisfy (D.46) with equality:

$$d_l(\hat{A}_2) > d_l(A).$$

To check which of the matrices $\hat{A}_1$ and $\hat{A}_2$ yields a greater objective value of the *full-size* SIS network reconstruction (5.10) at time $n_1 + \kappa_l + 1$, we compute the difference of the

objective function (D.45) as

$$\begin{aligned} f_{n_1+\kappa_l+1}(\hat{A}_1) - f_{n_1+\kappa_l+1}(\hat{A}_2) &= f_{n_1}(\hat{A}_1) - f_{n_1}(\hat{A}_2) + \kappa_l \log\left(1-\delta_{\Delta t} - \beta_{\Delta t} d_l(\hat{A}_1) - \beta_{\Delta t}(\hat{A}_1)_{1l}\right) \\ &\quad - \kappa_l \log\left(1-\delta_{\Delta t} - \beta_{\Delta t} d_l(\hat{A}_2) - \beta_{\Delta t}(\hat{A}_2)_{1l}\right) \\ &= f_{n_1}(\hat{A}_1) - f_{n_1}(\hat{A}_2) + \kappa_l \gamma_l, \end{aligned} \tag{D.50}$$

where

$$\gamma_l = \log\left(\frac{1-\delta_{\Delta t} - \beta_{\Delta t} d_l(\hat{A}_1) - \beta_{\Delta t}(\hat{A}_1)_{1l}}{1-\delta_{\Delta t} - \beta_{\Delta t} d_l(\hat{A}_2) - \beta_{\Delta t}(\hat{A}_2)_{1l}}\right).$$

It holds $d_l(\hat{A}_2) > d_l(A) = d_l(\hat{A}_1)$ and, as stated by (D.48), $(\hat{A}_1)_{1l} = (\hat{A}_2)_{2l}$. Thus, it holds $\gamma_l > 0$. Since the difference $f_{n_1}(\hat{A}_1) - f_{n_1}(\hat{A}_2)$ is finite, there is a number $\kappa_l \in \mathbb{N}$ of occurrences of the transition $\mathfrak{A}_l$, such that the right-hand side of (D.50) is positive, which implies $f_{n_1+\kappa_l+1}(\hat{A}_1) > f_{n_1+\kappa_l+1}(\hat{A}_2)$. Hence, the matrix $\hat{A}_1$ results in a greater objective value of the optimisation problem (5.10) than the matrix $\hat{A}_2$ for a sufficiently large number of transitions κ_l, and the matrix $\hat{A}_2$ cannot be a solution of (5.10). Thus, if the number of transitions κ_l is sufficiently great, then the matrix A_{ML} that solves the full-size SIS network reconstruction (5.10) has to be of the kind $\hat{A}_1$ and satisfy equation (D.49): $d_l(A_{\mathrm{ML}}) = d_l(A)$. As stated by (D.47), the equation $d_l(A_{\mathrm{ML}}) = d_l(A)$ is equivalent to $(A_{\mathrm{ML}})_{ml} = a_{ml}$ for all nodes $m \geq 2$.

In order to complete the proof of the first statement of Lemma 5.14, it needs to hold $(A_{\mathrm{ML}})_{ml} = a_{ml}$ for all nodes $m \geq 2$ and *additionally* for all nodes $l \geq 2$. We achieve $(A_{\mathrm{ML}})_{ml} = a_{ml}$ for all nodes $m, l \geq 2$ as follows. We design the viral state sequence $x[n_1+1], \ldots, x[n_2]$ such that it solely consists of two kind of viral transitions: Firstly, the transitions $\mathfrak{E}_{ij}$ given by (D.38) for all links $(i,j) \in \bar{\mathcal{L}}$. Secondly, the transitions $\mathfrak{A}_l$ given by (D.41), which occur κ_l times for all nodes $l \geq 2$.

Finding a *shortest*[3] walk which traverses every link in a graph is known as the Chinese Postman Problem (CPP) or route intersection problem [291]. The CPP is solvable in polynomial time. Since every link $(i,j) \in \bar{\mathcal{L}}$ has to be traversed by an infection, we define the graph $\bar{G} = (\mathcal{N}, \bar{\mathcal{L}})$ and denote the solution to the CPP as

$$\left((i_1, j_1), \ldots, (i_r, j_r)\right) = \mathrm{CPP}\left(\bar{G}\right),$$

where $i_1, \ldots, i_r$ and $j_1, \ldots, j_r$ denote the successive nodes of the walk, where $i_{l+1} = j_l$, and $(i_l, j_l) \in \bar{\mathcal{L}}$ denote the traversed links. Algorithm D.2 illustrates in pseudo-code how the required viral state sequence $x[n_1+1], \ldots, x[n_2]$ can be constructed.

With the construction of the viral state sequence $x[n_1+1], \ldots, x[n_2]$ as described by Algorithm D.2, the objective function (D.37) at time n_2 becomes

$$f_{n_2}(\hat{A}) = f_{n_1}(\hat{A}) + \sum_{l=2}^{N} \kappa_l \log\left(1-\delta_{\Delta t} - \beta_{\Delta t} d_l(\hat{A}) - \beta_{\Delta t} \hat{a}_{1l}\right) + \zeta, \tag{D.51}$$

where ζ is finite and depends on the transition probabilities $\Pr\left[\mathfrak{E}_{ij} \middle| \hat{A}\right] = \beta_{\Delta t} \delta_{\Delta t} \hat{a}_{ij}$, given by (D.39), for the links $(i,j) \in \bar{\mathcal{L}}$.

[3] There is no necessity to use the shortest walk here, as long as the walk visits every link $(i,j) \in \bar{\mathcal{L}}$.

Algorithm D.2 Construction of Viral State Sequence for Full-Size SIS Network Reconstruction

Input: graph $\bar{G} = (\mathcal{N}, \bar{\mathcal{L}})$, multiplicities $\kappa_2, ..., \kappa_N$
Output: viral state sequence $x[n_1+1], ..., x[n_2]$
$\big((i_1, j_1), ..., (i_r, j_r)\big) \leftarrow \mathrm{CPP}\big(\bar{G}\big)$
$\mathcal{D} \leftarrow \emptyset$ ▷ set of visited nodes
$k \leftarrow 1$
for $l = 1, ..., r$ **do**
  $p \leftarrow i_l$, $q \leftarrow j_l$
  $x[k] \leftarrow e_p$
  $k \leftarrow k+1$
  if $p \notin \mathcal{D} \wedge p \neq 1$ **then**
    $(x[k], x[k+1], ..., x[k+\kappa_p-1]) \leftarrow (e_p, e_p, ..., e_p)$ ▷ κ_p times constant transition $\mathfrak{A}_p$
    $k \leftarrow k+\kappa_p$
    $\mathcal{D} \leftarrow \mathcal{D} \cup \{p\}$
  end if
  $x[k] \leftarrow e_p + e_q$ ▷ essential part of transition $\mathfrak{E}_{pq}$ (infection from node p to q)
  $k \leftarrow k+1$
end for
$x[k] \leftarrow e_q$
$k \leftarrow k+1$

By choosing the number of transitions κ_l sufficiently great for all nodes $l \geq 2$, we finally obtain that the matrix A_{ML} that solves the full-size SIS network reconstruction (5.10) at time n_2 with the objective function (D.51) has to satisfy $(A_{\mathrm{ML}})_{ij} = a_{ij}$ for all links $(i,j) \in \bar{\mathcal{L}}$.

D.5.3. SECOND STATEMENT OF LEMMA 5.14

As given by the first statement of Lemma 5.14, the solution $\hat{A}_{\mathrm{ML}}$ to the full-size SIS network reconstruction (5.10) with the objective function (D.51) has to satisfy $(\hat{A}_{\mathrm{ML}})_{ij} = a_{ij}$ for $(i,j) \in \bar{\mathcal{L}}$. Hence, the full-size SIS network reconstruction problem (5.10) at time n_2 becomes

$$\begin{aligned} \hat{A}_{\mathrm{ML}} = \arg\max_{\hat{A}} \quad & f_{n_1}(\hat{A}) + \sum_{l=2}^{N} \kappa_l \log\big(1 - \delta_{\Delta t} - \beta_{\Delta t} d_l(\hat{A}) - \beta_{\Delta t} \hat{a}_{1l}\big) + \zeta \\ \text{s.t.} \quad & \hat{a}_{ij} \in \{0,1\}, \quad i,j = 1,...,N, \\ & \hat{a}_{ij} = \hat{a}_{ji}, \quad i,j = 1,...,N, \\ & \hat{a}_{ii} = 0, \quad i = 1,...,N, \\ & \hat{a}_{ij} = a_{ij}, \quad \forall (i,j) \in \bar{\mathcal{L}}, \end{aligned} \tag{D.52}$$

where the objective function follows from (D.37) and (D.51). Since the optimisation variables $\hat{a}_{ij}$ in (D.52) are fixed to a_{ij} for $(i,j) \in \bar{\mathcal{L}}$, the optimisation takes place only with respect to the elements $\hat{a}_{13}, ..., \hat{a}_{1N}$. Furthermore, the term ζ does not depend on the

links $\hat{a}_{13},...,\hat{a}_{1N}$ and can be omitted in (D.52). By the formal replacement

$$\Pr\left[x[1],...,x[n_1]\middle|\hat{a}_{13},...,\hat{a}_{1N}\right] = f_{n_1}(\hat{A}) \quad \text{if} \hat{a}_{ij} = a_{ij} \quad \forall (i,j) \in \bar{\mathcal{L}},$$

we obtain the second statement of Lemma 5.14.

D.6. PROOF OF THEOREM 5.15

To show that the optimisation problem (5.22) is NP-hard, we consider the addends in the sum of its objective function, which equal

$$\begin{aligned}\kappa_l \log\left(1-\delta_{\Delta t}-\beta_{\Delta t} d_l(\hat{A})-\beta_{\Delta t}\hat{a}_{1l}\right) =& \kappa_l \log\left(1-\delta_{\Delta t}-\beta_{\Delta t} d_l(A)\right) \\ &+ \hat{a}_{1l}\kappa_l \log\left(\frac{1-\delta_{\Delta t}-\beta_{\Delta t} d_l(A)-\beta_{\Delta t}}{1-\delta_{\Delta t}-\beta_{\Delta t} d_l(A)}\right),\end{aligned} \tag{D.53}$$

where we used the fact that $d_l(A) = d_l(\hat{A})$ as stated Subsection D.5.2. The first addend in (D.53) is constant with respect to the links $\hat{a}_{1m}$ for all nodes m and thus the term has not to be considered in the optimisation problem (5.22). However, the second addend in (D.53) given by $\hat{a}_{1l}\chi_l$, where

$$\chi_l = \kappa_l \log\left(\frac{1-\delta_{\Delta t}-\beta_{\Delta t} d_l(A)-\beta_{\Delta t}}{1-\delta_{\Delta t}-\beta_{\Delta t} d_l(A)}\right),$$

is not constant with respect to the elements $\hat{a}_{1m}$ and has to be considered in the optimisation problem (5.22). Hence, the optimisation problem (5.22) is of the form (5.20) when the coefficients c_l in (5.20) are replaced by $c_l + \chi_l$, and the optimisation problem (5.22) becomes

$$\begin{aligned}\max_{\hat{a}_{13},...,\hat{a}_{1N}} \quad & \sum_{i=3}^{N}\sum_{j=i+1}^{N} c_{ij}\hat{a}_{1i}\hat{a}_{1j} + \sum_{l=3}^{N}(c_l+\chi_l)\hat{a}_{1l} \\ \text{s.t.} \quad & \hat{a}_{1i} \in \{0,1\}, \quad i = 3,...,N.\end{aligned} \tag{D.54}$$

Since the term χ_l is constant with respect to the elements $\hat{a}_{1m}$, it follows from Lemma 5.12 that the coefficient c_l can be set such that the coefficient $(c_l + \chi_l)$ approaches any real number arbitrarily close. If the coefficients c_{ij} in (D.54) equal the coefficients b_{ij} in the zero-one UQP (5.12) and the difference of the coefficients $(c_l + \chi_l)$ in (D.54) to the coefficients b_l in (5.12) is positive and smaller than $1/N$, then it follows from Lemma 5.13 that the solution to (D.54) is also a solution to (5.12). Hence, solving the optimisation problem (D.54), which resulted from the full-size SIS network reconstruction (5.10) as stated by Lemma 5.14, implies solving the NP-hard zero-one UQP (5.12).

D.7. NETWORK RECONSTRUCTION AS CONVEX OPTIMISATION PROBLEM

To overcome the challenge of the non-convexity of the optimisation problem (5.9), we consider the following reformulation of the objective function

$$\begin{aligned} f_{\text{obj}}(\theta) = &-\log(\Pr[A]) - \sum_{k\in H_{10}} \left(\log\left(\beta_{\Delta t}\right) + \log\left(\frac{\delta_{\Delta t}}{\beta_{\Delta t}}\right)\right) \\ &- \sum_{i=1}^{N} \sum_{k\in H_{01}[i]} \log\left(\beta_{\Delta t}\right) + \log\left(\frac{\epsilon_{\Delta t}}{\beta_{\Delta t}} + \sum_{j=1}^{N} x_j[k]a_{ij}\right) \\ &- \sum_{k\in H_{\text{const}}} \log\left(\beta_{\Delta t}\right) + \log\left(\frac{1-N\epsilon_{\Delta t}}{\beta_{\Delta t}} + \frac{\epsilon_{\Delta t}-\delta_{\Delta t}}{\beta_{\Delta t}} u^T x[k] + \sum_{j,i} x_j[k](x_i[k]-1)a_{ij}\right) \end{aligned}$$

We transform the parameters θ according to

$$h(\theta) = (A, \beta_{\Delta t}^{-1}, \frac{\delta_{\Delta t}}{\beta_{\Delta t}}, \frac{\epsilon_{\Delta t}}{\beta_{\Delta t}}),$$

and denote the transformed parameters by

$$\tilde{\theta} = (A, \tilde{\beta}, \tilde{\delta}, \tilde{\epsilon}) = h(\theta).$$

Expressing the objective in terms of the transformed parameters $\tilde{\theta}$ gives, since $n = |H_{10}| + |H_{\text{const}}| + \sum_i |H_{01}[i]|$,

$$\begin{aligned} f_{\text{obj}}(\tilde{\theta}) =& n\log\left(\tilde{\beta}\right) - \log(\Pr[A]) - |H_{10}|\log\left(\tilde{\delta}\right) - \sum_{i=1}^{N} \sum_{k\in H_{01}[i]} \log\left(\tilde{\epsilon} + \sum_{j=1}^{N} x_j[k]a_{ij}\right) \\ &- \sum_{k\in H_{\text{const}}} \log\left(\tilde{\beta} - N\tilde{\epsilon} + (\tilde{\epsilon}-\tilde{\delta})u^T x[k] + \sum_{j,i} x_j[k](x_i[k]-1)a_{ij}\right) \\ =& n\log\left(\tilde{\beta}\right) + g\left(\tilde{\theta}\right), \end{aligned}$$

where $g(\tilde{\theta}) = f_{\text{obj}}(\theta) - n\log(\tilde{\beta})$. Given the convex relaxation of the integer constraint $a_{ij} \in [0,1]$, the function $g(\tilde{\theta})$ is convex as the function $g(\tilde{\theta})$ is a sum of composition of negative logarithms and linear functions of $\tilde{\theta}$ and since $\log(\Pr[A])$ is concave by assumption, but the remaining term $\log(\tilde{\beta})$ is not convex. Based on the above form of the objective function f_{obj}, a convex approximation is stated in the following. We consider a piecewise-linear (or, more accurately, piecewise-affine) approximation of the non-convex term $\log(\tilde{\beta})$. We denote the number of segments of the piecewise-linear approximation by w, the more line segments, the more accurate the resulting approximation.

Given the range of β, it holds that

$$\tilde{\beta} = (\beta\Delta t)^{-1} \in [(\Delta t\beta_{\max})^{-1}, (\Delta t\beta_{\min})^{-1}].$$

Hence, the image of the non-convex term $\log(\tilde{\beta})$ is given by $[-\log(\Delta t\beta_{\max}), -\log(\Delta t\beta_{\min})]$. For stating a piecewise-linear approximation, we divide the image of $\log(\tilde{\beta})$ into w sub-intervals of equal size. These intervals are denoted by $[\log(t_l), \log(t_{l+1})]$, $l = 1, ..., w$, where $(\log(t_{l+1}) - \log(t_l))$ is constant with respect to l. Furthermore, it holds that $\log(t_1) = -\log(\Delta t\beta_{\max})$ and $\log(t_{w+1}) = -\log(\Delta t\beta_{\min})$. The piecewise-linear approximation is then given by the line segments connecting the points $(t_l, \log(t_l))$ of the intervals:

$$\log(\tilde{\beta}) \approx h_l(\tilde{\beta}) := c_l\tilde{\beta} + d_l, \quad \text{for} \quad \tilde{\beta} \in [t_l, t_{l+1}],$$

where

$$c_l = \frac{\log(t_{l+1}) - \log(t_l)}{t_{l+1} - t_l}$$

and

$$d_l = \frac{t_l \log(t_{l+1}) - t_{l+1}\log(t_l)}{t_l - t_{l+1}}$$

Each line segment l of the piecewise-linear approximation gives rise to a convex optimisation problem when the integer constraint on A is relaxed to $a_{ij} \in [0,1]$. Considering the feasible regions for $\tilde{\beta}, \tilde{\delta}$ and $\tilde{\epsilon}$ as constraints in the optimisation problem, we obtain for each line segment l

$$\begin{aligned} \underset{\tilde{\theta}}{\text{minimise}} \quad & g(\tilde{\theta}) + nh_l(\tilde{\beta}) \\ \text{subject to} \quad & a_{ij} \in [0,1] \quad \forall i,j \\ & t_l \le \tilde{\beta} \le t_{l+1} \\ & 0 \le \tilde{\delta} \le \delta_{\max}\Delta t\tilde{\beta} \\ & 0 \le \tilde{\epsilon} \le \epsilon_{\max}\Delta t\tilde{\beta} \end{aligned} \tag{D.55}$$

We denote the solution to the convex optimisation problem (D.55) by

$$\tilde{\theta}_{\text{cvx},l} = (A_{\text{cvx},l}, \tilde{\beta}_{\text{cvx},l}, \tilde{\delta}_{\text{cvx},l}, \tilde{\epsilon}_{\text{cvx},l}).$$

E

APPENDIX TO CHAPTER 6

E.1. PROOF OF PROPOSITION 6.6

Proposition 6.6 states there exists a logistic function $f(t)$ with $f(0) = y_1, f(t_{\text{obs}}/2) = y_2$ and $f(t_{\text{obs}}) = y_3$ if and only if $\Phi\left(y_1, y_2, y_3\right) > 0$. Subsection E.1.1 shows the "only if" direction: if the three points y_1, y_2, y_3 satisfy $f(0) = y_1, f(t_{\text{obs}}/2) = y_2$ and $f(t_{\text{obs}}) = y_3$ for some logistic function $f(t)$, then it holds that $\Phi\left(y_1, y_2, y_3\right) > 0$. In Subsection E.1.2, we prove the "if" direction: for any three points y_1, y_2, y_3 that satisfy $\Phi\left(y_1, y_2, y_3\right) > 0$, we construct a logistic function $f(t)$ with $f(0) = y_1, f(t_{\text{obs}}/2) = y_2$ and $f(t_{\text{obs}}) = y_3$.

E.1.1. FIRST PART

Lemma E.1. *For some observation time $t_{\text{obs}} > 0$, consider three points $y_1 = f(0), y_2 = f(t_{\text{obs}}/2)$ and $y_3 = f(t_{\text{obs}})$ on a logistic function $f(t)$. Then, the growth metric $\Phi\left(y_1, y_2, y_3\right)$ defined in (6.7) equals*

$$\Phi\left(y_1, y_2, y_3\right) = \frac{e^{Kt_0}}{1 + e^{Kt_0}} \frac{\left(1 - e^{-Kt_{\text{obs}}/2}\right)^2}{1 + e^{-K(t_{\text{obs}}/2 - t_0)}}, \tag{E.1}$$

which implies that $0 < \Phi\left(y_1, y_2, y_3\right) < 1$.

Proof. Since $y_1 = f(0)$, $y_2 = f(t_{\text{obs}}/2)$ and $y_3 = f(t_{\text{obs}})$, we obtain from the definition of the logistic function $f(t)$ in (6.3) that

$$y_1 = \frac{y_\infty}{1 + e^{Kt_0}},$$
$$y_2 = \frac{y_\infty}{1 + e^{-K(t_{\text{obs}}/2 - t_0)}}$$

and

$$y_3 = \frac{y_\infty}{1 + e^{-K(t_{\text{obs}} - t_0)}}. \tag{E.2}$$

We define the two constants α and c as

$$\alpha = e^{Kt_0} \tag{E.3}$$

and

$$c = e^{-Kt_{\text{obs}}/2}. \tag{E.4}$$

Thus, we can write the three points y_1, y_2 and y_3 more compactly as

$$y_1 = \frac{y_\infty}{1+\alpha}, \tag{E.5}$$

$$y_2 = \frac{y_\infty}{1+\alpha c} \tag{E.6}$$

and

$$y_3 = \frac{y_\infty}{1+\alpha c^2}.$$

From the definition of the growth metric $\Phi(y_1, y_2, y_3)$ in (6.7), we obtain that

$$\begin{aligned}\Phi(y_1, y_2, y_3) &= \frac{1+\alpha c^2}{1+\alpha c} - \frac{1+\alpha c}{1+\alpha} \\ &= \frac{(1+\alpha c^2)(1+\alpha) - (1+\alpha c)^2}{(1+\alpha c)(1+\alpha)}.\end{aligned}$$

Hence, it holds that

$$\Phi(y_1, y_2, y_3) = \frac{1+\alpha+\alpha c^2+\alpha^2 c^2 - 1 - 2\alpha c - \alpha^2 c^2}{(1+\alpha c)(1+\alpha)},$$

which simplifies to

$$\Phi(y_1, y_2, y_3) = \frac{\alpha}{1+\alpha}\frac{1}{1+\alpha c}(1-c)^2. \tag{E.7}$$

Since $\alpha > 0$ and $c > 0$, we obtain that $\Phi(y_1, y_2, y_3) > 0$. Furthermore, $t_{\text{obs}} > 0$ implies that $c < 1$. Thus, we obtain from (E.7) that $\Phi(y_1, y_2, y_3) < 1$. To finish the proof, we substitute α, c in (E.7) and arrive at (E.1). □

E.1.2. SECOND PART

For $i = 1, 2, 3$, the point y_i is on the logistic function (6.3) if and only if

$$y_i + y_i e^{-K((i-1)t_{\text{obs}}/2 - t_0)} - y_\infty = 0.$$

Dividing by y_i yields that

$$e^{-K((i-1)t_{\text{obs}}/2 - t_0)} - \frac{1}{y_i}y_\infty + 1 = 0.$$

Thus, we arrive at a set of three non-linear equations

$$e^{Kt_0}e^{-K(i-1)t_{\text{obs}}/2} - \frac{1}{y_i}y_\infty + 1 = 0, \quad i = 1,2,3. \tag{E.8}$$

With (E.3) and (E.4), we can express the second exponential in (E.8) as

$$e^{-K(i-1)t_{\text{obs}}/2} = \begin{cases} 1 & \text{if} \quad i = 1, \\ c & \text{if} \quad i = 2, \\ c^2 & \text{if} \quad i = 3. \end{cases}$$

Then, we obtain from (E.8) a set of non-linear equations for the three unknowns α, c and y_∞ as

$$\alpha - \frac{1}{y_1}y_\infty + 1 = 0, \tag{E.9}$$

$$\alpha c - \frac{1}{y_2}y_\infty + 1 = 0, \tag{E.10}$$

$$\alpha c^2 - \frac{1}{y_3}y_\infty + 1 = 0. \tag{E.11}$$

The first equation (E.9) yields that

$$y_\infty = y_1(\alpha + 1). \tag{E.12}$$

Combining (E.12) with the second equation (E.10) gives that

$$\alpha c - \frac{y_1}{y_2}(\alpha + 1) + 1 = 0,$$

from which we obtain that

$$c = \frac{1}{\alpha}\left(\frac{y_1}{y_2}(\alpha + 1) - 1\right).$$

Hence, it holds that

$$c = \frac{1}{\alpha}\left(\frac{y_1}{y_2} - 1\right) + \frac{y_1}{y_2}. \tag{E.13}$$

Combining the expressions for y_∞ and c in (E.12) and (E.13), respectively, with the third equation (E.11) yields that

$$\alpha\left(\frac{1}{\alpha}\left(\frac{y_1}{y_2} - 1\right) + \frac{y_1}{y_2}\right)^2 - \frac{y_1}{y_3}(\alpha + 1) + 1 = 0,$$

which is equivalent to

$$\frac{1}{\alpha}\left(\frac{y_1}{y_2} - 1\right)^2 + 2\left(\frac{y_1}{y_2} - 1\right)\frac{y_1}{y_2} + \alpha\frac{y_1^2}{y_2^2} - \frac{y_1}{y_3}(\alpha + 1) + 1 = 0.$$

Multiplication with α and rearranging gives that

$$\alpha^2\left(\frac{y_1^2}{y_2^2}-\frac{y_1}{y_3}\right)+\alpha\left(2\frac{y_1}{y_2}\left(\frac{y_1}{y_2}-1\right)-\frac{y_1}{y_3}+1\right)+\left(\frac{y_1}{y_2}-1\right)^2=0. \tag{E.14}$$

The quadratic equation (E.14) has two solutions. The first solution is $\alpha=-1$ leads to a contradiction, since α, defined in (E.3), is positive. The second solution of (E.14) is

$$\alpha=-\frac{\left(\frac{1}{y_2}-\frac{1}{y_1}\right)^2}{\frac{1}{y_2^2}-\frac{1}{y_1y_3}},$$

which is equivalent to

$$\alpha=\frac{\left(y_1-y_2\right)^2}{y_1y_2}\frac{1}{\frac{y_2}{y_3}-\frac{y_1}{y_2}}.$$

E

Thus, we obtain with the definition of the growth metric $\Phi(y_1,y_2,y_3)$ in (6.7) that

$$\alpha=\frac{\left(y_1-y_2\right)^2}{y_1y_2}\frac{1}{\Phi(y_1,y_2,y_3)}. \tag{E.15}$$

Since $y_1>0$ and $y_2>0$, the expression (E.15) for α is positive only if

$$\Phi(y_1,y_2,y_3)>0.$$

Hence, if and only if (6.8) holds true, there is a solution for the unknown α, and, hence, for the logistic growth rate K and the inflection point t_0. From (E.15) and (E.12), we obtain the steady-state y_∞ as

$$y_\infty=y_1+\frac{\left(y_1-y_2\right)^2}{y_2}\frac{1}{\Phi(y_1,y_2,y_3)}.$$

From (E.13) and (E.15), it follows that the unknown c equals

$$c=\frac{y_1}{y_2}+\left(\frac{y_1}{y_2}-1\right)\frac{y_1y_2}{\left(y_1-y_2\right)^2}\Phi\left(y_1,y_2,y_3\right),$$

which simplifies to

$$c=\frac{y_1}{y_2}+\frac{y_1}{y_1-y_2}\Phi\left(y_1,y_2,y_3\right). \tag{E.16}$$

The definition of c in (E.4) implies that

$$K=-\frac{2}{t_{\text{obs}}}\log(c),$$

which yields with (E.16) that

$$K = -\frac{2}{t_{\text{obs}}} \log\left(\frac{y_1}{y_2} + \frac{y_1}{y_1 - y_2}\Phi\left(y_1, y_2, y_3\right)\right).$$

Finally, we obtain the inflection point t_0 from (E.3) as

$$\begin{aligned} t_0 &= \frac{1}{K}\log(\alpha) \\ &= \frac{1}{K}\log\left(\frac{\left(y_1 - y_2\right)^2}{y_1 y_2}\frac{1}{\Phi(y_1, y_2, y_3)}\right), \end{aligned}$$

where the last equality follows from (E.15).

E.2. PROOF OF PROPOSITION 6.7

E.2.1. CONDITION NUMBER OF ESTIMATING THE STEADY STATE

From the definition of the condition number $\kappa_1(t_{\text{obs}})$ in (6.13), we obtain that

$$\kappa_1(t_{\text{obs}}) = -\frac{\left(y_1 - y_2\right)^2}{y_2}\frac{1}{\Phi^2(y_1, y_2, y_3)}\frac{\partial\Phi(y_1, y_2, y_3)}{\partial y_3}.$$

The definition of the growth metric $\Phi(y_1, y_2, y_3)$ in (6.7) yields that

$$\frac{\partial\Phi(y_1, y_2, y_3)}{\partial y_3} = -\frac{y_2}{y_3^2}. \tag{E.17}$$

Thus, the condition number $\kappa_1(t_{\text{obs}})$ follows as

$$\kappa_1(t_{\text{obs}}) = \frac{\left(y_1 - y_2\right)^2}{y_3^2}\frac{1}{\Phi^2(y_1, y_2, y_3)}.$$

E.2.2. CONDITION NUMBER OF ESTIMATING THE LOGISTIC GROWTH RATE

With (6.10), we define the condition number $\kappa_2(t_{\text{obs}})$ with respect to the growth rate estimate $\hat{K}(t_{\text{obs}})$ as

$$\kappa_2(t_{\text{obs}}) = \frac{\partial}{\partial y_3}\left(-\frac{2}{t_{\text{obs}}}\log\left(\frac{y_1}{y_2} + \frac{y_1}{y_1 - y_2}\Phi\left(y_1, y_2, y_3\right)\right)\right).$$

Hence, it holds that

$$\kappa_2(t_{\text{obs}}) = -\frac{2}{t_{\text{obs}}}\frac{1}{\frac{y_1}{y_2} + \frac{y_1}{y_1 - y_2}\Phi\left(y_1, y_2, y_3\right)}\frac{y_1}{y_1 - y_2}\frac{\partial}{\partial y_3}\Phi\left(y_1, y_2, y_3\right).$$

Thus, we obtain with (E.17) that

$$\kappa_2(t_{\text{obs}}) = \frac{2}{t_{\text{obs}}}\frac{1}{\frac{y_1}{y_2} - 1 + \Phi\left(y_1, y_2, y_3\right)}\frac{y_2}{y_3^2},$$

which simplifies to

$$\kappa_2(t_{\text{obs}}) = \frac{2}{t_{\text{obs}}}\frac{y_2^2}{y_3^2}\frac{1}{y_1 - y_2 + y_2\Phi\left(y_1, y_2, y_3\right)}. \tag{E.18}$$

E

E.2.3. CONDITION NUMBER OF ESTIMATING THE INFLECTION POINT

With (6.11), we define the condition number $\kappa_3(t_{\text{obs}})$ with respect to the inflection point estimate $\hat{t}_0(t_{\text{obs}})$ as

$$\kappa_3(t_{\text{obs}}) = \frac{\partial}{\partial y_3}\left(\frac{1}{K}\log\left(\frac{(y_1-y_2)^2}{y_1 y_2}\frac{1}{\Phi(y_1,y_2,y_3)}\right)\right),$$

which becomes

$$\begin{aligned}\kappa_3(t_{\text{obs}}) = &-\frac{1}{K^2}\log\left(\frac{(y_1-y_2)^2}{y_1 y_2}\frac{1}{\Phi(y_1,y_2,y_3)}\right)\frac{\partial K}{\partial y_3}\\ &-\frac{1}{K}\frac{1}{\frac{(y_1-y_2)^2}{y_1 y_2}\frac{1}{\Phi(y_1,y_2,y_3)}}\frac{(y_1-y_2)^2}{y_1 y_2}\frac{1}{\Phi^2(y_1,y_2,y_3)}\frac{\partial}{\partial y_3}\Phi(y_1,y_2,y_3).\end{aligned}$$

Thus, it holds that

$$\begin{aligned}\kappa_3(t_{\text{obs}}) = &-\frac{1}{K^2}\log\left(\frac{(y_1-y_2)^2}{y_1 y_2}\frac{1}{\Phi(y_1,y_2,y_3)}\right)\frac{\partial K}{\partial y_3}\\ &-\frac{1}{K}\frac{1}{\Phi(y_1,y_2,y_3)}\frac{\partial}{\partial y_3}\Phi(y_1,y_2,y_3).\end{aligned}$$

With (6.11), (E.17) and (E.18), we obtain that

$$\begin{aligned}\kappa_3(t_{\text{obs}}) = &-\frac{1}{K}t_0\frac{1}{t_{\text{obs}}}\frac{y_2^2}{y_3^2}\frac{1}{y_1-y_2+y_2\Phi(y_1,y_2,y_3)}\\ &+\frac{1}{K}\frac{1}{\Phi(y_1,y_2,y_3)}\frac{y_2}{y_3^2},\end{aligned}$$

which simplifies to

$$\kappa_3(t_{\text{obs}}) = \frac{1}{K}\frac{y_2}{y_3^2}\left(\frac{1}{\Phi(y_1,y_2,y_3)} - \frac{t_0 y_2}{t_{\text{obs}}}\frac{1}{y_1-y_2+y_2\Phi(y_1,y_2,y_3)}\right).$$

The expression (6.16) for the condition number $\kappa_3(t_{\text{obs}})$ follows from $t_{\text{obs}} = t_{\text{obs}}/2$.

E.3. PROOF OF PROPOSITION 6.8

E.3.1. AUXILIARY LEMMAS

Lemma E.2. *For some observation time $t_{\text{obs}} > 0$, consider three points $y_1 = f(0), y_2 = f(t_{\text{obs}}/2)$ and $y_3 = f(t_{\text{obs}})$ on a logistic function $f(t)$. Then, the difference of the points y_2 and y_1 equals*

$$y_2 - y_1 = \frac{y_\infty}{1-e^{-\frac{1}{2}Kt_{\text{obs}}}}\Phi(y_1,y_2,y_3).$$

Proof. From (E.5) and (E.6), we obtain that

$$y_2 - y_1 = y_\infty \left(\frac{1}{1+\alpha c} - \frac{1}{1+\alpha} \right),$$

where α and c are defined by (E.3) and (E.4). We simplify and obtain that

$$y_2 - y_1 = y_\infty \frac{\alpha}{1+\alpha} \frac{1-c}{1+\alpha c}.$$

Comparing with (E.7) yields that

$$y_2 - y_1 = \frac{y_\infty}{1-c} \Phi\left(y_1, y_2, y_3\right).$$

□

E.3.2. LOWER BOUND FOR THE CONDITION NUMBER OF ESTIMATING THE STEADY STATE

From Lemma E.2, we obtain that the condition number $\kappa_1(t_{\text{obs}})$ in (6.14) equals to

$$\kappa_1(t_{\text{obs}}) = \frac{y_\infty^2}{y_3^2} \frac{1}{\left(1 - e^{-\frac{1}{2}Kt_{\text{obs}}}\right)^2}.$$

From the expression for y_3 in (E.2) and $2t_{\text{obs}} = t_{\text{obs}}$, it follows that

$$\kappa_1(t_{\text{obs}}) = \left(\frac{1 + e^{-K(t_{\text{obs}} - t_0)}}{1 - e^{-\frac{1}{2}Kt_{\text{obs}}}} \right)^2.$$

Hence, we obtain that

$$\begin{aligned} \kappa_1(t_{\text{obs}}) &\geq \left(\frac{1}{1 - e^{-\frac{1}{2}Kt_{\text{obs}}}} \right)^2 + \left(\frac{e^{-K(t_{\text{obs}} - t_0)}}{1 - e^{-\frac{1}{2}Kt_{\text{obs}}}} \right)^2 \\ &\geq 1 + \left(\frac{e^{-K(t_{\text{obs}} - t_0)}}{1 - e^{-\frac{1}{2}Kt_{\text{obs}}}} \right)^2. \end{aligned} \tag{E.19}$$

A basic inequality [282] for the exponential function is $e^{-x} \geq 1 - x$ for all $x \in \mathbb{R}$. Hence, the denominator in (E.19) is bounded by

$$\begin{aligned} 1 - e^{-\frac{1}{2}Kt_{\text{obs}}} &\leq 1 - \left(1 - \frac{1}{2}Kt_{\text{obs}}\right) \\ &= \frac{1}{2}Kt_{\text{obs}}, \end{aligned}$$

which finally implies that

$$\kappa_1(t_{\text{obs}}) \geq 1 + \frac{4}{K^2 t_{\text{obs}}^2} e^{-2K(t_{\text{obs}} - t_0)}.$$

E.3.3. LOWER BOUND FOR THE CONDITION NUMBER OF ESTIMATING THE LOGISTIC GROWTH RATE

We consider the denominator of the last factor in (6.15), which equals

$$y_1 - y_2 + y_2\Phi(y_1, y_2, y_3) = -(y_2 - y_1)\left(1 - \frac{y_2}{y_2 - y_1}\Phi(y_1, y_2, y_3)\right).$$

With Lemma E.2 we obtain that

$$y_1 - y_2 + y_2\Phi(y_1, y_2, y_3) = -(y_2 - y_1)\left(1 - \frac{y_2}{y_\infty}\left(1 - e^{-\frac{1}{2}Kt_{\text{obs}}}\right)\right).$$

Since $y_2 > y_1$, $y_\infty > y_2$ and $t_{\text{obs}} > 0$, it holds that

$$y_1 - y_2 + y_2\Phi(y_1, y_2, y_3) < 0.$$

Thus, it follows from (6.15) that

$$\begin{aligned}|\kappa_2(t_{\text{obs}})| &= -\kappa_2(t_{\text{obs}}) \\ &= \frac{2}{t_{\text{obs}}}\frac{y_2^2}{y_3^2}\frac{1}{y_2 - y_1 - y_2\Phi(y_1, y_2, y_3)}.\end{aligned}$$

With Lemma E.2

$$\begin{aligned}|\kappa_2(t_{\text{obs}})| &= \frac{2}{t_{\text{obs}}}\frac{y_2^2}{y_3^2}\left(\frac{y_\infty}{1 - e^{-\frac{1}{2}Kt_{\text{obs}}}} - y_2\right)^{-1}\frac{1}{\Phi(y_1, y_2, y_3)} \\ &= \frac{2}{t_{\text{obs}}}\frac{y_2^2}{y_3^2}\frac{1 - e^{-\frac{1}{2}Kt_{\text{obs}}}}{y_\infty - y_2\left(1 - e^{-\frac{1}{2}Kt_{\text{obs}}}\right)}\frac{1}{\Phi(y_1, y_2, y_3)}.\end{aligned}$$

Since

$$y_2\left(1 - e^{-\frac{1}{2}Kt_{\text{obs}}}\right) > 0,$$

it holds that

$$|\kappa_2(t_{\text{obs}})| > \frac{2}{t_{\text{obs}}}\frac{y_2^2}{y_3^2}\frac{1}{y_\infty}\left(1 - e^{-\frac{1}{2}Kt_{\text{obs}}}\right)\frac{1}{\Phi(y_1, y_2, y_3)}. \tag{E.20}$$

To further bound (E.20), we consider the term

$$\frac{2}{t_{\text{obs}}}\left(1 - e^{-\frac{1}{2}Kt_{\text{obs}}}\right) = K\frac{1 - e^{-\xi}}{\xi}, \tag{E.21}$$

where $\xi = \frac{1}{2}Kt_{\text{obs}}$. Since $\xi > -1$, we obtain that

$$K\frac{1 - e^{-\xi}}{\xi} > K\frac{1}{1 + \xi}$$

Thus, with (E.21) and the definition of ξ, we obtain that

$$\frac{2}{t_{\text{obs}}}\left(1-e^{-\frac{1}{2}Kt_{\text{obs}}}\right) \geq K\frac{1}{1+\frac{1}{2}Kt_{\text{obs}}}.$$

Finally, (E.20) yields that

$$|\kappa_2(t_{\text{obs}})| > \frac{y_2^2}{y_3^2}\frac{1}{y_\infty}\frac{K}{1+\frac{1}{2}Kt_{\text{obs}}}\frac{1}{\Phi\left(y_1,y_2,y_3\right)}.$$

E.3.4. LOWER BOUND FOR THE CONDITION NUMBER OF ESTIMATING THE INFLECTION POINT

With (6.15), the expression for the condition number $\kappa_3(t_{\text{obs}})$ in (6.16) is equivalent to

$$\kappa_3(t_{\text{obs}}) = \frac{1}{K}\frac{y_2}{y_3^2}\left(\frac{1}{\Phi(y_1,y_2,y_3)} - \frac{t_0 y_3^2}{y_2}\kappa_2(t_{\text{obs}})\right).$$

Since $\kappa_2(t_{\text{obs}}) < 0$, we obtain a lower bound as

$$\kappa_3(t_{\text{obs}}) > \frac{1}{K}\frac{y_2}{y_3^2}\frac{1}{\Phi(y_1,y_2,y_3)}.$$

F

APPENDIX TO CHAPTER 7

F.1. DERIVATION OF THE DISCRETE-TIME GEMF MODEL

In Subsection F.1.1, we give a brief description the continuous-time GEMF model [136] for completeness. In Subsection F.1.2, we extend the continuous-time GEMF model to *heterogeneous* spreading parameters. In Subsection F.1.3, we show that applying Euler's method to the continuous-time GEMF model of Sahneh *et al.* [136] results in the discrete-time model (7.4).

F.1.1. CONTINUOUS-TIME GEMF WITH HOMOGENEOUS PARAMETERS

There are two kinds of transition in the GEMF model. First, there are *nodal transitions*. Node i changes from compartment p to compartment q with the transition rate δ_{pq}. The $C \times C$ *nodal transition rate matrix* A_δ is defined as

$$(A_\delta)_{pq} = \delta_{pq}, \quad 1 \leq p, q \leq C.$$

The second kind of transitions in the GEMF model are *edge-based* transitions. The GEMF model is formulated for multi-layer networks. The layers are denoted by $l = 1, ..., L$, where L denotes the number of layers. For every layer l, there is an $N \times N$ adjacency matrix A_l with elements $a_{l,ij}$ for every pair of nodes i, j. If there is a directed link on layer l from node j to node i, then it holds $a_{l,ij} = 1$. If there is no link on layer l from node j to node i, then it holds $a_{l,ij} = 0$. To every network layer l, there is exactly one influencer compartment $c_l \in \{1, ..., C\}$. If a node i has neighbours j on graph layer l, i.e. $a_{l,ij} = 1$, which are in compartment c_l, then node i changes from compartment p to compartment q with the transition rate $\beta_{l,pq}$. For every layer l, the $C \times C$ *edge-based transition rate matrix* A_{β_l} is defined as

$$\left(A_{\beta_l}\right)_{pq} = \beta_{l,pq}, \quad 1 \leq p, q \leq C.$$

The matrices A_δ and A_{β_l} are adjacency matrices and define the nodal transition rate graph and, for every layer l, an edge-based transition rate graph. The Laplacian matrix

of the nodal transition rate graph and the edge-based transition rate graphs, respectively, are denoted by

$$Q_\delta = \operatorname{diag}(A_\delta u) - A_\delta$$

and

$$Q_{\beta,l} = \operatorname{diag}\left(A_{\beta_l} u\right) - A_{\beta_l}.$$

Finally, the GEMF model in continuous time describes the evolution of the $C \times 1$ viral state vector $v_i(t)$ as

$$\frac{dv_i(t)}{dt} = -Q_\delta^T v_i(t) - \sum_{l=1}^{L} \left(\sum_{j=1}^{N} a_{l,ij} v_{j,c_l}(t) \right) Q_{\beta,l}^T v_i(t) \tag{F.1}$$

for every node i. We refer the reader to [136] for further details of the GEMF model.

F.1.2. CONTINUOUS-TIME GEMF WITH HETEROGENEOUS PARAMETERS

In real-world epidemics, heterogeneous spreading parameters are more likely than homogeneous spreading parameters. For instance, in an SIS epidemic process, an elderly individual is more susceptible to getting infected than younger individuals. Hence, if β_{1j} and β_{2j} denote the infection rates from an individual j to an elderly individual 1 and a younger individual 2, respectively, then it holds that $\beta_{1j} > \beta_{2j}$. Similarly, the curing rate δ_1 of an elderly individual 1 is lower than the curing rate δ_2 of a younger individual 2.

To consider heterogeneous spreading parameters, we replace the nodal transition rates δ_{pq} from compartment p to compartment q by the rates $\delta_{pq,i}$, which depend on the node i. Hence, the $C \times C$ nodal transition rate matrix A_δ is replaced by the $C \times C$ matrix $A_{\delta,i}$ whose elements are given by

$$\left(A_{\delta,i}\right)_{pq} = \delta_{pq,i}, \quad 1 \le p, q \le C,$$

for every node i. Analogously, we replace the edge-based transition rates $\beta_{l,pq}$ from compartment p to compartment q on layer l by the rates $\beta_{l,pq,ij}$, which depend on the nodes i, j. Hence, the $C \times C$ adjacency matrix A_{β_l} of the edge-based transition rates on layer l is replaced by the $C \times C$ adjacency matrix $A_{\beta_l,ij}$ whose elements are defined by

$$\left(A_{\beta_l,ij}\right)_{pq} = \beta_{l,pq,ij}, \quad 1 \le p, q \le C.$$

With heterogeneous spreading parameters, the GEMF model (F.1) becomes

$$\frac{dv_i(t)}{dt} = -Q_{\delta,i}^T v_i(t) - \sum_{l=1}^{L} \sum_{j=1}^{N} v_{j,c_l}(t) a_{l,ij} Q_{\beta,l,ij}^T v_i(t), \tag{F.2}$$

Here, the Laplacian matrix of the nodal transition rate graph and the edge-based transition rate graphs, respectively, with heterogeneous spreading parameters are denoted by

$$Q_{\delta,i} = \operatorname{diag}\left(A_{\delta,i} u\right) - A_{\delta,i}$$

and

$$Q_{\beta,l,ij} = \operatorname{diag}\left(A_{\beta,l,ij} u\right) - A_{\beta,l,ij}.$$

F.1.3. DISCRETE-TIME GEMF WITH HETEROGENEOUS PARAMETERS

Before formulating the GEMF model in discrete time, we rewrite the differential equation (F.2). We define the set of layers l whose influence compartment c_l equals m as

$$\mathcal{L}_m = \{l = 1, ..., L | c_l = m\}.$$

Then, we can rewrite (F.2) as

$$\frac{dv_i(t)}{dt} = -Q_{\delta,i}^T v_i(t) - \sum_{j=1}^{N} \sum_{m=1}^{C} \sum_{l \in \mathcal{L}_m} v_{j,m}(t) a_{l,ij} Q_{\beta,l,ij}^T v_i(t),$$

which is equivalent to

$$\frac{dv_i(t)}{dt} = -Q_{\delta,i}^T v_i(t) - \sum_{j=1}^{N} \sum_{m=1}^{C} v_{j,m}(t) \left(\sum_{l \in \mathcal{L}_m} a_{l,ij} Q_{\beta,l,ij}^T \right) v_i(t). \tag{F.3}$$

Euler's method approximates the derivative as

$$\left. \frac{dv_i(t)}{dt} \right|_{t=k\Delta t} \approx \frac{v_i((k+1)\Delta t) - v_i(k\Delta t))}{\Delta t} \tag{F.4}$$

for a small sampling time Δt and a discrete time slot $k \in \mathbb{N}$. We denote $v_i[k] = v_i(k\Delta t)$ and, using Euler's method (F.4) with equality, obtain from (F.3) that

$$v_i[k+1] = v_i[k] - \Delta t Q_{\delta,i}^T v_i[k] - \sum_{j=1}^{N} \sum_{m=1}^{C} v_{j,m}[k] \left(\Delta t \sum_{l \in \mathcal{L}_m} a_{l,ij} Q_{\beta,l,ij}^T \right) v_i[k].$$

Finally, we identify the Laplacian matrices of the discrete-time GEMF model (7.4) as

$$Q_i = \Delta t Q_{\delta,i}$$

and

$$Q_{m,ij} = \Delta t \sum_{l \in \mathcal{L}_m} a_{l,ij} Q_{\beta,l,ij}.$$

Thus, the nodal transition probability matrix S_i and the edge-based transition probability matrix $B_{m,ij}$ of the discrete-time GEMF model (7.4) are related to the matrices $A_{\delta,i}$, $A_{\beta,l,ij}$ of the continuous-time GEMF model (F.2) via

$$S_i = \Delta t A_{\delta,i}$$

and

$$B_{m,ij} = \Delta t \sum_{l \in \mathcal{L}_m} a_{l,ij} A_{\beta,l,ij}. \tag{F.5}$$

From (F.5) follows that the edge-based transition probability matrix $B_{m,ij}$ describes the influence of individuals of group j in compartment m on node i, *summed* over all layers l that are in the set $\mathcal{L}_m$.

F.2. PROOF OF LEMMA 7.4

The GEMF model (7.4) model with a time-varying nodal transition matrix $\tilde{S}_i[k] = S_i + S_{\text{con},i}[k]$ is given by

$$\nu_i[k+1] = \left(I_C - Q_i^T - Q_{\text{con},i}^T[k]\right)\nu_i[k] - \sum_{j=1}^{N}\sum_{m=1}^{C}\nu_{j,m}[k]Q_{m,ij}^T\nu_i[k]$$

for every group $i = 1,...,N$. Here, the $C \times C$ Laplacian matrix of the known control matrix $S_{\text{con},i}[k]$ equals

$$Q_{\text{con},i}^T[k] = \text{diag}\left(S_{\text{con},i}[k]\,u\right) - S_{\text{con},i}[k].$$

For any $C \times C$ matrix A and any $C \times 1$ vector x, it holds that

$$Ax = \left(I_C \otimes x^T\right)\text{vec}(A^T),$$

which follows from the definition of the matrix vectorisation and the Kronecker product. Hence, we can rewrite the GEMF equations (7.4) as

$$\begin{aligned}\nu_i[k+1] - \nu_i[k] + Q_{\text{con},i}^T[k]\nu_i[k] = &-\left(I_C \otimes \nu_i^T[k]\right)\text{vec}(Q_i) \\ &- \sum_{j=1}^{N}\sum_{m=1}^{C}\nu_{j,m}[k]\left(I_C \otimes \nu_i^T[k]\right)\text{vec}(Q_{m,ij}). \qquad \text{(F.6)}\end{aligned}$$

To complete the proof, we stack (F.6) for the observation times $k = 1,...,n$ and obtain that

$$\begin{pmatrix}\nu_i[2] - \nu_i[1] + Q_{\text{con},i}^T[1]\nu_i[1] \\ \vdots \\ \nu_i[n+1] - \nu_i[n] + Q_{\text{con},i}^T[n]\nu_i[n]\end{pmatrix} = -\begin{pmatrix}I_C \otimes \nu_i^T[1] \\ \vdots \\ I_C \otimes \nu_i^T[n]\end{pmatrix}\text{vec}(Q_i)$$
$$- \sum_{j=1}^{N}\sum_{m=1}^{C}\begin{pmatrix}\nu_{j,m}[1]\left(I_C \otimes \nu_i^T[1]\right) \\ \vdots \\ \nu_{j,m}[n]\left(I_C \otimes \nu_i^T[n]\right)\end{pmatrix}\text{vec}(Q_{m,ij}).$$

F.3. SIR EPIDEMIC MODEL

Stacking the SIR equations (7.5) for $\mathcal{I}_i[k+1]$ and $\mathcal{R}_i[k+1]$ for the observation times $k = 1,...,n$ yields with (7.6) Lemma F.1.

Lemma F.1. *For any node i, the curing probability constant $\delta_{\Delta t,i}$ and the infection probabilities $\beta_{\Delta t,i1},...,\beta_{\Delta t,iN}$ of the discrete-time SIR epidemic model (7.5) with time-varying curing rates $\tilde{\delta}_{\Delta t,i}[k] = \delta_{\Delta t,i} + \delta_{\text{con},i}[k]$ satisfy*

$$V_{\text{SIR},i} = F_{\text{SIR},i}\left(\delta_{\Delta t,i}, \beta_{\Delta t,i1},..., \beta_{\Delta t,iN}\right)^T.$$

Here, the $2n \times 1$ vector $V_{\text{SIR},i}$ equals

$$V_{\text{SIR},i} = \left(V_{\text{SIR},i}^T[1],..., V_{\text{SIR},i}^T[n]\right)^T,$$

with the 2×1 *vectors*

$$V_{\mathrm{SIR},i}[k] = \begin{pmatrix} \mathcal{I}_i[k+1] - (1-\delta_{\mathrm{con},i}[k])\mathcal{I}_i[k] \\ \mathcal{R}_i[k+1] - (1+\delta_{\mathrm{con},i}[k])\mathcal{R}_i[k] \end{pmatrix}.$$

Furthermore, the $2n \times (N+1)$ *matrix* $F_{\mathrm{SIR},i}$ *equals*

$$F_{\mathrm{SIR},i} = \begin{pmatrix} F^T_{\mathrm{SIR},i}[1] & \dots & F^T_{\mathrm{SIR},i}[n] \end{pmatrix}^T$$

with the $2 \times (N+1)$ *matrices*

$$F_{\mathrm{SIR},i}[k] = \begin{pmatrix} -\mathcal{I}_i[k] & \mathcal{S}_i[k]\mathcal{I}_1[k] & \dots & \mathcal{S}_i[k]\mathcal{I}_N[k] \\ \mathcal{I}_i[k] & 0 & \dots & 0 \end{pmatrix}.$$

F.4. SEIR EPIDEMIC MODEL

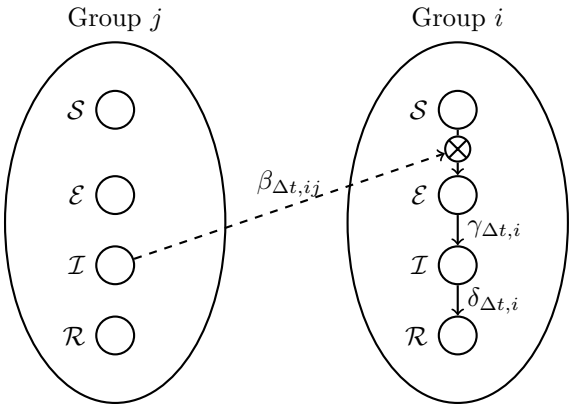

Figure F.1: **SEIR transition graph.** The transition graph for the discrete-time SEIR epidemic model in Definition F.2.

From Figure F.1, we obtain the nodal-based transition matrix S_i and the edge-based transition matrices $B_{3,ij}$ of the SEIR model as

$$S_i = \begin{pmatrix} 0 & 0 & 0 & 0 \\ 0 & 0 & \gamma_{\Delta t,i} & 0 \\ 0 & 0 & 0 & \delta_{\Delta t,i} \\ 0 & 0 & 0 & 0 \end{pmatrix},$$

and

$$B_{3,ij} = \begin{pmatrix} 0 & \beta_{\Delta t,ij} & 0 & 0 \\ 0 & 0 & 0 & 0 \\ 0 & 0 & 0 & 0 \\ 0 & 0 & 0 & 0 \end{pmatrix}.$$

For the compartments $m = 1,2,4$, the edge-based transition matrices equal $B_{1,ij} = B_{2,ij} = B_{4,ij} = 0$. Thus, the Laplacian matrices equal

$$Q_i = \begin{pmatrix} 0 & 0 & 0 & 0 \\ 0 & \gamma_{\Delta t,i} & -\gamma_{\Delta t,i} & 0 \\ 0 & 0 & \delta_{\Delta t,i} & -\delta_{\Delta t,i} \\ 0 & 0 & 0 & 0 \end{pmatrix}, \tag{F.7}$$

and

$$Q_{3,ij} = \begin{pmatrix} \beta_{\Delta t,ij} & -\beta_{\Delta t,ij} & 0 & 0 \\ 0 & 0 & 0 & 0 \\ 0 & 0 & 0 & 0 \\ 0 & 0 & 0 & 0 \end{pmatrix}. \tag{F.8}$$

For the compartments $m = 1,2,4$, the Laplacian matrices equal $Q_{1,ij} = Q_{2,ij} = Q_{4,ij} = 0$. With (F.7) and (F.8), the SEIR model specified by Figure F.1 follows with (7.4) as:

Definition F.2 (Discrete-time SEIR epidemic model)**.** For every group i, the viral state of the SEIR epidemic model equals $v_i[k] = (\mathcal{S}_i[k], \mathcal{E}_i[k], \mathcal{I}_i[k], \mathcal{R}_i[k])^T$. Here, $\mathcal{S}_i[k]$, $\mathcal{E}_i[k]$, $\mathcal{I}_i[k]$ and $\mathcal{R}_i[k]$ denote the fraction of susceptible, exposed, infectious, and recovered individuals in group i at time $k \in \mathbb{N}$, respectively. For every group i, the viral state evolves in discrete time k according to

$$\begin{aligned} \mathcal{S}_i[k+1] &= \mathcal{S}_i[k] - \mathcal{S}_i[k] \sum_{j=1}^{N} \beta_{\Delta t,ij} \mathcal{I}_j[k] \\ \mathcal{E}_i[k+1] &= (1-\gamma_{\Delta t,i})\mathcal{E}_i[k] + \mathcal{S}_i[k] \sum_{j=1}^{N} \beta_{\Delta t,ij} \mathcal{I}_i[k] \\ \mathcal{I}_i[k+1] &= (1-\delta_{\Delta t,i})\mathcal{I}_i[k] + \gamma_{\Delta t,i} \mathcal{E}_i[k] \end{aligned} \tag{F.9}$$

and the fraction of recovered individuals follows as

$$\mathcal{R}_i[k] = 1 - \mathcal{S}_i[k] - \mathcal{E}_i[k] - \mathcal{I}_i[k]$$

at any time $k \in \mathbb{N}$. Here, $\beta_{\Delta t,ij}$ denotes the *infection probability* from group j to group i, $\gamma_{\Delta t,i}$ denotes the *incubation probability* of group i, and $\delta_{\Delta t,i}$ denotes the *curing probability* of group i.

Stacking the SEIR equations (F.9) for $\mathcal{S}_i[k+1]$, $\mathcal{E}_i[k+1]$ and $\mathcal{I}_i[k+1]$ for the observation times $k = 1, ..., n$ yields Lemma F.3.

Lemma F.3. *For any node i, the incubation probability $\gamma_{\Delta t,i}$, the curing probability constant $\delta_{\Delta t,i}$ and the infection probabilities $\beta_{\Delta t,i1}, ..., \beta_{\Delta t,iN}$ of the discrete-time SIR epidemic model (F.9) with time-varying curing rates $\tilde{\delta}_{\Delta t,i}[k] = \delta_{\Delta t,i} + \delta_{\text{con},i}[k]$ satisfy*

$$V_{\text{SEIR},i} = F_{\text{SEIR},i} \left(\gamma_{\Delta t,i}, \delta_{\Delta t,i}, \beta_{\Delta t,i1}, ..., \beta_{\Delta t,iN}\right)^T.$$

Here, the $3n \times 1$ *vector* $V_{\text{SEIR},i}$ *equals*

$$V_{\text{SEIR},i} = \begin{pmatrix} V_{\text{SEIR},i}^T[1] & \dots & V_{\text{SEIR},i}^T[n] \end{pmatrix}^T,$$

with the 3×1 *vectors*

$$V_{\text{SEIR},i}[k] = \begin{pmatrix} \mathcal{S}_i[k+1] - \mathcal{S}_i[k] \\ \mathcal{E}_i[k+1] - \mathcal{E}_i[k] \\ \mathcal{I}_i[k+1] - (1 - \delta_{\text{con},i}[k])\mathcal{I}_i[k] \end{pmatrix}.$$

Furthermore, the $3n \times (N+2)$ *matrix* $F_{\text{SEIR},i}$ *equals*

$$F_{\text{SEIR},i} = \begin{pmatrix} F_{\text{SEIR},i}^T[1] & \dots & F_{\text{SEIR},i}^T[n] \end{pmatrix}^T$$

with the $3 \times (N+2)$ *matrices*

$$F_{\text{SEIR},i}[k] = \begin{pmatrix} 0 & 0 & -\mathcal{S}_i[k]\mathcal{I}_1[k] & \dots & -\mathcal{S}_i[k]\mathcal{I}_N[k] \\ -\mathcal{E}_i[k] & 0 & \mathcal{S}_i[k]\mathcal{I}_1[k] & \dots & \mathcal{S}_i[k]\mathcal{I}_N[k] \\ \mathcal{E}_i[k] & -\mathcal{I}_i[k] & 0 & \dots & 0 \end{pmatrix}.$$

F

F.5. SISIR EPIDEMIC MODEL

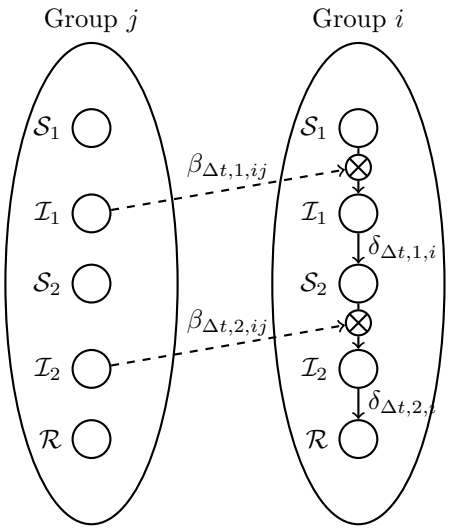

Figure F.2: **SISIR transition graph.** The transition graph for the discrete-time SISIR epidemic model in Definition F.4.

From Figure F.2, we obtain the nodal-based transition matrix S_i and the edge-based

transition matrices $B_{2,ij}$ and $B_{4,ij}$ of the SISIR model as

$$S_i = \begin{pmatrix} 0 & 0 & 0 & 0 & 0 \\ 0 & 0 & \delta_{\Delta t,1,i} & 0 & 0 \\ 0 & 0 & 0 & 0 & 0 \\ 0 & 0 & 0 & 0 & \delta_{\Delta t,2,i} \\ 0 & 0 & 0 & 0 & 0 \end{pmatrix}$$

and

$$B_{2,ij} = \begin{pmatrix} 0 & \beta_{\Delta t,1,ij} & 0 & 0 & 0 \\ 0 & 0 & 0 & 0 & 0 \\ 0 & 0 & 0 & 0 & 0 \\ 0 & 0 & 0 & 0 & 0 \\ 0 & 0 & 0 & 0 & 0 \end{pmatrix}$$

and

$$B_{4,ij} = \begin{pmatrix} 0 & 0 & 0 & 0 & 0 \\ 0 & 0 & 0 & 0 & 0 \\ 0 & 0 & 0 & \beta_{\Delta t,2,ij} & 0 \\ 0 & 0 & 0 & 0 & 0 \\ 0 & 0 & 0 & 0 & 0 \end{pmatrix}.$$

F

For the compartments $m = 1,3,5$, the edge-based transition matrices and their Laplacians equal $B_{1,ij} = B_{3,ij} = B_{5,ij} = 0$ and $Q_{1,ij} = Q_{3,ij} = Q_{5,ij} = 0$. The other Laplacian matrices equal

$$Q_i = \begin{pmatrix} 0 & 0 & 0 & 0 & 0 \\ 0 & \delta_{\Delta t,1,i} & -\delta_{\Delta t,1,i} & 0 & 0 \\ 0 & 0 & 0 & 0 & 0 \\ 0 & 0 & 0 & \delta_{\Delta t,2,i} & -\delta_{\Delta t,2,i} \\ 0 & 0 & 0 & 0 & 0 \end{pmatrix}$$

and

$$Q_{2,ij} = \begin{pmatrix} \beta_{\Delta t,1,ij} & -\beta_{\Delta t,1,ij} & 0 & 0 & 0 \\ 0 & 0 & 0 & 0 & 0 \\ 0 & 0 & 0 & 0 & 0 \\ 0 & 0 & 0 & 0 & 0 \\ 0 & 0 & 0 & 0 & 0 \end{pmatrix}$$

and

$$Q_{4,ij} = \begin{pmatrix} 0 & 0 & 0 & 0 & 0 \\ 0 & 0 & 0 & 0 & 0 \\ 0 & 0 & \beta_{\Delta t,2,ij} & -\beta_{\Delta t,2,ij} & 0 \\ 0 & 0 & 0 & 0 & 0 \\ 0 & 0 & 0 & 0 & 0 \end{pmatrix}.$$

Thus, the SISIR specified by Figure F.2 follows with (7.4) as:

Definition F.4 (Discrete-time SISIR epidemic model)**.** For every group i, the viral state of the SISIR epidemic model equals $v_i[k] = (\mathcal{S}_{1,i}[k], \mathcal{I}_{1,i}[k], \mathcal{S}_{2,i}[k], \mathcal{I}_{2,i}[k], \mathcal{R}_i[k])^T$. Here, $\mathcal{S}_{l,i}[k]$ and $\mathcal{I}_{l,i}[k]$ denote the fraction of individuals in group i at time $k \in \mathbb{N}$ that are susceptible to and infected by disease $l = 1,2$, respectively. At time $k \in \mathbb{N}$, $\mathcal{R}_i[k]$ denotes the fraction of recovered individuals in group i. For every group i, the viral state evolves in discrete time k according to

$$\begin{aligned}
\mathcal{S}_{1,i}[k+1] &= \mathcal{S}_{1,i}[k] - \mathcal{S}_{1,i}[k] \sum_{j=1}^{N} \beta_{\Delta t,1,ij} \mathcal{I}_{1,j}[k] \\
\mathcal{I}_{1,i}[k+1] &= (1 - \delta_{\Delta t,1,i}) \mathcal{I}_{1,i}[k] + \mathcal{S}_{1,i}[k] \sum_{j=1}^{N} \beta_{\Delta t,1,ij} \mathcal{I}_{1,j}[k] \\
\mathcal{S}_{2,i}[k+1] &= \mathcal{S}_{2,i}[k] + \delta_{\Delta t,1,i} \mathcal{I}_{1,i}[k] - \mathcal{S}_{2,i}[k] \sum_{j=1}^{N} \beta_{\Delta t,2,ij} \mathcal{I}_{2,j}[k] \\
\mathcal{I}_{2,i}[k+1] &= (1 - \delta_{\Delta t,2,i}) \mathcal{I}_{2,i}[k] + \mathcal{S}_{2,i}[k] \sum_{j=1}^{N} \beta_{\Delta t,2,ij} \mathcal{I}_{2,j}[k]
\end{aligned} \tag{F.10}$$

and the fraction of recovered individuals follows as

$$\mathcal{R}_i[k] = 1 - \mathcal{S}_{1,i}[k] - \mathcal{I}_{1,i}[k] - \mathcal{S}_{2,i}[k] - \mathcal{I}_{2,i}[k]$$

at any time $k \in \mathbb{N}$. Here, for the disease $l = 1,2$, $\beta_{\Delta t,l,ij}$ denotes the *infection probability* from group j to group i, and $\delta_{\Delta t,l,i}$ denotes the *curing probability* of group i.

Stacking the SISIR equations (F.10) for $\mathcal{S}_{l,i}[k+1]$ and $\mathcal{I}_{l,i}[k+1]$, where $l = 1,2$, for the observation times $k = 1,...,n$ yields Lemma F.5.

Lemma F.5. *For any node i, the curing probability constants $\delta_{\Delta t,l,i}$ and the infection probabilities $\beta_{\Delta t,l,1i}, ..., \beta_{l,iN}$, for both diseases $l = 1,2$, of the discrete-time SISIR epidemic model (F.10) with time-varying curing rates $\tilde{\delta}_{\Delta t,l,i}[k] = \delta_{\Delta t,l,i} + \delta_{\text{con},l,i}[k]$ satisfy*

$$V_{\text{SISIR},i} = F_{\text{SISIR},i} \left(\delta_{\Delta t,1,i}, \delta_{\Delta t,2,i}, \beta_{\Delta t,1,i1}, ..., \beta_{\Delta t,1,iN}, \beta_{\Delta t,2,i1}, ..., \beta_{\Delta t,2,iN} \right)^T.$$

Here, the $4n \times 1$ vector $V_{\text{SISIR},i}$ equals

$$V_{\text{SISIR},i} = \begin{pmatrix} V_{\text{SISIR},i}^T[1] & ... & V_{\text{SISIR},i}^T[n] \end{pmatrix}^T,$$

with the 4×1 vectors

$$V_{\text{SISIR},i}[k] = \begin{pmatrix} \mathcal{S}_{1,i}[k+1] - \mathcal{S}_{1,i}[k] \\ \mathcal{I}_{1,i}[k+1] - (1 - \delta_{\text{con},1,i}[k]) \mathcal{I}_{1,i}[k] \\ \mathcal{S}_{2,i}[k+1] - \mathcal{S}_{2,i}[k] - \delta_{\text{con},1,i} \mathcal{I}_{1,i}[k] \\ \mathcal{I}_{2,i}[k+1] - (1 - \delta_{\text{con},2,i}[k]) \mathcal{I}_{2,i}[k] \end{pmatrix}$$

for any time $k = 1,...,n$. Furthermore, the $4n \times (2N+2)$ matrix $F_{\text{SISIR},i}$ equals

$$F_{\text{SISIR},i} = \begin{pmatrix} F_{\text{SISIR},i}^T[1] & ... & F_{\text{SISIR},i}^T[n] \end{pmatrix}^T$$

where the $4 \times (2N+2)$ *matrices* $F_{\mathrm{SISIR},i}[k]$ *are given by*

$$F_{\mathrm{SISIR},i}[k] = \begin{pmatrix} 0 & 0 & -F^{(1)}_{\mathrm{SISIR},i}[k] & 0 \\ -\mathcal{I}_{1,i}[k] & 0 & F^{(1)}_{\mathrm{SISIR},i}[k] & 0 \\ \mathcal{I}_{1,i}[k] & 0 & 0 & -F^{(2)}_{\mathrm{SISIR},i}[k] \\ 0 & -\mathcal{I}_{2,i}[k] & 0 & F^{(2)}_{\mathrm{SISIR},i}[k] \end{pmatrix}$$

for any time $k = 1, \ldots, n$, *and the* $1 \times N$ *vectors* $F^{(l)}_{\mathrm{SISIR},i}[k]$ *equal*

$$F^{(l)}_{\mathrm{SISIR},i}[k] = \begin{pmatrix} \mathcal{S}_{l,i}[k]\mathcal{I}_{l,1}[k] & \ldots & \mathcal{S}_{l,i}[k]\mathcal{I}_{l,N}[k] \end{pmatrix}.$$

F.6. PROOF OF LEMMA 7.6

From the definition of the matrix $F_{\mathrm{SIS},i}$ in (7.10), it follows that

$$\operatorname{rank}\left(F_{\mathrm{SIS},i}\right) \leq 1 + \operatorname{rank}\left(\tilde{F}_{\mathrm{SIS},i}\right), \tag{F.11}$$

where the $n \times N$ matrix $\tilde{F}_{\mathrm{SIS},i}$ equals

$$\tilde{F}_{\mathrm{SIS},i} = \begin{pmatrix} \mathcal{S}_i[1]\mathcal{I}_1[1] & \ldots & \mathcal{S}_i[1]\mathcal{I}_N[1] \\ \vdots & \ddots & \vdots \\ \mathcal{S}_i[n]\mathcal{I}_1[n] & \ldots & \mathcal{S}_i[n]\mathcal{I}_N[n] \end{pmatrix}.$$

The bound (F.11) holds with equality if the first column of the matrix $F_{\mathrm{SIS},i}$ does not equal to a linear combination of the columns of the matrix $\tilde{F}_{\mathrm{SIS},i}$. The k-th row of the matrix $\tilde{F}_{\mathrm{SIS},i}$ is given by

$$\begin{aligned} r_k &= \mathcal{S}_i[k]\mathcal{I}^T[k] \\ &= \sum_{l=1}^{m} \left(\mathcal{S}_i[k]c_l[k]\right) y_l^T, \end{aligned} \tag{F.12}$$

where the second equality follows from the POD (2.1). From (F.12), we obtain that every row r_k of the matrix $\tilde{F}_{\mathrm{SIS},i}$ equals to the linear combination of m vectors $y_1, \ldots, y_m$. Thus, the row rank of $\tilde{F}_{\mathrm{SIS},i}$ equals m, which completes the proof with (F.11).

F.7. PROOF OF THEOREM 7.9

Analogous steps to the derivations in Chapter 5 yield that (7.15) is equivalent to

$$\hat{\theta}_i = \underset{\theta_i \geq 0}{\operatorname{argmax}} \log\left(\Pr\left[\theta_i\right]\right) + \sum_{k=1}^{n} \log\left(\Pr\left[v_i[k+1] \middle| v[k], \theta_i\right]\right) \tag{F.13}$$

The probability $\Pr\left[v_i[k+1] \middle| v[k], \theta_i\right]$ is determined by the distribution of the error $w_i[k]$. Similar steps as in Appendix F.2 yield for GEMF *with* model errors (7.13) that

$$\begin{pmatrix} w_i[1] \\ \vdots \\ w_i[n] \end{pmatrix} = V_i - F_i\theta_i.$$

Hence, under Assumption 7.8 on the prior $\Pr[\theta_i]$, the optimisation problem (F.13) becomes

$$\begin{aligned}\hat{\theta}_i = \underset{\theta_i}{\operatorname{argmax}} \quad & \log(\alpha) - \sum_{j\notin\Omega_i} (\theta_i)_j \\ & + \sum_{k=1}^{n} \log\left(\Pr\left[w_i[k] = (V_i)_k - \sum_{j=1}^{N} (F_i)_{kj}(\theta_i)_j\right]\right) \\ \text{s.t.} \quad & \theta_i \geq 0, \\ & (\theta_i)_j = 0, \quad \forall j \in \Omega_i.\end{aligned}$$

The term $\log(\alpha)$ is constant with respect to the parameter vector θ_i and can be omitted, which yields that

$$\begin{aligned}\max_{\theta_i} \quad & \sum_{k=1}^{n} \log\left(\Pr\left[w_i[k] = (V_i)_k - \sum_{j=1}^{N} (F_i)_{kj}(\theta_i)_j\right]\right) - \sum_{j\notin\Omega_i} (\theta_i)_j \\ \text{s.t.} \quad & \theta_i \geq 0, \\ & (\theta_i)_j = 0, \quad \forall j \in \Omega_i.\end{aligned}$$

Under Assumption 7.7, the errors $w_i[k]$ follow a Gaussian distribution, which results in the minimisation problem

$$\begin{aligned}\min_{\theta_i} \quad & \sum_{k=1}^{n} \log\left(\sqrt{2\pi}\sigma_w\right) + \frac{1}{2\sigma_w^2}\left((V_i)_k - \sum_{j=1}^{N} (F_i)_{kj}(\theta_i)_j\right)^2 + \sum_{j\notin\Omega_i} (\theta_i)_j \\ \text{s.t.} \quad & \theta_i \geq 0, \\ & (\theta_i)_j = 0, \quad \forall j \in \Omega_i.\end{aligned}$$

Omitting the constant term $\log(\sqrt{2\pi}\sigma_w)$ and multiplying with $2\sigma_w^2$ gives

$$\begin{aligned}\min_{\theta_i} \quad & \sum_{k=1}^{n} \left((V_i)_k - \sum_{j=1}^{N} (F_i)_{kj}(\theta_i)_j\right)^2 + 2\sigma_w^2 \sum_{j\notin\Omega_i} (\theta_i)_j \\ \text{s.t.} \quad & \theta_i \geq 0, \\ & (\theta_i)_j = 0 \quad \forall j \in \Omega_i.\end{aligned}$$

By identifying $\rho_i = 2\sigma_w^2$, we obtain the LASSO (7.14), which completes the proof.

F.8. SIMULATION PARAMETERS

We describe the precise setting of the simulation parameters for Subsection 7.4.2. In [76], an upper bound $\Delta t_{\max}$ on the sampling time Δt of Euler's method was derived that ensures the stability of the steady-state $\mathcal{I}_\infty$ of the discrete-time SIS[1] epidemic model (4.1). We set the sampling time to $\Delta t = \Delta t_{\max}/100$. (Then, for the Barabási-Albert graph of Figure 3, the resulting sampling time Δt ranges from $5.4 \cdot 10^{-4}$ to $1.2 \cdot 10^{-3}$.) If there

[1] The stability of the equilibria of the general discrete-time GEMF model (7.4) is an open question.

is a link between node i and j, then we set the infection probabilities $\beta_{\Delta t,ij}$ and $\beta_{\Delta t,ji}$ (respectively, $\beta_{\Delta t,l,ij}$ and $\beta_{\Delta t,l,ji}$ for the SISIR model) to a uniform random number in $[0.5\Delta t, 0.6\Delta t]$. Hence, $\beta_{\Delta t,ij} \neq \beta_{\Delta t,ji}$ in general, and $\beta_{\Delta t,ii} > 0$ due to infections between individuals in the same group i. If there is no link between node i and j, then we set the infection rates to $\beta_{\Delta t,ij} = 0$ and $\beta_{\Delta t,ji} = 0$. We set the "initial curing probabilities" $\delta_i^{(0)}$ to a uniformly distributed random number in $[0.5\Delta t, 0.6\Delta t]$. Then, we set the curing probabilities $\delta_{\Delta t,i}$ to a multiple of the initial curing rates $\delta_i^{(0)}$, i.e., $\delta_{\Delta t,i} = \sigma\delta_i^{(0)}$ for every node i and some scalar σ such that the basic reproduction number equals $R_0 = 1.5$. For every group i of the SIS, SIR and SEIR epidemic models, the initial fraction of infected individuals $\mathcal{I}_i[1]$ is set to a uniformly distributed random number in $[0,1]$, and the initial fraction of susceptible individuals $\mathcal{S}_i[1]$ is set to $\mathcal{S}_i[1] = 1 - \mathcal{I}_i[1]$. For the SEIR epidemic model, the incubation probability $\gamma_{\Delta t,i}$ is set to a uniform random number in $[0.5\Delta t, 0.6\Delta t]$ For every group i and both diseases $l = 1,2$ in the SISIR epidemic model, the initial fractions of infected individuals $\mathcal{I}_{l,i}[1]$ is set to a uniformly distributed random number in $[0, 0.5]$, and the initial fraction of susceptible individuals is set to $\mathcal{S}_{l,i}[1] = (1 - \mathcal{I}_{1,i}[1] - \mathcal{I}_{2,i}[1])/2$ for $l = 1,2$. Hence, the initial fraction of recovered individuals in the SIR, SEIR and SISIR model and the initial fraction of exposed individuals in the SEIR model are $\mathcal{R}_i[1] = 0$ and $\mathcal{E}_i[1] = 0$, respectively. The observation length is set to $n = 1000$.

F

F.9. DETAILS OF THE NETWORK RECONSTRUCTION ALGORITHM

In Subsection F.9.1, we provide the details of the network reconstruction algorithm in the presence of model errors $w_i[k]$. Subsection F.9.2 gives the network reconstruction algorithm in case of no model errors $w_i[k]$.

F.9.1. NETWORK RECONSTRUCTION IN THE PRESENCE OF MODEL ERRORS

To determine the regularisation parameter $\rho_i > 0$ in the LASSO (7.14), we consider 20 candidate values, specified by the set $\Theta_i = \{\rho_{\min,i}, ..., \rho_{\max,i}\}$. If $\rho_i > 2\|F_i^T V_i\|_\infty$, then [292] the solution to the LASSO (7.14) equals $\theta_i = 0$. We set the maximum value to $\rho_{\max,i} = 2\|F_i^T V_i\|_\infty \cdot 10^{-4}$ and the minimum value to $\rho_{\min,i} = 10^{-4}\rho_{\max,i}$. For every value of the regularisation parameter $\rho_i \in \Theta_i$, we compute the mean squared error $\mathrm{MSE}\left(\hat{\theta}_i(\rho_i)\right)$ by 5-fold cross-validation [141]. For every fold, the rows of the matrix F_i and the vector V_i are divided into a training set $F_{\text{train},i}$, $V_{\text{train},i}$ and a validation set $F_{\text{val},i}$, $V_{\text{val},i}$. We compute the solution θ_i to the LASSO (7.14) on the training set $F_{\text{train},i}$, $V_{\text{train},i}$ of every fold. Then, the mean squared error $\mathrm{MSE}\left(\hat{\theta}_i(\rho_i)\right)$ is computed with the validation set as

$$\mathrm{MSE}\left(\hat{\theta}_i(\rho_i)\right) = \left\| V_{\text{val},i} - F_{\text{val},i}\theta_i \right\|_2^2,$$

averaged over all folds. Finally, we set the regularisation parameter ρ_i to the minimiser of the mean square error $\mathrm{MSE}\left(\hat{\theta}_i(\rho_i)\right)$. The final estimate θ_i is obtained by solving the LASSO (7.14) on the whole matrix F_i and vector V_i. To solve the LASSO (7.14) numerically, we make use of the Matlab command `quadprog`. Our network reconstruction method is given in pseudo-code by Algorithm F.1.

Algorithm F.1 GEMF network reconstruction

Input: viral states $v_i[1]$, ..., $v_i[n+1]$ and $S_{\mathrm{con},i}[1]$, ..., $S_{\mathrm{con},i}[n]$ for all nodes i
Output: estimate for the GEMF parameter vector $\hat{\theta}_i$ for all nodes i
for $i = 1, ..., N$ **do**
  $\rho_{\max,i} \leftarrow 2\|F_i^T V_i\|_\infty \cdot 10^{-4}$
  $\rho_{\min,i} \leftarrow 10^{-4}\rho_{\max,i}$
  $\Theta_i \leftarrow$ 20 logarithmically equidistant values from $\rho_{\min,i}$ to $\rho_{\max,i}$
  for $\rho_i \in \Theta_i$ **do**
    estimate MSE$\left(\hat{\theta}_i(\rho_i)\right)$ by 5-fold cross validation on F_i, V_i and solving (7.14) on the respective training set
  end for
  $\rho_{\mathrm{opt},i} \leftarrow$ minimiser of the estimates of MSE$\left(\hat{\theta}_i(\rho_i)\right)$
  $\hat{\theta}_i \leftarrow$ the solution $\hat{\theta}_i(\rho_{\mathrm{opt},i})$ to (7.14) on the whole data set F_i, V_i
end for

F.9.2. NETWORK RECONSTRUCTION IN THE ABSENCE OF MODEL ERRORS

If there are no model errors, i.e., $w_i[k] = 0$ at every time k for every group i, then the linear system (7.8) is satisfied with equality. Depending on the (numerical) rank of the matrix F_i, we employ two methods to estimate the parameter vector θ_i. First, if the rank of the matrix F_i equals the number of unknown components of the parameter vector θ_i, then we solve the linear system $F_i\theta_i = V_i$ with the QR-solver provided by the Matlab command `mldivide`. Second, if the rank of the matrix F_i is lower than the number of unknown components of the parameter vector θ_i, then we estimate the parameter vector θ_i by *basis pursuit* [144]:

$$\begin{aligned} \hat{\theta}_i = \arg\min_{\theta_i} \quad & \|\theta_i\|_1 \\ \text{s.t.} \quad & F_i\theta_i = V_i \\ & \theta_i \geq 0 \\ & (\theta_i)_j = 0 \quad \forall\, j \in \Omega_i \end{aligned} \tag{F.14}$$

To solve the linear programme (F.14) numerically, we apply the dual simplex algorithm provided by the Matlab command `linprog`.

G

APPENDIX TO CHAPTER 8

G.1. PROOF OF LEMMA 8.2

We prove Lemma 8.2 by induction with respect to time k. The base case at the initial time $k = 1$, i.e., $\mathcal{I}_i[1] \geq 0$, $\mathcal{R}_i[1] \geq 0$ and $\mathcal{S}_i[1] \geq 0$, is satisfied by assumption. For the inductive step from time $k \geq 1$ to $k+1$, suppose that $\mathcal{I}_i[k] \geq 0$, $\mathcal{R}_i[k] \geq 0$ and $\mathcal{S}_i[k] \geq 0$ for all nodes i. Since $\mathcal{S}_i[k] = 1 - \mathcal{I}_i[k] - \mathcal{R}_i[k]$, we obtain that

$$\mathcal{I}_i[k] + \mathcal{R}_i[k] \leq 1. \tag{G.1}$$

Under Assumption 8.1 it holds that $0 \leq \delta_{\Delta t,i} \leq 1$ and $\beta_{\Delta t,ij} \geq 0$. Thus, (G.1) and the SIR equations (7.5) yield that both $\mathcal{I}_i[k+1]$ and $\mathcal{R}_i[k+1]$ equal to a sum of non-negative addends, which implies that $\mathcal{I}_i[k+1] \geq 0$ and $\mathcal{R}_i[k+1] \geq 0$ for all nodes i. Thus, it remains to show that $\mathcal{S}_i[k+1] \geq 0$ for all nodes i. From (7.5), we obtain that

$$\mathcal{I}_i[k+1] + \mathcal{R}_i[k+1] = \mathcal{I}_i[k] + \mathcal{R}_i[k] + (1 - \mathcal{I}_i[k] - \mathcal{R}_i[k]) \sum_{j=1}^{N} \beta_{\Delta t,ij} \mathcal{I}_j[k]. \tag{G.2}$$

From $\mathcal{I}_i[k] \geq 0$, $\mathcal{R}_i[k] \geq 0$ and (G.1), it follows that

$$\mathcal{I}_i[k] + \mathcal{R}_i[k] \in [0, 1], \tag{G.3}$$

which implies that $\mathcal{I}_i[k] \leq 1$ for all nodes i. Thus, it holds that

$$\sum_{j=1}^{N} \beta_{\Delta t,ij} \mathcal{I}_j[k] \leq \sum_{j=1}^{N} \beta_{\Delta t,ij} \leq 1$$

under Assumption 8.1. With (G.3), it follows that the right side of (G.2) is a convex combination of 1 and $\sum_{j=1}^{N} \beta_{\Delta t,ij} \mathcal{I}_j[k] \in [0, 1]$. Thus, it holds that $\mathcal{I}_i[k+1] + \mathcal{R}_i[k+1] \leq 1$ for all nodes i, which implies that $\mathcal{S}_i[k+1] \geq 0$.

Identifier i	City	Population $N_{\text{pop},i}$
1	Wuhan	10,607,700
2	Huanggang	6,291,000
3	Jingzhou	5,705,900
4	Xiangyang	5,614,000
5	Xiaogan	4,878,000
6	Xiantao	1,155,000
7	Yichang	4,115,000
8	Shiyan	3,383,000
9	Enshi (autonomous prefecture)	3,327,000
10	Jingmen	2,896,300
11	Xianning	2,507,000
12	Huangshi	2,458,000
13	Suizhou	2,190,800
14	Ezhou	1,059,500
15	Tianmen	1,292,000
16	Qianjiang	958,000

Table G.1: **Cities (prefecture-level divisions) in the province Hubei.** Here, we do not consider the city Shennongjia, since the number of SARS-CoV-2 infections in Shennongjia is very small.

G.2. DATA OF THE COVID-19 OUTBREAK IN HUBEI

Table G.1 shows the cities of the province Hubei and the respective population size $N_{\text{pop},i}$ for every city i, which is obtained from the Hubei Statistical Yearbook [293]. The time series of the reported number of infections $N_{\text{rep},i}[k]$ is stated in Table G.2.

G.3. DETAILS OF NIPA

Algorithm G.1 describes the NIPA prediction method in pseudo-code. In line 4, the Matlab command `smoothdata` is called to remove erratic fluctuations of the raw data $\mathcal{I}_{\text{rep},i}[k]$. We denote the $N \times 1$ infection state vector by $\mathcal{I}[k] = (\mathcal{I}_1[k], ..., \mathcal{I}_N[k])^T$ at any time k. The loop starting in line 7 iterates over all candidate values of the curing probability $\delta_{\Delta t,i}$ in the set Ω. Algorithm G.1 calls the `Network inference` method, which is stated in pseudo-code by Algorithm G.2. For a fixed curing probability $\delta_{\Delta t,i}$, the network inference in line 11 returns an estimate for the infection probabilities $\beta_{\Delta t,ij}(\delta_{\Delta t,i})$ for all $j = 1, ..., N$. Furthermore, the network inference returns the mean squared error $\text{MSE}(\delta_{\Delta t,i})$, which corresponds to the first term in the objective of (8.1). The smaller the mean squared error $\text{MSE}(\delta_{\Delta t,i})$, the better the fit of the SIR model (7.5) to the data $\mathcal{I}_i[1], ..., \mathcal{I}_i[n]$. In line 13, the final estimate $\hat{\delta}_{\Delta t,i}$ for the curing probability is obtained as the minimiser of the mean squared error $\text{MSE}(\delta_{\Delta t,i})$. The estimate $\hat{\delta}_{\Delta t,i}$ determines the final estimates $\hat{\beta}_{\Delta t,i1}$, ..., $\hat{\beta}_{\Delta t,iN}$ for the infection probabilities in line 14. From line 16 to line 26, the SIR model (7.5) is iterated, which results in the predicted fraction of infections $\hat{\mathcal{I}}_i[n+1], ..., \hat{\mathcal{I}}_i[n+n_{\text{pred}}]$ for all nodes i.

City	21-1	22-1	23-1	24-1	25-1	26-1	27-1	28-1	29-1	30-1	31-1	1-2	2-2	3-2	4-2	5-2	6-2	7-2	8-2	9-2	10-2	11-2
Wuhan	105	62	70	65	46	80	892	315	356	378	576	894	1033	1242	1967	1766	1501	1985	1378	1921	1552	1104
Huanggang	0	0	0	64	58	32	59	111	172	77	153	276	244	176	223	162	90	144	96	115	80	66
Jingzhou	0	6	2	2	23	14	24	30	50	70	66	46	166	114	100	88	84	56	56	48	30	35
Xiangyang	0	0	0	0	2	34	34	61	32	123	61	94	107	84	103	52	51	69	55	57	44	25
Xiaogan	0	0	22	4	29	45	73	101	125	142	87	121	169	202	342	424	255	172	123	105	101	109
Xiaotao	0	0	2	8	1	1	15	5	23	35	7	43	29	19	37	40	42	52	20	37	22	22
Yichang	0	0	1	0	19	11	20	12	54	50	109	77	39	60	44	67	47	23	71	45	23	12
Shiyan	0	0	1	4	15	20	25	23	31	31	27	35	44	35	27	35	42	43	29	14	24	31
Enshi	0	0	0	11	6	8	13	13	15	9	12	18	6	12	15	6	13	3	6	21	8	8
Jingmen	0	1	0	20	17	52	24	28	49	36	24	78	16	55	22	86	45	35	41	12	15	40
Xianning	0	0	0	0	43	21	27	21	18	36	40	40	50	52	36	15	44	33	17	14	8	10
Huangshi	0	0	0	0	31	5	17	33	27	55	41	43	82	71	104	57	69	68	50	52	30	39
Suizhou	0	0	0	5	31	16	18	46	27	85	76	80	74	183	65	128	81	38	31	65	46	34
Ezhou	0	0	0	1	0	19	37	27	39	66	38	51	28	26	50	41	48	98	67	89	65	71
Tianmen	0	0	0	3	2	8	10	11	10	23	15	17	16	2	11	10	25	16	18	20	44	32
Shennongjia	0	0	0	0	0	0	1	2	2	2	0	0	0	3	0	0	0	0	0	0	0	0
Qianjiang	0	0	0	0	0	5	2	1	2	2	15	8	0	9	10	10	10	6	2	3	5	0

Table G.2: **Reported SARS-CoV-2 infections in Hubei.** The time series of the reported number of infections $N_{\text{rep},i}[k]$ for every city i in Hubei.

Algorithm G.1 `Network-Inference-based Prediction Algorithm (NIPA)`

Input: reported fraction of infections $\mathcal{I}_{\text{rep},i}[1],...,\mathcal{I}_{\text{rep},i}[n]$ for all nodes i; prediction time n_{pred}

Output: predicted fraction of infections $\hat{\mathcal{I}}_i[n+1],...,\hat{\mathcal{I}}_i[n+n_{\text{pred}}]$ for all nodes i

Step 1 – Data preprocessing

$\mathcal{I}_i[1],...,\mathcal{I}_i[n] \leftarrow$ `smoothdata`$(\mathcal{I}_{\text{rep},i}[1],...,\mathcal{I}_{\text{rep},i}[n])$ for all nodes i

$\mathcal{I}[k] \leftarrow (\mathcal{I}_1[k],...,\mathcal{I}_N[k])^T$ for all $k = 1,...,n$

Step 2 – Network inference

for $i = 1,...,N$ **do**

  $\mathcal{R}_i[1] \leftarrow 0$

  for $\delta_{\Delta t,i} \in \Omega$ **do**

    $\mathcal{R}_i[k] \leftarrow \mathcal{R}_i[k-1] + \delta_{\Delta t,i}\mathcal{I}_i[k-1]$ for all $k = 2,...,n$

    $\mathcal{S}_i[k] \leftarrow 1 - \mathcal{I}_i[k] - \mathcal{R}_i[k]$ for all $k = 1,...,n$

    $\nu_i[k] \leftarrow (\mathcal{S}_i[k], \mathcal{I}_i[k], \mathcal{R}_i[k])^T$ for all $k = 1,...,n$

    $\left(\beta_{\Delta t,i1}(\delta_{\Delta t,i}),...,\beta_{\Delta t,iN}(\delta_{\Delta t,i}), \text{MSE}(\delta_{\Delta t,i})\right) \leftarrow$ `Network inference`$\left(\delta_{\Delta t,i}, \nu_i[1],...,\nu_i[n], \mathcal{I}[1],...,\mathcal{I}[n]\right)$

  end for

  $\hat{\delta}_{\Delta t,i} \leftarrow \underset{\delta_{\Delta t,i} \in \Omega}{\text{argmin}}\ \text{MSE}\left(\delta_{\Delta t,i}\right)$

  $(\hat{\beta}_{\Delta t,i1},...,\hat{\beta}_{\Delta t,iN}) \leftarrow \beta_{\Delta t,i1}\left(\hat{\delta}_{\Delta t,i}\right),...,\beta_{\Delta t,iN}\left(\hat{\delta}_{\Delta t,i}\right)$

end for

Step 3 – Iterating SIR model

for $i = 1,...,N$ **do**

  $\hat{\mathcal{I}}_i[n] \leftarrow \mathcal{I}_i[n]$

  $\hat{\mathcal{R}}_i[1] \leftarrow 0$

  $\hat{\mathcal{R}}_i[k] \leftarrow \hat{\mathcal{R}}_i[k-1] + \hat{\delta}_{\Delta t,i}\mathcal{I}_i[k-1]$ for all $k = 2,...,n$

end for

for $k = n+1,...,n+n_{\text{pred}}$ **do**

  for $i = 1,...,N$ **do**

    $\hat{\mathcal{I}}_i[k] \leftarrow \left(1 - \hat{\delta}_{\Delta t,i}\right)\hat{\mathcal{I}}_i[k-1] + \left(1 - \hat{\mathcal{I}}_i[k-1] - \hat{\mathcal{R}}_i[k-1]\right)\sum_{j=1}^{N}\hat{\beta}_{\Delta t,ij}\hat{\mathcal{I}}_j[k-1]$

    $\hat{\mathcal{R}}_i[k] \leftarrow \hat{\mathcal{R}}_i[k-1] + \hat{\delta}_{\Delta t,i}\hat{\mathcal{I}}_i[k-1]$

  end for

end for

The pseudo-code of `Network inference` is given by Algorithm G.2, which is a direct adaptation of Algorithm F.1. We refer to Chapter 7 for more details.

Algorithm G.2 `Network inference`

Input: curing probability $\delta_{\Delta t,i}$; viral state $v_i[k]$ for $k = 1,...,n$; infection state vector $\mathcal{I}[k]$ for $k = 1,...,n$
Output: infection probability estimates $\beta_{\Delta t,i1}(\delta_{\Delta t,i}),...,\beta_{\Delta t,iN}(\delta_{\Delta t,i})$; mean squared error $\mathrm{MSE}(\delta_{\Delta t,i})$
Compute $V_{\mathrm{SIR},i}$ and $F_{\mathrm{SIR},i}$ by Lemma F.1
$\rho_{\max,i} \leftarrow 2\|F_{\mathrm{SIR},i}^T V_{\mathrm{SIR},i}\|_\infty$
$\rho_{\min,i} \leftarrow 10^{-4}\rho_{\max,i}$
$\Theta_i \leftarrow 100$ logarithmically equidistant values from $\rho_{\min,i}$ to $\rho_{\max,i}$
for $\rho_i \in \Theta_i$ **do**
    estimate $\mathrm{MSE}(\delta_{\Delta t,i},\rho_i)$ by 3-fold cross-validation on $F_{\mathrm{SIR},i}$ $V_{\mathrm{SIR},i}$ and solving (8.1) on the respective training set
end for
$\rho_{\mathrm{opt},i} \leftarrow \operatorname{argmin}_{\rho_i \in \Theta_i} \mathrm{MSE}\left(\delta_{\Delta t,i},\rho_i\right)$
$(\beta_{\Delta t,i1}(\delta_{\Delta t,i}),...,\beta_{\Delta t,iN}(\delta_{\Delta t,i})) \leftarrow$ the solution to (8.1) on the whole data set $F_{\mathrm{SIR},i}, V_{\mathrm{SIR},i}$ for $\rho_i = \rho_{\mathrm{opt},i}$
$\mathrm{MSE}(\delta_{\Delta t,i}) \leftarrow \mathrm{MSE}(\delta_{\Delta t,i},\rho_{\mathrm{opt},i})$

H

APPENDIX TO CHAPTER 9

H.1. PROOF OF LEMMA 9.1

We derive the matrix S that minimises the error $\epsilon_{\text{eigen}}(S)$. The Frobenius norm of an $N \times N$ matrix M is defined as [32]

$$\|M\|_F = \sqrt{\sum_{i=1}^{N}\sum_{j=1}^{N}(M)_{ij}^2}. \tag{H.1}$$

For a symmetric matrix M, the Frobenius norm can be expressed in terms of the eigenvalues $\lambda_i(M)$ of the matrix M as

$$\|M\|_F = \sqrt{\sum_{i=1}^{N}\lambda_i^2(M)}.$$

Thus, the Frobenius norm of a symmetric matrix M is completely determined by the eigenvalues of M. For any orthogonal matrix B and any symmetric matrix M, the matrix $\tilde{M} = BMB^T$ is symmetric and has the same set of eigenvalues as the matrix M. Hence, the Frobenius norm of the matrices M and $\tilde{M}$ is equal, i.e.,

$$\|M\|_F = \left\|BMB^T\right\|_F$$

for any symmetric matrix M and any orthogonal matrix B.

In particular, by identifying $M = (W - XSX^T)$ and $B = X^T$, the definition of the error $\epsilon_{\text{eigen}}(S)$ in (9.5) is equivalent to

$$\begin{aligned}
\epsilon_{\text{eigen}}(S) &= \left\|(W - XSX^T)\right\|_F \\
&= \left\|X^T(W - XSX^T)X\right\|_F \\
&= \left\|X^TWX - X^TXSX^TX\right\|_F \\
&= \left\|X^TWX - S\right\|_F,
\end{aligned}$$

where the last equality follows from the orthogonality of the matrix X. Minimising the non-negative error $\epsilon_{\text{eigen}}(S)$ is equivalent to minimising its square $\epsilon^2_{\text{eigen}}(S)$. With the definition of the Frobenius norm in (H.1), we obtain that

$$\begin{aligned}\epsilon^2_{\text{eigen}}(S) &= \sum_{i=1}^{N}\sum_{j=1}^{N}(X^T W X - S)^2_{ij} \\ &= \sum_{i=1}^{N}\left(\left((X^T W X)_{ii} - s_i\right)^2 + \sum_{j=1,j\neq i}^{N}(X^T W X)^2_{ij}\right),\end{aligned} \tag{H.2}$$

where the last equality follows from the fact that the matrix S is diagonal. The second addend in (H.2) does not depend on the matrix S. Hence, minimising the error $\epsilon_{\text{eigen}}(S)$ is equivalent to minimising

$$\begin{aligned}\tilde{\epsilon}_{\text{eigen}}(S) &= \sum_{i=1}^{N}\left((X^T W X)_{ii} - s_i\right)^2 \\ &= \sum_{i=1}^{N}\left(x_i^T W x_i - s_i\right)^2,\end{aligned}$$

which is minimal if $x_i^T W x_i = s_i$ for all nodes $i = 1,...,N$, where x_i denotes the i-th column of the matrix X. Thus, the matrix S that results in the best fit of the eigenmode approach equals

$$S = \operatorname{diag}\left(x_1^T W x_1, ..., x_N^T W x_N\right).$$

H.2. PROOF OF LEMMA 9.2

We derive the coefficients c_m that minimise the error $\epsilon_{\text{series}}(c)$. The coefficients c_m can be obtained by minimising the difference of the left-hand side to the right-hand side in (9.3). Since the matrix A is symmetric, it holds that

$$\left\|A^m\right\|_2 = \lambda_1^m. \tag{H.3}$$

A similar calculation as in Appendix H.1 yields that minimising the error

$$\epsilon_{\text{series}}(c) = \left\| W - \sum_{m=1}^{d}\frac{c_m}{\|A^m\|_2} X D^m X^T \right\|_F \tag{H.4}$$

is equivalent to minimising

$$\tilde{\epsilon}_{\text{series}}(c) = \sum_{i=1}^{N}\left(x_i^T W x_i - \sum_{m=1}^{d} c_m \frac{\lambda_i^m}{\lambda_1^m}\right)^2. \tag{H.5}$$

Rewriting equation (H.5) in terms of the vector v and the matrix M completes the proof of Lemma 9.2.

H.3. PROOF OF LEMMA 9.3

We prove Lemma 9.3 by two steps. As the first step, we rewrite the error $\epsilon_{\text{series}}(c)$ of the series approach. From (H.3) and (H.4), we obtain that the error $\epsilon_{\text{series}}(c)$ of the series approach can be expressed, for any coefficient vector c, as

$$\epsilon_{\text{series}}(c) = \left\| W - XYX^T \right\|_F, \tag{H.6}$$

where the $N \times N$ matrix Y equals

$$Y = \text{diag}\left(\sum_{m=1}^{d} c_m \frac{\lambda_1^m}{\lambda_1^m}, ..., \sum_{m=1}^{d} c_m \frac{\lambda_N^m}{\lambda_1^m} \right).$$

The expression (H.6) of the error $\epsilon_{\text{series}}(c)$ closely resembles the error $\epsilon_{\text{eigen}}(S)$ of the eigenmode approach (9.5). Particularly, as the second step of the proof, we notice that by choosing the eigenmode coefficients s_i as

$$s_i = \sum_{m=1}^{d} c_m \frac{\lambda_i^m}{\lambda_1^m}, \quad i = 1, ..., N, \tag{H.7}$$

the diagonal matrix $S = \text{diag}(s_1, ..., s_N)$ equals $S = Y$. Hence, for any matrix Y, we obtain from (9.5), by choosing $S = Y$, that

$$\begin{aligned} \epsilon_{\text{eigen}}(Y) &= \left\| W - XYX^T \right\|_F \\ &= \epsilon_{\text{series}}(c), \end{aligned}$$

where the last equality follows from (H.6). Thus, for any coefficients c, the choice (H.7) for the eigenmode coefficients s_1, ..., s_N results in $\epsilon_{\text{eigen}}(Y) = \epsilon_{\text{series}}(c)$. Hence, we obtain that

$$\min_S \epsilon_{\text{eigen}}(S) \leq \epsilon_{\text{eigen}}(Y) = \min_c \epsilon_{\text{series}}(c), \tag{H.8}$$

which proves Lemma 9.3. Please note that the argument used is analogous to the classical linear algebra idea used to compute the remainder term (and the associated error) of a Taylor polynomial of a matrix function [294]. We emphasise that (H.8) almost always holds true *with strict inequality*, i.e.,

$$\min_S \epsilon_{\text{eigen}}(S) < \min_c \epsilon_{\text{series}}(c). \tag{H.9}$$

To arrive at (H.9), we stack (H.7) and obtain a linear system for the coefficients c_1, ..., c_d as

$$\begin{pmatrix} \frac{\lambda_1}{\lambda_1} & \cdots & \frac{\lambda_1^d}{\lambda_1^d} \\ \vdots & \ddots & \vdots \\ \frac{\lambda_N}{\lambda_1} & \cdots & \frac{\lambda_N^d}{\lambda_1^d} \end{pmatrix} \begin{pmatrix} c_1 \\ \vdots \\ c_d \end{pmatrix} = \begin{pmatrix} s_1 \\ \vdots \\ s_N \end{pmatrix}.$$

With Lemma 9.1, we obtain that (H.8) holds with equality if and only if

$$\begin{pmatrix} \frac{\lambda_1}{\lambda_1} & \cdots & \frac{\lambda_1^d}{\lambda_1^d} \\ \vdots & \ddots & \vdots \\ \frac{\lambda_N}{\lambda_1} & \cdots & \frac{\lambda_N^d}{\lambda_1^d} \end{pmatrix} \begin{pmatrix} c_1 \\ \vdots \\ c_d \end{pmatrix} = \begin{pmatrix} x_1^T W x_1 \\ \vdots \\ x_N^T W x_N \end{pmatrix}. \tag{H.10}$$

The linear system (H.10) is *overdetermined* since there are N equations but only d unknowns $c_1, ..., c_d$. More specifically, the linear system (H.10) can be solved for the coefficients $c_1, ..., c_d$ only if the $N \times 1$ vector

$$\begin{pmatrix} x_1^T W x_1 \\ \vdots \\ x_N^T W x_N \end{pmatrix} \tag{H.11}$$

is element of the image (or range) of the $N \times d$ matrix

$$\begin{pmatrix} \frac{\lambda_1}{\lambda_1} & \cdots & \frac{\lambda_1^d}{\lambda_1^d} \\ \vdots & \ddots & \vdots \\ \frac{\lambda_N}{\lambda_1} & \cdots & \frac{\lambda_N^d}{\lambda_1^d} \end{pmatrix}. \tag{H.12}$$

Thus, (H.8) holds with equality only if the vector (H.11) is in the image of (H.12). Since the image of the matrix (H.12) is a subspace of $\mathbb{R}^N$ with dimension not greater than d, this is a highly restrictive condition.

H.4. PROCESSING PIPELINE FOR DATASET 4

The HCP 100 unrelated subjects resting state fMRI dataset (REST1) was included for this project, which was already pre-processed using the optimized HCP minimal processing pipeline before downloading, including normalization, motion correction and intensity normalization [295]. Subsequently, the data were motion-corrected again using ICA-AROMA (v0.4-beta 2017, Nijmegen, the Netherlands), which identifies which ICA-based components are strongly correlated with already available motion parameters, and removed these components from the data. All subsequent processing was performed using[1] FSL 5.09. 3D T1-weighted data from the dataset was processed using SIENAX, to create grey matter (GM) and white matter (WM) as well as cerebrospinal fluid (CSF) masks, which were registered to the functional images using inverted boundary-based registration (BBR) parameters. WM and CSF masks were used to regress out average signals within these masks on the ICA-AROMA processed data. The automated anatomical labelling atlas (AAL) was registered to T1-weighted images using inverted FNIRT parameters [222], after which SIENAX-derived GM masks were used to mask the cortical atlas in T1-space. Subsequently, this modified atlas was transferred to the fMRI images, again using inverted BBR parameters. Finally, mean time series were calculated for each region within the atlas.

[1] See https://fsl.fmrib.ox.ac.uk/fsl/fslwiki/.

BIBLIOGRAPHY

[1] N. T. J. Bailey, *The Mathematical Theory of Infectious Diseases and Its Applications*, 2nd edition (Charles Griffin & Company, London, 1975).

[2] R. M. Anderson and R. M. May, *Infectious diseases of humans: dynamics and control* (Oxford University Press, 1992).

[3] D. Bernoulli, *Essai d'une nouvelle analyse de la mortalité causée par la petite vérole et des avantages de l'inoculation pour la prévenir,* Histoire de l'Acad. Roy. Sci.(Paris) avec Mém. des Math. et Phys. and Mém **1**, 1 (1760).

[4] J. Snow, *On the mode of communication of cholera* (John Churchill, 1855).

[5] R. Pastor-Satorras, C. Castellano, P. Van Mieghem, and A. Vespignani, *Epidemic processes in complex networks,* Reviews of Modern Physics **87**, 925– (2015).

[6] C. Nowzari, V. M. Preciado, and G. J. Pappas, *Analysis and control of epidemics: A survey of spreading processes on complex networks,* IEEE Control Systems Magazine **36**, 26 (2016).

[7] I. Z. Kiss, J. C. Miller, and P. L. Simon, *Mathematics of epidemics on networks,* Cham: Springer **598** (2017).

[8] A.-L. Barabási and R. Albert, *Emergence of scaling in random networks,* Science **286**, 509 (1999).

[9] R. Pastor-Satorras and A. Vespignani, *Epidemic spreading in scale-free networks,* Physical Review Letters **86**, 3200 (2001).

[10] F. Liljeros, C. R. Edling, L. A. N. Amaral, H. E. Stanley, and Y. Åberg, *The web of human sexual contacts,* Nature **411**, 907 (2001).

[11] T. Britton, F. Ball, and P. Trapman, *A mathematical model reveals the influence of population heterogeneity on herd immunity to SARS-CoV-2,* Science **369**, 846 (2020).

[12] M. Ogura and V. M. Preciado, *Stability of spreading processes over time-varying large-scale networks,* IEEE Transactions on Network Science and Engineering **3**, 44 (2016).

[13] N. Masuda and P. Holme, *Temporal Network Epidemiology* (Springer, 2017).

[14] P. E. Paré, C. L. Beck, and A. Nedić, *Epidemic processes over time-varying networks,* IEEE Transactions on Control of Network Systems **5**, 1322 (2017).

[15] N. Masuda and R. Lambiotte, *A Guide to Temporal Networks*, Vol. 6 (World Scientific, 2020).

[16] F. Schlosser, B. F. Maier, O. Jack, D. Hinrichs, A. Zachariae, and D. Brockmann, *COVID-19 lockdown induces disease-mitigating structural changes in mobility networks,* Proceedings of the National Academy of Sciences **117**, 32883 (2020).

[17] M. Hayhoe, F. Barreras, and V. M. Preciado, *Data-driven control of the COVID-19 outbreak via non-pharmaceutical interventions: A geometric programming approach,* arXiv preprint arXiv:2011.01392 (2020).

[18] A. Lajmanovich and J. A. Yorke, *A deterministic model for gonorrhea in a nonhomogeneous population,* Mathematical Biosciences **28**, 221 (1976).

[19] P. Van Mieghem and J. Omic, *In-homogeneous virus spread in networks,* arXiv preprint arXiv:1306.2588 (2014).

[20] P. Van Mieghem, J. Omic, and R. Kooij, *Virus spread in networks,* IEEE/ACM Transactions on Networking **17**, 1 (2009).

[21] P. Van Mieghem, *The N-Intertwined SIS epidemic network model,* Computing **93**, 147 (2011).

[22] A. Fall, A. Iggidr, G. Sallet, and J.-J. Tewa, *Epidemiological models and Lyapunov functions,* Mathematical Modelling of Natural Phenomena **2**, 62 (2007).

[23] Y. Wan, S. Roy, and A. Saberi, *Designing spatially heterogeneous strategies for control of virus spread,* IET Systems Biology **2**, 184 (2008).

[24] B. Prasse and P. Van Mieghem, *Network reconstruction and prediction of epidemic outbreaks for NIMFA processes,* arXiv preprint arXiv:1811.06741 (2018).

[25] P. E. Paré, J. Liu, C. L. Beck, B. E. Kirwan, and T. Başar, *Analysis, estimation, and validation of discrete-time epidemic processes,* IEEE Transactions on Control Systems Technology (2018).

[26] H. W. Hethcote, *The mathematics of infectious diseases,* SIAM review **42**, 599 (2000).

[27] J. A. P. Heesterbeek, *A brief history of R_0 and a recipe for its calculation,* Acta Biotheoretica **50**, 189 (2002).

[28] O. Diekmann, J. A. P. Heesterbeek, and J. A. Metz, *On the definition and the computation of the basic reproduction ratio R_0 in models for infectious diseases in heterogeneous populations,* Journal of Mathematical Biology **28**, 365 (1990).

[29] P. Van den Driessche and J. Watmough, *Reproduction numbers and sub-threshold endemic equilibria for compartmental models of disease transmission,* Mathematical Biosciences **180**, 29 (2002).

[30] W. O. Kermack and A. G. McKendrick, *A contribution to the mathematical theory of epidemics,* Proceedings of the Royal Society of London. Series A, Containing papers of a mathematical and physical character **115**, 700 (1927).

[31] M. Youssef and C. Scoglio, *An individual-based approach to SIR epidemics in contact networks,* Journal of Theoretical Biology **283**, 136 (2011).

[32] P. Van Mieghem, *Graph spectra for complex networks* (Cambridge University Press, 2010).

[33] A. Clauset, C. Moore, and M. E. Newman, *Hierarchical structure and the prediction of missing links in networks,* Nature **453**, 98 (2008).

[34] E. Abbe, *Community detection and stochastic block models: recent developments,* The Journal of Machine Learning Research **18**, 6446 (2017).

[35] T. P. Peixoto, *Hierarchical block structures and high-resolution model selection in large networks,* Physical Review X **4**, 011047 (2014).

[36] A. Arenas, A. Diaz-Guilera, and C. J. Pérez-Vicente, *Synchronization reveals topological scales in complex networks,* Physical Review Letters **96**, 114102 (2006).

[37] N. O'Clery, Y. Yuan, G.-B. Stan, and M. Barahona, *Observability and coarse graining of consensus dynamics through the external equitable partition,* Physical Review E **88**, 042805 (2013).

[38] S. Bonaccorsi, S. Ottaviano, D. Mugnolo, and F. D. Pellegrini, *Epidemic outbreaks in networks with equitable or almost-equitable partitions,* SIAM Journal on Applied Mathematics **75**, 2421 (2015).

[39] A. C. Antoulas, *Approximation of large-scale dynamical systems*, Vol. 6 (SIAM, 2005).

[40] G. Kerschen, J.-c. Golinval, A. F. Vakakis, and L. A. Bergman, *The method of proper orthogonal decomposition for dynamical characterization and order reduction of mechanical systems: an overview,* Nonlinear Dynamics **41**, 147 (2005).

[41] S. L. Brunton and J. N. Kutz, *Data-driven science and engineering: Machine learning, dynamical systems, and control* (Cambridge University Press, 2019).

[42] H. K. Khalil, *Nonlinear systems,* Prentice-Hall, New Jersey **2**, 5 (1996).

[43] A. J. Schwenk, *Computing the characteristic polynomial of a graph,* in *Graphs and Combinatorics* (Springer, 1974) pp. 153–172.

[44] M. T. Schaub and L. Peel, *Hierarchical community structure in networks,* arXiv preprint arXiv:2009.07196 (2020).

[45] D. Mugnolo, *Semigroup methods for evolution equations on networks*, Vol. 20 (Springer, 2014).

[46] S. Ottaviano, F. De Pellegrini, S. Bonaccorsi, and P. Van Mieghem, *Optimal curing policy for epidemic spreading over a community network with heterogeneous population,* Journal of Complex Networks **6**, 800 (2018).

[47] P. L. Simon, M. Taylor, and I. Z. Kiss, *Exact epidemic models on graphs using graph-automorphism driven lumping,* Journal of Mathematical Biology **62**, 479 (2011).

[48] J. A. Ward and M. López-García, *Exact analysis of summary statistics for continuous-time discrete-state Markov processes on networks using graph-automorphism lumping,* Applied Network Science **4**, 108 (2019).

[49] K. Devriendt and P. Van Mieghem, *Unified mean-field framework for Susceptible-Infected-Susceptible epidemics on networks, based on graph partitioning and the isoperimetric inequality,* Physical Review E **96**, 052314 (2017).

[50] M. Timme, *Revealing network connectivity from response dynamics,* Physical Review Letters **98**, 224101 (2007).

[51] B. Barzel and A.-L. Barabási, *Universality in network dynamics,* Nature Physics **9**, 673 (2013).

[52] E. Laurence, N. Doyon, L. J. Dubé, and P. Desrosiers, *Spectral dimension reduction of complex dynamical networks,* Physical Review X **9**, 011042 (2019).

[53] B. Prasse and P. Van Mieghem, *Predicting dynamics on networks hardly depends on the topology,* arXiv preprint arXiv:2005.14575 (2020).

[54] M. Egerstedt, S. Martini, M. Cao, K. Camlibel, and A. Bicchi, *Interacting with networks: How does structure relate to controllability in single-leader, consensus networks?* IEEE Control Systems Magazine **32**, 66 (2012).

[55] L. M. Pecora, F. Sorrentino, A. M. Hagerstrom, T. E. Murphy, and R. Roy, *Cluster synchronization and isolated desynchronization in complex networks with symmetries,* Nature Communications **5**, 1 (2014).

[56] M. T. Schaub, N. O'Clery, Y. N. Billeh, J.-C. Delvenne, R. Lambiotte, and M. Barahona, *Graph partitions and cluster synchronization in networks of oscillators,* Chaos: An Interdisciplinary Journal of Nonlinear Science **26**, 094821 (2016).

[57] K. Devriendt and R. Lambiotte, *Non-linear network dynamics with consensus-dissensus bifurcation,* arXiv preprint arXiv:2002.08408 (2020).

[58] P. Van Mieghem, *Performance Analysis of Complex Networks and Systems* (Cambridge University Press, 2014).

[59] P. Van Mieghem, *SIS epidemics with time-dependent rates describing ageing of information spread and mutation of pathogens,* Delft University of Technology **1** (2014).

[60] P. W. Holland, K. B. Laskey, and S. Leinhardt, *Stochastic blockmodels: First steps,* Social Networks **5**, 109 (1983).

[61] A. Saade, F. Krzakala, and L. Zdeborová, *Spectral clustering of graphs with the Bethe Hessian,* in *Advances in Neural Information Processing Systems*, Vol. 27, edited by Z. Ghahramani, M. Welling, C. Cortes, N. Lawrence, and K. Q. Weinberger (Curran Associates, Inc., 2014).

[62] J. Kunegis, *Konect: the Koblenz network collection,* in *Proceedings of the 22nd International Conference on World Wide Web* (ACM, 2013) pp. 1343–1350.

[63] M. Girvan and M. E. Newman, *Community structure in social and biological networks,* Proceedings of the National Academy of Sciences **99**, 7821 (2002).

[64] J. Stehlé, N. Voirin, A. Barrat, C. Cattuto, L. Isella, J. Pinton, M. Quaggiotto, W. Van den Broeck, C. Régis, B. Lina, and P. Vanhems, *High-resolution measurements of face-to-face contact patterns in a primary school,* PLOS ONE **6**, e23176 (2011).

[65] B. Hayes, *Connecting the dots,* American Scientist **94**, 400 (2006).

[66] B. Prasse and P. Van Mieghem, *Time-dependent solution of the NIMFA equations around the epidemic threshold,* Journal of Mathematical Biology , 1 (2020).

[67] M. G. Kitzbichler, M. L. Smith, S. R. Christensen, and E. Bullmore, *Broadband criticality of human brain network synchronization,* PLOS Computational Biology **5**, e1000314 (2009).

[68] M. Nykter, N. D. Price, M. Aldana, S. A. Ramsey, S. A. Kauffman, L. E. Hood, O. Yli-Harja, and I. Shmulevich, *Gene expression dynamics in the macrophage exhibit criticality,* Proceedings of the National Academy of Sciences **105**, 1897 (2008).

[69] P. Van Mieghem and R. van de Bovenkamp, *Accuracy criterion for the mean-field approximation in susceptible-infected-susceptible epidemics on networks,* Physical Review E **91**, 032812 (2015).

[70] P. Van Mieghem, *The viral conductance of a network,* Computer Communications **35**, 1494 (2012).

[71] P.-F. Verhulst, *Notice sur la loi que la population suit dans son accroissement,* Corresp. Math. Phys. **10**, 113 (1838).

[72] P. Van Mieghem, *Universality of the SIS prevalence in networks,* arXiv preprint arXiv:1612.01386 (2016).

[73] D. G. Kendall, *On the generalized birth-and-death process,* The Annals of Mathematical Statistics **19**, 1 (1948).

[74] P. Erdős and A. Rényi, *On the evolution of random graphs,* Publ. Math. Inst. Hung. Acad. Sci **5**, 17 (1960).

[75] D. J. Watts and S. H. Strogatz, *Collective dynamics of "small-world" networks,* Nature **393**, 440 (1998).

[76] B. Prasse and P. Van Mieghem, *The viral state dynamics of the discrete-time NIMFA epidemic model,* IEEE Transactions on Network Science and Engineering (2019).

[77] J. Stoer and R. Bulirsch, *Introduction to numerical analysis*, Vol. 12 (Springer Science & Business Media, 2013).

[78] H. J. Ahn and B. Hassibi, *Global dynamics of epidemic spread over complex networks,* in *Proc. 52nd IEEE Conference on Decision and Control, CDC* (IEEE, 2013) pp. 4579–4585.

[79] A. Khanafer, T. Başar, and B. Gharesifard, *Stability of epidemic models over directed graphs: A positive systems approach,* Automatica **74**, 126 (2016).

[80] D. J. Daley and J. Gani, *Epidemic modelling: an introduction*, Vol. 15 (Cambridge University Press, 2001).

[81] Z. He and P. Van Mieghem, *The spreading time in SIS epidemics on networks,* Physica A: Statistical Mechanics and its Applications **494**, 317 (2018).

[82] R. van de Bovenkamp and P. Van Mieghem, *Time to metastable state in SIS epidemics on graphs,* in *2014 Tenth International Conference on Signal-Image Technology and Internet-Based Systems* (IEEE, 2014) pp. 347–354.

[83] B. Prasse and P. Van Mieghem, *Exact network reconstruction from complete SIS nodal state infection information seems infeasible,* IEEE Transactions on Network Science and Engineering **6**, 748 (2018).

[84] B. Prasse and P. Van Mieghem, *Maximum-likelihood network reconstruction for SIS processes is NP-hard,* arXiv preprint arXiv:1807.08630 (2018).

[85] P. Van Mieghem and E. Cator, *Epidemics in networks with nodal self-infection and the epidemic threshold,* Physical Review E **86**, 016116 (2012).

[86] P. Van Mieghem and F. Wang, *Time dependence of susceptible-infected-susceptible epidemics on networks with nodal self-infections,* Physical Review E **101**, 052310 (2020).

[87] A. Vajdi and C. Scoglio, *Identification of missing links using susceptible-infected-susceptible spreading traces,* IEEE Transactions on Network Science and Engineering (2018).

[88] Z. Shen, W.-X. Wang, Y. Fan, Z. Di, and Y.-C. Lai, *Reconstructing propagation networks with natural diversity and identifying hidden sources,* Nature Communications **5**, 1 (2014).

[89] T. P. Peixoto, *Network reconstruction and community detection from dynamics,* Physical Review Letters **123**, 128301 (2019).

[90] S. Boyd and L. Vandenberghe, *Convex Optimization* (Cambridge University Press, 2004).

[91] L. Pronzato and A. Pázman, *Asymptotic properties of M, ML, and maximum a posteriori estimators,* in *Design of Experiments in Nonlinear Models* (Springer, 2013) pp. 79–104.

[92] C. R. Rao, *Information and the accuracy attainable in the estimation of statistical parameters,* in *Breakthroughs in Statistics* (Springer, 1992) pp. 235–247.

[93] H. Cramér, *Mathematical Methods of Statistics*, Vol. 9 (Princeton University Press, 2016).

[94] P. Netrapalli and S. Sanghavi, *Learning the graph of epidemic cascades,* ACM SIGMETRICS Performance Evaluation Review **40**, 211 (2012).

[95] A. Braunstein and A. Ingrosso, *Network reconstruction from infection cascades,* arXiv preprint arXiv:1609.00432 (2016).

[96] Q. Duong, M. P. Wellman, and S. Singh, *Modeling information diffusion in networks with unobserved links,* in *Privacy, Security, Risk and Trust (PASSAT) and 2011 IEEE Third International Conference on Social Computing (SocialCom)* (IEEE, 2011) pp. 362–369.

[97] S. Myers and J. Leskovec, *On the convexity of latent social network inference,* in *Advances in Neural Information Processing Systems* (2010) pp. 1741–1749.

[98] E. Sefer and C. Kingsford, *Convex risk minimization to infer networks from probabilistic diffusion data at multiple scales,* in *2015 IEEE 31st International Conference on Data Engineering (ICDE)* (IEEE, 2015) pp. 663–674.

[99] M. Gomez Rodriguez, J. Leskovec, and A. Krause, *Inferring networks of diffusion and influence,* in *Proceedings of the 16th ACM SIGKDD International Conference on Knowledge Discovery and Data Mining* (ACM, 2010) pp. 1019–1028.

[100] H. L. Bodlaender, *On the complexity of the maximum cut problem*, Vol. 91 (Unknown Publisher, 1991).

[101] K. Devriendt and P. Van Mieghem, *Tighter spectral bounds for the cut size, based on Laplacian eigenvectors,* Linear Algebra and its Applications **572**, 68 (2019).

[102] P. Van Mieghem and K. Devriendt, *An epidemic perspective on the cut size in networks,* Delft University of Technology **1** (2015).

[103] M. R. Garey, D. S. Johnson, and L. Stockmeyer, *Some simplified NP-complete graph problems,* Theoretical Computer Science **1**, 237 (1976).

[104] T. H. Cormen, *Introduction to algorithms* (MIT press, 2009).

[105] A. Caprara, *Constrained 0–1 quadratic programming: Basic approaches and extensions,* European Journal of Operational Research **187**, 1494 (2008).

[106] E. Boros and P. L. Hammer, *Pseudo-boolean optimization,* Discrete Applied Mathematics **123**, 155 (2002).

[107] I. G. Rosenberg, *Reduction of bivalent maximization to the quadratic case,* Cahiers du Centre d'etudes de Recherche Operationnelle **17**, 71 (1975).

[108] M. R. Garey and D. S. Johnson, *A Guide to the Theory of NP-Completeness,* WH Freemann, New York **70** (1979).

[109] J.-C. Picard and H. D. Ratliff, *Minimum cuts and related problems,* Networks **5**, 357 (1975).

[110] P. M. Pardalos and S. Jha, *Graph separation techniques for quadratic zero-one programming,* Computers & Mathematics with Applications **21**, 107 (1991).

[111] F. Barahona, *A solvable case of quadratic 0–1 programming,* Discrete Applied Mathematics **13**, 23 (1986).

[112] S. Diamond, R. Takapoui, and S. Boyd, *A general system for heuristic minimization of convex functions over non-convex sets,* Optimization Methods and Software , 1 (2017).

[113] W. W. Zachary, *An information flow model for conflict and fission in small groups,* Journal of Anthropological Research **33**, 452 (1977).

[114] L. C. Freeman, S. C. Freeman, and A. G. Michaelson, *On human social intelligence,* Journal of Social and Biological Structures **11**, 415 (1988).

[115] B. Prasse, M. A. Achterberg, and P. Van Mieghem, *On the accuracy of predicting epidemic outbreaks,* Submitted (2020).

[116] H. W. Hethcote, *Qualitative analyses of communicable disease models,* Mathematical Biosciences **28**, 335 (1976).

[117] P. Cirillo and N. N. Taleb, *Tail risk of contagious diseases,* Nature Physics , 1 (2020).

[118] M. Castro, S. Ares, J. A. Cuesta, and S. Manrubia, *Predictability: Can the turning point and end of an expanding epidemic be precisely forecast?* arXiv preprint arXiv:2004.08842 (2020).

[119] M. Paggi, *Simulation of Covid-19 epidemic evolution: are compartmental models really predictive?* arXiv preprint arXiv:2004.08207 (2020).

[120] T. Alberti and D. Faranda, *On the uncertainty of real-time predictions of epidemic growths: a COVID-19 case study for China and Italy,* Communications in Nonlinear Science and Numerical Simulation , 105372 (2020).

[121] Q. Liu and P. Van Mieghem, *Evaluation of an analytic, approximate formula for the time-varying SIS prevalence in different networks,* Physica A: Statistical Mechanics and its Applications **471**, 325 (2017).

[122] K. Biswas, A. Khaleque, and P. Sen, *Covid-19 spread: Reproduction of data and prediction using a SIR model on euclidean network,* arXiv preprint arXiv:2003.07063 (2020).

[123] Y.-C. Chen, P.-E. Lu, C.-S. Chang, and T.-H. Liu, *A time-dependent SIR model for COVID-19 with undetectable infected persons,* IEEE Transactions on Network Science and Engineering (2020).

[124] B. F. Maier and D. Brockmann, *Effective containment explains subexponential growth in recent confirmed COVID-19 cases in China,* Science (2020).

[125] J. Kumar and K. Hembram, *Epidemiological study of novel coronavirus (COVID-19),* arXiv preprint arXiv:2003.11376 (2020).

[126] B. Prasse, M. A. Achterberg, L. Ma, and P. Van Mieghem, *Network-inference-based prediction of the COVID-19 epidemic outbreak in the Chinese province Hubei,* Applied Network Science **5**, 1 (2020).

[127] G. Vattay, *Predicting the ultimate outcome of the COVID-19 outbreak in Italy,* arXiv preprint arXiv:2003.07912 (2020).

[128] M. Löytönen and P. Maasilta, *Multi-drug resistant tuberculosis in Finland—a forecast,* Social Science & Medicine **46**, 695 (1998).

[129] Y. Yang and E. Williams, *Logistic model-based forecast of sales and generation of obsolete computers in the U.S.* Technological Forecasting and Social Change **76**, 1105 (2009).

[130] A. C. Harvey, *Time Series Forecasting Based on the Logistic Curve,* The Journal of the Operational Research Society **35**, 641 (1984).

[131] H. Schultz, *The Standard Error of a Forecast from a Curve,* Journal of the American Statistical Association **25**, 139 (1930).

[132] R. Pearl and L. J. Reed, *On the rate of growth of the population of the United States since 1790 and its mathematical representation,* Proceedings of the National Academy of Sciences of the United States of America **6**, 275 (1920).

[133] G. H. Golub and C. F. Van Loan, *Matrix computations,* Vol. 3 (JHU Press, 2012).

[134] E. Dong, H. Du, and L. Gardner, *An interactive web-based dashboard to track COVID-19 in real time,* The Lancet Infectious Diseases **20**, 533 (2020).

[135] B. Prasse and P. Van Mieghem, *Network reconstruction and prediction of epidemic outbreaks for general group-based compartmental epidemic models,* IEEE Transactions on Network Science and Engineering (2020).

[136] F. D. Sahneh, C. Scoglio, and P. Van Mieghem, *Generalized epidemic mean-field model for spreading processes over multilayer complex networks,* IEEE/ACM Transactions on Networking (TON) **21**, 1609 (2013).

[137] A. Khanafer and T. Başar, *On the optimal control of virus spread in networks,* in *2014 7th International Conference on Network Games, Control and Optimization (NetGCoop)* (IEEE, 2014) pp. 166–172.

[138] M. Gomez-Rodriguez, L. Song, H. Daneshmand, and B. Schölkopf, *Estimating diffusion networks: Recovery conditions, sample complexity & soft-thresholding algorithm,* The Journal of Machine Learning Research **17**, 3092 (2016).

[139] M. Timme and J. Casadiego, *Revealing networks from dynamics: an introduction,* Journal of Physics A: Mathematical and Theoretical **47**, 343001 (2014).

[140] J. Casadiego, M. Nitzan, S. Hallerberg, and M. Timme, *Model-free inference of direct network interactions from nonlinear collective dynamics,* Nature Communications **8**, 2192 (2017).

[141] T. Hastie, R. Tibshirani, and M. Wainwright, *Statistical learning with sparsity: the lasso and generalizations* (CRC press, 2015).

[142] W.-X. Wang, Y.-C. Lai, and C. Grebogi, *Data based identification and prediction of nonlinear and complex dynamical systems,* Physics Reports **644**, 1 (2016).

[143] A.-L. Barabási, *Network Science* (Cambridge University Press, 2016).

[144] S. S. Chen, D. L. Donoho, and M. A. Saunders, *Atomic decomposition by basis pursuit,* SIAM review **43**, 129 (2001).

[145] E. T. Jaynes, *Information theory and statistical mechanics,* Physical Review **106**, 620 (1957).

[146] A. Papoulis and S. U. Pillai, *Probability, random variables, and stochastic processes* (Tata McGraw-Hill Education, 2002).

[147] R. C. Aster, B. Borchers, and C. H. Thurber, *Parameter estimation and inverse problems* (Elsevier, 2018).

[148] R. Tibshirani, *Regression shrinkage and selection via the lasso,* Journal of the Royal Statistical Society. Series B (Methodological) , 267 (1996).

[149] T. Fawcett, *An introduction to ROC analysis,* Pattern Recognition Letters **27**, 861 (2006).

[150] L. Isella, J. Stehlé, A. Barrat, C. Cattuto, J.-F. Pinton, and W. Van den Broeck, *What's in a crowd? Analysis of face-to-face behavioral networks,* Journal of Theoretical Biology **271**, 166 (2011).

[151] V. J. Munster, M. Koopmans, N. van Doremalen, D. van Riel, and E. de Wit, *A novel coronavirus emerging in China — key questions for impact assessment,* New England Journal of Medicine (2020).

[152] Q. Yang, C. Yi, A. Vajdi, L. W. Cohnstaedt, H. Wu, X. Guo, and C. M. Scoglio, *Short-term forecasts and long-term mitigation evaluations for the COVID-19 epidemic in Hubei Province, China,* medRxiv (2020).

[153] L. Lorch, W. Trouleau, S. Tsirtsis, A. Szanto, B. Schölkopf, and M. Gomez-Rodriguez, *A spatiotemporal epidemic model to quantify the effects of contact tracing, testing, and containment,* arXiv preprint arXiv:2004.07641 (2020).

[154] S. Y. Chang, E. Pierson, P. W. Koh, J. Gerardin, B. Redbird, D. Grusky, and J. Leskovec, *Mobility network modeling explains higher SARS-CoV-2 infection rates among disadvantaged groups and informs reopening strategies,* medRxiv (2020).

[155] M. Al-qaness, A. Ewees, H. Fan, and M. Abd El Aziz, *Optimization Method for Forecasting Confirmed Cases of COVID-19 in China,* J. Clin. Med. **9**, 674 (2020).

[156] Z. Yang, Z. Zeng, K. Wang, S. Wong, W. Liang, M. Zanin, P. Liu, X. Cao, Z. Gao, Z. Mai, J. Liang, X. Liu, S. Li, Y. Li, F. Ye, W. Guan, Y. Yang, F. Li, S. Luo, Y. Xie, B. Liu, Z. Wang, S. Zhang, Y. Wang, N. Zhong, and J. He, *Modified SEIR and AI prediction of the epidemics trend of COVID-19 in China under public health interventions,* Journal of Thoracic Disease **12** (2020).

[157] A. Kergassner, C. Burkhardt, D. Lippold, S. Nistler, M. Kergassner, P. Steinmann, D. Budday, and S. Budday, *Meso-scale modeling of COVID-19 spatio-temporal outbreak dynamics in Germany,* medRxiv (2020).

[158] S. He, Y. Peng, and K. Sun, *SEIR modeling of the COVID-19 and its dynamics,* Nonlinear Dynamics (2020).

[159] C. Pizzuti, A. Socievole, B. Prasse, and P. Van Mieghem, *Network-based prediction of COVID-19 epidemic spreading in Italy,* Applied Network Science **5**, 1 (2020).

[160] R. J. Hyndman and A. B. Koehler, *Another look at measures of forecast accuracy,* International Journal of Forecasting **22**, 679 (2006).

[161] J. L. Elman, *Finding Structure in Time,* Cognitive Science **14**, 179 (1990).

[162] I. Goodfellow, Y. Bengio, and A. Courville, *Deep Learning* (MIT Press, 2016).

[163] T. Young, D. Hazarika, S. Poria, and E. Cambria, *Recent Trends in Deep Learning Based Natural Language Processing [Review Article],* IEEE Computational Intelligence Magazine **13**, 55 (2018).

[164] S. Hochreiter and J. Schmidhuber, *Long Short-Term Memory,* Neural Computation **9**, 1735 (1997).

[165] F. A. Gers and J. Schmidhuber, *LSTM recurrent networks learn simple context-free and context-sensitive languages,* IEEE Transactions on Neural Networks **12 6**, 1333 (2001).

[166] F. A. Gers, J. Schmidhuber, and F. Cummins, *Learning to Forget: Continual Prediction with LSTM,* Neural Computation **12**, 2451 (2000).

[167] R. Jozefowicz, W. Zaremba, and I. Sutskever, *An Empirical Exploration of Recurrent Network Architectures,* in *In Proc. of ICML (32nd International Conference on Machine Learning)*, PMLR, Vol. 37, edited by F. Bach and D. Blei (Lille, France, 2015) pp. 2342–2350.

[168] Y. Yu, X. Si, C. Hu, and J. Zhang, *A Review of Recurrent Neural Networks: LSTM Cells and Network Architectures,* Neural Computation **31**, 1235 (2019), pMID: 31113301.

[169] D. P. Kingma and J. Ba, *Adam: A Method for Stochastic Optimization,* In Proc of ICLR (International Conference for Learning Representations), San Diego, 2015 **abs/1412.6980** (2015).

[170] S. Makridakis, E. Spiliotis, and V. Assimakopoulos, *The M4 Competition: 100,000 time series and 61 forecasting methods,* International Journal of Forecasting **36**, 54 (2020), m4 Competition.

[171] E. Bullmore and O. Sporns, *The economy of brain network organization,* Nature Reviews Neuroscience **13**, 336 (2012).

[172] S. N. Sotiropoulos, S. Jbabdi, J. Xu, J. L. Andersson, S. Moeller, E. J. Auerbach, M. F. Glasser, M. Hernandez, G. Sapiro, M. Jenkinson, *et al.*, *Advances in diffusion MRI acquisition and processing in the Human Connectome Project,* NeuroImage **80**, 125 (2013).

[173] Z. Wang, Z. Dai, G. Gong, C. Zhou, and Y. He, *Understanding structural-functional relationships in the human brain: a large-scale network perspective,* The Neuroscientist **21**, 290 (2015).

[174] A. M. Fjell, M. H. Sneve, H. Grydeland, A. B. Storsve, I. K. Amlien, A. Yendiki, and K. B. Walhovd, *Relationship between structural and functional connectivity change across the adult lifespan: a longitudinal investigation,* Human Brain Mapping **38**, 561 (2017).

[175] A. Avena-Koenigsberger, B. Misic, and O. Sporns, *Communication dynamics in complex brain networks,* Nature Reviews Neuroscience **19**, 17 (2018).

[176] C. J. Honey, O. Sporns, L. Cammoun, X. Gigandet, J.-P. Thiran, R. Meuli, and P. Hagmann, *Predicting human resting-state functional connectivity from structural connectivity,* Proceedings of the National Academy of Sciences **106**, 2035 (2009).

[177] M. D. Greicius, K. Supekar, V. Menon, and R. F. Dougherty, *Resting-state functional connectivity reflects structural connectivity in the default mode network,* Cerebral Cortex **19**, 72 (2009).

[178] G. C. O'Neill, P. Tewarie, D. Vidaurre, L. Liuzzi, M. W. Woolrich, and M. J. Brookes, *Dynamics of large-scale electrophysiological networks: A technical review,* NeuroImage **180**, 559 (2018).

[179] G. Rosenthal, F. Váša, A. Griffa, P. Hagmann, E. Amico, J. Goñi, G. Avidan, and O. Sporns, *Mapping higher-order relations between brain structure and function with embedded vector representations of connectomes,* Nature Communications **9**, 1 (2018).

[180] B. Mišić, R. F. Betzel, M. A. De Reus, M. P. Van Den Heuvel, M. G. Berman, A. R. McIntosh, and O. Sporns, *Network-level structure-function relationships in human neocortex,* Cerebral Cortex **26**, 3285 (2016).

[181] C. J. Honey, R. Kötter, M. Breakspear, and O. Sporns, *Network structure of cerebral cortex shapes functional connectivity on multiple time scales,* Proceedings of the National Academy of Sciences **104**, 10240 (2007).

[182] M. Forrester, J. J. Crofts, S. N. Sotiropoulos, S. Coombes, and R. D. O'Dea, *The role of node dynamics in shaping emergent functional connectivity patterns in the brain,* Network Neuroscience **4**, 467 (2020).

[183] R. Ton, G. Deco, and A. Daffertshofer, *Structure-function discrepancy: inhomogeneity and delays in synchronized neural networks,* PLOS Computational Biology **10**, e1003736 (2014).

[184] A. F. Alexander-Bloch, P. E. Vértes, R. Stidd, F. Lalonde, L. Clasen, J. Rapoport, J. Giedd, E. T. Bullmore, and N. Gogtay, *The anatomical distance of functional connections predicts brain network topology in health and schizophrenia,* Cerebral Cortex **23**, 127 (2013).

[185] P. Tewarie, A. Hillebrand, E. van Dellen, M. M. Schoonheim, F. Barkhof, C. Polman, C. Beaulieu, G. Gong, B. W. van Dijk, and C. J. Stam, *Structural degree predicts functional network connectivity: a multimodal resting-state fMRI and MEG study,* NeuroImage **97**, 296 (2014).

[186] C. Stam, E. Van Straaten, E. Van Dellen, P. Tewarie, G. Gong, A. Hillebrand, J. Meier, and P. Van Mieghem, *The relation between structural and functional connectivity patterns in complex brain networks,* International Journal of Psychophysiology **103**, 149 (2016).

[187] J. Goñi, M. P. Van Den Heuvel, A. Avena-Koenigsberger, N. V. De Mendizabal, R. F. Betzel, A. Griffa, P. Hagmann, B. Corominas-Murtra, J.-P. Thiran, and O. Sporns, *Resting-brain functional connectivity predicted by analytic measures of network communication,* Proceedings of the National Academy of Sciences **111**, 833 (2014).

[188] A. Kuceyeski, S. Shah, J. Dyke, S. Bickel, F. Abdelnour, N. Schiff, H. Voss, and A. Raj, *The application of a mathematical model linking structural and functional connectomes in severe brain injury,* NeuroImage: Clinical **11**, 635 (2016).

[189] F. Abdelnour, H. U. Voss, and A. Raj, *Network diffusion accurately models the relationship between structural and functional brain connectivity networks,* NeuroImage **90**, 335 (2014).

[190] G. Deco, M. L. Kringelbach, V. K. Jirsa, and P. Ritter, *The dynamics of resting fluctuations in the brain: metastability and its dynamical cortical core,* Scientific Reports **7**, 1 (2017).

[191] G. Deco and M. L. Kringelbach, *Metastability and coherence: extending the communication through coherence hypothesis using a whole-brain computational perspective,* Trends in Neurosciences **39**, 125 (2016).

[192] V. Wens, M. Bourguignon, M. Vander Ghinst, A. Mary, B. Marty, N. Coquelet, G. Naeije, P. Peigneux, S. Goldman, and X. De Tiège, *Synchrony, metastability, dynamic integration, and competition in the spontaneous functional connectivity of the human brain,* NeuroImage **199**, 313 (2019).

[193] G. Deco and V. K. Jirsa, *Ongoing cortical activity at rest: criticality, multistability, and ghost attractors,* Journal of Neuroscience **32**, 3366 (2012).

[194] G. Deco, A. Ponce-Alvarez, D. Mantini, G. L. Romani, P. Hagmann, and M. Corbetta, *Resting-state functional connectivity emerges from structurally and dynamically shaped slow linear fluctuations,* Journal of Neuroscience **33**, 11239 (2013).

[195] P. Tewarie, B. A. Hunt, G. C. O'Neill, A. Byrne, K. Aquino, M. Bauer, K. J. Mullinger, S. Coombes, and M. J. Brookes, *Relationships between neuronal oscillatory amplitude and dynamic functional connectivity,* Cerebral Cortex **29**, 2668 (2019).

[196] G. Deco, A. Ponce-Alvarez, P. Hagmann, G. L. Romani, D. Mantini, and M. Corbetta, *How local excitation–inhibition ratio impacts the whole brain dynamics,* Journal of Neuroscience **34**, 7886 (2014).

[197] G. Deco, A. R. McIntosh, K. Shen, R. M. Hutchison, R. S. Menon, S. Everling, P. Hagmann, and V. K. Jirsa, *Identification of optimal structural connectivity using functional connectivity and neural modeling,* Journal of Neuroscience **34**, 7910 (2014).

[198] M. L. Saggio, P. Ritter, and V. K. Jirsa, *Analytical operations relate structural and functional connectivity in the brain,* PLOS One **11**, e0157292 (2016).

[199] J. Meier, P. Tewarie, A. Hillebrand, L. Douw, B. W. van Dijk, S. M. Stufflebeam, and P. Van Mieghem, *A mapping between structural and functional brain networks,* Brain Connectivity **6**, 298 (2016).

[200] P. A. Robinson, *Interrelating anatomical, effective, and functional brain connectivity using propagators and neural field theory,* Physical Review E **85**, 011912 (2012).

[201] M. Gilson, N. E. Kouvaris, G. Deco, and G. Zamora-López, *Framework based on communicability and flow to analyze complex network dynamics,* Physical Review E **97**, 052301 (2018).

[202] C. O. Becker, S. Pequito, G. J. Pappas, M. B. Miller, S. T. Grafton, D. S. Bassett, and V. M. Preciado, *Spectral mapping of brain functional connectivity from diffusion imaging,* Scientific Reports **8**, 1 (2018).

[203] P. Robinson, S. Sarkar, G. M. Pandejee, and J. Henderson, *Determination of effective brain connectivity from functional connectivity with application to resting state connectivities,* Physical Review E **90**, 012707 (2014).

[204] G. Mehta-Pandejee, P. A. Robinson, J. A. Henderson, K. Aquino, and S. Sarkar, *Inference of direct and multistep effective connectivities from functional connectivity of the brain and of relationships to cortical geometry,* Journal of Neuroscience Methods **283**, 42 (2017).

[205] R. G. Bettinardi, G. Deco, V. M. Karlaftis, T. J. Van Hartevelt, H. M. Fernandes, Z. Kourtzi, M. L. Kringelbach, and G. Zamora-López, *How structure sculpts function: unveiling the contribution of anatomical connectivity to the brain's spontaneous correlation structure,* Chaos: An Interdisciplinary Journal of Nonlinear Science **27**, 047409 (2017).

[206] P. Van Mieghem, K. Devriendt, and H. Cetinay, *Pseudoinverse of the Laplacian and best spreader node in a network,* Physical Review E **96**, 032311 (2017).

[207] P. E. Vértes, A. F. Alexander-Bloch, N. Gogtay, J. N. Giedd, J. L. Rapoport, and E. T. Bullmore, *Simple models of human brain functional networks,* Proceedings of the National Academy of Sciences **109**, 5868 (2012).

[208] N. C. Gabay, T. Babaie-Janvier, and P. A. Robinson, *Dynamics of cortical activity eigenmodes including standing, traveling, and rotating waves,* Physical Review E **98**, 042413 (2018).

[209] F. Abdelnour, M. Dayan, O. Devinsky, T. Thesen, and A. Raj, *Functional brain connectivity is predictable from anatomic network's Laplacian eigen-structure,* NeuroImage **172**, 728 (2018).

[210] P. Tewarie, R. Abeysuriya, Á. Byrne, G. C. O'Neill, S. N. Sotiropoulos, M. J. Brookes, and S. Coombes, *How do spatially distinct frequency specific MEG networks emerge from one underlying structural connectome? The role of the structural eigenmodes,* NeuroImage **186**, 211 (2019).

[211] M. B. Wang, J. P. Owen, P. Mukherjee, and A. Raj, *Brain network eigenmodes provide a robust and compact representation of the structural connectome in health and disease,* PLOS Computational Biology **13**, e1005550 (2017).

[212] S. Atasoy, I. Donnelly, and J. Pearson, *Human brain networks function in connectome-specific harmonic waves,* Nature Communications **7**, 10340 (2016).

[213] P. A. Robinson, X. Zhao, K. M. Aquino, J. Griffiths, S. Sarkar, and G. Mehta-Pandejee, *Eigenmodes of brain activity: Neural field theory predictions and comparison with experiment,* NeuroImage **142**, 79 (2016).

[214] A. Tokariev, J. A. Roberts, A. Zalesky, X. Zhao, S. Vanhatalo, M. Breakspear, and L. Cocchi, *Large-scale brain modes reorganize between infant sleep states and carry prognostic information for preterms,* Nature Communications **10**, 1 (2019).

[215] N. C. Gabay and P. Robinson, *Cortical geometry as a determinant of brain activity eigenmodes: Neural field analysis,* Physical Review E **96**, 032413 (2017).

[216] P. Van Mieghem, *Interconnectivity structure of a general interdependent network,* Physical Review E **93**, 042305 (2016).

[217] P. Robinson, *Physical brain connectomics,* Physical Review E **99**, 012421 (2019).

[218] E. Estrada and N. Hatano, *Communicability in complex networks,* Physical Review E **77**, 036111 (2008).

[219] S. Boyd and L. Vandenberghe, *Introduction to Applied Linear Algebra: Vectors, Matrices, and Least Squares* (Cambridge University Press, 2018).

[220] V. Y. Pan, *How bad are Vandermonde matrices?* SIAM Journal on Matrix Analysis and Applications **37**, 676 (2016).

[221] G. Gong, Y. He, L. Concha, C. Lebel, D. W. Gross, A. C. Evans, and C. Beaulieu, *Mapping anatomical connectivity patterns of human cerebral cortex using in vivo diffusion tensor imaging tractography,* Cerebral Cortex **19**, 524 (2009).

[222] N. Tzourio-Mazoyer, B. Landeau, D. Papathanassiou, F. Crivello, O. Etard, N. Delcroix, B. Mazoyer, and M. Joliot, *Automated anatomical labeling of activations in SPM using a macroscopic anatomical parcellation of the MNI MRI single-subject brain,* NeuroImage **15**, 273 (2002).

[223] J. A. Brown, J. D. Rudie, A. Bandrowski, J. D. Van Horn, and S. Y. Bookheimer, *The UCLA multimodal connectivity database: a web-based platform for brain connectivity matrix sharing and analysis,* Frontiers in Neuroinformatics **6**, 28 (2012).

[224] K. B. Nooner, S. Colcombe, R. Tobe, M. Mennes, M. Benedict, A. Moreno, L. Panek, S. Brown, S. Zavitz, Q. Li, *et al.*, *The NKI-Rockland sample: a model for accelerating the pace of discovery science in psychiatry,* Frontiers in Neuroscience **6**, 152 (2012).

[225] R. C. Craddock, G. A. James, P. E. Holtzheimer III, X. P. Hu, and H. S. Mayberg, *A whole brain fMRI atlas generated via spatially constrained spectral clustering,* Human Brain Mapping **33**, 1914 (2012).

[226] J. D. Power, A. L. Cohen, S. M. Nelson, G. S. Wig, K. A. Barnes, J. A. Church, A. C. Vogel, T. O. Laumann, F. M. Miezin, B. L. Schlaggar, *et al.*, *Functional network organization of the human brain,* Neuron **72**, 665 (2011).

[227] D. C. Van Essen, S. M. Smith, D. M. Barch, T. E. Behrens, E. Yacoub, K. Ugurbil, W.-M. H. Consortium, *et al.*, *The WU-Minn human connectome project: an overview,* NeuroImage **80**, 62 (2013).

[228] D. S. Bassett and O. Sporns, *Network neuroscience,* Nature Neuroscience **20**, 353 (2017).

[229] D. S. Bassett, N. F. Wymbs, M. A. Porter, P. J. Mucha, J. M. Carlson, and S. T. Grafton, *Dynamic reconfiguration of human brain networks during learning,* Proceedings of the National Academy of Sciences **108**, 7641 (2011).

[230] C. J. Stam, *Modern network science of neurological disorders,* Nature Reviews Neuroscience **15**, 683 (2014).

[231] R. T. Canolty and R. T. Knight, *The functional role of cross-frequency coupling,* Trends in Cognitive Sciences **14**, 506 (2010).

[232] M. X. Cohen, *Multivariate cross-frequency coupling via generalized eigendecomposition,* ELife **6**, e21792 (2017).

[233] O. Jensen and L. L. Colgin, *Cross-frequency coupling between neuronal oscillations,* Trends in Cognitive Sciences **11**, 267 (2007).

[234] T. Womelsdorf, T. A. Valiante, N. T. Sahin, K. J. Miller, and P. Tiesinga, *Dynamic circuit motifs underlying rhythmic gain control, gating and integration,* Nature Neuroscience **17**, 1031 (2014).

[235] M. J. Brookes, P. K. Tewarie, B. A. Hunt, S. E. Robson, L. E. Gascoyne, E. B. Liddle, P. F. Liddle, and P. G. Morris, *A multi-layer network approach to MEG connectivity analysis,* NeuroImage **132**, 425 (2016).

[236] P. Tewarie, A. Hillebrand, B. W. van Dijk, C. J. Stam, G. C. O'Neill, P. Van Mieghem, J. M. Meier, M. W. Woolrich, P. G. Morris, and M. J. Brookes, *Integrating cross-frequency and within band functional networks in resting-state MEG: a multi-layer network approach,* NeuroImage **142**, 324 (2016).

[237] S. Boccaletti, G. Bianconi, R. Criado, C. I. Del Genio, J. Gómez-Gardenes, M. Romance, I. Sendina-Nadal, Z. Wang, and M. Zanin, *The structure and dynamics of multilayer networks,* Physics Reports **544**, 1 (2014).

[238] M. De Domenico, A. Solé-Ribalta, E. Cozzo, M. Kivelä, Y. Moreno, M. A. Porter, S. Gómez, and A. Arenas, *Mathematical formulation of multilayer networks,* Physical Review X **3**, 041022 (2013).

[239] M. Kivelä, A. Arenas, M. Barthelemy, J. P. Gleeson, Y. Moreno, and M. A. Porter, *Multilayer networks,* Journal of Complex Networks **2**, 203 (2014).

[240] S. F. Muldoon and D. S. Bassett, *Network and multilayer network approaches to understanding human brain dynamics,* Philosophy of Science **83**, 710 (2016).

[241] M. De Domenico, S. Sasai, and A. Arenas, *Mapping multiplex hubs in human functional brain networks,* Frontiers in Neuroscience **10**, 326 (2016).

[242] M. De Domenico, *Multilayer modeling and analysis of human brain networks,* Giga Science **6**, gix004 (2017).

[243] J. J. Crofts, M. Forrester, and R. D. O'Dea, *Structure-function clustering in multiplex brain networks,* EPL (Europhysics Letters) **116**, 18003 (2016).

[244] R. F. Betzel and D. S. Bassett, *Multi-scale brain networks,* NeuroImage **160**, 73 (2017).

[245] A. Ashourvan, Q. K. Telesford, T. Verstynen, J. M. Vettel, and D. S. Bassett, *Multi-scale detection of hierarchical community architecture in structural and functional brain networks,* PLOS One **14**, e0215520 (2019).

[246] J. Guillon, M. Chavez, F. Battiston, Y. Attal, V. La Corte, M. Thiebaut de Schotten, B. Dubois, D. Schwartz, O. Colliot, and F. de Vico Fallani, *Disrupted core-periphery structure of multimodal brain networks in Alzheimer's disease,* Network Neuroscience **3**, 635 (2019).

[247] K. Mandke, J. Meier, M. J. Brookes, R. D. O'Dea, P. Van Mieghem, C. J. Stam, A. Hillebrand, and P. Tewarie, *Comparing multilayer brain networks between groups: Introducing graph metrics and recommendations,* NeuroImage **166**, 371 (2018).

[248] F. Battiston, V. Nicosia, M. Chavez, and V. Latora, *Multilayer motif analysis of brain networks,* Chaos: An Interdisciplinary Journal of Nonlinear Science **27**, 047404 (2017).

[249] M. Yu, M. M. Engels, A. Hillebrand, E. C. Van Straaten, A. A. Gouw, C. Teunissen, W. M. Van Der Flier, P. Scheltens, and C. J. Stam, *Selective impairment of hippocampus and posterior hub areas in Alzheimer's disease: an MEG-based multiplex network study,* Brain **140**, 1466 (2017).

[250] J. M. Buldú and M. A. Porter, *Frequency-based brain networks: From a multiplex framework to a full multilayer description,* Network Neuroscience **2**, 418 (2018).

[251] V. Jirsa and V. Müller, *Cross-frequency coupling in real and virtual brain networks,* Frontiers in Computational Neuroscience **7**, 78 (2013).

[252] E. Florin and S. Baillet, *The brain's resting-state activity is shaped by synchronized cross-frequency coupling of neural oscillations,* NeuroImage **111**, 26 (2015).

[253] J. L. Soto, J.-P. Lachaux, S. Baillet, and K. Jerbi, *A multivariate method for estimating cross-frequency neuronal interactions and correcting linear mixing in MEG data, using canonical correlations,* Journal of Neuroscience Methods **271**, 169 (2016).

[254] J. Aru, J. Aru, V. Priesemann, M. Wibral, L. Lana, G. Pipa, W. Singer, and R. Vicente, *Untangling cross-frequency coupling in neuroscience,* Current Opinion in Neurobiology **31**, 51 (2015).

[255] M. X. Cohen, *Assessing transient cross-frequency coupling in EEG data,* Journal of Neuroscience Methods **168**, 494 (2008).

[256] F. Siebenhühner, S. H. Wang, G. Arnulfo, A. Lampinen, L. Nobili, J. M. Palva, and S. Palva, *Genuine cross-frequency coupling networks in human resting-state electrophysiological recordings,* PLOS Biology **18**, e3000685 (2020).

[257] C. von Nicolai, G. Engler, A. Sharott, A. K. Engel, C. K. Moll, and M. Siegel, *Corticostriatal coordination through coherent phase-amplitude coupling,* Journal of Neuroscience **34**, 5938 (2014).

[258] R. F. Helfrich, C. S. Herrmann, A. K. Engel, and T. R. Schneider, *Different coupling modes mediate cortical cross-frequency interactions,* NeuroImage **140**, 76 (2016).

[259] F. Siebenhühner, S. H. Wang, J. M. Palva, and S. Palva, *Cross-frequency synchronization connects networks of fast and slow oscillations during visual working memory maintenance,* Elife **5**, e13451 (2016).

[260] B. Gohel, S. Lim, M.-Y. Kim, K.-m. An, J.-E. Kim, H. Kwon, and K. Kim, *Evaluation of phase-amplitude coupling in resting state magnetoencephalographic signals: effect of surrogates and evaluation approach,* Frontiers in Computational Neuroscience **10**, 120 (2016).

[261] V. V. Nikulin and T. Brismar, *Phase synchronization between alpha and beta oscillations in the human electroencephalogram,* Neuroscience **137**, 647 (2006).

[262] T. Stankovski, V. Ticcinelli, P. V. McClintock, and A. Stefanovska, *Neural cross-frequency coupling functions,* Frontiers in Systems Neuroscience **11**, 33 (2017).

[263] Y. Kuramoto, *Chemical oscillations, waves, and turbulence* (Courier Corporation, 2003).

[264] E. A. Martens, E. Barreto, S. H. Strogatz, E. Ott, P. So, and T. M. Antonsen, *Exact results for the Kuramoto model with a bimodal frequency distribution,* Physical Review E **79**, 026204 (2009).

[265] J. Cabral, M. L. Kringelbach, and G. Deco, *Exploring the network dynamics underlying brain activity during rest,* Progress in Neurobiology **114**, 102 (2014).

[266] B. Pietras, N. Deschle, and A. Daffertshofer, *Equivalence of coupled networks and networks with multimodal frequency distributions: Conditions for the bimodal and trimodal case,* Physical Review E **94**, 052211 (2016).

[267] P. Grindrod, *Range-dependent random graphs and their application to modeling large small-world proteome datasets,* Physical Review E **66**, 066702 (2002).

[268] A. Taylor and D. J. Higham, *Contest: A controllable test matrix toolbox for MATLAB,* ACM Transactions on Mathematical Software (TOMS) **35**, 1 (2009).

[269] L. J. Larson-Prior, R. Oostenveld, S. Della Penna, G. Michalareas, F. Prior, A. Babajani-Feremi, J.-M. Schoffelen, L. Marzetti, F. de Pasquale, F. Di Pompeo, *et al.*, *Adding dynamics to the Human Connectome Project with MEG,* NeuroImage **80**, 190 (2013).

[270] A. Hillebrand, G. R. Barnes, J. L. Bosboom, H. W. Berendse, and C. J. Stam, *Frequency-dependent functional connectivity within resting-state networks: an atlas-based MEG beamformer solution,* NeuroImage **59**, 3909 (2012).

[271] A. Hillebrand, P. Tewarie, E. Van Dellen, M. Yu, E. W. Carbo, L. Douw, A. A. Gouw, E. C. Van Straaten, and C. J. Stam, *Direction of information flow in large-scale resting-state networks is frequency-dependent,* Proceedings of the National Academy of Sciences **113**, 3867 (2016).

[272] P. Tewarie, L. Liuzzi, G. C. O'Neill, A. J. Quinn, A. Griffa, M. W. Woolrich, C. J. Stam, A. Hillebrand, and M. J. Brookes, *Tracking dynamic brain networks using high temporal resolution MEG measures of functional connectivity,* NeuroImage **200**, 38 (2019).

[273] G. L. Colclough, M. J. Brookes, S. M. Smith, and M. W. Woolrich, *A symmetric multivariate leakage correction for MEG connectomes,* NeuroImage **117**, 439 (2015).

[274] J.-P. Lachaux, E. Rodriguez, J. Martinerie, and F. J. Varela, *Measuring phase synchrony in brain signals,* Human Brain Mapping **8**, 194 (1999).

[275] M. Tamura, T. J. Spellman, A. M. Rosen, J. A. Gogos, and J. A. Gordon, *Hippocampal-prefrontal theta-gamma coupling during performance of a spatial working memory task,* Nature Communications **8**, 1 (2017).

[276] R. M. Reinhart and J. A. Nguyen, *Working memory revived in older adults by synchronizing rhythmic brain circuits,* Nature Neuroscience **22**, 820 (2019).

[277] O. Jensen, E. Spaak, and H. Park, *Discriminating valid from spurious indices of phase-amplitude coupling,* Eneuro **3** (2016).

[278] B. C. van Wijk, M. Beudel, A. Jha, A. Oswal, T. Foltynie, M. I. Hariz, P. Limousin, L. Zrinzo, T. Z. Aziz, A. L. Green, *et al.*, *Subthalamic nucleus phase–amplitude coupling correlates with motor impairment in Parkinson's disease,* Clinical Neurophysiology **127**, 2010 (2016).

[279] B. Nandi, P. Swiatek, B. Kocsis, and M. Ding, *Inferring the direction of rhythmic neural transmission via inter-regional phase-amplitude coupling (ir-PAC),* Scientific Reports **9**, 1 (2019).

[280] S. I. Dimitriadis, N. A. Laskaris, P. G. Simos, J. M. Fletcher, and A. C. Papanicolaou, *Greater repertoire and temporal variability of cross-frequency coupling (CFC) modes in resting-state neuromagnetic recordings among children with reading difficulties,* Frontiers in Human Neuroscience **10**, 163 (2016).

[281] S. Friedberg, A. Insel, and L. Spence, *Linear Algebra* (Prentice Hall, 1989).

[282] M. Abramowitz and I. A. Stegun, *Handbook of mathematical functions: with formulas, graphs, and mathematical tables*, Vol. 55 (Courier Corporation, 1965).

[283] E. Kamke, *Zur Theorie der Systeme gewöhnlicher Differentialgleichungen. II.* Acta Mathematica **58**, 57 (1932).

[284] M. Müller, *Über das Fundamentaltheorem in der Theorie der gewöhnlichen Differentialgleichungen,* Mathematische Zeitschrift **26**, 619 (1927).

[285] R. A. Horn and C. R. Johnson, *Matrix analysis* (Cambridge University Press, 1990).

[286] Z. He and P. Van Mieghem, *Prevalence expansion in NIMFA,* Physica A: Statistical Mechanics and its Applications **540**, 123220 (2020).

[287] J. N. Issos, *The field of values of non-negative irreducible matrices*, Ph.D. thesis, Auburn University (1966).

[288] J. Maroulas, P. Psarrakos, and M. Tsatsomeros, *Perron–Frobenius type results on the numerical range,* Linear Algebra and its Applications **348**, 49 (2002).

[289] C.-K. Li, B.-S. Tam, and P. Y. Wu, *The numerical range of a nonnegative matrix,* Linear Algebra and its Applications **350**, 1 (2002).

[290] G. B. Arfken and H. J. Weber, *Mathematical methods for physicists,* (1999).

[291] J. Edmonds and E. L. Johnson, *Matching, Euler tours and the Chinese postman,* Mathematical Programming **5**, 88 (1973).

[292] S.-J. Kim, K. Koh, M. Lustig, S. Boyd, and D. Gorinevsky, *An interior-point method for large-scale l_1-regularized least squares,* IEEE Journal of Selected Topics in Signal Processing **1**, 606 (2007).

[293] T. Li and X. Xu, *Hubei Statistical yearbook* (China Statistics Press, 2016).

[294] E. Deadman and S. D. Relton, *Taylor's theorem for matrix functions with applications to condition number estimation,* Linear Algebra and its Applications **504**, 354 (2016).

[295] M. F. Glasser, S. N. Sotiropoulos, J. A. Wilson, T. S. Coalson, B. Fischl, J. L. Andersson, J. Xu, S. Jbabdi, M. Webster, J. R. Polimeni, *et al.*, *The minimal preprocessing pipelines for the Human Connectome Project,* NeuroImage **80**, 105 (2013)

ACKNOWLEDGEMENTS

First of all, I would like to thank my supervisor Professor Piet Van Mieghem for his guidance during my PhD studies. I am grateful for his honest and elaborate feedback, which allowed me to grow as a scientist. While PhD studies are a time-consuming undertaking, I truly enjoyed conducting research under his supervision, not least due to his genuine enthusiasm for science. The initial focus of my PhD studies was system identification, and epidemics on networks constituted merely an exemplary application (at a time before COVID-19). After some surprising results, the focus of my research shifted towards epidemics on networks, and Prof. Van Mieghem continuously gave me the freedom to explore my research ideas.

I would also like to thank Dr. Prejaas Tewarie for introducing me to the field of neuroscience. Thank you, Massimo Achterberg, for helping me with the Dutch summary of this thesis. Verena, thank you for your help with the cover design. I would like to thank my colleagues at the Network Architectures and Services group for creating a pleasant and stimulating working atmosphere: Massimo Achterberg, Dr. Hannah Bos, Dr. Edgar van Boven, Gabriel Budel, Dr. Hale Çetinay İyicil, Karel Devriendt, Dr. Zhidong He, Ivan Jokić, Dr. Maksim Kitsak, Prof. Rob Kooij, Dr. Remco Litjens, Dr. Qiang Liu, Long Ma, Dr. Marcus Märtens, Dr. Jil Meier, Rogier Noldus, Maria Raftopoulou, Dr. Jaron Sanders, Albert Senén Cerdà, Dr. Mattia Sensi, Dr. Eric Smeitink, Peng Sun, Misa Taguchi, Qingfeng Tong and Fenghua Wang.

Curriculum Vitæ

Bastian Prasse
Born on 15 March 1991 in Troisdorf, Germany

Professional Experience

Since 04/2017	**Network Architectures and Services Group, Delft University of Technology** PhD candidate • Promoter: Prof. dr. Piet Van Mieghem • PhD thesis: "Epidemics on Networks: Analysis, Network Reconstruction and Prediction"
10/2015–03/2017	**abiturma GbR** Tutor and event coordinator (for six one-week courses)
04/2011–02/2016	**Institute for Communication Technologies and Embedded Systems, RWTH Aachen University** Research and teaching assistant (for 26 of the 59 months)
09/2014–02/2015	**Netherlands Organization for Applied Scientific Research (TNO), Delft** Research intern at the network technology department
07/2011–02/2013	**Institute for Theoretical Information Technology, RWTH Aachen University** Research assistant

Academic Background

10/2012–09/2015	**Double Degree Programme "Top Industrial Managers of Europe"** • Three-year programme at KTH Royal Institute of Technology and RWTH Aachen University with the aim of educating engineers for the international job market • Thesis jointly done at both universities: "Optimization Methods for Localization in Distributed Wireless Sensor Networks" (best grade at both universities)

08/2013–07/2014 **KTH Royal Institute of Technology, Stockholm**
Master of Science in Electrical Engineering
- Specialisation: Systems and Control Theory

10/2012–07/2013 **RWTH Aachen University**
Master of Science in Electrical Engineering
- Specialisation: Computer Engineering
- Final grade: 1.2 (1.0 is the best grade, 4.0 is passed)

10/2009–09/2012 **RWTH Aachen University**
Bachelor of Science in Electrical Engineering
- Specialisation: Computer Engineering
- Final grade: 1.9 (1.0 is the best grade, 4.0 is passed)
- Bachelor thesis: "Interference Mitigation in Hybrid-Cognitive-Radio Systems" (1.0)

Scholarships and Awards

12/2015 **Dean's List of RWTH Aachen University**
Among the best five percent of graduates of the master's programme in Electrical Engineering

10/2012–09/2015 **German National Scholarship**
Students "whose academic performance so far leads to expect outstanding achievement at university" are supported by the German Ministry of Education and business sponsors

12/2012 **Texas Instruments and ICE Bachelor Thesis Award for 2012**

12/2012 **Dean's List of RWTH Aachen University**
Among the best five percent of graduates of the bachelor's programme in Electrical Engineering

10/2011–09/2012 **North Rhine-Westphalia Scholarship**
Predecessor of the German National Scholarship, confined to the federal state of North Rhine-Westphalia

Other Qualifications

02/2016 **Certificate International of RWTH Aachen University**
Awarded for various activities relating to intercultural competences and extracurricular activities

Languages German (native), English (fluent), Dutch (very good command), Swedish (basic command)

LIST OF PUBLICATIONS

Peer-reviewed journal publications

18. C. Pizzuti, A. Socievole, **B. Prasse**, and P. Van Mieghem, *Network-based prediction of COVID-19 epidemic spreading in Italy*, Applied Network Science, **5**(1), pp.1–22 (2020).

17. M. A. Achterberg, **B. Prasse**, L. Ma, S. Trajanovski, M. Kitsak, and P. Van Mieghem, *Comparing the Accuracy of Several Network-based COVID-19 Prediction Algorithms*, International Journal of Forecasting, to appear.

16. **B. Prasse**, and P. Van Mieghem, *Time-Dependent Solution of the NIMFA Equations around the Epidemic Threshold*, Journal of Mathematical Biology, **81**(6), pp.1299–1355 (2020).

15. **B. Prasse**, M. A. Achterberg, L. Ma, and P. Van Mieghem, *Network-inference-based prediction of the COVID-19 epidemic outbreak in the Chinese province Hubei*, Applied Network Science, **5**(1), pp.1–11 (2020).

14. **B. Prasse**, and P. Van Mieghem, *Network Reconstruction and Prediction of Epidemic Outbreaks for General Group-Based Compartmental Epidemic Models*, IEEE Transactions on Network Science and Engineering, to appear.

13. P. Tewarie*, **B. Prasse***, J. M. Meier, F. A. N. Santos, L. Douw, M. Schoonheim, C. J. Stam, P. Van Mieghem, and A. Hillebrand, *Mapping functional brain networks from the structural connectome: relating the series expansion and eigenmode approaches*, NeuroImage, **216**, 116805 (2020). *P. Tewarie and B. Prasse contributed equally.

12. **B. Prasse**, and P. Van Mieghem, *The Viral State Dynamics of the Discrete-Time NIMFA Epidemic Model*, IEEE Transactions on Network Science and Engineering, **7**(3), pp.1667–1674 (2020).

11. **B. Prasse**, and P. Van Mieghem, *Exact Network Reconstruction from Complete SIS Nodal State Infection Information Seems Infeasible*, IEEE Transactions on Network Science and Engineering, **6**(4), pp.748–759 (2018).

10. S. Schlupkothen*, **B. Prasse***, and G. Ascheid*, *Backtracking-based dynamic programming for resolving transmit ambiguities in WSN localization*, EURASIP Journal on Advances in Signal Processing, **2018**(1) (2018). *S. Schlupkothen, B. Prasse, and G. Ascheid contributed equally.

Peer-reviewed conference publications

9. S. Schlupkothen, **B. Prasse**, and G. Ascheid, *A Dynamic Programming Algorithm for Resolving Transmit-Ambiguities in the Localization of WSN*, In 2016 Ad Hoc Networking Workshop (Med-Hoc-Net), pp.1–8, IEEE, 20–22 June, 2016, Vilanova i la Geltru, Spain.

In preparation

8. **B. Prasse**, K. Devriendt, and P. Van Mieghem, *Clustering for epidemics on networks: a geometric approach.*

7. **B. Prasse**, and P. Van Mieghem, *Mobile smartphone tracing can detect almost all SARS-CoV-2 infections*, preprint available on arXiv:2006.14285.

6. **B. Prasse**, M. A. Achterberg, and P. Van Mieghem, *On the Accuracy of Predicting Epidemic Outbreaks.*

5. **B. Prasse**, and P. Van Mieghem, *Predicting Dynamics on Networks Hardly Depends on the Topology*, preprint available on arXiv:2005.14575.

4. P. Tewarie, J. M. Meier, **B. Prasse**, K. Mandke, S. Warrington, C. J. Stam, M. J. Brookes, P. Van Mieghem, S. N. Sotiropoulos, and A. Hillebrand, *Predicting time-resolved electrophysiological brain networks from structural eigenmodes.*

3. P. Tewarie, **B. Prasse**, J. M. Meier, Á. Byrne, M. De Domenico, C. J. Stam, M. J. Brookes, A. Hillebrand, A. Daffertshofer, S. Coombes, and P. Van Mieghem, *Interlayer connectivity reconstruction for multilayer brain networks using phase oscillator models.*

Technical reports

2. **B. Prasse**, and P. Van Mieghem, *Network Reconstruction and Prediction of Epidemic Outbreaks for NIMFA Processes*, arXiv preprint arXiv:1811.06741 (2018).

1. **B. Prasse**, and P. Van Mieghem, *Maximum-Likelihood Network Reconstruction for SIS Processes is NP-Hard*, arXiv preprint arXiv:1807.08630 (2018).

Talks and presentations

5. *Prediction of epidemics on networks*, Seminar of the Leiden Complex Networks Network (LCN2), Leiden, The Netherlands, 27 November 2020.

4. *Prediction of Epidemic Outbreaks for General Group-Based Epidemic Models*, regular talk, NetSci 2020: International School and Conference on Network Science, September 2020.

3. *The Solution of the NIMFA Epidemic Model around the Epidemic Threshold*, talk at an invited session, 21st IFAC World Congress, Berlin, Germany, 12-17 July 2020.

2. *Network Reconstruction from NIMFA Viral State Observations of Multiple Epidemic Outbreaks*, regular talk, 7th International Conference on Complex Networks and Their Applications, Cambridge, UK, December 2018.

1. *Network Reconstruction from Viral State Observations of SIS Models seems Infeasible*, contributed talk, NetSci 2018: International School and Conference on Network Science, Paris, France, June 2018.